Numerical Investigation of a Free standing Horizontal Axis Tidal Turbine

Chirath Assalaarachchi

Degree Sought: PhD - Full Time

Cranfield University

School of Engineering

Department of Power & Propulsion Engineering

Cranfield University

School of Engineering

Department of Power & Propulsion Engineering

PhD THESIS

Academic Year 2009 - 2010

Chirath Assalaarachchi

Numerical Investigation of a Free standing Horizontal Axis Tidal Turbine

Supervisor: Dr. Joao Amaral Teixeira

21st January 2011

This thesis is submitted in partial fulfillment of the requirements for the degree of Doctor of Philosophy

Abstract

The thesis describes a set of studies carried out in parallel with a tidal turbine design program which was undertaken by the Turbomachinery Group to which the author belonged to during the duration of this project. Therefore the work presented in this thesis constitutes an exploration of the physics of horizontal axis tidal turbines and of the modelling issues associated with the simulation of these devices. Specifically the investigation centered on the behaviour of the turbine when exposed to the influence of tidal channel waves. The numerical analysis of the free standing, gravity stabilised horizontal axis tidal turbine (HATT) was carried out with the application of Speziale's Reynolds Stress Model (hereafter know as Speziale, Sarkar and Gatski or SSG model) available in the CFX CFD code. The use of a number of turbulence models was investigated but poor convergence or starting difficulties led to the employment of the SSG Reynolds Stress turbulence model.

Simulations for a range of test cases were undertaken ranging from single blade passage cases to transient simulations which included the motion of the turbine and the variation of the flow velocity due to the combined action of waves and the shearing effects of the sea bed boundary layer. A number of CFD results were compared to experimental data acquired from tests conducted on a scale model in the summer of 2009 at the IFREMER test flume in France. An additional source of comparison is provided by data obtained from a BEMT code produced by the CU consultant, Mr Chris Freeman, (Freeman et al., 2009a). A number of numerical models were assembled to analyse the effects of the presence of the pylon and blade-pylon spacing. These were run as steady and unsteady cases. For the steady cases several angular positions were examined to investigate the effects of the transit of the blades through the pylon potential field and across the sea bed boundary layer shear flow. An idealised no-pylon case was analysed to compare with the equivalent model with pylon. On average there was a performance increase of 2% for this configuration when compared to the case with pylon for the datum spacing.

The simulations covered four turbine rotational speed cases. These correspond to a start-up condition and to rated power, with an intermediate point, and to an overspeed regime. In the overspeed condition the power is essentially unchanged but the thrust reduction is strong. Additional investigations covered the performance of the turbine when yawed and

the influence of inflow turbulence. The comparisons between the solutions obtained from steady-state and transient simulations showed that the unsteady approach is preferable to describe these types of flow. Two waves were employed in conjunction with the transient models. The first corresponded to a moderate sea state ($1.5m$ height and $10.0s$ time period) of the type occurring more frequently. The second case involved a substantial wave ($3.0m$ height and $14.0s$ time period) which is associated with storm conditions. The datum models which incorporated the most energetic wave showed similar values for the torque observed on the transient simulations without waves for the overspeed and rated power cases respectively. This is a significant finding given that the $15m$ diameter turbine is immersed in a $35m$ tidal channel. The peak value for the axial thrust and torque on the large wave simulation is on average 86% and 90% higher than the steady state thrust and torque respectively for the rated power case. The loads imposed on the rotor system for the large wave are approximately 3% higher than those of the regular wave.

Similar detailed studies for tidal turbines are non-existent at time of publication. The work is therefore unique in the scope and breath of the simulations it contains. The computational resources required were vast. Transient simulations including wave effects took three weeks of computation time utilizing sixteen processors. Each of these cases required about several terabytes of storage space to record the intermediate transient results.

Acknowledgements

I would like to take this opportunity to thank Professor Pericles Pilidis, for believing in me, and for giving me the opportunity to work on this PhD project at Cranfield. The project was not always easy, but I can think of no other topic that would have given me more rounded experience. Peri's advice has always been spot on, and I thank him from the bottom of my heart for his guidance, from the first turbulent year to the end of the project.

The rounded experience and the key skills that I have gained would not have been possible without my supervisor, Dr. Joao Teixeira. Joao was, to put it simply, much more than a supervisor to me, and probably to most of his students. It is rare for a researcher to describe a supervisor as a father figure, but for me, he was just that. He will be forever remembered for his humour, his larger-than-life personality, and for his quirky way with words. On behalf of his students, I would like to thank him and his family for minding us and understanding our needs. After everything that he has done for me, I would like to think that the one thing that I gave him was the *Middle Path Doctrine* of the Buddhist philosophy, which seemed to fascinate him.

My thanks also go to Professor David Mba, for his words of encouragement during the little corridor talks that we shared. Thanks also go to Chris Freeman for sharing his great ideas and advising me on this project. He is one of the most conversant people I have ever met, with expertise not only in turbomachinery, but also in several other fields of interest. I would also like to thank Dr. Evgeniy Shapiro for his expert advice on CFD during my reviews. His constructive criticism on my approach made be a better person, and I thank him for that. I am grateful to Dr. Les Oswald, without whom I would have been lost in the world of parallel computing, Linux based operating systems, and every other possible issue involved in high performance computing. A special mention must be given for the departmental administration team and especially Josh, for helping me out with the administrative issues.

My past and present office colleagues, namely Joel, Emidio, Omid, Michael and Luca have all in some way, deliberately or otherwise, contributed to my work, from a simple word of encouragement to a serious transfer of knowledge. Thank you all for literally making the office a better and brighter place to work. I would like to thank my team mates from the

University cricket team from 2007 to 2010 for providing me with the perfect opportunity to channel my PhD stresses and in the process made some lifelong friends. Thanks also go to Shahab, my CFX buddy, for his advice, Cinzia for her simple words of encouragement, and Krish for his ridiculous claims that his BMW is the best on campus, and for redefining the standards of a role model researcher. I would like to thank all my childhood friends living abroad and in the UK for appreciating me as a person, understanding me and backing me up, no matter what.

Last but by no means least, I would like to thank my parents (Ammi and Appachchi), without whose effort, time and sacrifice I would not be here. I am grateful too to my Loku Ammi and Loku Appachchi and my fiancee's parents, for their encouragement and support, and to my three sisters and my brother. Thank you for looking after me, and keeping me on the straight and narrow.

Finally, a very big thank you and appreciation to the sacrifice and effort put in by my beloved fiance Ninoshi, without whom this three year research programme would be a complete failure. You are the blood that carries oxygen to my body. Thank you isn't just enough. I love you.

Chirath Assalaarachchi

“To be idle is a short road to death and to be diligent is a way of life; foolish people are idle, wise people are diligent”

- Lord Gautama Buddha

Contents

List of Figures

List of Tables

Nomenclature

Roman Symbols

$\tilde{u}$	Superimposed fluctuating velocity with zero mean
A	Rotor swept area
a	Axial flow induction factor
a_w	Amplitude
B	Number of blades
b	Rotational flow induction factor
c	Chord length
c	Wave celerity
D	Drag
d	Water depth
dF_A	Axial force
dF_T	Tangential force
dT	Axial torque
f	Frequency
$F_{D,x}$	Differential Force of the Sun or the Moon
F_G	Gravitational Force
F_{red}	Circulation reduction factor
f_s	Solidity of the rotor
F_X	Thrust about the X - axis (Axial Thrust)

F_Y Thrust about the Y - axis

F_Z Thrust about the Z - axis

H Wave height

I Turbulent intensity

I_x Reference turbulent intensity

k Turbulent kinetic energy

k_w Wave number

L Lift

l Turbulent length scale

M_1 Mass of first object

M_2 Mass of second object

M_X Torque about the X - axis (Axial Torque)

M_x Mass of the Moon or the Sun

M_Y Torque about the Y - axis

M_Z Torque about the Z - axis

N Number of samples

$N-1$ Degrees of freedom (Bessel's correction)

N_s Sample at the s^{th}term

P Power generated by the turbine

p Ambient static pressure

p_c Critical pressure at which cavitation occurs

p_l Local pressure

R Tip radius

r^2 Distance between the centre of M_1 and M_2

r_x^3 Distance to the Moon or the Sun from the Earth

Re Reynolds number

T Time period

t Instantaneous time

U Instantaneous velocity

u_i An observation from the sample

U_m Short term mean velocity

U_{ref} Reference Velocity

U_r Velocity at the rotor plane

U_x Horizontal velocity

v Resultant velocity

v/V The ratio of instantaneous velocity to the maximum velocity

V_∞ Freestream velocity

x Instantaneous axial coordinate

y Instantaneous tangential coordinate

y/a The ratio of instantaneous height to the amplitude

y^+ Non dimensional wall distance

Z Instantaneous height

z Instantaneous vertical coordinate

Z_{ref} Reference height

Greek Symbols

α Empirical constant

β Empirical constant

Δt short term mean time period

ϵ Turbulent dissipation

Γ Circulation at a radial location

Γ_∞ Corresponding circulation for rotor with an infinite number of blades

λ Wavelength

λ_{TSR} Tip Speed Ratio

Ω Angular velocity of the rotor

ω Flow angular velocity

ϕ Angle of the local flow to the plane of rotation

ρ Density of medium

σ Coefficient of cavitation

σ_{crit} Critical coefficient of cavitation

σ_u Standard deviation of the current velocity

Constants & Coefficients

μ Coefficient of friction

π Mathematical constant -3.14159265

C_μ Model constant -5.48^{-2}

C_D Coefficient of drag

C_L Coefficient of lift

C_P Coefficient of Power

C_p Coefficient of pressure

C_T Coefficient of Thrust

G Gravitational Constant $-6.67 \times 10^{-11} Nm^2/Kg^2$

g Gravitational acceleration $-9.98 ms^{-2}$

M_E Mass of Earth $-6 \times 10^{24} Kg$

M_M Mass of Moon $-7.4 \times 10^{22} Kg$

M_S Mass of Sun $-2 \times 10^{30} Kg$

R_E Radius of the Earth $-6378 \times 10^3 m$

Abbreviations

$ADCP$ Acoustic Doppler Current Profiler

$ADCP$ Acoustic Doppler Current Profilers

$BEMT$ Blade Element Momentum Theory

BL Boundary Layer

BSL Baseline

CCL CFX Command Language

CCS Carbon dioxide Capture and Storage

CEL CFX Expression Language

CFD Computational Fluid Dynamics

CU Cranfield University

D Diameter

DES Detached Eddy Simulation

DNS Direct Numerical Simulation

DTI Department of Trade and Industry

GGI General Grid Interface

GH Garrad Hassan

GHG Green House Gases

GUI Graphical User Interface

$HATT$ Horizontal Axis Tidal Turbine

$HAWT$ Horizontal Axis Wind Turbine

$IFREMER$ French Research Institute for Exploitation of the Sea

LES Large Eddy Simulation

$LRR - IP$ Lauder, Reece and Rodi - Isotropization of Production

$LRR - QI$ Lauder, Reece and Rodi - Quasi-Isotropic

MCT Marine Current Turbines

MPI Message Passing Interface

$NACA$ National Advisory Committee for Aeronautics

NOC National Oceanography Centre

$OENA$ Offshore Engineering and Naval Architecture Group

$PSURF$ Pressure Surface

$RANS$ Reynolds Averaged Navier Stokes

RMS Root Mean Square

RNG Re-Normalisation Group

RPM Revolutions Per Minute

RSM Reynolds Stress Model

$SERG$ Sustainable Energy Research Group - University of Southampton

SGS Sub-grid Scale

SMC Second Moment Closure

SSG Speziale, Sarkar and Gatski

SST Shear Stress Transport

$SSURF$ Suction Surface

TBT Tributyltin

TEL Tidal Energy Ltd

$THGL$ Tidal Hydraulic Generators Ltd

TI Turbulence Intensity

TSR Tip Speed Ratio

$URANS$ Unsteady Reynolds Averaged Navier Stokes

Chapter 1

Introduction

Scientists, engineers and developers have identified the sea as a 'hot spot' for renewable energy generation opportunities. Although oceans cover more than 70% of the Earth there is only a restricted number of sites that could produce a suitable amount of power with the available technology at present, (Balme et al., 2007). This said, the energy from even this limited amount of locations, could make an enormous contribution to the total electricity supply of the countries within the reach of those energetic ocean sites. Johnstone et al. (2006), highlights this importance and state that numerous research and industrial institutions spend considerable amounts of time exploring the endless possibilities of harnessing power from oceans. According to these authors the marine renewable energy sector is one of the most promising sources of renewable energy for the future.

The two main criteria for producing power from the ocean are the availability of energetic wave or tidal climates and the existence of these energy sources within reasonable reach of the energy markets. These two conditions are widely available in many of the European coastlines. Hammons (1993), states that the United Kingdom has 48% of the European tidal energy resource, while France has 42%. His research shows that the United Kingdom is a prime location for the marine renewable energy sector. Hence it is no surprise that out of the $£12.0bn$ allocated by the British government for the renewable energy sector in the coming years, $£5.0bn$ has been apportioned for marine energy projects.

In the subsequent decade or so, at least a 3% increase in power consumption per year is expected worldwide, therefore an additional power generation of approximately $7500TWh$ is estimated, (Webb et al., 2005). This sustained energy demand increase occurs against a background of reduced availability of fossil fuels, high costs and environmental concerns. The quest for fossil fuel-free power has prompted research by energy developers for many decades. Factors such as global warming, due to the large increase in the atmospheric concentration of greenhouse gases (GHG) especially of carbon dioxide through the usage

of fossil fuels, the sharp increase in oil and gas prices, together with the primary issue of expanding demand mentioned above, act as strong drivers for the research of alternative solutions.

As a result a true replacement for fossil fuels is needed with a minimum impact in the environment. This is behind the remarkable expansion of the renewable energy sector as witnessed in the last decade. The impetus for this new and lucrative energy sector was due to the ratification of the Kyoto protocol by the majority of the international community. This treaty places obligations on the main industrial nations to reduce their GHG emissions according to an agreed schedule.

In order to meet the Kyoto protocol commitments national energy sectors must promote industrial, research and energy tariff policies that will enable the expansion of various types of renewable energy sectors. In some more mature sectors, such as wind, the issue is essentially one off expansion. In other areas such as wet renewables the picture regarding the merits of particular technologies is less clear. Here the most viable approaches to harnessing a suitable and abundantly available energy to produce power will eventually be encouraged to improve its techniques before being pushed in the market as a suitable and worthy replacement for traditional power generation methods, (Baddour, 2004).

Currently there are several types of renewable energy sectors namely solar, wind, geothermal, hydro, wave and tidal energy. This thesis focuses on the last of the listed items. Specifically the technology addressed in this work is concerned with the production of power from tidal streams not depending on the impounding of a body of water as is practiced by tidal barrages or tidal mills. Rather the generation of power is due to the placement of a turbine in a naturally occurring tidal current. All the other renewable sectors have their own economical and social implications together with their pros and cons as laid out briefly in the subsequent paragraphs.

Solar power utilizes the sun's energy to convert into electricity; this can be achieved in several ways. The main method of conversion is by a solar cell or photovoltaic cell, this device converts light into electricity using the photoelectric principles. Solar power stations are very expensive to build and solar cells are too expensive in comparison to the electricity they can produce. And one of the major limitations of this type of renewable method is that the system itself thrives on a very sunny climate thus a very large panel needs to be implemented to produce sufficient amount of electricity in the United Kingdom.

Wind generators use wind turbines to convert wind energy in to any useful form such as electricity. The basic system utilizes wind energy to rotate the wind turbines thus rotating the coupled shaft; this shaft in turn drives a gear box to increase its rotation speed. This

is enough to drive the generator which produces electricity. Highly efficient research can be traced back to at least four decades and the experience gained in this field is of vital importance to the work carried out in this thesis and other tidal energy projects. Wind power turbines tend to be noisy and can be expensive to build and install. A major constraint would be that the wind is not always predictable. It can be considered as an environment hazard - tend to be noisy (affecting the tranquility of the environment), utilisation of vast amount of land and could kill birds. Nevertheless, wind power is a vital part of the renewable sector and is necessary to kick start UK renewable energy development. By the end of 2010 the wind power industry plans to produce at least 8% of the UK's electricity demands (Geographical, 2003).

Hydropower is the force/energy of moving water and converting this energy to a useful form like electricity. This method is a very good example of the application of potential energy. A dam or barrage is built across a bay or estuary. When the tide sets in the gate is open and fills the basin with water and then the gates close when the tide has stopped. As the tide recedes, the gates open and the back flow causes the turbines in the gates to turn thus producing electricity. In certain systems power could be achieved both ways as the turbines are designed to rotate both ways. This method of renewable energy is very expensive as a lot of engineering has to be put in for its structure and a special consideration has to be given when choosing a site. Flooding a large area upstream could cause problems for animals and more importantly the impact on residents and the environment is unacceptable.

Wave energy is derived from the ocean's wave columns. Generators are driven by floating devices such as buoys or air been displaced by waves in hollow concrete structures to produce electricity. One of the major issues prevailing in this type of energy system is that is hard to find an appropriate site which has consistently strong waves and also due to its unpredictability. Technical issues such as very strong structures to withstand rough seas contribute to extra expenses. It is noted that the UK has a potential recoverable resource of $50 - 90TWh$ of electricity per year, which easily accounts for at least $15 - 25\%$ of the current UK electricity demands, (Pelamis Wave power, 2008).

Geothermal power is energy derived from the heat that is present below the Earth's surface. The primary limitation of this type of system is finding an appropriate site to build a station. The type of rock and the depth of the hole to be drilled present another issue before implementing a geothermal system. Environmental issues such as hazardous gases and minerals could come up to the surface and if too much cold water is pumped down to the rocks, it might get cooled down and might run-out of steam for a while.

Finally, another less known technology to add to the renewable energy sector is that of *Carbon dioxide Capture and Storage* (CCS). This method works by capturing and

sequestering from prime sources that emit this gas. The incentive for this type of method is that it allows for continued use of fossil fuels without seriously effecting the environment therefore NOT contributing to global warming, (Pessé), 2008). Therefore, this method along with the other methods mentioned above and also methods such and nuclear energy should play a significant role in reducing our GHG emissions and contribute positively to global warming.

In the United Kingdom, tidal stream energy alone can account for approximately $18TWh/year$ which equates to roughly 5% of the UK's current electricity demands, (Baldock, 2005). There are several variations of tidal stream generators namely Horizontal Axis Tidal Turbines, Vertical Axis Tidal Turbines, Cross-axis Tidal Turbines, Ducted Tidal Turbines and non-turbomachine like devices such as the Stingray tidal generator. The most widely researched variation is the Horizontal Axis Tidal Turbine (HATT). This is not an altogether surprising situation given the similarities between these devices and the most widespread configuration employed for wind turbines - the Horizontal Axis Wind Turbine (HAWT).

The resemblance between horizontal axis wind and tidal turbines is based on the fact that the two devices are exposed to flows of similar power densities despite the vast difference in the density of the respective media. Average flow conditions for the operation of tidal and wind turbines, are typically $2.0m/s$ $(4.5kts)$ and $18.0m/s$ $(35kts)$ respectively and yield similar power densities approximately around $2kW/m^2$. The operation of the blades of the two devices is itself very similar. The Reynolds number of a section of a blade, taken at 90% of the span and with similar chords, for a tidal turbine and wind turbine are approximately 1.97×10^6 and 1.14×10^6 respectively. Although these values are not exactly the same they are of the same order, aero and hydrodynamically. The Table 1.1 below employed by Le Gouriérès, (2008) highlights the similarities and benefits of these two systems.

Tidal Turbine		Wind Turbine	
Power	$500kW$	Power	$500kW$
Tidal Velocity	$3ms^{-1}$	Wind Velocity	$13ms^{-1}$
Rotor Diameter	$10.5m$	Rotor Diameter	$33.0m$
Rotational Velocity	$27.5rev/min$	Rotor Velocity	$53.0rev/min$
Axial Force	$397kN$	Axial Force	$92kN$

Table 1.1 Comparison of Tidal and Wind Turbine operation parameters (Le Gouriérès, 2008)

However as is also apparent in this table, the axial thrust imposed on the tidal turbine, despite its diameter being a third of the diameter of the wind turbine, is more than four times that exerted by the air on the wind turbine. The magnitude of the torque is also substantially different with that of the tidal turbine, to continue employing this example, being some two times the torque of the wind turbine. To put it briefly the difference between these two devices lies hence in the comparative size of the turbines for similar powers, and the large size of the forces exerted by the tidal current on the device.

To the differences, and similarities, highlighted above one must consider the main operational characteristic of tidal turbine - the highly predictable nature of the marine tidal current flows and hence the very predictable power yield of these devices. It is this predictability, together with the intrinsically non visually intrusive nature of its operation, that remains critical to convince industries and governments to financially back this potentially promising sector.

1.1 The DeltaStream Device

Tidal Hydraulic Generators Ltd (THGL) was founded by a marine engineer, Richard Ayre. His experience in the marine sector led him to envisage the extraction of power from tidal currents employing an array of small horizontal axis rotors mounted on a ballasted frame resting on the seabed. This initial design consisted of simple paddle blade turbines which were coupled to water pumps such that the power was transferred ashore via hydraulic lines and was used by turbines coupled to electric generators as displayed on Figure 1.1.

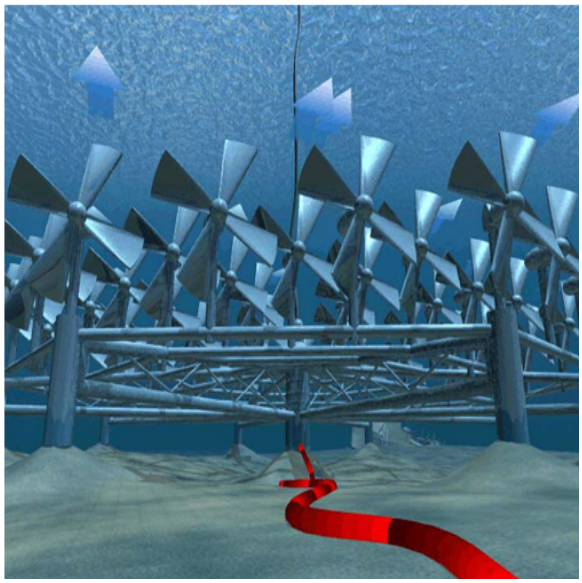

Figure 1.1 Early THGL multiple turbine ballasted unit concept (TEL)

The follow on design employed profiled blades and a lower number of turbines in each unit

unit. A prototype employing a $5.5m$ diameter full-scale turbine with blades aimed at 30% efficiency was tested with a dynamometer and generator in the tidal river Cleddau in Wales at between $2-3knot$ flows as shown on Figure 1.2.

Figure 1.2 Turbine testing in the in Cleddau estuary (Egarr, 2004)

These tests enabled the obtaining of power and efficiency data and provided information on the scale of power extraction and the tip speed and torque relationship together with useful experience on the operation of these machines. This was one of the first full scale tests of a power generation turbine in a tidal stream and was completed in 2002, (Egarr et al., 2004).

Tidal Energy Ltd (TEL) was then set up as the successor to THGL in support of a newly conceived design. This consisted of a three turbine freestanding system termed DeltaStream. The unit power was rated at $1.2MW$. A triangular base is utilised as the supporting structure and at each vertex stands a $15m$ diameter tidal turbine. The frame would be ballasted to resist the current forces while allowing swift installation and retrieval. The decision to utilise a triangular base was based on the inherent stability of a tripod arrangement, i.e. to ensure that every foot is in contact with the sea surface. A generic arrangement of the DeltaStream device, is illustrated on Figure 1.3.

The site for the location of the prototype was chosen to be the Ramsey Sound in Pembrokeshire, Wales. The average depth of the tidal channel in this location is between $25-45m$. Current velocities may reach up to 4.5 m/s at certain times of the year. TEL is currently planning to install the prototype by the middle of 2011.

Since late 2007 Cranfield University (CU) has been working alongside TEL to develop the design. Cranfield University supports the research activities via two research Groups, the Offshore Engineering and Naval Architecture Group (OENA) which was tasked with the

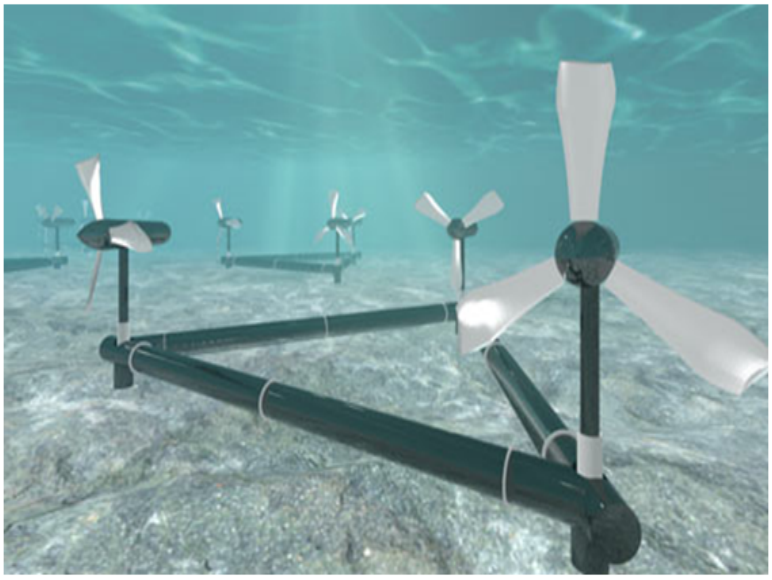

Figure 1.3 Illustration of the proposed model (TEL)

naval architecture work and the Turbomachinery and Icing Group which was essentially responsible for the design and development of the turbine.

1.2 Project Overview

At present, there is not a considerable amount of literature analysing the design and operation of a tidal stream generators when compared with the vast body of literature covering wind turbine technologies. In addition there is virtually no reported data on the application of a full size or large scale tidal turbine device. A very limited number of experiments, employing small scale turbine models, have been reported with the bulk of the remaining articles covering theoretical analysis dealing with performance prediction and modelling issues. The focus for many authors has been to analytically model these turbines using conventional methods such as the Blade Element Momentum Theory (BEMT).

These mathematical approximations have serious limitations placed upon them and these methods together with their limitations are discussed in more detail in the subsequent chapters. An alternative to these mathematical simulations is the manufacturing of scaled-down models and their testing in water flumes. This process incurs heavy costs and is not also without its own limitations as is discussed in the following chapters.

The application of computational fluid dynamics (CFD) techniques to this new sector offers a much cheaper alternative to testing and incorporates much more physics than what is possible with the analytical methods. The main objection is commonly that of the large computational costs and run times. However these are relative factors and ones that tend to become less problematic with the advancement of computational resources.

There is however a second set of limitations regarding these simulations: how realistic can their predictions be and how significant can the insights gained this way be for turbine designers and operators? These are some of the questions that this thesis seeks to address. The work carried out on this thesis investigates the current capabilities of a commercial code to simulate a free standing horizontal axis tidal turbine in operation in a realistic marine flow environment. This thesis also attempts to show the benefits of using CFD for this problem and discusses appropriate methods and best practice approaches. The academic project which the thesis covers was conducted in support of an industrial project concerning the design and development of a horizontal axis freestanding tidal turbine.

The Turbomachinery and Icing Group was commissioned to design the DeltaStream turbine while the Offshore Engineering and Naval Architecture Group was tasked with the analysis of the support structure and the model testing of the complete device. Throughout the duration of this research the author belonged to the first of these groups and was involved thus in the turbine design process.

The first phase of the academic project can be further broken down in to two major work packages. The first part corresponded to the development of the computational models, grids and solution methods to be employed in the research. The second part consisted of the single blade steady state analysis that set to investigate and corroborate the performance predictions obtained though BEMT methods.

In the second phase of the research steady state simulations which included the complete turbine, nacelle and pylon were carried out to investigate issues of separation of the blades and the tower as well as the loads experienced by the turbine when positioned in discrete angular positions. Other investigations in this phase included the effects of yawing the turbine with respect to the incident flow.

In the third part of the work transient analysis were carried out to extend physics of the previously employed models to the description of time accurate behaviour of the turbine when operating in a steady but shearing flow characteristic of tidal channels.

The fourth and the final part of the CFD project was the analysis of the effects of waves on the turbine and the combined interaction with the turbine and pylon. The final part of the research project was especially complex from the point of view of usage of resources with these simulations requiring extended run times and generating many terabytes of transient flow field data.

The validation of the numerical results was partially addressed by the scale tests carried out at the IFREMER (French Research Institute for Exploitation of the Sea) flume tank in

Boulogne-sur-Mer, France in the summer of 2009. In these experiments a 1:20th scale single rotor model and a 1:30th scale three rotors DeltaStream device were tested.

1.3 Project Objectives

Although the academic project provided support to the industrial programme described above, its ultimate objective was the deepening the knowledge of the physics, and of the modelling techniques, for these devices.

Examples of deepening the understanding of the physics are:

- Tidal turbine blade pylon interaction
- Characterisation of the turbine wakes
- Effects of the interaction of waves with the turbines

The investigation of the modelling techniques that were required for the achievement of the objectives listed above was also seen as a contribution to knowledge by itself.

At present there is hardly any published work related to numerical analysis of wake behaviour and blade-pylon interactions for marine current turbines. This work therefore offers a broadening of the understanding of these subjects areas.

1.4 Thesis Structure

The thesis is composed of eight chapters. In the first chapter there is a brief introduction to the background of the DeltaStream project and the relationship between that project and this research.

Chapter 2 introduces the reader to the theoretical aspects of the tidal resource and of the turbines used to harvest that energy source. The chapter seeks to describe the theories and principles behind such topics as tides and currents and the sources of turbulence in tidal flows. In addition turbine design and analysis methods, focused around the BEMT approach are discussed together with a reference to cavitation.

A review of the literature on the analytical modelling of tidal turbines, blade-pylon interaction, wake phenomena and other important topics has been documented in Chapter 3. The contents of this chapter could be broadly categorised in to three main sections, namely: analytical, numerical and experimental investigations.

Chapter 4 comprises two main parts, an introduction to the code employed in the simulations and a presentation of the modelling techniques employed in the work. In the first section the capabilities and limitations of the commercial software package ANSYS CFX and of its turbulence models have been discussed. In the second, the model geometry, meshing approach and solution strategies are presented and justified.

The reader is then introduced to steady state simulations documented in Chapter 5 where the turbine performance is examined and the blade-pylon interaction effects investigated for set of different models.

The chapter that follows, covers the transient analysis carried out both as part of a comparison with steady state computations and when seeking to extend the level of fidelity of the numerical models and is documented in Chapter 6. This section comprises of transient cases without waves.

The final technical Chapter 7 presents the concluding observations derived from the work and discusses the outcomes of the model when exposed to time varying velocities (wave interaction) with a combination of BL shear profiles with a standard medium TI profile. The comparison of transient cases without waves and with waves are discussed.

The final chapter documented in Chapter 8 of the thesis draws the general conclusions in addition to the chapter conclusions and contains recommendations for future work.

Following the final chapter is the references used in the thesis and a section on the bibliography for the work as extra reading material yet still beneficial for this HATT project.

Appendices are listed on chapter wise order. Appendix A is dedicated for the extra material for Chapter 4, Appendix B is exclusively for Chapter 5, Appendix C for Chapter 6 and finally Appendix D holds additional material for Chapter 7.

Chapter 2

Marine Flow Characteristics and Tidal Turbine Principles

2.1 Introduction

This chapter introduces some of the theories and principles that are relevant to the understanding and modelling of tidal turbine devices. The chapter encompasses topics such as: tides, currents, turbulence, boundary layer velocity profiles, waves and etc to name a few.

2.2 Tide Characterisation

Tides are created by the rotation of the Earth within the gravitational fields of the Sun and the Moon. Newton's Law of Gravitation combined with his Second Law of Motion explain why the Moon has a dominant effect in relation to tides despite its mass being a small fraction of that of the Sun. There are two components for the generation of tidal forces. They are - *differential* forces between the gravitational forces i.e. Earth-Sun and Earth-Moon gravitational attraction, and the *centrifugal* forces on the Earth produced by the Earth's orbit around the Sun and the Moon's orbit around the Earth.

Recalling Newton's Law of Gravitation, the gravitational force between two bodies is given by;

$$F_G = \frac{G\, M_1\, M_2}{r^2} \tag{2.1}$$

It is now possible to estimate the Earth-Moon and Earth-Sun gravitational forces using the Equation 2.1.

Earth-Moon Gravitational force:

Substituting the mass of Earth as, $6 \times 10^{24} Kg$ and the mass of the Moon as $7.4 \times 10^{22} Kg$ and the distance between the masses as $384,000 Km$. The gravitational force would be $2 \times 10^{20} N$.

Earth-Sun Gravitational force:

Substituting the mass of Earth as, $6 \times 10^{24} Kg$ and the mass of the Sun as $2.0 \times 10^{30} Kg$ and the distance between the masses as $150,000,000 Km$. The gravitational force would then be $3.56 \times 10^{22} N$.

These calculations clearly show that the Earth-Sun gravitational force is extremely high when compared with that of the Earth-Moon gravitational force. However, from ancient civilizations people have been conscious of the fact that the Moon is the primary factor that governs the time and height of tides. Therefore, this argument arrives to the point where the gravitational forces are not the ONLY reason that affect tides. Figure 2.1 below shows the Earth's sole gravity field due to the Moon. All vectors in this figure are pointed towards the centre of the Moon. The greatest force is experienced at point B as this is the nearest to the Moon and the least experienced force would be at point A. The points C and D experience moderate amounts of forces when compared with points A and B.

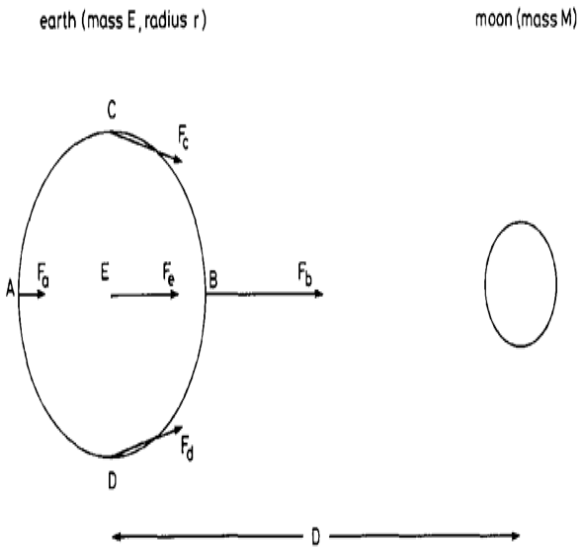

Figure 2.1 Vector field representing the Moon's gravitational force (Baker, 1991)

When the average force at the centre is subtracted from the force on each point, the resulting forces would be as shown on Figure 2.2.

The Figure 2.2 illustrates the principal forces that affect tides and is called differential forces. The horizontal components of these differential forces are the principal tide-generating

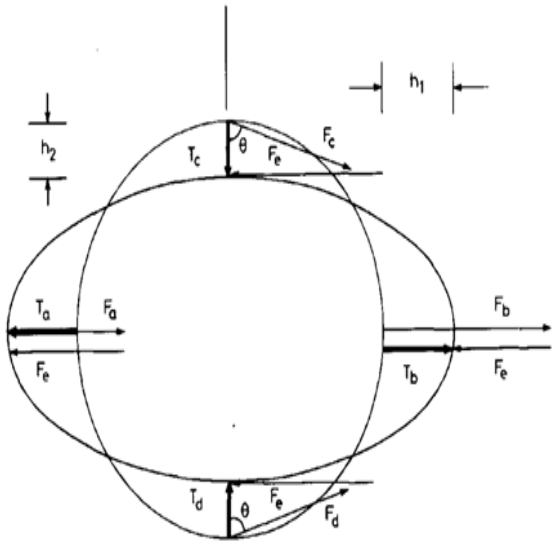

Figure 2.2 The tidal generating forces (Baker, 1991)

forces and these are often called tractive forces.

Differential forces

As previously mentioned, Newton's Law of Gravitation and his Second Law of Motion can be combined to formulate differential forces at any point on the Earth. These tidal forces are inversely proportional to the cube of the distance between the bodies and as a result their direction and magnitude plays a vital role in the tidal forces. The equation is also known as the cube law and is;

$$F_{D,x} = \frac{GM_x R_E}{r_x^3} \tag{2.2}$$

Differential force of the Moon:

Substituting, mass of the Moon as $7.4 \times 10^{22} Kg$ and the radius of the Earth taken approximately as $6378 Km$ and the distance between the Earth and Moon as $384,000 Km$. Then the differential force is $5.56 \times 10^{-7} N$.

Differential force of the Sun:

Substituting, mass of the Sun as $2 \times 10^{30} Kg$ and the radius of the Earth and the distance between the Earth and Sun as in previous calculations. The differential force is $2.5 \times 10^{-7} N$.

Therefore, the moon has a 55% dominance for tidal forces as shown from the calculations above.

2.2.1 Characteristics of tides

A tide behaves in sinusoidal form i.e. the sea surface rises until it reaches its maximum height, called the high tide and then falls to a minimum called low tide. The tide begins to rise very slowly at first and tends to increase to about half way to the highest point, there is another decrease in rate as it moves from the mid way to the highest point and gradually ceases. The return happens much the same way therefore the rate of rise and fall is considered non-uniform. According to the features of the tidal pattern, tides are categorised in to three types, they are as follows;

- Semidiurnal tide
- Diurnal tide
- Mixed tide

Semidiurnal tide

This tidal regime consists of two high tides and two low tides in each tidal day. Generally there is a low height difference between the high and low waters. The high-water level reached during one of the high tide stages is usually higher than the other high point, and the low water level reached during one of the low tide stages is usually lower than the other low tide point. This difference is called the diurnal inequality of the tides.

Diurnal tide

A single high tide and a single low tide occur in each tidal day. These generally tend to have a fairly large height difference.

Mixed tide

A diurnal tide produces a large difference in height and/or durations of successive high and/or low tides. This type of tide applies to tides in between semidiurnal and diurnal types.

A graphical illustration of the types of tides mentioned above is shown in Figure 2.3.

Though a tide at a particular place can be classified as belonging to one of the types mentioned above, there are many variations that can occur during a month. The range of the tide varies according to the intensity of the tide-producing forces, though there may be a lag of a day or two between a particular astronomic cause and the tidal effect. The combined lunar-solar effect is obtained by summing the Moon's tractive forces to the Sun's

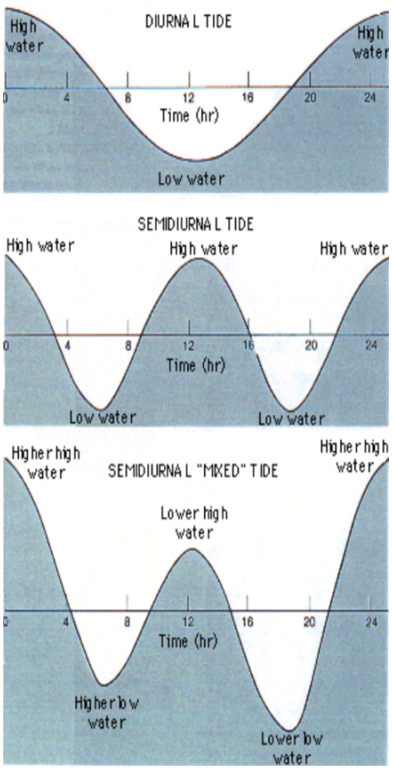

Figure 2.3 The types of tides (Thai Marine Meteorological Centre, 2010)

tractive forces through vectors. It has been shown that the resulting tidal bulge will be caused predominantly by the Moon's effects with modifying effects from the Sun.

Spring and Neap tides

With the Earth, Moon and Sun lying approximately on the same line, the tractive forces of the Sun are acting in the same direction as the Moon's tractive forces. The resultant tides are called spring tides, whose ranges are greater than average. Between spring tides, the Moon is at the first and third quarters. At those times, the tractive forces of the Sun are acting at approximately right angles to the Moon's tractive forces. Then the tides are called neap tides, whose ranges are less than average. This is shown in Figure 2.4.

When the Moon's positions are such that it is in between the quadrature and new or full, the effect of the Sun is to cause the tidal bulge to lag or precede the Moon. These effects are called the priming and lagging of the tides, (Bowditch, 1995).

2.3 Currents

A tidal current is the wave motion associated with a tide and is essentially a shallow water wave of known period, (Thomas, 2003). In other words, tides represent the rise and fall of water levels, whilst the tidal current floods and ebbs correspond to the horizontal motion

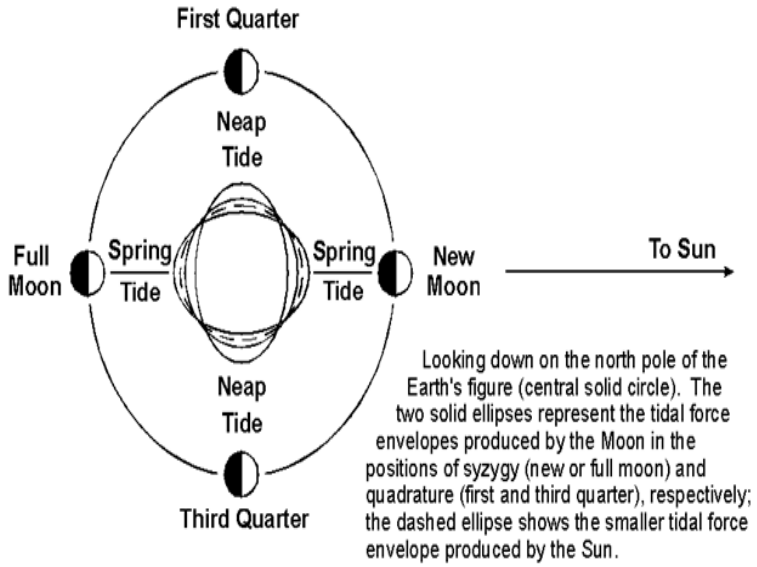

Figure 2.4 Spring and Neap tides - (NOAA Tides and Currents, 2010)

of the water. The horizontal movement of water, called a current, could be either tidal or non-tidal. Tidal current is the periodic horizontal flow of water accompanying the rise and fall of the tides. Non-tidal currents as the name implies includes all currents not due to the tidal movement. Non-tidal currents include the permanent currents in the general circulatory system of the oceans as well as temporary currents arising from meteorological conditions. The current experienced at any given time is usually a combination of both tidal and non-tidal currents.

As discussed by Thomas (2003) the term marine currents describe a large class of currents with considerable variability in structure and origin and not all have potential for power generation. Marine currents could include oceanographic currents, estuary flows and flows around headlands. In Figure 2.5 a basic graph for the variation of tides and currents with time is presented, (Le Gouriérès, 2008).

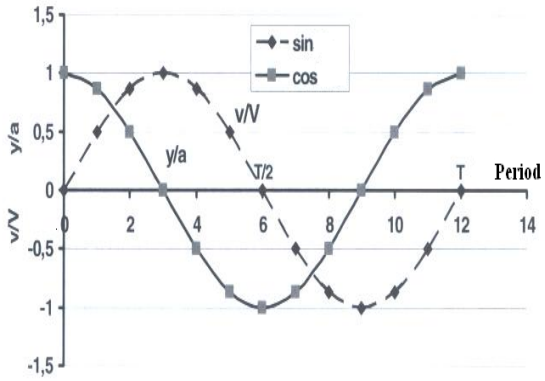

Figure 2.5 Amplitudes of water currents (Le Gouriérès, 2008)

The cosine plot represents the tidal variation in terms of y/a, a non-dimensional tidal half-

range where a is the amplitude and y which denotes the water displacement from the zero datum. The sine plot displays in a non-dimensional form the current variation in terms of v, the instantaneous tidal velocity and V the peak velocity of the tide. What this plot makes clear is that there is a lag of approximately three hours between the peak water height and the top current velocity. Although local bathymetry conditions contribute to change this generic pattern, the Figure 2.5 essentially remains valid.

2.4 Tidal Stream Locations in the United Kingdom

Figure 2.6 shows a map of the UK's tidal resources. In this chart the lighter shades correspond to the locations with the greater current velocities. The most favoured areas for tidal stream sites are due to a combination of the local tidal range and the particular geometry of the coast. As can be seen the quality of the resource around the Cardiff area, Anglesey Island, the Channel Islands, the Norfolk coast and around the Shetlands is excellent and it is in some of these locations that prototypes have been or are planed to be installed. Usually the water velocities should reach at least $2.0ms^{-1}$ for the installation to be commercially viable.

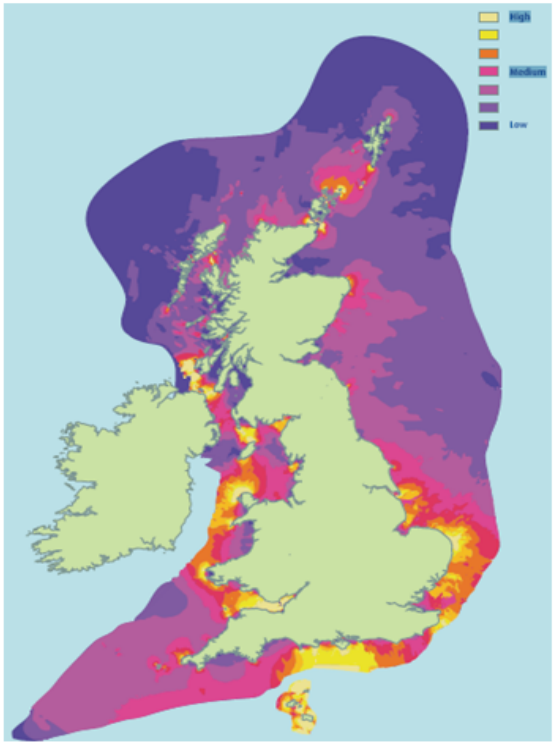

Figure 2.6 'hot-spots' for tidal turbine sites around the UK - (Sustainable Development Commission, 2007)

2.5 Marine Flows - Velocity Variation

The power law in general is a relationship variation between the flow speeds at one height, and those at another. The velocity profile of the marine atmospheric boundary layer is generally logarithmic in nature and is best approximated using the log law profile equation that accounts for surface roughness (sea-bed topography), shape of the sea-bed (bathymetry), shoreline orography (shape of the land) and marine/sea atmospheric stability.

The velocity profile power law relationship shown below is often used as a substitute for the log law profile when detailed information of surface roughness or stability is not available.

$$\frac{U}{U_{ref}} = \left(\frac{Z}{Z_{ref}}\right)^{\frac{1}{\alpha}} \tag{2.3}$$

The exponent α is an empirically derived coefficient that is dependant upon the stability of the atmosphere in question. A widely accepted value for in neutral stability conditions for the wind energy sectors is approximately $1/7$, or 0.143, hence is referred to as the $1/7^{th}$ power law profile. The $1/7^{th}$ power law is also a heavily utilised velocity profile for the marine tidal energy sector as reviewed by authors such as McCann (2007) and Barltrop et al. (2006) which are documented in the Literature Review Chapter 3. However Masters et al., (2007) employed a $1/10^{th}$ power law profile while acknowledging the fact that most authors tend to use the $1/7^{th}$ power law profile. A technical article reviewed by the Carbon Trust (2005) discusses the application of the $1/7^{th}$ power law to marine flows borrowed from the wind turbine sector.

The $1/7^{th}$ power law equation was used to obtain the vertical profiles for four tidal velocities, Figure 2.7. The turbine hub height and channel depth are those of the DeltaStream prototype and location. The turbine diameter is $15m$. The horizontal red dotted line denotes the hub height, $13.75m$ measured from the seabed. The black dotted line represents the highest point reached by the blade relative to the sea bed, $21.25m$, while the light blue dotted line represents the lowest point of the blade sweep, $6.25m$.

Hence, the area between the highest and the lowest blade points denotes the freestream flow velocities the turbine blades would operate in. The design calculations were based on these flow velocities.

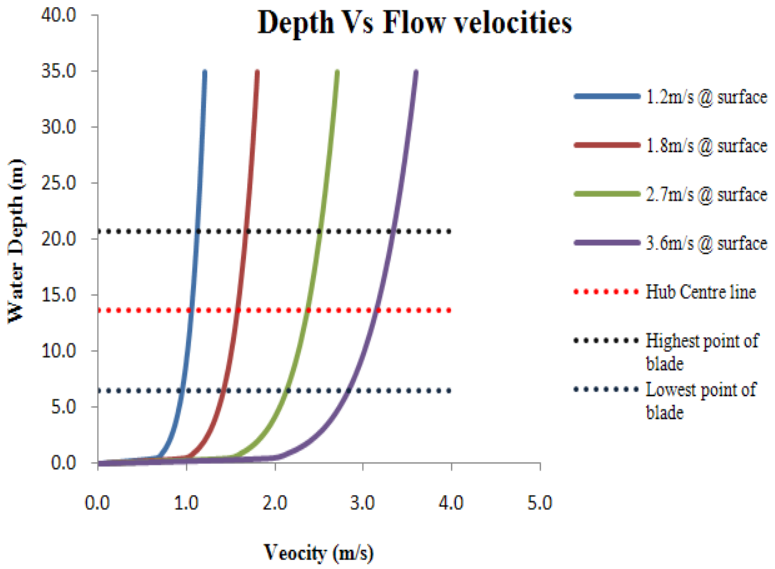

Figure 2.7 Velocity profiles exhibiting various surface velocities

2.6 Marine Flows - Turbulence Variation

Turbulence in a flow is associated with the dissipation of kinetic energy into thermal energy through a cascade of increasingly smaller eddies. Turbulence is not ”attached” to a specific liquid or gas but it is in fact is an attribute/quality of the fluid in itself. Randomness is a key characteristic of turbulence because every turbulent flow has unique and precise features which are very much associated with the initial and boundary conditions together with the inherent and common characteristics. This point can be better expressed in a graphical format, Figure 2.8. The graph represents a typical velocity measurement obtained during an experiment. The measurement was said to have been conducted in “seemingly identical conditions”, although the velocity histories shown below in Figure 2.8 suggests otherwise due to the minute variations during the experimentation. In spite of these variations, the time-averaged values of the velocities are identical. The random/chaotic and unsteady motion in space and time are the most “referred to” characteristics of turbulent flows.

As is mentioned above, a central element of the turbulent process are the vortical structures known as eddies. These are organised motions which occur at random locations at different time instants. The three dimensional nature of the vortices, plays an important and significant role in the analysis and prediction of turbulent flows. The larger vortices continually form and break down into smaller ones which eventually break in to even smaller vortices and are then finally dissipated as heat. The transport of mass, momentum and energy are greatly enhanced due to convective effects in turbulent flows. Consequently, the surrounding fluid will be surrounded by these charged turbulent scales and the velocity fluctuations spread in space. This is often termed as mixing and dispersion in turbulent

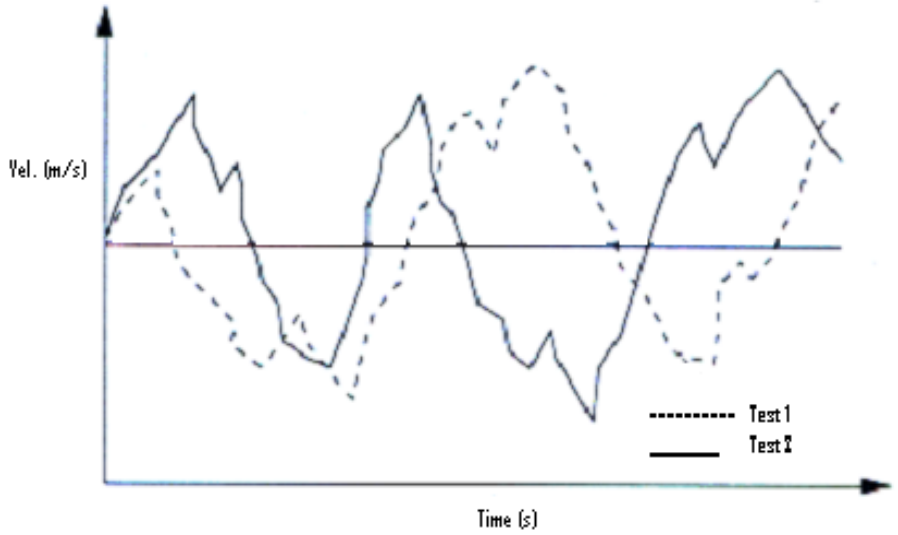

Figure 2.8 Velocity histories under identical experiment conditions (Davidson, 2004)

flows.

The characterization of turbulence is expressed through a number of statistical properties, turbulence intensity, probability density functions, auto and cross correlations and integral time and length scales. Of these the most used is turbulence intensity.

The common way to describe a turbulent velocity, taking a single flow direction as an example, is to decompose it into a short term mean and a fluctuating component;

$$U = U_m + \tilde{u} \tag{2.4}$$

where U is the instantaneous speed, U_m, the short term mean and ũ is a superimposed fluctuating velocity with zero mean. It is worth noting that the short term mean time period mentioned here, Δt, is much longer than the characteristic time of the turbulent fluctuations. In the wind industry this time is never longer than one hour and is in generally taken to be ten minutes. The equation form of U is then;

$$U_m = \frac{1}{\Delta t} \int_0^{\Delta t} U \mathrm{d}r \tag{2.5}$$

However, for measurement purposes the flow is sampled at discrete intervals not continuously and therefore it is necessary to assemble an equivalent sampled format;

$$U_m = \frac{1}{N}\sum_{i=1}^{N_s} u_i \tag{2.6}$$

where N is the number of samples.

Turbulence intensity is defined as the ratio of the standard deviation of the current velocity to the short term mean velocity;

$$I = \frac{\sigma_u}{U_m} \tag{2.7}$$

The standard deviation in sampled form is then given by;

$$\sigma_u = \sqrt{\frac{1}{N-1}\sum_{i=1}^{N_s} u_i - U_m} \tag{2.8}$$

The values of turbulence intensity in tidal flows have not been sufficiently documented. In the wind industry values ranging from 0.1 to 0.4 have been identified.

The turbulence that has been mentioned so far is that which is present in the incoming flow. However the turbine operation is in itself a source of turbulence generation. Various experiments and analytical studies have demonstrated that strong turbulence is generated by the degradation of the blade tip vortices and by shear production in the first two diameters downstream of a rotor. Further downstream the turbulence properties recover to their upstream values and thus, atmospheric turbulence controls the growth of the wake. Therefore, a model taking both shear generated and atmospheric turbulence into account is a minimum requirement. A review of experimental and analytical work on the turbulence interaction and generation in horizontal axis turbines has been carried out in Chapter 3. Nonetheless Alinot and Masson's (2002) work is presented here to keep with the nature of this section.

The equations given below were obtained from the standard turbulence model and the constants were modified to reflect the standard atmospheric turbulence in wind as discussed by Alinot and Masson (2002). The turbulent kinetic energy on Equation 2.9 and Equation 2.10 for turbulent dissipation are shown below;

$$k = \frac{3}{2}\left(U_{ref} I_x\right)^2 \tag{2.9}$$

$$\epsilon = C_{\mu}^{3/4}\left(\frac{k^{3/2}}{l}\right) \tag{2.10}$$

The standard turbulence profile is given by the following equation;

$$\frac{I}{I_{ref}} = \left(\frac{Z}{Z_{ref}}\right)^{\frac{1}{\beta}} \tag{2.11}$$

A widely accepted value for β in stable neutral atmospheric conditions for wind turbines is approximately -0.47. This value has been adopted for this thesis work as well.

It is usually common to express the turbulent length scale as a percentage of $4-5\%$ of a typical dimension of the problem. For this model approximately 4% of the domain height of $35m$ equates to approximately $1.5m$. Model constant C_{μ} has a typical value of 0.09 for the standard $k-\epsilon$ model although authors such as Alinot and Masson (2002) have modified the standard model to reflect the neutral atmospheric conditions for standard wind turbine simulations. Therefore a value of 5.48^{-2} has been adopted to stay in line with the neutral atmospheric conditions. Figure 2.9 displays typical turbulence profiles for 5% and 10% turbulent intensities together with a velocity profile of $2.7ms^{-1}$ at the water surface.

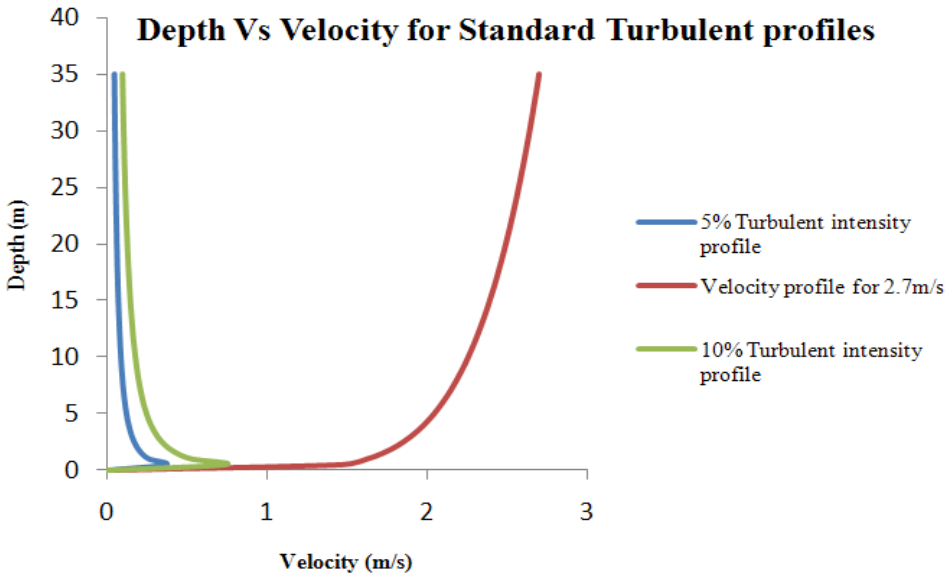

Figure 2.9 Turbulent profiles with a velocity profile

As is shown in Figure 2.9, the velocity profile achieves a maximum at the sea surface and a minimum at the sea-bed while the turbulent profiles exhibits its lowest value at the surface and the highest at a location close to the sea-bed. This is the typical turbulent boundary layer distribution where the turbulence source is the roughness of the solid surface. In tidal channels the sea surface conditions can also act as sources of turbulence and then situation

become more complex. However, in the absence of firm site specific experimental data those effects tend to be neglected.

2.7 Marine Flows - Wave Theory

Although tidal turbines work on the principle of extraction of the kinetic energy from the tidal current and are therefore not concerned with the exploitation of wave energy they are nonetheless exposed to the action of waves during their operation. Therefore, it is imperative that the action of waves need to be modelled when investigating the performance of a tidal turbine in a "realistic" marine flow. In the following section an introduction to the principles governing the modelling of waves is carried out.

The Airy or linear water wave theory is concerned with the representation of disturbances to the free surface of an inviscid, incompressible and irrotational fluid flow with a mean depth d, and constant uniform density ρ. This disturbance could be generated by the wind, the passage of a ship, an earthquake, the movement of the Moon, tidal action and/or atmospheric pressure gradients. Gravity together with surface tension will act as restoring forces that would tend to drive the fluid towards its equilibrium state. It is the balance between fluid inertia and restoring forces that gives rise to free surface waves. Waves which are created through the action of atmospheric pressure differences are ultimately derived from solar energy effects. The heating of the Earth from solar radiation causes pressure differences in the atmosphere, which produces wind and this in turn causes waves in the sea.

According to Billingham and King (2000), in British coastal waters, where typical sea depths range from a few metres to a hundred metres, 40% of the observed waves have amplitudes of $2m$ or less with much longer wavelengths. It would therefore seem worthwhile and appropriate to develop a linear theory for such waves, based on the assumption that their amplitude is much smaller than their wavelength.

2.7.1 Linear/Airy Wave Theory

In the real world, a wave would be characterised by different wave heights, periods and directions of travel, all in the same time and in the same location. Statistical methods can model this random behaviour to replicate the variation of waves. Some advanced and complex mathematical wave theories could model describe irregular sea waves. The linear wave theory, based on the linearisation of the mathematical model of gravity waves, is the simplest of these theories. Since, the wavelength is far greater than its wave height, an alternative name for linear wave theory is also known as small amplitude wave theory. The general assumptions for this model include;

- Irrotational fluid flow
- Fluid flow is assumed to have a uniform density with constant depth
- The square of the particle velocities are neglected
- Viscosity and surface tension are neglected

The equations used for this model and for numerical modelling purposes are based on the progressive small amplitude water waves as given below and Figure 2.10 displays a graphical form of the properties;

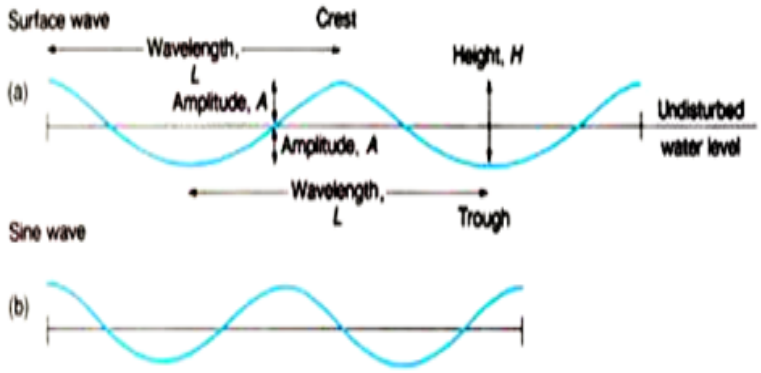

Figure 2.10 Wave nomenclature (The University of Maine, 2010)

$$a_w = \frac{H}{2} \tag{2.12}$$

$$\lambda = \frac{gT^2}{2\pi} \tag{2.13}$$

$$k_w = \frac{2\pi}{\lambda} \tag{2.14}$$

$$\omega = 2\pi f \tag{2.15}$$

$$T = \frac{2\pi}{\omega} \tag{2.16}$$

$$T = \frac{1}{f} \tag{2.17}$$

$$c = \lambda f \tag{2.18}$$

$$U_x = \omega a_w \frac{\cosh k\,(z+d)}{\sinh\,(kd)} \cos\,(kx - \omega t) \tag{2.19}$$

The numerical model only utilises the horizontal velocity components of the linear wave theory. The horizontal and vertical velocity components are $90deg$ out of phase if examined as a function of position. The computational fluid model was designed to model the whole sea below the water surface as explained in more detail in Chapter 4. Therefore, no surface waves are modelled and the horizontal movement of the water particles were considered far more important to model than that of the vertical components. This is because the vertical velocity components tend to become very weak towards the depths that the rotor system operates and essentially zero at the sea bed. Dean et al. (1991) states that the horizontal particle has a constant distance for all particles under the wave and the vertical particle increases linearly with elevation, zero at the bottom and H at the mean water surface. The intermediate water wave depth states that the ratio of water depth to the wave length should lie within 0.05 and 0.5.The wave parameters used in Chapter 7 in accordance with the wave equations shown above sits in comfortably with this theory and a $35m$ water depth is regarded as an intermediate water depth. The Figure 2.11 represents a flow velocity variation with the relative depth for waves and boundary layer shear flows. The surface velocity for the shear flow was set at $3.6ms^{-1}$.

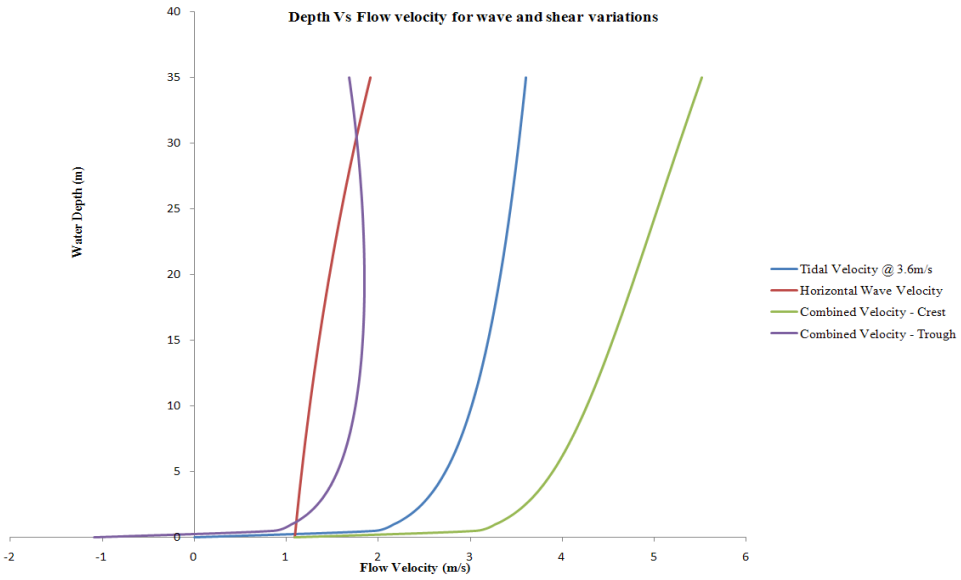

Figure 2.11 Effects of the variation of waves on the shear BL profile

2.8 Hydrodynamics

Fluid dynamics is a sub category of fluid mechanics dealing with fluids in motion. It has several branches in itself including aerodynamics and hydrodynamics. Aerodynamics is the study of gases in motion whilst hydrodynamics is the study of fluids in motion. Fluid dynamics have a wide range of applications in many different fields of study ranging from forces acting on aircrafts, calculating the mass flow rate of liquids through ducts, predicting weather, and understanding space to even predicting and controlling traffic by treating the traffic flow as a fluid in motion.

2.8.1 Lift and Drag Forces

When an aerofoil shaped body moves through a fluid, it generates a force perpendicular to the motion called lift. Aerofoils used for subsonic flights have a characteristic shape of a rounded leading edge, followed by a sharp trailing edge, often with asymmetric camber. Foils of similar function designed for working in water are generally called hydrofoils.

The lift on an aerofoil is primarily the result of its shape and its angle of attack. When either is positive, the resulting flow field about the airfoil has a higher average velocity on the upper surface than on the lower surface. This velocity difference is accompanied by a pressure difference, via the Bernoulli's principle for incompressible inviscid flow, which in turn produces the lift force. The lift force can also be related directly to the average top/bottom velocity difference, without invoking the pressure, by using the concept of circulation and the Kutta-Joukowski theorem.

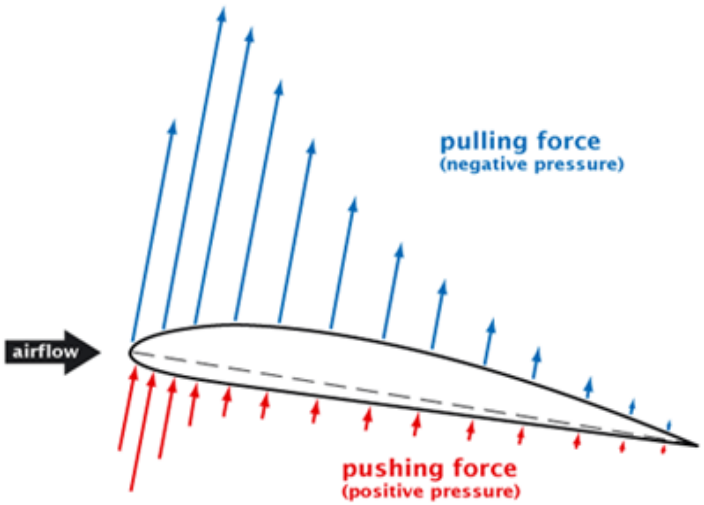

Figure 2.12 Positive and negative pressure gradients on an aerofoil (Open University, 2010a)

Consider an aerofoil facing a stream of air at an angle as illustrated on Figure 2.12. The pressure distribution is as shown on Figure 2.12. The resultant force on the negative pressure distribution (Lift) increases till about 15 degrees or so and then the aerofoil experiences stall by having a large increase in drag and a decrease in lift. Figure 2.13 represents the variation of the coefficients of lift and drag. Carpenter (1996) perfectly summarises the definition of lift as generated by the production of circulation around the aerofoil, by which some velocity is added to the streamwise velocity over the top of the aerofoil and some is subtracted from the velocity beneath the lower side of the aerofoil. As mentioned earlier, by Bernoulli's principle the resulting velocity difference produces a lower pressure on the top surface than on the bottom surface, thereby, this pressure difference producing lift. This circulation is generated by means of separation of the flow at the sharp trailing edge of the top surface of the aerofoil and this flow separation occurs because the fluid possesses some viscosity, and thus, has a boundary layer which separates because of the strong adverse pressure gradient around the sharp corner of the trailing edge.

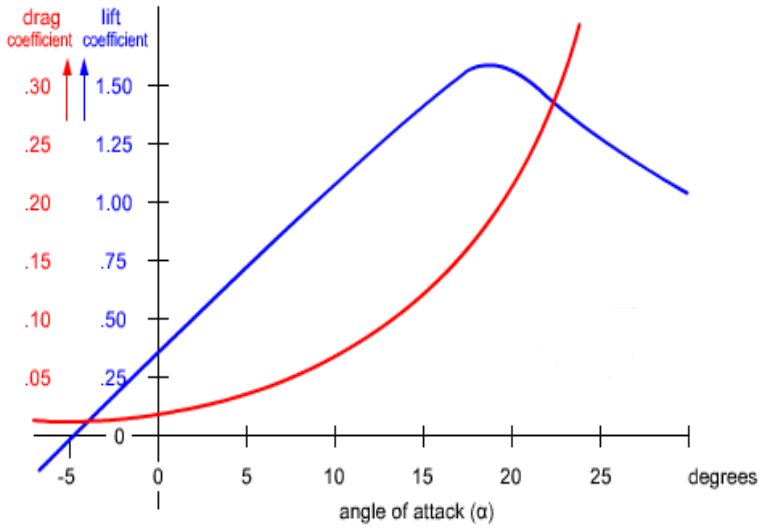

Figure 2.13 A typical C_L & C_D variation for an aerofoil (Open University, 2010b)

The coefficient of pressure can be expressed as the ratio of the local pressure to the dynamic pressure;

$$C_p = \frac{p_l}{1/2\rho V_\infty^2} \tag{2.20}$$

Lift and drag over the aerofoil could be expressed by Equation 2.21 and Equation 2.22 respectively.

$$L = \frac{1}{2}\rho V_{\infty}^{2} c C_L \tag{2.21}$$

$$D = \frac{1}{2}\rho V_{\infty}^{2} c C_D \tag{2.22}$$

2.8.2 Blade Element Momentum Theory (BEMT)

The equations and the theory used in this section are based on the work carried out by Griffiths and Woollard (1978). The equations used below are used on the basis that the flow is incompressible and can be used with different fluid densities.

The relative velocity of the fluid flow approaching the blade is the vector combination of the flow speed, the blade rotational speed and the interference velocity from the complex structure of trailing vortices shedded from the blade due to its three-dimensional nature. The design procedure determines the shape of the blade so that ideally the resultant velocity is inclined to the blade aerofoil section at that angle of incidence giving the maximum Lift/drag ratio at all points along the blade i.e. from the hub to the tip.

The air that passes through the rotor cannot slow down as the air in front needs to stay away from the air at the back which is moving towards the air at the front. Therefore at the rotor the energy is extracted through a pressure drop. i.e. the air directly behind the rotor is at sub atmospheric level in comparison to the air in front of the rotor which hovers around slightly greater than atmospheric pressure. This high pressure in front of the turbine deflects some of the upstream air around the turbine. Therefore, this causes the actual air passing through the rotor to have a smaller velocity than the free upstream velocity. This ratio of decelerated velocity to the free stream velocity is called the axial induction factor and is given by;

$$a = \frac{U_r}{V_{\infty}} \tag{2.23}$$

The rotational flow interference factor is given by;

$$b = \frac{\omega}{\Omega} \tag{2.24}$$

ω is the angular velocity of the flow which rotates in the opposite direction to the rotor rotation denoted by Ω.

Using the Prandtl method, where the trailing vortices are assumed to lie on the surface of a circular cylinder and a circulation reduction factor F_{red} is introduced;

$$F_{red} = \frac{B\Gamma}{\Gamma_\infty} \tag{2.25}$$

Prandtl shows F_{red} is given by;

$$F_{red} = \frac{2}{\pi} \cos^{-1} e^{-f_s} \tag{2.26}$$

Where, f_s, is the solidity of the rotor and given by;

$$f_s = \frac{B}{2}\left[1 - \frac{r}{R}\right]\sqrt{1 + \lambda_{TSR}^2} \tag{2.27}$$

And tip speed ratio is given by;

$$\lambda_{TSR} = \frac{\Omega R}{V_\infty} \tag{2.28}$$

The nomenclature of the blade is as shown on Figure 2.14, the momentum equations given below are based on this illustration.

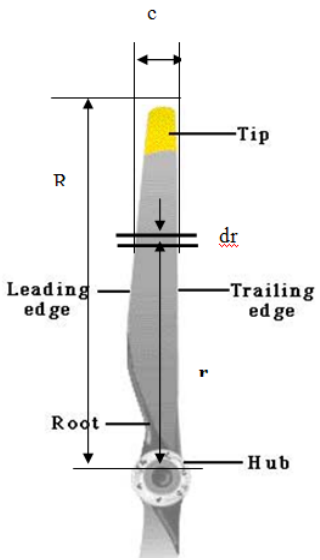

Figure 2.14 Blade element nomenclature (Thai Technics, 2008)

$$\frac{\mathrm{d}F_A}{\mathrm{d}r} = 4\pi\rho U^2 r\left(1 - a\right)aF \tag{2.29}$$

$$\frac{\mathrm{d}T}{\mathrm{d}r} = 4\pi\rho U\Omega r^3\left(1-a\right)bF \tag{2.30}$$

Consider the aerodynamic forces acting on an aerofoil section, as shown below on Figure 2.15.

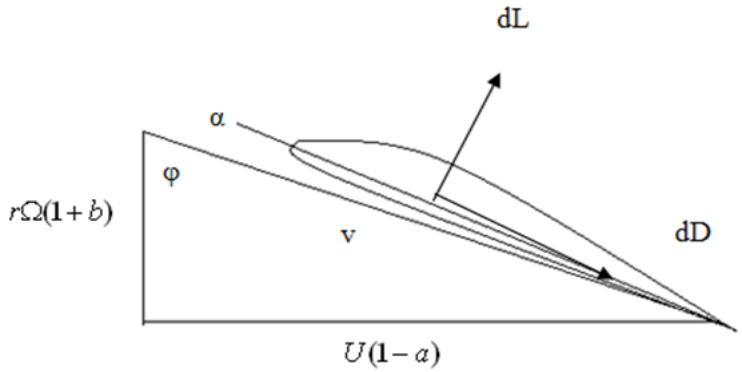

Figure 2.15 Aerodynamic forces on an airfoil

The axial and tangential forces acting on this blade section is give by Equation 2.31 and Equation 2.32 respectively.

$$\mathrm{d}F_A = \mathrm{d}L\cos\phi + \mathrm{d}D\sin\phi \tag{2.31}$$

$$\mathrm{d}F_T = \frac{\mathrm{d}T}{\mathrm{r}} = \mathrm{d}L\sin\phi - \mathrm{d}D\cos\phi \tag{2.32}$$

The above equations in terms of lift and drag coefficients are given by;

$$\frac{\mathrm{d}F_A}{\mathrm{d}r} = B\frac{1}{2}\rho v^2 c\left(C_L\cos\phi + C_D\sin\phi\right) \tag{2.33}$$

$$\frac{\mathrm{d}T}{\mathrm{d}r} = B\frac{1}{2}\rho v^2 cr\left(C_L\sin\phi - C_D\cos\phi\right) \tag{2.34}$$

The axial and torque force for any values of U & Ω may be calculated by an iterative procedure by obtaining a value for the circulation reduction factor F_{red} for a given radius and selecting arbitrary values for a and b. The angle of attack of the aerofoil is known and ϕ & v could be found by applying simple trigonometry. Before calculating the axial and tangential forces from the equations above, it should be noted that lift and drag coefficients should be obtained from the aerofoil characteristics. This process is repeated for a number

of radial stations and the forces may be calculated using numerical integration along the length of the blade as given by;

$$T = \int \frac{\mathrm{d}T}{\mathrm{d}r}\mathrm{d}r \tag{2.35}$$

$$F_A = \int \frac{\mathrm{d}F_A}{\mathrm{d}r}\mathrm{d}r \tag{2.36}$$

2.8.3 Cavitation

Under specific conditions, areas of low pressure can take place locally in a flowing fluid. If the pressure in the areas in question falls below the vapour pressure of the fluid, there would be local boiling together with a cloud of vapour bubbles. This phenomenon is known as *cavitation* and can cause serious damage, since the flow of liquid will sweep this cloud of bubbles on into an area of higher pressure where the bubbles will collapse in an explosive manner. If this occurs when in contact with a solid surface, very serious damage can result due to the very large force with which the liquid hits the surface. Cavitation can affect the performance of hydraulic machinery, turbines in this context and the impact of collapsing bubbles can cause local erosion of metal surfaces.

Douglas et al. (2005) states that cavitation could also occur if a liquid contains dissolved air or other gasses, since the solubility of gases in a liquid decreases as the pressure is reduced. Gas or air bubbles will be released in the same way as vapour bubbles, with the same damaging effects. Usually, this release occurs at higher pressures and, therefore, before vapour cavitation commences.

In a flowing system, the liquid may be subjected to changes in velocity and consequently, changes in pressure. When the velocity increases, the pressure falls and, if it falls to a sufficiently low level, cavitation may occur. The most general and widely used formulae for the coefficient of cavitation, σ, defined as;

$$\sigma = \frac{(p - p_c)}{\left(\frac{1}{2}\rho V_\infty^2\right)} \tag{2.37}$$

The value of σ at which cavitation occurs is often called the critical coefficient of cavitation σ_{crit} and is also referred to as the inception point. Since cavitation occurs when the pressure falls to the value of the vapour pressure of the liquid it is governed by the function of temperature. This helps explain why a system working well in the wintery conditions might

fail during the summer where the temperature is higher and as a result the vapour pressure being higher.

2.9 Chapter Closure

Background information on tides and currents governing the performance of the HATT has been discussed for clarity and closure. Boundary conditions involving the the shear flows, turbulence profiles and wave variations has been discussed in time for the modelling sections in the subsequent chapters. BEMT and cavitation has been discussed in the hydrodynamics section in this chapter to provide a base to understand the works done by other authors in the HATT field which is documented in the Chapter 3 and the subsequent chapters in the thesis.

Chapter 3

Literature Review

3.1 Introduction

The literature covering tidal turbines is limited. This chapter reviews some of the articles that have appeared in press according to a thematic structure. The main themes are site selection, analytically modelling of tidal turbines and its comparisons with the experimental data, blade-pylon interaction (employing wind turbines), turbine wake phenomena and modelling of realistic marine flow environments. The main reason to discuss the blade-pylon interaction employing wind turbine references is because of the availability of data on this subject in contrast to the situation regarding tidal turbines. The chapter concludes with an examination of the main areas of research currently undertaken within the field of the numerically modelling of tidal turbines.

3.2 Site Selection

Site selection is an important aspect of a marine current turbine design procedure. In fact all tidal turbine developers prior to committing to fundamental design aspects decide on the site in which its tidal stream generator operates. This is essential in determining the operational parameters or what is also termed the "operational envelope of the turbine". As was mentioned in Chapter 1, the site for the location of the DeltaStream prototype was chosen to be the Ramsey Sound in Pembrokeshire, Wales. The site was chosen after an analysis of the tidal climate, current velocity, depth, bathymetry, turbulence in the channel and the nature of waves.

The necessity to design site-specific tidal turbines have been discussed by Thomas (2003). In order to produce a substantial amount of power from the turbines the tidal velocities must vary from at least 1.5 to $3.0ms^{-1}$. The difficulty in realistically modelling a site as stated by

Thomas (2003) is as follows;

- Shear forces (vertical and horizontal) acting on the current profile
- Sea bed roughness causing turbulence
- Turbulence effects together with wave-current fields

In the UK, the National Oceanography Centre (NOC) administers the UK Tide Gauge Network. This network, managed by the Tide Gauge Inspectorate, includes 45 gauges distributed around the British Isles. Tidal data is collected, processed and stored as long time series (extending over several decades). For the DeltaStream project tidal statistics are extrapolated from data obtained at the neighbouring Milford Haven site.

Wind induced waves can be measured by a number of techniques; buoys or remote sensing techniques such as wave radar or satellites. Of the remote sensing techniques the most common approach is to employ wave radars. The usage of wave radars has its own limitations and techniques such as laser altimeters and microwave range finders help overcome some of these limitations. Wave measurement by radars is dependent on the digitizing of the image obtained by the device. By comparing successive images and introducing an empirical method of wave spectrum scaling the wave field can be characterised in terms of amplitude, direction and surface current. Tucker (1991) presented a comprehensive survey of various radar techniques for the remote sensing of waves.

Sea-bed mounted, Acoustic Doppler Current Profilers (ADCP) can also be used to monitor and record water levels, current and wave data and turbulent profile data for site specific knowledge as described by Holmes and Brydan (2003). ADCP's employ sonar technology which depends on the emission and receiving of sound pulses. The sound energy leaving and arriving at the transducer face suffers a shift in frequency due to the Doppler effect caused by the tidal stream velocity. Once the Doppler shift is determined the velocity vector relative to a known direction can be known. ADCP's are used to obtain a profile of the tidal flow at a set of depths. Given their high sampling rate, which can run into several megahertz, turbulence quantities can be obtained in addition to steady current velocities.

3.3 Analytical Modelling of Tidal Turbines

The main technique employed in the analysis of wind turbines is by using the BEMT code as introduced in the Chapter 2, and this technique of performance analysis is also used with the tidal turbines together with some extensions to the existing code. Masters et al. (2007) analysed the behaviour of a horizontal axis turbine when exposed to a dynamic marine flow

environment using a modified Blade Element Momentum Theory formulation. The sea conditions described by these authors include tidal currents and waves but turbulent effects were omitted. The task was accomplished by representing the three dimensional velocity effects and applying these to the conventional BEMT equations thus taking into account the wave-current interactions together with the boundary layer gradient. The code for this model is based on the work done by Griffiths and Woollard (1978) although a few aspects are modified to simulate marine flow environments. This work has a close correlation with the basic code written in a simulation software called MATLAB by Chapman et al. (2006).

Two plots extracted from the work of Masters et al. (2007) are presented in Figure 3.1. The first of these plots, Figure 3.1(a), shows the power coefficient with varying tip-speed ratios and turbine yaw angles. As is to be expected the power coefficient varies as a result of the variation of yaw angle, defined as being the angle subtended between the direction of the incoming flow and the axis of rotation of the turbine, which alters the local angle of incidence of the flow on the discrete sections of the turbine. As is seen in Figure 3.1(a) the power coefficient drop is fairly unimportant for low yaw angles but becomes sizeable at higher yaw values.

In Figure 3.1(b) a hypothetical $9m$ diameter blade is plotted against eight tidal channel depths ranging from 15 to $80m$. Superimposed on the eight turbine sizes are the plots of the power of the fluid and the velocity profile. These are plotted as non-dimensional quantities, u/U and p/P where the lower cases denote the values at a given depth and the upper cases indicate peak values. The depth is itself plotted in the same manner as y/I. This plot highlights an important fact. The operation of the turbine in a shear flow exposes the device to substantial gradients of velocity and power which become more marked as the depth increases.

The cyclic loading associated with the operation of the turbine in a shear flow is further documented in Figure 3.2 from Masters et al. (2007). The teeter torque oscillates with blade rotation as the rotor sweeps through its area of operation during its rotation. A way of lessening this torque is to fit a hinge to the shaft about which the turbine is free to teeter, i.e. to oscillate in and out of a plane perpendicular to the shaft. In the teetering rotor, the rotor yaw and pitch moments are largely decoupled from tower torsion or bending, thus permitting a less stiff and hence more cost-effective tower design to be manufactured, (Hau, 2003).

As is shown in Figure 3.2 for a one full revolution it can be clearly seen that the loading is repeated three times, this is due to the 3 bladed design. At first glance, the Figure 3.2 displays the magnitude of the teeter torque decreases with the increase in depth. Although, the magnitude of the teeter torque decreases with the increase in depth, the magnitude of

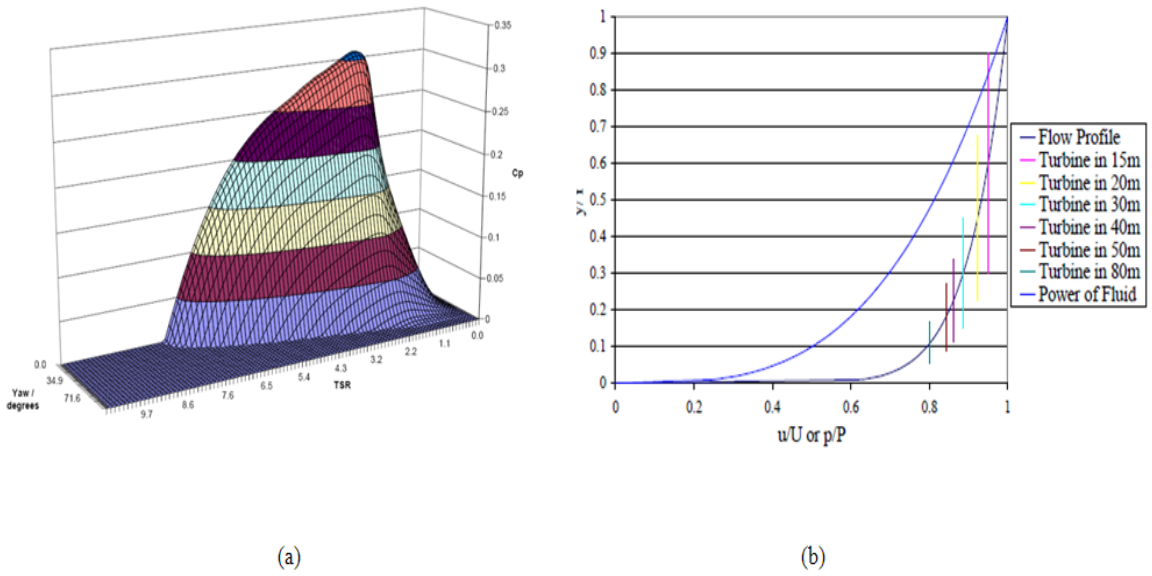

(a) (b)

Figure 3.1 (a) Variation of power coefficient with tip speed ratios and yaw angles (Masters, 2007). (b) Power law variation with depth (Masters, 2007)

the oscillation or the variation of the oscillation is less significantly affected. This could be explained by the fact that the boundary layer profile varies sharply with the increase of depth and this counterbalances the fact that turbine utilises a smaller portion of the boundary layer profile at increased depths therefore the turbine does not see a sharp variation of flow speed at the top and bottom blade positions.

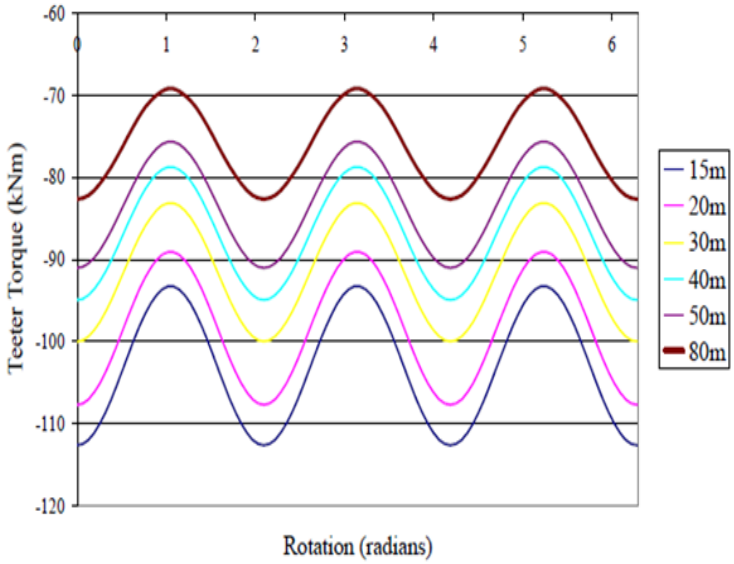

Figure 3.2 Variation of teeter torque with varying water depths (Masters, 2007)

Cyclic pitch variation and speed control have been devised to minimise the transient loading on blades and hence minimising the risk of fatigue failure of the rotor-pylon system.

This approach has been discussed by McCann (2007) for a $2MW$ tidal turbine. This author employed a commercial code, GH-Tidal Bladed, to simulate the transient loading

and performance of a tidal turbine. This code was developed combining both the momentum theory and the Blade Element theory with some additional changes to the equations to be able to perform in the marine environments.

If the performance and loading of the tidal turbine is to be accurately predicted, it is essential that engineers understand the marine environment in which the turbine is to operate and also gain a sound knowledge of how the device interacts with the environment. The sea-state (wave action) and the turbulence present in the flow are likely to have a significant influence on the turbine loadings. In Figure 3.3 contour plots of velocity time history for $5m$ waves with a period of $6s$ when the tidal flow is zero are plotted. The depth of the channel shown in this plot is $45m$.

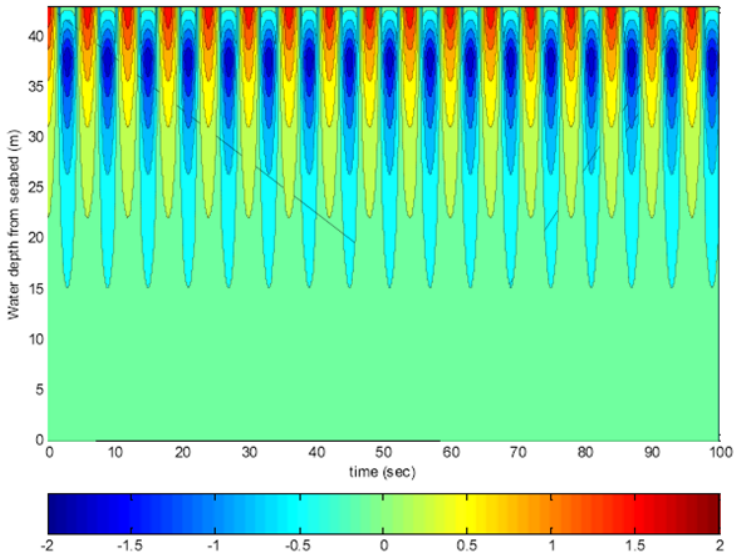

Figure 3.3 Velocity time-history for 5m 6s wave - zero tidal flow (McCann, 2007)

What this plot makes clear is that the wave interaction with a submerged turbine is to be expected even in a channel with the depth of McCann's example. However it is not only waves that affect the vertical profile of velocity. When turbulence effects are superimposed onto a steady velocity field comprising of a $1/7^{th}$ power law with a surface velocity of $2.7ms^{-1}$ the resulting velocity field as a function of time is shown in Figure 3.4.

The picture is further complicated by the gathering of all the marine flow effects; boundary layer velocity gradient, wave variation and turbulent perturbations as shown in Figure 3.5.

For the DeltaStream prototype a water depth of $35m$ is anticipated with the turbine hub centre line being located at $13.75m$ from the sea bed. The distance to the highest point of the blade tip is at $21.25m$ from the seabed with a rotor diameter of $15m$. The diameter of the turbine used by McCann is $22.8m$ and the hub height is located at $29m$ above the sea bed. This means that the highest point of the blade tip is almost at $40m$ from the sea bed, or in

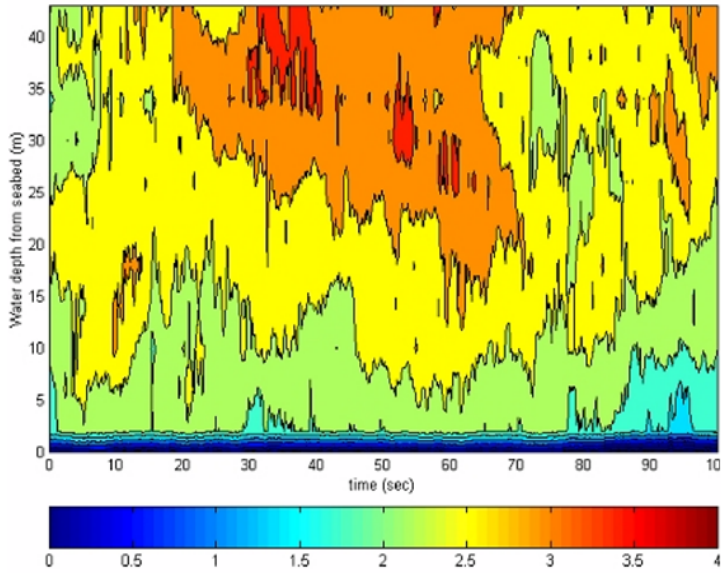

Figure 3.4 Velocity time-history of turbulent flow superimposed on tidal flow (McCann, 2007)

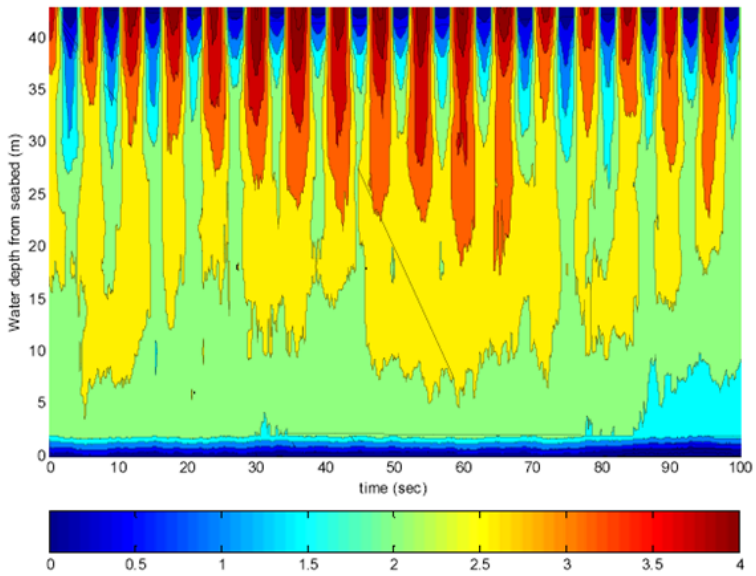

Figure 3.5 Velocity time-history of tidal, wave and turbulent flow (McCann, 2007)

other words, just $5m$ from the sea surface. therefore, the turbine undergoes severe unsteady loading as shown by the work carried out by Masters et al., (2007). The implications for the turbine in terms of loading variation as the blades are exposed to this highly unsteady environment would be discussed in the subsequent paragraphs.

In McCann's prominent paper a number of cases with 0, 5, 7, 10 and 12% turbulence intensities were simulated with the assumption of zero wave height and time period i.e. no waves. This exercise sought to clarify the effects of turbulence fluctuation alone in the operation of the turbine while employing a time history of turbulence.

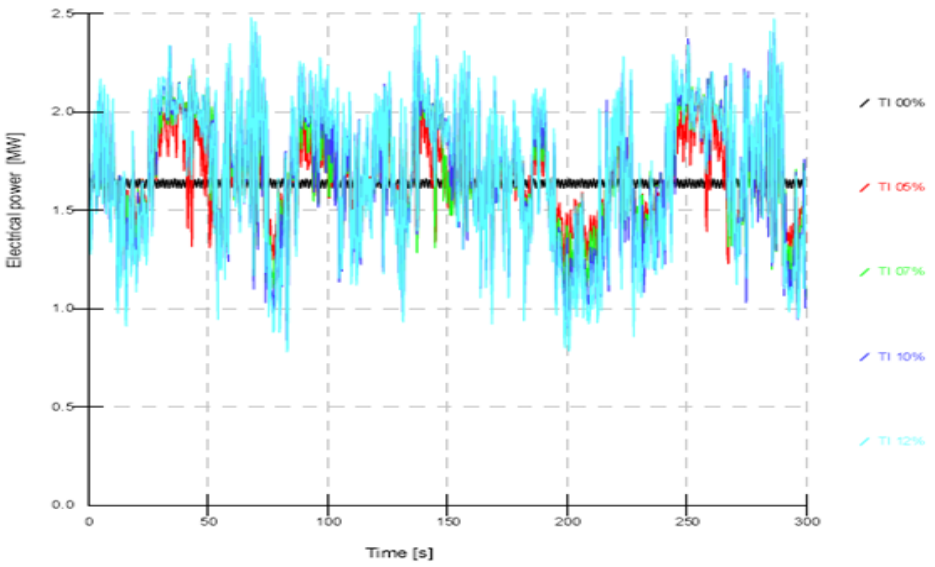

Figure 3.6 Time-history of power with turbulence (McCann, 2007)

In the plots of Figure 3.6 where power at a tidal velocity of $3.0ms^{-1}$ is plotted, it is evident the large variation in power due to the turbulent fluctuations. If the case of 12% turbulence intensity is considered (cyan trace), a very plausible figure in terms of marine environments, the power variation reaches about $0.9MW$ either side of the steady power set at about $1.6MW$. That is the fluctuation in power is greater or of the order of the steady power. This variation is even more disquieting as it takes place in times of the order of a very few seconds, five or less in this case.

Another scenario investigated by McCann (2007) corresponds to a current with varying sea-state conditions (waves) and a prescribed flow velocity with turbulent intensity. The plots of Figure 3.7 were obtained for a tidal velocity of $3.0ms^{-1}$, 10% turbulence intensity and for four wave conditions, $1.5m$, $3.0m$, $4.5m$ and $6.0m$ wave heights. Once again the extreme fluctuation in power is apparent. For a comparatively mild wave height of $3.0m$ and a period of 14 seconds (red trace), a relatively modest figure in terms of marine environments, the power variation reaches on average about $2.2MW$ over the marked $1.6MW$ and $1.2MW$ below the rated power for most part of the plot.

McCann's paper formalised at the date it was published what was already understood by some practitioners in the field. The dynamic loading imposed on tidal turbines is extremely unforgiving given its frequency and size of loads. It is therefore hardly surprising that Peter Fraenkel of Marine Current Turbines chose to describe these devices as fatigue test rigs, (Marsh, 2004). This also helps explain the catalogue of failures that have plagued this technology.

In the absence of full scale turbine data some authors have employed scaled down models

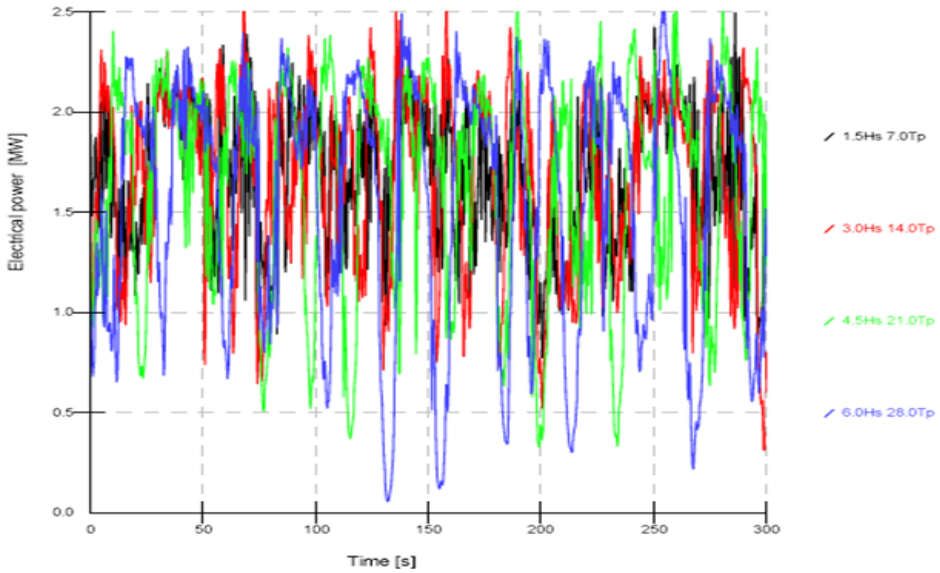

Figure 3.7 Time-history of power with 10% turbulence and various wave conditions (McCann, 2007)

to obtain experimental information against which performance prediction methods can be validated. Balme et al. (2007) presented simulation results obtained from a BEMT code and a comparison with experimental data acquired from a $0.8m$ marine current turbine scale model. The tests were conducted at a current velocity of approximately $1.5ms^{-1}$. A C_P of 0.32 was calculated by the BEMT model as opposed to a C_P of 0.36 obtained in the experimental tests.

Further information on comparisons between performance predictions and experimental data is presented in section 3.8.

3.4 Blade-Pylon Interaction

Blade-pylon interaction is an important aspect of the marine current turbine operation that needs to be understood perfectly as misinterpretation of this phenomenon can lead to a possible high cycle fatigue failure of the blades and an eventual failure of the rotor system.

No work has been published with regards to the marine current blade-pylon interaction. That was not the case with wind turbines as there were a number of articles covering this topic that have appeared in the literature. McNerney et al. (2003) amongst others investigated the interaction from the point of view of noise. Other authors such as Murtagh et al. (2005) centred on the structural aspects of the interaction. Yet another group concentrated their analysis on the performance implications of the blade tower interactions both in the case of a downwind wind turbine, Janajreh et al. (2010) or as done experimentally by Simms et al. (2001) for an upwind turbine. Zahle et al. (2009) employed CFD to model a wind

turbine operating in close proximity of a tower. Two simulations have been presented in this paper. The first of these simulations employed a rotor only configuration while in the other a rotor and tower were modelled. Zahle et al. (2009) results were the compared with experimental data. This work showed that at low wind speeds the data produced by the simulated results fall in line with the observed experimental values. However at high wind speeds the accuracy of the model was seen to drop. This could be due to the turbulence model used in the simulation and also due to the quality of the mesh utilised for this work. The interaction might have been better captured with a Second Moment Closure (SMC) model such as implemented in the CFD analysis of the DeltaStream project. This hypothesis has also been mentioned as part of the conclusions of the paper. Zahle utilized a $k - \omega$ turbulence model for the CFD simulations.

3.5 Wake Characteristics

Marine current turbines extract energy from the flow thereby causing a reduction in momentum of the flow downstream of the rotor. This momentum deficit is defined as the wake of the turbine. There are several aspects that guide the studies on the wakes of tidal turbines namely the extent of the wake of an isolated turbine, the way it behaves in a channel whose surface is exposed to waves (unsteady wake) and the structure that wakes adopt when produced by arrays of turbines.

Bahaj et al. (2007c) noted that the wake created by a tidal device is unique and could be a complex phenomenon, although the fundamental physics involved might be the same in every case. Near wakes usually occur at $0-1$ diameters (D) downstream and are created by the turbine extracting energy from the flow, whilst conserving mass. As mentioned earlier in a previous section, blade tip vortices and support structure vortices (tower shedding) aid the discontinuity of the velocity profile hence contributing to wake characteristics. Convection and turbulent mixing contribute to the far wake characteristics. The flow in the wake would convect slowly downstream when compared with the free stream flow. However because of turbulent mixing, the slower moving flow will get energised from the free stream flow until it reaches the free stream velocity.

A set of experimental results have been presented using a scaled down mesh disc rotor in the $21m$ tilting flume at the Chilworth hydraulics laboratory in the University of Southampton, (Bahaj et al., 2007c). A velocity deficit graph has been shown in Figure 3.8 at various diameters downstream of the rotor. As is to be expected the greatest deficit is found to be just downstream of the rotor (dark blue line) and this reduces further downstream. According to the Betz momentum theory the minimum velocity in the streamtube enclosing the turbine will be registered at the point of greatest enlargement of the streamtube. At this axial station

the velocity of the flow will be $1/3$ of the freestream velocity. It is useful to compare that value (corresponding to a velocity deficit of 0.67) with the peak deficit, dark blue line, of Figure 3.8.

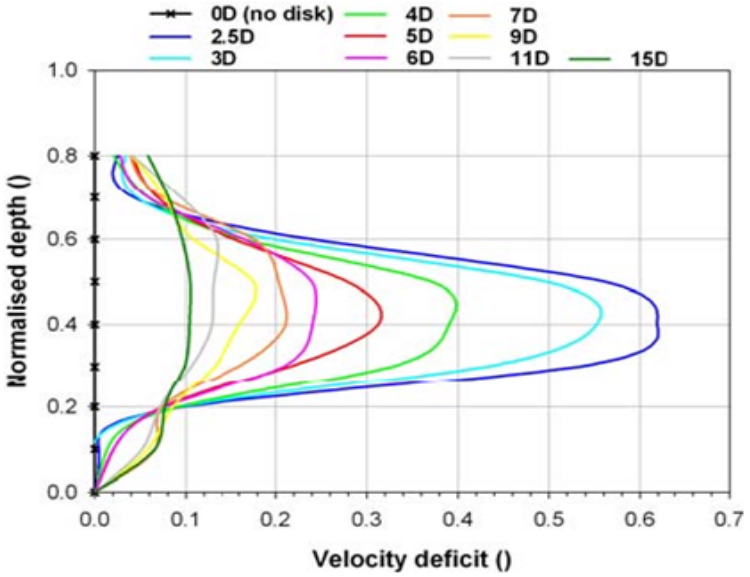

Figure 3.8 Velocity deficit downstream of the rotor (Bahaj, 2007c)

It is interesting to note that a slight wake pattern is still distinguishable $15D$ downstream of the rotor. Here the velocity deficit is approximately 90% of the upstream flow stream.

The bounding surfaces i.e. sea bed and the free surface acts to restrict the wake expansion vertically - propinquity to flow boundaries. As described, the extraction of energy from the flow will cause a change in momentum across the whole streamtube the magnitude of this change in momentum will be affected by changes to the streamtube which may be enforced by the proximity of boundaries, in the form of a solid boundary at the channel floor and at the channel surface. Sea bed materials, changes in bathymetry, and sea bed topography are the principle catalysts in ambient turbulence at lower depths. Waves and swell will cause turbulence towards the surface with length scales that decrease in a logarithmic manner with the increase in depth. The velocity profile which is present the marine environment can also account for wake characteristics, as disproportionate amounts of flow may pass above and below the rotor system and also the velocity gradient may affect the wake mixing down stream of the rotor as well. Finally flow velocity also plays a key role in the wake formation as faster the free stream velocity travels, the further downstream the wake is carried with the same time frame. The Figure 3.9 below summarises the variables that affect the wake structure and device performance. Further investigation is necessary to understand the effects of water depth, proximity to sea bed and ambient turbulence has on wake characteristics.

An investigation of the interaction of the turbine with the channel surface was carried out by

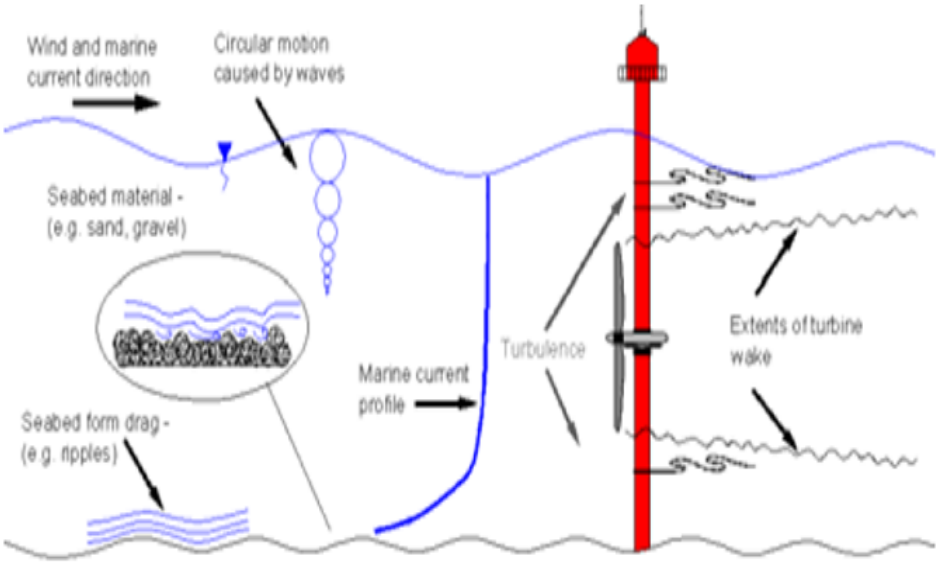

Figure 3.9 Variables affecting the performance and wake characteristics (Bahaj, 2007c)

Bahaj et al., (2006) utilising a $1:30th$ scale horizontal axis turbine. The rotor was operated upstream of a vertical tower. In Figure 3.10 the surface elevation of the flume water is shown for the condition where only the pylon is present in the flow and where the turbine is extracting power. In both cases there is a change in the surface of the channel downstream of the obstructions. However when the turbine is extracting power that change becomes quite marked. A sharp decrease in water height occurred immediately downstream of the rotor when in operation and a strong standing wave (hydraulic jump) was present between 6-7D downstream, (Bahaj et al., 2006).

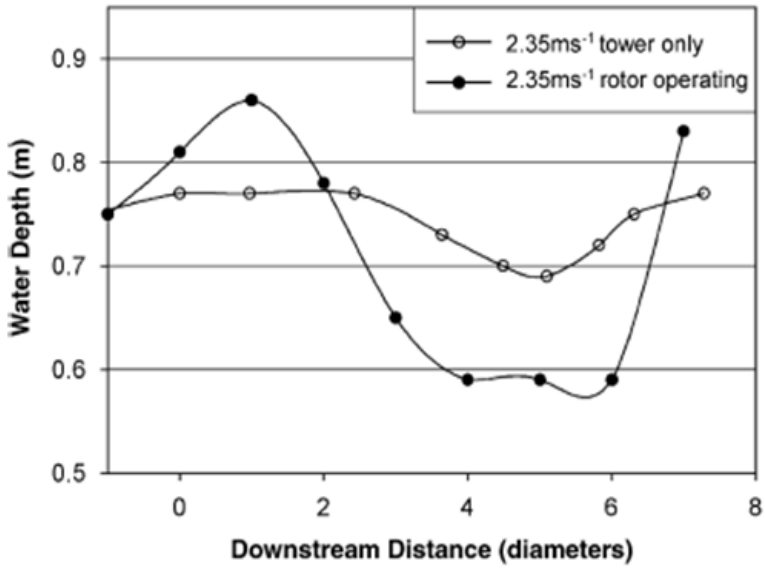

Figure 3.10 Water surface elevation for $2.35ms^{-1}$ (Bahaj, 2006)

Although it is accepted that the conditions of the test were compromised by the dimensions

of the circulating water channel test facility, maximum water depth of $0.84m$, width of $1.4m$ and working channel length of approximately $4.4m$ and the relative size of the model, rotor diameter of $0.4m$, it is apparent that rotors operating at shallow depths will interfere substantially with the sea surface.

3.6 Sea-State Conditions

The importance of modelling realistic sea-state (wave and currents) conditions for marine current energy extractors have been emphasized before. The waves could be in line, at an angle or opposing the current direction. The height and period of the wave is as important as the type of wave i.e. long wave or steep wave. Barltrop et al. (2006) conducted research on the dynamic bending moments experienced by the blades when exposed to variable sea-state conditions. The scaled down experimental results were compared with a mathematical simulation. When the sea state is characterised by long waves the linear wave model (mathematical simulation) follows the experimental results regarding the dynamic bending moments acting on the blades. However, in steep waves the modelling approach provides an underestimate when compared to the experimental results.

The possible problems that could be encountered by the rotor in the presence of a combination of waves and currents are two fold. Firstly, given the contribution of the waves to the overall velocity field, as shown by McCann (2007), this will affect the forces acting on the rotor, and add to the transient loading. In addition the variable pressure field could, in combination with the dynamic velocity field, cause cavitation depending on the depth and, as seen in the section above, the behaviour of the sea surface caused through the action of the turbine. The problem is evidently complex in nature and will required a sophisticated modelling approach. However in the spirit of separating the causes and effects for simplification, it is possible to concentrate on a set of effects, axial loading for example, while neglecting other factors. This is the approach taken in this study where the primary concern is the identification of the thrust in steady and transient conditions. In this scenario the analysis of the horizontal components of the waves is of primary importance.

The computation of the horizontal wave velocity component is given by;

$$U = \frac{\pi H}{T_w} \frac{\cosh\left[k_w\left((zr - ds) + d\right)\right]}{\sinh k_w d} \cosh\left(\phi_w\right) \tag{3.1}$$

Although the vertical wave velocities contribute to modify the lift and drag forces, by changing the angle of incidence of the flow, their contribution to thrust generation is secondary, (Freeman et al., 2009b).

Vertical wave particle;

$$V = \frac{\pi H}{T_w} \frac{\sinh\left[k_w\left((zr - ds) + d\right)\right]}{\cosh k_w d} \sinh\left(\phi_w\right) \tag{3.2}$$

Where;
d=Water depth
ds=Rotor axis depth
H=Wave height
k_w=Wave number
T_w=Wave period
zr=Instantaneous vertical position of centroid of blade section with respect to rotor axis
ϕ_w=Angle of attack

If the waves are regular waves, the wave effects on the rotor are periodical. If the rotor is positioned at sizeable depths the wave effects are reduced as the wave kinematics decrease with depth. In extreme weather, when the wave effects are much larger than the current flow, then simulating waves is even more important. If the wave effects are significantly smaller than that of the current, then it is safe to neglect the wave effects, (Barltrop et al., 2006). The relevant parameters in Baltrop's study concerning the turbine characteristics and the marine climate conditions are presented in Table 3.1.

Diameter	$20m$
No. of blades	3
Rotation rate	$12revmin^{-1}$
Immersion of shaft	$20m$
Water depth	$40m$
Current velocity	$2.5ms^{-1}$
Maximum wave height	$9m$

Table 3.1 Dimensions and operating conditions (Barltrop, 2006)

In Table 3.2 the horizontal and vertical wave particle velocities are tabulated for two sea states together with the percentage of the current velocity that the waves contribute to the velocity field. This is a clear illustration of the importance of the waves to the turbine velocity field.

	Wave period set at 12 seconds					
	Up right position		Down right position		Horizontal	
	$u(ms^{-1})$	$v(ms^{-1})$	$u(ms^{-1})$	$v(ms^{-1})$	$u(ms^{-1})$	$v(ms^{-1})$
H_{wave}=8m	1.99	1.02	1.64	0.46	1.78	0.73
% current velocity	79.65	40.99	65.44	18.38	71.81	29.13
H_{wave}=2m	0.50	0.26	0.41	0.11	0.44	0.18
% current velocity	19.91	10.25	16.36	4.59	17.79	7.28

Table 3.2 Horizontal and vertical wave particle velocities at 0.7R (Barltrop, 2006)

Final concluding remarks are that the simulated results fall in line with the experimental findings when the wave is long (waves with long wavelengths), but when the wave is steep due to non linearities the results are skewed. It is noted that high bending moments are acting on blades when the waves are normal to the rotor. Further more, the Reynolds numbers used in the experiment are very low compared to the simulated Reynolds numbers, therefore, this could be a source of discrepancy between simulated and the experimental results.

When the wave contribution effects are superimposed on a shear boundary layer profile the shear distribution in the current can be plotted for the trough and crest variations. Figure 3.11 from Guena et al. (2006) displays these conditions for a $30m$ deep channel and a $2m$, $9s$ wave superimposed on a $3.0ms^{-1}$ current obeying the $1/7^{th}$ power law.

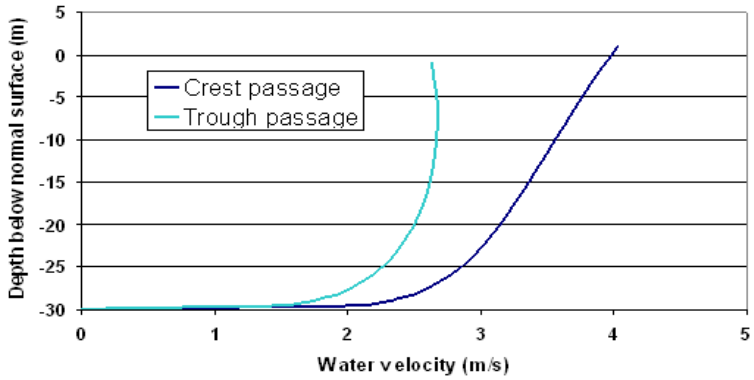

Figure 3.11 Influence of the swell on the velocity profiles (Guena, 2006)

It has been shown that the water velocity fluctuates with the inclusion of wave effects. There is evidence in the literature, from experimental work and through analytical calculations, that turbines react quite quickly to the change in flow conditions. This has been seen in tests conducted as part of DeltaStream development program (not reported here for confidentiality reasons) and is illustrated below in a theoretical study conducted by Guena

et al. (2006). The plot of Figure 3.12 details the time history of a rotor velocity and power when the turbine is exposed to a $3.0ms^{-1}$ current and a wave height of $2m$ with a wave period of $9s$. The power as can be observed is limited to $200kW$. Both power and turbine velocity are seen to vary with the wave action.

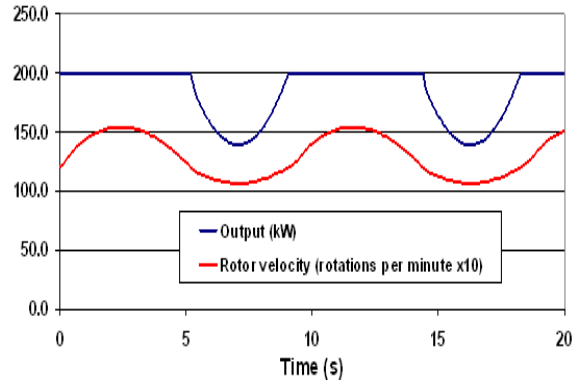

Figure 3.12 Power and velocity variation with wave action (Guena, 2006)

What is not plotted but will vary too is the torque and thrust of the turbine. Another way to look at this phenomenon is that of Figure 3.13. In this figure the power variation for different wave heights and periods is plotted together with the power available when there are no waves, $H = 0$. As displayed, there is a positive outcome when the device operates in a higher sea state regime. In practice, this plot represents a map of power and waves and a real sea state environment will mean that the output of the turbine will correspond to track over this map as the different waves that correspond to a real sea wave which pass the turbine. This somewhat erratic power output can be smoothed out by spacing the turbines in the array such that there is minimum interference with the wake of its sister turbines and also in conjunction with the use of intelligent generators, as is practiced in wind turbine technology.

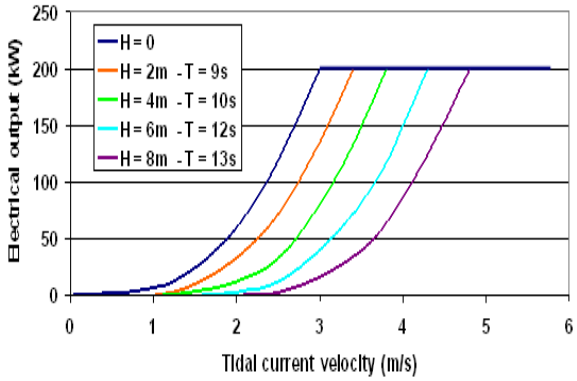

Figure 3.13 Power output of a single turbine operating with a range of waves (Guena, 2006)

Given the importance played by waves on the operation of tidal turbines a certain amount of effort was dedicated to the understanding of the interaction of tidal flows and waves

in shallow bodies of water. The presence of wave-current interactions in the shallow and intermediate depths of the sea has long been acknowledged and there is a considerable amount of literature associated with the subject. The breakthrough review is that of Peregrine (1976) and other notable contributions include that of Jonsson (1990) and Thomas & Klopman (1997). In each of these review articles there is an acknowledgement of the drawbacks as well as acknowledgement of validated models. Accurate numerical modelling of the marine environment is an extremely difficult task. Experimental simulations are in the preliminary phase and further light needs to be shed for site-specific studies. The main difficulty as addressed by Thomas (2003) is that the phenomenon is very complex in nature and there are many aspects that contribute to this complex environment; horizontal and vertical shear in the current profile, the variation of the sea-bed boundary layer and the presence of turbulence.

3.7 Turbulence Modelling of Wind Turbines

The state of the art in terms of the understanding and of the modelling of turbulence in tidal channels is not very advanced. There is a scarcity of real data and no established models that can be used to supply trustworthy results when used for tidal turbines. Of the scarce work conducted in this area the review paper of Burchard et al. (2008)is unique in its comprehensiveness and depth of analysis. As the authors point out, as long as consistent observational data sets are missing, the development of mathematical models for the reproduction of near-surface processes will also be delayed. The paper contains however some very insightful comments. Amongst this is the following one due to Kemp and Simons (1983): Given the rapid oscillatory nature of wave-induced motion, a wave boundary layer is typically much smaller in height (a few centimeters) than a current boundary layer (meters to tens of meters). This leads to steeper velocity gradients and more intense turbulence in the wave boundary layer. When wave and current boundary layers co-exist, the overlying currents appear to perceive the wave boundary layer as an additional bed roughness contribution, leading to increased bottom friction and modified mean current profiles.

To improve the understanding of the use turbulence models in the modelling of marine current turbines, it is worthwhile to discuss the importance of wind turbine modelling as this gives an insight as to how to customise turbulence models. The 3 major contributors for turbulence in the wake of a wind or marine turbine are atmospheric (environment) turbulence, wake shear turbulence and blade created viscous and pressure effects. Due to the shedding of tip vortices and shear forces, strong turbulence is created between $0 - 2D$ and this has been discussed extensively at the start of this chapter. Various experiments also support these claims. Further downstream the turbulence properties recover to the original

upstream values therefore the atmospheric turbulence controls the wake.

As with tidal turbines, turbulence is the source of both the extreme gust loading and a large part of the blade fatigue loading, (Ahlström, 2005). This author developed an aeroelastic simulation tool to deal with horizontal axis wind turbines. Ahlström, (2005) developed the code FAST (Fatigue, Aerodynamics, Structures, and Turbulence) to generate aerodynamic forces along the blade.

Pesmajoglou and Graham (2000) employed an unsteady vortex lattice method to investigate yaw loads. In order to evaluate the effects of turbulence induced rotor yaw loads, an incident turbulence field was reconstructed. A pseudo-turbulence time history was stimulated from an assumed Dryden spectrum (in alternative to the more common von-Karman form) of the longitudinal and lateral turbulent velocity components. Dryden spectrum utilises integral powers and therefore, is more easily generated than the more accurate von-Karman form. These signals were then inserted as inputs to the vortex lattice model of the rotor aerodynamics and the resulting output of the yawing moment due to the veering of the incident velocity was analysed. These results were compared with experimental data obtained for three turbines of radius $0.262m$, $1.45m$ and $27.5m$ respectively and a good agreement was demonstrated.

Whether employing panel methods or BEMT derivatives the scheme adopted by turbulence models for analytic solutions is similar, Butterfield (2008);

- 3 components are considered
- Based on the von Karman isotropic spectrum
- Ten minute simulations are standard
- A spatial coherence model is included
- Turbulence intensity set according to site specific turbulence intensity and turbine design class

3.8 Comparison of Analytical Models with Experimental Measurements

Bahaj et al. (2007a) compared the predictions of two blade element momentum codes, a commercial code (GH-Tidal Bladed) and an academic in-house code (SERG-Tidal) with experimental measurements obtained from a $0.8m$ diameter turbine model. The tests were conducted on in a cavitation tunnel and a towing tank. The commercial code

called GH-Tidal Bladed is a design tool to simulate the loading and performance of tidal stream generators developed from the GH-Bladed code for Horizontal Axis wind turbines while SERG-Tidal is a tidal turbine prediction programme developed by the University of Southampton. Shown below are results for the performance of the model turbine obtained from the two codes compared with two sets of experimental results. These correspond to a blade setting angle of 0 to 13 degrees.

In Figure 3.14 the variation of coefficient of power and thrust, C_P and C_T, with Tip Speed Ratio (TSR) at 0 degree set angle is shown. In the TSR 4-6 range the experiments and the numerical simulations are in general agreement but at high TSR the prediction results of both codes fail to predict the sharp drop in both parameters as seen.

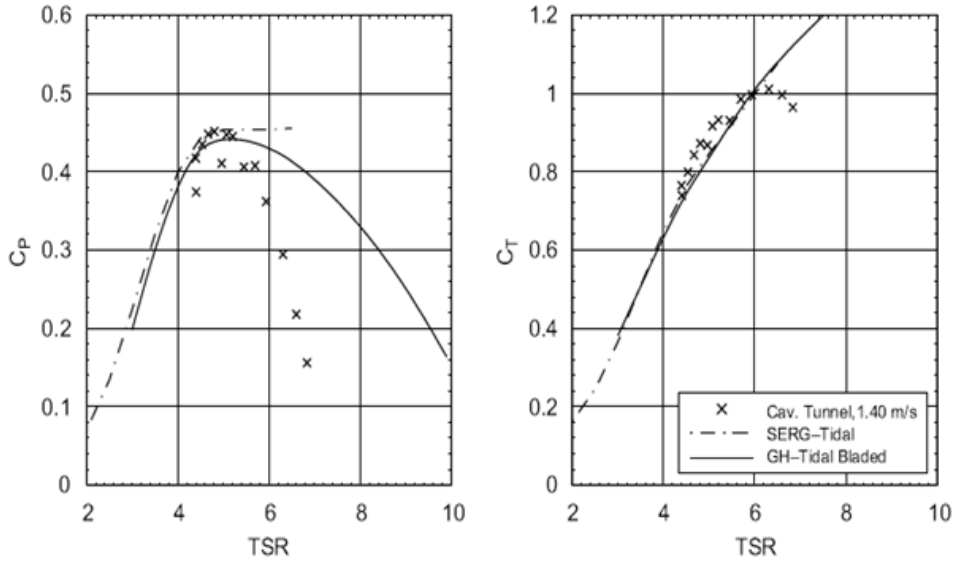

Figure 3.14 Comparisons between experiments and simulations with a 0 degree set angle (Bahaj, 2007a)

The variation of C_P and C_T, with TSR at 5 degree set angle, corresponding to the design setting, is shown in Figure 3.15. The prediction results are now in better agreement generally although the accuracy is greatest near the operation point. The expression "design point" is deliberately avoided since, unlike in other turbomachinery applications, the turbine is expected to commonly operate over a significant range of flows. The source of discrepancy between the codes and the experimental data is the object of discussion in Bahaj's paper. Model turbines operating in confined water tunnels experience conditions that are not similar to those modelled in the BEMT codes. Therefore empiric blockage corrections are employed to transpose the experimental results to free stream conditions. As a result the validation exercise is somewhat compromised by the chain of approximations that are employed on both the codes and to the experimental data.

In Figure 3.15 and Figure 3.16 for the 5 and 10 degree set angle respectively, the results

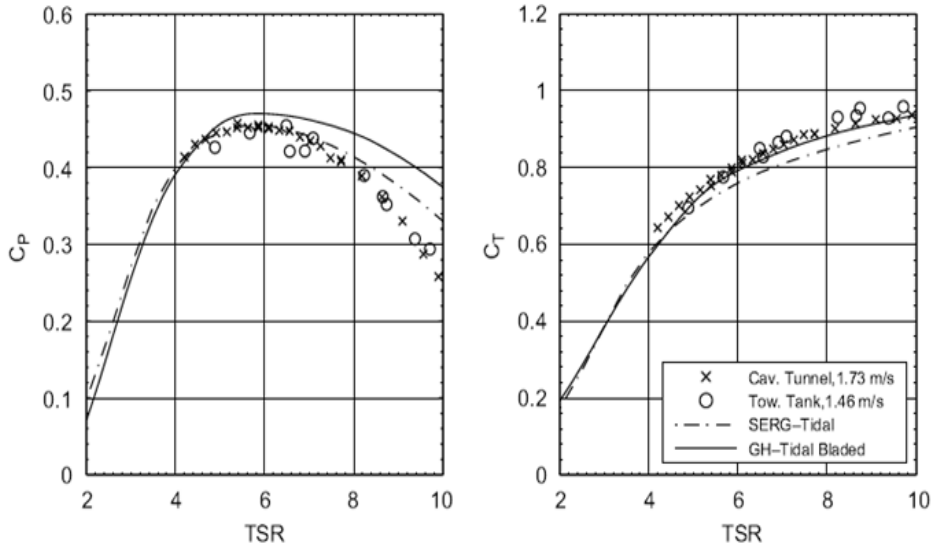

Figure 3.15 Comparisons between experiments and simulations with a 5 degree set angle (operation point) (Bahaj, 2007a)

are in better agreement and which in turn credits the appropriate usage of the blockage corrections and also the usage of the still water towing tank. Since the BEMT does not utilise the boundary effects of the sea bed and the free surface. These effects should be taken in to account especially when the ratio of the diameter of the turbine to depth is large.

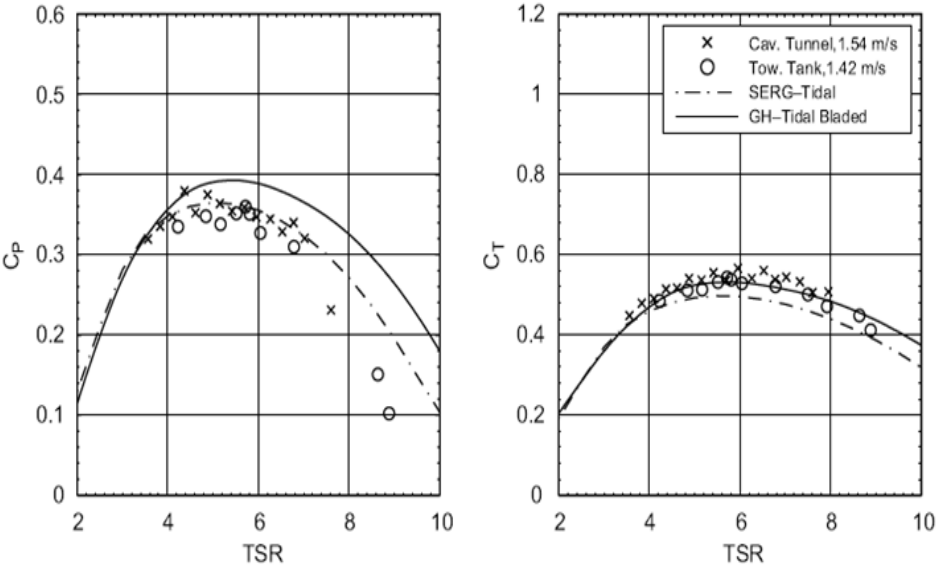

Figure 3.16 Comparisons between experiments and simulations with a 10 degree set angle (operation point) (Bahaj, 2007a)

These correctional effects should be taken in to account especially when the ratio of the diameter of the turbine to the dimensions of the tunnel cross section is large. Table 3.3 contains the correction factors to be applied to the two tunnels for a particular C_T value. In Bahaj et al., (2007b) a methodology to compute these corrections is presented.

	Cavitation tunnel	Towing tank
Blockage area ratio(%)	17	7.5
Reduction in $C_P(\%)$	18	5
Reduction in $C_T(\%)$	11	5

Table 3.3 Blockage corrections for $C_T = 0.8$ (Bahaj, 2007a)

Bahaj et al. (2007b) took power and thrust measurements of a $0.8m$ diameter turbine under various hydrodynamic flow conditions on a cavitation tunnel and a towing tank. The results shown in Figure 3.17 corresponds to the variation of C_P with TSR for a combination of five blade setting angles and flow velocities.

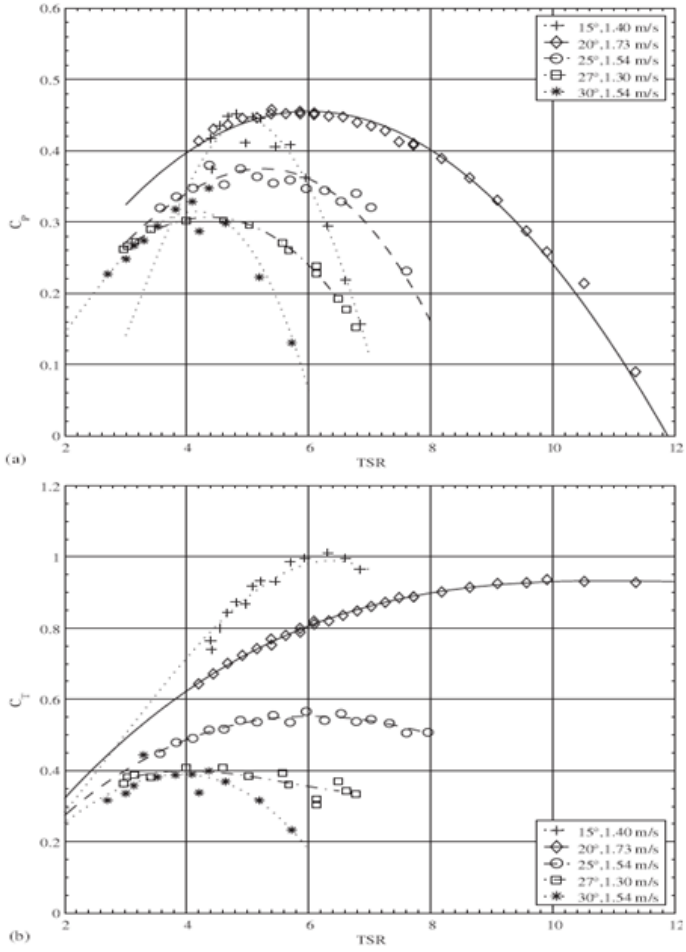

Figure 3.17 Comparisons of hub at pitch angles at the cavitation tunnel - zero yaw (Bahaj, 2007b)

The trends shown in Figure 3.17 are not consistent for both C_P and C_T. For C_T, it is apparent that there is a rise as the hub pitch angle is reduced. However in some instances the C_T is

seen to be rising for higher TSR values while in other cases C_T falls with increasing TSR. This observation was to form the basis of the DeltaStream blade design principle. However the C_P situation is less clear. The highest C_P is achieved by the second lowest stagger and in addition, those values appear to be much more stable, i.e. show less scatter, than the 15 degree setting angle case. However, it is the combination of high, though not highest, C_P together with a desirable C_T that can suggest a solution for a fixed pitch, gravity held, tidal turbine.

Figure 3.18 compares the results from the towing tank and the cavitation tunnel for a pitch angle of 20 degrees. In Figure 3.18 there is hardly any difference between the $1.0ms^{-1}$ and $1.7ms^{-1}$ cavitation tunnel case, also at low TSR the deep tip-immersion case for the towing tank is in close agreement with the cavitation tunnel case. Therefore this confirms the acceptability of using the towing tank and the cavitation tunnel during these experiments. The C_P for the shallow tip-immersion cases in Figure 3.15 and Figure 3.16 are $10 - 15\%$ lower than that of deep-immersion results and the C_T cases are about 5% lower. This is due to the proximity of the rotor to the free surface. This prevents the streamtube being able to develop and that in turn causes a reduction in the pressure difference across the turbine resulting in a reduction in both power and thrust. Because the rotor is being operated close the free surface there are additional losses that arise from the creation of waves, as seen above, and this would account of an increase in thrust. It is due to these factors that a small change is seen on the turbine thrust but accompanied by large reduction in power.

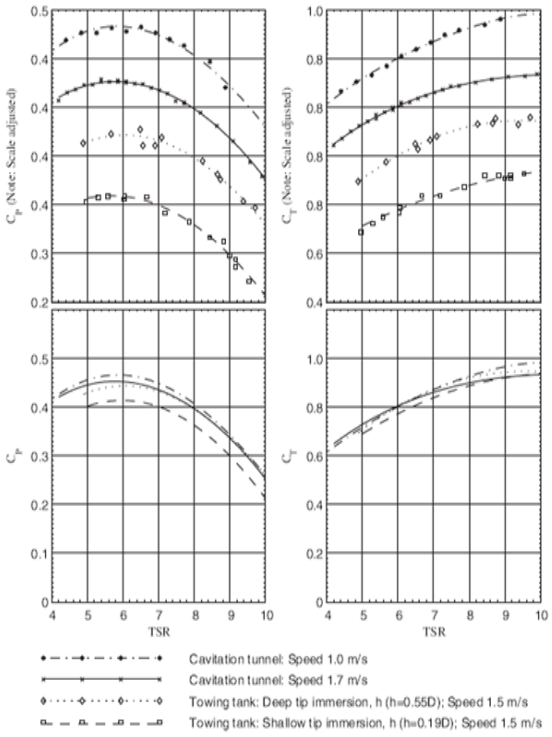

Figure 3.18 Test tank Vs cavitation tunnel - 20 degree hub pitch angle (Bahaj, 2007b)

Bahaj et al. (2007b) also investigated the effect of operating the turbine at a yaw angle to the inflow. Figure 3.19 shows the profiles for different yaw angles at 20 degree pitch angle. The most noteworthy feature is that for both cases the power and thrust coefficients decrease with the increase in yaw angle. Power tends to decrease approximately as a function of the cosine of the yaw angle squared and thrust as cosine of the yaw angle. It is stated that with a 30 degree yaw, a reduction of 30% of C_P is seen whilst the C_T was reduced to about 15%. A reduction of almost 9% in C_P was seen at 15 degree yaw and a 5% decrease in C_T.

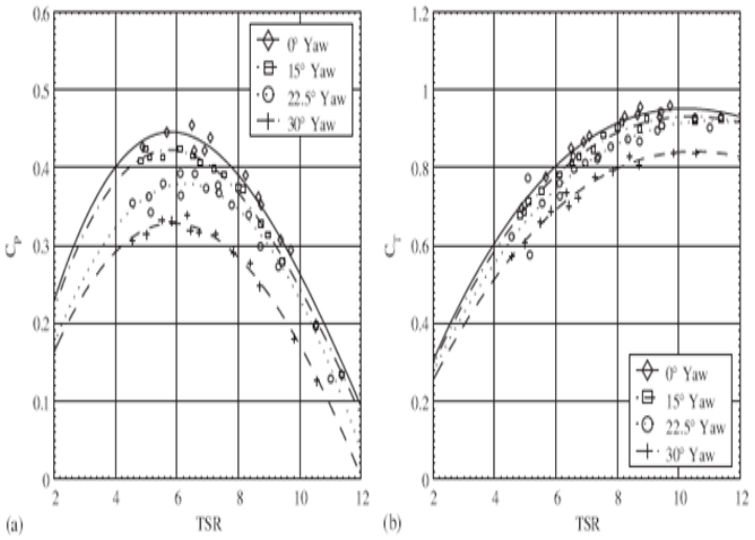

Figure 3.19 Comparison of the effect of yaw with 20 degree pitch at towed speed of 1.4m/s (Bahaj, 2007b)

3.9 Blade Fouling

The performance of moving parts of the turbine, i.e. the rotor and hub, could be affected by marine fouling. This concern has prompted the studies of Bahaj and Myers (2003) and also the extensive study done by Batten et al. (2008). A significant decrease in power with the increase of fouling was seen in the experiments carried out by Batten et al. (2008) at high tip speed ratios. A 50% increase in drag is assumed to have occurred with the increase in blade roughness for anti fouling measures. The effect of roughness had an effect in the stall characteristics of the blades but little or no change in the C_L was observed. For a TSR of 6 there is little change in span wise C_L but a significant increase in span wise C_D was observed. Further to these observations there was a $6 - 8\%$ decrease in C_P for a tip speed ratio of 6.

These observations are very important for this project since blade fouling has been an area of concern in the absence of concrete information. It has been suggested that one way of reducing the effect of blade fouling is by operating the turbine close to the sea bed. This can

both stir up sea bed debris and or place the turbine in the path of suspended abrasive matter, sand and shells transported in the tidal current. It is hypothesised that these particles could help clean a substantial section of the blade span. This solution however is not without its downside since to place the turbine closer to sea floor will expose the device to the sharp change in velocity gradient and high turbulence levels that are observed close to the sea bed. The rotor operational area would be compromised as the it is operating close to the sea bed, therefore, power generated from the turbine wold be reduced.

More research needs to be carried out in order to find a suitable solution for the prevailing issue of fouling. Anti fouling methods such as paints and sonic and ultra sonic devices are being tested and researched currently. The most commonly used anti fouling agent is tributyltin (TBT). However this can only be used very sparingly because of its hazardous nature to marine organisms. Different paints and metal treatments are being researched to be incorporated in the moving parts of similar structures.

3.10 Numerical Modelling of Tidal Turbines

Numerical analysis of tidal turbines are very rare in the literature. This is partly due to smaller organizations not being able to model tidal turbines given that commercial software is very expensive and because the solutions require significant computing power which can be quite expensive as well. Some work has however been published in collaboration with universities as was the case of the work done by Cardiff University in collaboration with the predecessors of Tidal Energy Limited, Tidal Hydraulic Generators based in Cardiff.

Egarr et al. (2004) presented results for a four bladed tidal turbine modelled using the computational fluid dynamic (CFD) package Fluent and validated using a full scale experimental model manufactured by the company. The experimental testing was done in 2002 on the Cleddau River near Milford Haven, Pembrokeshire, UK. The computational results for the turbine is compared with the experimental data in Figure 3.20. There is a 4% drop in peak power and approximately 15% difference in the angular velocity at which peak power occurs as shown in this figure.

Since the four bladed design was expensive to manufacture it was decided to replace this by three bladed turbine for the same power. In order for it to produce the same power the turbine diameter had to be increased to $6m$. The blade pitch was investigated to achieve the optimum power. This could be achieved by plotting the efficiency versus the blade angle as shown in Figure 3.21.

An optimum blade pitch of 2.6 degrees was identified and the turbine designed accordingly. The maximum efficiency that could be attained for this blade is 31%. However, it was

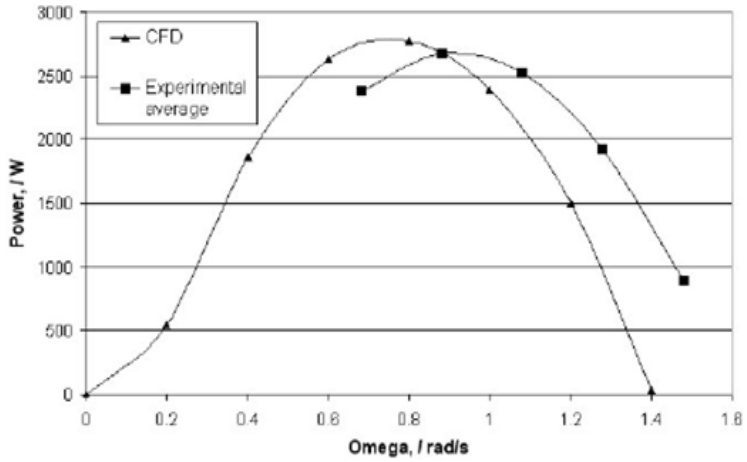

Figure 3.20 Comparison of CFD and experimental power for a $5.5m$ diameter turbine in a $0.9ms^{-1}$ tidal flow (Egarr, 2004)

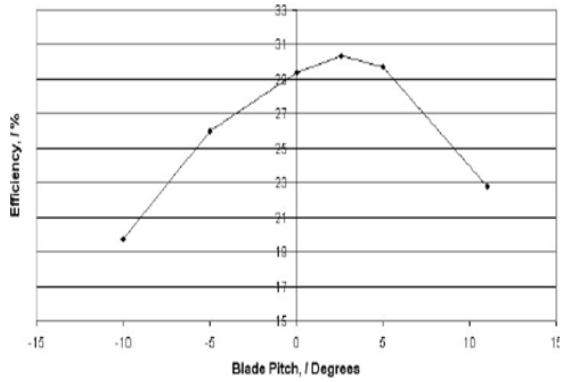

Figure 3.21 Variation in efficiency with blade pitch of a 3 blade, $6m$ diameter turbine in a $3.09ms^{-1}$ flow (Egarr, 2004)

thought that this could be improved with further design improvements. After establishing the optimum blade pitch the turbine was modelled in a range of tidal flows as shown in Figure 3.22 and Figure 3.23. Figure 3.22 shows the variation of power with angular velocity for different flow conditions.

Figure 3.23 shows the variation of the force with angular velocity for different flow conditions. To attain the optimum power extraction of the turbine, the force exerted on the turbine by the blades cannot be ignored as the structure supporting the turbine would need to be held in place by an anchor or would need to be piled into the sea bed. As shown in Figure 3.23, the force tends to even out when the turbine appears to be freewheeling. Therefore, the peak force occurs on the turbine when it is freewheeling.

Figure 3.24 illustrates velocity variation along the turbine axis at peak power extraction in a $3.09ms^{-1}$ tidal flow. The turbine is positioned at $0m$. When the fluid approaches the turbine the velocity drops. The velocity drop to $0ms^{-1}$ corresponds to the stagnation point at the hub . The flow then encounters a recirculation zone immediately after passing the turbine

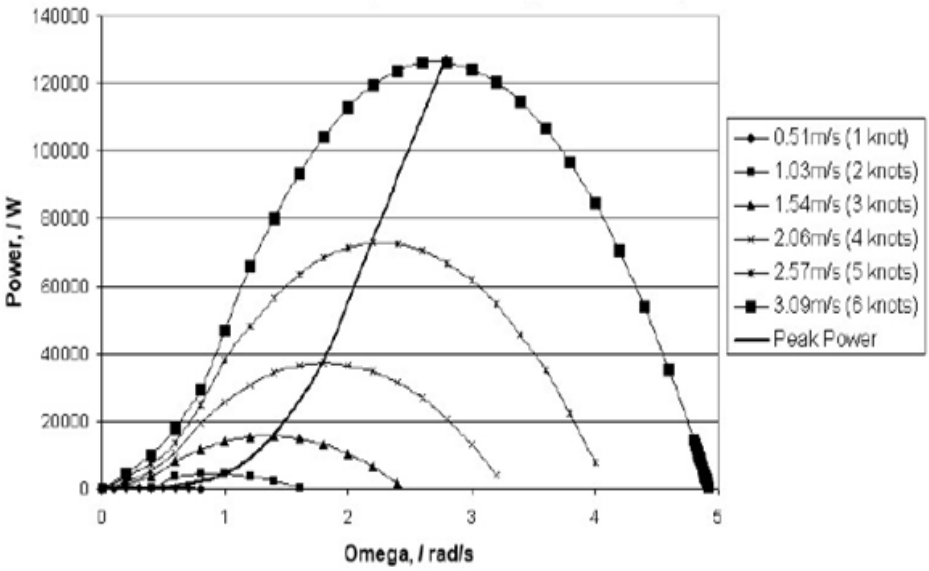

Figure 3.22 Variation power with a range of flow velocities (Egarr, 2004)

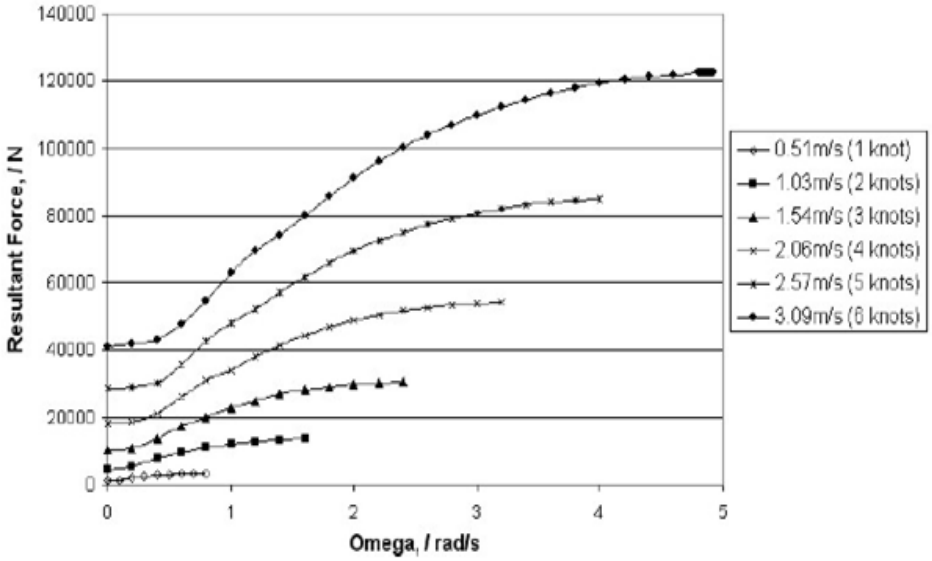

Figure 3.23 Variation of thrust with a range of flow velocities (Egarr, 2004)

which forces the velocity to peak and the sudden drop. After this the flow gradually reaches 90% of the free stream velocity at $75m$ downstream of the rotor i.e. approximately $12D$ of the rotor. However 80% recovery is achieved at $40m$ aft of the rotor ($7D$ of the rotor) i.e. indicating the closest position of the neighbouring turbine in a farm should be placed at least $7D$ downstream of the preceding rotor.

Some numerical results need to be received with a sceptical mind since the accuracy of the models is directly related to the rigour of the boundary conditions namely whether gradients of velocity and turbulence are modelled and other features of the model such as the extent of the computational domain, blade-pylon interactions, the treatment of near wall flows, etc. Akwensivie (2004) from the University of Strathclyde modelled a marine current turbine

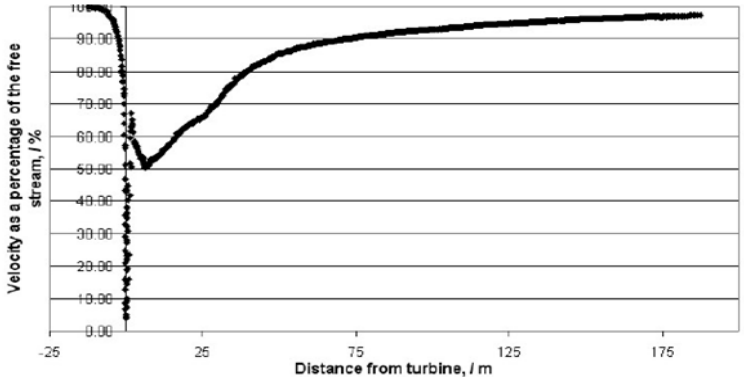

Figure 3.24 Development of flow downstream from the turbine at peak power extraction (Egarr, 2004)

using CFD (Fluent) for his Master's thesis. This author discusses the possible use of a number of turbulence models including the Reynolds stress model. However the $k - \epsilon$ model was employed in the study. The turbine was modelled in isolation discounting the blade-pylon interaction.

Fan et al. (2010) presented a numerical analysis of a tidal turbine based on Reynolds Averaged Navier Stokes (RANS) simulations. All computations were performed under the set conditions discussed in sub chapter 3.8. The whole computing area was divided into a rotational domain and a far field domain. GGI (General Grid Interface) connections were applied to connect these two domains. All three blades passages were simulated instead of the $1/3$ periodic rotation. The run was initiated with a $k - \epsilon$ turbulence model but later on the authors employed the $k - \omega$ SST (Shear Stress Transport) model for the remaining iterations. The $k - \omega$ SST, is a two equation eddy viscosity model used extensively with a low Reynolds number formulation as discussed in Chapter 4.

The results of the CFD simulations are compared with the results of a set of experimental tests and with the results of the analytical BEMT code (SERG-Tidal) mentioned previously. The results are compared for the design case with the blade pitch angle set at 20 degrees, Figure 3.25. The closest agreement was found to be for the design case and both simulations tend to overpredict the C_P. For the same cases the C_T for the experimental tests are higher. The code fails to predict the sharp drop in power after TSR 6 and increase in C_T after TSR 6, although the CFD is able to clearly predict this on both cases. This discrepancy of the analytical analysis method points to the added physical description inherent to the RANS approach when compared to the BEMT method being able to capture loss mechanisms akin to what is happening in the real blade.

Concluding remarks of the authors were such that the predictions for marine current turbines using CFD were satisfactory meaning in turn that this may become the preferred tool of

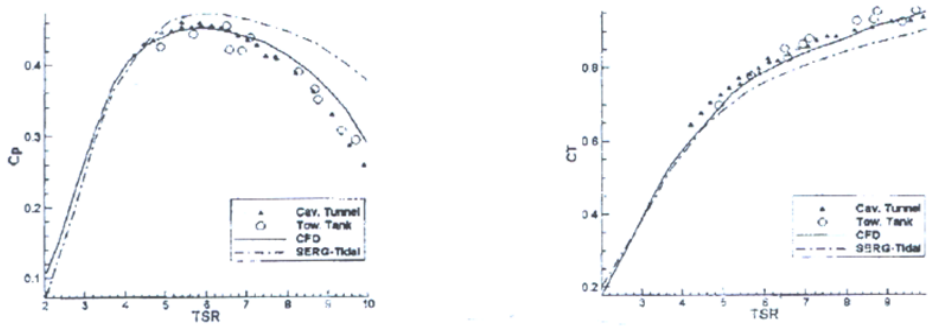

(a) (b)

Figure 3.25 (a) Power coefficient at 20 degree pitch (Fan, 2010). (b) Thrust coefficient at 20 degree pitch (Fan, 2010)

analysis method for these type of devices in the not so distant future.

3.11 Performance Enhancement Techniques used in Horizontal Axis Tidal Turbine (HATT)

As discussed above the turbine and its support structure are subjected to large transient loads. Therefore different methods of counteracting these harsh loading conditions have been developed. One such method is the use of fatigue resistant composite materials which can also offer potential improvements in the hydrodynamic performance of HATT's. Three dimensional tailoring of the blade deformation could thus be achieved because of the anisotropy of the laminated fibre composites. Consequently, the composite material is benefited by the high strength-to-mass and strength-to-stiffness ratios making these composites very promising materials for tidal turbine blades. Passive blade control could be achieved integrating advanced composites in to the manufacturing process of the blades. Anisotropic materials show different levels of elastic coupling and could exhibit bend-twist coupling. This behaviour is said to have reduce loads and enhance stall control in wind turbines, (Nicholls-Lee et al., 2007). This principle could be used in the marine environment as well, therefore incorporating a simple bend-twist coupled blade enables the turbine to deal with the extreme cyclic loads induced upon it whilst also maintaining a more consistent power output and hence maximising the energy capture of the device since the turbine could operate efficiently along a wider spectrum of tip speed ratios.

Using this simple technique eliminates the necessity to have a variable pitch blade as it is expensive and extremely demanding to maintain. This concept has been investigated using a BEMT code and a 3D surface panel code. The work carried out by Nicholls-Lee was for a 3-bladed $20m$ diameter turbine operating at the inflow velocity of approximately $2.5ms^{-1}$. The aerofoil section used for this research is the NACA$63-815$. This initial study comprised

of research on cavitation effects and the appropriate blade twist.

In order to check the effects on performance the section shape was simply altered by numerically deflecting the trailing end of the foil, Figure 3.26. As discussed on Chapter 2 cavitation occurs when the local pressure on the section falls to, or below, that of the vapour pressure of the fluid. It has been understood that increasing the proximity to the free surface of the ocean also increases the risk of cavitation and air may be sucked down from the surface at shallow depths causing ventilation. Cavitation can also be explained using the equation given below which is similar to the equation discused in Chapter 2.

$$\sigma = \frac{(P_{ref} - P_v)}{\left(\frac{1}{2}\rho V_\infty^2\right)} = \frac{(P_{AT} + \rho g h) - P_v}{\left(\frac{1}{2}\rho V_\infty^2\right)} = -C_p \tag{3.3}$$

Where;
P_{ref}=Reference pressure
P_v=Vapour pressure
P_{AT}=Total atmospheric pressure
h=Head of water
All other symbols are listed on the Nomenclature list.

As shown below in Figure 3.26, C_p becomes more positive with the increase in trailing edge deflection. The cavitation number was calculated at 1.8 for a blade diameter of $20m$ operating in an inflow velocity of $2.5ms^{-1}$ and at a rotating speed of $10revsmin^{-1}$. As shown on the figure, the datum aerofoil section or the section with slight deflections produce a negative C_p greater than the cavitation number. This means that the occurrence of cavitation is inevitable. The graph shows that by increasing the deflection C_p become more positive and therefore it would be less likely for the blade to cavitate, which is the desired effect. Therefore a blade section whose trailing edge deflects as it approaches the free surface would reduce the risk of cavitation.

Figure 3.27 below illustrates the pressure distribution over the NACA$63-815$ section with a variation of the deflection of the latter part of the foil at an angle of attack of 0 degrees. As seen in the previous figure the pressure distribution over the upper section gets more positive with the increase in trailing edge deflection, although the lower surface gets increasingly more negative in this case.

Cavitation occurs at the upper surface of the aerofoil when it is at an angle of attack at 8 degrees and at 0 degrees the lower surface experiences cavitation. Analysing both Figure 3.26 and Figure 3.27, it is evident that a section exhibiting less twist in the latter of

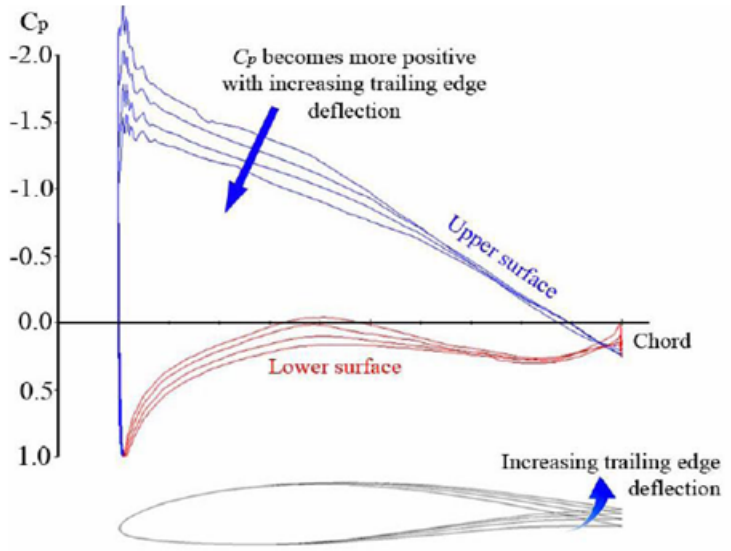

Figure 3.26 Pressure distribution over the NACA$63-815$ section with a variation in the deflection of the latter part of the foil at an angle of attack of 8 degrees (Nicholls-Lee, 2007)

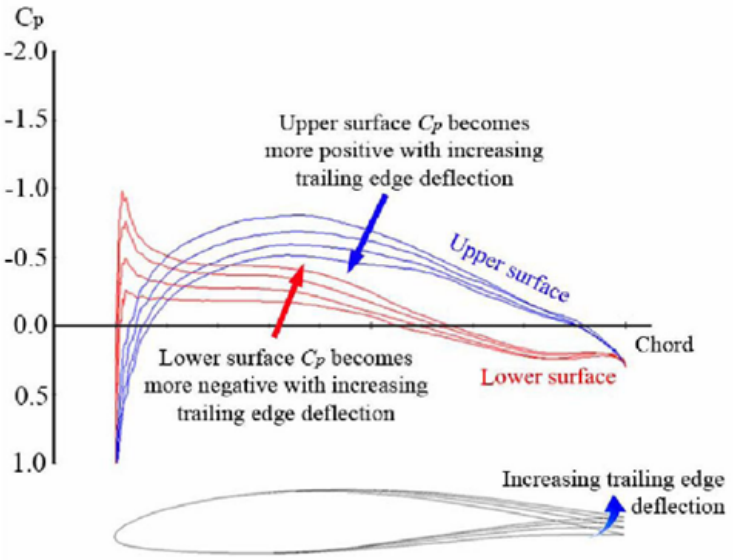

Figure 3.27 Pressure distribution over the NACA$63-815$ section with a variation in the deflection of the latter part of the foil at an angle of attack of 0 degrees (Nicholls-Lee, 2007)

the foil is more efficient at lower angle of attack and the contrary for the increased angle of attack. Therefore, this experiment highlights the important fact that designers need to bear in mind what the turbine is supposed to achieve and then a design compromise needs to be implemented accordingly.

This analytical study of adaptive blades using trailing edge twist confirms the much anticipated performance advantages of reduced cavitation and also more optimal performance in yawing flows. Many tidal sites are subjected to bi-directional flows, some sites vary from

as little as 10 degrees to complete opposite directions to 180 degrees. It has been confirmed by experimentation and by statistical analysis that an increase in turbine yaw angle causes a consistent power decrease and ideally a fully rectilinear flow is the more desired approach.

Performance and energy calculations were done from the modified BEMT code produced in MATLAB. A blade with constant twist with span and linear twist with span was analysed. The first configuration effectively models the variable pitch device and the latter configuration models the passively adaptive blades. In addition to the blade twist configuration, a couple of different twist distributions were imposed as well. One being a linear variation with wind speed and the second a square root variation with wind speed. The Figure 3.28 represents the variation of the C_P with the TSR. The solid power curve denotes the reference pressure variation for a fixed pitch configuration.

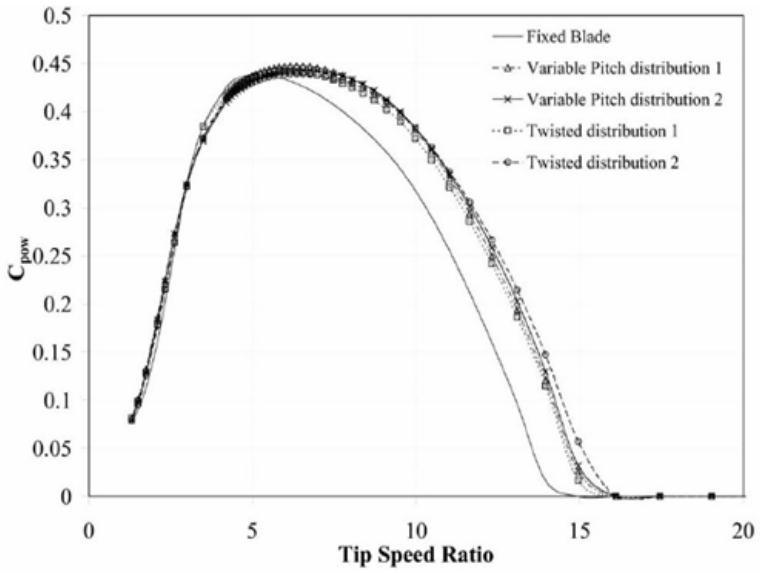

Figure 3.28 C_P **as a function of tip speed ratio for the various twist distributions and configurations overlaid on the reference power curve (Nicholls-Lee, 2007)**

At the first glance on the power variation graph it can be generally agreed that all of the twist distributions produce the curve to widen and higher values of C_P are maintained at the lower flow velocities which correspond to the higher TSR on the graph. The blade twist configurations are more efficient at higher flow velocities as there is no difference in the values. When comparing the two twist configurations, the passively adaptive blades show a marginally lower and less extensive C_P, therefore, producing poor performance than that of the variable pitch configuration.

The thrust force acting on the rotor is directly applied to the blades, hub and its support structure hence is a prime factor in the design process of the tidal turbine. The Figure 3.29 illustrates the variation of the C_T as a function of the TSR over the several configurations. It

can be seen that higher TSR's produce less thrust, indicating that the turbine generates less thrust at low velocities. The profile which has the best variation is that of the variable pitch configuration with the second twist distribution as shown below in Figure 3.29.

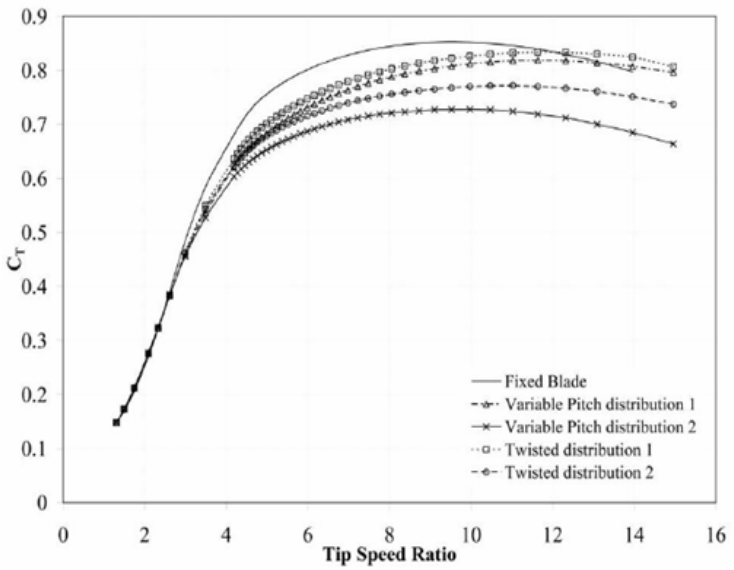

Figure 3.29 C_T **as a function of tip speed ratio for the various twist distributions and configurations overlaid on the reference thrust curve (Nicholls-Lee, 2007)**

Table 3.4 shows the percentage increase of both C_P and annual energy capture and percentage decrease of C_T from the fixed blade configuration. As seen, all configurations has increased the annual energy capture and decreased the undesirable thrust loading. What is important is not the peak C_P but rather the extensiveness of the high C_P illustrated by the wider C_P graph.

Blade Configuration	C_P	Annual Energy Capture	C_T
	(%)	(%)	(%)
Fixed	0	0	0
VP distribution 1	2.20	2.65	−3.93
VP distribution 2	1.17	1.56	−14.62
Twisted distribution 1	0.90	1.80	−2.19
Twisted distribution 2	0.29	1.35	−9.45

Table 3.4 Percentage of C_P, annual energy capture, and C_T from the reference blade configuration (Nicholls-Lee, 2007)

The first configuration for both variable pitch and linear twist yields the greatest energy capture, the increase is just over 2.5% over the reference energy capture. This can be calculated to an extra $60.5GWh/year$ and a $£4.84m$ increase in energy sales when the price is taken to be $8p/kWh$. These same configurations has a fairly moderate reduction in C_T. Considering the design, manufacturing and maintenance cost over a said period, these configurations would produce a good return of income.

As seen from the Table 3.4, the greatest decrease in C_T was experienced by the second configuration of the variable pitch system, which has a reduction of over 14%. However, this configuration has one of the lowest energy capture percentages and also utilises the more expensive and complex variable pitch mechanism. Therefore, it is essentially clear that a compromise between the annual energy capture and C_T needs to be attained. Passively twisted blades yield less energy capture but it more than compensates for the easy and lighter and more dynamic design rather than the more expensive and complex variable pitch approach.

The surface panel code Palisupan was used to model the performance of different blade twist configurations at an agreed single TSR of 5 corresponding to a flow velocity of $2.1ms^{-1}$. This analysis helps to gather a detailed knowledge of the actual blade surface loading. The red areas in the Figure 3.30 are the areas of high negative pressure and hence show where cavitation is most likely to occur. The green demonstrates areas of more even and less negative pressure. Ultimately it is the role of the designer to produce a more even distribution of pressure whilst maintaining the maximum C_P greater than the value of cavitation.

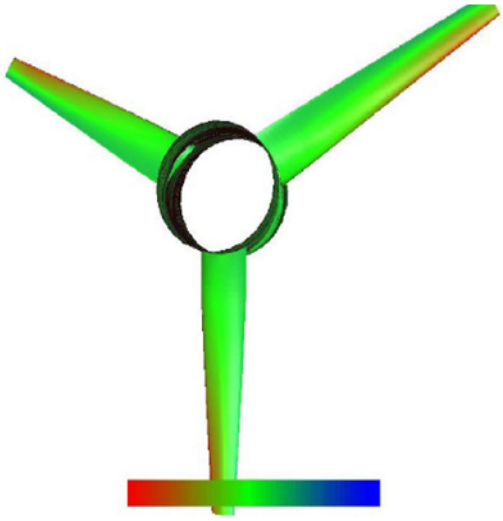

Figure 3.30 Pressure plot over the three bladed turbine (Nicholls-Lee, 2007)

The Figure 3.31 represents the C_p as a function of the turbine radius for the various blade

twist configurations and distributions.

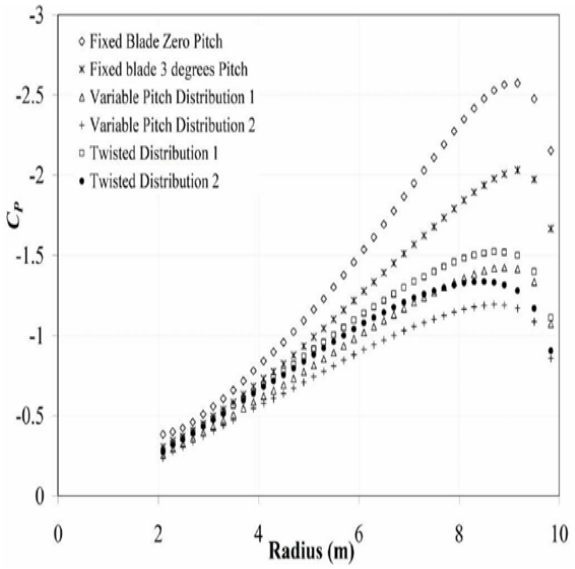

Figure 3.31 Pressure coefficient,C_p, with turbine radius for various configurations (Nicholls-Lee, 2007)

At this flow velocity the cavitation number is calculated at 2 and both the fixed blade configurations exhibit a maximum C_p of less than -2 and thus is most likely to cavitate. The blade twist configuration causes the C_p over the latter two thirds of the blade to decrease significantly. The Table 4.5 provides the C_p values for all configurations.

Blade Configuration	Maximum negative C_p
Fixed blade, no pitch	-2.57
Fixed blade, 3 degree pitch	-2.03
VP distribution 1	-1.42
VP distribution 2	-1.19
Twisted distribution 1	-1.52
Twisted distribution 2	-1.33

Table 3.5 C_p for all configurations (Nicholls-Lee, 2007)

All configurations expect that of the fixed blade configuration has significantly reduced the occurrence of cavitation. The most desirable model is that of the second distribution of the variable pitch configuration, it not only has a reduced maximum negative coefficient of pressure but also exhibits most even spanwise pressure distribution as well.

As expected, the concept of blade twisting has been a success and further work needs to be carried out using CFD and finite element analysis to test the blade theoretically and ultimately an experimental test needs to be done in order to validate the numerically obtained results.

3.12 Best Practice

After reviewing the literature, it was apparent that a best practice guide must be followed. The list below highlights some of the best practice methods suitable for the smooth advancement of this project;

- Site selection for a site specific design namely water depth, turbulence data, wave information, bathymetry, etc.
- Design specifics to yield the desired power output e.g. power per turbine, size of blades, type of aerofoil and thrust estimates - design operation criteria.
- Careful design of the domains for simulations e.g. possibility to add, delete or edit domains later on in the project life cycle.
- Leading edges and trailing edges are to have a greater amount of nodes to ensure proper resolution of the stagnation points
- Sufficient amounts of nodes on the hub, pylon and immediate front and rear of the blade areas to ensure sufficient capture of the physics and more importantly streamlining computational costs.
- Use of the best possible turbulence models
- Sufficient steady state simulations
- Transient simulations involving time-dependent waves

3.13 Chapter Closure

This literature review has shown that for most industrial applications, RANS based models give the best modelling accuracy despite the computational cost. Their behaviour has been well documented enabling the user to have a good degree of confidence in their use. The $k-\omega$ SST and $k-\epsilon$ turbulence models have shown to be the RANS model of choice although with limited accuracy. When predicting unsteady effects at high Reynolds numbers the mentioned models under perform quiet significantly, therefore more work must be done

to develop these models in order to fully predict the unsteady effects from vortices, wakes, environmental turbulence, waves etc.

Chapter 4

Numerical Model

4.1 Introduction

A few of the inadequacies of the turbulence models used currently for these types of research have been discussed in the preceding, Chapter 3. Such drawbacks are particularly common with flows comprising of high pressure gradients, shear flows with strong anisotropy (swirl components), complex boundary conditions, geometry curvature, inherently high Reynolds's numbers. Therefore, this chapter is dedicated to in providing a respectable and suitable turbulence model for the analysis of HATT project whilst carefully introducing the geometry and meshing of the model together with its initial physics ready for the steady state simulations. Modelling improvements, model variations and etc, made necessary for several future simulations are described in more detail in the relevant subsequent chapters.

4.2 An Overview of CFD

The use of computational fluid dynamics has increased immensely in the last decades, propelled by continuous fall in cost of computational power and the realisation of the benefits this technology brings to organisations dealing with fluid dynamics analysis requirements. Along with the advent of three-dimensional (3D) CFD, the need for actual experiments either with scaled down or full scale models has been drastically reduced. As defined by Versteed and Malalasekera (1995), CFD is the analysis of systems involving fluid flow, heat transfer and associated phenomena such as chemical reactions by means of computer-based simulations.

The time and costs involved in the building and running of experiments are far more expensive when compared to utilising CFD techniques - although commercial CFD packages don't come cheap. With the increase in the usage of 3D CFD there has been an

overall reduction in the length of the design life cycle process and its associated costs. Both CFD and experimental testing can be categorised as data gathering techniques. Therefore, there has to be a sensible compromise between the use of CFD and experimental testing whilst keeping the time and expenses in check. The Table 4.1 highlights the general strengths and weakness of CFD and experimental techniques.

A few of the benefits of using CFD modelling for this HATT project would be the ability to understand the problem far more comprehensively than with the actual experimental methods i.e. numerical models have commonly millions of data sampling locations which enable the clarification of phenomena that is very difficult to capture experimentally. In addition numerical models allow the quick varying of the depth and size of the rotor, varying the physics, changing the blade-pylon distances and also adding wave and other phenomena to the model and etc.

4.3 Types of CFD Software

At present there are several commercial CFD packages available, ANSYS FLUENT, ANSYS CFX, STAR-CD, Cobalt, etc. Packages offered by ANSYS are extremely user-friendly and have a good solid market therefore customer care and training are good. Softwares such as OpenFOAM, an open source code, are emerging in the CFD market. However this code does not have a Graphical User Interface (GUI) but since it is free to use its customer base is building rapidly.

Some companies and institutions also have their own CFD codes. These are often academic codes that have been further developed in-house. One such case is Prof. J.D. Denton's Multip code now used, in a improved manner, in a number of companies. These codes can be very fast and provide fairly accurate results when simulating models that related to its main field of operation. Essentially they may be more accurate than commercial codes, with general capabilities, because organisations have worked many years on adapting their code to a specific, well calibrated, use. Table 4.2 below highlights the advantages and disadvantages of commercially available CFD codes to in-house codes.

	In-house codes	Commercial codes
Advantages	User knowhow	Good technical support
	Usually solves quicker than commercial codes	Latest technologies
	Easily developed	Can run wider range of applications
	Post-processing is optimised for companies	Very good general post-processing capabilities
	Code optimised for specifics for company design	Larger customer base

		Support widely available from user forums Versatility between family packages
Disadvantages	In-house support Developer support can be slow Documentation could be obsolete and of poor quality GUI could be poor or not at all	Computationally more expensive Extremely expensive packages Processing limited by licenses Uncertainty of its codes

Table 4.2 Advantages and Disadvantages of Commercial codes vs. In-house codes

4.3.1 ANSYS CFX

The software employed in this HATT project was ANSYS CFX because of its wide availability, versatility and the technical support ANSYS provides to the University.

Today's ANSYS CFX package has over 20 years of experience behind it. Any CFD model can be broken down in to 3 segments. A Pre-Processor - where all the geometry and meshing is done together with the addition of the physics of the simulation. A Solver which is the part of the code where the equations are solved. Lastly, the Post-processor where the computed data is retrieved and analysed into meaningful qualitative and quantitative information. Shown in Figure 4.1 is an illustration of this 3 segment concept as used in ANSYS CFX.

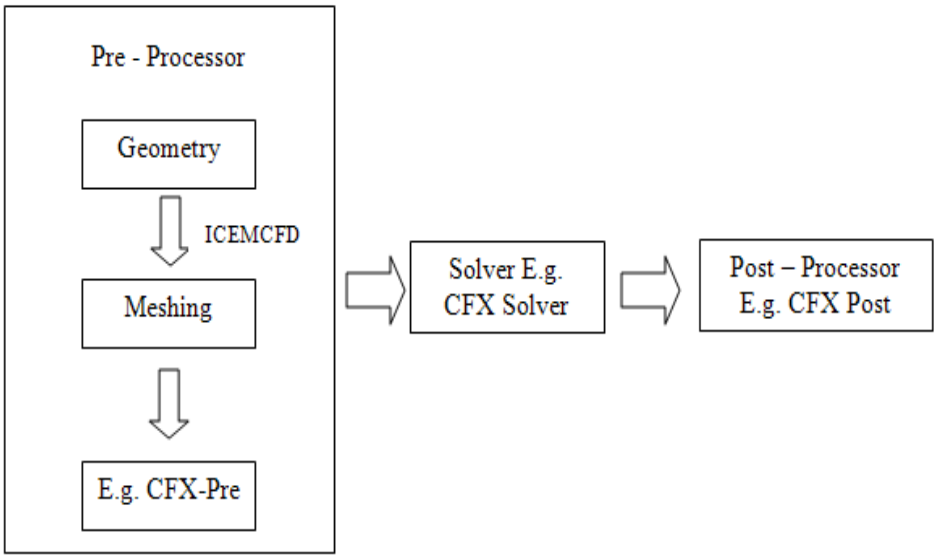

Figure 4.1 CFD code structure

	Experimental Testing	CFD
Advantages	Best for accuracy e.g. waves, turbulence, etc. Data for a wide range of conditions All geometric details Accurate performance evaluation Captures all physics	No scaling issues Relatively quick to acquire results Comprehensive flow details Multiple simulations and easy to manage new configurations Relatively low initial and maintenance costs Easily available anywhere and repeatable Can simulate experimental tests
Disadvantages	High initial and running expenses Instrumentation limitations Expensive and time consuming to repeat experiments and to set up new configurations Scaled-down effects need to be addressed Sensor probes, etc could affect result	Limited by computational resources Results are in direct relation to the user and the code Accurate unsteady effects are difficult to model Not highly accurate Least effective at predicting losses

Table 4.1 Advantages and Disadvantages of CFD to experimental testing

4.4 Turbulence Models in ANSYS CFX

The CFX code used for the most of the part of the project was the version 11.0. It was upgraded to version 12.1 in mid 2010, which coincided with the final simulation stages of the project. CFX version 10.0 was also employed in the initial stages of the project as the transition from version 10.0 to 11.0 was performed during mid 2007. This change had no effect on the main solver or its turbulence models.

During the project a mixture of Reynolds Averaged Navier-Stokes (RANS) and Unsteady Reynolds Averaged Navier-Stokes (URANS) simulations were carried out. CFX is a coupled finite-volume solver. A coupled solver is one where all the hydrodynamic equations are solved as a single system. This code, as indeed most commercial codes, employs turbulence models to predict the effects of turbulence on the flow without resolving all scales of the turbulent fluctuations. The turbulence model used in this project was the SSG (Speziale, Sarkar and Gatski) Reynolds Stress Model (RSM). These Reynolds Stress Models are often referred to as the Second Moment Closure (SMC) models. The SSG Reynolds Stress Model is based on the $k-\epsilon$ two equation model. As stated in the ANSYS CFX-Solver Theory Guide manual the RANS based turbulence models are also known as Statistical Turbulence Models as their equations are statistically averaged. The only two exceptions in ANSYS CFX are Large Eddy Simulation (LES) and Detached Eddy Simulation (DES).

A brief description and some of their physical properties are outlined in the subsequent sections.

4.4.1 Zero equation Model

The zero equation model is a very simple eddy viscosity model that solves for a global value for the turbulent viscosity, μ_t, from the mean turbulent velocity, U_t, and the turbulent length scale, l_t. A constant turbulent eddy viscosity is calculated for the entire flow domain and is given by;

$$\mu_t = \rho f_\mu U_t l_t \tag{4.1}$$

Where;
f_μ = proportionality constant
All other symbols are listed on the Nomenclature list.

The turbulent length scale is is calculated using the fluid domain volume equation;

$$l_t = \frac{\left(V_D^{\frac{1}{3}}\right)}{7} \tag{4.2}$$

Where;
V_D = fluid domain volume

This model is called Zero-equation because, it has no additional transport equations to be computed.

4.4.2 $k-\epsilon$ model

$k-\epsilon$ models are categorised as two-equation models and is very popular among the industrial and academic communities, as the model offers a good compromise between computational resource and computational accuracy. The term "two-equations" derives from the fact that both the turbulent velocity and length scales are solved using separate transport equations.

These models are much more superior and sophisticated than the zero-equation models. The momentum equation is given by;

$$\frac{\partial \rho U}{\partial t} + \nabla \cdot (\rho U \otimes U) - \nabla \cdot (\mu_{eff} \nabla U) = -\nabla p^{'} + \nabla \cdot (\mu_{eff} \nabla U)^T + B \tag{4.3}$$

Where;
B = the sum of body forces
$p^{'}$ = modified pressure
μ_{eff} = is the effective viscosity (includes the effects of turbulence in the flow)

$$\mu_{eff} = \mu + \mu_t \tag{4.4}$$

Turbulent viscosity is given by;

$$\mu_t = C_\mu \rho \frac{k^2}{\epsilon} \tag{4.5}$$

All other symbols are listed on the Nomenclature list.

In general two-equation models, the turbulent velocity term is solved from the turbulent kinetic energy, k, which is derived from the solution of its dedicated transport equation. The turbulent length scale is estimated from two properties of the turbulence field, usually the turbulent kinetic energy, k, and its dissipation rate, ϵ. The dissipation rate is also derived from the solution of its transport equation. The transport equations used for k and ϵ are;

Turbulent kinetic energy

$$\frac{\partial (\rho k)}{\partial t} + \nabla \cdot (\rho U k) = \nabla \cdot \left[\left(\mu + \frac{\mu_t}{\sigma_k} \right) \nabla k \right] + P_k - \rho \epsilon \tag{4.6}$$

Dissipation rate

$$\frac{\partial (\rho \epsilon)}{\partial t} + \nabla \cdot (\rho U \epsilon) = \nabla \cdot \left[\left(\mu + \frac{\mu_t}{\sigma_\epsilon} \right) \nabla \epsilon \right] + \frac{\epsilon}{k} \left(C_{\epsilon 1} P_k - C_{\epsilon 2} \rho \epsilon \right) \tag{4.7}$$

Where $C_{\epsilon 1}$, $C_{\epsilon 2}$, C_μ, σ_k and σ_ϵ are empirically derived model constants. P_k is the turbulence production rate due to viscous and buoyancy forces, and is given by;

$$P_k = \mu_t \nabla U \cdot \left(\nabla U + \nabla U^T \right) - \frac{2}{3} \nabla \cdot U \left(3 \mu_t \nabla \cdot U + \rho k \right) + P_{kb} \tag{4.8}$$

Within ANSYS CFX, this model uses the scalable wall-function approach to improve robustness and accuracy when the near-wall mesh is very fine. Whilst this model is widely used in many engineering applications, there are areas in which this model has been found to produce inaccurate results. These shortcomings would be discussed in more detail in the subsequent sub chapters.

Another variation to this model is the RNG$k - \epsilon$. The transport equations for the turbulent kinetic energy and the dissipation rate are the same as those of the $k - \epsilon$ model, although the empirically derived constants are different and also the constant $C_{\epsilon 1}$ is now replaced by $C_{\epsilon 1 RNG}$ and so on. In general, the model offers little improvement to the standard $k - \epsilon$ model.

The dissipation rate equation is;

$$\frac{\partial (\rho \epsilon)}{\partial t} + \nabla \cdot (\rho U \epsilon) = \nabla \cdot \left[\left(\mu + \frac{\mu_t}{\sigma_{\epsilon RNG}} \right) \nabla \epsilon \right] + \frac{\epsilon}{k} \left(C_{\epsilon 1 RNG} P_k - C_{\epsilon 2 RNG} \rho \epsilon \right) \tag{4.9}$$

And;

$$C_{\epsilon 1RNG} = 1.42 - f_{\eta} \tag{4.10}$$

$$f_{\eta} = \frac{\eta\left(1 - \frac{\eta}{4.38}\right)}{(1 + \beta_{RNG}\eta^3)} \tag{4.11}$$

$$\eta = \sqrt{\frac{P_k}{\rho C_{\mu RNG}\epsilon}} \tag{4.12}$$

4.4.3 $k - \omega$ model

These models assume that the turbulence viscosity is linked to the turbulent kinetic energy and turbulent frequency by;

$$\mu_t = \rho\frac{k}{\omega} \tag{4.13}$$

One of the advantages of the $k - \omega$ formulation is the near wall treatment for low-Reynolds number computations. The model does not require the complex non-linear damping function as required by the $k - \epsilon$ model, hence, is more accurate and more robust. At low-Reynolds numbers a $k - \epsilon$ model would require a typical near wall resolution of $y+ < 0.2$, while for the same Reynolds number $k - \omega$ model would require at least a $y+ < 2$. This model is also called the Wilcox $k - \omega$ model. It solves for two transport equations, one for the turbulent kinetic energy and one for the turbulent frequency. The transport equations are given by;

Turbulent kinetic energy

$$\frac{\partial(\rho k)}{\partial t} + \nabla \cdot (\rho U k) = \nabla \cdot \left[\left(\mu + \frac{\mu_t}{\sigma_k}\right)\nabla k\right] + P_k - \beta^{'}\rho k\omega \tag{4.14}$$

Turbulent frequency

$$\frac{\partial(\rho\omega)}{\partial t} + \nabla \cdot (\rho U \omega) = \nabla \cdot \left[\left(\mu + \frac{\mu_t}{\sigma_\omega}\right)\nabla\omega\right] + \alpha\frac{\omega}{k}P_k - \beta\rho\omega^2 \tag{4.15}$$

P_k is the production rate of turbulence and is calculated the same way as in the $k - \epsilon$ model.

β, α, $\beta^{'}$, σ_k and σ_ω are standard model constants. Since the HATT model has high Reynolds numbers, this model is not suited for these highly turbulent applications, therefore, is not discussed any further in this thesis.

There are 2 more $k-\omega$ based models namely the Baseline (BSL) $k-\omega$ and the $k-\omega$ Shear Stress Transport (SST) models.

One of the main issues in turbulence modelling is the accurate prediction of flow separation from a smooth surface. Standard two-equation turbulence models fail to predict the inception of the flow separation and in $k-\epsilon$ based models the prediction is too late and then under predicts the amount of separation later on under adverse pressure gradient conditions. For this reason, the aerodynamic community has developed these two ω based models. The SST model in particular is recommended for high accuracy boundary layer simulations - at least a boundary layer of 10 points is required to benefit from this model.

4.4.4 Reynolds Stress Models

Two-equation turbulence models mentioned above offer good predictions of the characteristics and physics of most flows of industrial and or academic relevance. Unlike the two-equation models where the eddy viscosity hypothesis exists, the Reynolds Stress Models are based on solving transport equations for all components of the Reynolds stress and the dissipation rate. The RSM model has six additional transport equations that are solved for each time step or outer coefficient loop in the flow solver. The source terms in the Reynolds stress equations are also more complex than those compared to the two-equation models. Consequently, the outer loop convergence may be slower for the RSM models in comparison to the two-equation models. The eddy viscosity models fail to precisely capture the effects in flows where turbulent transport or non-equilibrium effects are important. As stated by the ANSYS CFX solver modelling guide and the Von Karman Institute for fluid dynamics Lecture series (2000-04), if the flow is complex and has the following characteristics, consider using RSM models;

- Buoyant flows
- Flows with sudden changes in the mean strain rate e.g. swirls, curvature
- Can be used for complex models (rotating fluids, curved surfaces)
- Strong pressure gradient (high acceleration and deceleration)
- Only initial and or boundary conditions need to be supplied
- Flow separation and recirculation

- Three-dimensional flow effects (cross-flows)
- Stagnation and streamlines reattachment

Standard RSM models in ANSYS CFX are based on the ϵ-equation. The ω based RSM models will not be discussed in this thesis as the model itself is not suited for the work criteria of the project. For example, the ϵ-equation models are generally suited for high Reynolds number turbulence problems where the ω based models are generally for low Reynolds number flows.

There are 3 types of the modified ϵ based RSM models in ANSYS CFX, they are as follows;

- Reynolds Stress Model (LRR-IP)
- QI Reynolds Stress Model (LRR-QI)
- SSG Reynolds Stress Model (SSG)

In general, the (SSG) Speziale, Sarkar and Gatski (1991) model is more accurate than the Lauder, Reece and Rodi (LRR-IP) (Isotropization of Production) versions for most flows and more practical than the LRR-QI (Quasi-Isotropic) models, (Von Karman Institute for fluid dynamics Lecture series, 2000-04). According to ANSYS CFX this is particularly true for swirling flows. The SSG model is a good compromise between the desired accuracy and computational economy which stands well with the industry and academic work. Hence the SSG model has been implemented in the project due to the inherent complexity of the flow which comprises most of the above mentioned flow characteristics.

The Reynolds averaged momentum equations for the mean velocity is;

$$\frac{\partial \rho U}{\partial t} + \nabla \cdot (\rho U \otimes U) - \nabla \cdot (\mu \nabla U) = -\nabla p^{''} - \nabla \cdot (\rho \overline{u \otimes u}) + B \tag{4.16}$$

Where, B is the sum of body forces, $\rho \overline{u \otimes u}$ is the Reynolds stress component. $p^{''}$ is the modified static thermodynamic pressure, given by;

$$p^{''} = p + \nabla \cdot U \left(\frac{2}{3}\mu - \zeta \right) \tag{4.17}$$

The ANSYS CFX-Solver solves the following equations for the transport of the Reynolds stresses;

$$\frac{\partial \rho \overline{u \otimes u}}{\partial t} + \nabla \cdot (\rho U \otimes \overline{u \otimes u}) = \left[P + \phi + \nabla \cdot \left\{ \left(\mu + \frac{2}{3} C_s \rho \frac{k^2}{\epsilon} \right) \nabla \overline{u \otimes u} \right\} - \frac{2}{3} \delta \rho \epsilon \right] \tag{4.18}$$

Where, ϕ, is the pressure-strain tensor, P, is shear turbulence production and C_s is a model constant.

As the turbulent dissipation term appears in every stress transport equation, a formulae for dissipation is given by;

$$\frac{\partial (\rho \epsilon)}{\partial t} + \frac{\partial}{\partial x_k} (\rho U_k \epsilon) = \frac{\epsilon}{k} (C_{\epsilon 1} P - C_{\epsilon 2} \rho \epsilon) + \frac{\partial}{\partial x_k} \left[\left(\mu + \frac{\mu_t}{\sigma_\epsilon} \right) \frac{\partial \epsilon}{\partial x_k} \right] \tag{4.19}$$

Where,$C_{\epsilon 1}$ and $C_{\epsilon 2}$ are model constants.

The two LRR models use a linear relation to the pressure-strain correlation, whilst the SSG model uses a quadratic relation.

The Table 4.3 below shows the values of the constants for each RSM model.

Model	$C_{\mu RS}$	S_{eRS}	C_s	$C_{\epsilon 1}$	$C_{\epsilon 2}$	C_{s1}	C_{s2}	C_{r1}	C_{r2}	C_{r3}	C_{r4}	C_{r5}
LRR-IP	0.1152	1.10	0.22	1.45	1.9	1.8	0.0	0.0	0.8	0.0	0.6	0.6
LRR-QI	0.1152	1.10	0.22	1.45	1.9	1.8	0.0	0.0	0.8	0.0	0.873	0.655
SSG	0.1	1.36	0.22	1.45	1.83	1.7	-1.05	0.9	0.8	0.65	0.625	0.2

Table 4.3 Constants for the 3 Reynolds Stress Models (ANSYS CFX-Solver Theory Guide version 11.0)

4.4.5 Large Eddy Simulations (LES)

The most accepted approach to predicting turbulent flows is the use of RANS equations, which solve for time averaged quantities. This has been extensively discussed in the previous sub chapters. In some complex flows the RANS approach has been found less effective, therefore, alternative approaches such as Large Eddy Simulation (LES) or Direct Numerical Simulation (DNS) are necessary to model turbulence. In DNS models, time dependant equations are solved with no approximations, or all relevant scales resolved or the equations are filtered to remove very fine time and length scales as in the LES approach.

Both these methods require fine grids and small timesteps. Any further discussions on DNS models will not be made in this thesis as it's very expensive computationally and is beyond the scope of this thesis. As stated by Ranga (2009), LES has emerged as a next generation modelling technique to simulate the turbulent flows based on the idea of separation of scales. During the last three decades, this technique of modelling turbulence has improved considerably while developing major theories, new models and more efficient numerical schemes, (Piomelli 1999).

As stated in the ANSYS CFX-Solver Modelling Guide, for high Reynolds numbers, consider using the LES approach when;

- The flow is unstable e.g. vortex shedding, due to structures in the model
- There are symmetries in the geometry and flow
- The flow is buoyant
- The noise from the flow is to be calculated
- Fluctuating data is required e.g. forces, gust of wind/water

One should also consider using LES when conventional RANS methods fail to simulate and also when there is access to high performance computing.

The non filtered Navier-Stokes equations are;

$$\frac{\partial\left(\rho U_i\right)}{\partial t}+\frac{\partial\left(\rho U_i U_j\right)}{\partial x_j}=-\frac{\partial p}{\partial x_i}+\mu\frac{\partial^2 U_i}{\partial x_j \partial x_j} \tag{4.20}$$

LES approach is about filtering of the equations of movement and the breakdown of the flow variables in to a large scale (resolved) and a small scale (unresolved) parts. Any flow variable f can be written such as;

$$f=\overline{f}+f^{'} \tag{4.21}$$

Where, $\overline{f}$, the large scale part is defined through volume averaging;

$$\overline{f}\left(x_i,t\right)=\int_{Vol} G\left(x_i-x_i^{'}\right) f\left(x_i^{'},t\right)\mathrm{d}x_i^{'} \tag{4.22}$$

Where, $G\left(x_i-x_i^{'}\right)$, is the filter function also called the *hat* filter or *Gaussian* filter.

Then, after assuming the density fluctuations to be negligible, the filtered Navier-Stokes equations become;

$$\frac{\partial\left(\rho\overline{U_i}\right)}{\partial t}+\frac{\partial\left(\rho\overline{U_iU_j}\right)}{\partial x_j}=-\frac{\partial\overline{p}}{\partial x_i}+\mu\frac{\partial^2\overline{U_i}}{\partial x_j\partial x_j} \tag{4.23}$$

The non linear transport term in the above equation can be developed as;

$$\overline{U_iU_j}=\overline{\left(\overline{U_i}+u_i^{'}\right)\left(\overline{U_j}+u_j^{'}\right)}=\overline{\overline{U_i}\,\overline{U_j}}+\overline{\overline{U_i}u_j^{'}}+\overline{\overline{U_j}u_i^{'}}+\overline{u_i^{'}u_j^{'}} \tag{4.24}$$

Introducing the sub-grid scale (SGS) stresses, τ_{ij} as;

$$\tau_{ij}=\overline{u_iu_j}-\overline{U_i}\,\overline{U_j} \tag{4.25}$$

You can then rewrite the filtered Navier-Stokes equations using SGS as;

$$\frac{\partial\left(\rho\overline{U_i}\right)}{\partial t}+\frac{\partial\left(\rho\tau_{ij}+\rho\overline{U_i}\,\overline{U_j}\right)}{\partial x_j}=-\frac{\partial\overline{p}}{\partial x_i}+\mu\frac{\partial^2\overline{U_i}}{\partial x_j\partial x_j} \tag{4.26}$$

$$\frac{\partial\left(\rho\overline{U_i}\right)}{\partial t}+\frac{\partial\left(\rho\overline{U_i}\,\overline{U_j}\right)}{\partial x_j}=-\frac{\partial\overline{p}}{\partial x_i}+\mu\frac{\partial^2\overline{U_i}}{\partial x_j\partial x_j}-\frac{\partial\left(\rho\tau_{ij}\right)}{\partial x_j} \tag{4.27}$$

With;

$$\begin{aligned}\tau_{ij} &= \overline{u_iu_j}-\overline{U_i}\,\overline{U_j}\\ &= \overline{\overline{U_i}\,\overline{U_j}}+\overline{\overline{U_i}u_j^{'}}+\overline{\overline{U_j}u_i^{'}}+\overline{u_i^{'}u_j^{'}}-\overline{U_i}\,\overline{U_j}\\ &= L_{ij}+C_{ij}+R_{ij}\\ C_{ij} &= \overline{\overline{U_i}u_j^{'}}+\overline{\overline{U_j}u_i^{'}}=\text{Cross Terms}\end{aligned} \tag{4.28}$$

Pioneering works on LES have been done by Smagorinsky (1963), Lilly (1967), Deardorff (1970), Schumann (1975) and several others. ANSYS CFX uses the Smagorinsky (1963) model and this combines the Reynolds averaging assumptions given by $L_{ij}+C_{ij}=0$ with a mixing-length based eddy viscosity model for the Reynolds SGS tensor. Therefore, it is assumed that the SGS stresses are proportional to the modulus of the strain rate, $|\overline{S_{ij}}|$ of the filtered large-scale flow;

$$\tau_{ij} - \frac{1}{3}\tau_{kk} = -2 \cdot \nu_{SGS} \cdot \overline{S_{ij}} = -\nu_{SGS} \cdot \left[\frac{\partial \overline{U_i}}{\partial x_j} + \frac{\partial \overline{U_j}}{\partial x_i}\right] \tag{4.29}$$

To improve the prediction of turbulence models in highly separated areas, a hybrid approach which combines the features of the RANS formulations with elements of LES methods was implemented. This concept has been termed Detached Eddy Simulation (DES) and is simply based on the idea of covering the boundary layer by a RANS model and switching the model to LES mode in the separated regions. Compared to the classical LES models the DES approach saves a lot of computation power. DES will not be discussed any further because the approach cannot be implemented in this project and the desired flow features for e.g. flows which are completely detached such as; flows around non-aerodynamic obstacles, etc, are not inherent in the HATT project.

Section Closure

After carefully reviewing the work done on the numerical analysis of HATT in the Literature Review, chapter 3, it was evident that a suitable turbulence model was necessary to get meaningful and accurate results. Most authors were of the opinion that different two-equation based models or a RSM model were to be trialled in order to be successful at the selection of the appropriate turbulence model. Although, several authors have had tried using most two-equation models and were fairly unimpressed with the physical capture of the data concluding that more research needs to be done on the usage of the appropriate turbulence model.

After several unsuccessful attempts with $k - \epsilon$ turbulence model for this HATT project, the author made a decision to model the turbine rotor and the domain with Reynolds Stress Model SSG as mentioned earlier. The HATT project is inherently a very high turbulent case and the flow features some of the above mentioned characteristics in the RSM sub chapter. In fact, the Reynolds numbers for the HATT model approximately varies between the ranges of $7 \times 10^7 \leq Re \leq 9 \times 10^7$. The strong 3D flows in the turbine arise as a result of the association of the velocity profiles together with the rotation of the blades. The situation gets even more involved with the inclusion of wave effects. Recirculation flows can occur because of the finite channel width for both currents or waves or both and is discussed by authors such as Groeneweg & Battjes (2002). For waves with steady flows these could be seen as asymmetries in turbulence flows. Nezu & Nakagawa (1993) discusses recirculation flows for various depth-width ratios. Rotating flows, curved surfaces and stagnation points are inherent in this model, whereby justifying the use of the SSG RSM model.

4.5 Geometry and Mesh Generation

ANSYS ICEM CFD has been utilized in creating the geometry comprising of several "building blocks" called domains and finally assembling all the domains to make up the whole model in 3D space. ICEM CFD is sophisticated software which provides complex geometry creation and editing, mesh generation and mesh editing capabilities. The meshes employed were unstructured and were generated with the Tetra version of ICEM. This is the variant of the software that generates unstructured meshes. This approach was preferred over the Hexa version since unstructured grids offer a better geometric flexibility when compared with the more unwieldy structured approach (which was initially considered but eventually discontinued).

4.5.1 Geometry and Domains

The CFD model of the device comprises a three-bladed turbine together with the nacelle and pylon. This assembly is placed into a volume corresponding to a parallelepiped of $72m$ in length, $40m$ in breadth and $35m$ in height (corresponding to the tidal channel depth). The model was created using just two basic coordinates. One being $(0, 0, 0)$ and the other being $(1, 0, 0)$. At the initial stages a very basic generic blade was designed and the hub and nose was designed accordingly. Then the support structure was designed and a few minor adjustments were made to the hub and the nose to align with the other features of the system. A reference depth of $35m$ was agreed upon initially and the domain was made to that depth with $20m$ on either side of the model and a length of $60m$ aft of the model - $60m$ was considered adequate to capture the immediate and far wakes as described by Bahaj et al., (2007c), in the Literature Review. A further distance of approximately about $10m$-$11m$ in front of the plane of the blades was decided so that the flow field could be successfully formed. The basic model comprising of a single blade with its support structure in the domains are shown in Figure 4.2 and Figure 4.3.

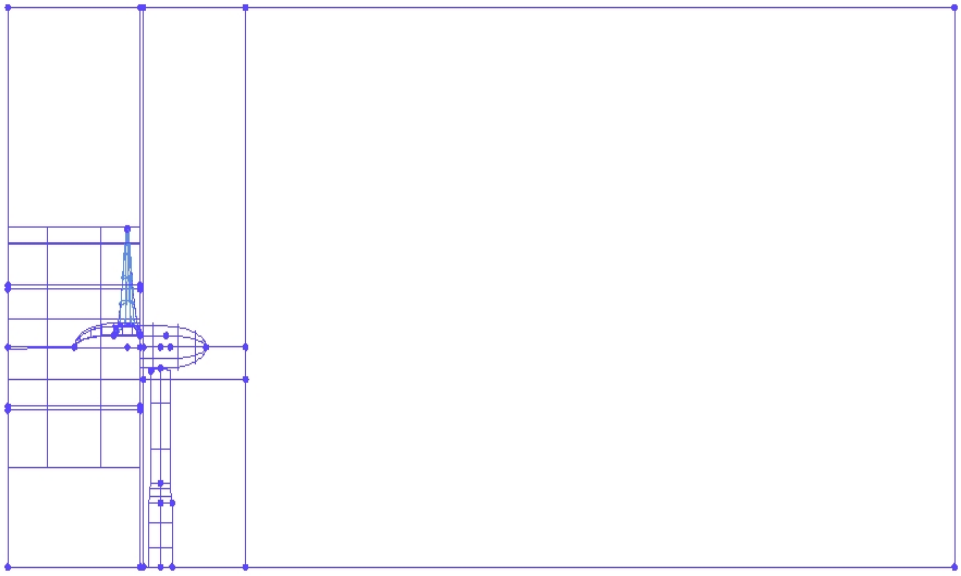

Figure 4.2 Side-on view of the model

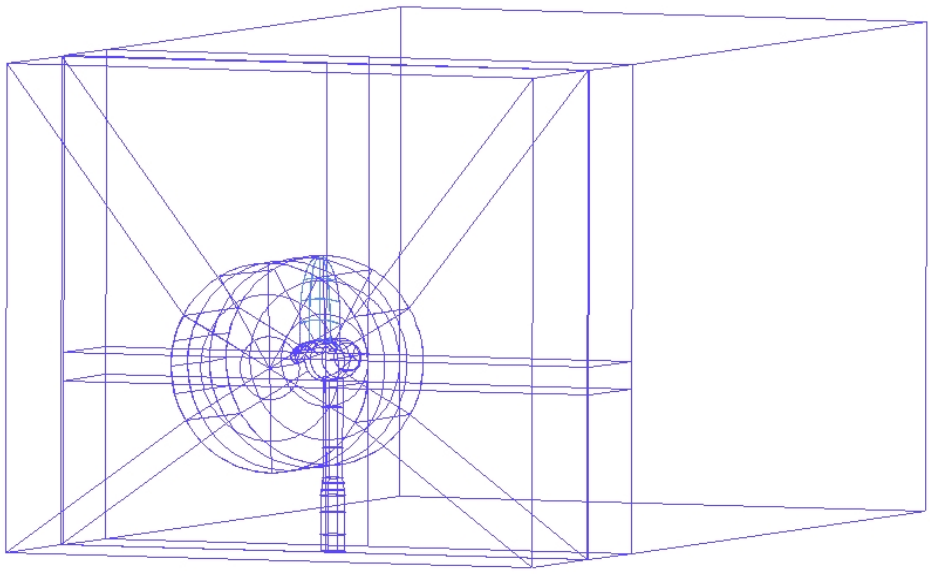

Figure 4.3 An isometric view of the model

The basic turbine component comprises a single blade, this could be easily replicated twice and rotated through 120° each to form the 3-bladed turbine. Figure 4.4 represents the domain blocks where each block fulfils a purpose. Figure 4.4(a) shows the “Frontpad”. This was designed to accommodate a frozen rotor interface. Details of this inter-block connection type are discussed in more detail in section 4.6. Figure 4.4(b) shows the “Blade-outer” block denoted as “Try”. This accommodates the rotor blocks shown in (c), and is called “Blade”. The mid section shown in Figure 4.4(d) corresponds to the back half of the hub and the pylon. This block is denoted as “ABC”. Finally the downstream block of the domain, called ”D”, was created to enable the flow to mix out after the blade and to analyse the near and far wake phenomena.

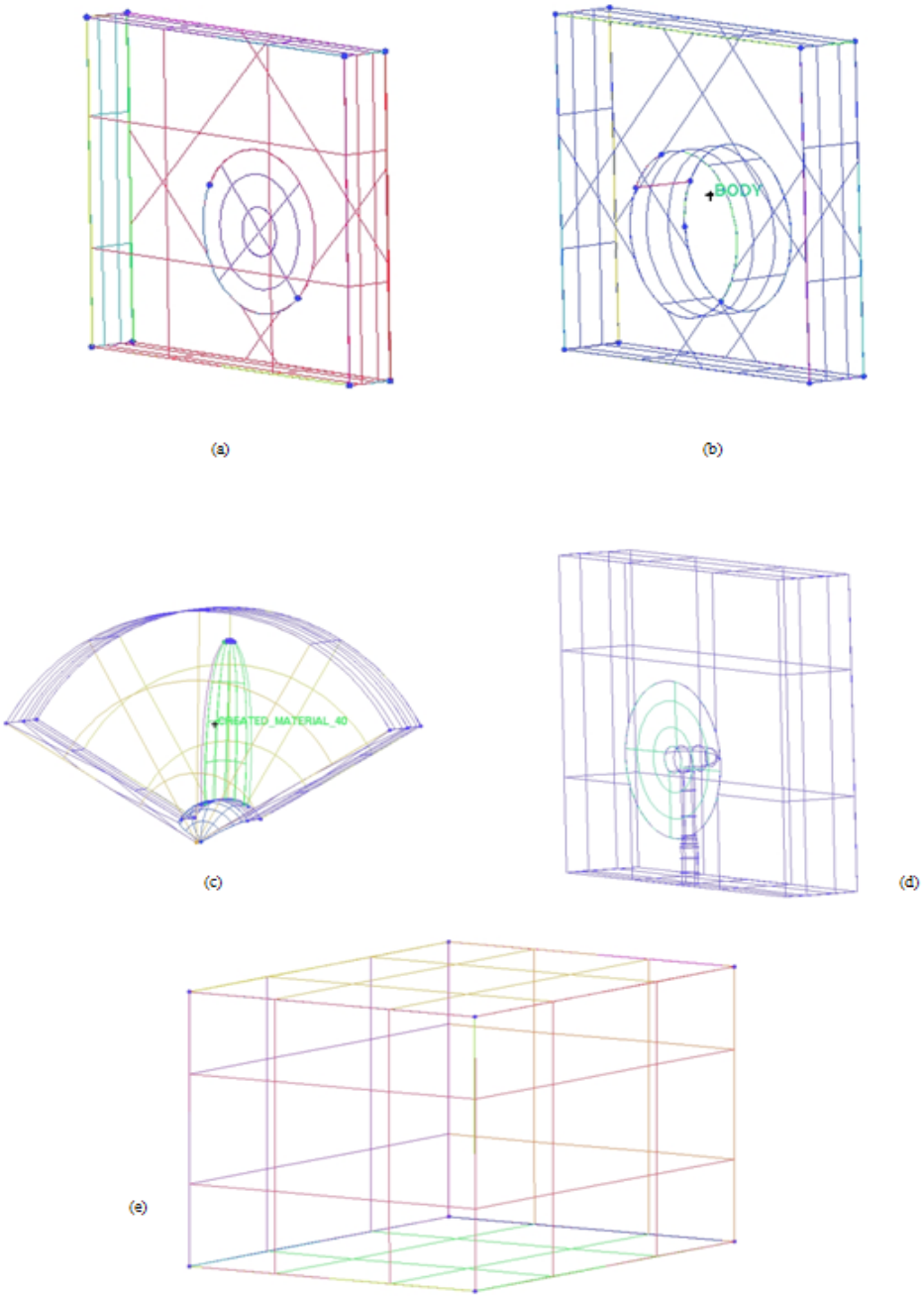

Figure 4.4 Views of separate domains

Each domain has its own unique face, correct and careful implementation of this helps in mating domains in ANSYS CFX-Pre, this is shown in Table 4.4 below.

Domain Name	Face/Part Description
Frontpad	IN OUT LEFT RIGHT TOP BOTTOM CIRCLE GEOM

Try	IN OUT LEFT RIGHT TOP BOTTOM DRUM GEOM
Blade	INFLOW DOWN FRONT BACK PR1 PR2 PSURF SSURF TOP HUB NOSE SHROUD GEOM
ABC	IN OUT LEFT RIGHT TOP BOTTOM DRUMFRONT HUB TUBE GEOM
D	IN OUT LEFT RIGHT TOP BOTTOM GEOM

Table 4.4 Part/face description of each domain

A NACA0015 blade profile was used in this model. The radius of the blade was $7.5m$ from the hub centre line. Some details about the profile thickness, blade twist, chord length, etc could be found in Appendix A, Table A.1. Only selected few profiles are displayed on the Table A.1 out of a possible $60,000$ profile sections on the actual blade geometry. The blade has an ogive like termination in the manner of a Spitfire wing, this gradual profiling from the blade root to blade tip was to reduce the blade tip vortices. In addition towards the tip the profiles become thinner. These subtle changes on the blade are enormously challenging to model and mesh.

4.5.2 Geometry Meshing

Mesh generation of all blocks were done on ANSYS ICEM CFD and the main model was created with three different mesh densities. At first, a very fine mesh was created consisting of around 7.5 million nodes. A second model was created with a node count of some 3.5 million nodes. The final model was created with approximately 1.8 million nodes. This enabled the possibility of performing a grid dependency study. However given the computation intensive requirements of the study all results presented in the thesis were obtained with the 1.8 million nodes model. The model generally was meshed using the volume mesh approach for tetrahedral/mixed meshes and the mesh methodology used was unstructured robust octree approach in conjunction with part mesh set up to control the mesh qualities at the faces of the geometry.

In Figure 4.5 the mesh used on the "Frontpad" block is shown. Tetrahedral unstructured mesh was utilised with the aid of the part mesh feature. The part mesh approach helped in maintaining a suitable number of nodes where necessary i.e. increasing the number of nodes at specific areas in the domain to capture the local flow physics better. The node count on this domain was approximately $113,000 nodes$. The maximum element size was set at 0.4 for all faces in the "Frontpad". Then this maximum element size was multiplied by the global element scale factor which was set to 1.0 to produce the actual maximum element size of 0.4 units. This method helps to globally control the mesh size instead of changing the mesh parameters for different entities.

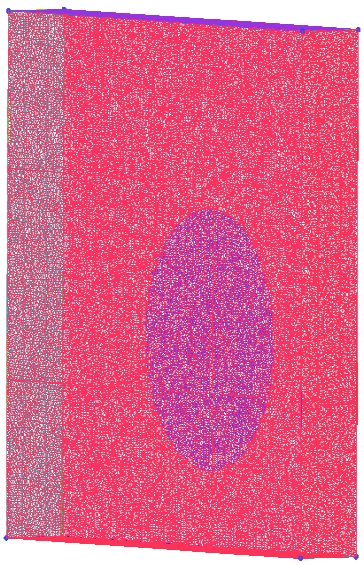

Figure 4.5 Meshed "Frontpad" block

The Figure 4.6 represents the "Try" block, also a tetrahedral unstructured mesh built with the aid of part mesh. The actual maximum element size on this domain was set at 0.6 units

and the node count is approximately $94,000$.

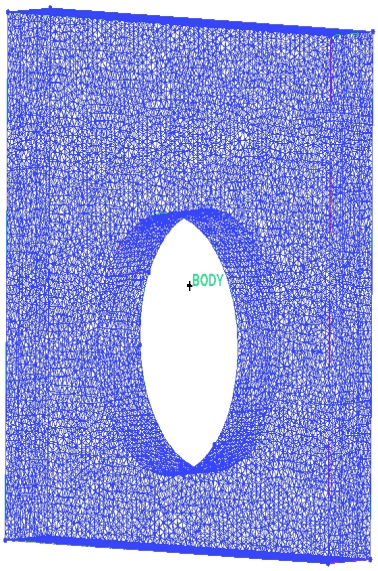

Figure 4.6 Meshed "Try" block

The Figure 4.7 shows the "Blade" block. This component was also meshed using the volume mesh with an unstructured prism mesh approach. The growth law in the global mesh parameters for prisms was selected as exponential. The number of layers was selected to be five in this case. The initial height was set to 0.00499 as the height of the first layer. The height ratio was set at 1.2. And the prism height of a particular layer is calculated using the following formulae;

$$\text{Prism height of a particular layer} = h \times r^{(n-1)} \tag{4.30}$$

$$\text{Total height at a layer, n} = \frac{h\,(1 - r^n)}{1 - r} \tag{4.31}$$

Where;
h = Initial layer height
r = Height ratio
n = Layer number

The part mesh was selected to be governed by the prism details as given above and the maximum element size was adjusted for each face to be 0.03 units for the leading and trailing edge, tip and pressure and suction surfaces. 0.6 units were set for the inflow, down and the shroud. Hub and the nose were set at 0.2 units. And finally the periodic 1 and 2 surfaces were set at 0.3 units. The total number of nodes was approximately $354,000$.

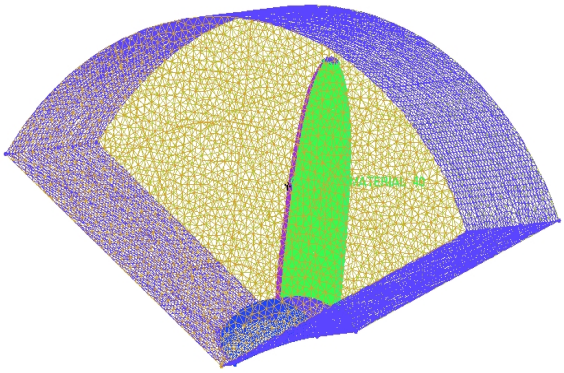

Figure 4.7 Meshed ”Blade” block

The rear section of the hub consisting of the pylon, “ABC”, was meshed together using the same methodology as the “Try” and the “frontpad”. The part mesh details include 0.8 units at the IN, OUT, LEFT, RIGHT, BOTTOM and TOP. 0.3 units at the HUB, DRUMFRONT and TUBE. The number of nodes are calculated to be approximately $138,927$. The Figure 4.8 illustrates the meshed geometry of the ”ABC”.

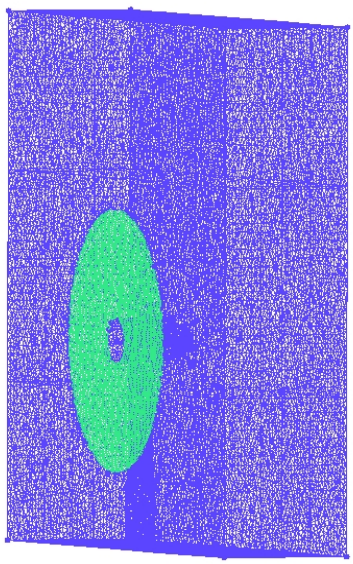

Figure 4.8 Meshed ”ABC” block

The last block “D” is meshed in the same manner as the other domains. Because of the large volume of this block, the number of nodes is higher than for the others, $250,000$ nodes approximately. The part mesh includes 0.9 units at the BOTTOM, IN, LEFT, RIGHT AND TOP surfaces. The OUT surfaces has been set at 1.0 unit as even reducing it to 0.9 will contribute to a large mesh. Figure 4.9 illustrates the meshed ”D” block.

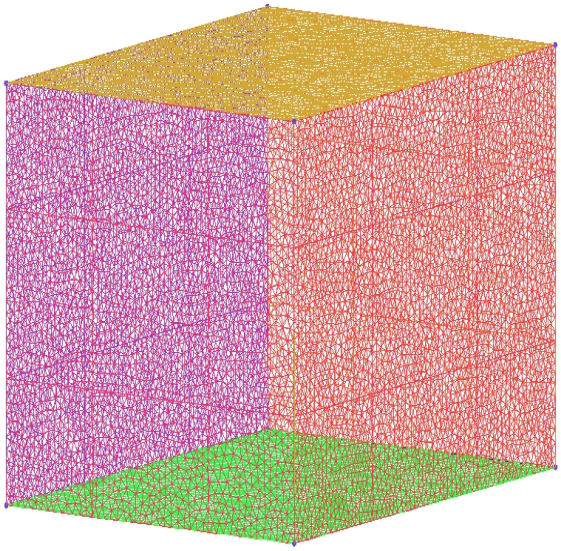

Figure 4.9 Meshed ”D” block

4.6 Model Initialisation

For the steady state simulations the blades were set at pre-defined locations. Three cases have been implemented as steady state computations. These are called Model_a, c and e. The three cases and reference angles of individual blades are detailed in Table 4.5. This was done so that the simulations capture positions that were interesting from a of blade-pylon interaction perspective (which was part of the objective of the steady state simulations).

Blade No.	Case Name		
	Model_a	Model_c	Model_e
1	79.61	34.61	139.61
2	199.61	154.61	259.61
3	319.61	274.61	19.61

Table 4.5 Steady state summary of cases

The Figure 4.10, through to Figure 4.12 illustrate the three cases with reference to the position of the blades (each of which is numbered in the figures) relative to the pylon. The rotors rotate in an anti-clockwise direction.

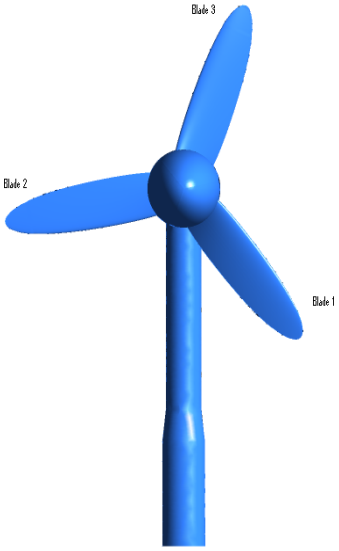

Figure 4.10 Model_a

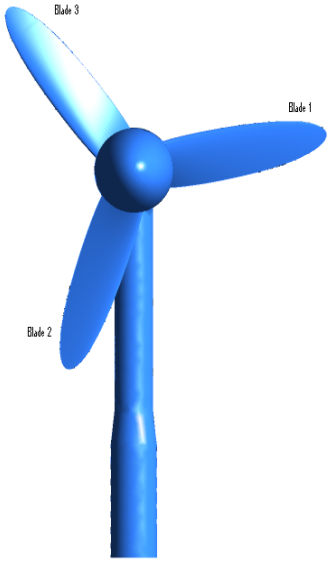

Figure 4.11 Model_c

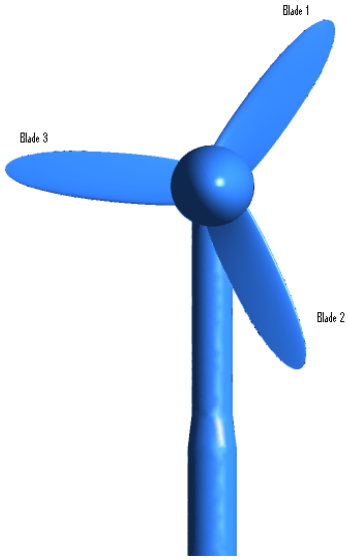

Figure 4.12 Model_e

The simulation type was initially set to steady state for initial solving purposes. The subsequent Chapters 5, 6 and 7 discuss the steady state and transient cases in more detail. A default domain was created which consists of all mesh blocks expect that of the rotor. The motion of the default domain was set to stationary, domain type was set to fluid and water was selected. Heat transfer option of the fluid was set to isothermal and fluid temperature at $5°C$ was set. A reference pressure of $1atm$ was selected and the non-buoyant option was also activated. The turbulence option was initially set to laminar to get initial results and then to turbulent employing the $k - \epsilon$ model or any other suitable model. As discussed earlier in section 4.4, the most suitable turbulence model was the Reynolds SSG model and this was implemented in all of the simulations. .

A boundary layer profile for $2.7ms^{-1}$ at the water surface was set at inlet together with a turbulence intensity of 5%. A part of the details of the boundary layer profile file can be found in Appendix A, Figure A.1 and its physics in section 2.5. At the outflow an average static pressure of $200,000Pa$ was used. The side walls were set as free slip zones (where the shear stress at the wall is zero and the velocity of the fluid by the wall is not retarded by the wall friction effects) and were identified for the left and right sides of the model. Top water surface was identified selecting all the TOP parts in the model and was selected as a wall with free slip, while the sea bed was set to no slip (fluid velocity at the wall is set to zero) with a roughness height of $0.05m$ to simulate the sea bed irregularity.

The rotor domain was set to rotating with an angular velocity of $-9.29rpm$ about the X - axis. The surface velocities for the boundary layer profiles and the angular rotation of the rotors are independent and have a fixed set of data corresponding to the sponsors needs in

relation to the design point calculations in mind. The reference pressures and the buoyancy were matched to be the same as that of the default domain.

The CIRCLE of the Frontpad was mated with the INFLOWS on the rotor block using a general connection, frozen rotor technique. General Grid Interface (GGI) was selected for the mesh connection type. The DOWNFLOW surfaces of the rotor was mated with the DRUMFRONT of the domain block ABC using the same principle as mentioned above. The periodic boundaries of the rotor blocks were set as fluid-fluid interfaces using a general connection. The SHROUD surfaces of the rotor domain were mated with the DRUM of the Try domain using the frozen rotor interface. In the frozen rotor principle, the relative positioning of the two frames of reference across the interface is fixed throughout the calculation but the pitch or the frame of reference is changed. This method is mainly used for steady state simulations.

The advection scheme was set to run on high resolution with 1000 iterations; the time scale option was selected to auto timescale and the length scale option was set to conservative with a timescale factor of 1.0. For the convergence criteria a RMS residual target of 1×10^{-6} was set. As a precautionary measure, back ups were created every 100 iterations.

4.7 Solver

After the initialization process a definition file was created ready to be solved in the ANSYS CFX-Solver either using serial or parallel processors. This model is incapable of running on a serial processor in local desktop machines due to the high level of memory and processor requirements. Therefore the simulation was set to be run either on the Cranfield University's Astral or Grid clusters.

Astral is an independent large Linux cluster intended for developing and/or running parallel "MPI" Distributed Memory applications with many processors per job. Astral is a major University-wide research facility. The system is based on the HP $DL140G3$ cluster. It has $214\times$ HP $DL140G3$ servers each with $2\times$ Intel 5160 Woodcrest processors clocked at $3.0GHz$, therefore a total of 856 user-accessible processors are available and each core has a theoretical performance of $12Gflops$ with a total theoretical performance (Rpeak) of around $10Teraflops$. It has two large Shared-Memory login nodes (front-ends) - $2\times$ H-P $DL580$ servers with 8 Intel Xeon 7130 cores and $64GB$ of RAM. The file server space is based on the H-P SATA (Serial Advanced Technology Attachment) RAID (Redundant Array of Independent Disks) array with $30TB$ useable storage offered as an HP SFS (StorageWorks Scalable File Share) parallel file system. The typical cost of an equivalent super computing facility is around $£1000,000$.

The Grid is a smaller Linux cluster primarily intended for running single processor applications with the capability to run small scale typically less that 4 processor jobs for parallel applications. The Grid is integrated with the University's Linux based PCs and hence is not totally independent as is the case with Astral where the user numbers are restricted to PhD and staff users. It has approximately 150 user accessible processors. Most of the processors are based on the Intel 5272 processor architecture clocked at $3.4Ghz$. Some processors are also based on the AMD technology as well. The typical cost of such a Grid system is approximately around $£80,000$.

4.8 Chapter Closure

This chapter described the choices made during the preliminary part of the project regarding the type of turbulence model to be employed. Preliminary investigations led to the identification of the SSG Reynolds Stress Model (RSM) as the model of choice for the analysis of the HATT. This model gave a consistent performance in terms of its predictions of the wake, blade-pylon interaction and fluid-rotor interactions. These predictions are discussed in more detail in the subsequent chapters. Several two-equation models mentioned in this chapter did not perform well due to the fact that the flow had inherent qualities of separation, adverse pressure gradients, swirls, high Reynolds numbers and finally its geometrical structure. In many trials the convergence was poor and the flow had an unphysical appearance in places and in some trials the solver was terminated with sudden physical errors.

Chapter 5

Turbine Design and Steady State Analysis

5.1 Introduction

The turbine employed in this study was designed by Mr. Chris Freeman, acting as a consultant to the Turbomachinery Group in Cranfield University. The design methodology employed is discussed in this chapter and design intent performance predictions obtained with a BEMT code are presented. These are complemented by a set of steady state numerical predictions run by the author as part of his academic program.

A set of flow conditions, comprising a range of tidal flows and rotational velocities, were identified as the most significant ones for investigation purposes. In addition a number of model variations were investigated. These sought to account for the effects of the presence of the pylon, the axial separation of the pylon and the blades and the effects due to the flow approaching the turbine with a yaw angle. The investigation also covered the effects of varying the inflow turbulence.

5.2 Rotor Design Intent

As discussed in Chapter 1, the main requirements for the design of the tidal turbine were guided by the design philosophy that the turbine needed to be simple and hence likely robust and requiring a minimum of maintenance. The essential quality was to survive the harsh marine environment.

5.2.1 Design Requirements

The design requirements are as follows;

- The structure should utilise a triangular base to ensure that all of its feet are in contact

with the sea bed

- The device should be freestanding, i.e. held in place by its own weight
- The total power output to be no less than $1.2MW$ across the 3 turbines at a flow velocity of $2.3ms^{-1}$.
- Maximum weight of the structure to be not more than 250 tonnes in air. This value corresponded to the lifting capacity of the Mersey Mammoth, the largest sea-going self propelled crane on the UK west coast, refer Figure 5.1
- Frictional resistance - the coefficient of friction, μ, is 0.75 with a safety factor of 1.35. The weight was assumed to be no more that 250 tonnes in air. Therefore the maximum axial thrust on the support frame and the turbines should not exceed the available friction which equates to a maximum thrust of 40.5 tonnes per turbine
- Cavitation - this is thought not to affect at the depths at which the turbine is designed to operate in
- Extreme loads - although the turbine is designed to operate in harsh conditions there might be extremely rare cases of abnormal behaviour in the marine flow, then the rotors can be furled to reduce the drag on the frame
- The structure to be made in sections for ease of transportation of the parts to the final assembly site
- The structure to be made of circular hollow sections in order to reduce manufacturing costs by employing standard pipe sections

Since the tidal turbine is freestanding the "management" of the axial thrust is of vital importance. Therefore, the tidal turbine had to be designed so that the total thrust on the structure and the rotor system is less than the frictional forces opposing any motion. This lead to a design requirement where the power-thrust ratio is a maximum for the turbine. Since, the design needs to be simple, reliable and robust the intent was to implement a fixed pitch turbine system. The professional experience of some of the TEL staff members with variable pitch mechanisms suggested that any performance benefits would be outweighed by the attending complexity and maintenance needs of this method.

Fixed pitch turbines employ stall regulation to keep the rotational speed within a given range. Usually stall regulated wind turbines operate at nearly constant speed and therefore the angle of attack of the relative velocity will increase as the flow velocity increases. When the wind reaches a certain value the angle of attack will exceed the lifting capability of

Figure 5.1 Mersey Mammoth - sea crane

the blade profiles and the blade will stall. The stall lowers the torque, and increases the drag, and the turbine is then kept within a given band of power. However, stall regulated wind turbines are prone to large transient loadings as the stall is an unsteady process which generates strong turbulent effects.

However there are some strong advantages to using fixed pitch turbines. The benefit of employing a variable pitch solution in terms of cost per MWh can be as little as 4% when compared to the fixed pitch alternative, (DTI, 2007). Therefore, considering all the available data, a decision was made to employ fixed pitch control. How this was achieved is explained in the following sections.

5.2.2 Design Philosophy

The primary constraint for the design of the tidal turbine is the limitation of the axial thrust because of the gravity based design approach for the support frame. Therefore to determine which TSR would yield the maximum power for a given thrust, calculations were made for a range of designs at different blade staggers (angle of the airfoil to the tangential direction) using a BEMT method, (Freeman, 2009c). The Figure 5.2 shows the C_P & C_T plotted against a range of TSR's corresponding to various 3 tip staggers from $2°$, $6°$ and $10°$.

From the plot, it can be shown that at low blade staggers the turbine thrust is increased when the TSR increases. The novel aspect of this design, which does not fit in the common classifications of fixed pitch control methods, is that through a combination of the selection of blade pitch, and hence, the shape of the C_T curve, and the enabling of the speeding up of the turbine, increasing the TSR, the growth in axial load can be checked and even lowered

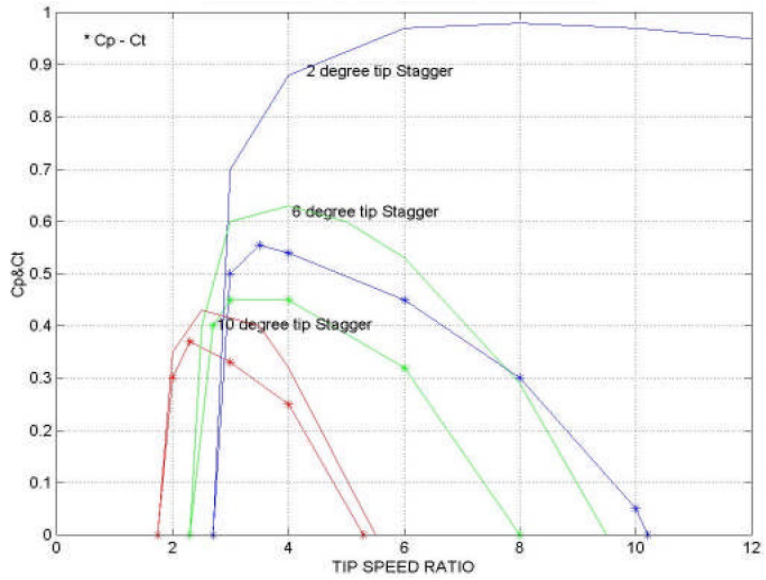

Figure 5.2 Coefficient of thrust and power with TSR over a range of blade staggers, (Freeman, 2009c)

as the TSR increases.

This means if the grid fails, and therefore ceases to absorb power, the turbine will speed up leading the thrust of these turbines to decrease. Conversely as shown on Figure 5.2, as the stagger increases, the TSR decreases along with the ratio of C_P / C_T max, therefore, the drag for a given power decreases. The drag at no load also reduces and the speed increase from full power to no power reduces. Therefore, low TSR has many advantages for the design requirement of the tidal turbine. But the size of the turbine for a give power increases. Issues of cavitation are minimised at lower TSR's as the local static pressure decreases with the lower velocities and larger chords.

A typical C_P and C_T plot against TSR for horizontal axis turbines is shown on Figure 5.3. It can be observed that as the TSR increases the turbine power coefficient decreases rapidly past the peak point. However the thrust coefficient hardly falls below the top thrust value. In fact, often this line shows an increasing trend after the point of inflection.

This is undesirable, as are the problems associated with stall control mentioned previously. The reader is directed to the work of Bahaj (2007a,b), Egarr (2004), Fan (2010) and Nicholls-Lee (2007) where C_P and C_T plots with the appearance of Figure 5.3 are shown. However the design philosophy in these turbine designs is to maximise power capture.

The design philosophy in the DeltaStream project was to manage the thrust first and foremost. To achieve this a lower C_P had to be accepted since this was part of the price to pay for the higher C_T control goal.

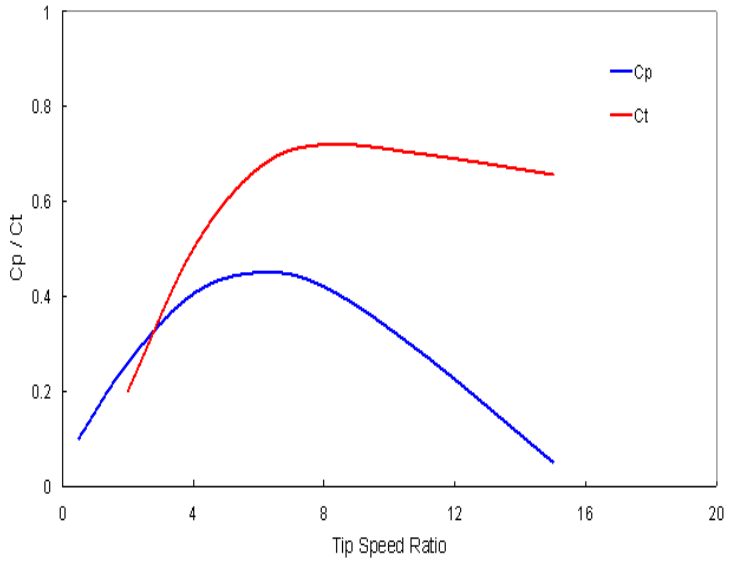

Figure 5.3 Stereotypical thrust and power coefficient with various Tip Speed Ratios

Figure 5.4 shows the C_P and C_T curves against TSR for the DeltaStream HATT.

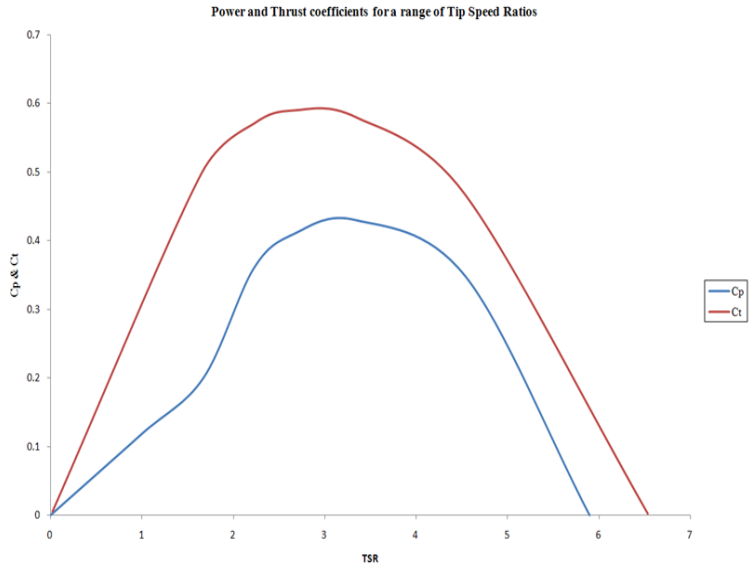

Figure 5.4 Coefficient of thrust and power with various Tip Speed Ratios (Freeman, 2009a)

5.3 Turbine Operational Schedule

The operational philosophy of the turbine is rooted in the design principles expressed above. Essentially, the turbine rotational speed increases with an increase in the tidal velocity. Once a threshold is reached the turbine is allowed to gather rotational speed, Figure 5.5. In this way power is shed from that point onwards, Figure 5.6, and given the shape of the C_T curve the thrust begins to drop from that point onwards, Figure 5.7. The variation of torque is shown in Figure 5.8.

Five points on the curves shown in Figure 5.5 to Figure 5.8 were selected for CFD simulations. In the first case, denoted (F1), the turbine rotates at $4.2\ RPM$ while the channel surface velocity is $1.2ms^{-1}$. The second case (F2) has a rotation of $6.2\ RPM$ and a surface water velocity of $1.8ms^{-1}$. The third (F3) is $9.29\ RPM$ at $2.7ms^{-1}$ at the surface and finally the last case, (F4) has a rotational speed of $21.0\ RPM$ at a surface water velocity of $3.6ms^{-1}$. In addition to all these simulation parameters, the turbine start-up case was also simulated, were the surface flow velocity was set to a relatively low speed of $0.8ms^{-1}$ with a rotational velocity of $0.0\ RPM$.

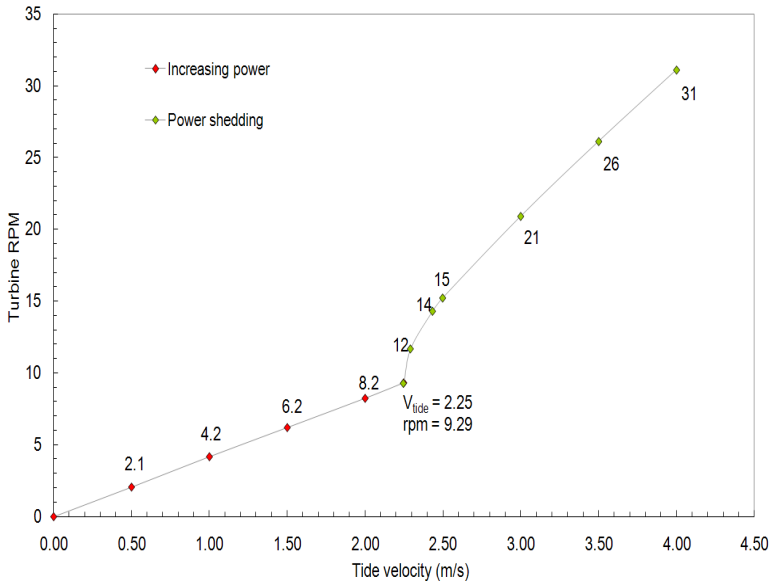

Figure 5.5 Variation of turbine RPM with tidal velocity

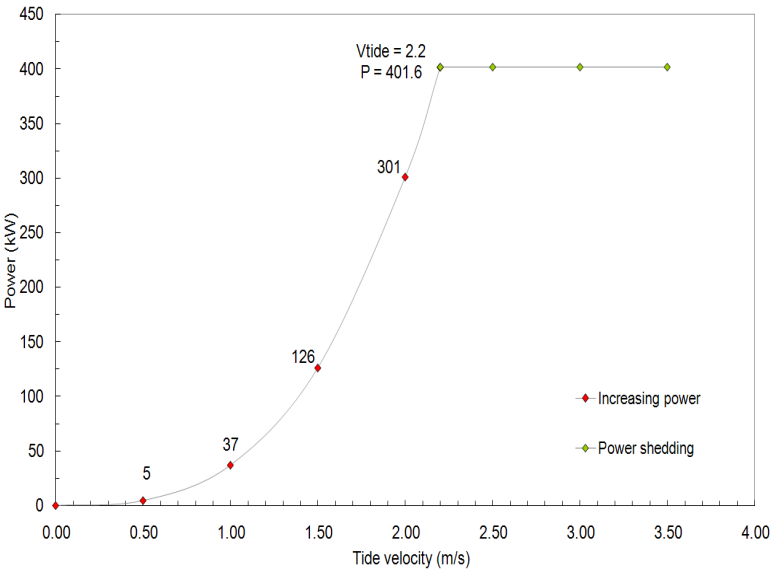

Figure 5.6 Variation of power with tidal velocity

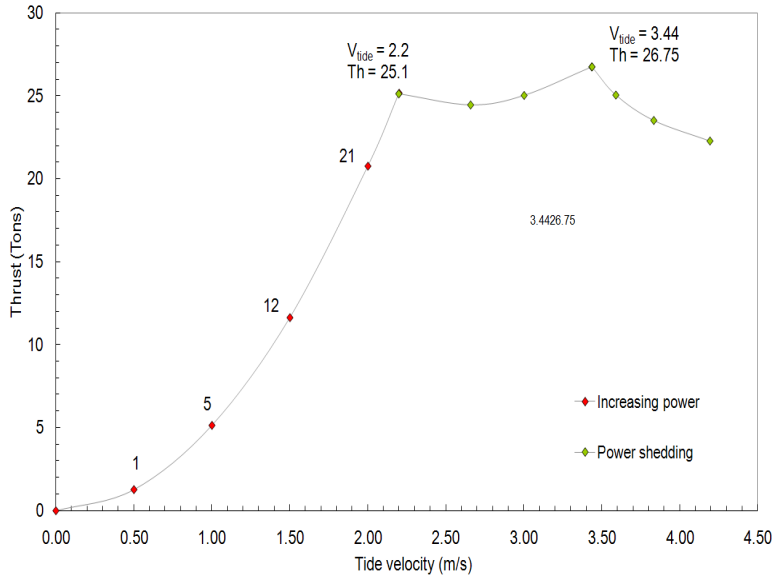

Figure 5.7 Variation of thrust with tidal

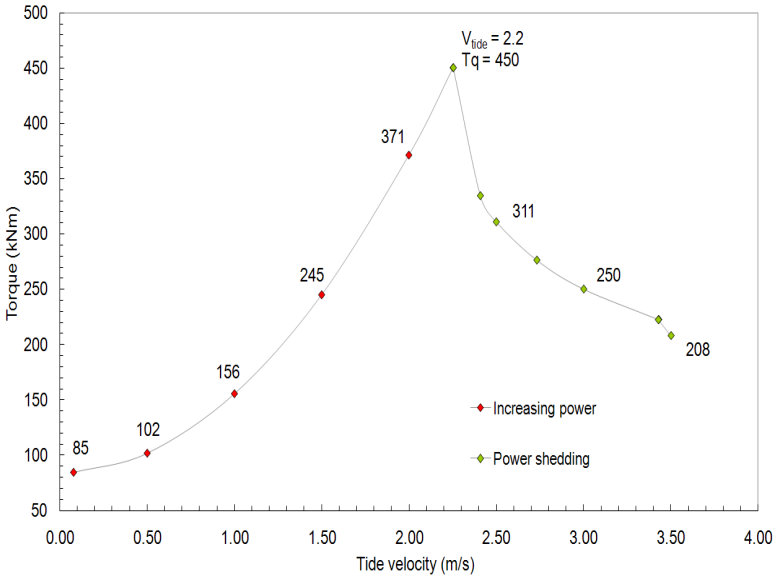

Figure 5.8 Variation of torque with tidal velocity

The steady state CFD simulations consisted of the three models at different angular settings for each of the flow conditions as discussed above.

5.4 Initial Model Overview

Soon after the key objectives and basic concepts of the project was specified and agreed by TEL and Cranfield University, the CFD domain dimensions were agreed upon. These initially agreed dimensions included the operational water depth, hub height, blade-pylon spacing, hub/nose and pylon specifications and the domain specifications. These dimensions

corresponded to an initial pass and were subject to change through the initial analysis phase of the project. The domain specifications have been stated in section 4.5.1. The dimensions of the hub height, blade-pylon spacing and pylon and hub thickness are shown in the 2D illustration on Figure 5.9.

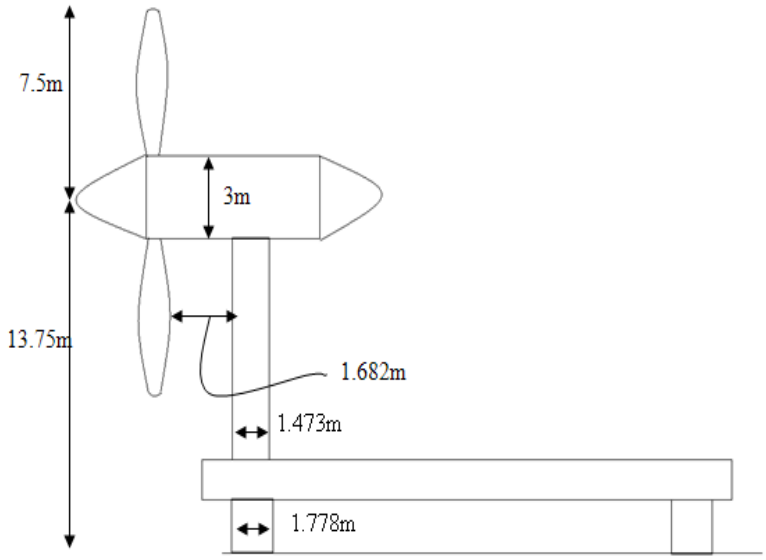

Figure 5.9 Side view of the rotor and support structure

The domain dimensions as stated in section 4.5.1 together with the dimensions shown in Figure 5.9 were applied to the model designated as the "normal_spacing_model".

5.5 Model Variations

In order to investigate the implications of the change of blade-pylon spacing several different blade-pylon spacing models along with the initial normal_spacing_model were created. This was done primarily to compare the loadings associated with the varied models. Besides factors such as pressure loading on the blades and blade-pylon interaction, cost effectiveness to building the rotor-pylon system was given a thought when selecting the most suitable model for further analysis and testing. The three models that were created to investigate and understand the blade-pylon spacing effects were a model with increased blade-pylon spacing and a model with reduced blade-pylon spacing with respect to the datum model. The flow conditions for the entire blade loading plots in the model variation section were set out in accordance with the parameters as described in more detail in section 5.3. The inlet velocity boundary layer at the surface was set to $2.7ms^{-1}$ with a turbine rotational speed of $9.29\ RPM$ corresponding to the F3 case, the nominal power condition.

5.5.1 Increased blade-pylon Spacing Model

A model with a blade-pylon spacing of $2.523m$ was created to study and analyse its interaction. This spacing was 1.5 times that of the normal_spacing_model and was achieved by creating an additional block between the rear hub/pylon block (ABC) and blade/mid-hub block (Blade). Apart from this additional block, all other blocks remain the same as in the normal_spacing_model. This model was termed as the "Inc_spacing_model". Meshing of this block was completed in exactly the same methodology as the other common blocks to the standard model.

Figures 5.10, 5.11 and 5.12 shown below are blade loading plots at 25%, 50% and 90% of the span against the streamwise (chord) position respectively. Figure 5.13 displays the blade positioning of the model.

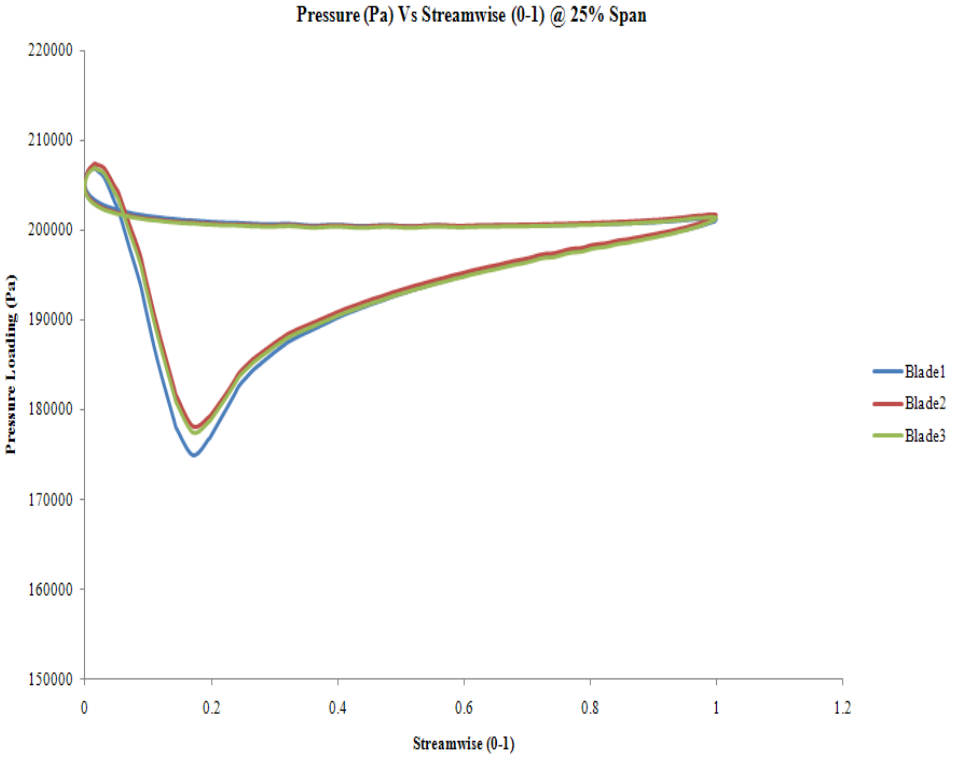

Figure 5.10 Pressure plot at 25% span - Inc_spacing_model

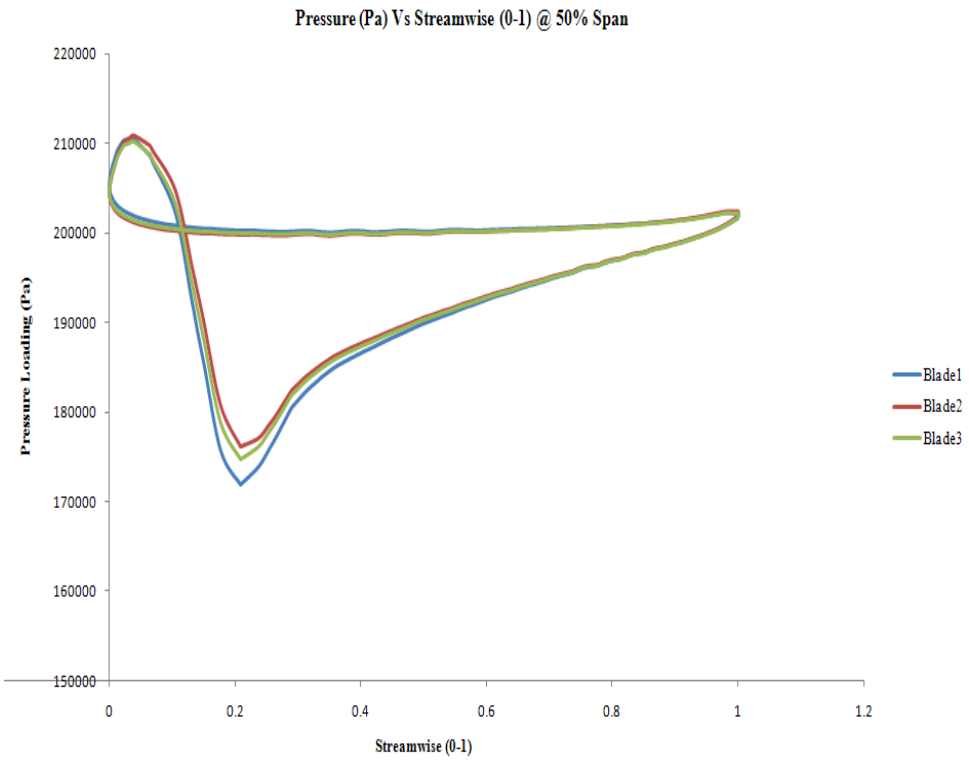

Figure 5.11 Pressure plot at 50% span - Inc_spacing_model

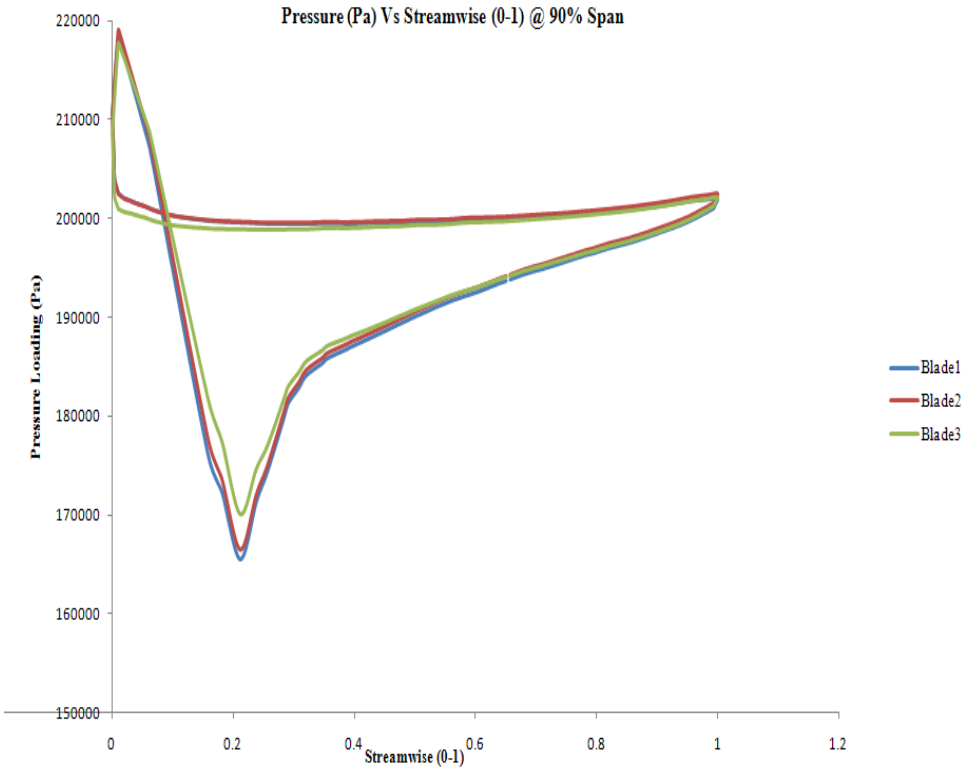

Figure 5.12 Pressure plot at 90% span - Inc_spacing_model

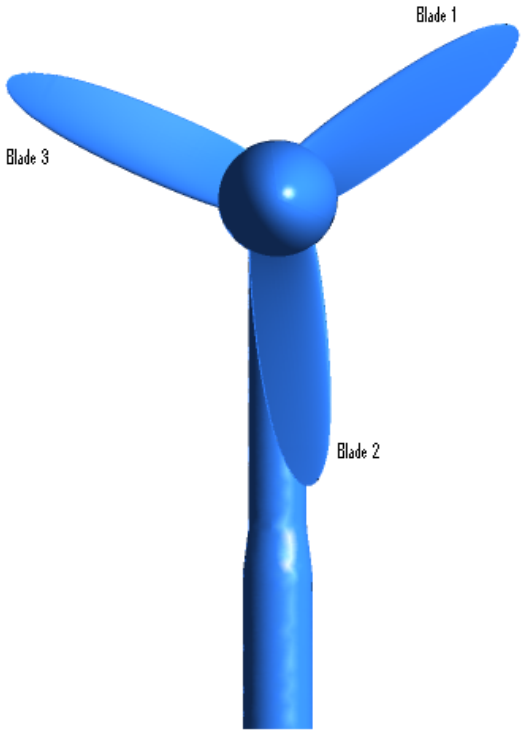

Figure 5.13 Blade positioning - Inc_spacing_model

The area between the curves on the pressure loading plot yields the force which is created by the blades. This force will have a tangential (the torque) and an axial component and these in turn have corresponding lift and drag forces. Therefore, the larger the area under the pressure loading plot, the larger the force generated. As seen from the pressure plots in Figures 5.10 to Figure 5.12, the area under the plot increases, as expected, with span and at 90% span produces the highest force. Blade 2 is positioned roughly upstream of the pylon, Figure 5.13, which accounts for yielding the least amount of force due to the high interference between the blade and pylon.

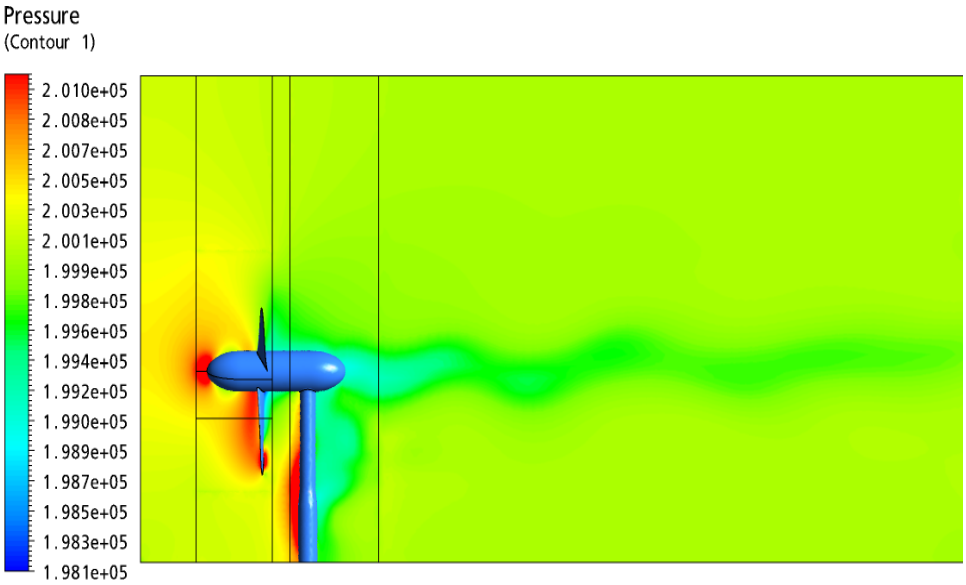

Figure 5.14 Pressure distribution in the meridional plane - Inc_spacing_model

Figure 5.14 shows the wake distribution of the model using a contour plot. The static pressure distribution associated with the wake is plotted in a meridional plane. The shape of the wake suggests that there are transient effects associated with it. The potential effects associated with the stagnation locations are apparent (coloured in red in this plot). Interestingly enough the section of the pylon immediately downstream of the blade sees a quasi absence of this effect. The pressure recovers quite promptly after only a few diameters, $1-3D$ downstream of the rotor. This is also noted by Bahaj et al., (2007c). In Figure 5.15 the pressure distribution in a plane located roughly 1/3 of the span is presented. The interaction between the blade and the tower is not marked, other than by the fact that the blade shadows the pylon.

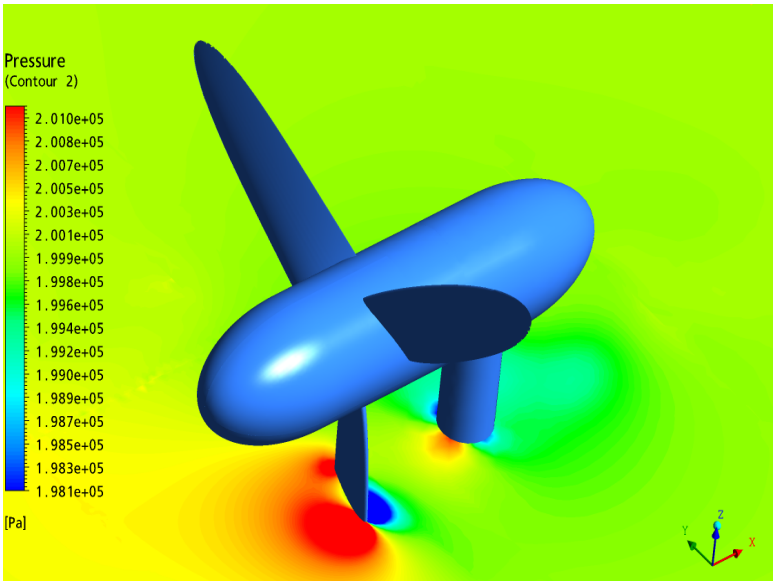

Figure 5.15 Blade-pylon interaction - Inc_spacing_model

The side on view of the increased spacing model is shown in Figure 5.16. The implications of this design is that the bending loads loadings created by the movement of the rotor impart additional stresses on the pylon and hub given the large separation.

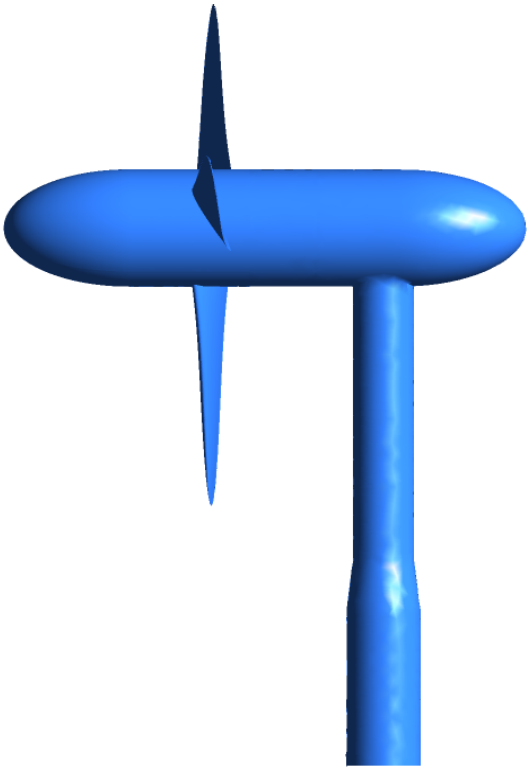

Figure 5.16 Side view of the Inc_spacing_model

5.5.2 Decreased blade-pylon Spacing Model

A model with half the blade-pylon spacing of the normal_spacing_model was created to understand the physics of interaction between the blades and pylon. The blade-pylon spacing was set at $0.841m$. This model is denoted as the Half_spacing_model. This was designed by shortening the blade/mid-hub domain from the normal_spacing_model. Figures 5.17, 5.18 and 5.19 show blade loading plots for this model. The blade orientation of the model is similar to that of the normal_spacing_model. The reduced pressure in blade 2, by comparison with the previous case is apparent.

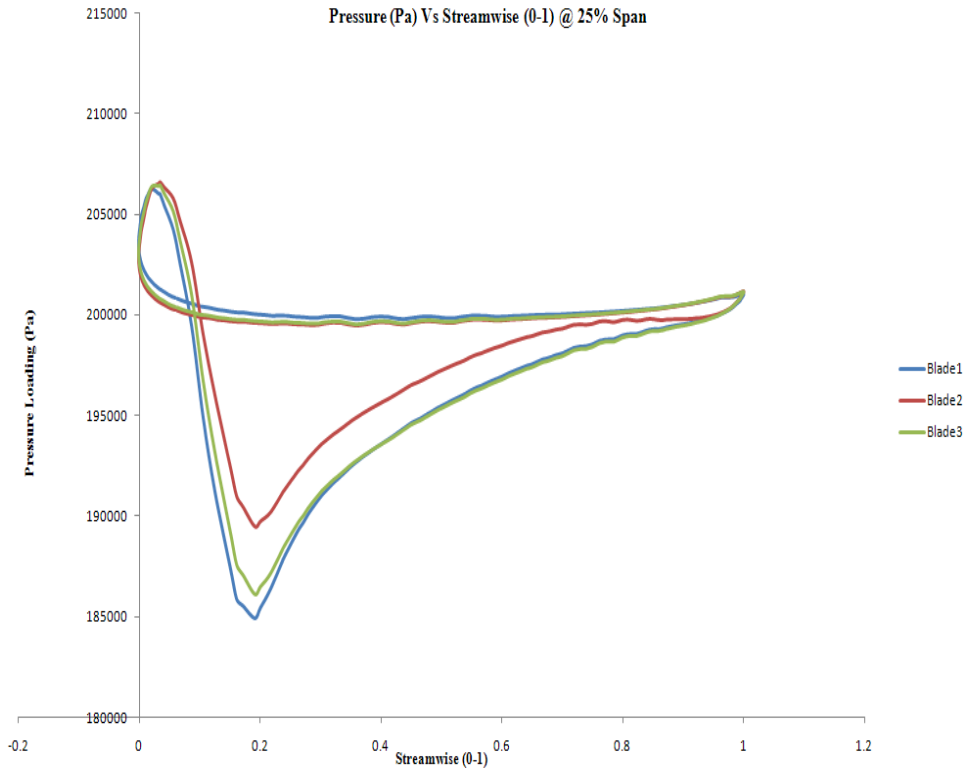

Figure 5.17 Pressure plot at 25% span - Half_spacing_model

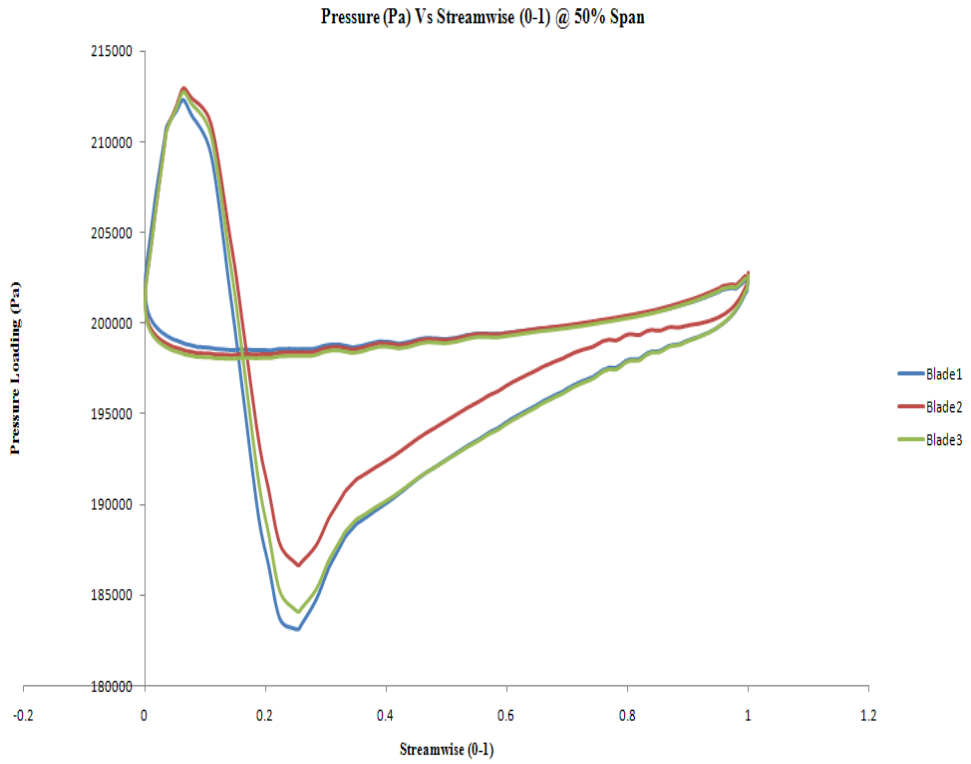

Figure 5.18 Pressure plot at 50% span - Half_spacing_model

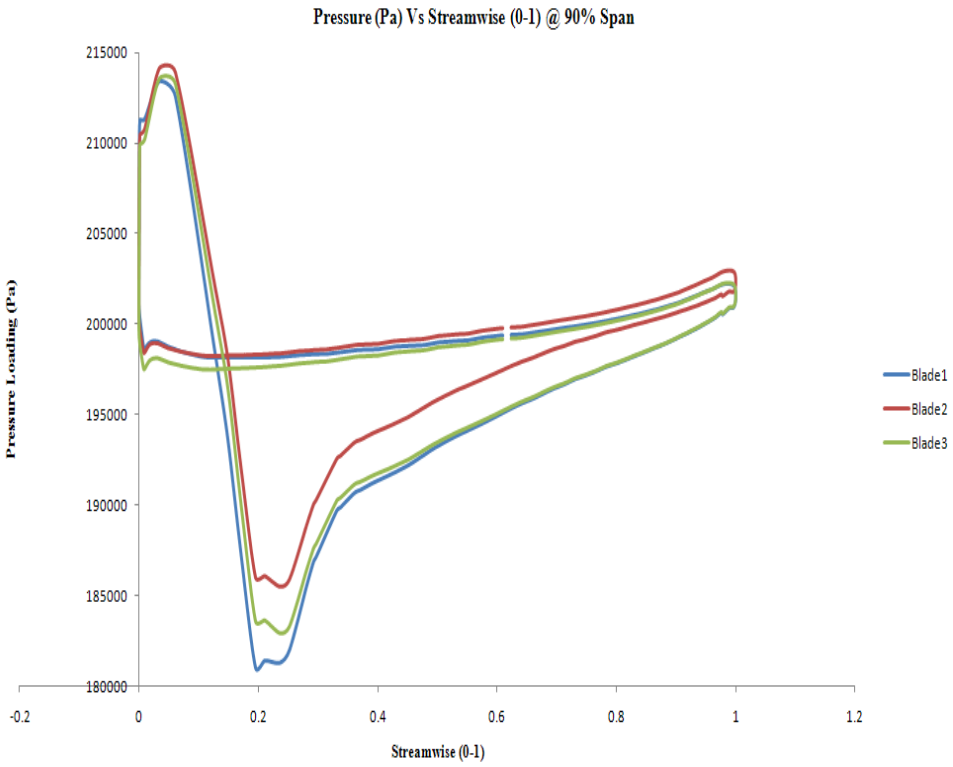

Figure 5.19 Pressure plot at 90% span - Half_spacing_model

Figure 5.20 shows the side view of the Half_spacing_model model.

Figure 5.20 Side view of the Half_spacing_model

Figure 5.21 shows the wake distribution for the model. The colour of the pressure contour is somewhat misleading. Whereas in the corresponding previous plot the stagnation point in the bullet end (nose), the blade span and the half section of the pylon were coloured red, now these appear in a much lighter colour. What happens though is that these regions do not in this plot correspond to the peak values in red. That region is associated with the tip of the blade as it sweeps past the pylon. Therefore in this spacing a strong interaction takes place at the blade tip when near the pylon.

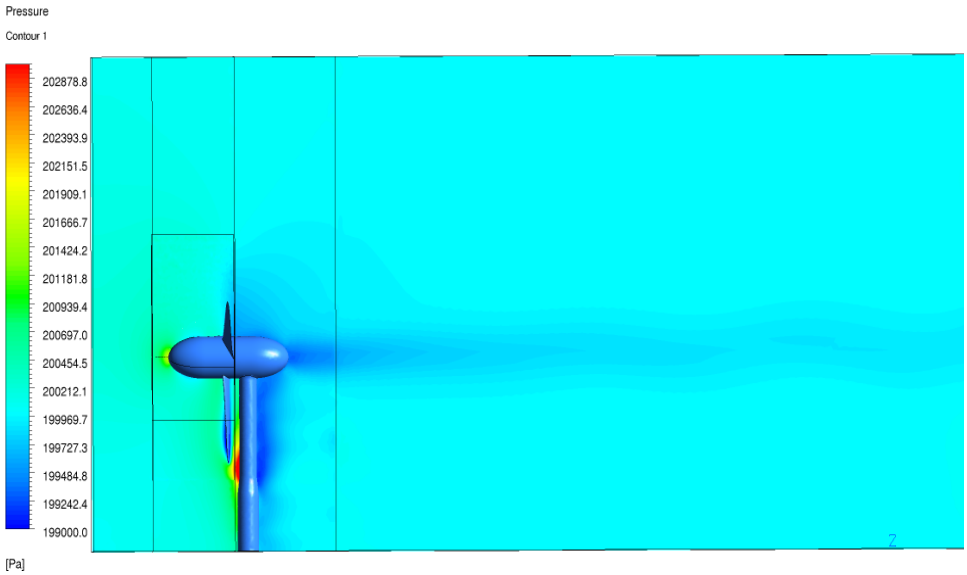

Figure 5.21 Pressure distribution in the meridional plane - Half_spacing_model

The Figure 5.22 below represents the blade-pylon interaction of the model using a contour plot of pressure plotted in a plane located approximately 1/3 of the blade span. The pressure reaches a higher value than for the large separation case.

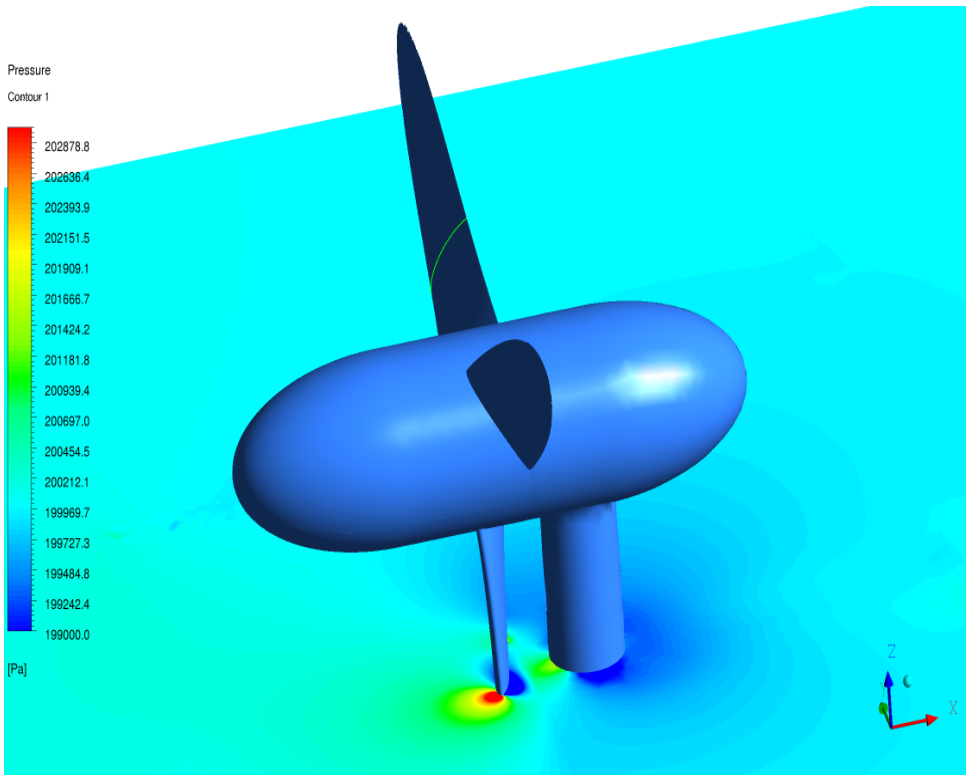

Figure 5.22 Blade-pylon interaction - Half_spacing_model

5.5.3 Normal blade-pylon Spacing Model

The blade-pylon spacing was set at $1.682m$ as mentioned at the start of this section. Figures 5.23, 5.24 and 5.25 represent the pressure (blade loading) vs streamwise positioning for 25, 50 and 90% of the blade span respectively.

The variation in the shape of the blade loading profiles between the normal_spacing_model case and the other two models is not marked. There are subtle variations in the shape of the side of the curves that correspond to the suction side. In common with the Half_spacing_model the pressure in blade 2 is somewhat lower (in terms of depression below the farstream value) than for the other blades. In any case it is the suction side that exhibits this difference. Since that pressure is related to the local velocity this is explained by the reduction in velocity provoked by the tower shadow.

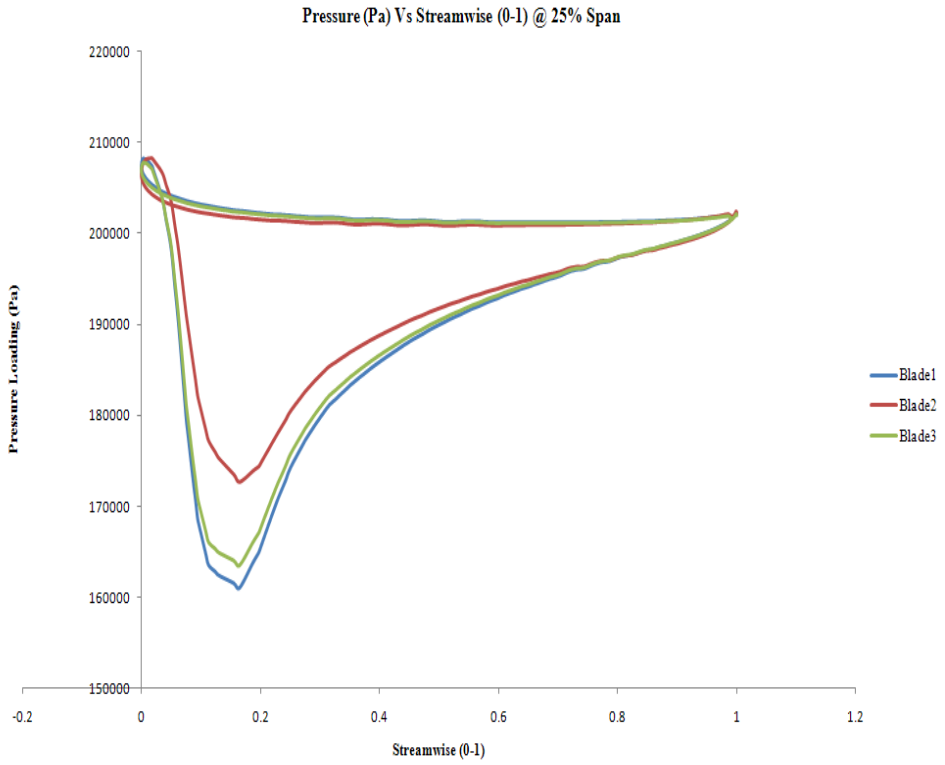

Figure 5.23 Pressure plot at 25% span - normal_spacing_model

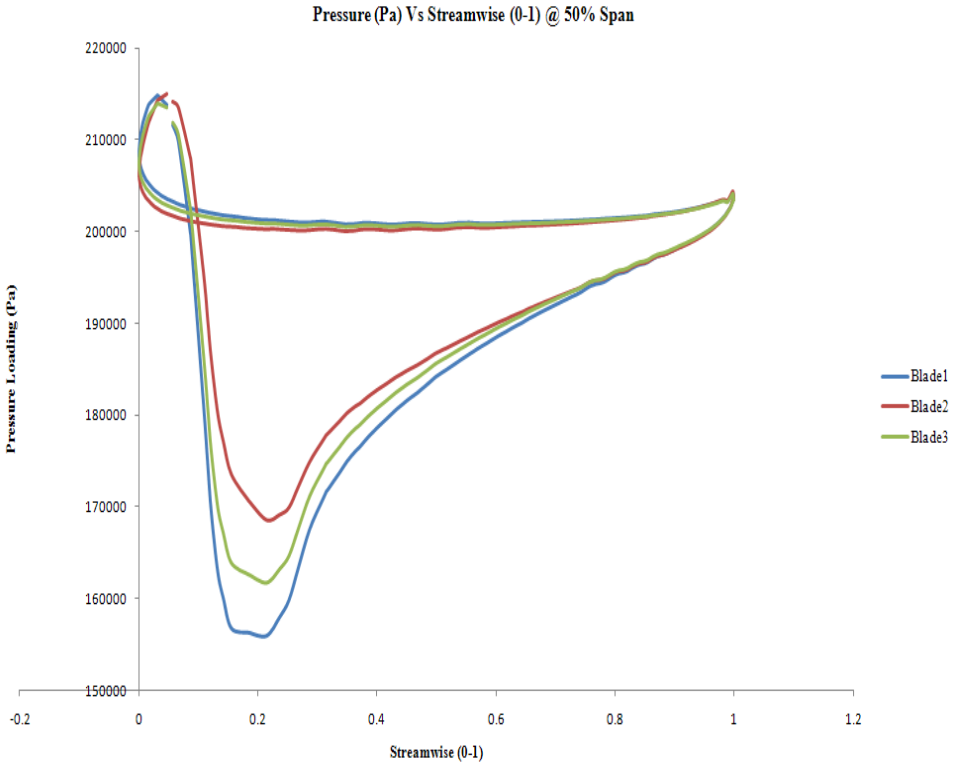

Figure 5.24 Pressure plot at 50% span - normal_spacing_model

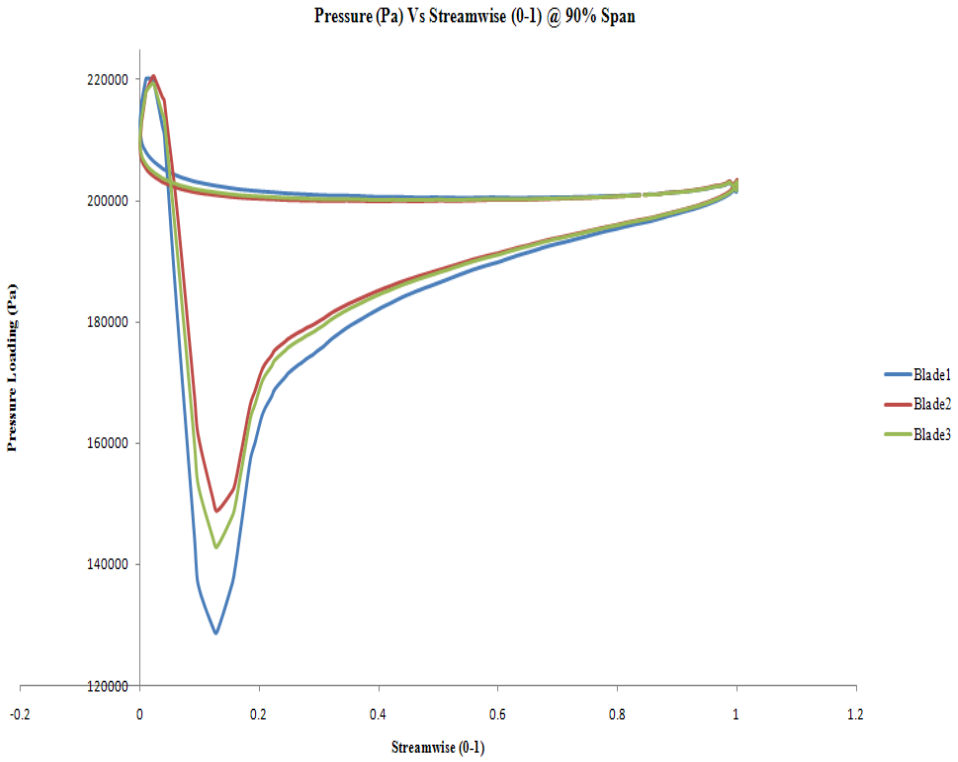

Figure 5.25 Pressure plot at 90% span - normal_spacing_model

In Figure 5.26 a vector plot corresponding to a mid-chord location in the blade domain is shown. The vectors are plotted in the relative frame. This plot is illustrative of the range of velocities that the turbine is exposed to.

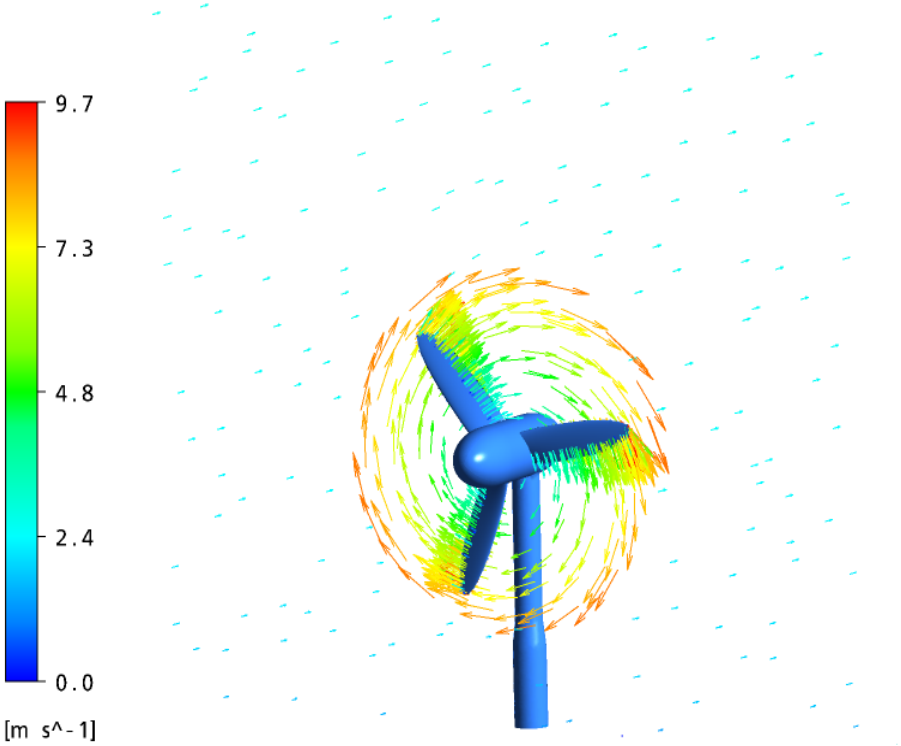

Figure 5.26 Vector plot on the rotor axis - normal_spacing_model

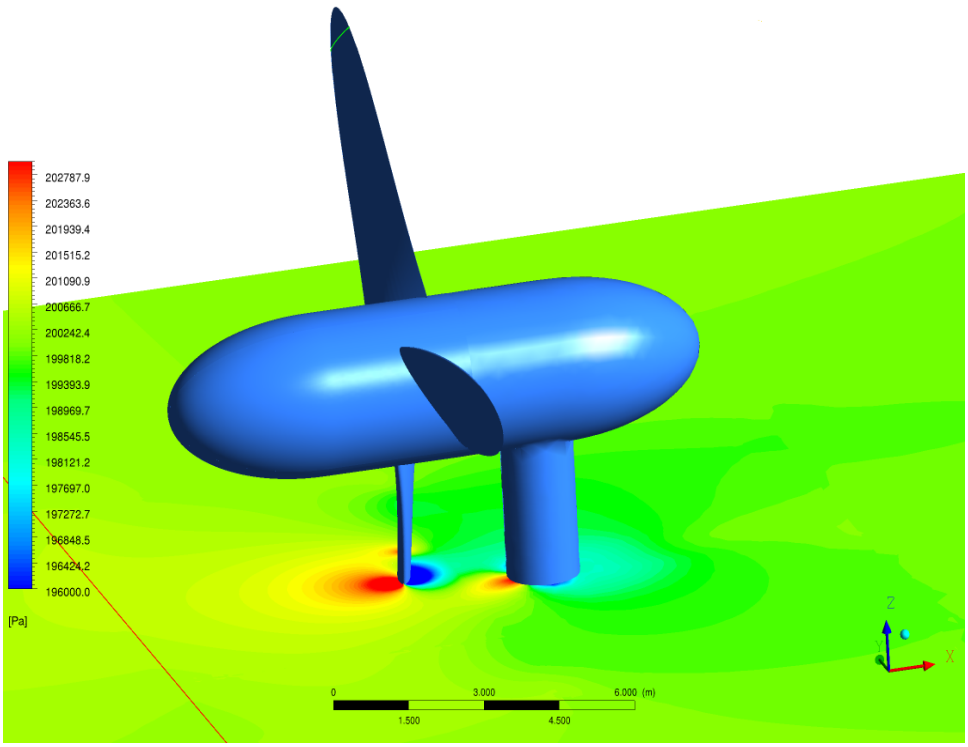

Figure 5.27 Blade-pylon interaction - normal_spacing_model

The blade-pylon interaction in the normal_spacing_model is plotted in Figure 5.27. This plot

portrays a situation that is intermediate between the interaction seen in the Inc_spacing_model and that of the Half_spacing_model.

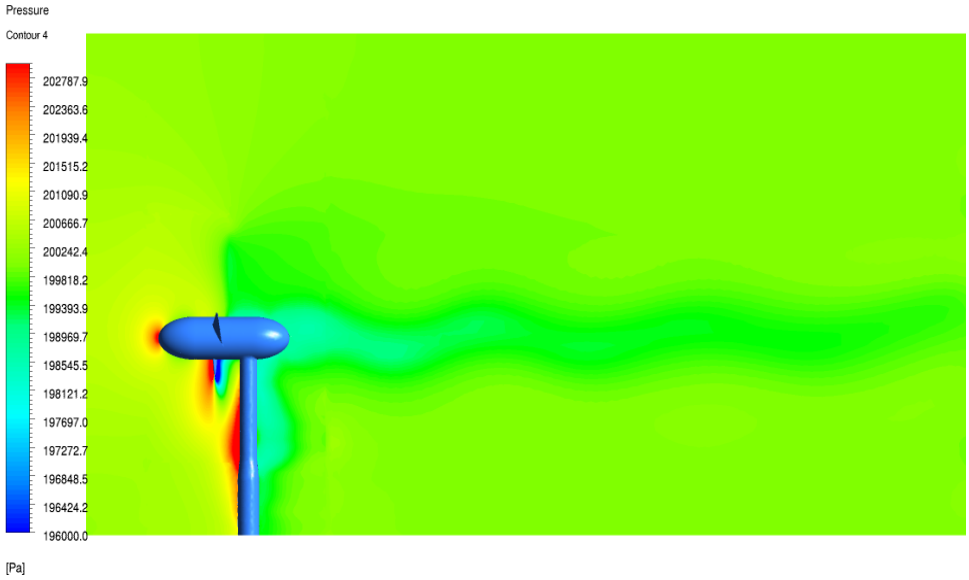

Figure 5.28 Pressure distribution in the meridional plane - normal_spacing_model

The meridional plane representation of the pressure for the normal_spacing_model is shown in Figure 5.28. The situation is as identified previously. The pressure distributions over the various components, and in the wake, are substantially intermediate between the other two cases presented before.

The Figure 5.29 shows the wake distribution aft of the rotor. The velocity deficit is plotted against the water depth at specific rotor diameters downstream of the rotor.

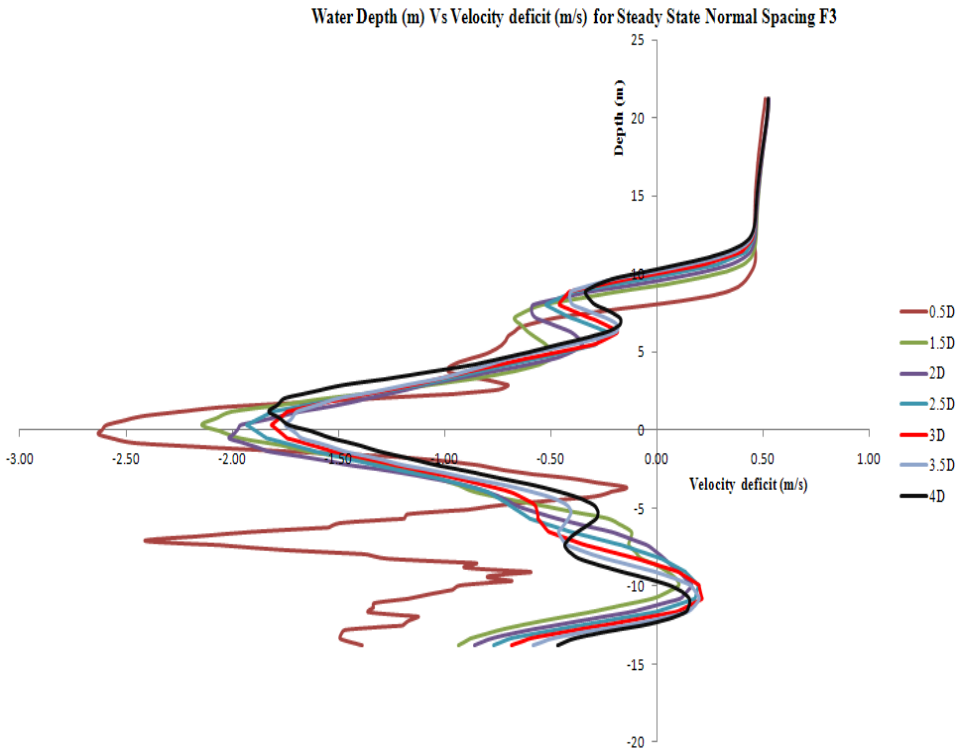

Figure 5.29 Velocity deficit downstream of the rotor - normal_spacing_model

The average flow speed of the rotor operating area was calculated to be $2.25ms^{-1}$. The flow velocities on the above plot in Figure 5.29 were subtracted from the average flow velocity of the rotor operating area to get the velocity deficit. It is apparent from the Figure 5.29 that the highest deficit occurs closest to the rotor and gradually increases to free stream velocities at many diameters downstream of the rotor. $3.5D$ - $4D$ show an increase of approximately $1ms^{-1}$ when compared to velocities just aft of the rotor axis.

A vortices created around the blades are displayed on Appendix B, Figure B.8. The total vorticity was calculated to be approximately $5.8s^{-1}$.

Discussion

The analysis of the overall blade loading plots for the three variations of the models make it evident that the normal_spacing_model experiences considerably less severe conditions than the closer spacing model. It is though that the cyclic variations experienced by the blades are not severe enough, when compared to other sources of transient loading, as shown by McCann, to warrant an undue concern. The stresses created from bending and twisting of the hub, as illustrated in Figure 5.30, on the Inc_spacing_model by the unsteady loads; cyclic and stochastic, would be large due to the extended blade-pylon distance. In contrast, the Half_spacing_model would expose the blade to high blade-pylon interactions which can be higher still when one considers that turbulence effects can lead to gust like velocity peaks.

Therefore this study enabled the progression of the design on the basis of the present spacing represented by the normal_spacing_model.

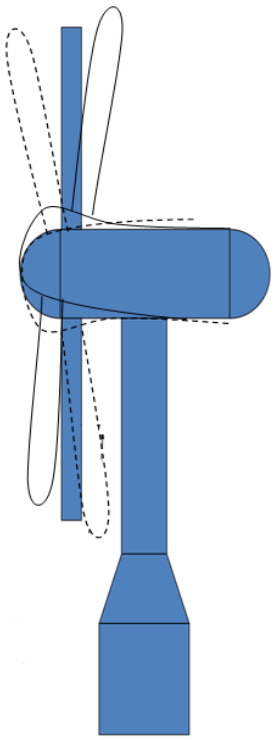

Figure 5.30 Illustration of the effects of cyclic loads acting on the rotor system

5.5.4 Double upstream Spacing Model

After establishing the desired blade-pylon spacing model for the project, a check was carried out on the axial extent of the upstream domain of the normal_spacing_model. This was done to analyse and understand if the inlet boundary condition of the domain was placed too close to the various components of the turbine. The scale of these effects was analysed and a "safe length" for the domain was established. The location of the inflow in the normal_spacing_model was set at $X = -11m$. The new axial location for the inlet plane was set at $X = -30m$. The model was termed New_frontpad_model. This is illustrated in Figure 5.31.

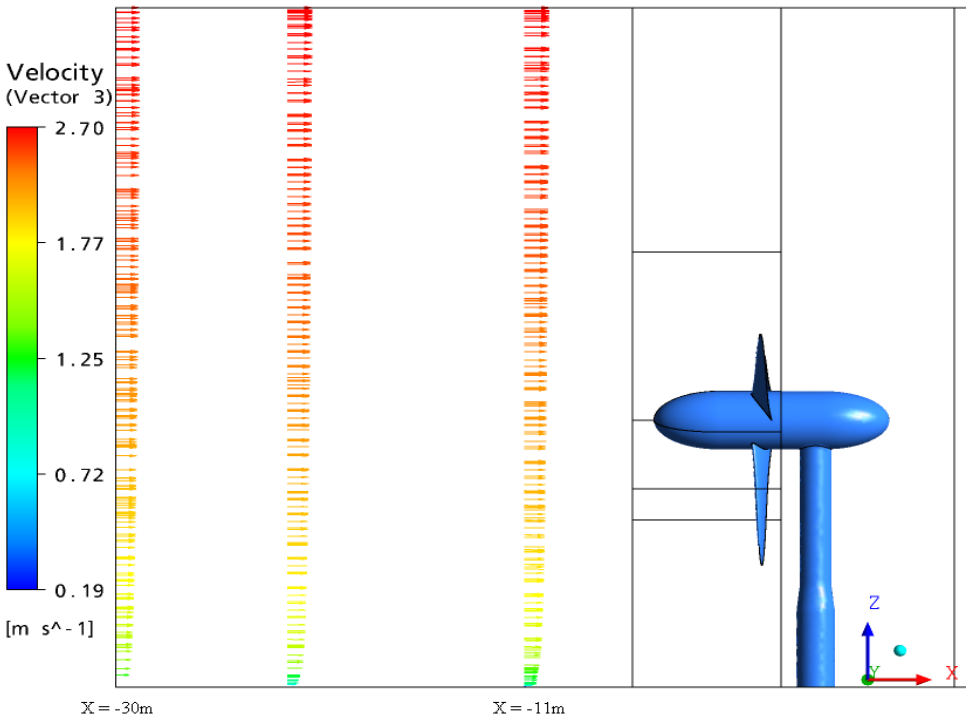

Figure 5.31 BL velocity profiles at various axial distances - New_frontpad_model

The length of the upstream block i.e. the distance from the rotor axis to the inflow of the upstream domain was initially set at $0.75D$. The extended upstream model was set at $2D$, Figure 5.31. Checks carried out confirmed that the shorter length approach had no impact on the solution.

5.5.5 No-Pylon Model

In order to address the importance of the blade-pylon spacing and pylon design in general, a No_pylon_model was created. The same domain specifications, rotor system, boundary conditions and physics as used in the other models were defined for this model, except for the fact that there was no pylon involved. The rotor system was suspended freely in the 3D domain. The Figures 5.32, 5.33 and 5.34 represents blade loading plots for 25%, 50% and 90% span locations respectively.

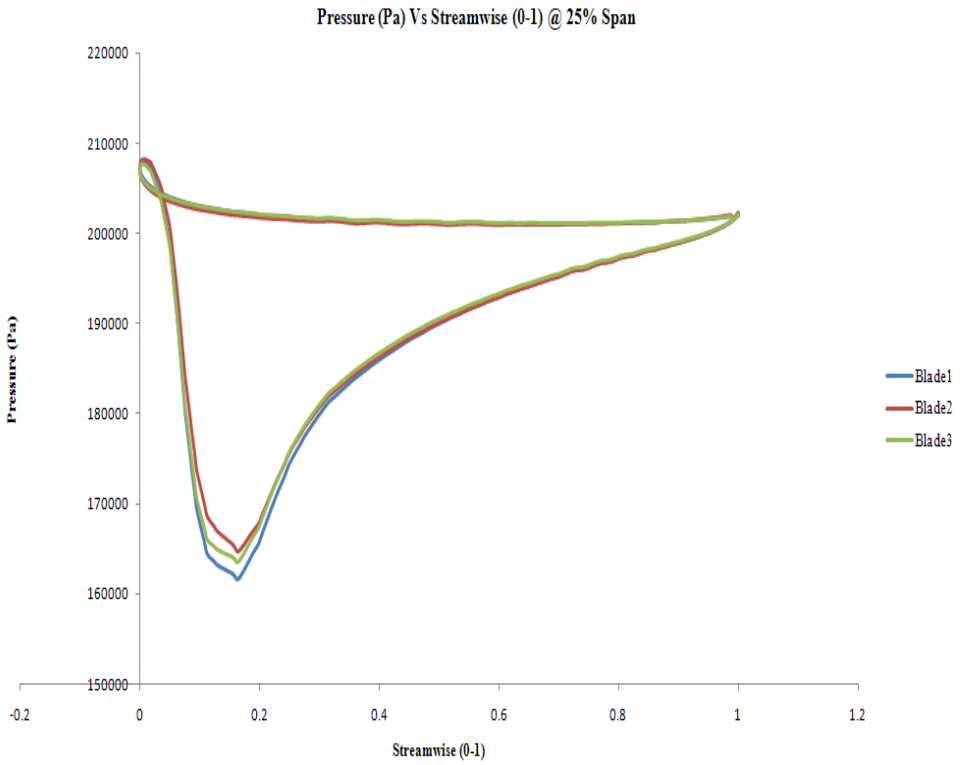

Figure 5.32 Pressure plot at 25% span - No_pylon_model

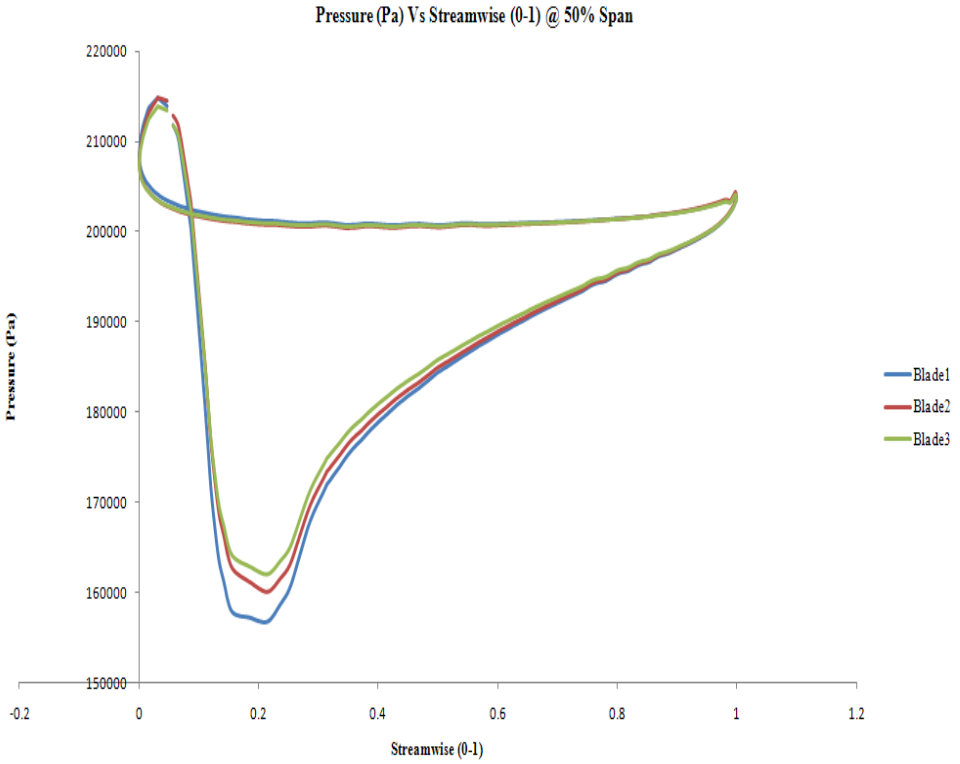

Figure 5.33 Pressure plot at 50% span - No_pylon_model

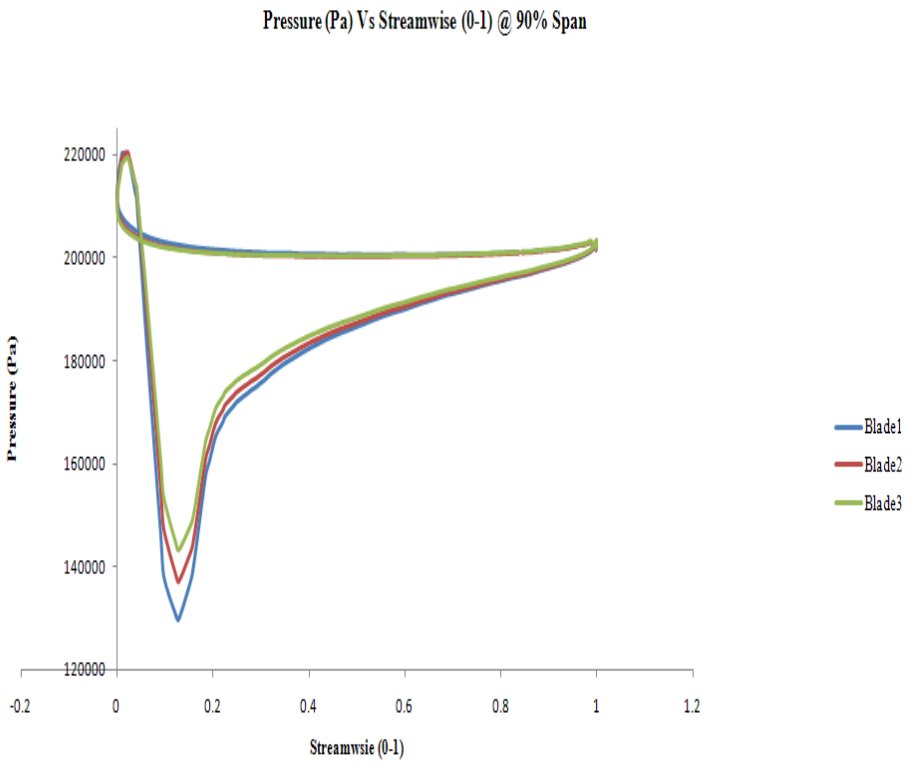

Figure 5.34 Pressure plot at 90% span - No_pylon_model

The collective areas under these plots are not very different to the normal_spacing_model blade loading plots presented in section 5.5.3. However some difference becomes apparent when each blade is analysed individually. The blade 2 in the normal_spacing_model loses lift because of the presence of the pylon. On the No_pylon_model there is still some difference between the three blades, because of the vertical flow gradient, but the variation is mild in comparison.

The model of the freely suspended No_pylon_model is shown in Figure 5.35.

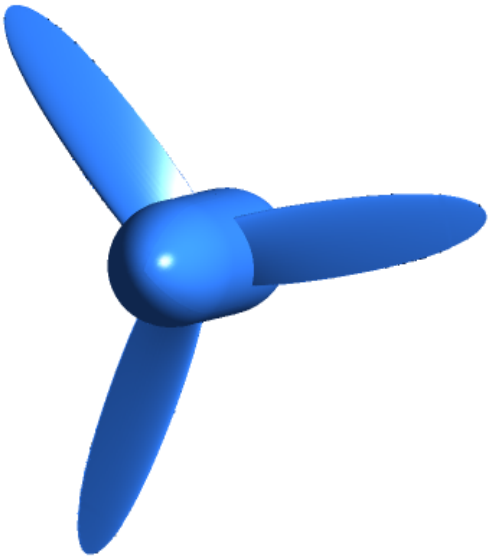

Figure 5.35 No_pylon_model

5.6 Steady State Analysis for the Datum Spacing Model

The results presented in section 5.5 were all obtained for the F3 case described previously. Therefore all model variations are strictly only valid for the flow conditions pertaining to the F3 case. The range of flow cases presented before are analysed in this part of the work. In this section the turbine performance characteristics are discussed employing the normal_spacing_model and all five cases are modelled and analysed in the subsequent sections. The Figure 5.36 displays the four CFD cases with the velocity profiles at the inlet except that of the start-up case.

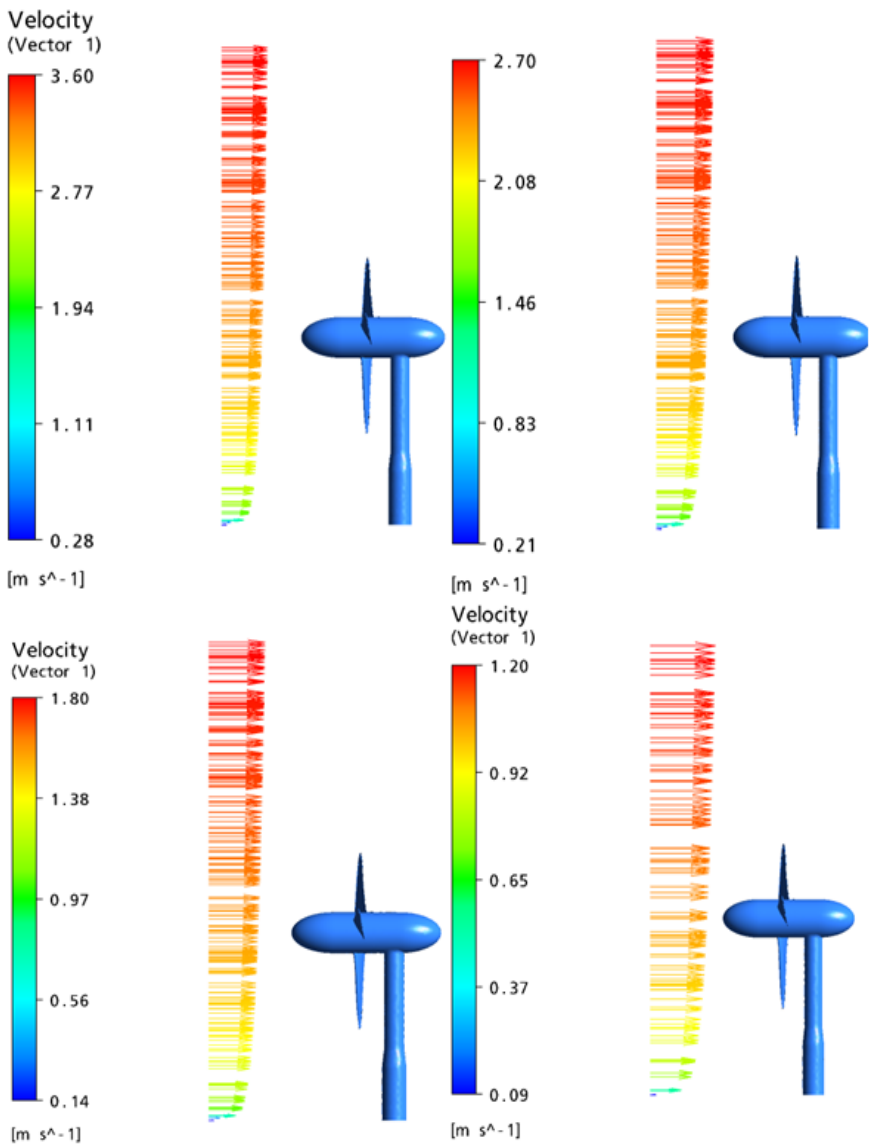

Figure 5.36 Four flow conditions analysed

5.6.1 Start-up torque

It is always important to understand at what flow velocity a turbine will start. The accepted notion is that flows below $1.0ms^{-1}$ do not provide a commercially attractive return. This case sought to simulate the start up conditions for the model. The tidal velocity is low, $0.8ms^{-1}$ at the surface. The rotational velocity of the turbine was set to $0.0\ RPM$. The turbine operating flow speed is approximately $0.65ms^{-1}$. In Figures 5.37 to 5.39 blade loading plots at 25, 50 and 90% of the span respectively are presented.

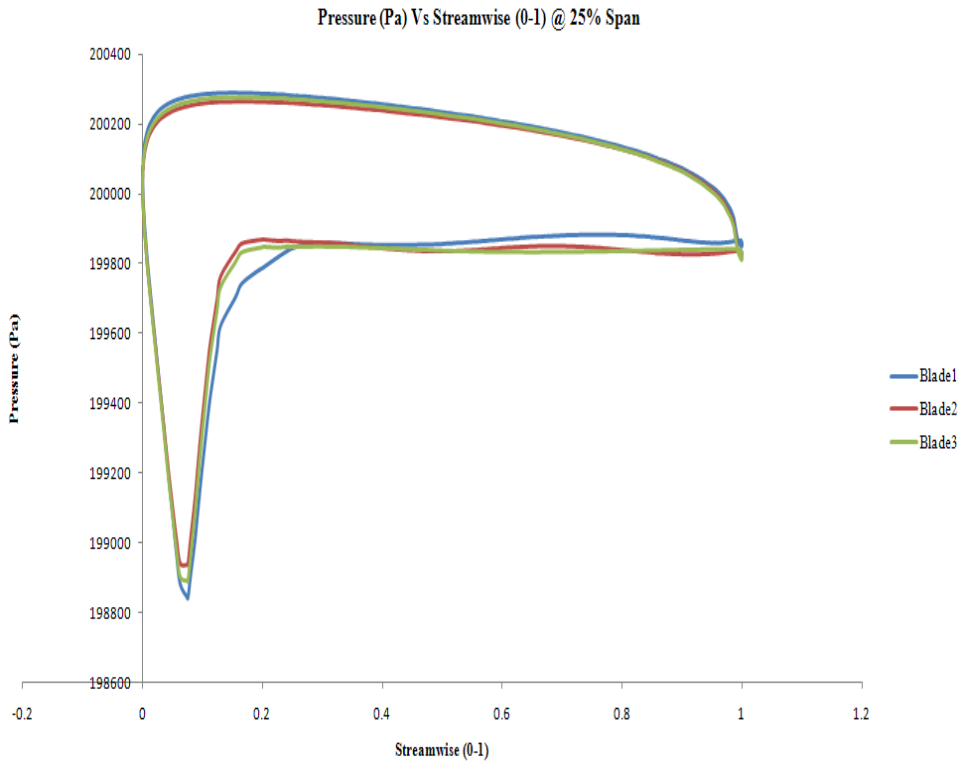

Figure 5.37 Pressure plot at 25% span - No_pylon_model

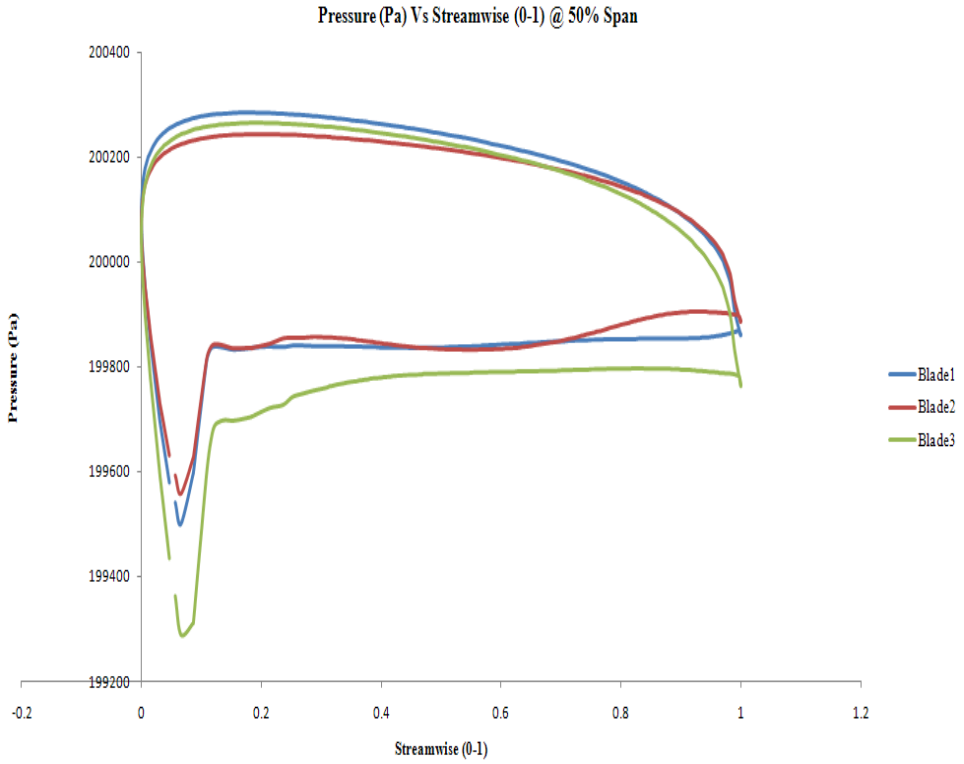

Figure 5.38 Pressure plot at 50% span - No_pylon_model

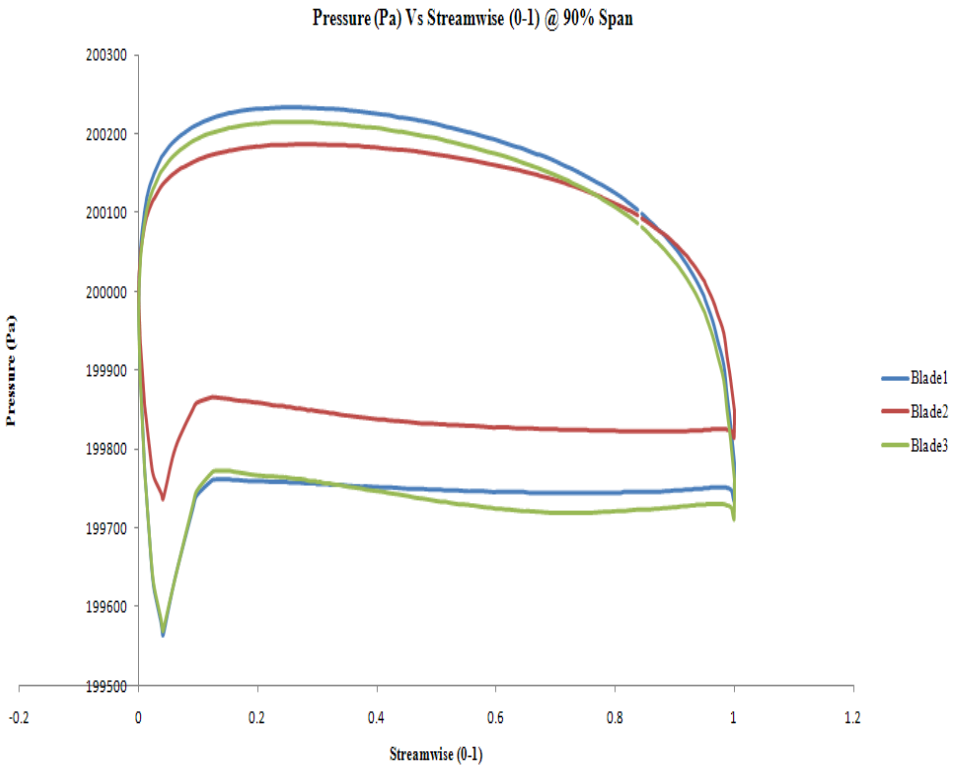

Figure 5.39 Pressure plot at 90% span - No_pylon_model

These blade loading plots, with a somewhat unusual shape for a Turbomachinery application, correspond to the distribution of the flow around profiled but stationary objects. The fact that blade 2 loading is the most affected comes as no surprise given its positioning. Interestingly enough the pressure side, pressure, corresponds to the upper part of the curve rather than the nearly flat part that corresponds to the suction side.

The total torque for this case was calculated as $13.5kNm$, which ties with the design estimates. The total thrust generated by the turbine is just over $9.0kN$. The Figure 5.40 shows the torque and thrust for each blade together with their respective angular positions. The datum for the plots presented against angular position is top dead centre, $0°$.

It is noteworthy that the angular distribution of torque and thrust is not symmetrical around the circumference. However the blade shape is itself not symmetric about the meridional plane.

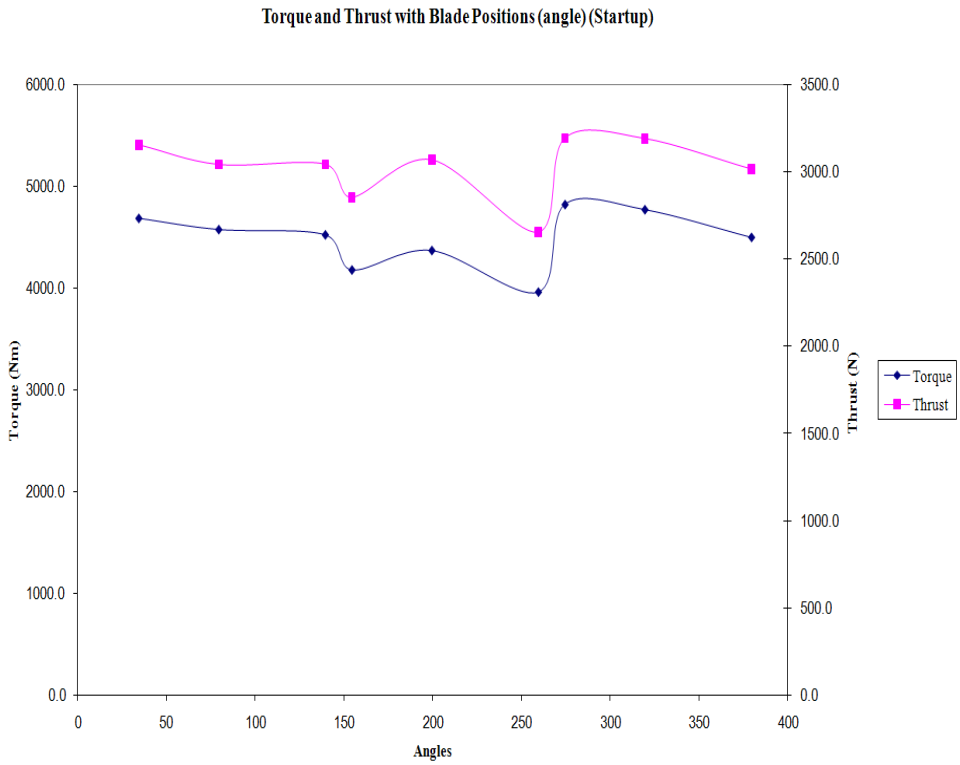

Figure 5.40 Torque and Thrust for the Start-up case

5.6.2 F1 Case (low-tidal velocity case)

The F1 case was simulated to study the torque and thrust variations for the low end tidal velocity spectrum. At the inlet, a surface velocity of $1.2ms^{-1}$ was set. The average flow velocity in the vicinity of the rotor was calculated to be approximately $1.0ms^{-1}$ and the rotational velocity of the rotor was set to $4.2\ RPM$. The turbulence intensity was set to medium intensity (5%) using the default value in CFX-Pre as described in section 4.6. The total torque was calculated to be $88.6kNm$, total thrust at approximately $51.0kN$ and the total power just over $39.0kW$. Figure 5.41 shows the torque and thrust for each blade with its respective angular positions. The lowest point in the two curves denotes that the blade is at its lowest point which is upstream of the pylon.

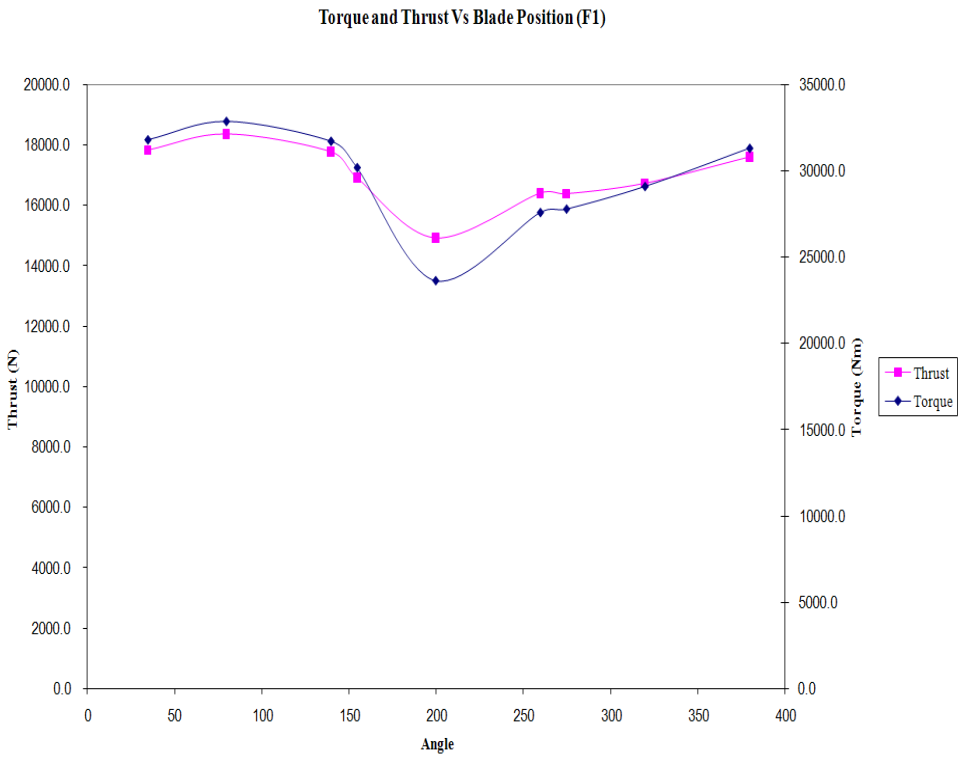

Figure 5.41 Torque and thrust for the F1 case

Once again symmetry is not a characteristic of this plot. This is not altogether surprising as well if it is considered that the hydrodynamics of the arrival and departure of the blade profiles around the pylon are itself not a symmetric event. Elsewhere, away from the immediate vicinity of the pylon too the blade-flow interaction is not symmetric. On one of the sides of the turbine the blade is sweeping in a rising gradient of velocity. On the opposite side the situation is reversed. The outcome is the pitchwise variation seen above and in following plots.

As noted in section 5.4 the design calculations for power at this flow was $37.0kW$, the thrust was calculated to be $5.0tons$ and the torque was just over $155.0kNm$. As expected the thrust and the power are similar to the numerical results but the torque is almost twice that of the computed CFD value.

5.6.3 F2 Case (moderate-tidal velocity case)

The most frequently recorded tidal velocities vary from $1.0ms^{-1}$ - $2.0ms^{-1}$, therefore a case with surface velocity of $1.8ms^{-1}$, average flow across the rotor of $1.5ms^{-1}$, was created with a turbine rotational velocity of $6.2\ RPM$. Total torque was approximately $202.0kNm$, total thrust just over $115.0kN$ and the power was $131.0kW$. The Figure 5.42 represents the torque and thrust for each blade with its respective positioning.

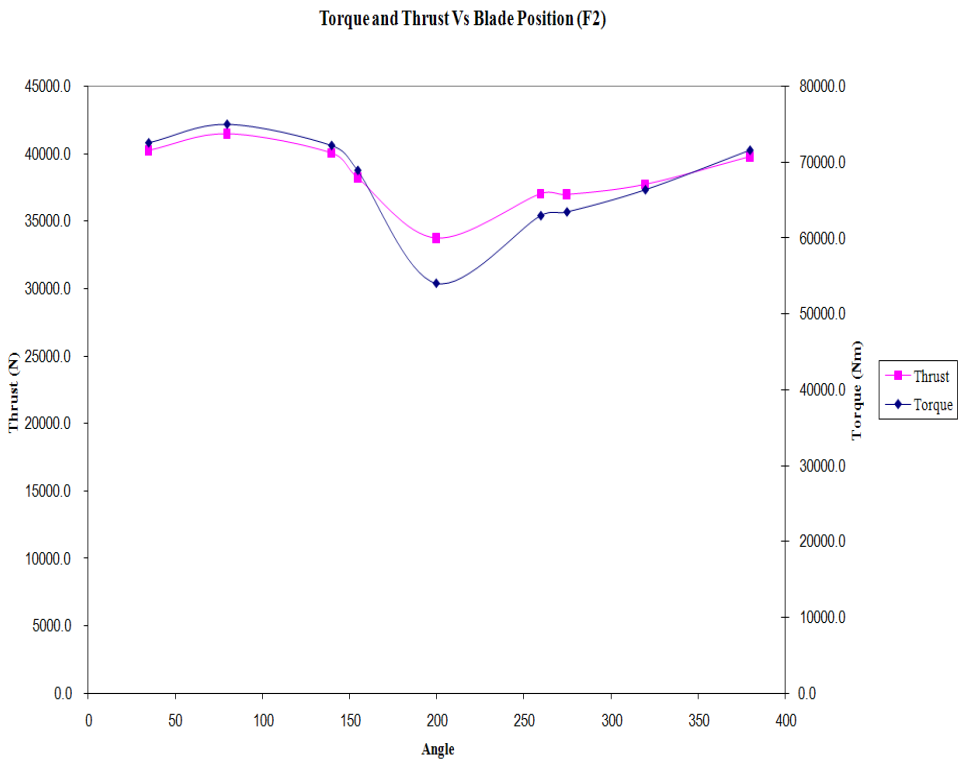

Figure 5.42 Torque and thrust for the F2 case

In comparison with the design calculations, $245.0kNm$, the numerically computed torque is slightly lower. The thrust was calculated by the BEMT design code to be just over $11.0tons$ and this is in agreement with the CFD calculations as well. The design power was calculated at $126.0kW$ and this is also in agreement with the CFD results.

5.6.4 F3 Case (maximum torque)

A maximum power/torque case was also calculated. This corresponds to the rated power condition of the turbine. It must be noted that velocities of the graphs denoting the operational schedule, presented in section 5.3 employ not surface velocities to characterise the flow condition but a uniform, farstream flow velocity that is roughly equivalent to that of the turbine hub in the CFD simulations. For the F3 case the flow velocity at the surface was $2.7ms^{-1}$, and the average rotor velocity $2.25ms^{-1}$. The rotational velocity is 9.29 RPM The total torque was computed to be $455.5kNm$, the thrust $259.0kN$ and the power $441.8kW$. Figure 5.43 below shows a representation of the thrust and torque variation with appropriate blade positions.

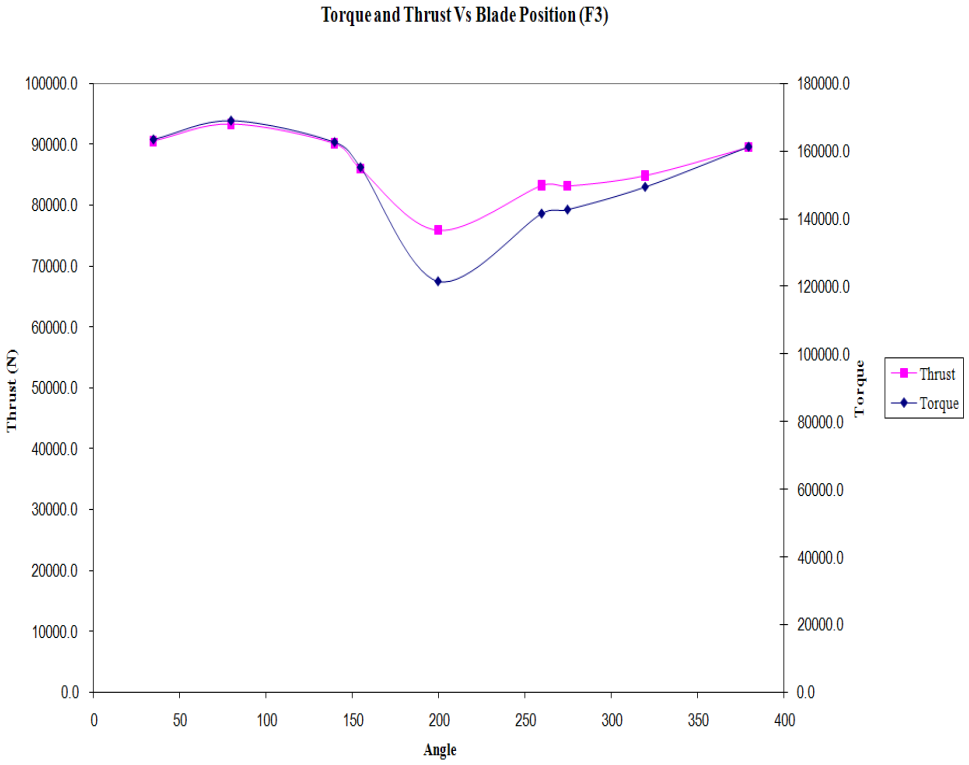

Figure 5.43 Torque and thrust for the F3 case

The power calculated using the BEMT code was just over $401.0kW$ which is compared to the $441kW$ generated by the CFD simulations. The design torque was calculated to be just over $450.0kNm$ and a design thrust of $250.5kN$ was recorded. The torque and thrust are in fair agreement with the CFD results although the power generated is somewhat different when compared to the CFD results.

5.6.5 F4 Case (maximum thrust)

An atypical case has also been investigated. This corresponds to a high surface velocity of $3.6ms^{-1}$ to which corresponds an average rotor flow velocity of $3.0ms^{-1}$ and a rotational velocity of $21.0\ RPM$. This case corresponds to a situation where the surface tidal velocity is over $2.7ms^{-1}$ and hence the thrust is contained by allowing the rotor to accelerate in relation to a linear RPM increase as was the case up to the power shedding threshold. The total torque calculated by the CFD simulation was $267.5kNm$, the thrust was $238.7kN$ and the power was $588.5kW$.

The power calculation on the design analysis was of the order of $548.0kW$ (of which $400kW$ are useful power), the thrust calculation was $249.5kN$ and is not far off when compared to the CFD results. The torque was calculated to be just over $250kNm$ and is also in agreement with the CFD data. Figure 5.44 below shows a representation of the thrust and torque

variation with appropriate blade positions.

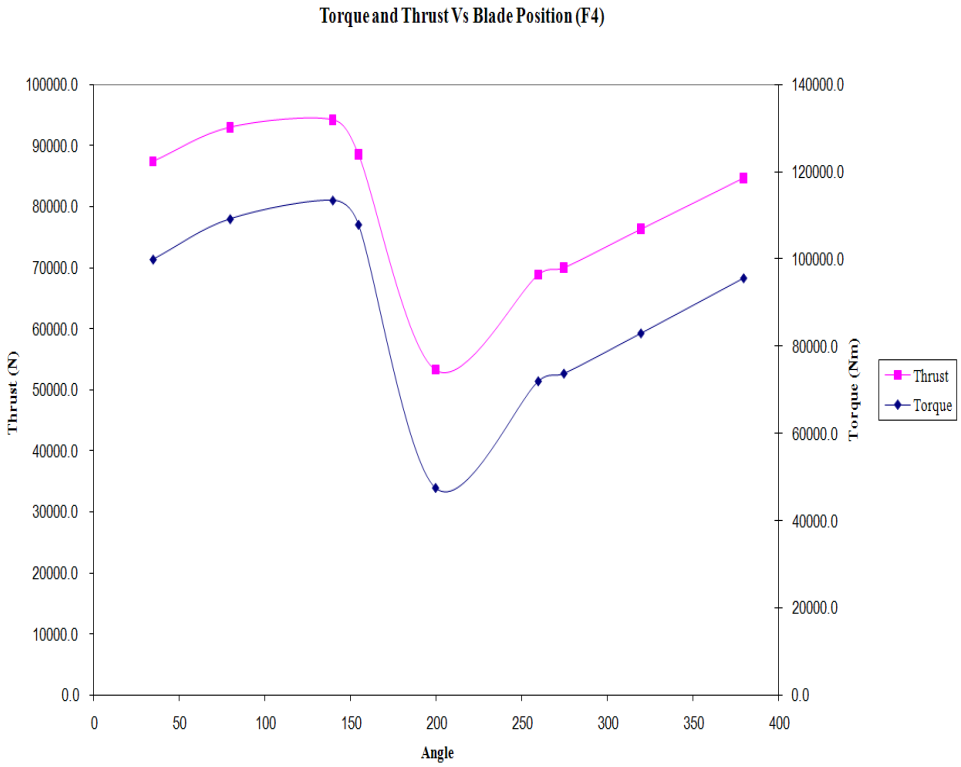

Figure 5.44 Torque and thrust for the F4 case

Vortices created around the blades are displayed on Appendix B, Figure B.9. The total vorticity was calculated to be approximately $13.5s^{-1}$.

5.6.6 Operational Schedule of the Turbine from CFD simulations

The turbine operating schedule in terms of the thrust generated against tidal velocity is presented in Figure 5.45. This shows that the thrust control approach is well-founded and feasible. The torque shows a substantial decrease also in response to the increase in speed, Figure 5.46. However the power generated by the turbine is larger than the target although much smaller than would have been the case had this control method not been active. At the time these simulations were run this was the situation which pointed to a need to re-stagger the blades.

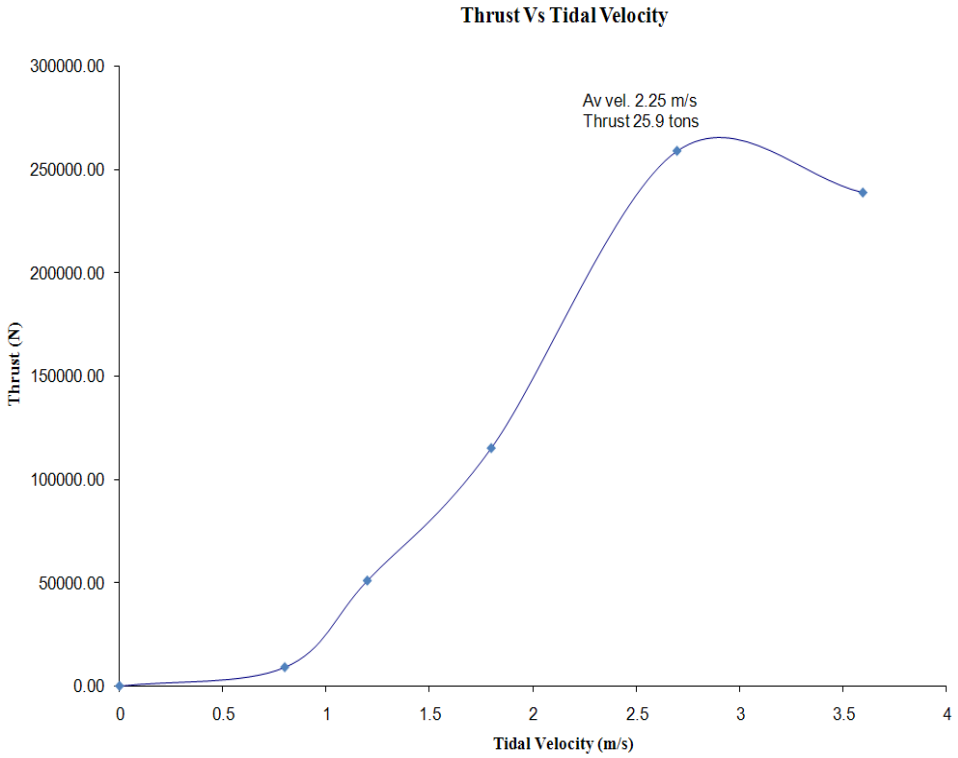

Figure 5.45 Thrust Vs Tidal Velocity

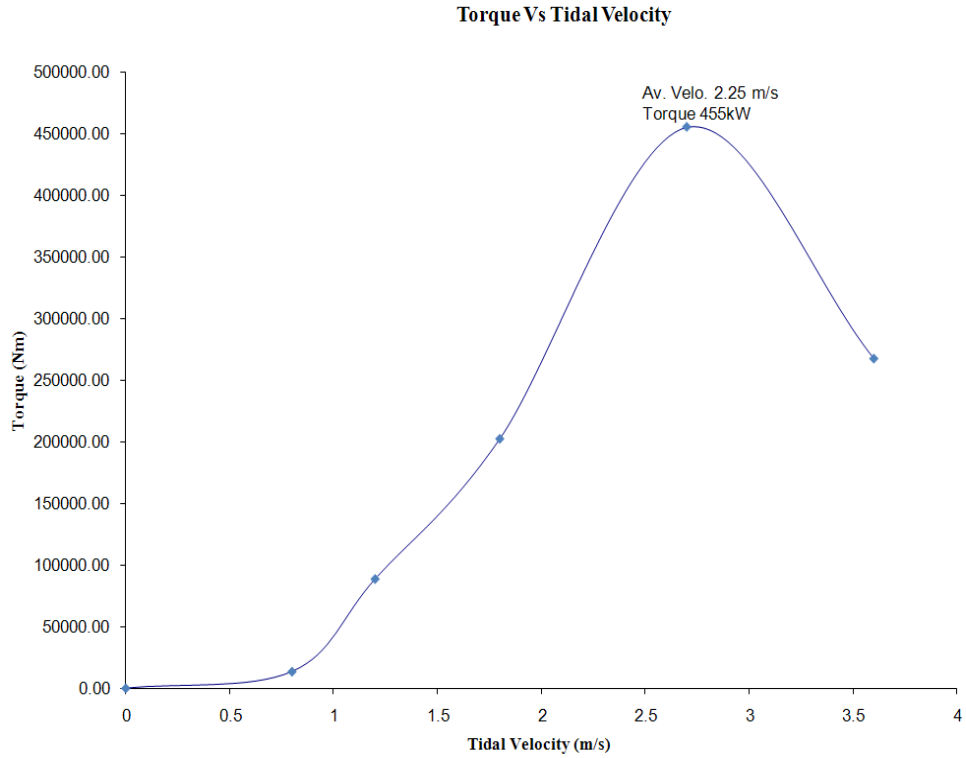

Figure 5.46 Torque Vs Tidal Velocity

5.6.7 Performance of the rotor

The performance of the turbine was initially calculated by Mr. Chirs Freeman using the BEMT code. The derivation of the model is very well known as it is widely used in rotating machinery as discussed in Chapter 2. The assumptions in deriving the model are;

- Steady state flow
- Viscous effects are ignored i.e. no drag and momentum diffusion
- Uniform thrust over the rotor area
- Flow is incompressible
- Tip losses are ignored
- Elementary blade sections analysed independently (though Prandtl's tip correction factor used to adjust this)

The BEMT code supplies information on the power and thrust experienced by the turbine at a given flow velocity but these figures are subject to a theoretical limit, the Betz condition. Additional losses, due to viscous effects for the most part reduce the power produced further.

The performance expressions are the non-dimensional coefficients of power and thrust;

$$C_P = \frac{P}{\left(\frac{1}{2}\rho V_\infty^3 A\right)} \tag{5.1}$$

$$C_T = \frac{F_X}{\left(\frac{1}{2}\rho V_\infty^2 A\right)} \tag{5.2}$$

The theoretical limit, know as the Betz law, limits the system from achieving 100% efficiency. These limits are $16/27$ for C_P and 0.8889 for C_T.

C_P and C_T are functions of the relative flow fields and these quantities can either be computed through the BEMT approach from knowledge of the performance of the profiles employed on the blades or directly through a numerical approach such as CFD. However the CFD results are subject to rectification since the computational domains are, even when these are quite extensive as is the case in the present study, finite in relation to the volume of an open channel.

This is coincidentally akin to a certain extent to what takes place in a water flume, i.e. the constriction of the tunnel by comparison with the vast expanse of the ocean. Bahaj et al. (2007a,b) who investigated this phenomenon derived correction factors applicable to the results of models operating in close proximity of boundaries. These models seek to account for blockage effects which would in turn change the performance of the turbine. Figure 5.47 displays the C_P and C_T curves with TSR. The graph consists of C_P and C_T profiles for a single-blade CFD (blue line for C_P and red line for C_T) run rotating at 0.96 $radss^{-1}$ ($9.1RPM$) with various flow speeds. The lines marked "corrected" correspond to the quantities just described after the blockage correction of Bahaj is applied (green line for C_P and purple for C_T).

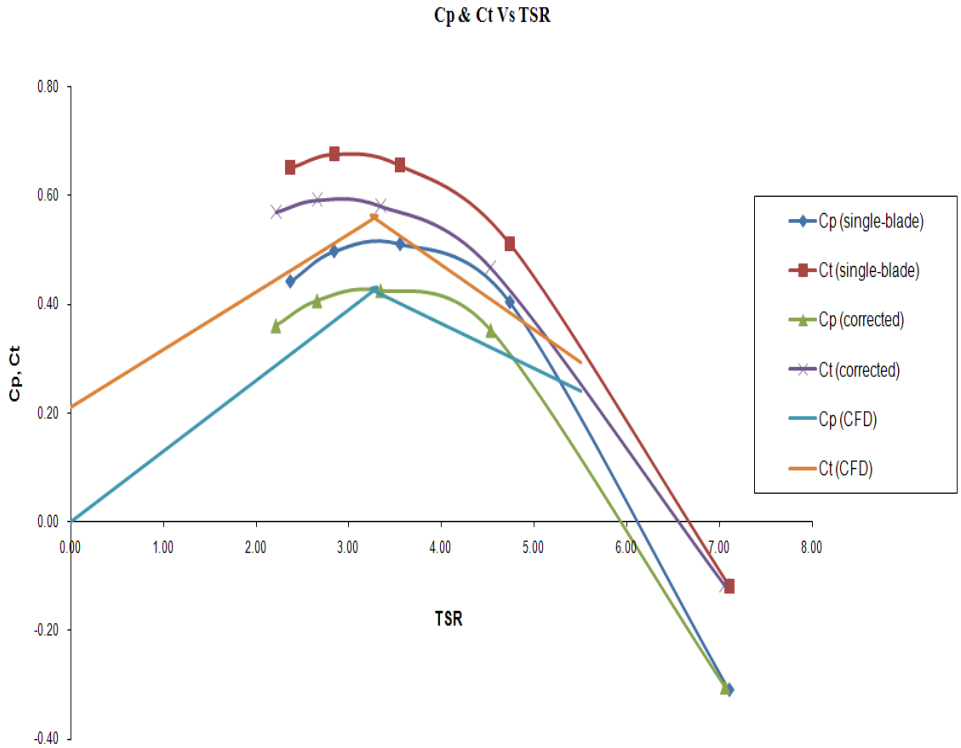

Figure 5.47 C_P and C_T Vs Tip Speed Ratio

The lines marked CFD in Figure 5.47 (shown as cyan for C_P and orange for C_T) correspond to the whole turbine simulations described above. The fact that these correlate more closely with the blockage corrected values is a vindication of the employment of a large computational domain by comparison to what was done in the single blade simulations. This comparison is done in the interest of illustrating the point while acknowledging the fact that the two CFD simulations were carried out at slightly different RPM values.

5.6.8 Turbulence Intensity Profile

The standard F3 case was simulated employing a medium value (5%) of turbulence intensity in CFX-Pre. A vertical distribution of turbulence intensity employing the relationship described in Chapter 2 was employed in order to compare the results with the turbine performance obtained with the standard ANSYS turbulence intensity mentioned previously. The vertical distribution equations were based on the Alinot & Masson (2002) paper described on Chapter 2. Therefore, an additional F3 case was launched with the manual introduction of k and ϵ using the turbulence intensity profile. Unlike for the boundary layer velocity profile, were the highest velocity occurs at the sea surface, the highest value of turbulence intensities occur near the bottom (sea-bed) of the domain. The peak turbulence intensity reaches approximately 30% when close to the sea-bed for a turbulence intensity case of 5% at the sea surface. Vertical profiles of turbulence intensity plots can be found in section 2.6.

The variation of torque and thrust was obtained for 2 different F3 cases as shown in Figure 5.48. The blue and the red profiles are the torque variations for the F3 default 5% turbulence intensity (uniform) and F3 5% intensity using the k and ϵ profile respectively. As expected, given the geometry of the profile, there is hardly any difference between the results due to the two methods. This same observation is valid for equivalent thrust plots, denoted in purple for the standard 5% intensity and cyan for the profiled 5% intensity case. The conclusion reached at this stage was therefore that for the DeltaStream geometry, essentially the vertical placement within the channel, the default turbulence intensity representation is wholly acceptable.

A further case was simulated using a 10% turbulence intensity for the F3 case. The profiled version predicts a substantial reduction of torque and trust when compared with the 5% equivalent model, as seen in Figure 5.48. The green profile displays the torque variation and the orange shows the thrust variation. Unfortunately the results obtained with the CFX-Pre uniform 10% turbulence intensity boundary condition do not show very good agreement with the results obtained with the equivalent TI profile version.

In fact, the high turbulence intensity function of ANSYS almost matches the F3 5% intensity case as if though there was no change in intensities. This means therefore that the conclusion derived above is invalid for other than low turbulence intensity cases. A part of the boundary condition profile data employed for the shear velocity profile together with the corresponding 5% turbulence intensity profile is presented in Appendix B, Figure B.1.

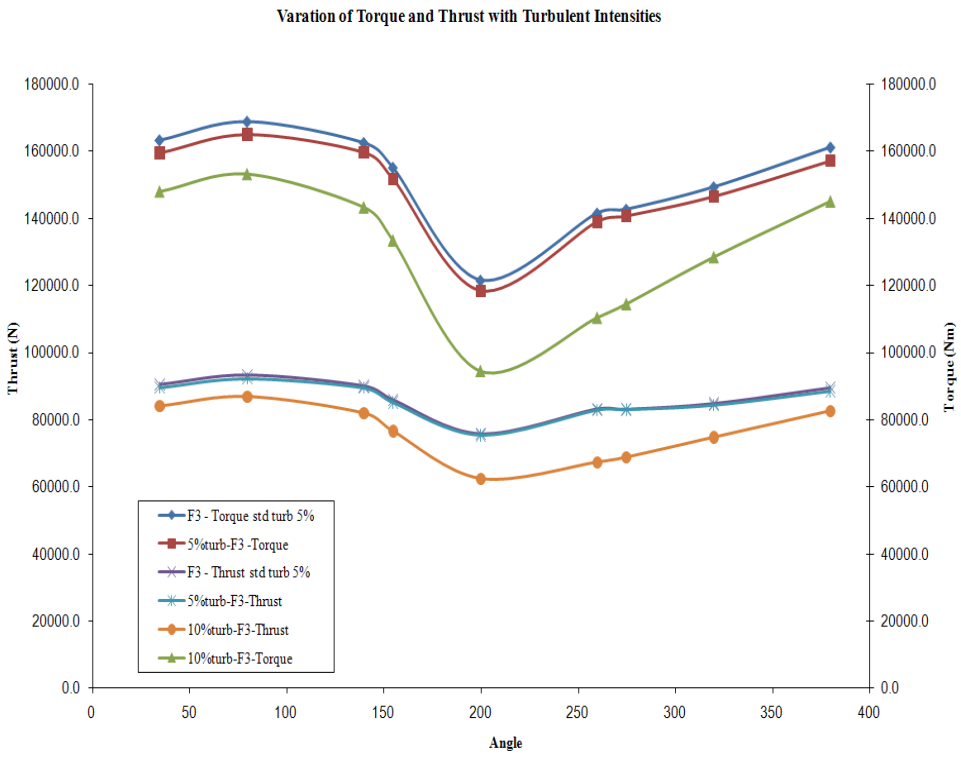

Figure 5.48 Variation of Thrust and Torque for the F3 case with 5% & 10% TI

5.6.9 Inflow angle change (10° yaw)

A model was simulated for the purpose of understanding the performance characteristics of the turbine when the inflow was angled (yawed). An inflow angle of 10° was set for the F3 case. A total torque of $437.0kNm$ was computed together with a total thrust of $247.5kN$ and a power of $424.3kW$. An average of 4% reduction in torque, thrust and power was seen when compared to the standard F3 case. The Figure 5.49 shows the variation of torque (red) and thrust (blue) with blade positions for the 10° case and also compares the torque (purple) and thrust (green) variations for the standard F3 case. It is evident from the figure that the 10° yaw case produces sharper variations of thrust and torque plots when compared to the standard F3 case. The crests and the troughs for the 10° yaw case is also much higher and lower than than of the standard case, implying that the 10° yaw model undergoes larger unsteady loadings.

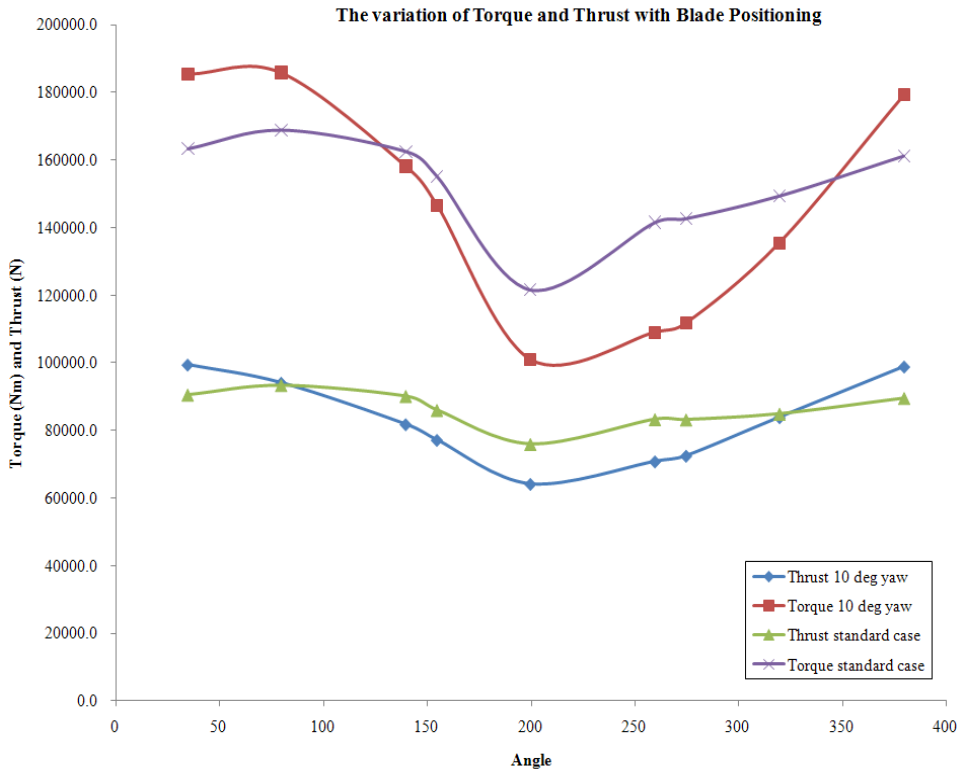

Figure 5.49 Comparison of the standard F3 case and 10° yaw case

This comparison was conducted in light of understanding the effects of yaw on the performance of the HATT. As expected and also documented by Bahaj et al. (2007b), the yaw has a negative effect on the performance characteristics. In addition to the is the CFD simulations confirm that the load variation experienced by the rotor is also higher than that of the standard case.

The profile data showing the 10° yaw is shown on Appendix B, Figure B.2.

A comparison of torque and thrust about the Y and Z axes are presented in Appendix B, Figure B.3 for the 10° yaw model and the standard F3 model. As seen from the comparisons the 10° yaw case produces a slightly higher torque and thrust plot about the Y and Z planes as compared with the standard case. This variation is very small and could be neglected. The interpretation of these plots mean is that the forces (torque and thrust) about the Y and Z axes are not very much affected by the yaw case but the axial forces (torque and thrust) are affected and hence would influence the unsteady transient loading characteristics of the rotor-pylon system.

5.7 Steady State CFD Analysis for the Half Spacing Model

As discussed previously in section 5.5, the Half_spacing_model was simulated with the F3 case parameters to analyse the torque, power and thrust variation. The torque was calculated to be $344.0kNm$, the thrust $211.0kN$ and the power was $335.0kW$. Therefore, for the same parameters, the Half_spacing_model under performs when compared to the normal_spacing_model. An average of 20% reduction in performance characteristics was seen when compared to the normal_spacing_model. Figure 5.50 below shows the torque (red)and thrust (blue) variation with blade position for the Half_spacing_model. The green shows the thrust and the purple shows the torque variation for the normal_spacing_model. If the variation pattern is examined, the shorter spacing plot shows a sharp profile when compared to the normal_spacing_model F3 case. The close blade-pylon spacing has an adverse effect on the performance of the rotor and its blade loading characteristics. The pressure plots in section 5.5.2 and 5.5.3 also confirms this effect of low thrust and torque production when compared for the Half_spacing_model and the normal_spacing_model respectively.

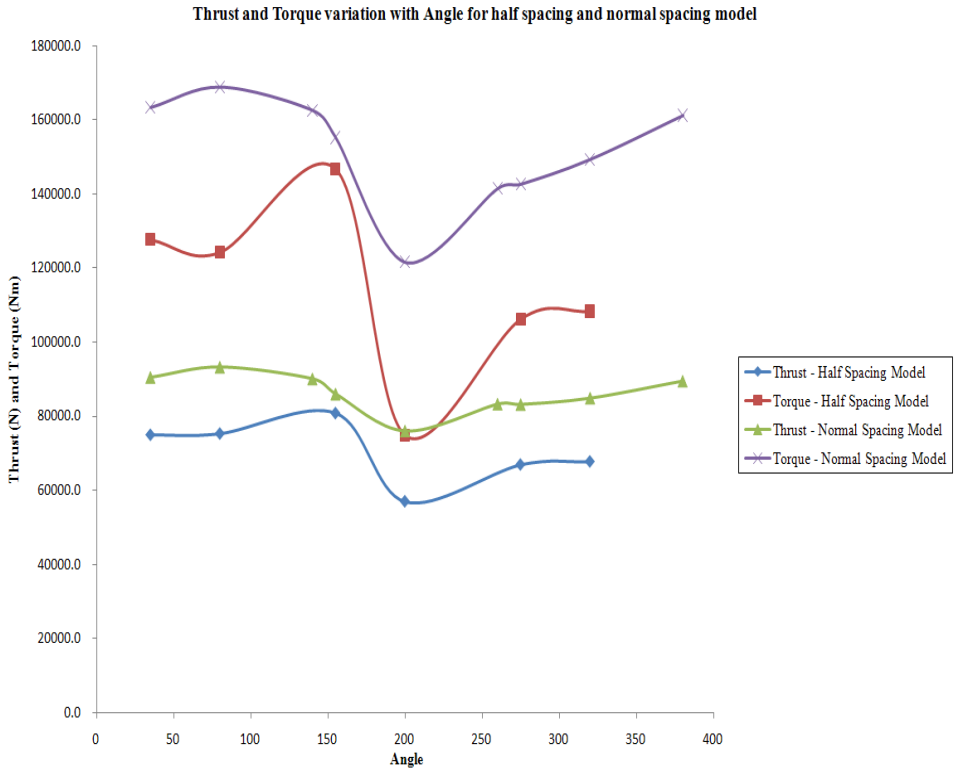

Figure 5.50 Comparison of the standard F3 case and the Half_spacing_model case

5.8 Steady State CFD Analysis for the Increased Spacing Model

Here again the F3 simulation parameters were utilised for the simulation. The total torque for the Inc_spacing_model was calculated to be $256kNm$, the thrust was $174.6kN$ and the power was $246kW$. A similar situation was confronted for the Inc_spacing_model as compared with the Half_spacing_model, although this simulation slightly under performs in performance characteristics and is less significant compared to the normal_spacing_model. Figure 5.51 represents the variation of thrust with blade positions for the three model variations. In Figure 5.51 the red line shows the thrust variation for the Inc_spacing_model, the blue plot displays the Half_spacing_model and the green shows the normal_spacing_model variation. Figure 5.52 represents the variation of torque for the Inc_spacing_model in the green plot, the Half_spacing_model in red and the normal_spacing_model in blue.

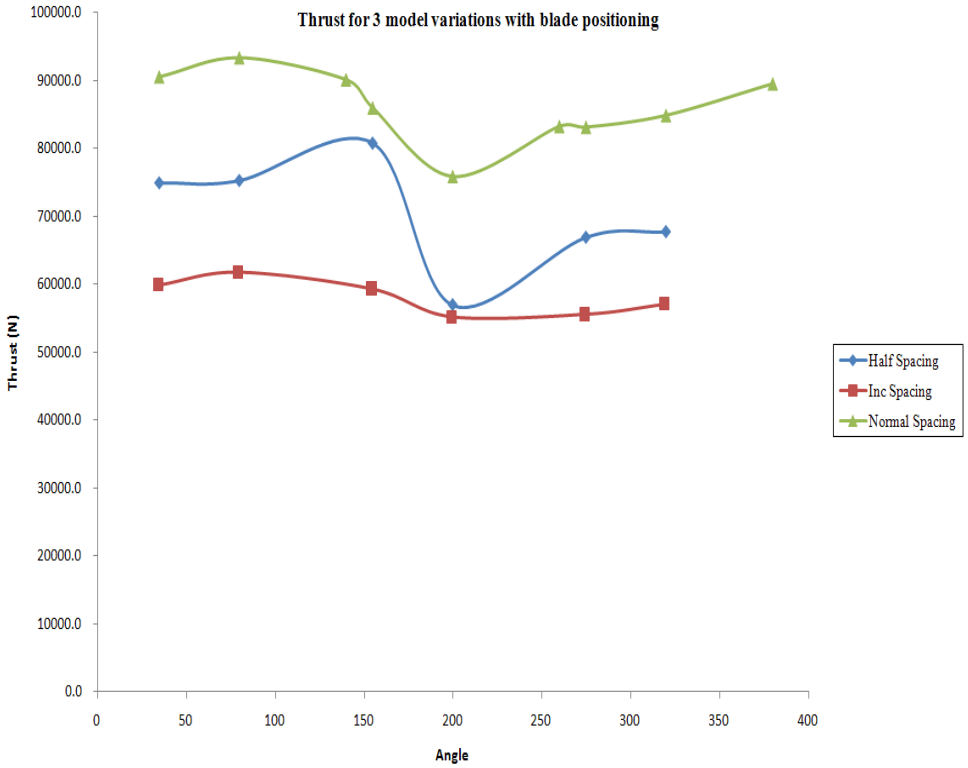

Figure 5.51 Comparison of the thrust variation of all 3 models for the F3 case

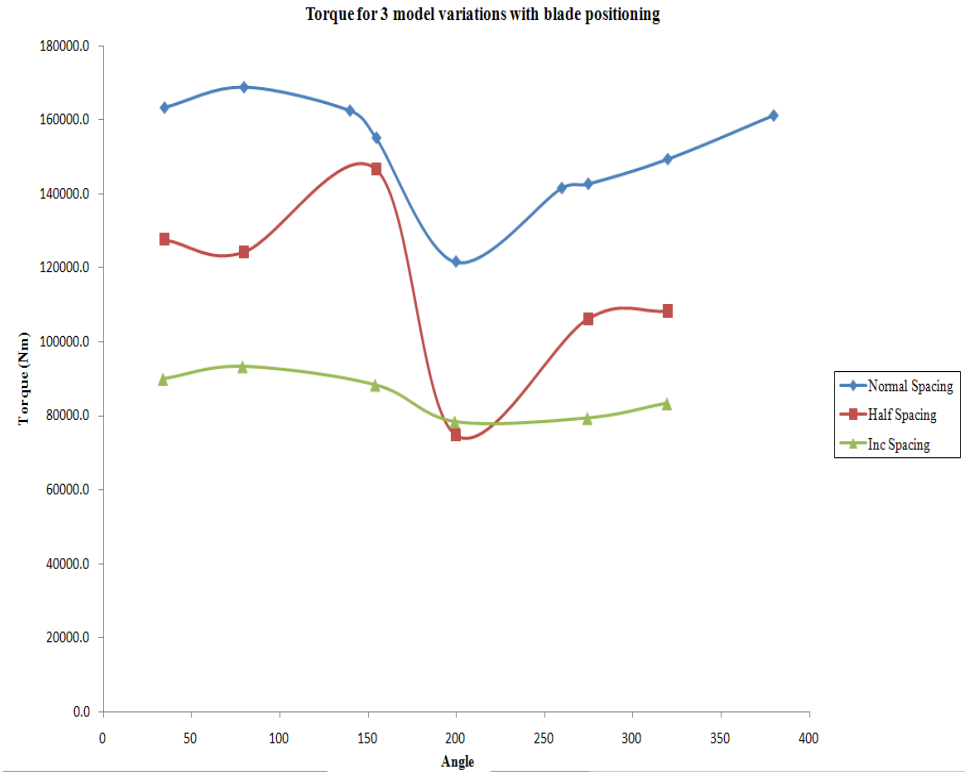

Figure 5.52 Comparison of the torque variation of all 3 models for the F3 case

The variation of the Inc_spacing_model is not as sharp as observed with the Half_spacing_model on both figures. Both plots interpret that the Inc_spacing_model experiences the least loading characteristics and is also confirmed in the pressure plots on section 5.5.1. However, due to the larger spacing the support system would undergo high bending and twisting as discussed on section 5.5. Coupled with the fact that the Inc_spacing_model under performs when compared to the datum model, further analysis of this model is unnecessary.

5.9 Steady State CFD Analysis for No-Pylon Model

The importance of appropriately designing the pylon and also correctly spacing the blades and the pylon has been discussed extensively in chapter 3 and section 5.5 in the model variations. A couple of simulations of the rotor have been analysed without the pylon to note the change in performance characteristics. The cases have been designed for the F2 and F3 parameters. The expected output of the results would be to achieve higher performance characteristics when compared to the normal_spacing_model. The performance characteristics for the F2 case was analysed and the total torque was calculated to be $207kNm$, the thrust was calculated to be $117kN$ and the power was to be $134kW$. These performance values are higher than that of the F2 normal_spacing_model. On average there was 2% increase in the performance criteria when compared with the normal_spacing_model F2 case.

The total torque was $466kNm$, the total thrust is $264kN$ and the total power was $452kW$ for the F3 case. Also, again on average there is an increase of 2% of performance characteristics when compared to the normal_spacing_model F3 case.

The Figure 5.53 shows the variation of torque for both model variations with blade positions for the F2 and F3 cases. The dip on the green and purple plots are for the F2 and F3 cases respectively for the datum model. This is due to the fact the blade is upstream of the pylon. Figure 5.54 shows the variation of thrust for all 3 model variations with blade positions for the F2 and F3 cases. Once again the dip shown on the green and purple plot are for the F2 and F3 cases for the normal_spacing_model.

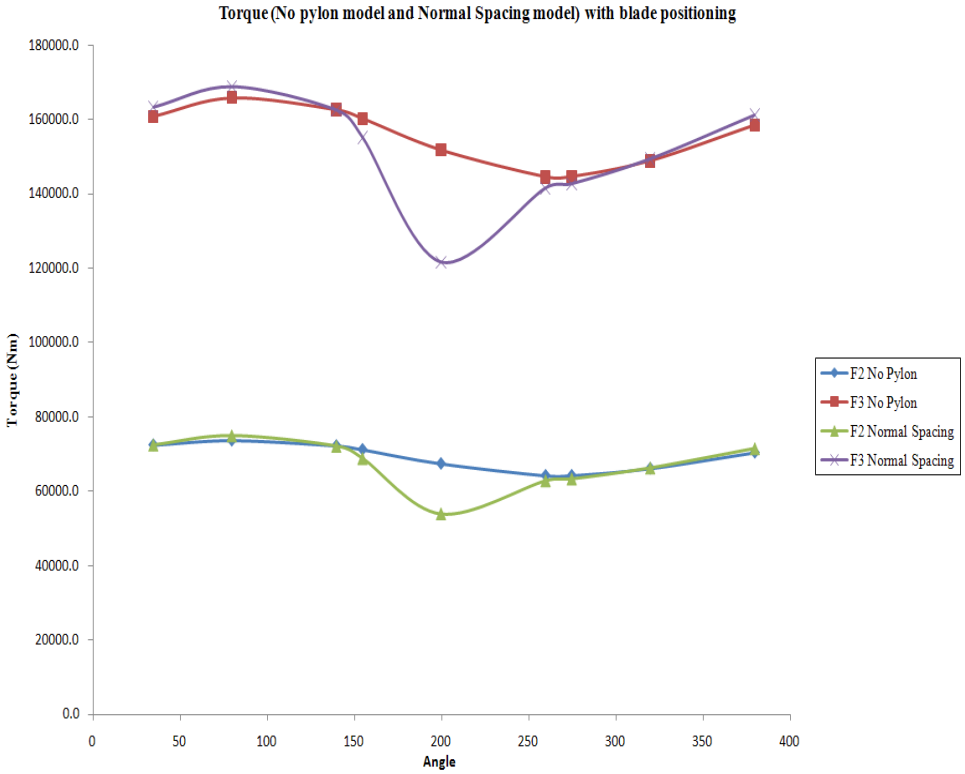

Figure 5.53 Comparison of the torque variation of datum F2 & F3 case with the No_pylon_model

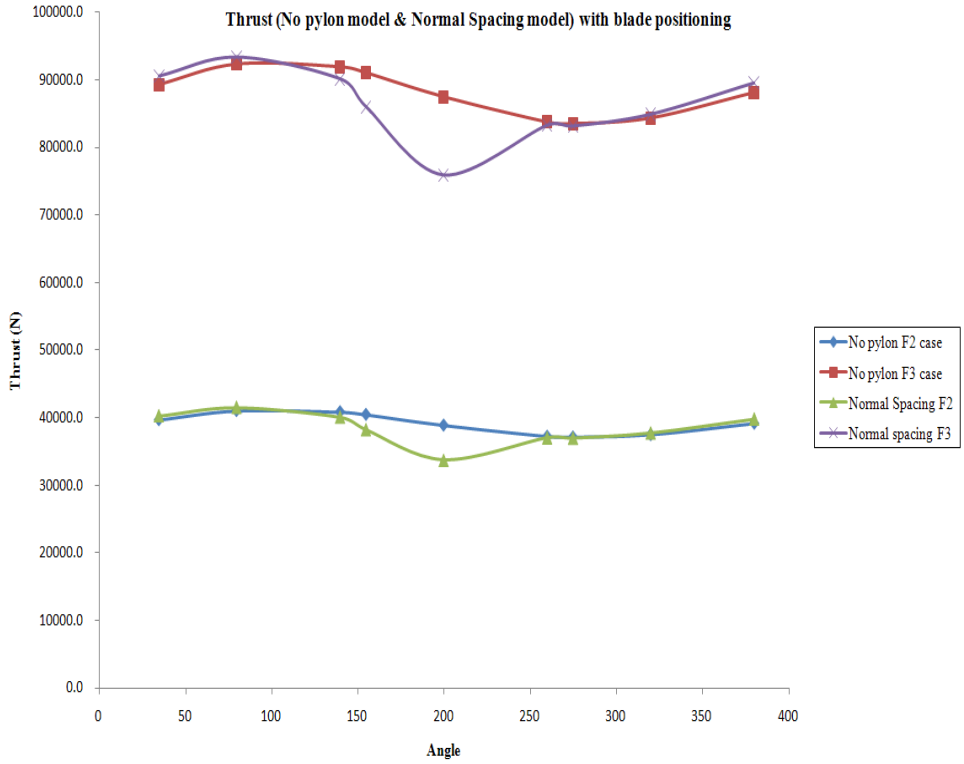

Figure 5.54 Comparison of the thrust variation of datum F2 & F3 case with the No_pylon_model

This analysis together with the pressure plots on section 5.5.4 highlights the importance of pylon spacing and pylon design. Large unsteady transient loadings could be experienced by the rotor-pylon system if the spacing and the pylon design is not optimised.

5.10 Chapter Closure

The design intent of the DeltaStream HATT has been presented together with a justification of the design philosophy. Steady state results and a number of model variations have been discussed and examined. A datum model called the normal_spacing_model has been described and analysed. Performance analysis were carried out on all model variations and the normal_spacing_model results were compared to the BEMT code results obtained by the turbine designer Mr. Chris Freeman. The accuracy of the CFD simulations is compromised to some extent by the relatively coarse size of the mesh. However, the model was kept deliberately light in terms of computational running costs in view of the fact that this model was always intended for use in transient simulations whose running and storage overheads are truly colossal (as the size of the storage requirements attest to).

The comparisons between BEMT derived results and the CFD output is in general quite good. However the main contribution of the numerical method lies beyond the integrated

performance parameters. It is to a large extent through qualitative plots that the contribution takes place. Indeed early in the project it was due to this method that the identification of separation regions near the hub led to the re-stagger of the section near the blade root.

The novel power shedding method to reduce thrust at high flow speeds, an essential requirement for a gravity anchored device such as the DeltaStream, was illustrated through the analysis of a high tidal flow case. Effective reductions in thrust and torque were recorded although the computed power exceeded the intended target.

A comparison of axial thrust and torque for all CFD models is presented in Appendix B, Figure B.4 and Figure B.5 respectively.

A comparison of the force about the Y and Z planes and the torque about the Y and Z planes are presented in Appendix B, Figure B.6 and Figure B.7 respectively with blade positions. As seen on Figure B.6, the forces produced are somewhat identical expect for those of the Inc_spacing_model and the Half_spacing_model. When compared with the other models, the Inc_spacing_model and the Half_spacing_model produces a marginally low variation and this could be confirmed with the pressure plots and the axial force plots for these models.

The Figure B.7 exhibits the same characteristics as with the previous figure. The torque about the Y and Z axes for the Inc_spacing_model and the Half_spacing_model are significantly less when compared to the other models.

Chapter 6

Transient Simulations

6.1 Introduction

The purpose of the transient computations was to investigate the behaviour of the turbine when exposed to the type of interactions that unsteady simulations can describe and which are absent from the steady state representation of the flow field. This is because fluid dynamics are inherently non-linear and some events such as boundary layer separations only take place when exposed to significantly dynamic conditions.

In addition the work shown in this chapter corresponded to the natural progression from the steady state representation of the flow conditions before the realistic effects of the environment are taken into account with the inclusion of the waves documented in the subsequent chapter.

Some of the steady state cases discussed in the previous chapter were repeated in this part of the work such that results between the two methods can be directly compared. Of the three blade-pylon spacing variants described previously, two were simulated in this phase of the work. These were the normal_spacing_model and the Half_spacing_model. The Inc_spacing_model was not considered in this part of the work because of the mechanically undesirable features of the extended shaft and because the normal or datum spacing was not seen to be associated with excessive pressure fluctuations.

The start-up, F1 and F2 cases were not modelled in the transient simulations as they were considered unnecessary and these would utilise precious CFD resources and storage space resources. The start-up, F1 and F2 cases were mainly modelled to compare the CFD simulated results with the BEMT derived data and to establish an operational envelope of the tidal turbine through the CFD results. The F3 and F4 cases, corresponding to the peak power situation (nominal power) and one point in the power shedding regime, were

considered worthy of further investigation.

6.2 Transient Model Set-up

In transient simulations real time information is required for the code to resolve at what time intervals the flow field is calculated. Unlike for the steady state cases, where the goal is to reach a flow solution that is invariant in time, convergence in a transient simulation sense is reached when the flow exhibits cyclic behaviour. In a transient simulation both physical timesteps and the maximum number coefficient iterations per timestep need to be set.

The transient timestep control can be carried out in the code through one of two systems. First, the user can select the Timesteps option which provides a manner for the code to track the progress of the real time during the simulation. Alternatively the user can employ the Time Duration approach where the user specifies a limit on the time-span thereby controlling the real time for the simulation to conclude. This latter approach was the one employed in this work.

The analysis type was set to transient and a total time of $25.8342s$ was used for the F3 case and a total time of $11.4286s$ was used for the F4 case. Both these timescales refer to 4 complete revolutions of the turbine. It was noted that the simulations needed at least 2.5 to 3 revolutions for the rotor and the flow field to reach a state of periodicity which, as mentioned above, is a measure of convergence in transient simulations. This is discussed more thoroughly in the subsequent sections. The timestep function was activated and a set timestep of $0.01794s$ and $0.0079s$ was selected for the F3 and F4 cases respectively. This corresponded to the rotor system being rotated at a rate of 1° in every timestep calculation.

At least a degree of rotation was found necessary to capture the main transient physics in the models. Initial time selection was selected as automatic with value and the value set to zero. Most of the domain interface specifics mentioned in the section 4.6 apply to these transient models. The frozen rotor principle used in the previous models was changed to transient interface. This method predicts the true transient interaction in the flow through the two frames of reference. The relative position of the frames of reference is updated in terms of angular displacement at every timestep.

Second order (high resolution) advection scheme was selected to calculate the advection terms in the discrete finite volume equations. Second Order Backward Euler is second order accurate and was used in the transient scheme that defines the discretisation algorithm for the transient term. This scheme is an implicit time stepping scheme. The timestep initialisation was set to automatic. In the convergence control, the minimum coefficient loop was set to 1 and the maximum coefficient loop was set to 5. Timescale control was set to coefficient

loops. The residual type was set to RMS and set to 1×10^{-6}. The transient results files were backed up between the third and the fourth revolution for every degree of rotation. The simulations (F3 and F4) utilised 16 processors to complete and roughly took around one and a half days to complete.

6.3 Normal Spacing model

The transient F3 and F4 cases for the normal_spacing_model are analysed and discussed in this section. The blade loading plots, blade-pylon interaction and wake distribution pressure contour plots for the F3 and F4 cases are discussed and analysed. The thrust and torque values are analysed and plotted against the simulation time.

6.3.1 F3 case (maximum torque)

Figures 6.1, 6.2, 6.3 display the individual blade loading plots at 25%, 50% and 90% span respectively.

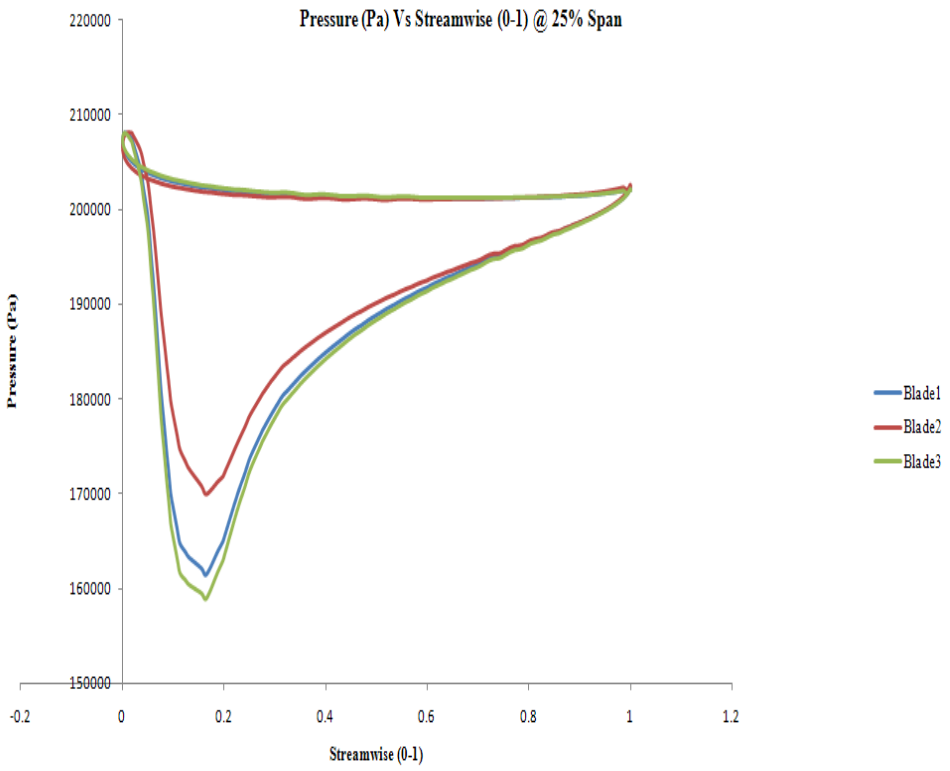

Figure 6.1 Pressure plot at 25% span - normal_spacing_model F3

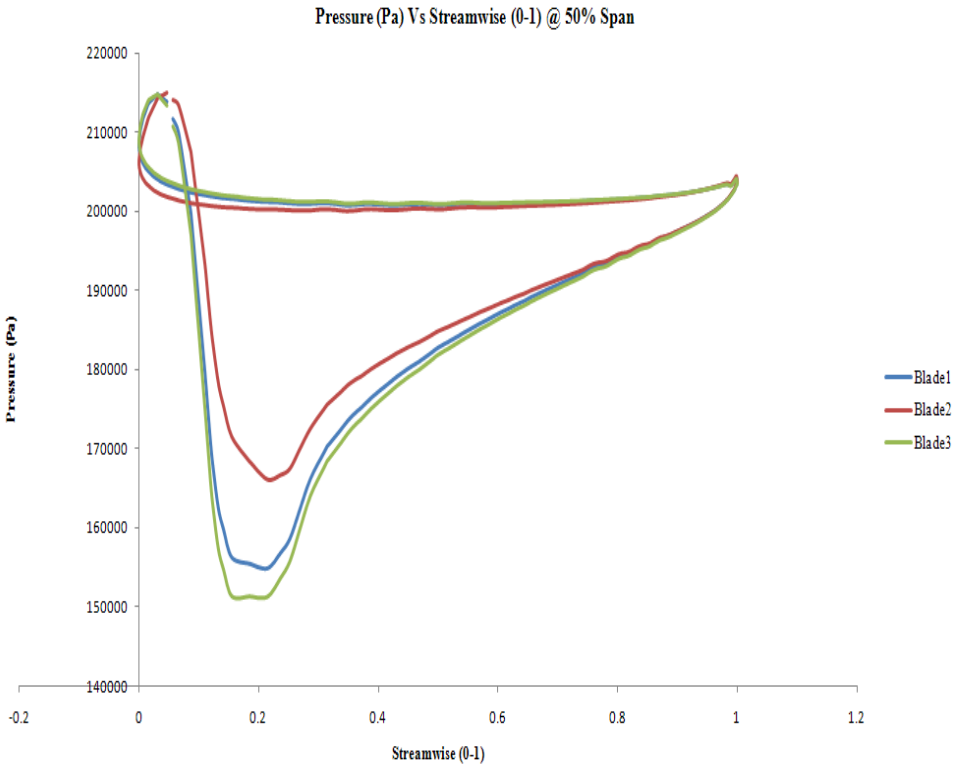

Figure 6.2 Pressure plot at 50% span - normal_spacing_model F3

The pressure plots extracted from the transient simulation, taken at 25%, 50% and 90% span, are quite similar to those obtained from the steady state analysis. The marginal differences are due to the position of the blades in these plots not exactly coinciding with those of the steady state case.

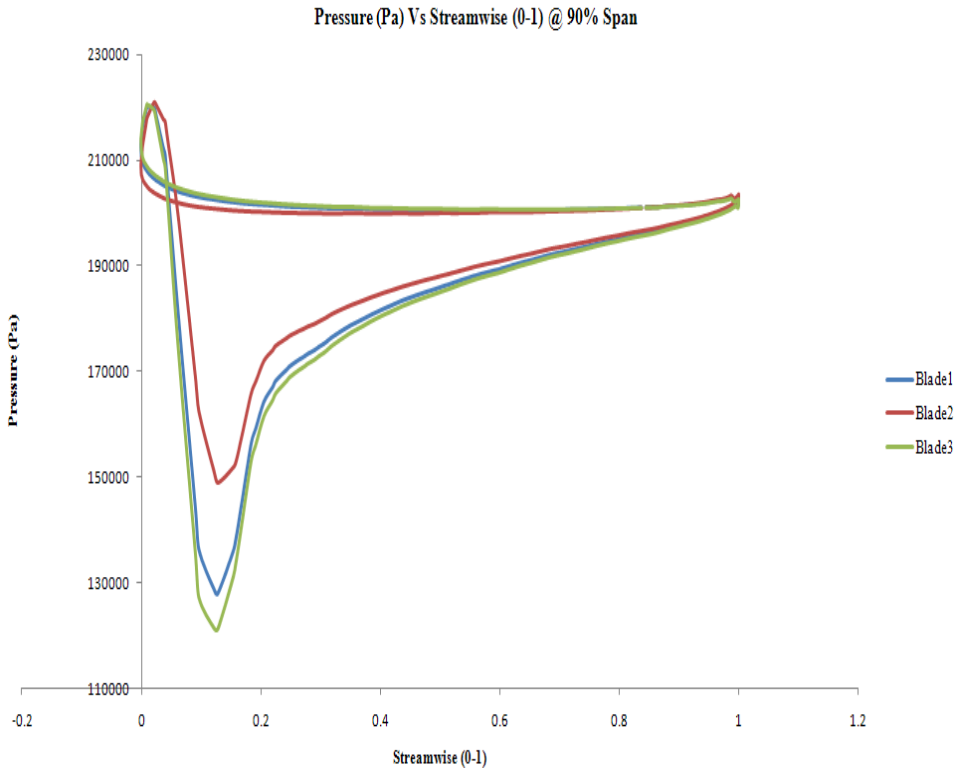

Figure 6.3 Pressure plot at 90% span - normal_spacing_model F3

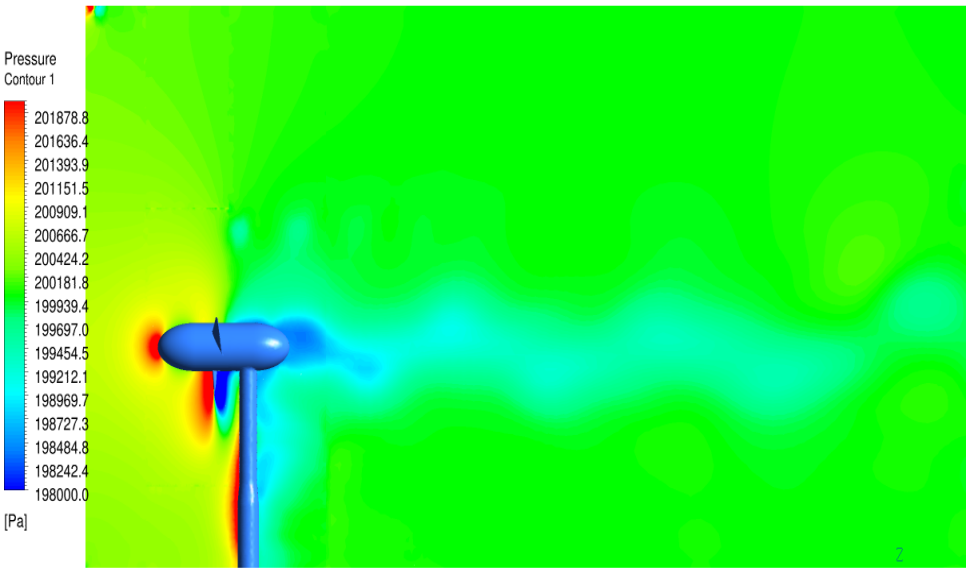

Figure 6.4 Pressure distribution in the meridional plane - normal_spacing_model F3

The pressure distribution in the meridional plane, Figure 6.4, is similar in several respects to its steady-state equivalent, on Figure 5.28, but there are significant differences worth commenting about. The pressure contours that correspond to the stagnation regions are similar in intensity and regarding their location. However the definition of the wake, including its spatial characterisation, is much more complex in the unsteady state case. This

suggests that the description of the wake requires a transient solution to fully achieve its full significance.

The Figure 6.5 shows the wake distribution aft of the rotor. The velocity deficit is plotted against the water depth at specific rotor diameters downstream of the rotor.

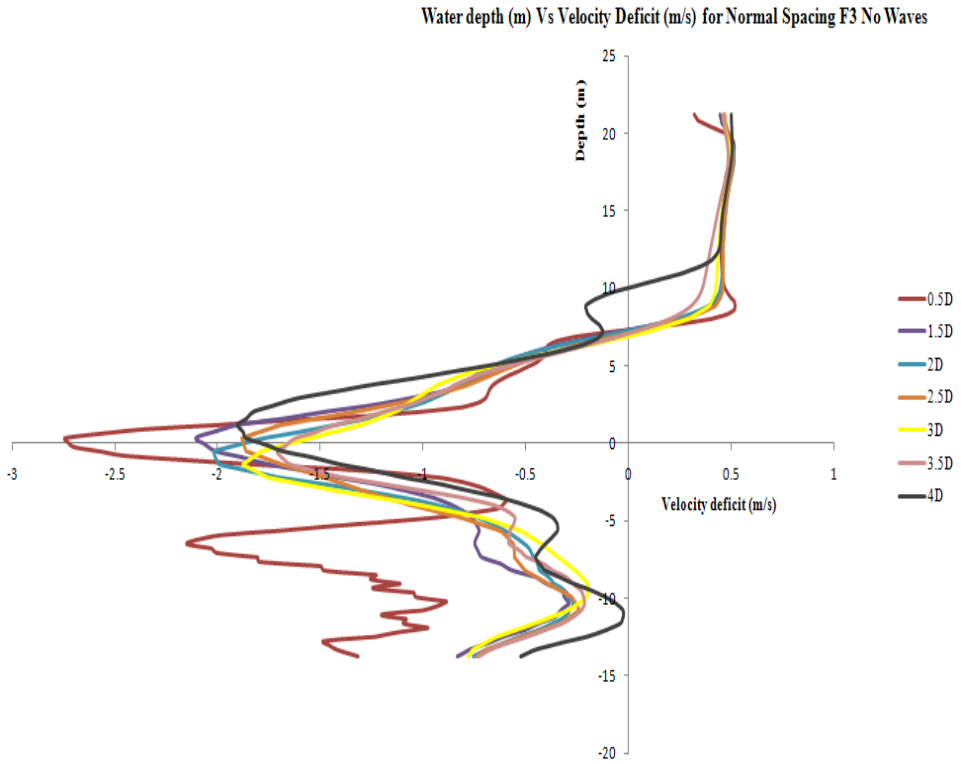

Figure 6.5 Velocity deficit downstream of the rotor for normal_spacing_model F3 case

The average flow speed of the rotor operating area was calculated to be $2.25ms^{-1}$. The flow velocities on the above plot in Figure 6.5 were subtracted from the average flow velocity of the rotor operating area to get the velocity deficit. It is apparent from the Figure 6.5 that the highest deficit occurs closest to the rotor and gradually increases to free stream velocities at many diameters downstream of the rotor as is evident in the steady state plot on Figure 5.29. As also seen from the steady state velocity deficit plot, $3.5D$ - $4D$ downstream of the rotor show an increase of approximately $1ms^{-1}$ when compared to velocities just aft of the rotor axis. The significant feature of Figure 6.5 is that the wake plots are slightly shifted towards the left side of the graph implying that the wakes are much more resolved when compared to the steady state generated wakes.

The similarity between the pressure distribution plots due to the two analysis methods is also present in Figure 6.6 showing the blade-pylon interaction pressure contour plot. It is worth noting that the presence and location of the two high pressure regions, denoted in this plot in red, together with the low pressure values which are shown in dark blue, correspond

strictly to the particular blade-pylon interaction process. The pressure distribution around the profile is elsewhere in the transit of the blade replaced by a conventional distribution.

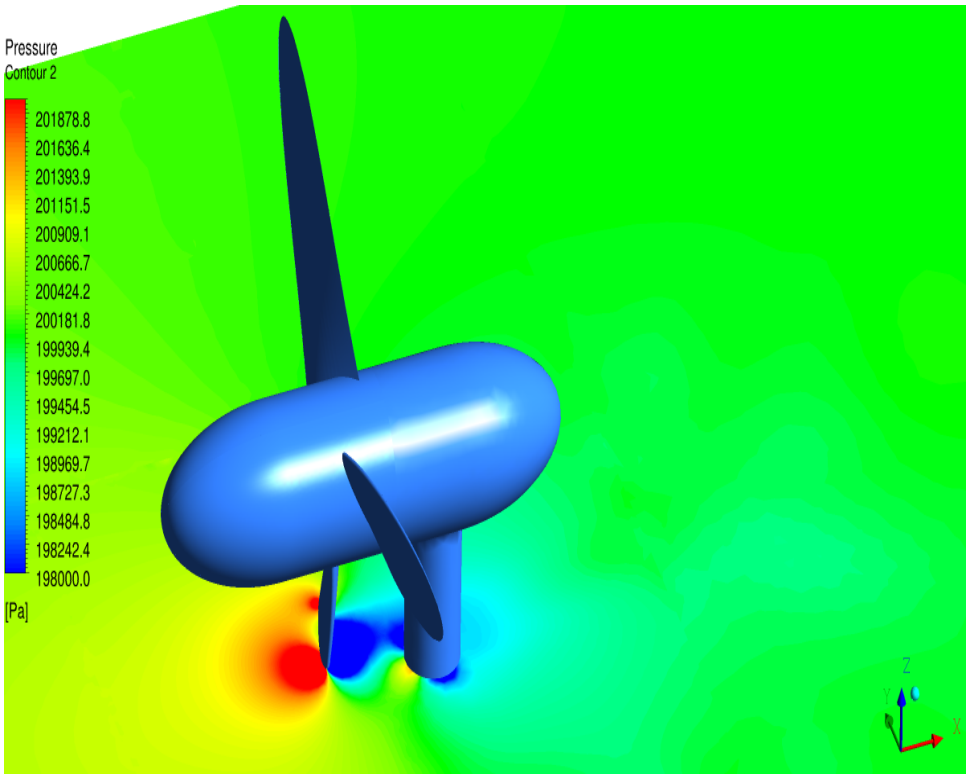

Figure 6.6 Blade-pylon interaction - normal_spacing_model F3

The conventional pressure distribution plots are shown of Figures 6.7 and 6.8 for the blade 3 and blade 1 respectively. Both these figures demonstrate a normal behaviour in representing the pressure and the suction sides of the blades. The low pressure area on Figure 6.6 displays an exaggerated area (dark blue) as compared to Figures 6.7 and 6.8. And also the low pressure area runs along the entire chord length on Figure 6.6 which is an abnormal behaviour but could be justified because of the blade interaction with the pylon.

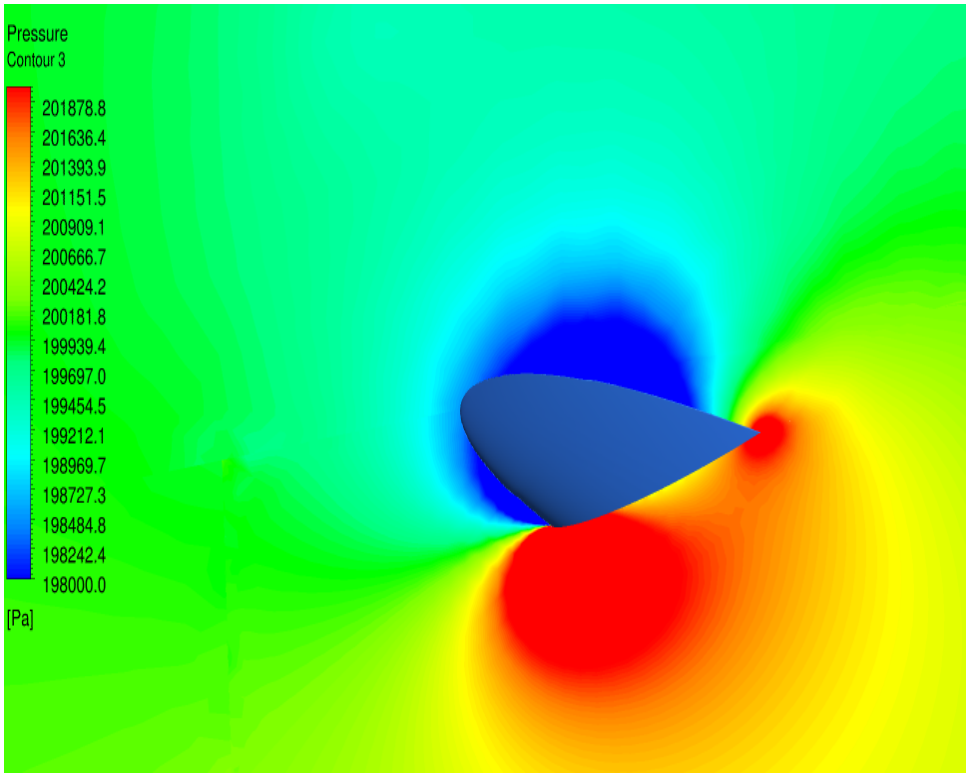

Figure 6.7 Pressure distribution over the Blade 3 (top)

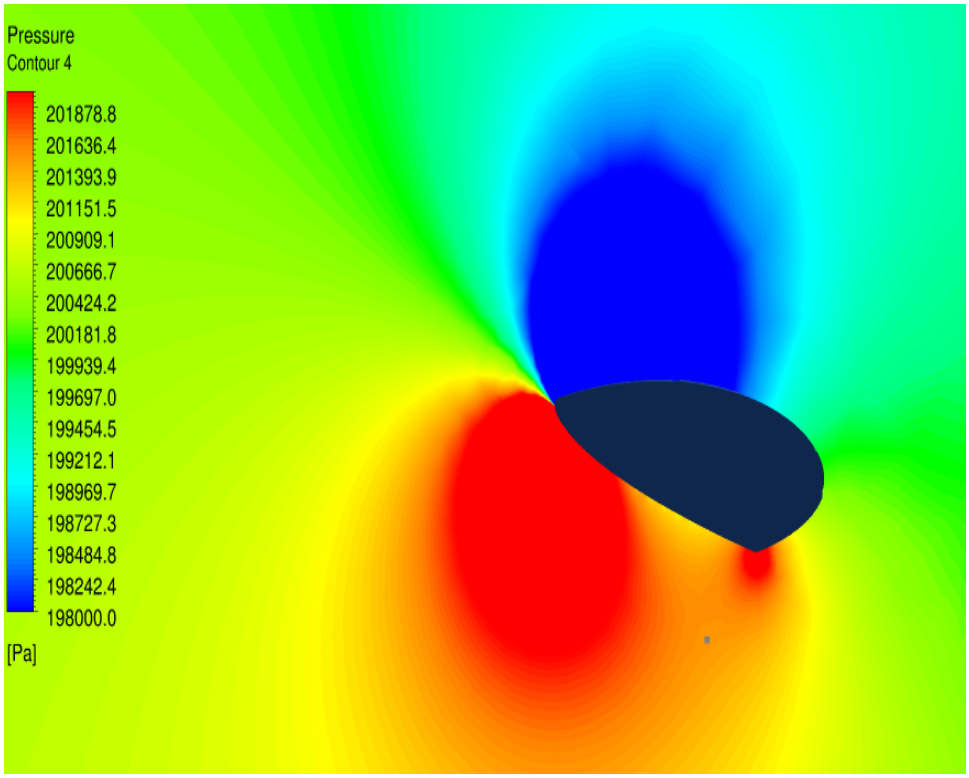

Figure 6.8 Pressure distribution over the Blade 1

Additional qualitative plots when the blade 2 first experiences the presence of the pylon, blade 2 in front of the pylon and after blade 2 had passed the pylon have been documented.

The three transient results at 2080, 2099 and 2132 corresponding to simulation time of $19.375s$, $19.716s$ and $20.308s$ were loaded on to ANSYS CFX and vector plots, vorticity plots, pressure plots and velocity plots were plotted for these timesteps.

A user-defined surface was created from the "DRUMFRONT" surface in the block "ABC" at $0.5m$ in front of the DRUMFRONT surface. The vorticity, pressure, circumferential velocity, and vector plots were created from this plane. A second user-defined surface was created in the same manner and placed at approximately $3D$ $(45m)$ downstream of the rotor and an axial velocity component plot was plot on this plane.

The vector plot on Figure 6.9 displays the flow field approximately a metre or so downstream of the rotor plane of rotation at the timestep corresponding to 2080. This plot clearly displays the vortices created just aft of the each blade and the flow field being disturbed by the rotation of the rotor.

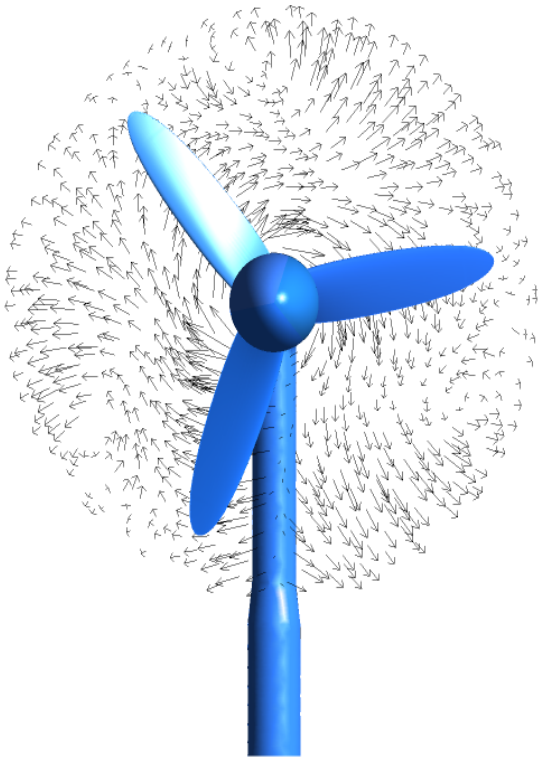

Figure 6.9 Vector plot at 2080 **timestep F3**

The vorticity plot on Figure 6.10 show the vortices created by the blades for the same axial location. The total vorticity was calculated to be approximately $5.8s^{-1}$, agreeing with the vorticity calculated for the steady state simulation.

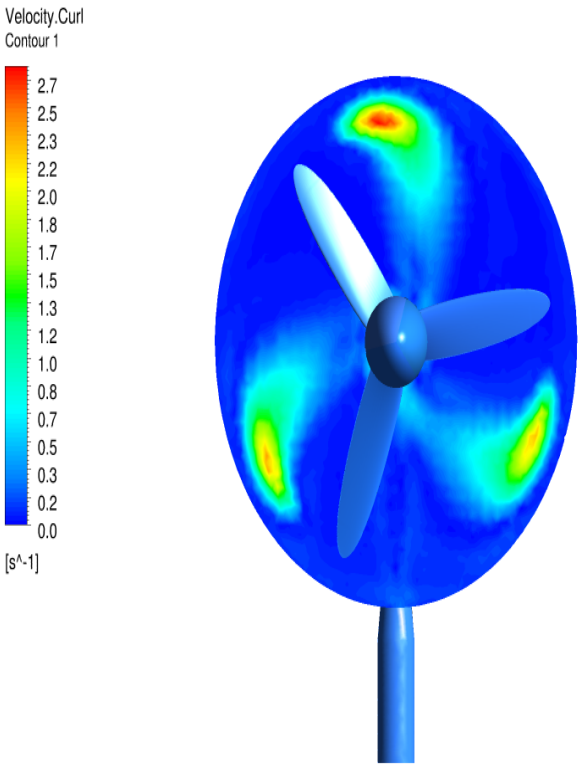

Figure 6.10 Vorticity plot at 2080 **timestep F3**

Figure 6.11 displays a pressure plot at the same location and on this plot it could be seen clearly that there is an increased activity just aft of the blade where the pylon is present.

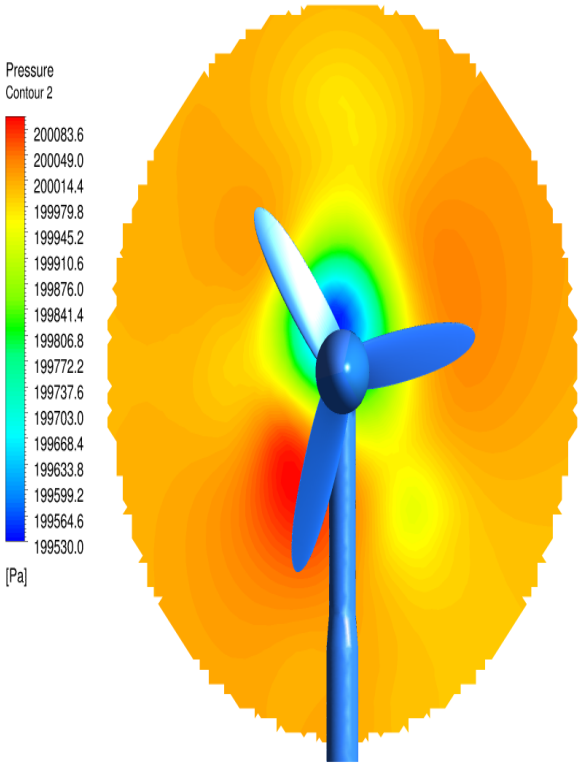

Figure 6.11 Pressure plot at 2080 **timestep F3**

The circumferential velocity is plot on Figure 6.12 at the same location.

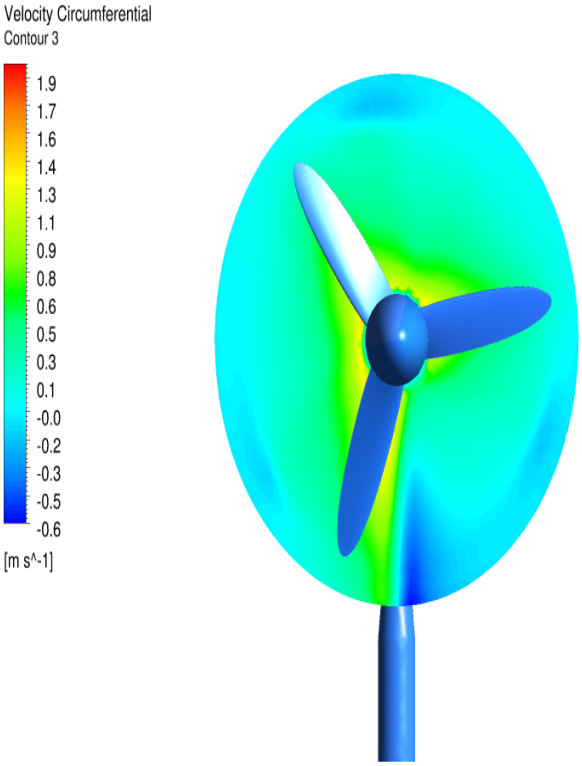

Figure 6.12 Circumferential velocity plot at 2080 **timestep F3**

Axial velocity is plotted on Figure 6.13 at the second user-defined location positioned approximately at $3D$ downstream of the rotor. The blades were made invisible for clarity. The blade orientation was unchanged. As described before, the wake has recovered to a certain extend at $3D$ downstream of the rotor, however, there is still some wake present even between $3D - 4D$ downstream of the rotor.

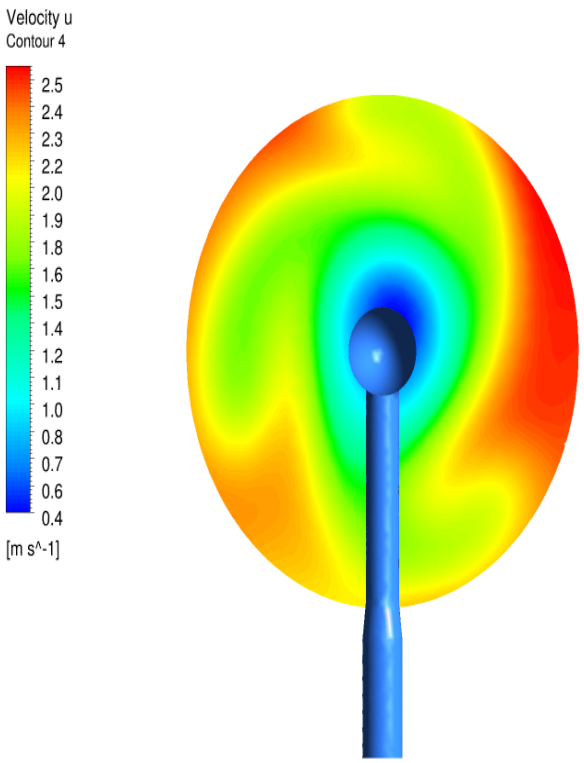

Figure 6.13 Axial velocity plot at 2080 **timestep F3**

The vector plot on Figure 6.14 displays the flow field at the 2099 timestep signified when the blade 2 is in front of the pylon. The general orientation of the flow field has changed and flow intensity has increased on the blade 2 due to the pylon as denoted by the larger arrows.

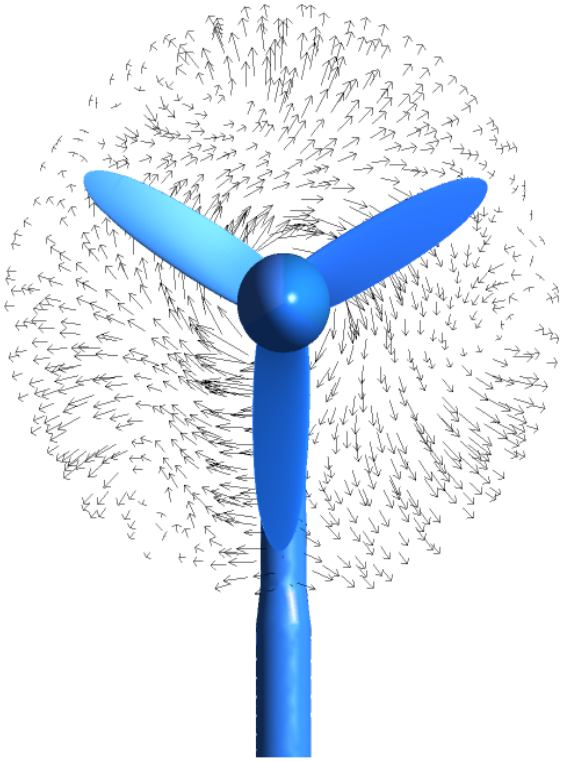

Figure 6.14 Vector plot at 2099 **timestep F3**

The vorticity plot on Figure 6.15 show the vortices created by the blades. This plot clearly displays that the vortices have moved with the blade when compared to the previous corresponding plot.

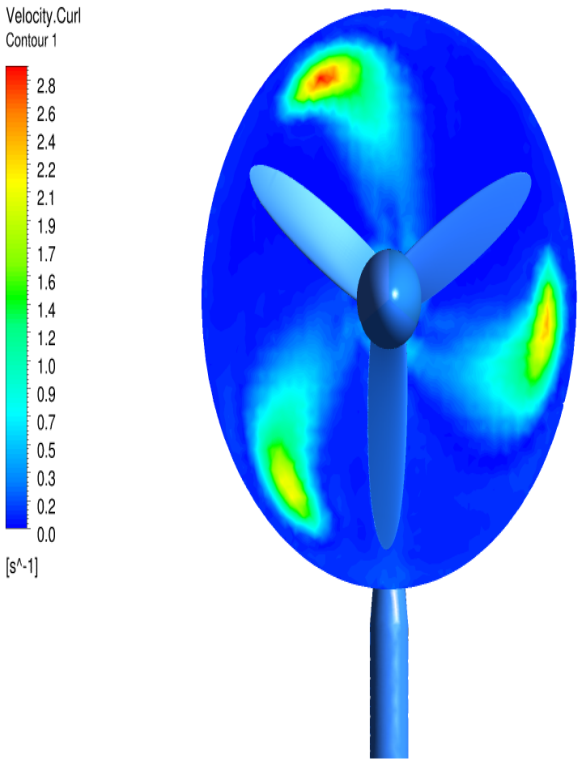

Figure 6.15 Vorticity plot at 2099 **timestep F3**

Figure 6.16 displays a pressure plot.

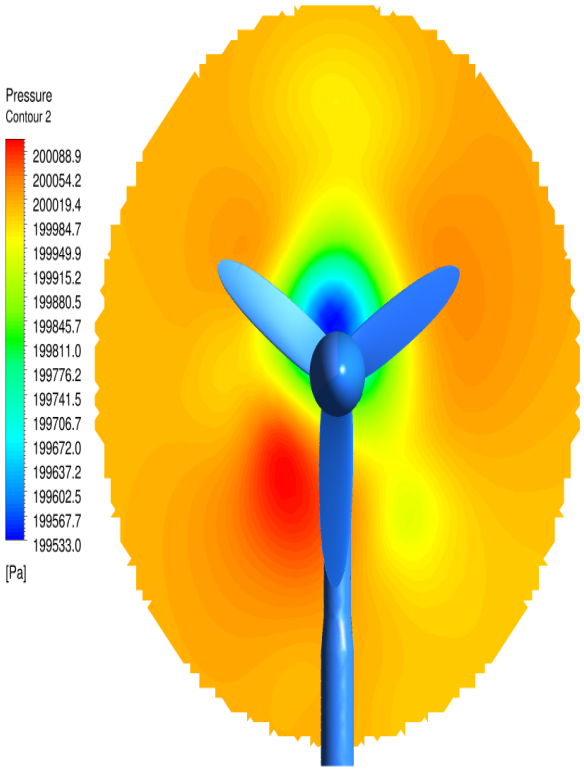

Figure 6.16 Pressure plot at 2099 **timestep F3**

The circumferential velocity is plot on Figure 6.17.

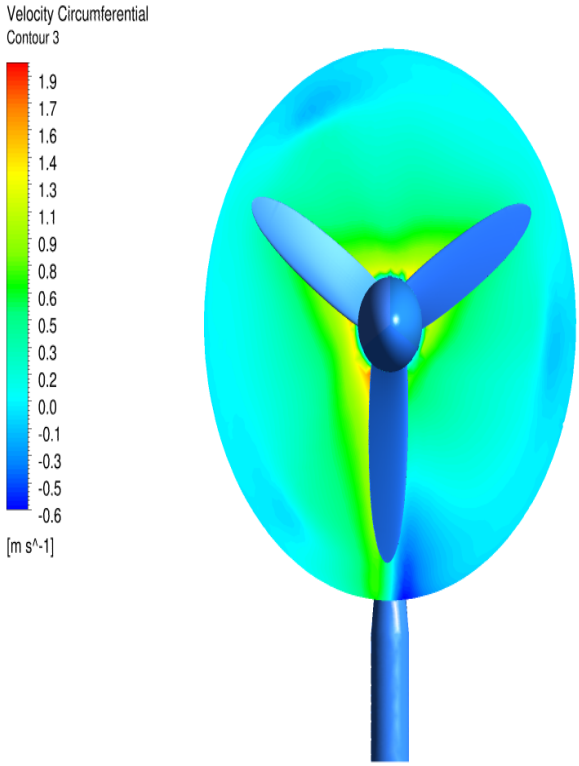

Figure 6.17 Circumferential velocity plot at 2099 **timestep F3**

Axial velocity plot is plotted on Figure 6.18 in the same manner as the previous corresponding plot.

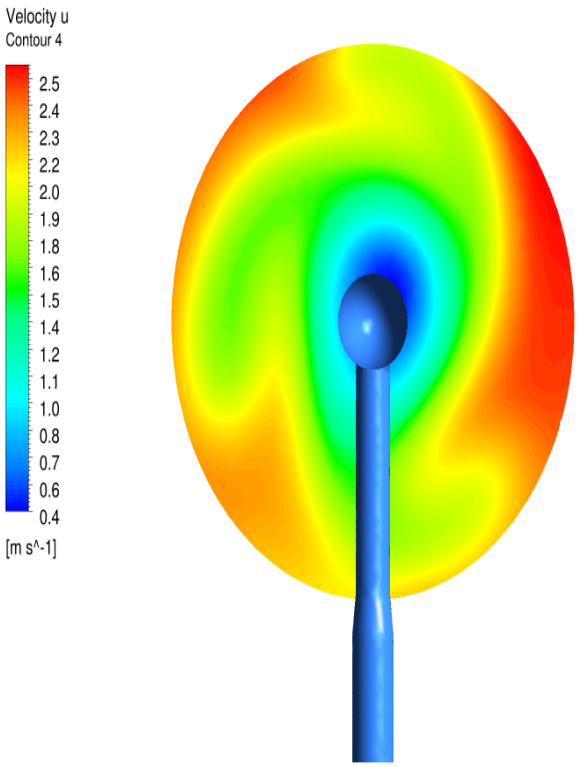

Figure 6.18 Axial velocity plot at 2099 **timestep F3**

The vector plot on Figure 6.19 displays the flow field at the 2132 timestep signified when the blade 2 has just passed the pylon. Again the general orientation of the flow field has changed and vorticity intensity has increased for the blade 2 as shown on the swirls just behind the blade 2.

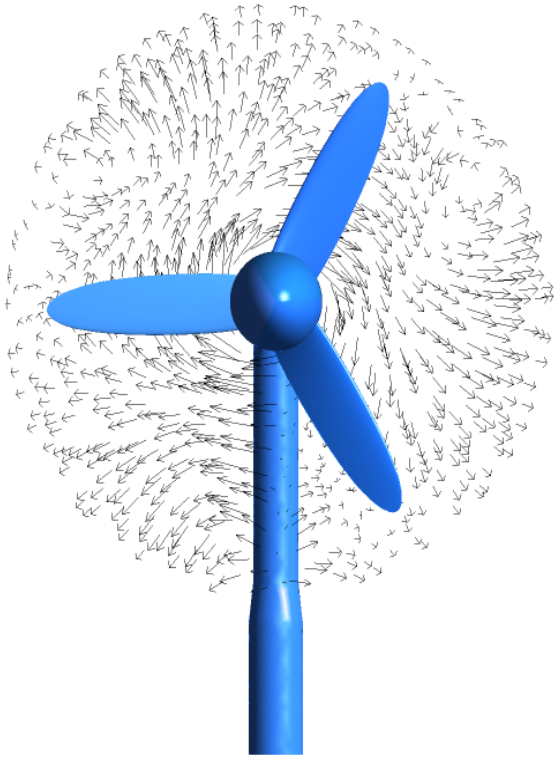

Figure 6.19 Vector plot at 2132 **timestep F3**

The vorticity plot on Figure 6.20 show the vortices created by the blades. This plot clearly displays that the vortices have moved with the blade when compared to the previous vorticity plots.

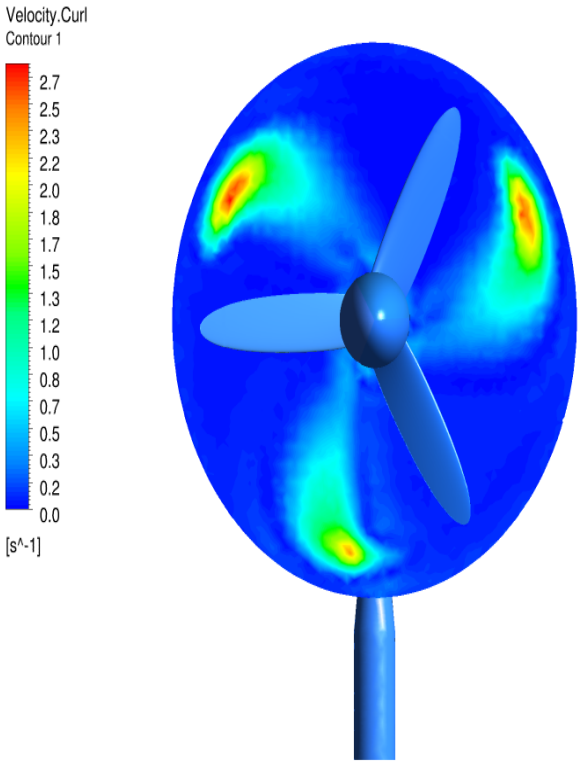

Figure 6.20 Vorticity plot at 2132 **timestep F3**

Figure 6.21 displays a pressure plot.

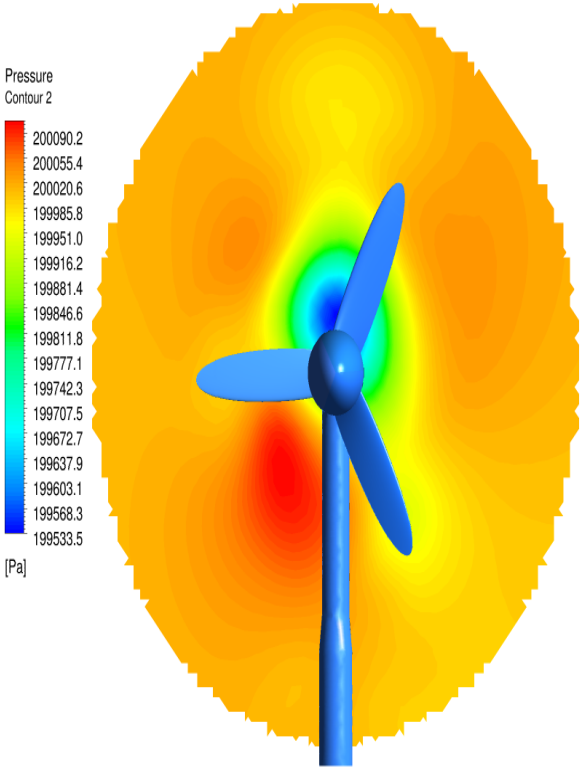

Figure 6.21 Pressure plot at 2132 **timestep F3**

The circumferential velocity is plot on Figure 6.22.

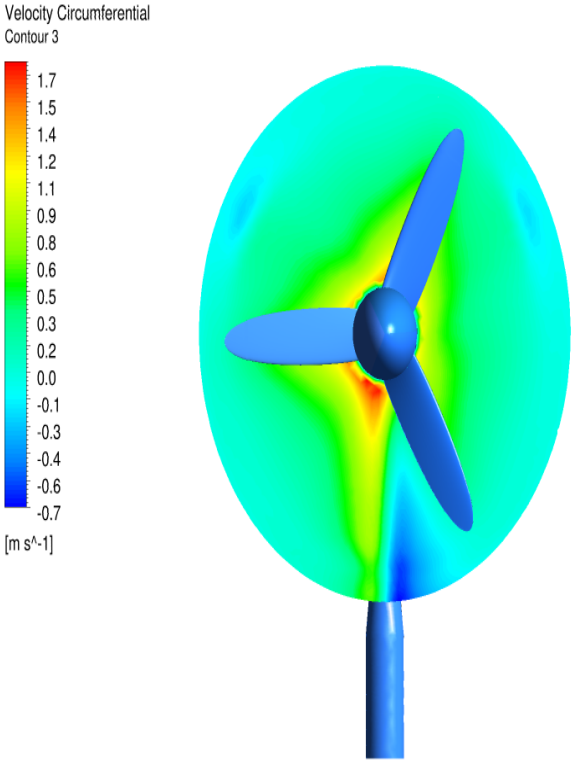

Figure 6.22 Circumferential velocity plot at 2132 **timestep F3**

Axial velocity plot is plotted on Figure 6.23 in the same manner as the previous axial velocity plots.

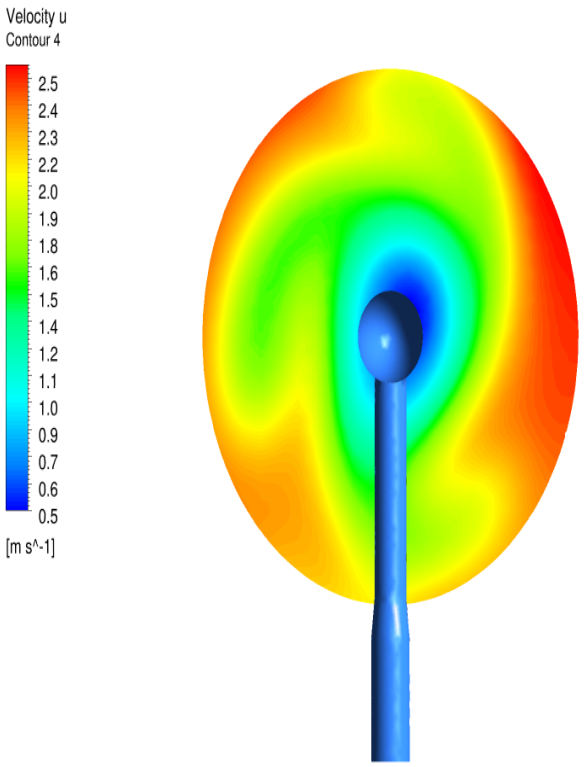

Figure 6.23 Axial velocity plot at 2132 timestep F3

The flow conditions used were exactly the same as the F3 steady state case. Figure 6.24 below represents the total axial thrust and torque loads for the turbine. The reason for the time frame to start at just over $18s$ rather than at $0s$ is that the simulation was abruptly ended through a computer fault and restarted from there. If restarted from a full back up file (.bak) or a transient results file (.trn) in ANSYS version 12.1, the previous data collected would have been available but this simulation was restarted from a full back up file from ANSYS version 11.0. Therefore, for some reason the previous timesteps were not loaded.

The time histories of the torque and thrust for the turbine, rather than individual blades, are seen in Figure 6.24. The variation of these two quantities is quasi sinusoidal and represents roughly a 5% deviation from the mean value. The total torque was calculated to be $506.0kNm$, the total thrust was approximately $290.0kN$ and the total power the turbine generates is approximately $491.0kW$.

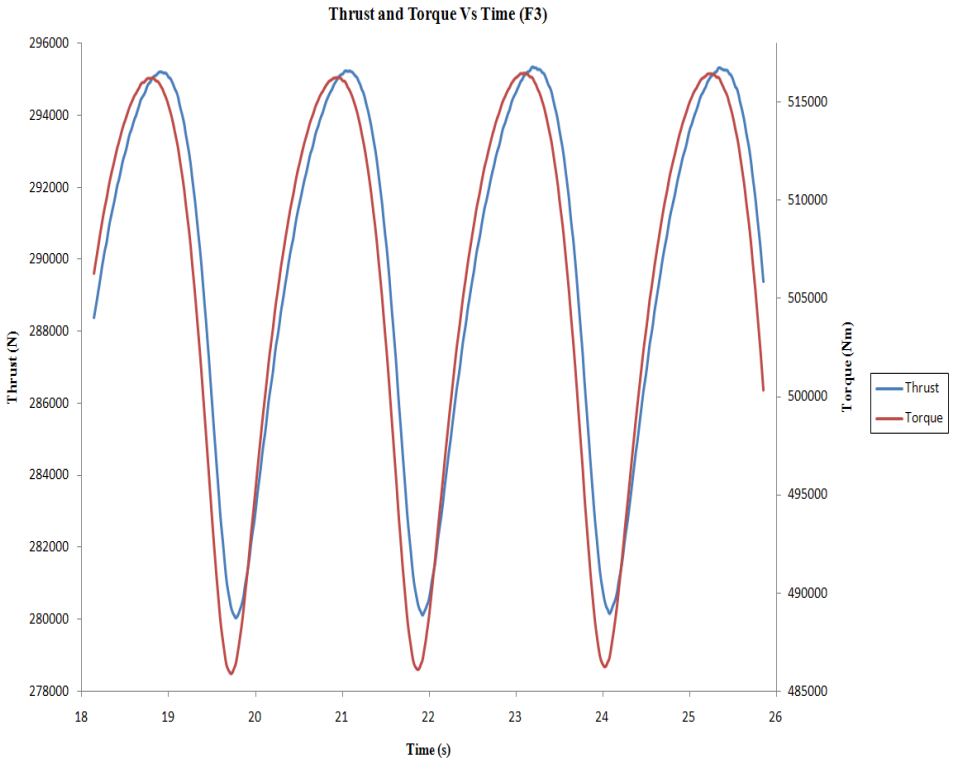

Figure 6.24 Thrust and Torque loads for F3 case

The axial thrust and axial torque variation per blade are shown on Figure 6.25 and Figure 6.26 respectively. The lowest point on all three figures denotes that the respective blade is in front of the pylon at the lowest point in the rotation.

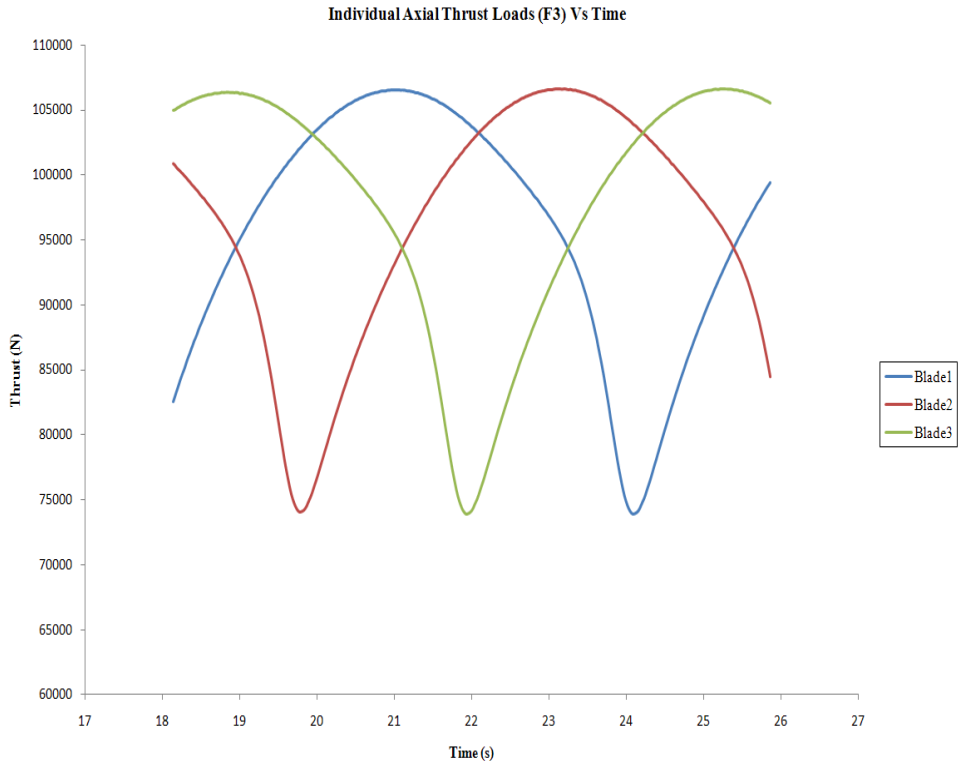

Figure 6.25 Individual Axial Thrust loads

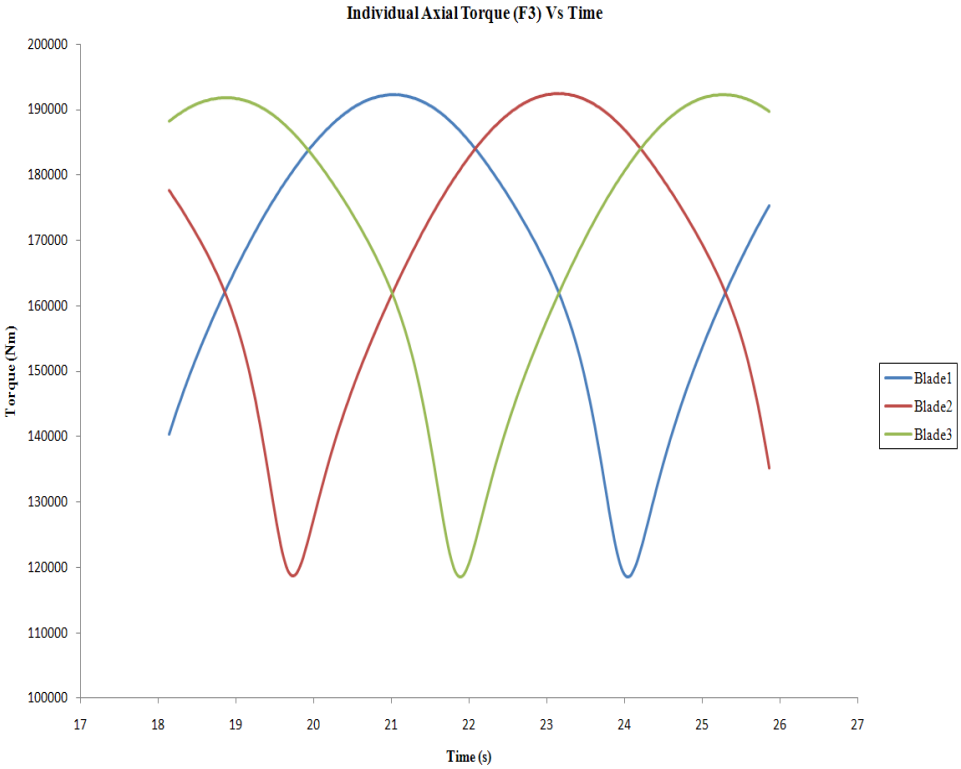

Figure 6.26 Individual Axial Torque loads

The graphs represent approximately just over one revolution. The individual plots on

Figures 6.25 and 6.26 show that the blade 2 goes past the pylon initially followed by blade 3 and blade 1.

6.3.2 F4 case (maximum thrust)

Figures 6.27, 6.28, 6.29 represent the blade loading plots for individual blades at 25%, 50% and 90% span respectively. As expected, given the higher relative velocities, the F4 blade loading plots indicate that the blades experience higher forces than those of the F3 case.

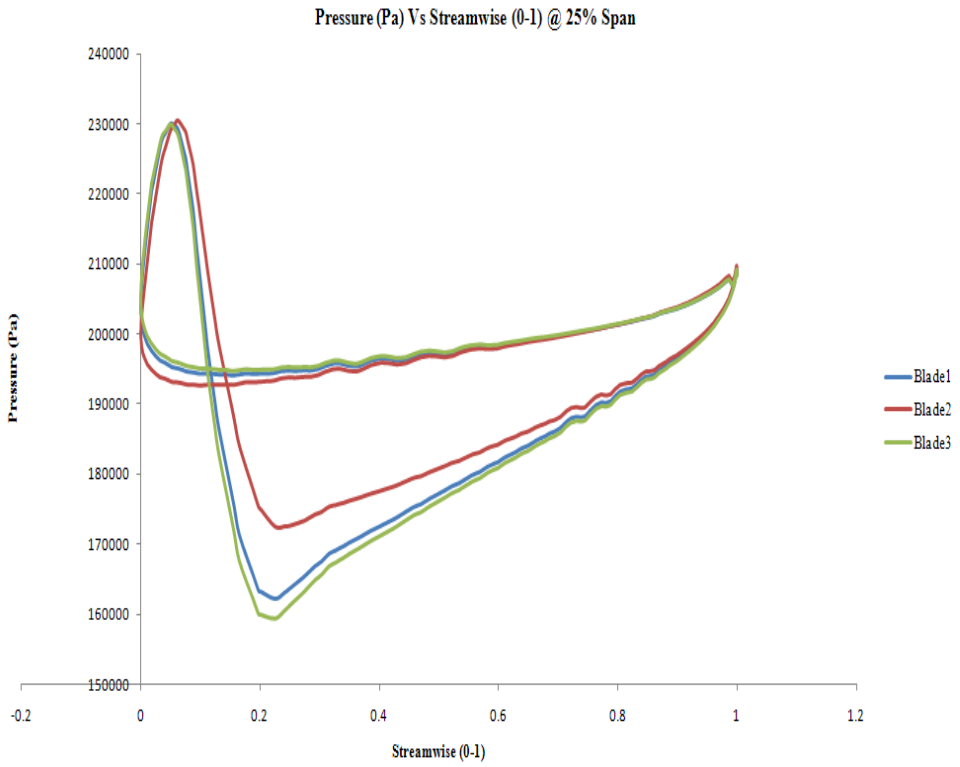

Figure 6.27 Pressure plot at 25% span - normal_spacing_model F4

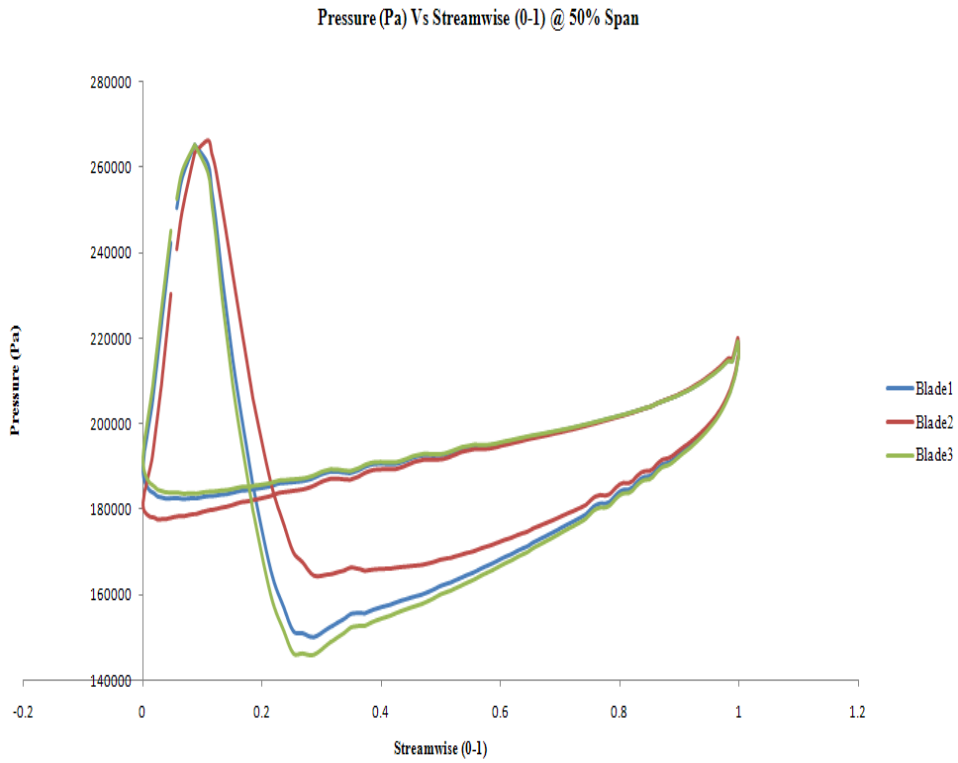

Figure 6.28 Pressure plot at 50% span - normal_spacing_model F4

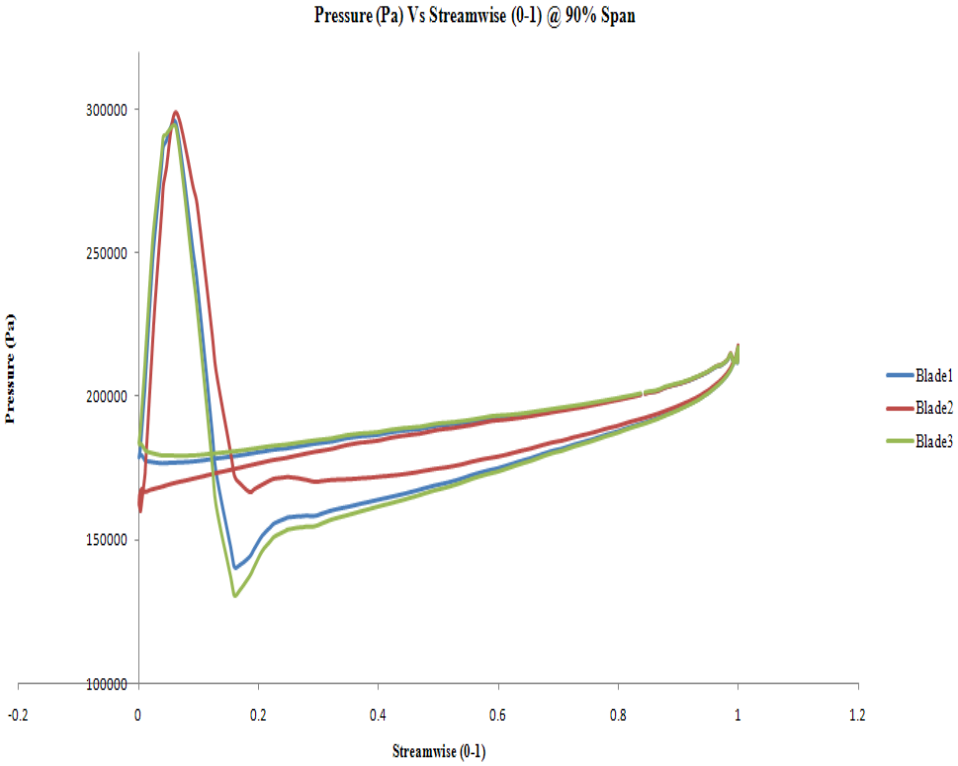

Figure 6.29 Pressure plot at 90% span - normal_spacing_model F4

The blade orientation is the same as that of the previous F3 case.

As shown in Figure 6.30, a strong wake is evident in the $1-3D$ downstream of the rotor. The stagnation points are relatively strong when compared to the F3 case as shown on the red pressure areas. The wake is clearly defined in the low pressure areas aft of the rotor.

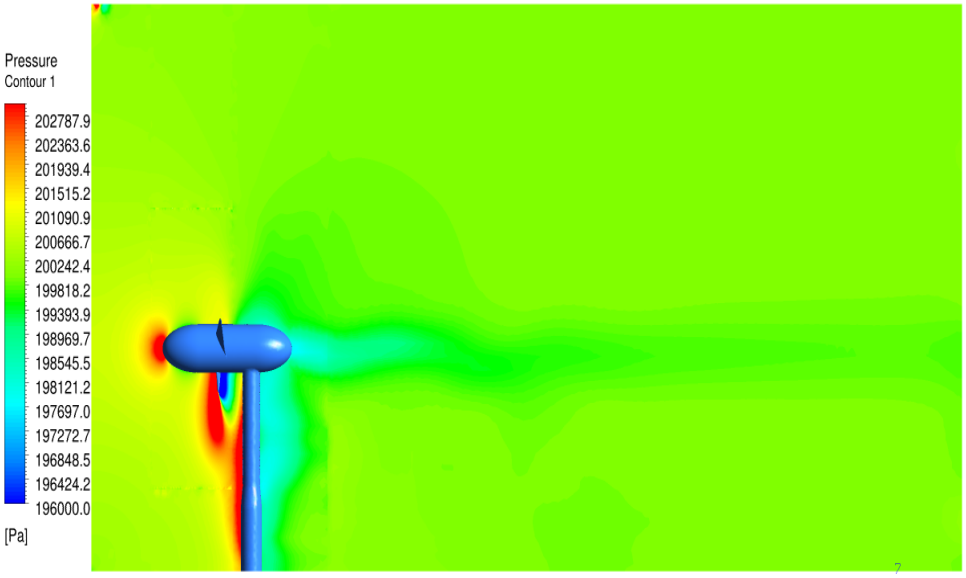

Figure 6.30 Pressure distribution in the meridional plane - normal_spacing_model F4

As shown in Figure 6.31, at higher flow speeds it is evident that the blade-pylon interaction is greater too.

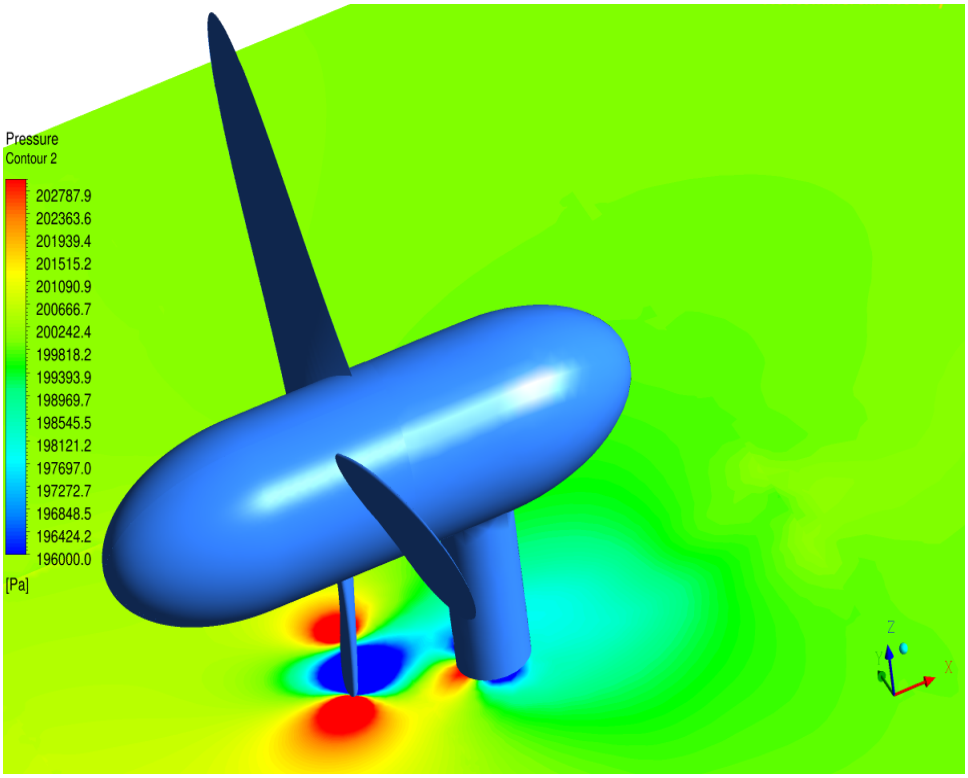

Figure 6.31 Blade-pylon interaction - normal_spacing_model F4

As with the F3 case, the three transient results at 2080, 2099 and 2132 corresponding to simulation time of $8.575s$, $8.726s$ and $8.988s$ were loaded on the ANSYS CFX and vector plots, vorticity plots, pressure plots and velocity plots were plotted for these timesteps.

The vector plot on Figure 6.32 displays the flow field approximately a metre or so downstream of the rotor at the 2080 timestep. This plot clearly displays the vortices created just aft of the each blade and the flow field being disturbed by the rotation of the rotor.

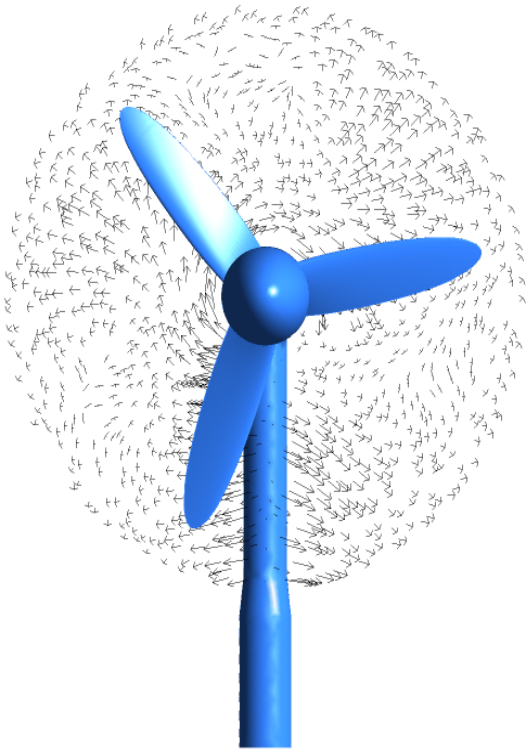

Figure 6.32 Vector plot at 2080 timestep F4

The vorticity plot on Figure 6.33 show the vortices created by the blades in the same manner as the F3 case. The intensity of this plot is far greater than that of the corresponding F3 plots. This is because the flow parameters are higher and the blade is rotating faster than that of the F3 case parameters. The total vorticity was calculated to be approximately $13.5s^{-1}$.

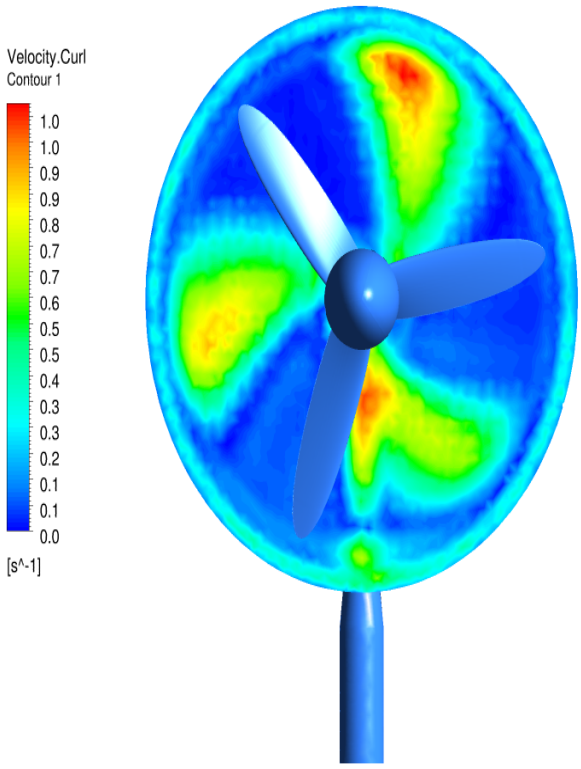

Figure 6.33 Vorticity plot at 2080 **timestep F4**

Figure 6.34 displays a pressure plot at the same location and on this plot it could be seen clearly that there is an increased activity just aft of the blade where the pylon is present.

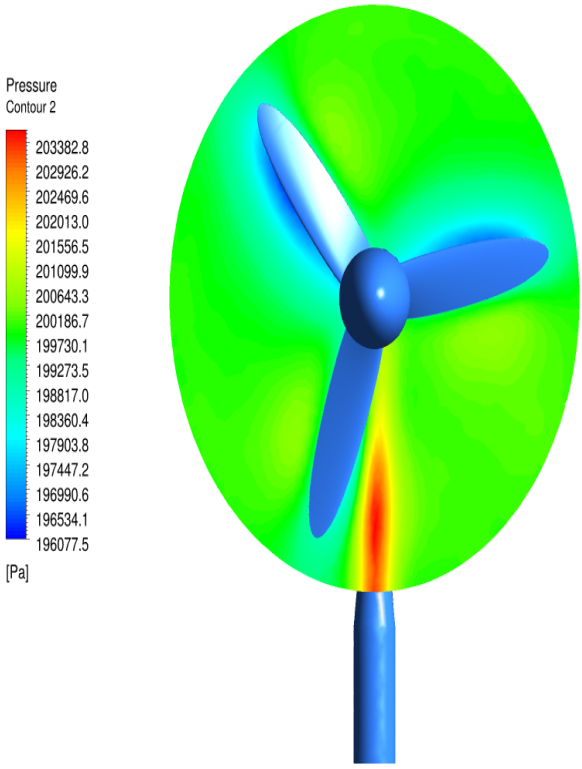

Figure 6.34 Pressure plot at 2080 **timestep F4**

The circumferential velocity is plot on Figure 6.35at the same location.

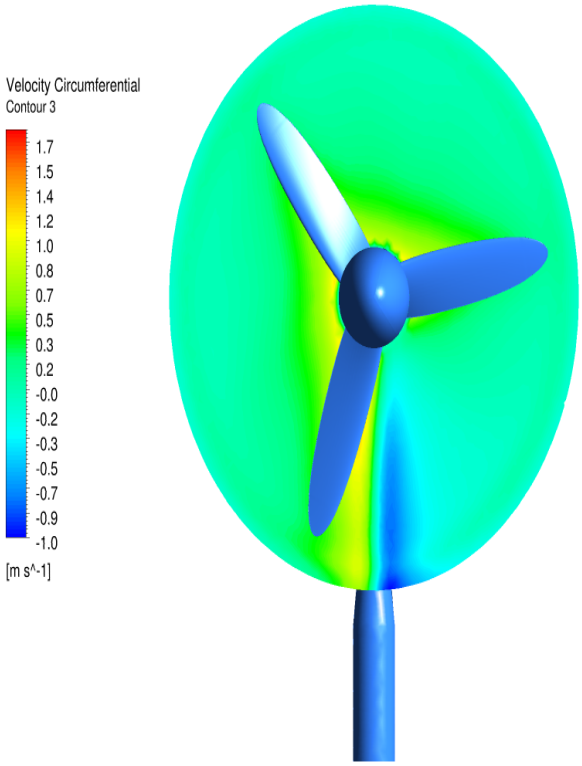

Figure 6.35 Circumferential velocity plot at 2080 **timestep F4**

Axial velocity is plotted on Figure 6.36 as in the same way as the F3 plots.

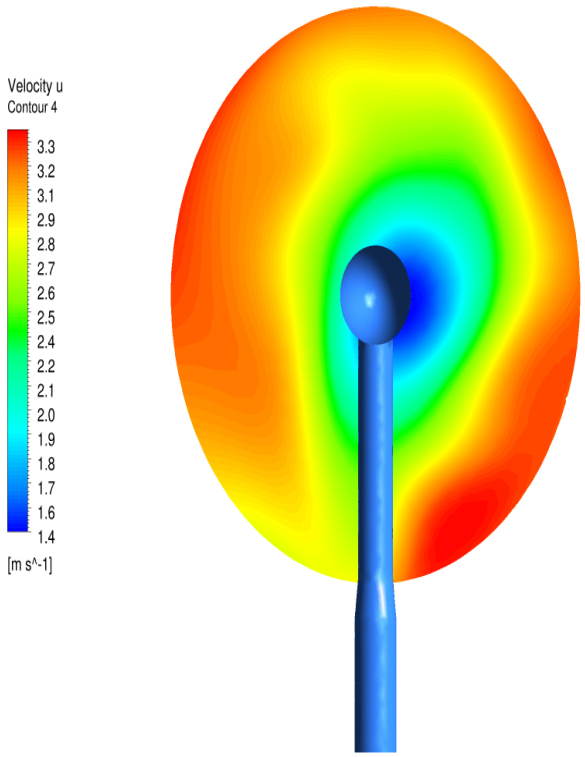

Figure 6.36 Axial velocity plot at 2080 **timestep F4**

The vector plot on Figure 6.37 displays the flow field at the 2099 timestep signified when the blade 2 is in front of the pylon. The changes to this plot are similar to the changes that took place for the F3 case.

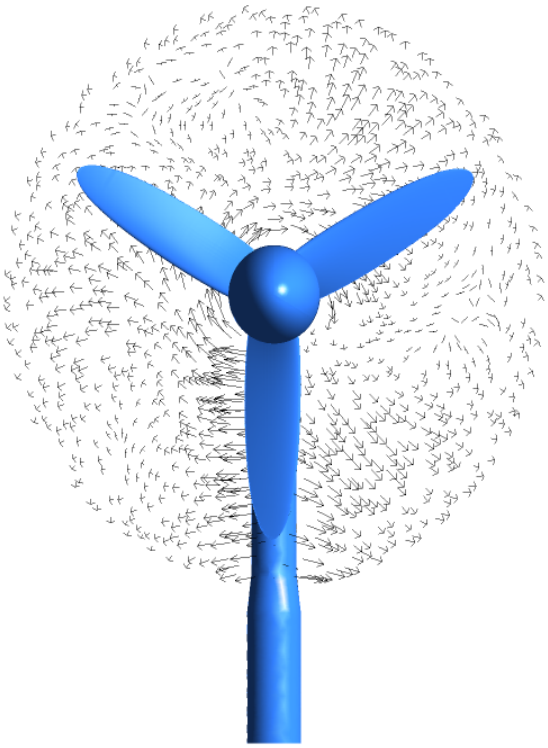

Figure 6.37 Vector plot at 2099 **timestep F4**

The vorticity plot on Figure 6.38 show the vortices created by the blades.

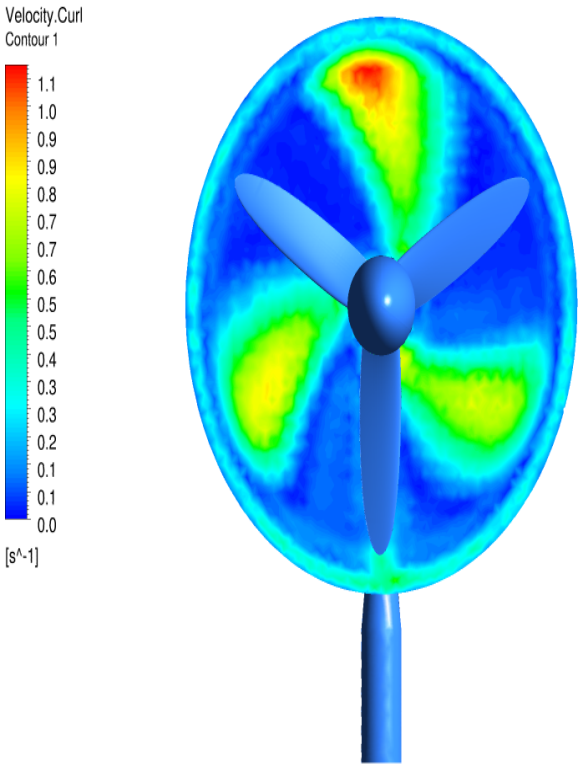

Figure 6.38 Vorticity plot at 2099 **timestep F4**

Figure 6.39 displays a pressure plot.

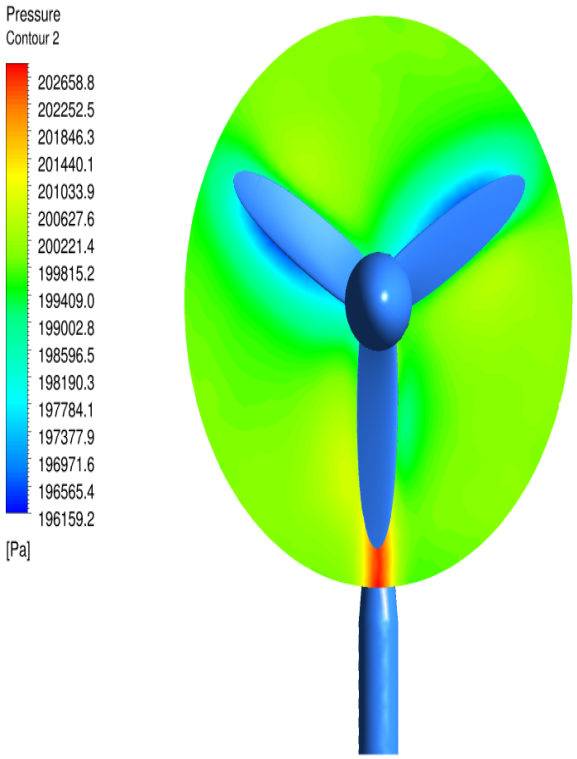

Figure 6.39 Pressure plot at 2099 **timestep F4**

The circumferential velocity is plot on Figure 6.40.

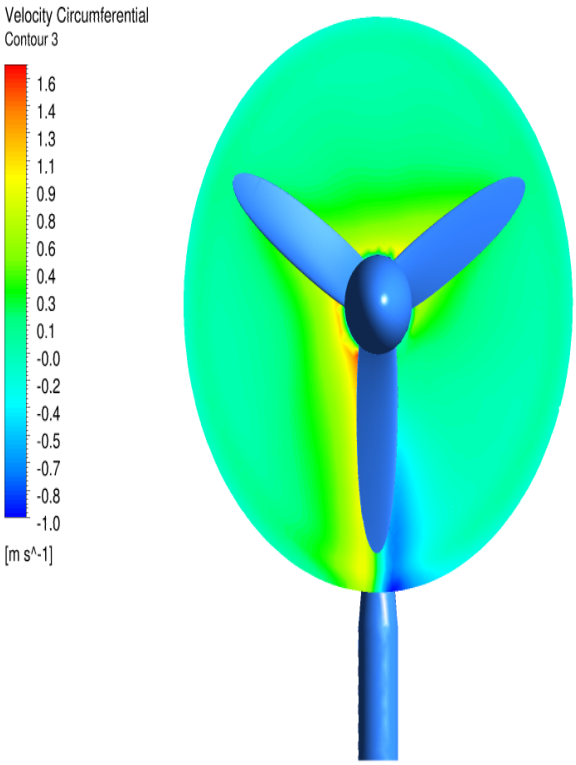

Figure 6.40 Circumferential velocity plot at 2099 **timestep F4**

Axial velocity plot is plotted on Figure 6.41 in the same manner as the previous corresponding plot.

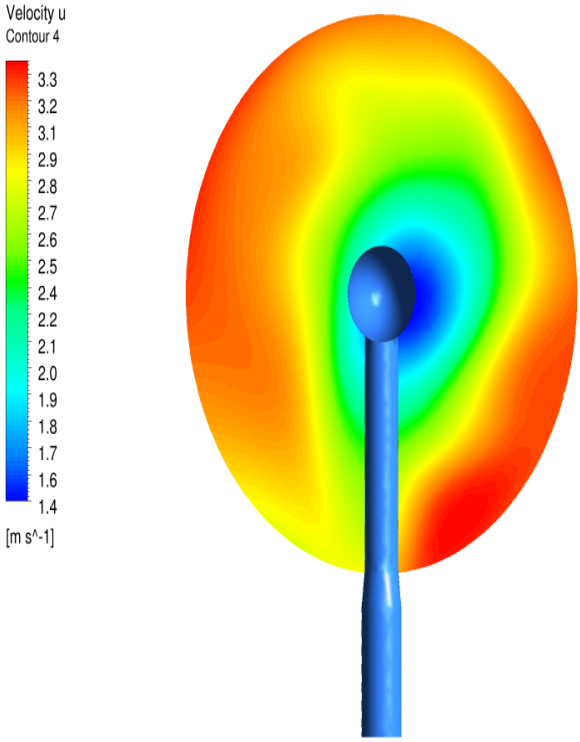

Figure 6.41 Axial velocity plot at 2099 **timestep F4**

The vector plot on Figure 6.42 displays the flow field at the 2132 timestep signified when the blade 2 has just passed the pylon.

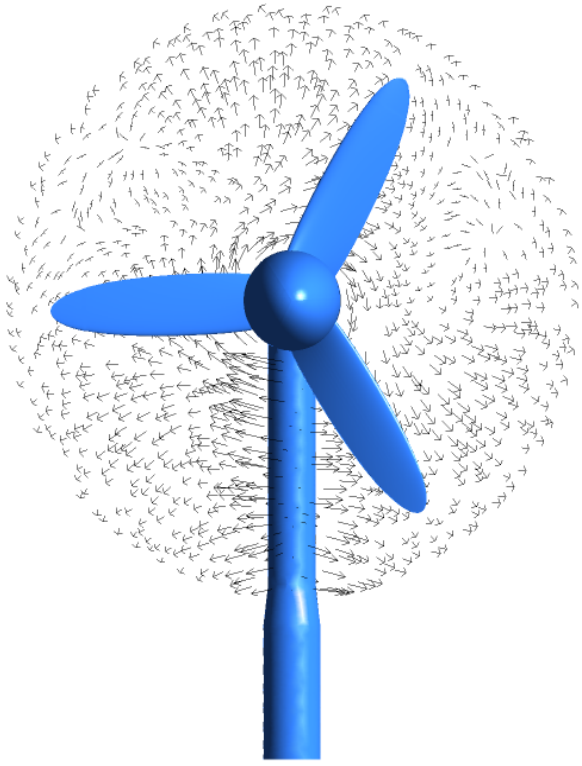

Figure 6.42 Vector plot at 2132 **timestep F4**

The vorticity plot on Figure 6.43 show the vortices created by the blades.

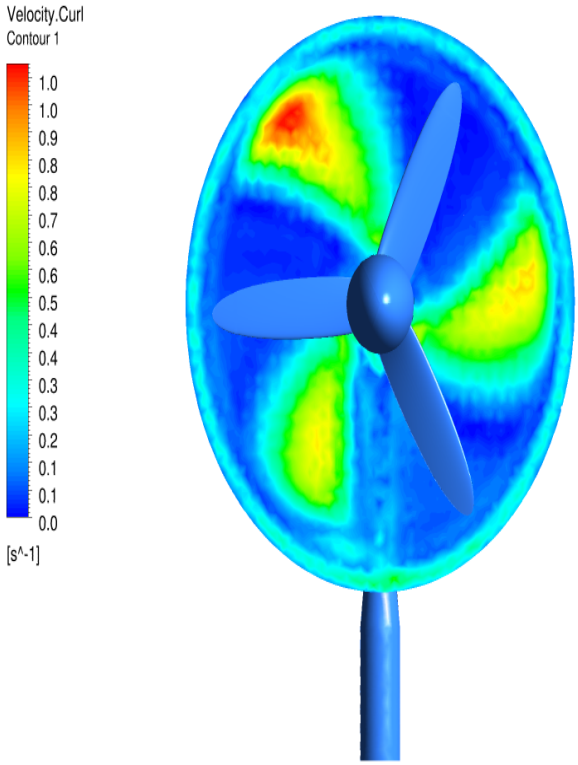

Figure 6.43 Vorticity plot at 2132 **timestep F4**

Figure 6.44 displays a pressure plot.

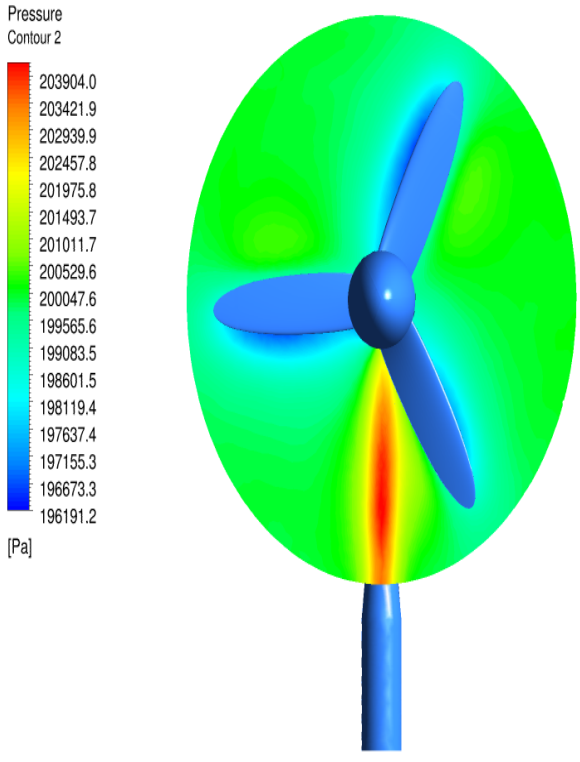

Figure 6.44 Pressure plot at 2132 **timestep F4**

The circumferential velocity is plot on Figure 6.45.

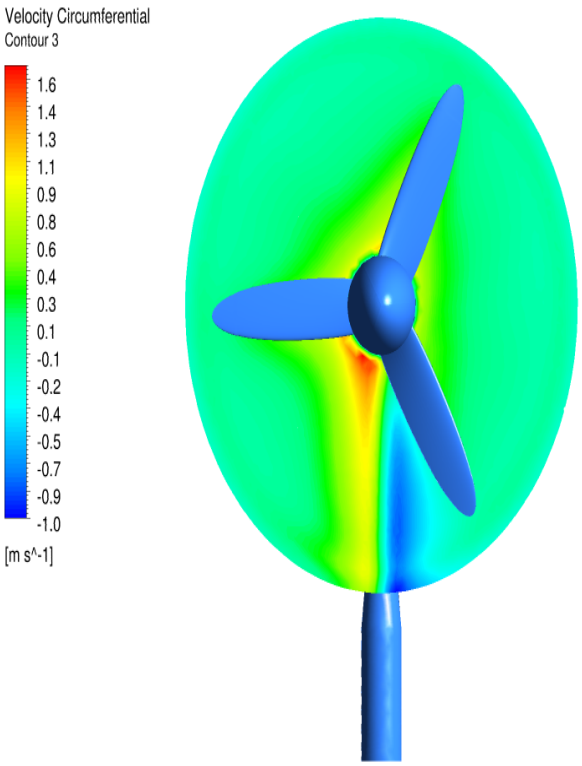

Figure 6.45 Circumferential velocity plot at 2132 **timestep F4**

Axial velocity plot is plotted on Figure 6.46 in the same manner as the previous axial velocity plots.

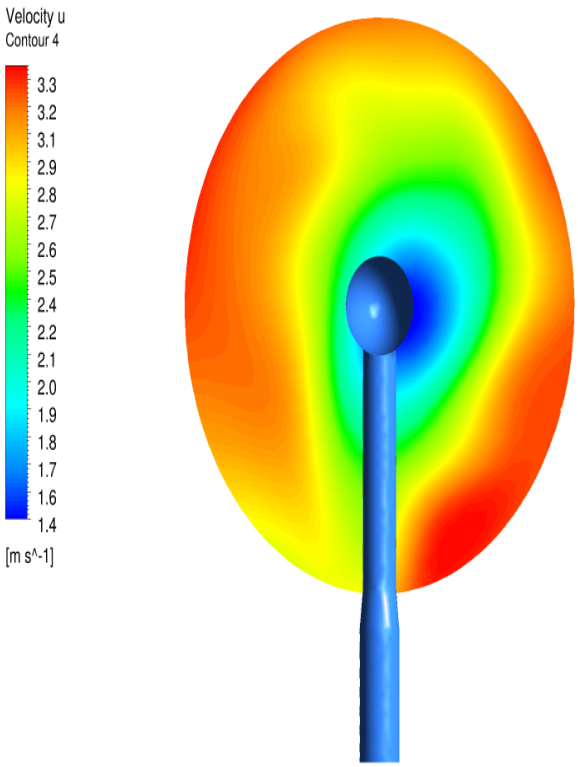

Figure 6.46 Axial velocity plot at 2132 **timestep F4**

Figure 6.47 displays the total axial thrust and torque loads for the turbine. The total torque was calculated to be $330.0kNm$, the total thrust $289.0kN$ and the total power $726.0kW$. The plot varies approximately by 14% and 10% from the mean thrust and torque values respectively.

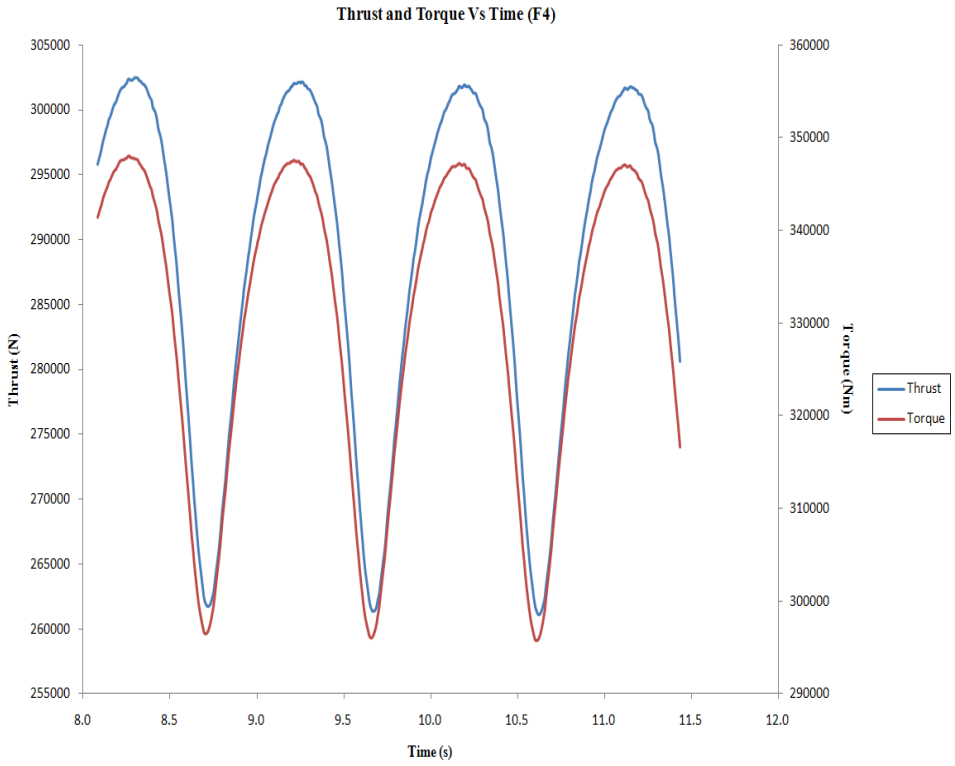

Figure 6.47 Thrust and Torque loads for F4 case

The axial thrust and axial torque variations per blade are shown on Figure 6.48 and Figure 6.49 respectively.

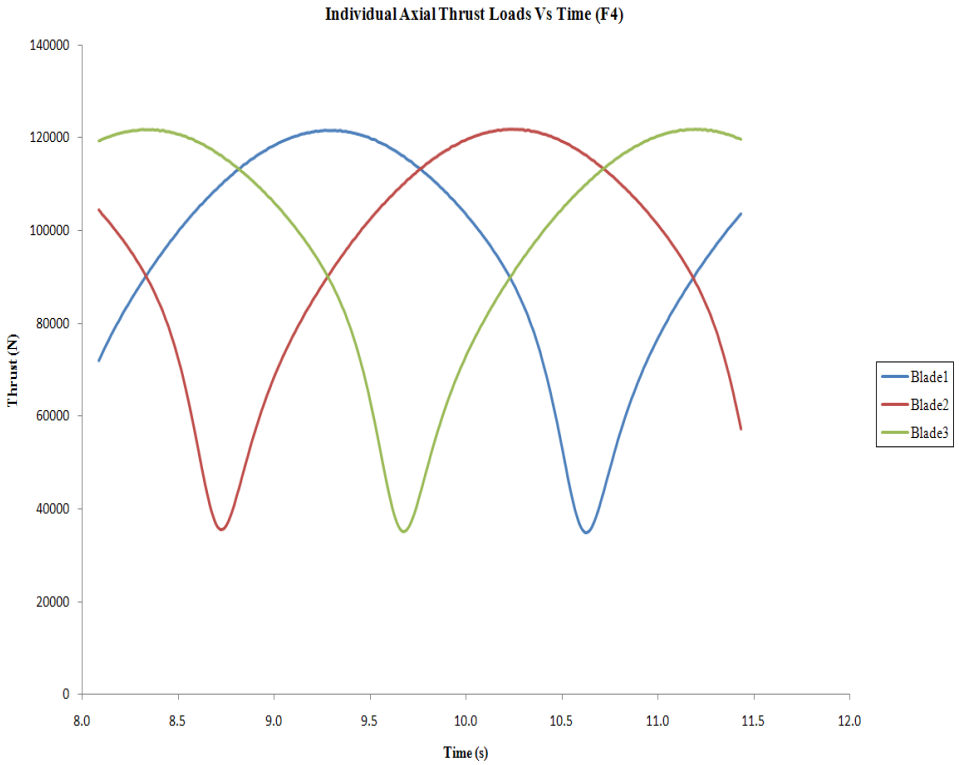

Figure 6.48 Individual Axial Thrust loads

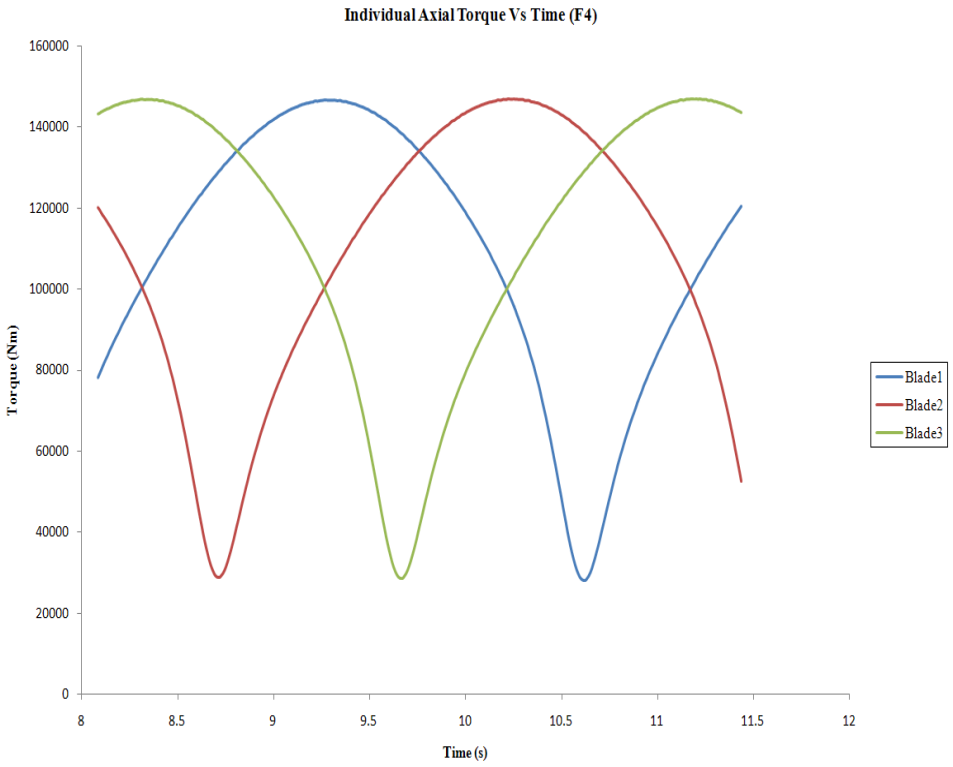

Figure 6.49 Individual Axial Torque loads

6.4 Half Spacing Model

The Half_spacing_model was also analysed and is discussed in this section using the flow conditions for the F3 and F4 cases.

6.4.1 F3 case (maximum torque)

Figures 6.50, 6.51, 6.52 display the individual blade loading plots at 25%, 50% and 90% span respectively.

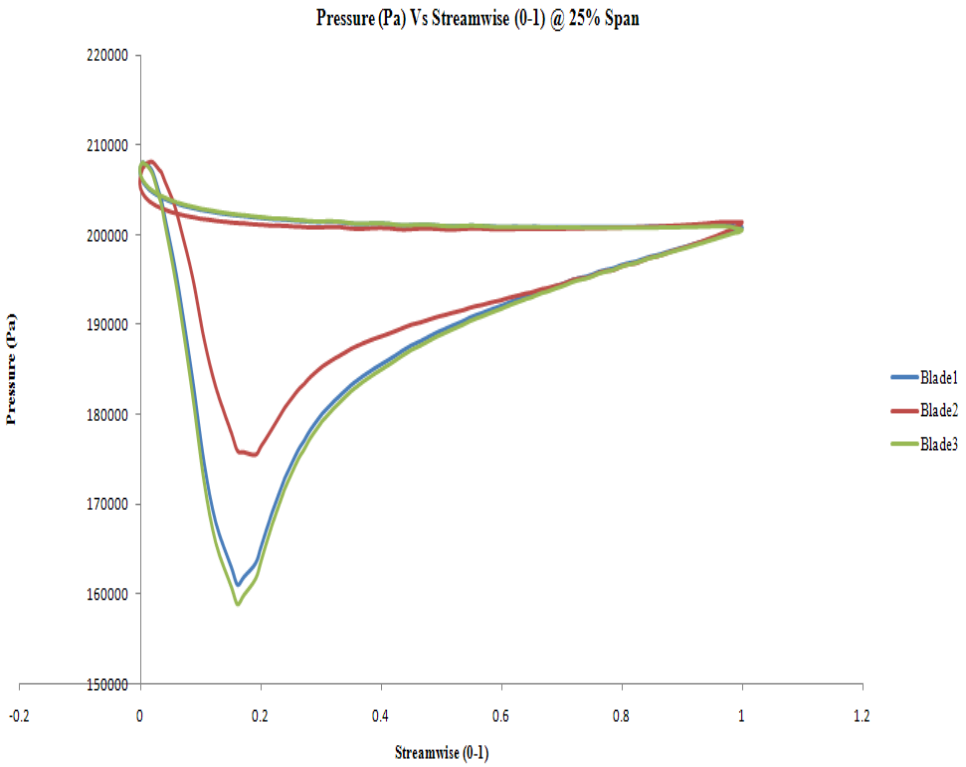

Figure 6.50 Pressure plot at 25% span - Half_spacing_model F3

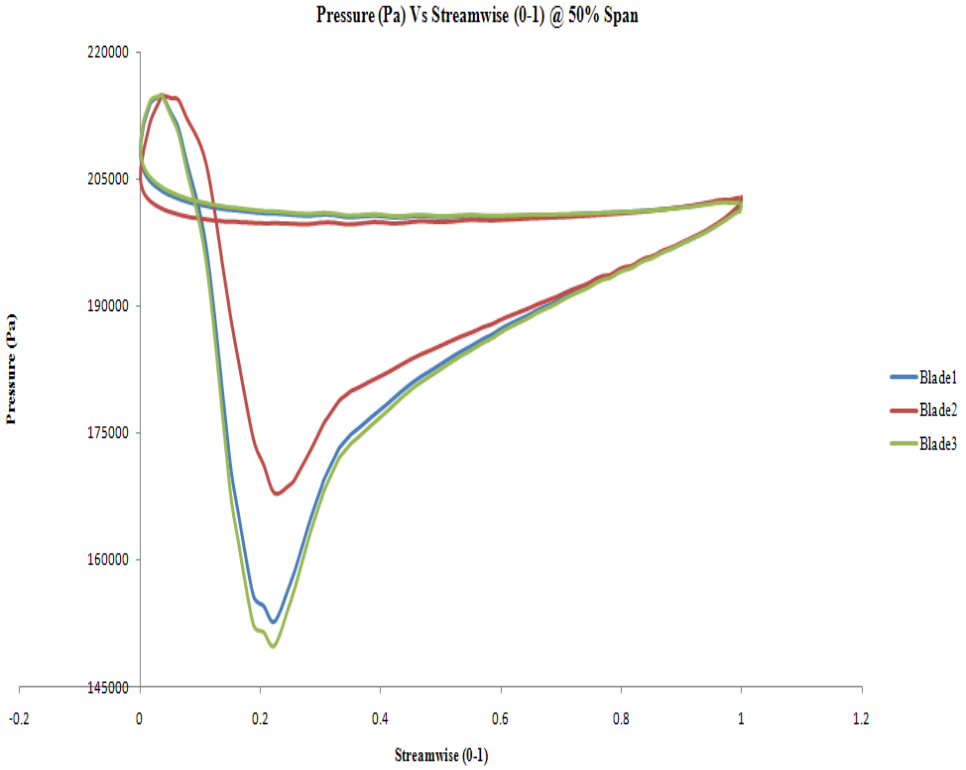

Figure 6.51 Pressure plot at 50% span - Half_spacing_model F3

Once again, the pressure plots extracted from the transient simulation, taken at 25%, 50% and 90% span, are quite similar to those obtained from the steady state analysis. The

orientation of the blades for the transient cases are relatively the same as a result the plots are very similar in nature. There is a however, a decrease in the force experienced by the blade 2, as the blade-pylon interaction is in close proximity. The pressure plots for the transient normal_spacing_model produces a marginally better pressure loading plot than that of the F3 Half_spacing_model.

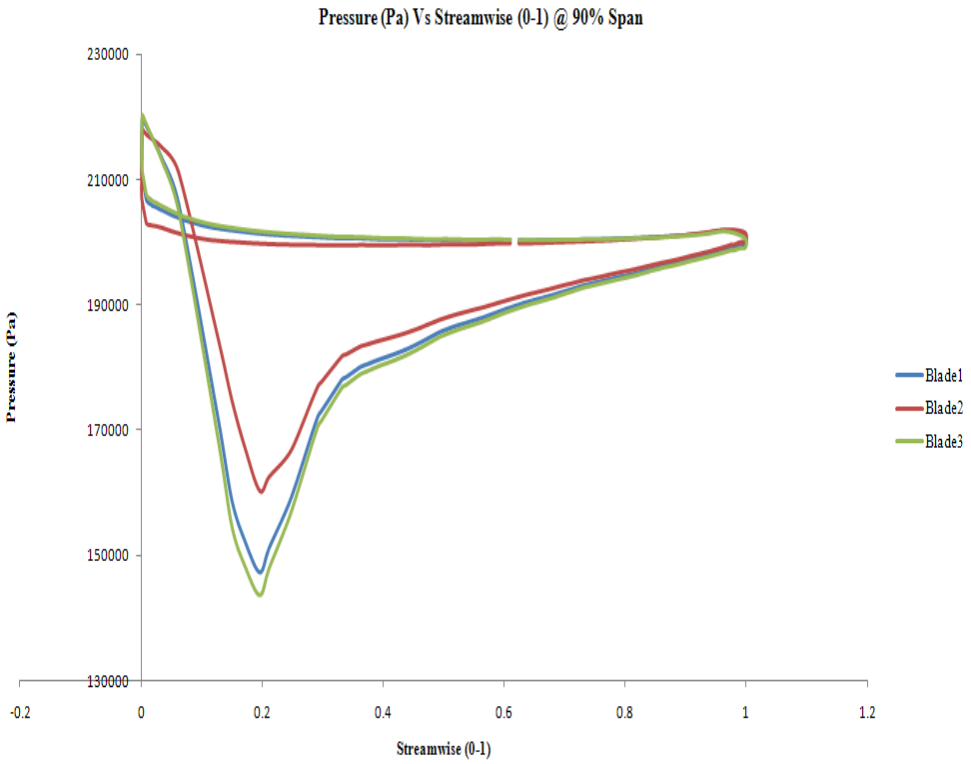

Figure 6.52 Pressure plot at 90% span - Half_spacing_model F3

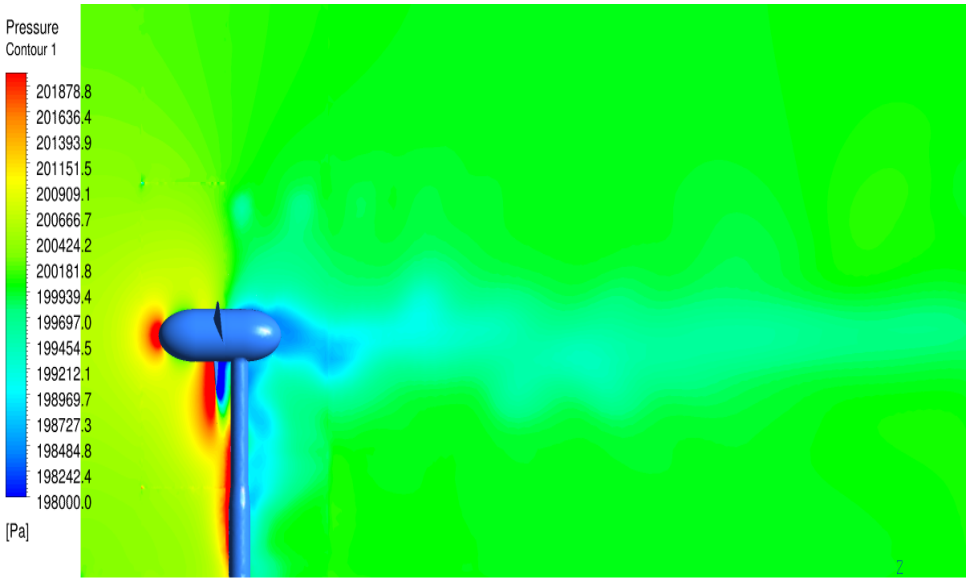

Figure 6.53 Pressure distribution in the meridional plane - Half_spacing_model F3

The pressure distribution in the meridional plane, Figure 6.53, is similar in several respects to its steady-state equivalent, on Figure 5.21, but as with the previous transient pressure plots, the Figure 6.53 captures more complex unsteady characteristics. The pressure contours that correspond to the stagnation regions are resolved fully and are corresponding to the normal_spacing_model transient plots.

The Figure 6.54 shows the wake distribution aft of the rotor. The velocity deficit is plotted against the water depth at specific rotor diameters downstream of the rotor.

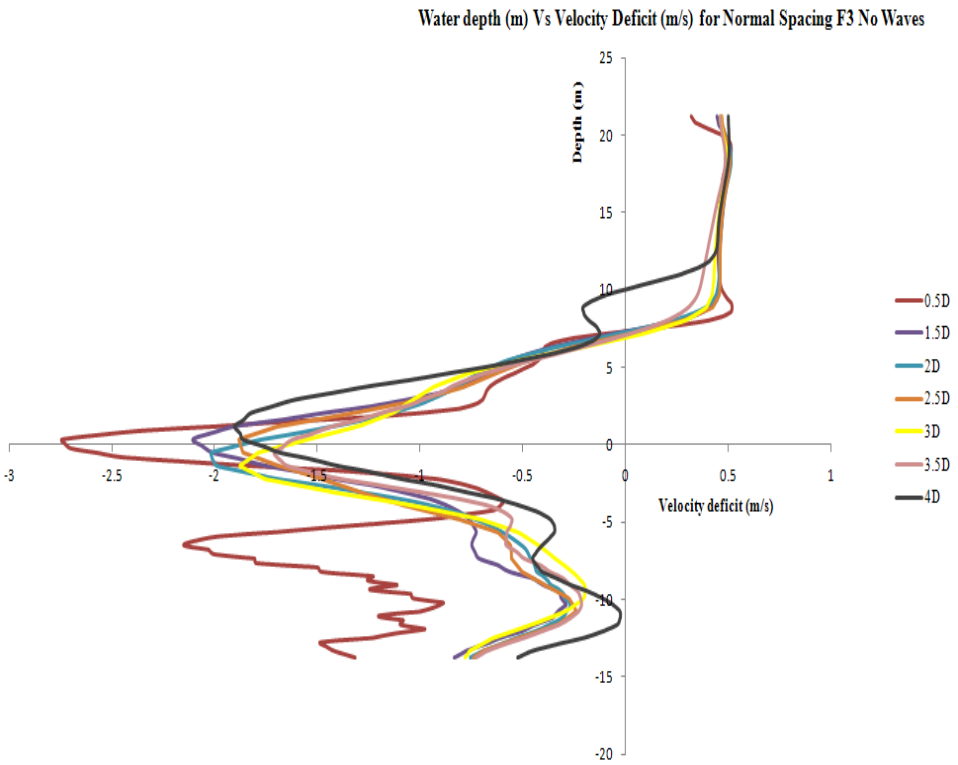

Figure 6.54 Velocity deficit downstream of the rotor for Half_spacing_model F3 case

The average flow speed of the rotor operating area was calculated to be $2.25ms^{-1}$ as with the previous transient normal_spacing_model velocity deficit plot. The flow velocities on the above plot in Figure 6.54 were subtracted from the average flow velocity of the rotor operating area to get the velocity deficit. This plot is very similar to the velocity deficit plot displayed on Figure 6.5. The plot suggests that the wake generated aft of the rotor is hardly affected by this pylon spacing when compared to the plot on Figure 6.5.

The Figure 6.55 represents the contour plot for the blade-pylon spacing.

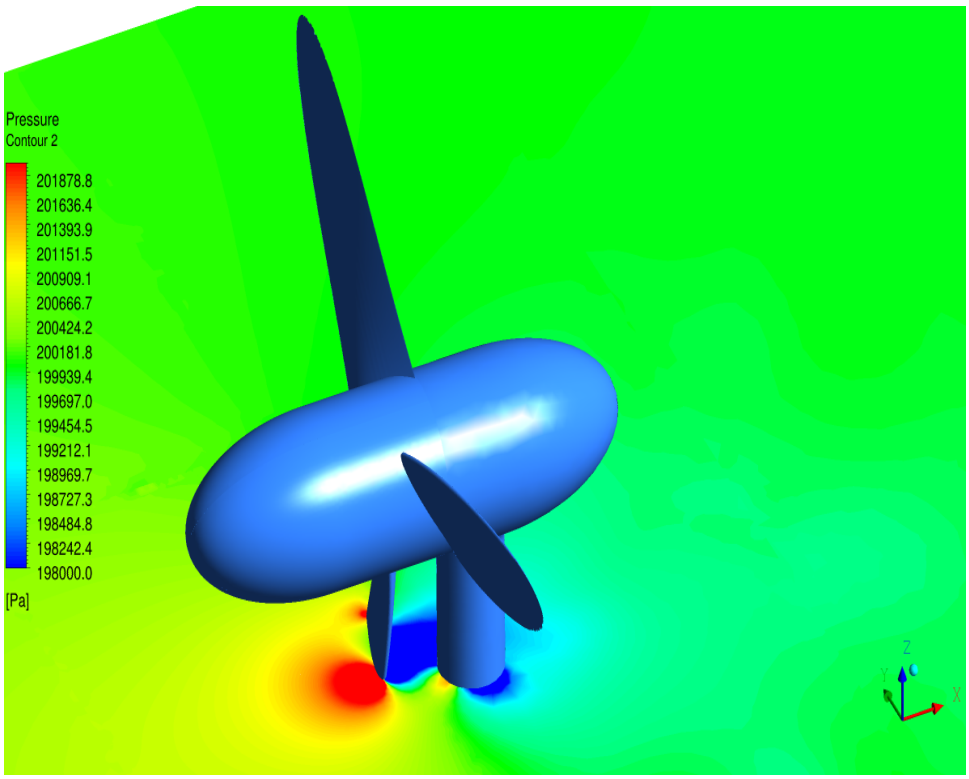

Figure 6.55 Blade-pylon interaction - Half_spacing_model F3

The flow interaction between the blade-pylon on Figure 6.55 is much more visible when compared to the plot shown on Figure 6.6 for the normal_spacing_model F3 model. The plot range is constant on both plots and the Figure 6.55 shows more interaction on the flow between the blade and the pylon. This confirms the fact that there is undoubtedly more interaction taking placing on the shorter hub than that of the normal hub spacing.

The flow conditions used were exactly the same as the F3 steady state case. Figure 6.56 below represents the total axial thrust and torque loads for the turbine. Unlike the normal_spacing_model transient cases, the Half_spacing_model transient cases were not interrupted, as a result the variation of thrust and torque is present for the entire simulation.

The time histories of the torque and thrust for the turbine are seen in Figure 6.56. The variation of these two quantities is quasi sinusoidal as seen from the previous transient plots as well. This figure clearly shows the last revolution (between the third and the fourth revolution) is the most stable variation, occurs roughly after $19.3s$. This means that turbine system needs a few revolutions to come to is equilibrium state of operation. The total torque was calculated to be $440kNm$, the total thrust was approximately $276kN$ and the total power the turbine generates is approximately $428kW$.

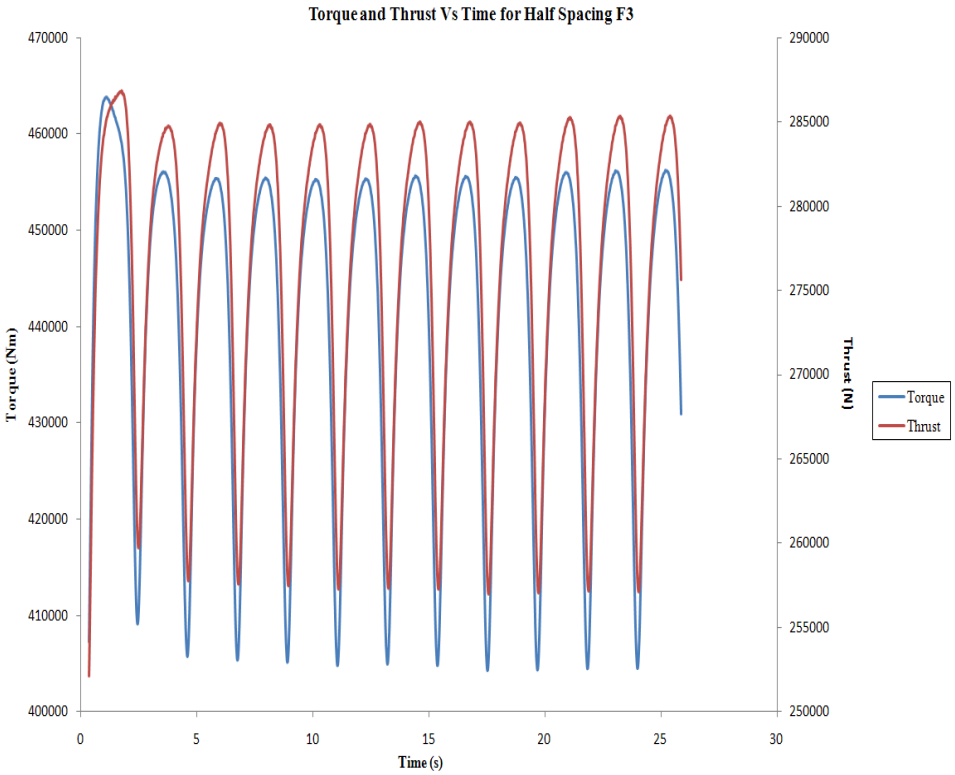

Figure 6.56 Thrust and Torque loads for Half_spacing_model F3 case

The axial thrust and axial torque variation per blade are shown on Figure 6.57 and Figure 6.58 respectively. The lowest point on all three figures denotes that the respective blade is in front of the pylon at the lowest point in the rotation.

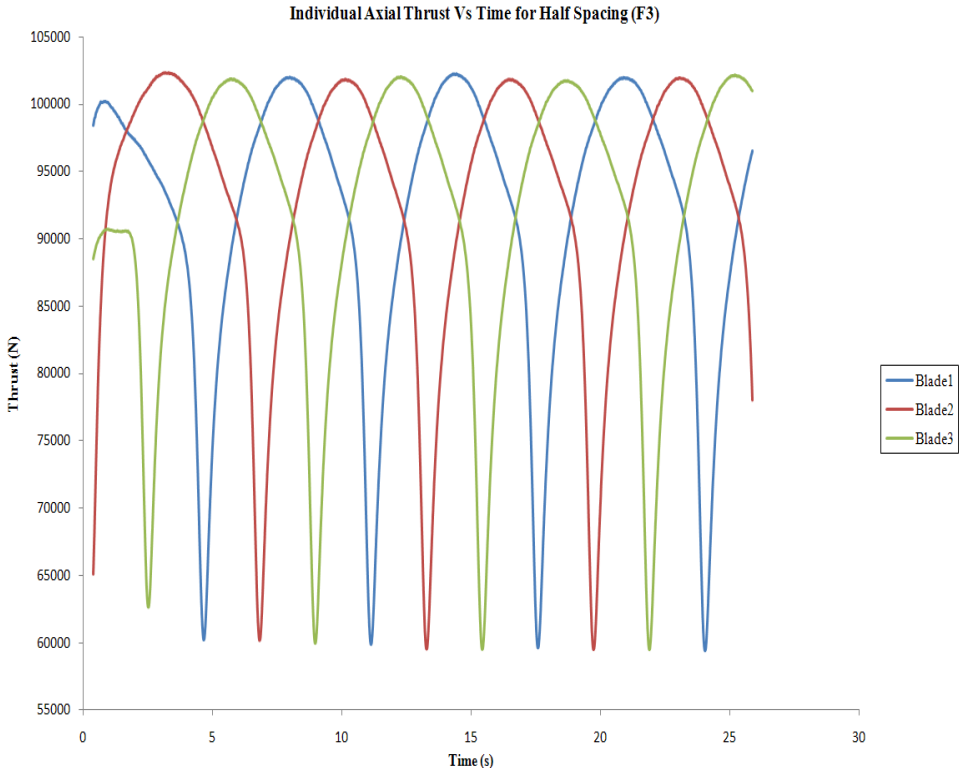

Figure 6.57 Individual Axial Thrust loads

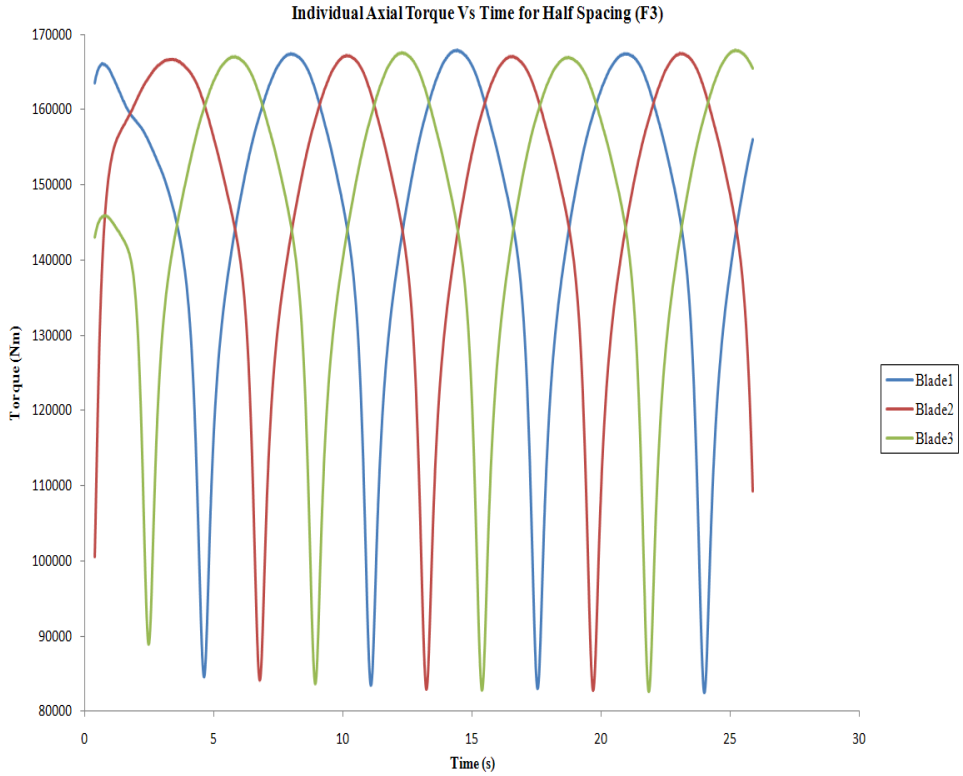

Figure 6.58 Individual Axial Torque loads

The above plots represent approximately all four revolutions. The individual plots on

Figures 6.57 and 6.58 shows that the blade 2 goes past the pylon initially followed by blade 3 and blade 1, this is the same layout as the other previous transient plots.

6.4.2 F4 case (maximum thrust)

Figures 6.59, 6.60, 6.61 display the individual blade loading plots at 25%, 50% and 90% span respectively.

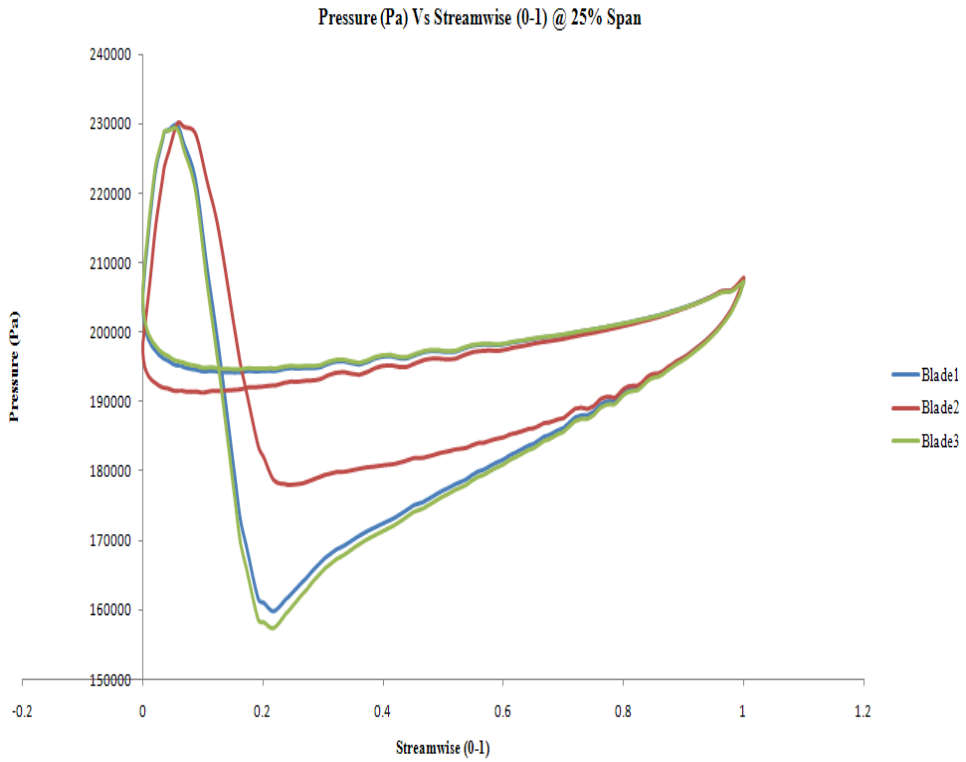

Figure 6.59 Pressure plot at 25% span - Half_spacing_model F4

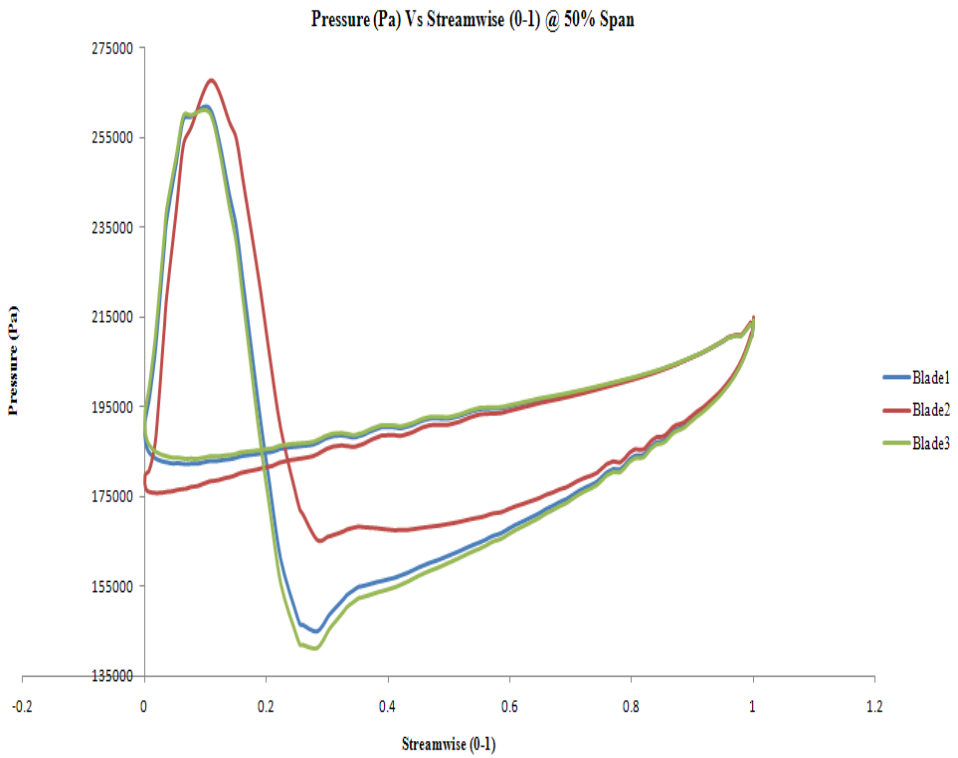

Figure 6.60 Pressure plot at 50% span - Half_spacing_model F4

The orientation of the blades for the transient cases are relatively the same as a result the plots are very similar in nature. The expected decrease in the force experienced by the blade 2, as the blade-pylon interaction is in close proximity is evident. This implies that higher flow velocities have a strong impact of the blade-pylon interaction. The pressure plots for the transient F4 normal_spacing_model produces a marginally better pressure loading plot than that of the F4 Half_spacing_model.

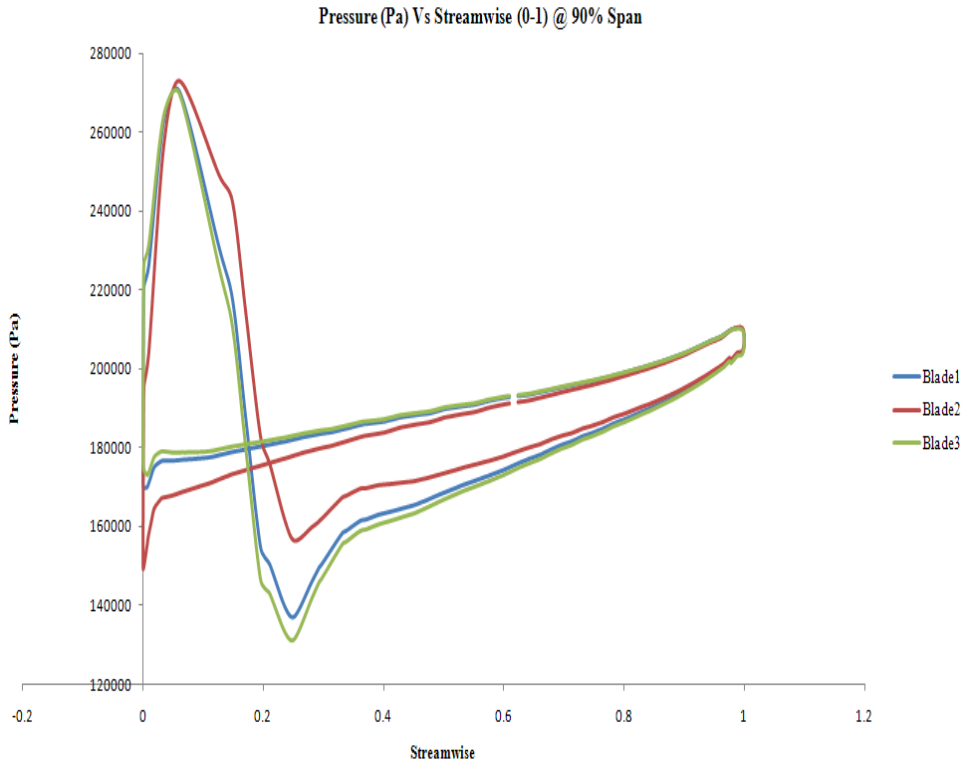

Figure 6.61 Pressure plot at 90% span - Half_spacing_model F4

The pressure distribution in the meridional plane, Figure 6.62. The pressure contours that correspond to the stagnation regions are resolved fully and are corresponding to the normal_spacing_model transient plots. The pressure contour plot notes that the wake is strong immediately behind the rotor and reduces several diameters downstream of the rotor. The stagnation points are clearly evident with the red zones marked on Figure 6.62. The high pressure areas between the blade-pylon are quite visible than when compared to the transient F4 normal_spacing_model shown on Figure 6.30. This also confirms that the higher velocities have an adverse affect on pressure fields around the blade-pylon areas.

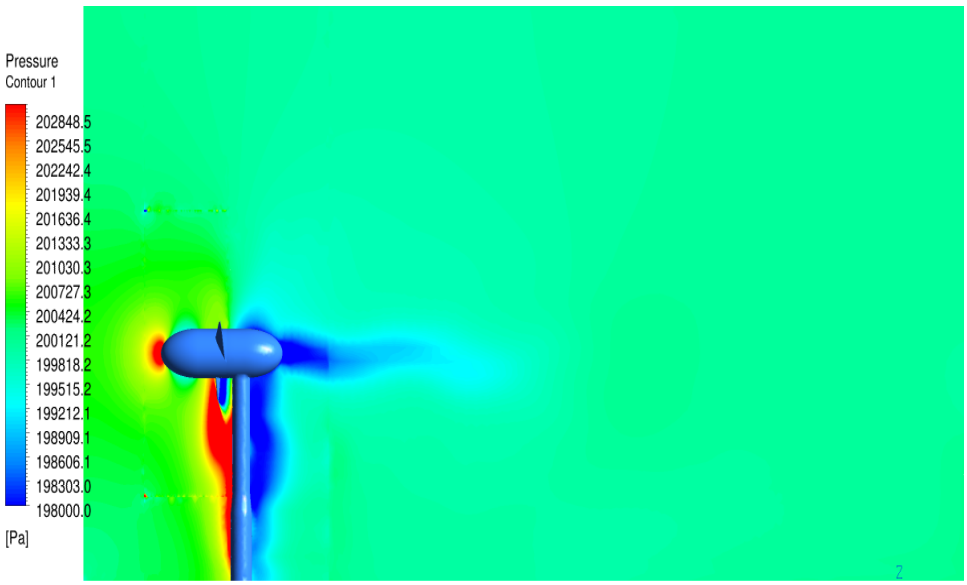

Figure 6.62 Pressure distribution in the meridional plane - Half_spacing_model F4

The Figure 6.63, display the pressure contour plot for the blade-pylon interaction. It is evident that there is lot of high pressure and low pressure areas close to the pylon and the blade respectively. This signifies that the activity between the blade-pylon is severe, thereby, confirming the remarks made from the plots above. The Figure 6.63 shows lot more activity than when compared to the transient F4 normal_spacing_model on Figure 6.31.

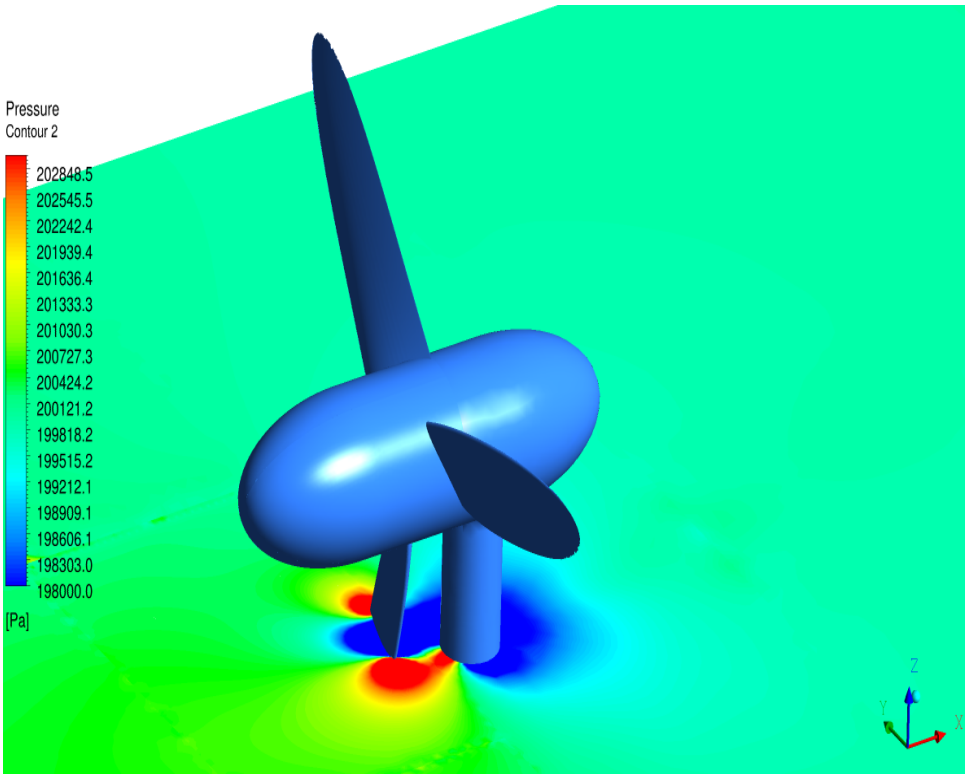

Figure 6.63 Blade-pylon interaction - Half_spacing_model F4

The Figure 6.64, represents the total axial thrust and torque loads for the turbine. The thrust and torque production gets stable after around $8.5s$ roughly corresponding to the end of 3 revolution. The Figure 6.64 confirms that the turbine generally needs a few revolutions to come to its equilibrium state of power production. The total torque was calculated to be $296kNm$, the total thrust was approximately $298kN$ and the total power that the turbine generates is approximately $651kW$.

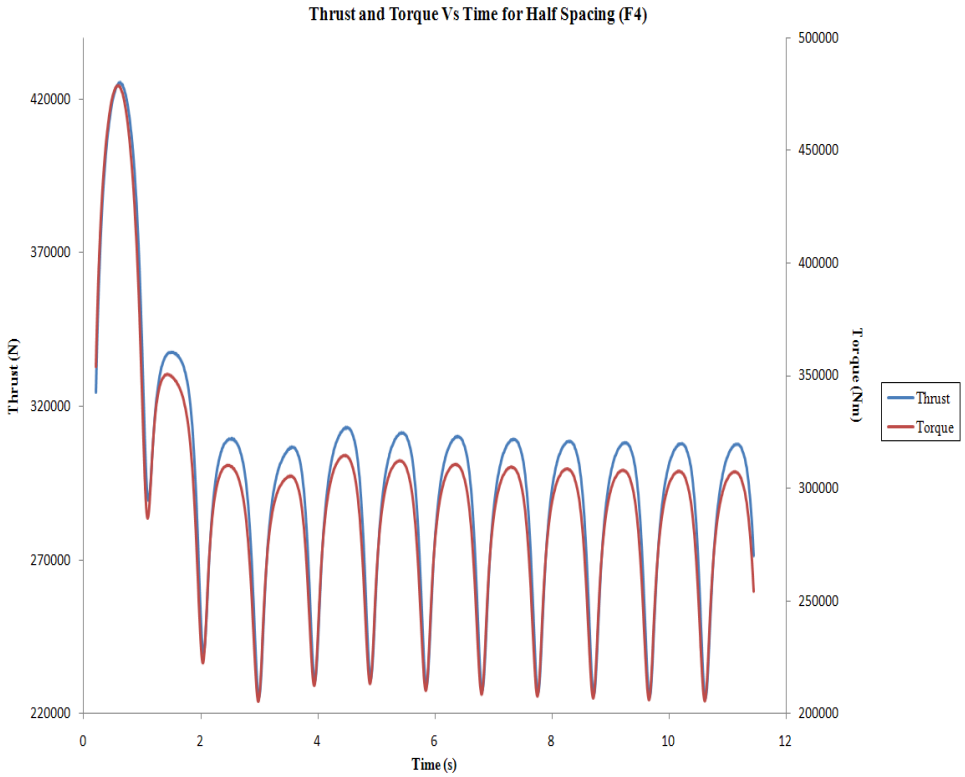

Figure 6.64 Thrust and Torque loads for Half_spacing_model F4 case

The F3 Half_spacing_model displays a significantly lower variation in this time period. This could be due to the high flow velocities seen on the F4 case.

The Figure 6.65 and Figure 6.66 represents the individual axial thrust and the individual axial torque loads per blade. Both these figures show the initial unstable variation of thrust and torque respectively and there after achieves an equilibrium state, approximately after $8.5s$.

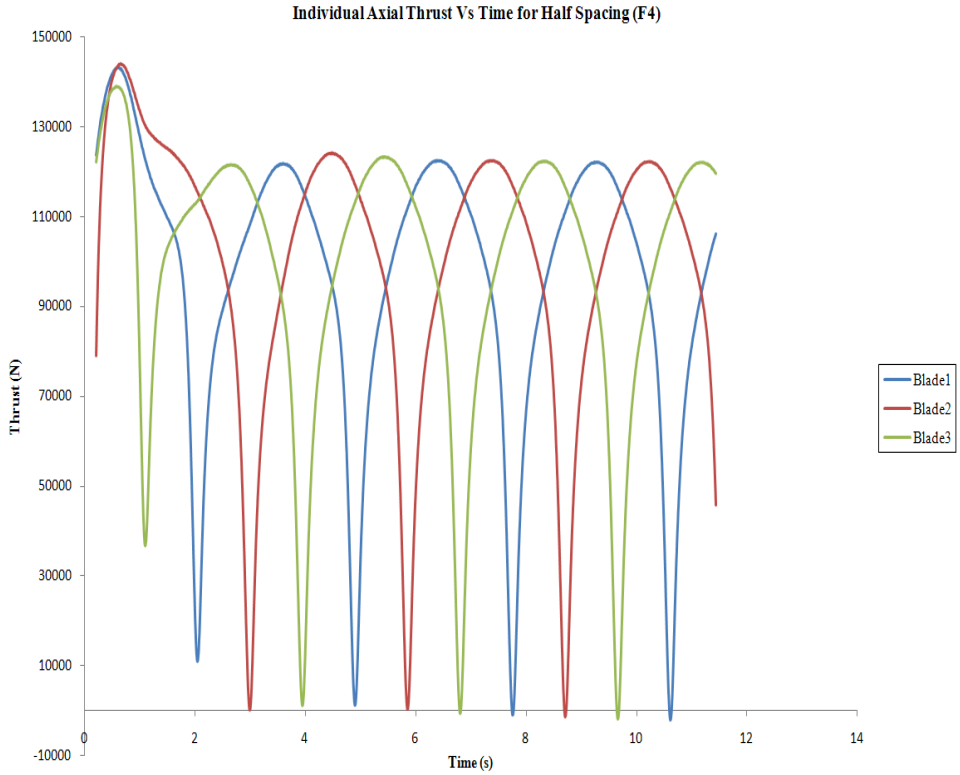

Figure 6.65 Individual Axial Thrust loads

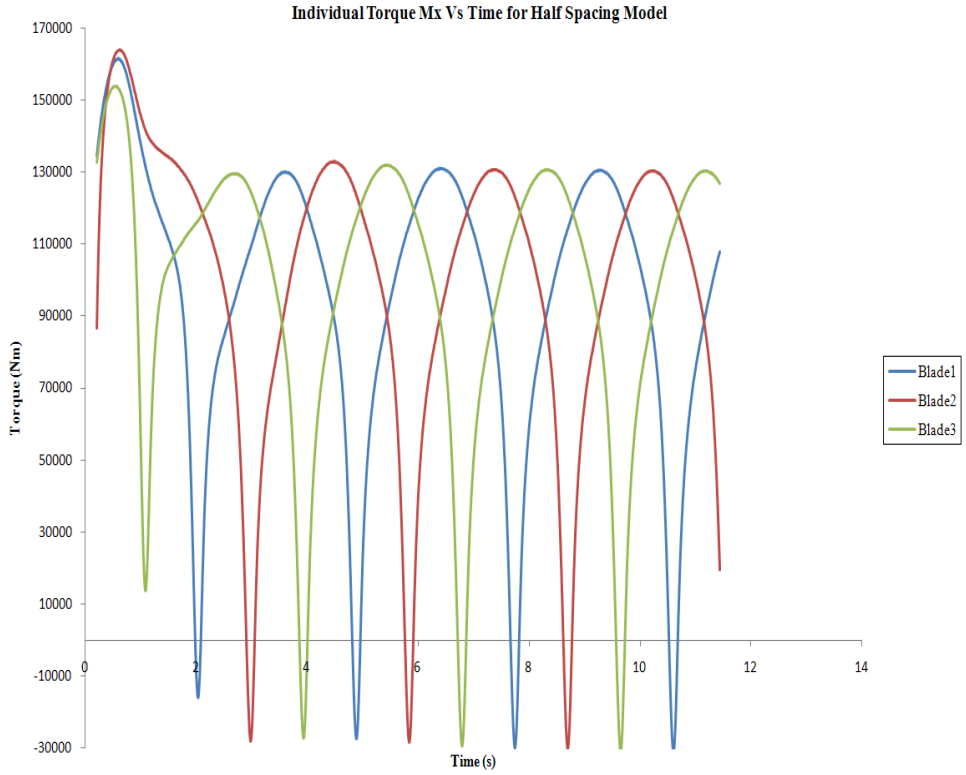

Figure 6.66 Individual Axial Torque loads

It is clearly evident from the Figures 6.65 and 6.66 that at certain points in the time histories the individual blades experiences negative thrust and torque loads. This phenomenon only

occurs for the F4 Half_spacing_model. The higher flow velocities and the shorter hub spacing causes the flow around the turbine system to experience severe pressure gradients and hence experiences negative thrust and torque loads.

The individual thrust and torque loads on Figure 6.48 and Figure 6.49 respectively for the F4 normal_spacing_model show a less severe variation as opposed to the forces experienced by the F4 Half_spacing_model shown above. This is quite evident for the total loads as well. This implies that the blades experience severe unsteady loadings for the Half_spacing_model than when compared to the normal_spacing_model for any given flow parameter.

6.5 Comparison of Steady State and Transient analysis

From the Figure 6.67, it is evident that the C_P and C_T curves for the transient normal_spacing_model and Half_spacing_model are marginally over predicting its values when compared to the steady state plots. Approximately a 10% difference is observed for the C_T and C_P for the transient normal_spacing_model when compared to the steady state plot. As expected, the Half_spacing_model produces marginally lower C_P and C_T values when compared to the transient normal_spacing_model.

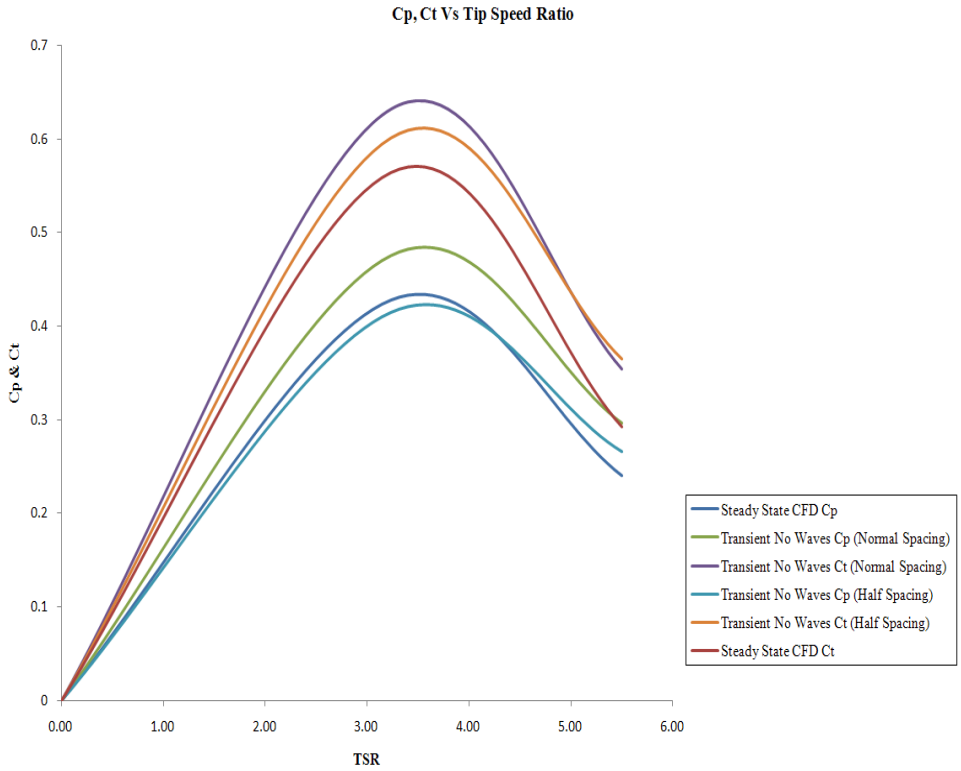

Figure 6.67 Comparison of C_P and C_T plots with various models

As discussed previously in the thesis, this CFD model is inherently unsteady and solving the model with steady state equations would account for losses like tip losses, vortices to

be neglected. But transient solvers captures everything in a time average frame, therefore, when compared to each other, the data is bound to be different. And the transient cases offer good convergence especially if the model in question is inherently unsteady.

6.6 Chapter Closure

The transient no waves results for the normal_spacing_model and the Half_spacing_model have been discussed. The convergence obtained for the transient results are significantly better than that of the steady state results discussed in Chapter 5. This confirms the principle, that if the problem is inherently unsteady and turbulent, one cannot use steady state analysis to obtain good convergence and rely on its results. As the quantities which vary with time i.e. pressure or density is set to zero (there is no change). Therefore, a transient case needs to be solved for and hence shown with the good convergence. It's not to say that the steady state results were a mere waste of time, it is far from that. In fact, it was regarded as the initial CFD data and was able to utilise it as the initial guess for the transient simulation.

The transient results are on average 1.2times the steady state results. This probably is because of the approximations done in the steady state results. Usually an unsteady problem solved in steady state solver is impossible to converge, this could also perhaps account for the difference in results.

These transient results could now be compared with the transient with waves results presented in the following chapter. The mass and momentum transient residual convergence for all simulations have been attached in Appendix C. The Figure C.1 and Figure C.2 display the residual convergence for the F3 and F4 normal_spacing_model respectively. Figure C.3 and C.4 show the residuals for the F3 and F4 Half_spacing_model respectively. The steady state convergence is shown until the 1000^{th} accumulated timestep for the Half_spacing_model. These plots show how good the transient convergence is when compared to the steady state convergence.

A comparison of the F3 total axial loads (thrust and torque) for both the normal_spacing_model and the Half_spacing_model is presented on Appendix C, Figure C.5. As clearly seen the F3 normal_spacing_model loads produces higher loads but are less severe in terms of the variation of the unsteady loading as also mentioned in concluding remarks for the sub chapter 6.4.1 and 6.4.2. Figure C.6 on Appendix C displays a similar plot for the F4 case and again the same remarks could be drawn to this plot as well. The thrust produced for the both the F4 models are roughly the same although the amount of cyclic unsteady loading variation is significantly higher in the Half_spacing_model. These plots conclude the discussion that the Half_spacing_model experiences significantly higher cyclic unsteady loadings than when

compared to the datum spacing model.

A few additional plots of the total loads about the Y and Z axis for the F3 normal_spacing_model is presented on Figures C.7 and C.8 respectively. Similar plots of the total loads about the Y and Z axis are presented for the F4 normal_spacing_model on Figures C.9 and C.10 respectively.

Finally, similar plots are presented for the loads about the Y and Z axis for the Half_spacing_model F3 and F4 on Figures C.11, C.12, C.13 and C.14 respectively.

Chapter 7

Transient Simulations - with Waves

7.1 Introduction

In this chapter, a combination of the boundary layer velocity profile and the progressive linear wave theory (small amplitude) profiles are introduced to simulate a realistic marine flow environment. The application and physics of the shear velocity profile and the linear wave theory were discussed in Chapter 2. In Chapter 6, the problem was simplified by only using the boundary layer velocity profile at the inlet of the domain. As a result the data from Chapter 6 would be compared and discussed in the final section of Chapter 7. This was done in order to understand the impact that the sea waves have on the rotor system. The same F3 and the F4 model parameters were utilised to model the normal_spacing_model and Half_spacing_model.

7.2 Wave Parameters

Ideally, wave parameters used for any form of analysis should be site specific as these parameters are obtained from a detailed investigation of the site environment. This data is often called the site wave scatter diagram. This helps to assess the loads that are being imposed on the turbine and its supporting structure by the waves. Unfortunately, there was no detailed information available to the author about the wave climate observed in Ramsey Sound which is the target location for the DeltaStream turbine. Therefore some detailed information about the wave climate data for the west of Cornwall was used instead. At the time of this analysis this was the only detailed source of information on wave climate data that was available to the author to utilise for the CFD simulations. Two wave types were selected to be modelled and simulated. It was decided that an energetic wave and a more benign, and hence more common, wave needed to be simulated. These waves represent a storm condition and a typical wave of the type which may be present most of the time the

device is operating. The prime reason to model only two waves was partly because of the computational cost and also to do with the vast disc space that is required to store these files.

The F4 case for the normal_spacing_model and the Half_spacing_model were simulated for every degree of rotation successfully with a combination of waves and shear boundary layer profile and it approximately took about four days to complete four revolutions on a full 16-processor simulation. Unfortunately, both the F3 case for the normal_spacing_model and the Half_spacing_model could not be successfully simulated with a timestep corresponding to an angular displacement of one degree. Therefore, the model simulation parameters had to be changed to a smaller degree of angular displacement to successfully simulate the F3 case. A number of attempts were performed from a rotation of one degree through to a timestep down to 0.2 degrees without success. When the model was operated at 0.1 degree of rotation the computation was successful. However, in order to do four complete revolutions at 0.1 degree per timestep, the simulation would have taken well over a month to complete on 16-processors. Therefore, a decision was made to only simulate the first two revolutions for the F3 model. Despite the reduction in the number of revolutions in light of saving precious computing resources, the simulation took no less than twenty one days to complete.

Bearing all these factors in mind, only two types of waves for the two different models for the F3 and F4 cases were modelled. Therefore a total of 8 wave simulations were carried out for this chapter. A high intensity, less frequent wave was selected to have a wave height of $3m$ and a wave period of $14s$. The frequency of the occurrence of this wave corresponded to 67 times in $100,000$ for the west of Cornwall site data. The other wave modelled was a more frequent wave, with a wave height of $1.5m$ and a wave period of $10s$. Waves of this type have been recorded 834 times in $100,000$ occurrences for the same site. Both these waves lie comfortably in the intermediate water wave depth range. The range is a ratio of the wave height to the wave length as discussed in Chapter 2. The extreme wave lies at 0.1 and the more frequent wave lies at 0.22 for the intermediate water wave depth.

7.3 Transient with Wave Solutions - Model Initialisation

The boundary conditions specified at the inlet for the steady state (chapter 5) and transient no waves (chapter 6) simulations were only a shear boundary layer velocity profile which was created employing the user functions section for CFX Expression Language (CEL) expressions of interpolated data as shown in the attached profile data file in Appendix A, Figure A.1 (shear layer velocity) and Appendix B, Figure B.1 and Figure B.2 (shear layer velocity with turbulence profile and yaw velocity respectively).

As is shown in these files to each corresponding x,y,z coordinate was assigned a specific

velocity value. This method of specifying the boundary conditions was limited to specific yet simple functions. Additional variables such as those of the input required by the wave model were extremely hard and cumbersome to implement in this manner as there was a requirement for extra equations with a considerable amount of data to be filled in. Therefore the best approach for the transient simulations including waves was to introduce CEL expressions as shown in the CFX Command Language (CCL) output in Appendix D, Figure D.1.

In order to utilise these equations, the model had to be redefined in a local coordinate frame. Global coordinate system (Coord 0) is the default coordinate system in ANSYS CFX-Pre, therefore, the solver always computes solutions in the global coordinate system. This origin is located at 0,0,0 and all material properties, boundary conditions, source terms and initial conditions are calculated from this point of reference. Since the inlet coordinates are different to the global coordinate system, a local coordinate system had to be introduced. For this case, the local coordinate frames were particularly useful in setting up quantities (velocity profile, wave profile, etc.) that were not aligned with the global coordinate system.

After assigning a suitable name (CELlcs) for the local coordinate system and the option of creating the frame set to axis points, it was a matter of simply entering the desired new coordinates and creating a new coordinate system. The coordinate frame type is always selected to Cartesian and the reference coordinate name is also set to Coord 0. Then the coordinates were entered for the origin of the new coordinate system set at $-11, -20, -13.75$. Then the Z axis is located from the new origin by $-11, 20, +21.25$ so that they lie in the same plane. The X-Y plane points were used to identify the positive X axis and could lie along the same plane as before. Therefore, $+10, -20, +5$ was selected as also shown in the part of the CCL output in Appendix D, Figure D.2. Once the new origins were established for the model, using CEL expressions at the inlet boundary conditions was significantly easier than using the previous method of interpolated values. The inlet coordinate frame was selected to be CELlcs. All the equations used for the F3 case extreme wave are presented in the Appendix D, Figure D.1. The F4 case frequent wave parameter equations are the same as above except for obvious changes in some of the parameters used.

For the solution the analysis type was set to as the one used in Chapter 6 - transient. The total time for the F3 cases was set at $28s$ but the simulation was stopped at just over $14s$ for the extreme waves and just over $13s$ for the more frequent wave. For the F4 cases the total simulation time was set to $14s$ (more than four revolutions) for the extreme waves and $11.43s$ (four revolutions) for the frequent waves. This was done in order to get at least one full wave time period. The timestep for the F3 cases was changed to $0.0018s$ from $0.01794s$ to reflect the 0.1 degree rotation. The F4 cases were set to the same timestep as used in

Chapter 6 corresponding to 1.0 degree of rotation. The initial time selection was selected as automatic with value and the value set to zero as per the transient no-wave models.

The boundary type for the left and right sides of the domain were selected to be symmetric. This created a plane of symmetry for both the geometry and fluid flow. The outlet was changed to an opening. In an opening, the flow can flow both in and out of the domain simultaneously. This was done to reduce the risk of an error occurring in the simulation due to flow recirculation at the outlet. The alternative to this solution was to increase the length of the domain but that entailed additional computational costs.

The discretisation algorithm for the transient term and the advection schemes were all set to the specific set-ups used in Chapter 6. The minimum and maximum coefficient loop was set between 1 and 3 loops respectively per timestep. This was done in order to reduce the unnecessary simulation time that would be needed if the loops were set between 1 and 5. ANSYS CFX recommends coefficient loops iterations between 1 to 3 to obtain good convergence. The residual time was set to stay in line with the accuracy achieved in Chapter 6. The transient results were backed up between the first and second revolution for the F3 cases and third and fourth for the F4 cases. The storage space required by these cases is truly staggering. The F3 data for one model uses approximately 4TB of space and the F4 data for one model uses approximately 600GB of space.

7.4 Extreme Wave for Normal Spacing F3 & F4 Cases

A combination of boundary layer velocities within the F3 and F4 parameters together with a large wave of $3m$ in wave height and $14s$ in wave period was analysed for the normal_spacing_model. As in the previous chapters, the blade loading plots are analysed and pressure contour plots are presented to discuss the behaviour of the models. Qualitative and quantitative analysis of the vorticity created by the turbine blades are discussed. Finally, axial torque and thrust plots are compared and its performance characteristics are compared.

7.4.1 F3 case (maximum torque)

The blade loading plots in Figures 7.1, 7.2 and 7.3 at 25%, 50% and 90% span respectively were taken from the results file corresponding to the last iteration of the simulation. At this timestep the positioning of the blades was such that blade one was at the highest position, blade two at the lowest position and blade three in between, refer Figure 7.4.

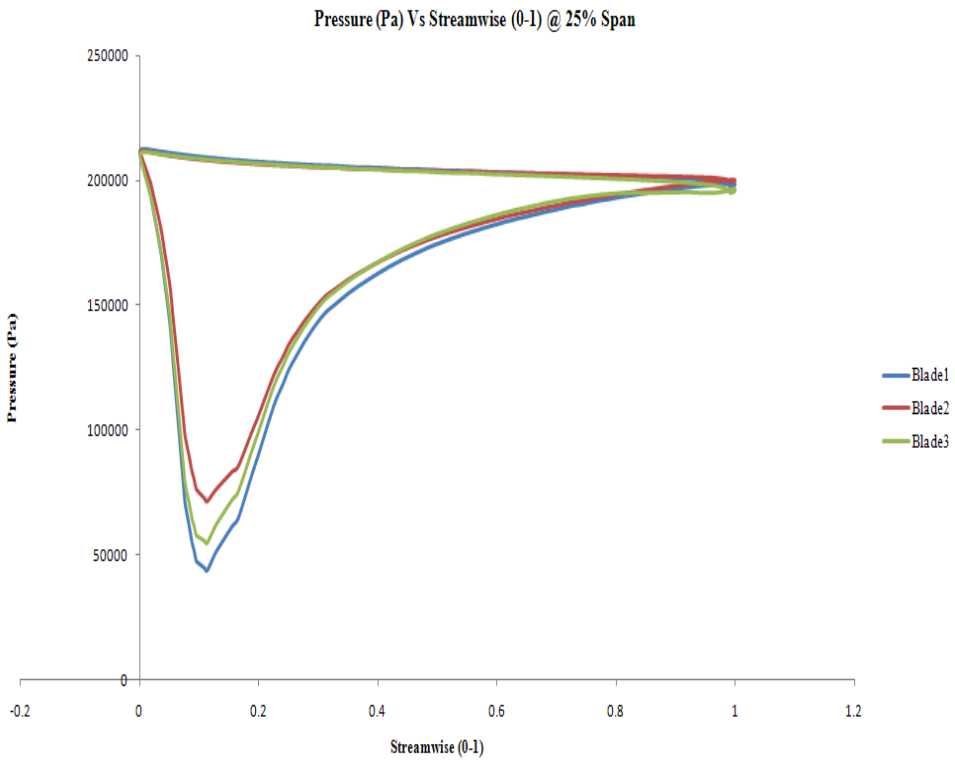

Figure 7.1 Pressure plot at 25% span - normal_spacing_model F3

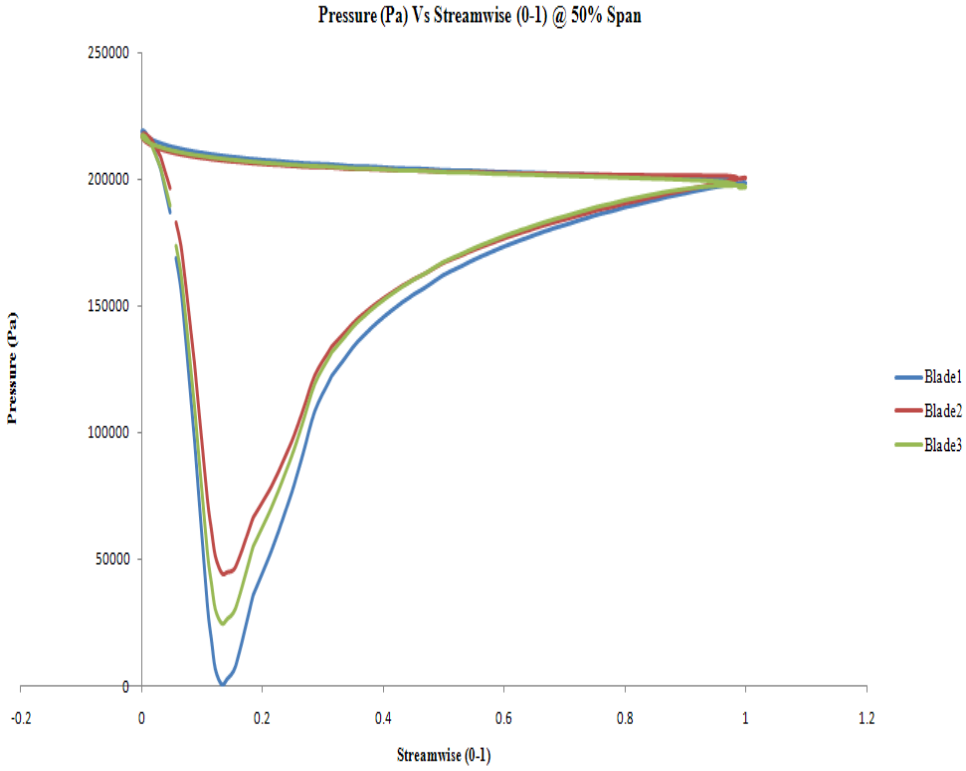

Figure 7.2 Pressure plot at 50% span - normal_spacing_model F3

One cannot compare these blade loading plots to the previous blade loading plots discussed in Chapter 5 and Chapter 6 as the current loading plots in this chapter have a horizontal

wave velocity component that varies with time. Therefore, at any instantaneous position in the simulation the flow velocities would be different, if evaluated. Therefore, it is clear that Figures 7.1 and 7.2 yields a standard blade loading plot than the Figure 7.3. Figure 7.3 is completely different to the normal loading plots discussed before, especially when considering the blade layout. According to the blade layout the red line being the blade 2 at the lowest level should have produced the least amount of force. On the contrary as shown in Figure 7.3, the blade 2 experiences highest flow velocity hence producing the largest force. The flow at this point in the simulation time would have been accelerating towards its peak velocity. The approximate combined flow speed of the rotor operating area at $14s$ would be around $3.2ms^{-1}$.

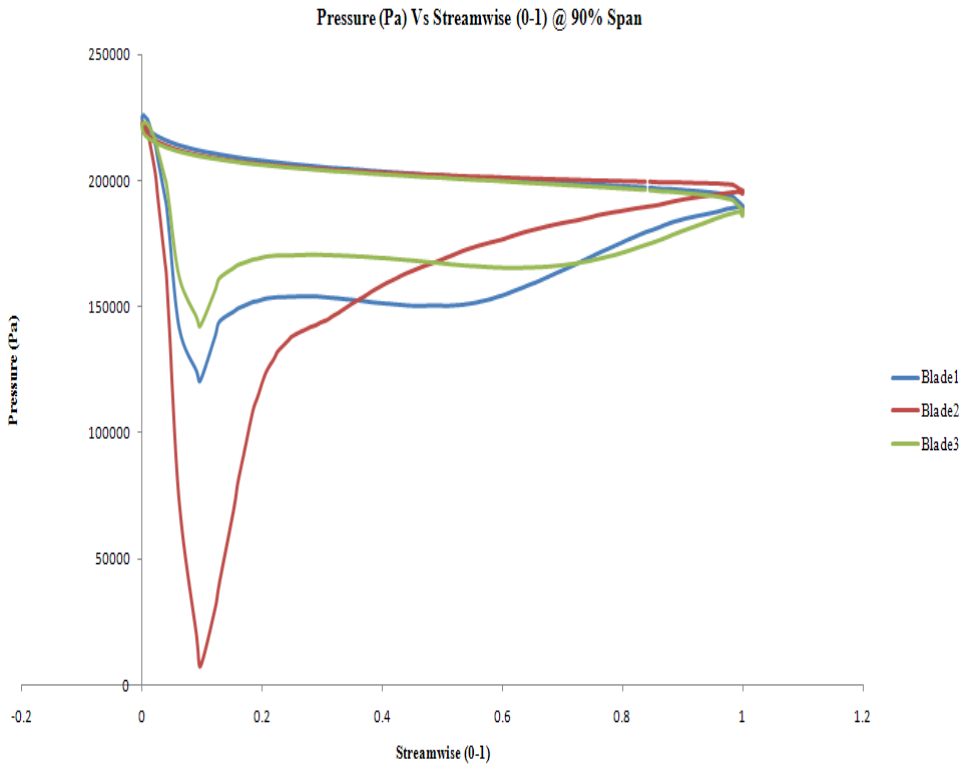

Figure 7.3 Pressure plot at 90% span - normal_spacing_model F3

Figure 7.4 depicts vectors of relative velocity taken in a plane $0.5m$ upstream of the plane of rotation of the turbine that corresponds to the axial position of the blade root. A certain amount of three dimensionality in the flow is visible in this plot around the root to about mid-span of the blades.

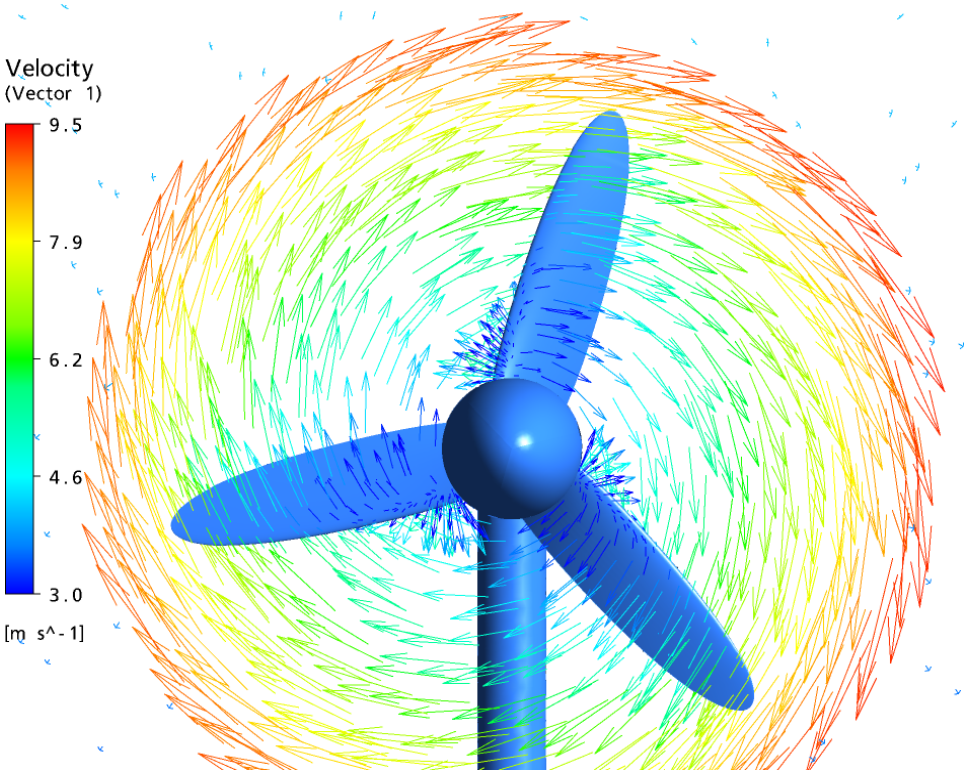

Figure 7.4 Velocity vector at $0.5m$ in front of the rotor axis

Figure 7.5 corresponds in turn to the flow in the plane of rotation that corresponds to the axial position of the blade tips. Here the flow, relative velocity vectors, departs substantially from a 2D behaviour in particular near the tip region.

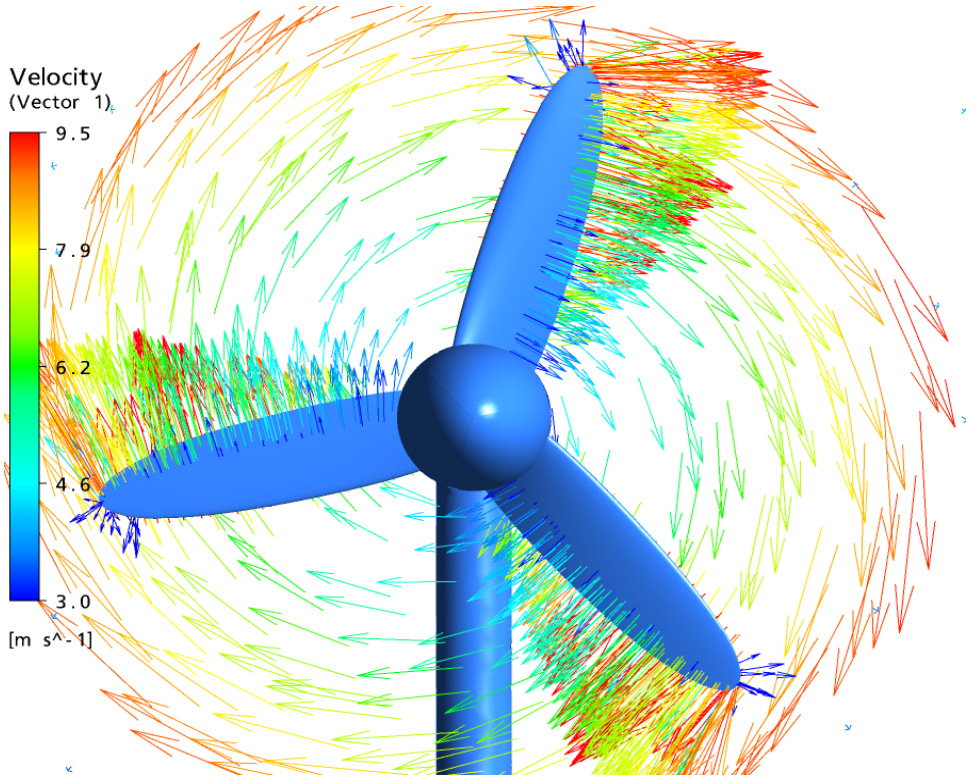

Figure 7.5 Velocity vector at the rotor axis

Moving back to the discussion on the varying velocity with time on the pressure loading plots refer to Figure 7.6, this figure displays three cosine wave plots varying with time. Figure 7.6a displays the combined velocity (shear profile and wave profile) at the sea bed. Figure b shows the combined velocity at hub height and figure c shows the combined velocity at the sea surface. This shows clearly that the velocity is a maximum at time $t = 0s$ and at time $t = 14s$. It's a minimum at time $t = 7s$ (half time period).

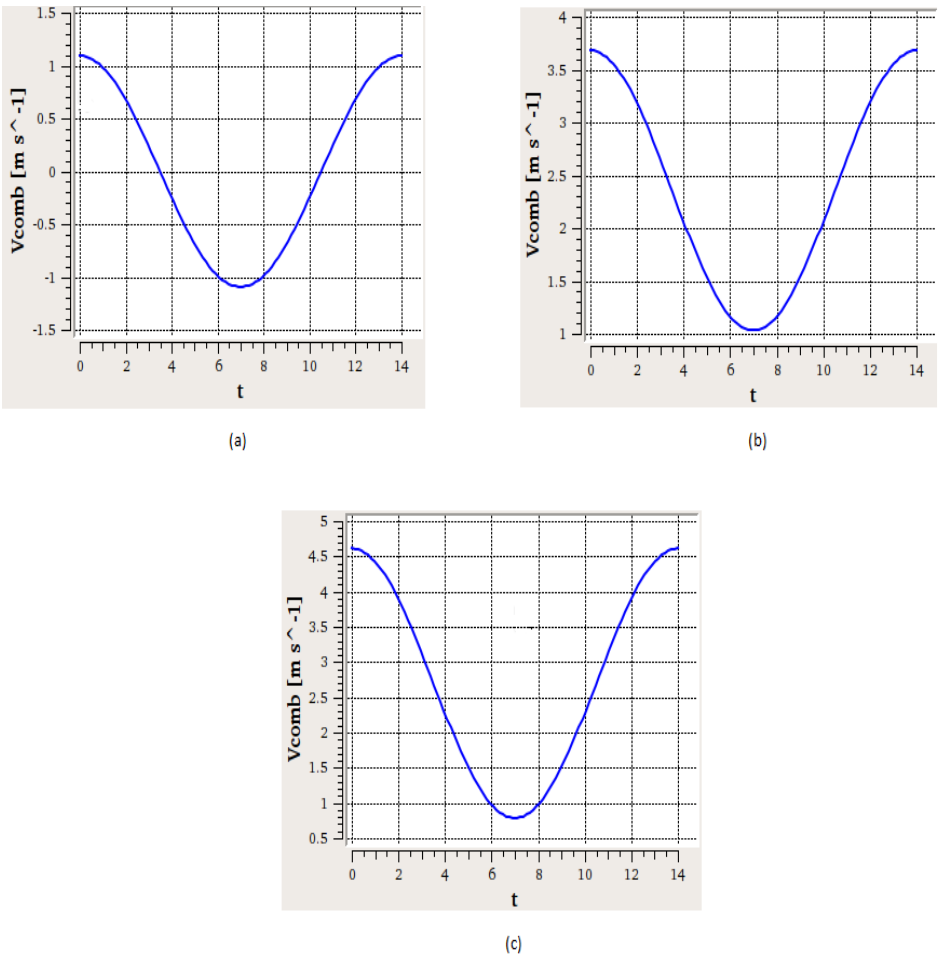

Figure 7.6 Combined velocities Extreme wave F3 case - (a) at sea bed, (b) at hub height, (c) at sea surface

If the pressure loading plots are analysed corresponding to the timestep at half wave period, the blade loading plots should be similar to the plots discussed above. The Figure 7.7, Figure 7.8 and Figure 7.9 represent the blade loading plots at 25%, 50% and 90% span respectively at exactly half the wave period. As expected the blade loading plots behave similarly as the blade loading plots in Figures 7.1, 7.2 and 7.3 except that these plots at half the wave period yields a significantly lower force. The orientation of the blades are roughly the same except that the blade 2 at the lowest location is almost infront of the pylon, therefore, the position of the other blades vary accordingly. This difference does not have a large impact on the plots. The averaged combined flow speed of the rotor operating area at $7s$ would be approximately around $1.2ms^{-1}$.

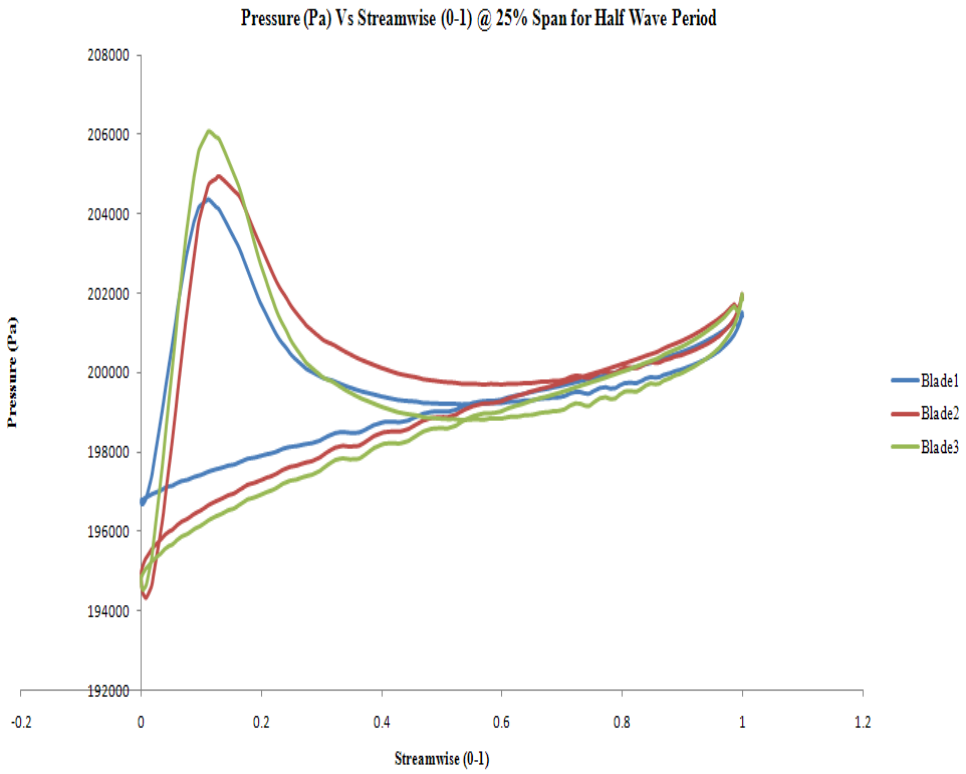

Figure 7.7 Pressure plot at 25% span - normal_spacing_model F3(Half wave period)

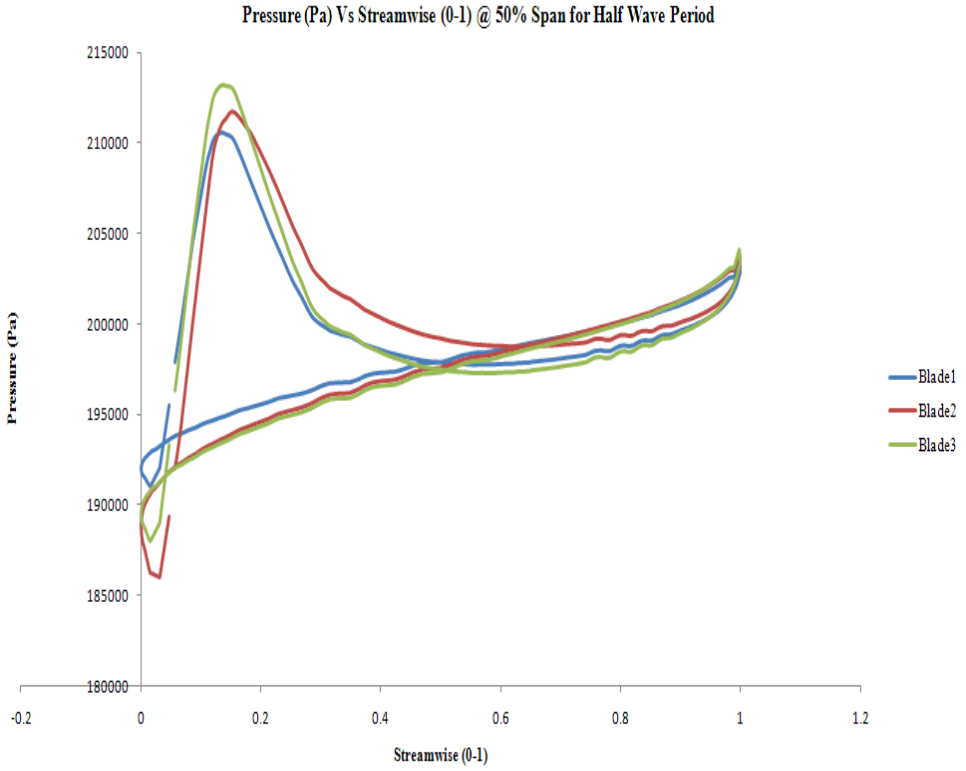

Figure 7.8 Pressure plot at 50% span - normal_spacing_model F3(Half wave period)

According to the new layout, the blade 3 should have a slightly higher force and the Figures 7.7 and 7.8 confirm this. The red line (blade 2) on Figure 7.9 behaves exactly the

same as the Figure 7.3, i.e. the blade 2 displays the highest force even though it's location suggests otherwise.

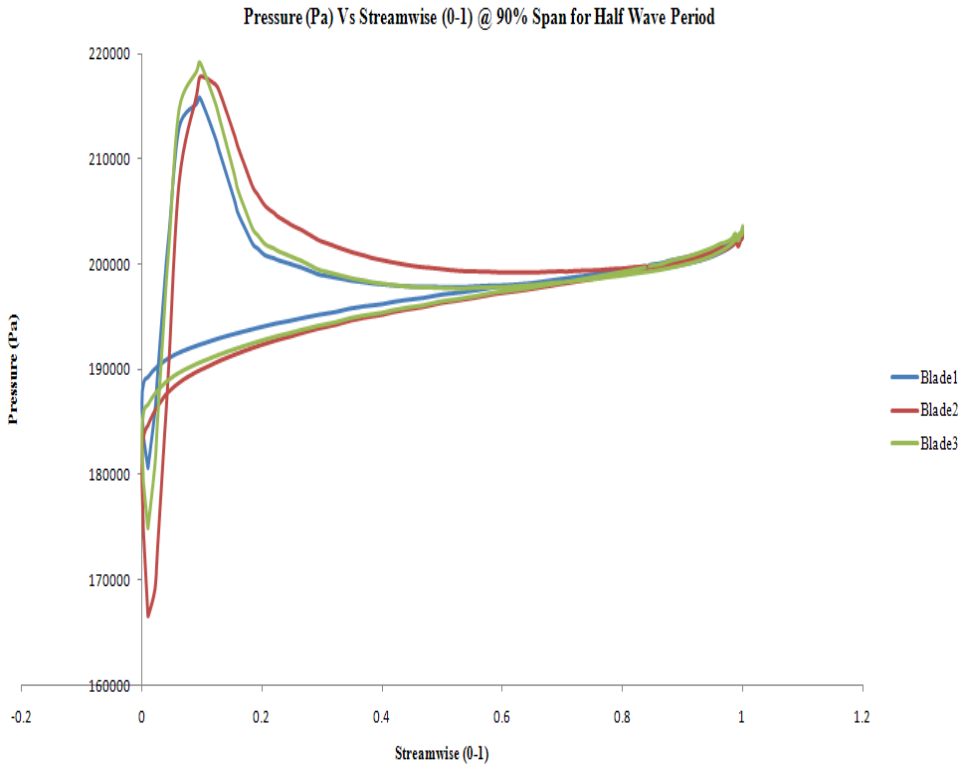

Figure 7.9 Pressure plot at 90% span - normal_spacing_model F3(Half wave period)

Moving on, the blade-pylon interaction is shown on the pressure contour plot in Figure 7.10. The stagnation points on the pylon are clearly marked by the high pressure zones and the low pressure area downstream of the rotor is clearly visible. Note the increase on the range of the pressure distribution than compared to the similar plots on displayed chapters 5 and 6. This suggests that there is a lot more activity as the flow is energised by superimposing the waves to the shear profile.

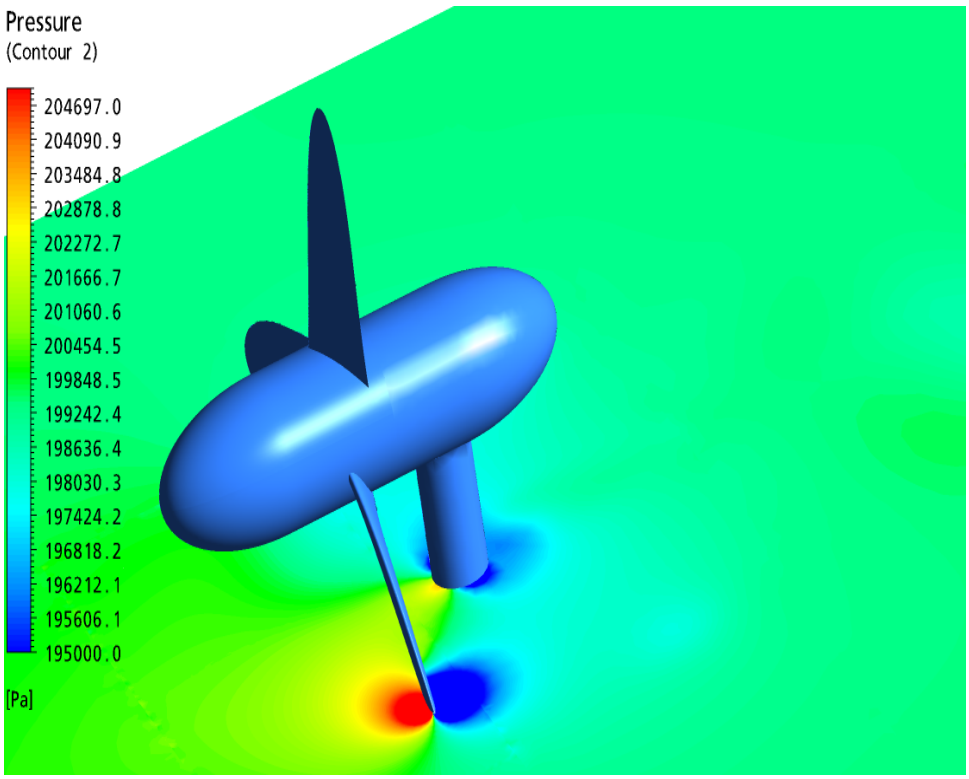

Figure 7.10 Blade-pylon interaction - normal_spacing_model F3

The Figure 7.11 represents the pressure contour for the wake distribution downstream of the rotor. The wake distribution plot shown on Figure 7.11 is very strong between 1-3D downstream of the rotor. The wake created by the combination of waves and the boundary layer velocity profile is more intense when compared with the models that consisted of only the shear flow.

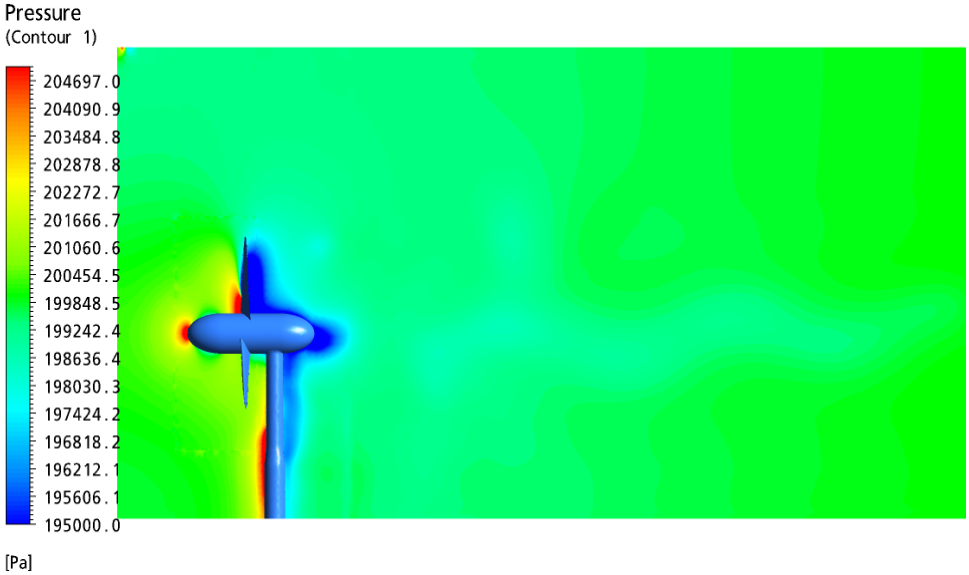

Figure 7.11 Pressure distribution in the meridional plane - normal_spacing_model F3

Similar qualitative plots presented in chapter 6 are presented in the subsequent paragraphs. Plots when the blade 2 first experiences the presence of the pylon, plots when the blade 2 is in front of the pylon and plots after blade 2 had passed the pylon have been documented. The three transient results at 4600, 4800 and 5100 corresponding to a simulation time of $6.4801s$, $6.8401s$ and $7.3801s$ were loaded on to ANSYS CFX and vector plots, vorticity plots, pressure plots and velocity plots were plotted for these timesteps.

As with chapter 6, a surface was created from the "DRUMFRONT" surface in the block "ABC" at $0.5m$ in front of the DRUMFRONT surface. Vorticity, pressure, circumferential velocity, and vector plots were created from this plane. A second surface was created in the same manner and placed at approximately $3D$ $(45m)$ downstream of the rotor and an axial velocity component plot was plot on this plane.

The vector plot on Figure 7.12 displays the flow field approximately a metre or so downstream of the rotor plane of rotation at the timestep corresponding to 4600.

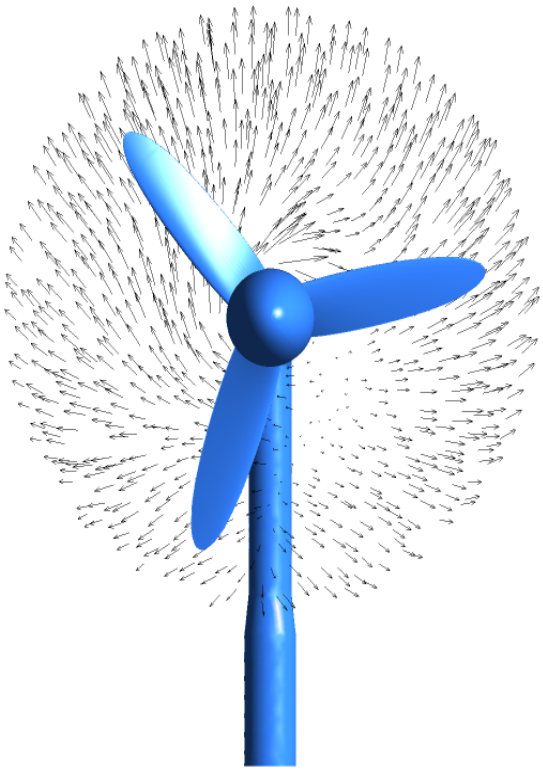

Figure 7.12 Vector plot at 4600 timestep - normal_spacing_model F3

The vorticity plot on Figure 7.13 show the vortices created by the blades for the same axial location. The vorticity was calculated to be approximately $6.0s^{-1}$.

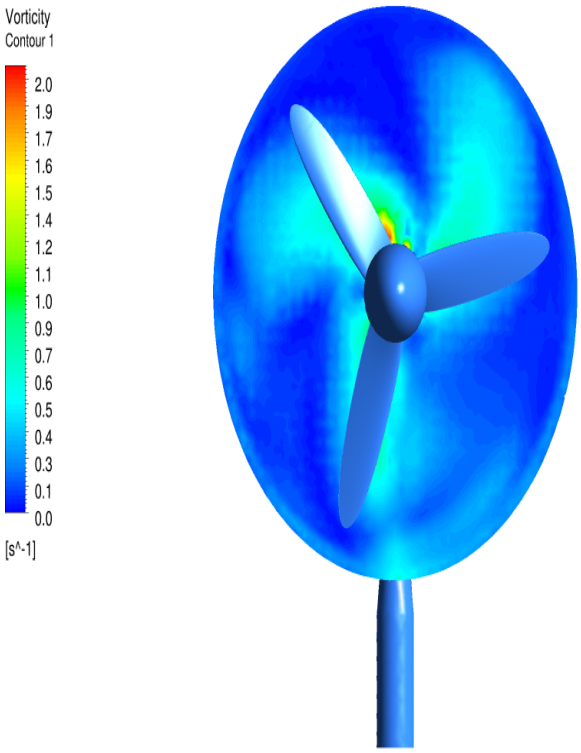

Figure 7.13 Vorticity plot at 4600 **timestep - normal_spacing_model F3**

Figure 7.14 displays a pressure plot at the same location and on this plot it could be seen clearly that there is an increased activity aft of the blade where the pylon is present. This increase in pressure area is certainly higher that that of the plot in chapter 6, implying that the pressures a lot higher in cases where waves are also involved.

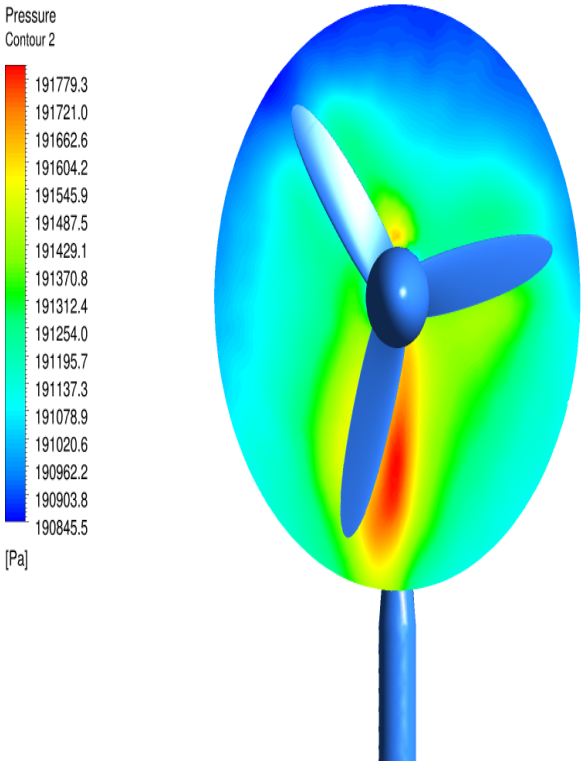

Figure 7.14 Pressure plot at 4600 **timestep - normal_spacing_model F3**

The circumferential velocity is plot on Figure 7.15at the same location.

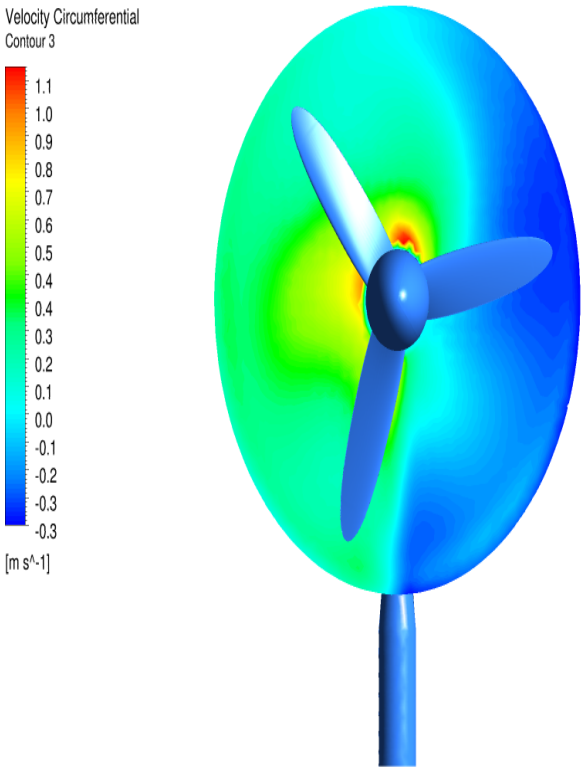

Figure 7.15 Circumferential velocity plot at 4600 **timestep - normal_spacing_model F3**

Axial velocity is plotted on Figure 7.16 at the second surface positioned approximately at $3D$ downstream of the rotor. The blades were made invisible for clarity. The blade orientation was unchanged. The wake generated for this location is higher than that of the corresponding plot in chapter 6. The range displayed in Figure 7.16 is smaller than that of the one in chapter 6, Figure 6.13 suggesting that velocities have not yet recovered.

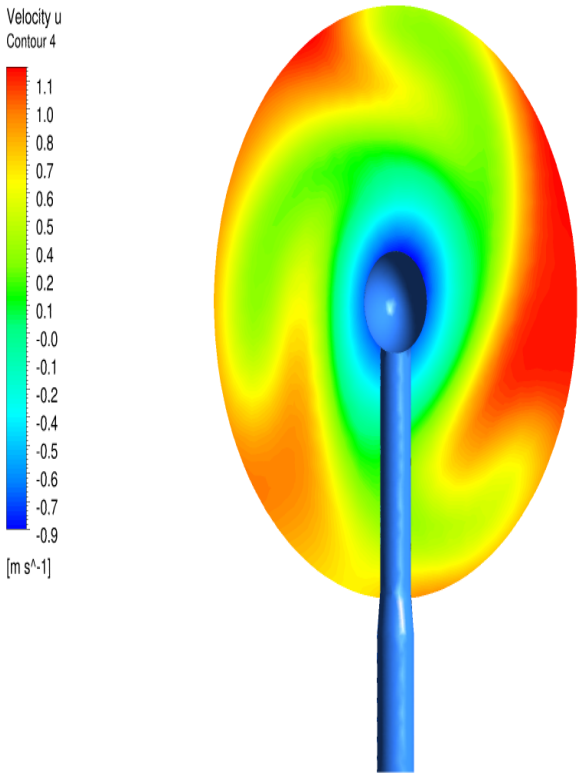

Figure 7.16 Axial velocity plot at 4600 **timestep - normal_spacing_model F3**

The vector plot on Figure 7.17 displays the flow field at the same location as previously except for the timestep which is now corresponding to 4800. The plot is similar to the previous plot at the timestep corresponding to 4600 but there is a disturbance at the blade 2 which is in front of the pylon.

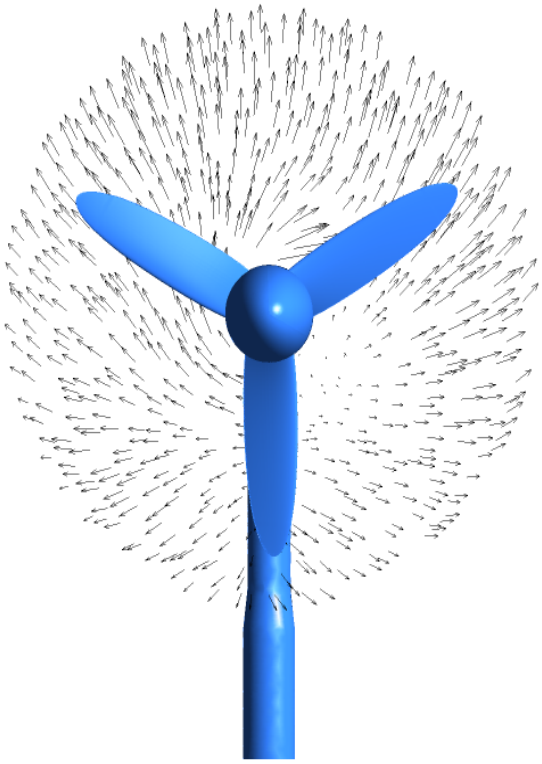

Figure 7.17 Vector plot at 4800 **timestep - normal_spacing_model F3**

The vorticity plot on Figure 7.18 show the vortices created by the blades. The range of the vorticity plot has slightly increased. This implies that the vorticity intensity has increased.

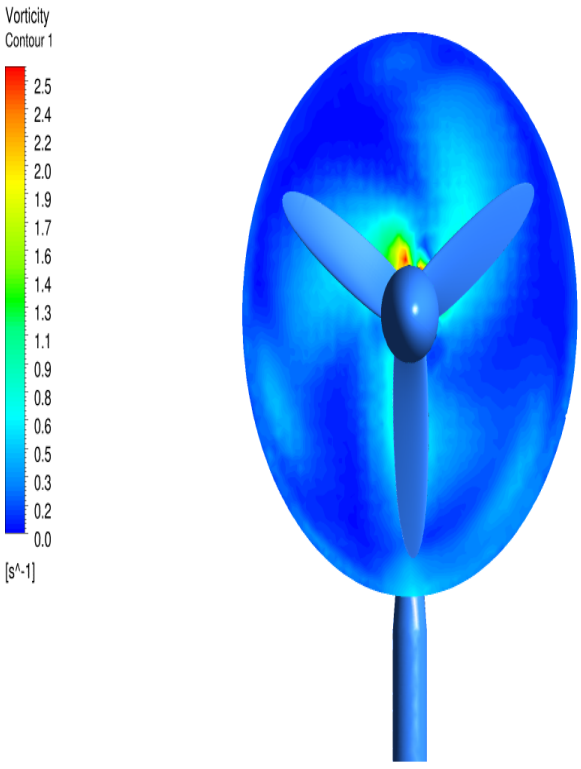

Figure 7.18 Vorticity plot at 4800 **timestep - normal_spacing_model F3**

Figure 7.19 displays a pressure plot, the range in the plot suggests that there is an increased activity when the blades are at that position. This could be due to the blade being right in front of the pylon thereby creating more activity around the vicinity.

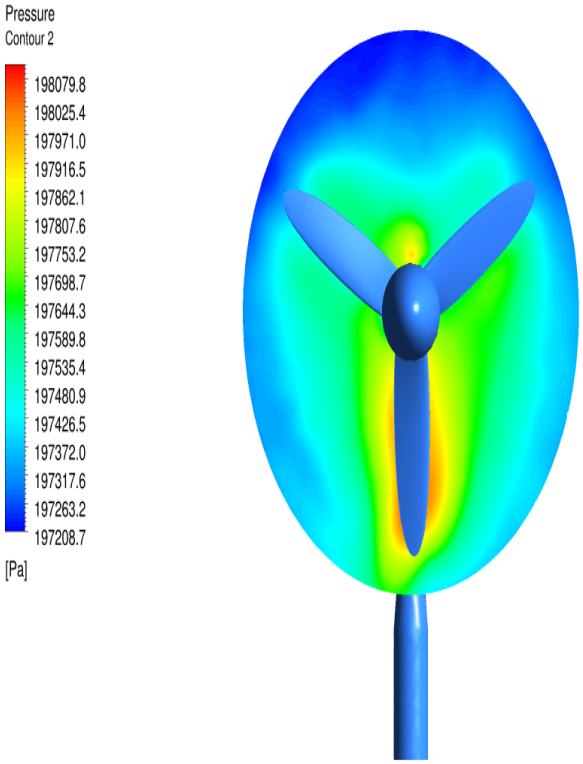

Figure 7.19 Pressure plot at 4800 **timestep - normal_spacing_model F3**

The circumferential velocity is plot on Figure 7.20at the same location. This plot is similar to the plot corresponding to the timestep of 4600.

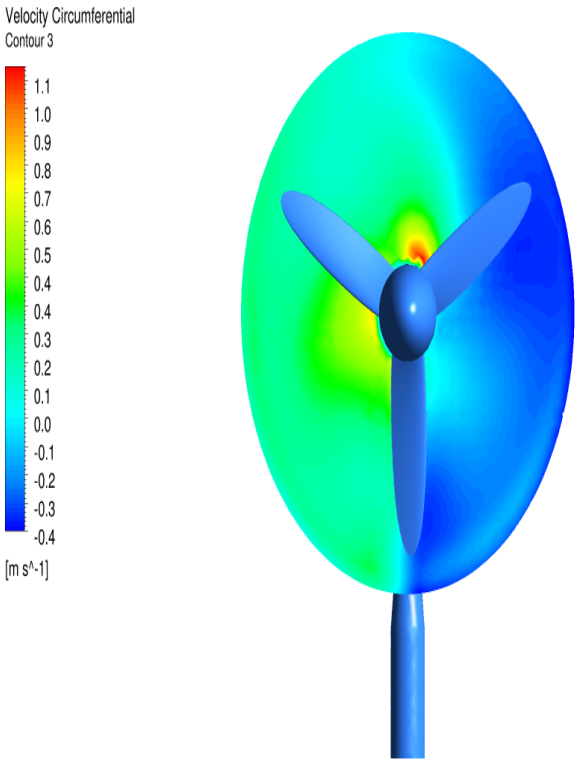

Figure 7.20 Circumferential velocity plot at 4800 **timestep - normal_spacing_model F3**

Axial velocity is plotted on Figure 7.21 at the second surface positioned approximately at $3D$ downstream of the rotor. This is also similar to the previous plot at 4600 timestep.

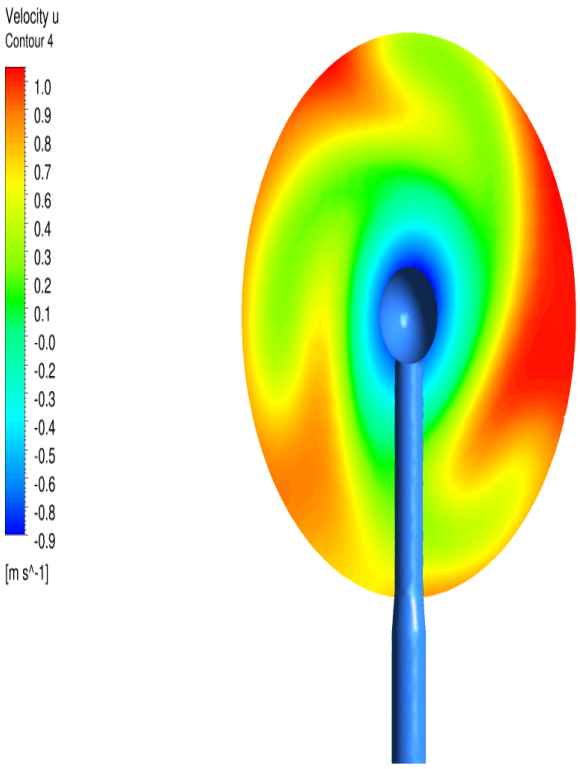

Figure 7.21 Axial velocity plot at 4800 **timestep - normal_spacing_model F3**

The vector plot on Figure 7.22 displays the flow field at the timestep corresponding to 5100.

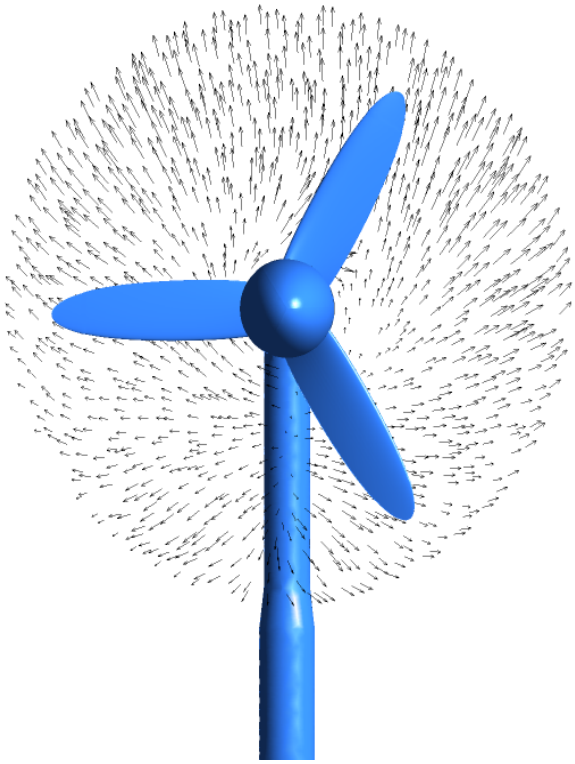

Figure 7.22 Vector plot at 5100 **timestep - normal_spacing_model F3**

The vorticity plot on Figure 7.23 show the vortices created by the blades. Although the range and the intensity seems to be the same as the plot corresponding to the timestep of 4800, the vorticity plot in this figure seems to have developed more.

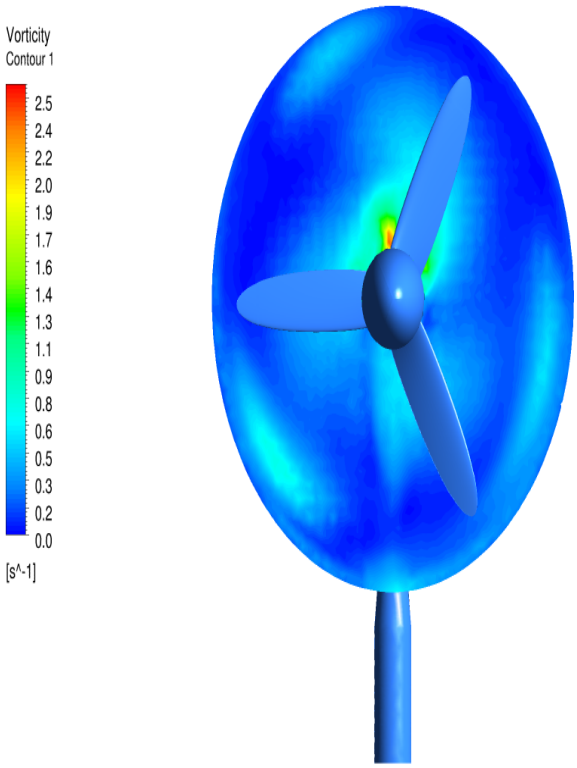

Figure 7.23 Vorticity plot at 5100 timestep - normal_spacing_model F3

Figure 7.24 displays a pressure plot, the range in this plot has increased.

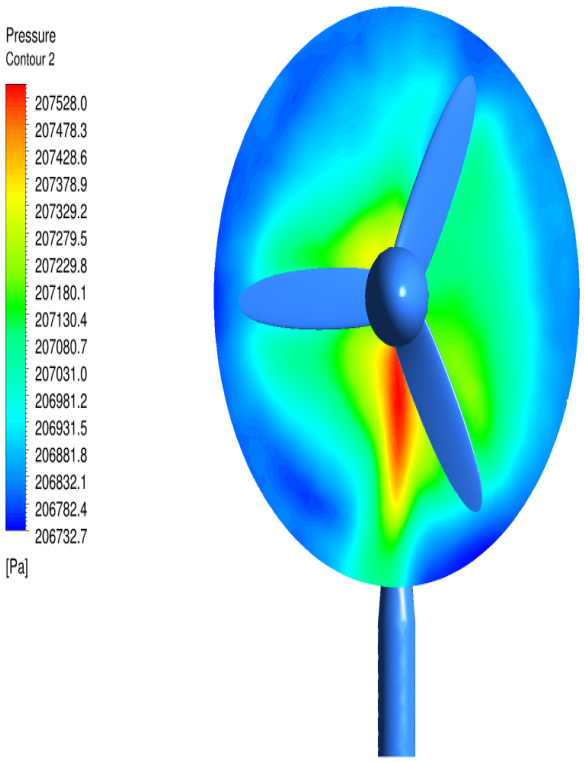

Figure 7.24 Pressure plot at 5100 timestep - normal_spacing_model F3

The circumferential velocity is plot on Figure 7.25.

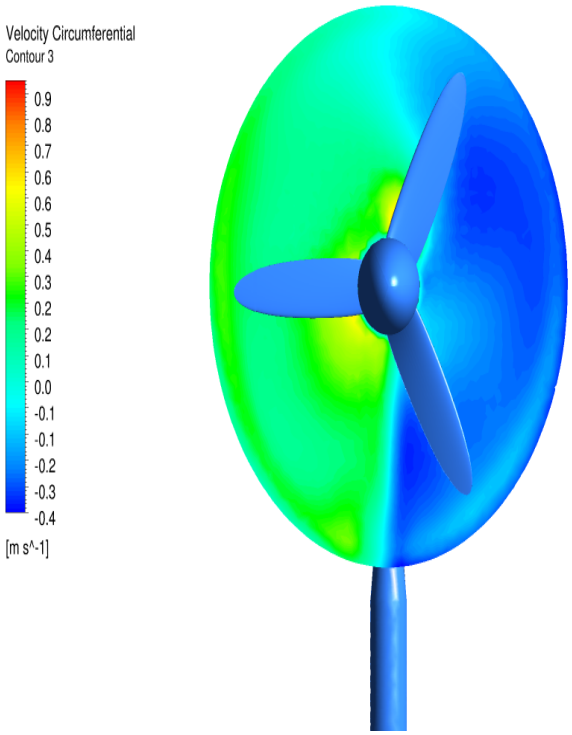

Figure 7.25 Circumferential velocity plot at 5100 timestep - normal_spacing_model F3

Axial velocity is plotted on Figure 7.26 in the same manner as before.

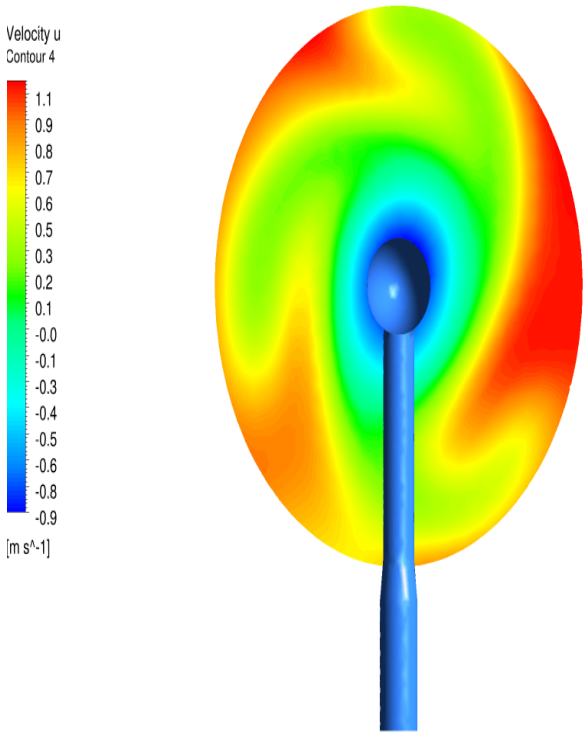

Figure 7.26 Axial velocity plot at 5100 timestep - normal_spacing_model F3

The total torque was calculated to be around $629kNm$ and the total thrust was calculated to be approximately $297kN$. The total power generated by the turbine with a combination of waves and shear flow velocities is equal to be approximately $612kW$. The total axial thrust and total axial torque curves are plotted on the Figure 7.27. The negative loads are due to the flow increasing and decreasing between the time spectrum. The lowest point in the plot signifies that it's half the wave time period.

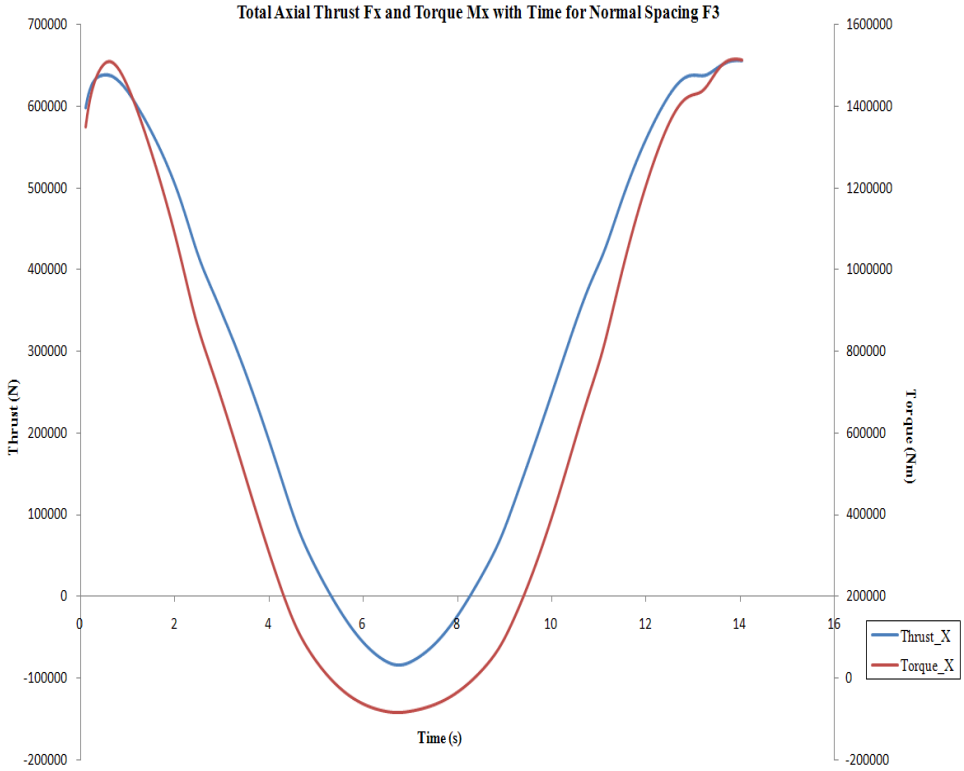

Figure 7.27 Thrust and Torque loads for normal_spacing_model F3

The axial thrust and axial torque variation per blade are shown on Figure 7.28 and Figure 7.29 respectively. The main difference on these individual blade load plots to the plots in chapter 6 is that there seems to be no sequence in the plots. This is because the one full rotation is approximately about $6.5s$ and also half wave period is roughly close to this value at $7.0s$. Therefore, the point at which the lowest loads are generated (half wave period) is superimposed to the one full revolution.

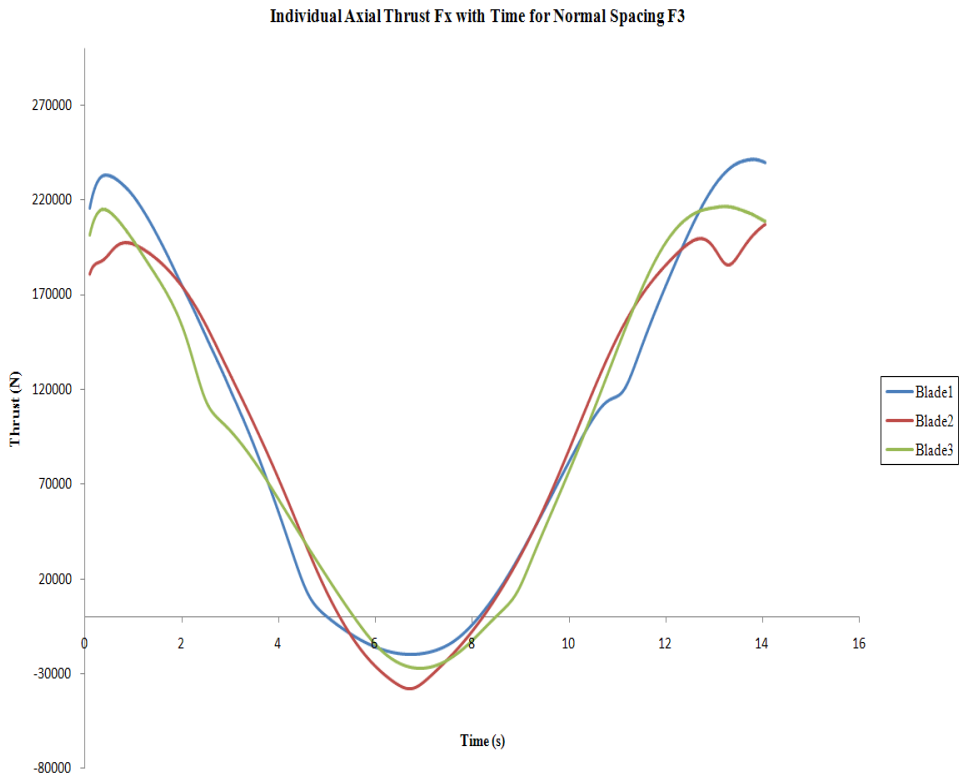

Figure 7.28 Individual Axial Thrust loads for normal_spacing_model F3

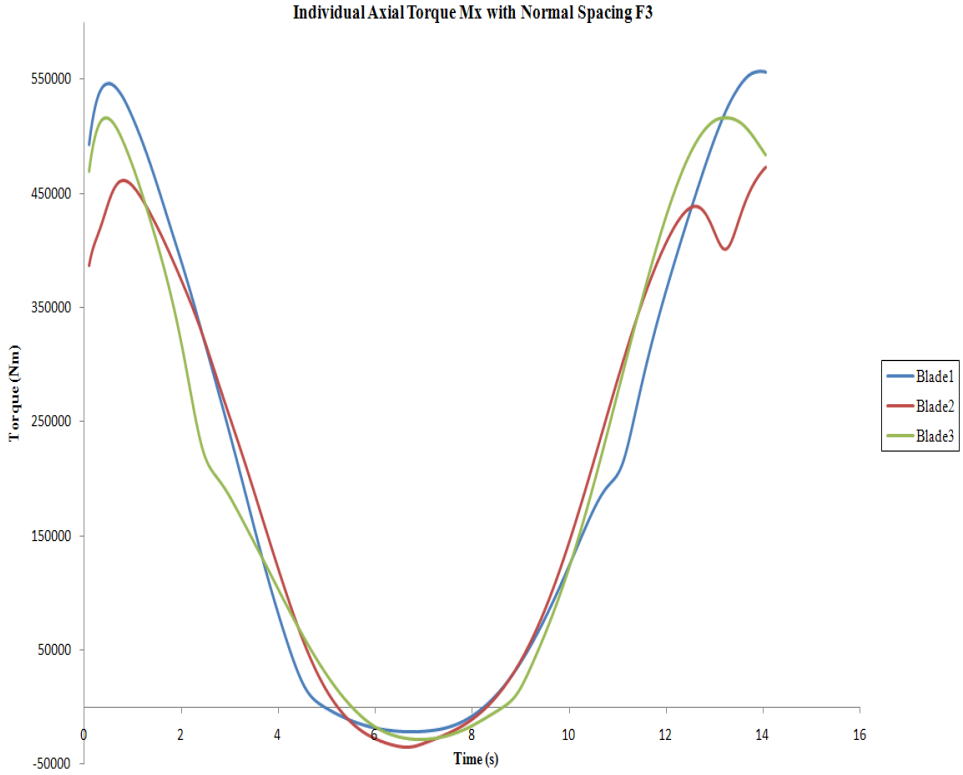

Figure 7.29 Individual Axial Torque loads for normal_spacing_model F3

7.4.2 F4 case (maximum thrust)

The Figure 7.30, Figure 7.31 and Figure 7.32 represents the blade loading plots for the F4 cases at 25%, 50% and 90% span locations. Again as expected, the F4 blade loading plots produce significantly higher blade loading characteristics than when compared with the F3 cases.

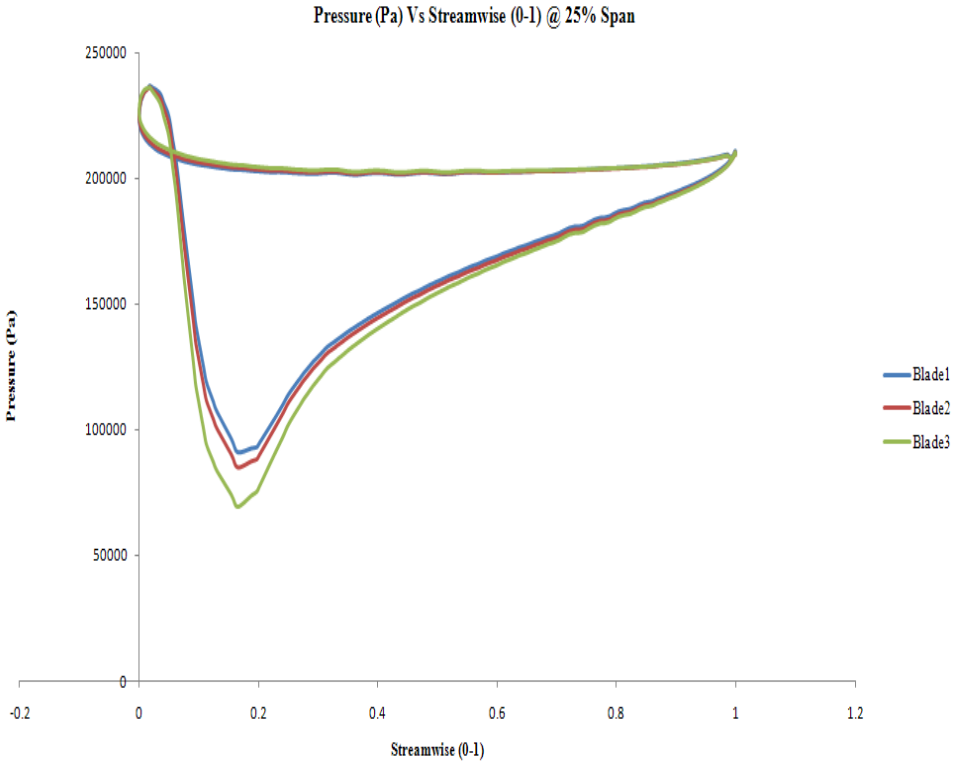

Figure 7.30 Pressure plot at 25% span - normal_spacing_model F4

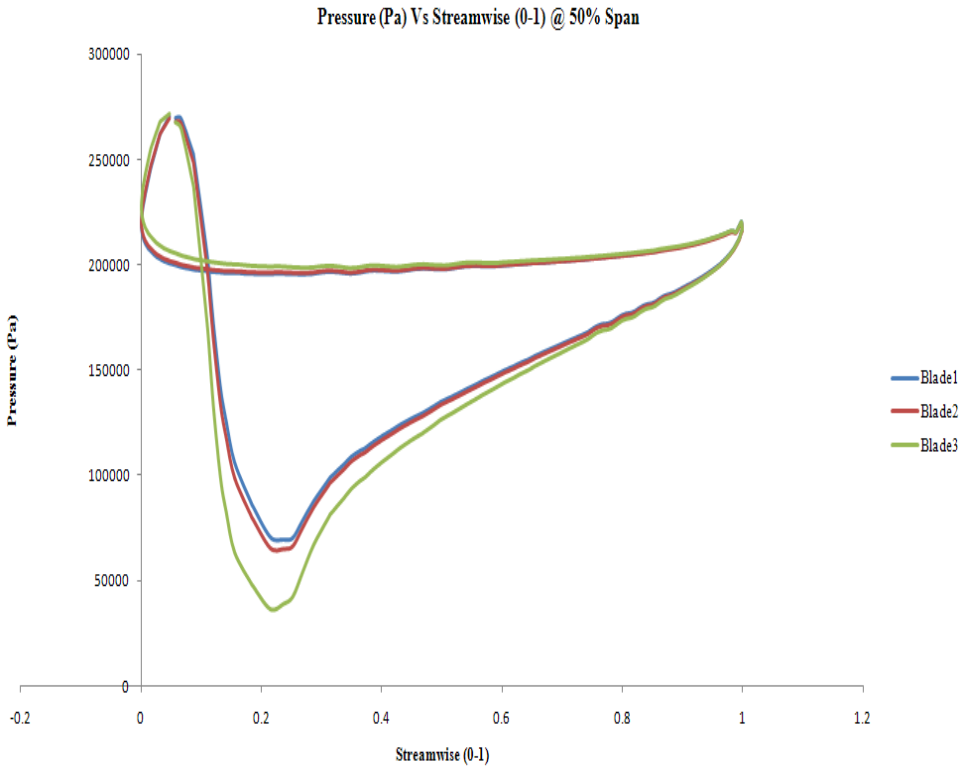

Figure 7.31 Pressure plot at 50% span - normal_spacing_model F4

The blade orientation is such that the blades 1 and 2 are in a lower position when compared to the blade 3. The blade three is at the highest position and hence experiences are larger force than when compared to the blade 1 and blade 2. The blade 1 and blade 2 are relatively in a similar position and is further confirmed by the blade loading plots.

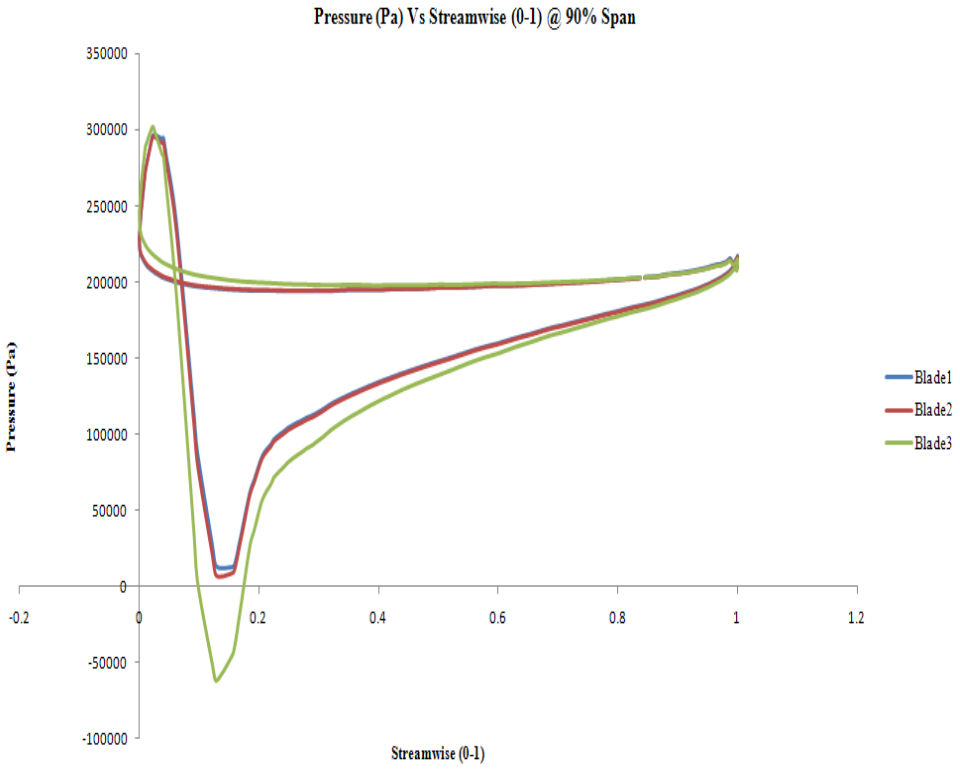

Figure 7.32 Pressure plot at 90% span - normal_spacing_model F4

The Figure 7.33 represents the blade-pylon pressure contour plot. The stagnation point on the pylon and the low pressure areas downstream of the rotor are clearly visible. The pressure distribution range is clearly higher than that of the similar plot in chapter 6. This suggests that the flow is energised and a lot more activity is going on.

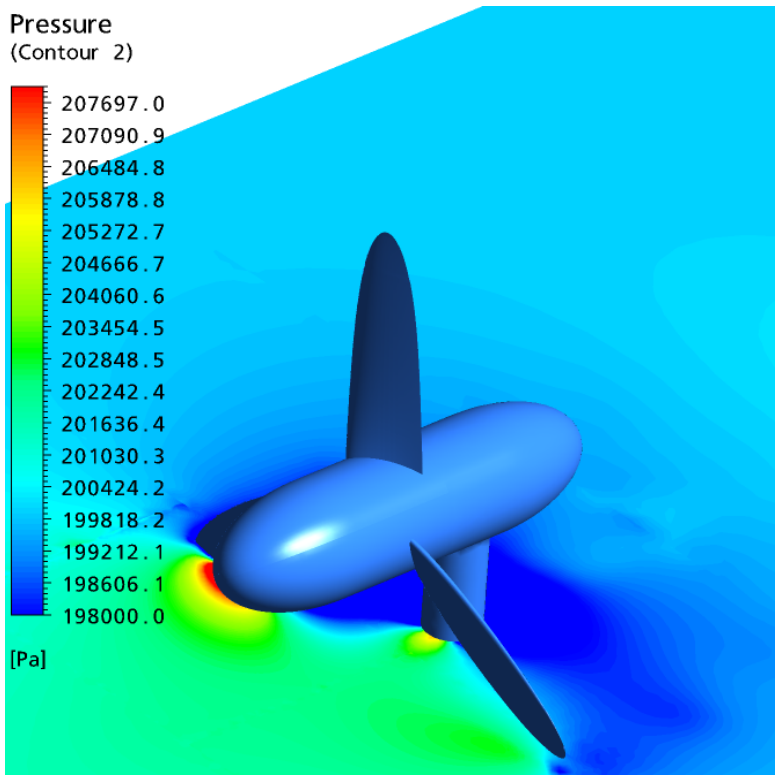

Figure 7.33 Blade-pylon interaction - normal_spacing_model F4

The Figure 7.34 displays the pressure contour plot for the wake distribution. There is a severe wake occurring between 1-2D downstream of the rotor. The wake improves slightly beyond this region. The stagnation points are clearly marked on as the red areas in front of the pylon, front of the nose and also in front of the blades.

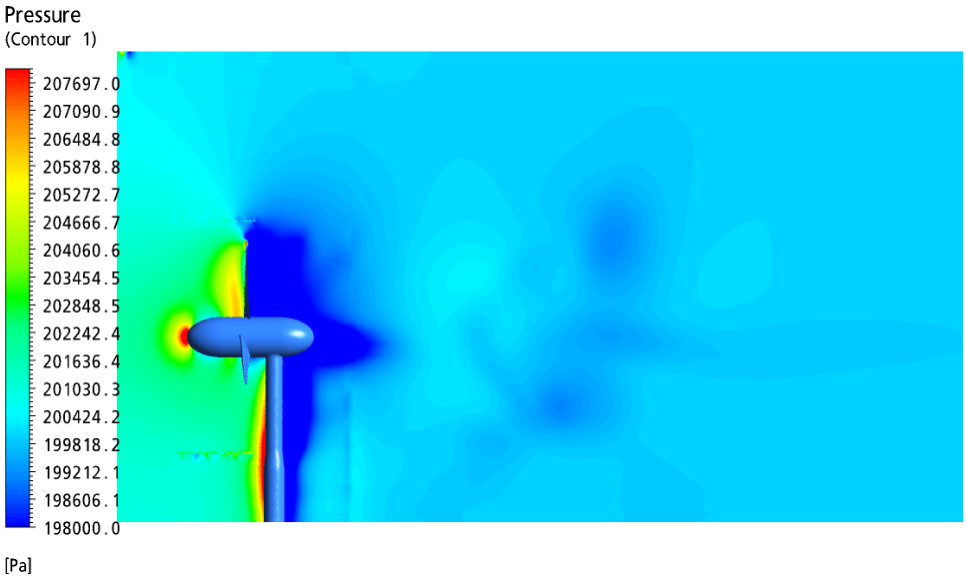

Figure 7.34 Pressure distribution in the meridional plane - normal_spacing_model F4

The Figure 7.35 and Figure 7.36 illustrate the vorticity around blades at the rotor axis with

and without the blades respectively.

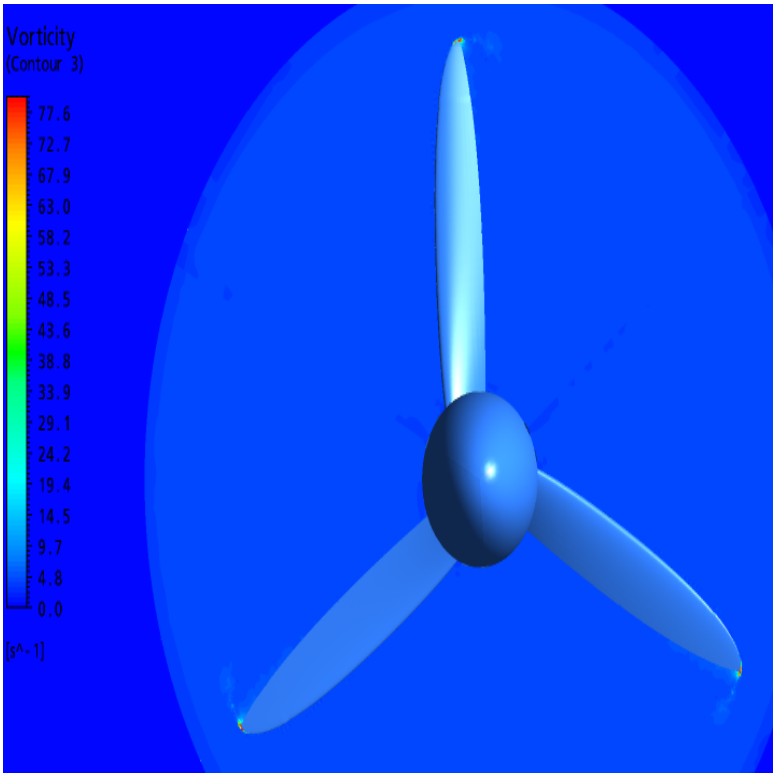

Figure 7.35 Vorticity at the blade tips on the rotor axis - normal_spacing_model F4

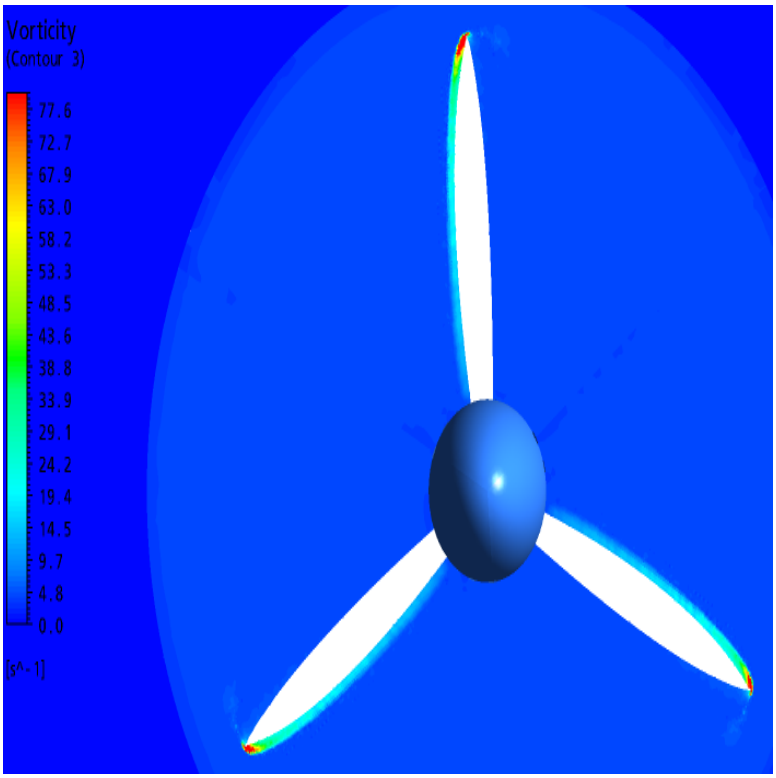

Figure 7.36 Vorticity on the rotor axis without blades - normal_spacing_model F4

The vortices created around the blade tips are just visible in Figure 7.35. The Figure 7.36 without the blades shows part of the vortices formed around the leading edge, the blade tip area clearly shows an high intensity vortex being formed and also like in the previous figure the vortices can be noticed just aft of the blade tips.

The total torque was calculated to be around $500kNm$, the total thrust was calculated to be roughly around $332kN$. The total power produced by the turbine is approximately $1100kW$. This simulation was allowed to solve for the full four revolutions and is clearly visible on the plot displayed on Figure 7.37 for the total axial loads with simulation time.

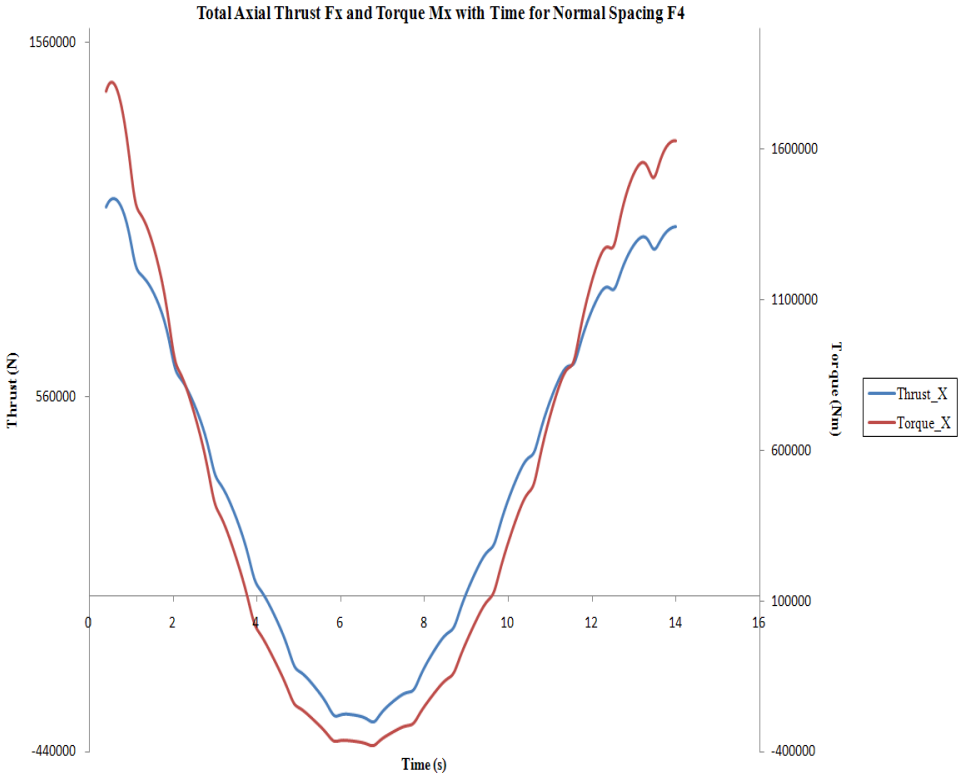

Figure 7.37 Thrust and Torque loads - normal_spacing_model F4

The individual axial thrust and axial torque per blade is presented in Figure 7.38 and Figure 7.39 respectively.

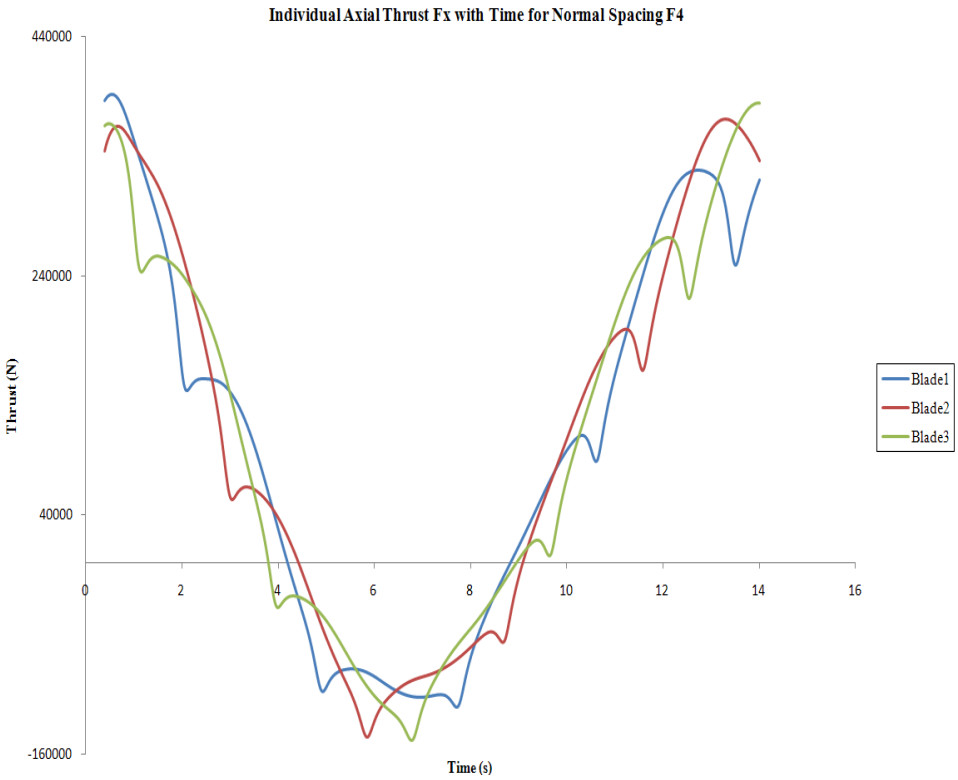

Figure 7.38 Individual Axial Thrust loads - normal_spacing_model F4

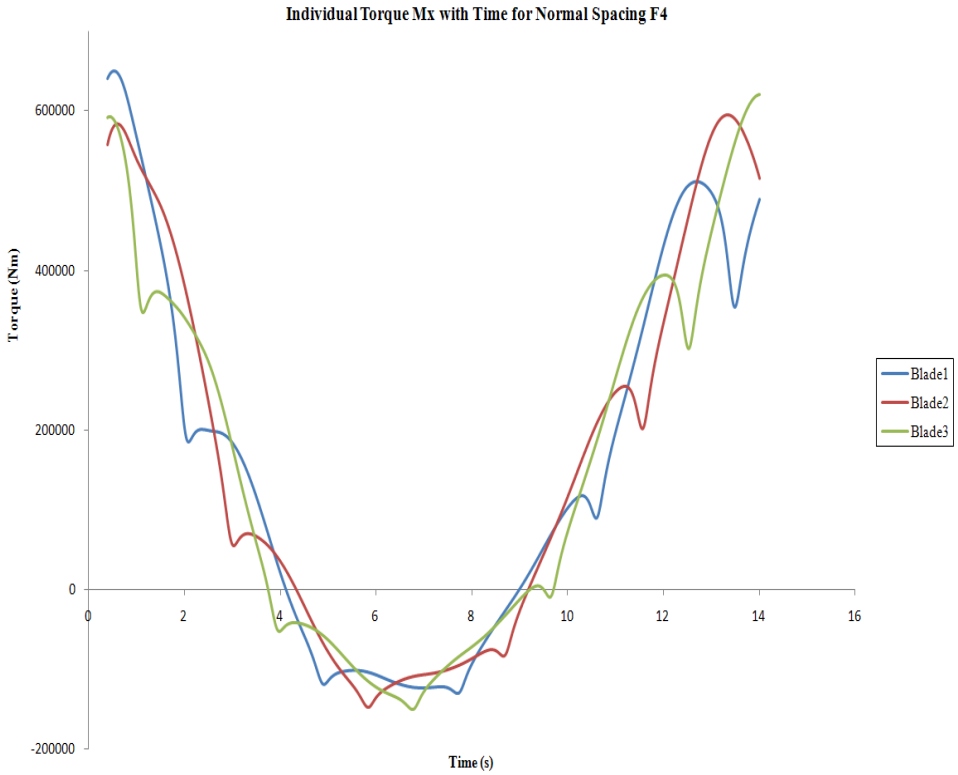

Figure 7.39 Individual Axial Torque loads - normal_spacing_model F4

Unlike the previous F3 performance plots, these plots clearly show each revolutions and on Figures 7.38 and 7.39 it is clear at just under $2.9s$ all three blades see the pylon, which

suggests that it had completed one full revolution during this time. And on all three figures, at half time period $(t = 7s)$ the rotor system experiences the lowest flow field therefore producing the lowest loads.

7.5 Extreme Wave for Half Spacing F3 & F4 Cases

The same wave and shear velocity profile parameters as in the previous section was now utilised for the analysis of the Half_spacing_model. The blade loading plots are analysed for the F3 and F4 cases and the pressure contour plots are discussed for the wake characteristics and blade-pylon interactions. The performance characteristics such as the total axial thrust and total axial torque variations are discussed together with the individual blade loadings.

7.5.1 F3 case (maximum torque)

The Figure 7.40, Figure 7.41 and Figure 7.42 represents pressure loading plots for the Half_spacing_model F3 cases at 25%, 50% and 90% span locations respectively.

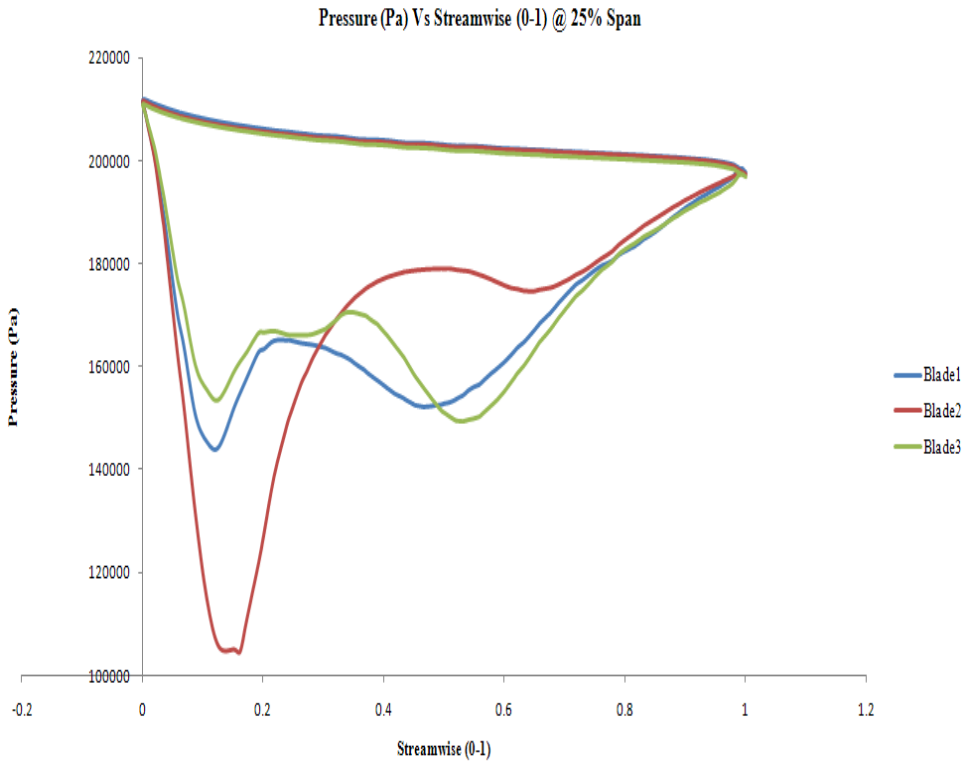

Figure 7.40 Pressure plot at 25% span - Half_spacing_model F3

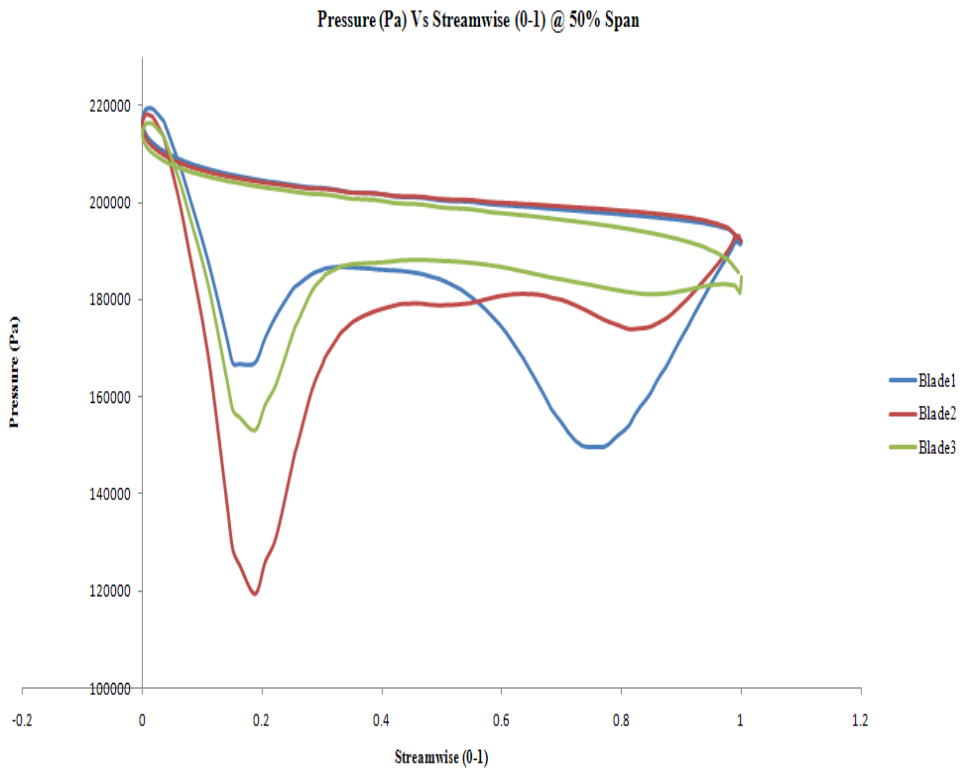

Figure 7.41 Pressure plot at 50% span - Half_spacing_model F3

The normal orientation of the blades is such that the blade one is at the highest location followed by the blade two (clockwise) and then the blade three. The blade two is slightly below the blade three. These blade loading plots are very similar to the plots observed for the normal_spacing_model F3 case. Typically the blade one plot denoted in blue should have experienced the highest force variation and followed closely by the blade three and then blade two. This could be seen on the Figure 7.42 at 90% span. At this point in the simulation, the blades would be experiencing different velocity components at different locations because of the time varying velocity components produced by the waves superimposed by the shear profile.

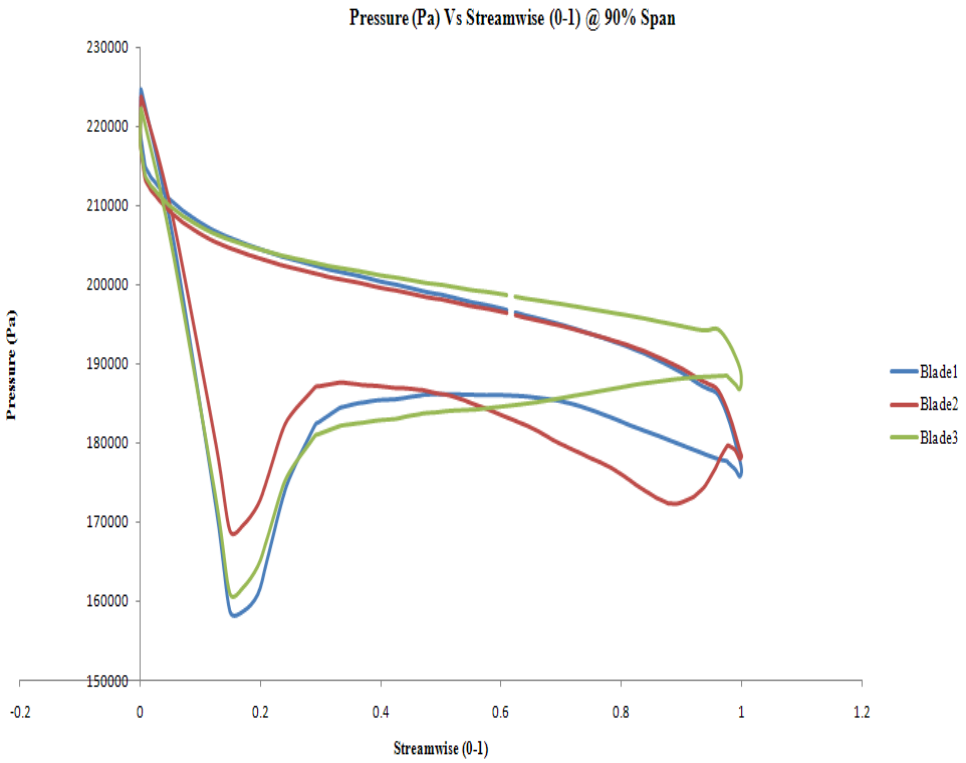

Figure 7.42 Pressure plot at 90% span - Half_spacing_model F3

The plot shown on Figure 7.43 represents the vorticity of each blade with the blade positioning at 99% span. The plots were taken at the plane of rotation of the rotor. The colour code for the vorticity plot and the blade loading plots shown above are the same. As shown, the blade one experiences the largest vortex, followed by the blade three and the smallest vorticity is produced by the blade two which is at the lowest point in the rotor operating area. The total vortex generated for all three blades were approximately equal to $4s^{-1}$.

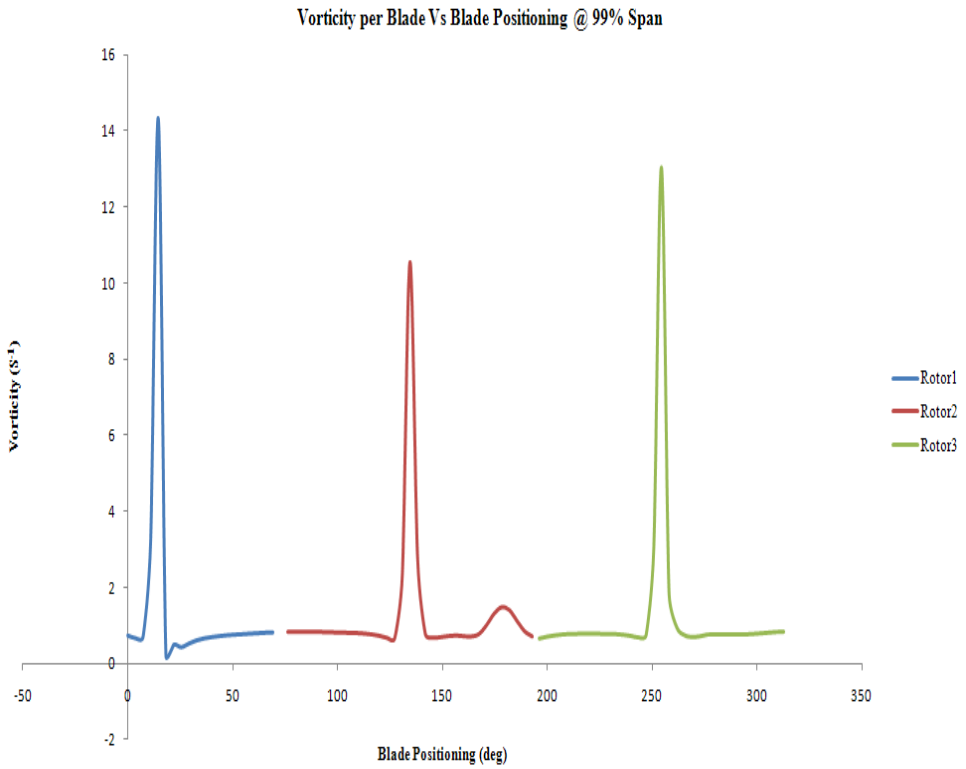

Figure 7.43 Vorticity plot with blade positioning at 99% span - Half_spacing_model F3

The pressure contour plot displayed on Figure 7.44 is for the blade-pylon interaction. The lower pressure areas and the high pressure stagnant areas are clearly visible from the dark blue areas and the yellow and red areas respectively.

The Figure 7.45 shows a pressure contour plot for the wake distribution of the model. The pressure ranges on the Figure 7.44 and Figure 7.45 are similar. The darker blue areas on the Figure 7.45 show that wake is at its greatest and reaches upstream pressure values several diameters downstream of the rotor. The stagnation points are defined by the red areas in front of the pylon, the nose of the hub and in front of the blades as shown on Figure 7.45.

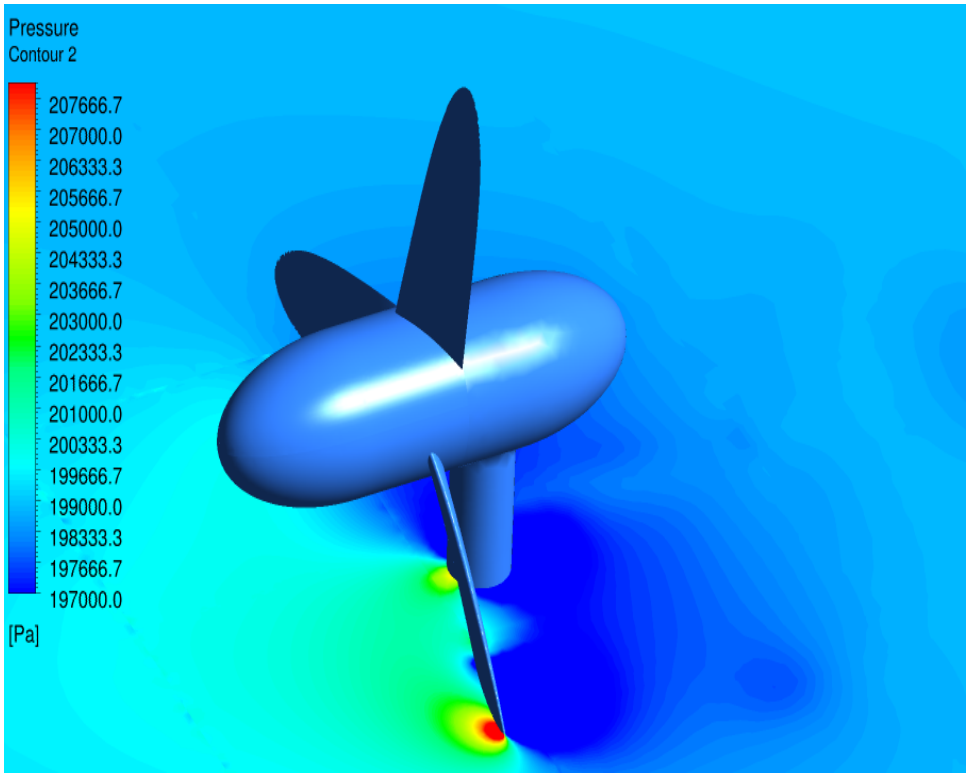

Figure 7.44 Blade-pylon interaction - Half_spacing_model F3

Both these pressure contour plots suggests that there is a lot more activity occurring in the Half_spacing_model than when compared the datum model. This was quite evident also in the transient plots on chapter 6. The variations of these pressure plots are definitely a lot higher than that of the datum model.

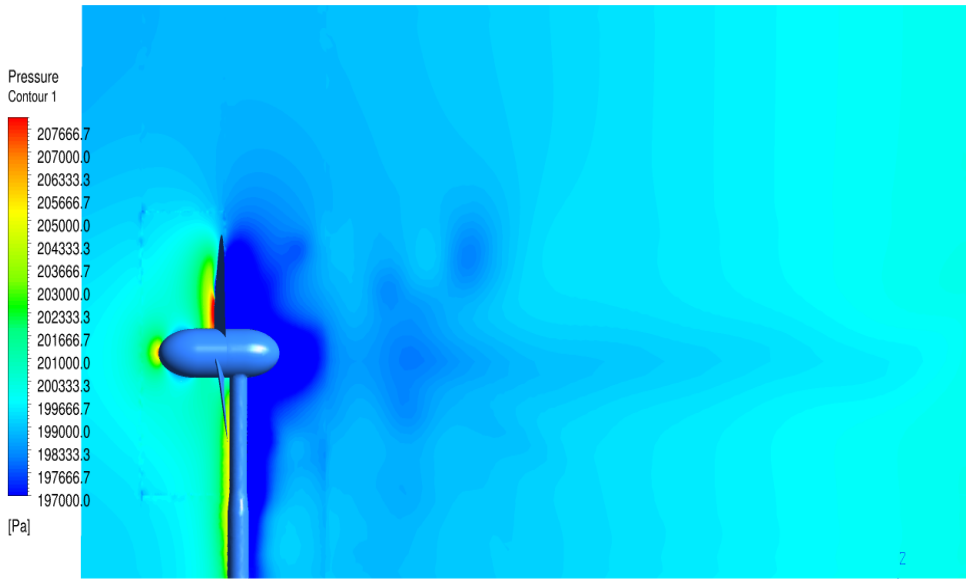

Figure 7.45 Pressure distribution in the meridional plane - Half_spacing_model F3

Figures 7.46, 7.47 and 7.48 represent vector plots a couple of metres downstream of the

rotor plane of rotation for timesteps at 4600, 4800 and 5100. As mentioned previously on sub section 7.4, these timesteps correspond to actual simulation times of $6.4801s$, $6.8401s$ and $7.3801s$ respectively.

The first feature that is clearly visible in these vector plots when compared to the vector plots in subsection 7.4 is that the size of the vector arrows relatively larger in size. The larger the size of these vector arrows, the greater the intensity. If looked deeper in to the Figure 7.46 and then compare it with a similar plot on Figure 7.12, it can be said that the vector plot for the latter is generally more organised than the former. This would suggest that there is more activity involved in the Half_spacing_model.

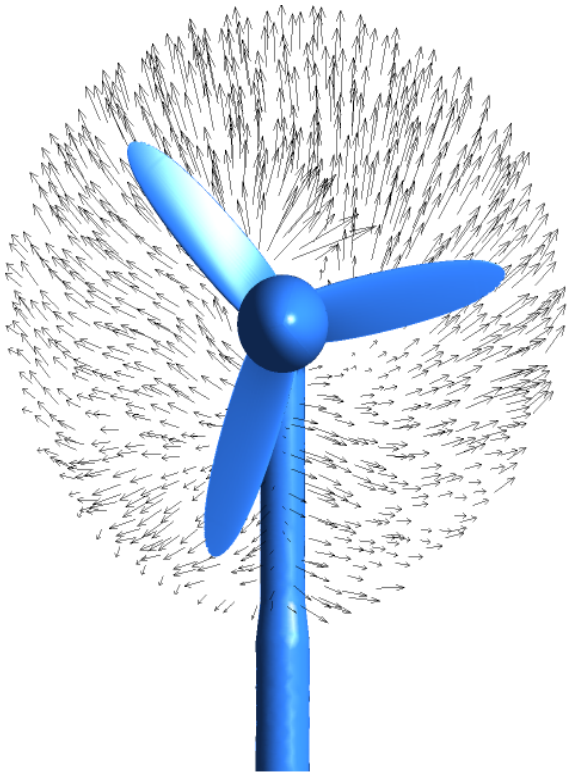

Figure 7.46 Vector plot at 4600 timestep - Half_spacing_model F3

Figure 7.47 also shows similar intensities as the previous plot and draws similar conclusions mentioned in the above paragraph when compared to Figure 7.17 on section 7.4.

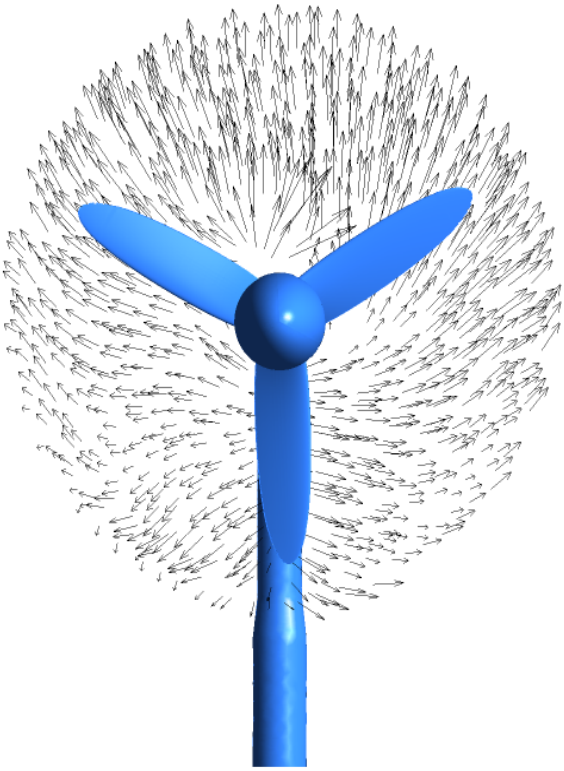

Figure 7.47 Vector plot at 4800 **timestep - Half_spacing_model F3**

Figure 7.48 draws similar conclusions as the above plots and its more disorganised when compared to its similar plot on Figure 7.22 on section 7.4.

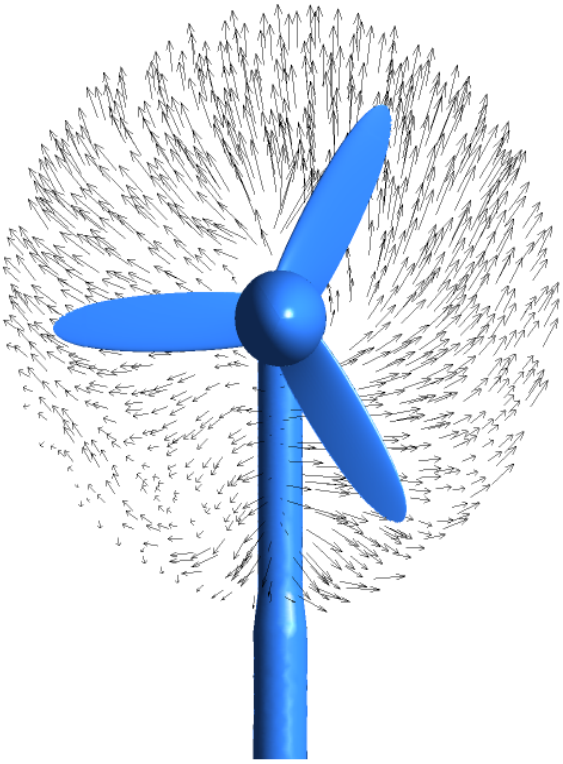

Figure 7.48 Vector plot at 5100 **timestep - Half_spacing_model F3**

The total torque was calculated to be around $420kNm$, the total thrust was calculated to be roughly around $282kN$. The total power produced by the turbine is approximately $409kW$. The total axial thrust and total axial torque curves are plotted on the Figure 7.49. As seen with all Half_spacing_model performance plots, the variations are large in comparison to the datum spacing plots and this plot in Figure 7.49 is no exception.

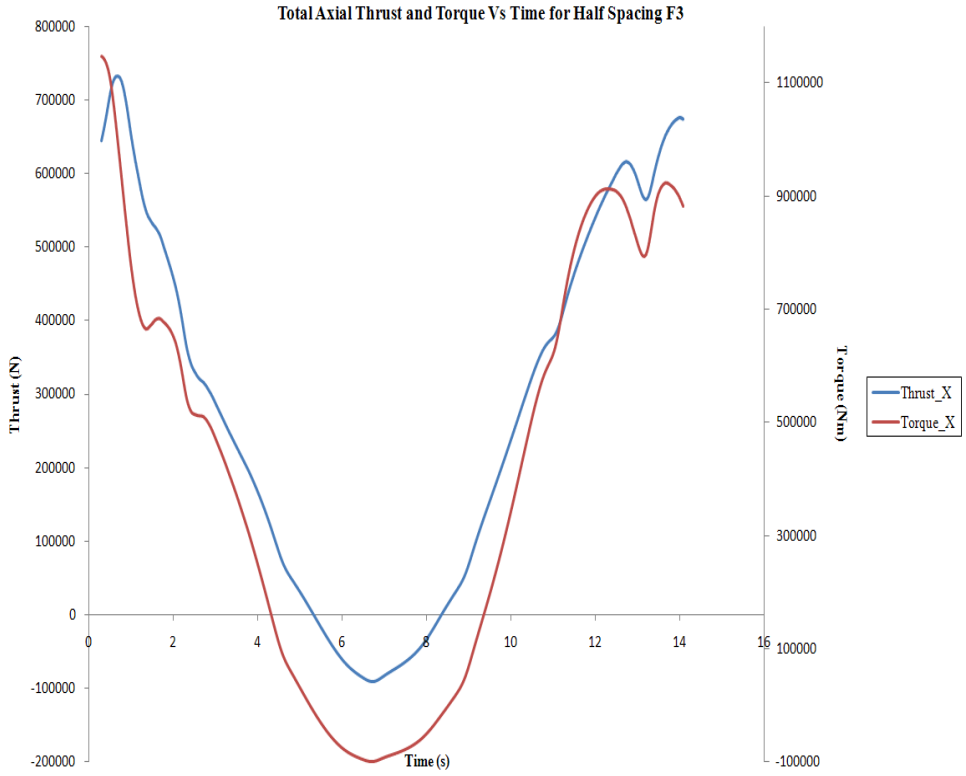

Figure 7.49 Thrust and Torque loads - Half_spacing_model F3

The individual axial thrust and axial torque per blade is presented in Figure 7.50 and Figure 7.51 respectively.

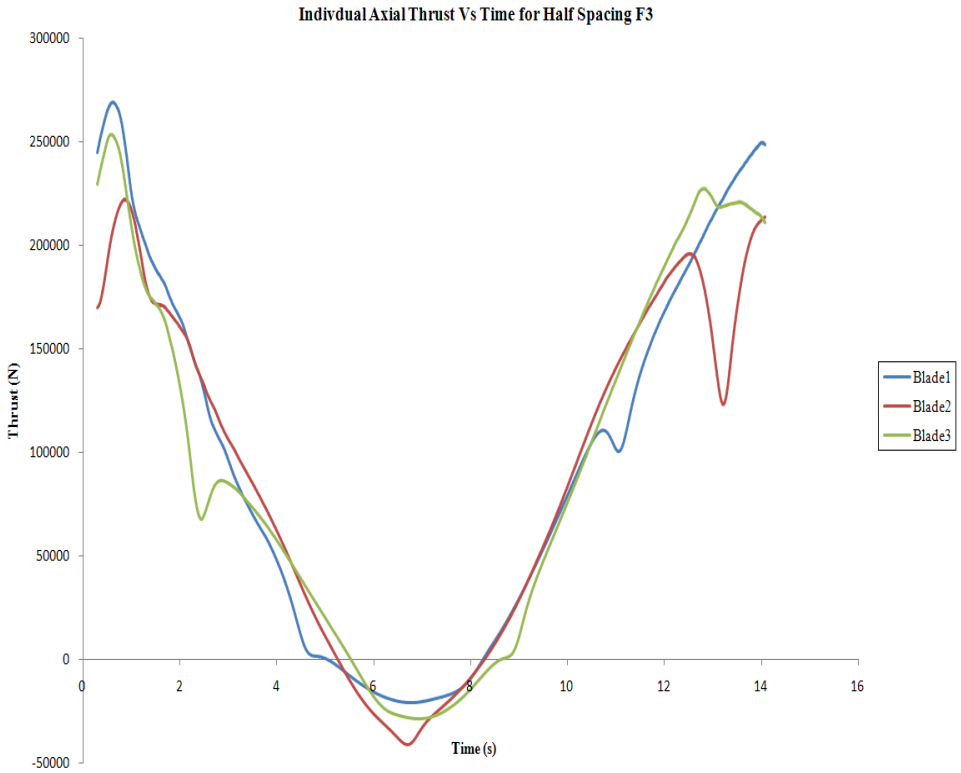

Figure 7.50 Individual Axial Thrust loads - Half_spacing_model F3

As discussed at the start of this chapter the F3 cases were only run for two full revolutions. The half wave period coincides with the one complete revolution of the model as a result the minimum is somewhat masked by this effect.

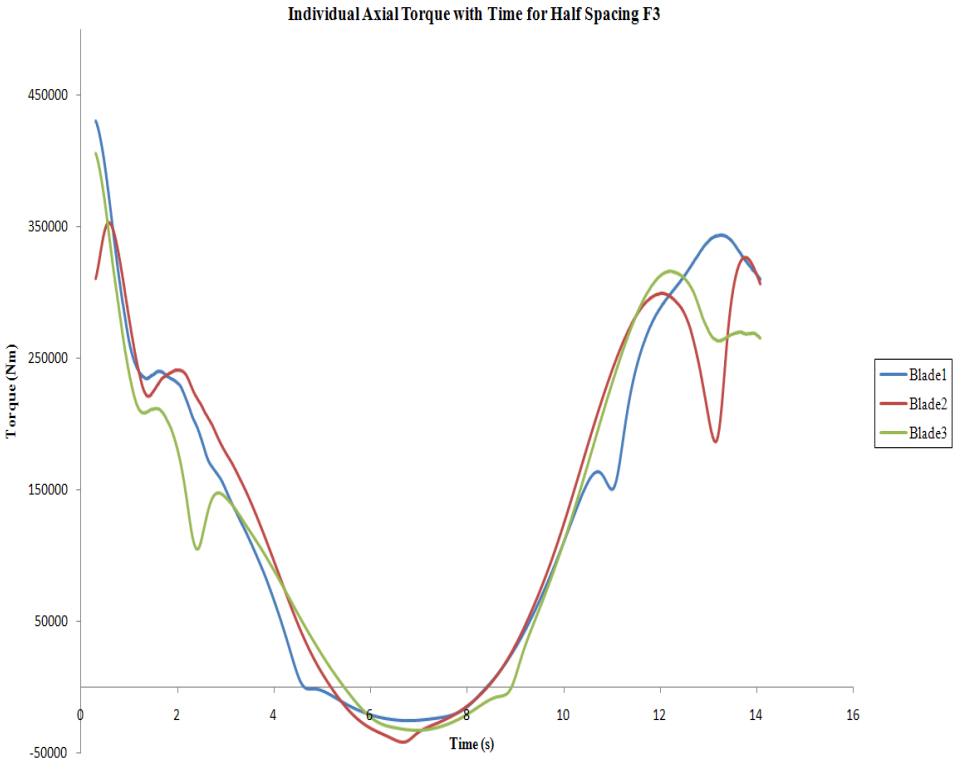

Figure 7.51 Individual Axial Torque loads - Half_spacing_model F3

Figure 7.50 for the individual axial thrust loads for each blade undergoes a higher unsteady cyclic load than when compared to its similar plot for the normal_spacing_model. The Figure 7.51 does not show that it experiences higher torque loads than the datum model. This suggests that the datum model is more efficient, i.e., producing more power at a given time for a specific flow condition.

7.5.2 F4 case (maximum thrust)

The Figure 7.52, Figure 7.53 and Figure 7.54 show the blade loading plots for the F4 Half_spacing_model at 25%, 50% and 90% span locations respectively.

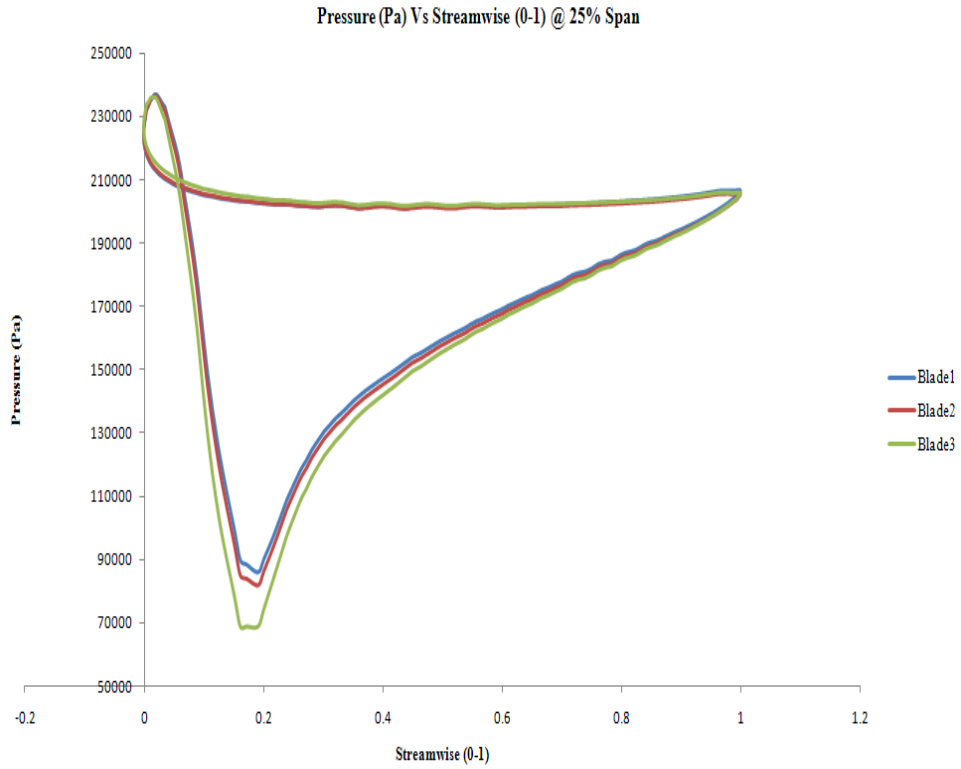

Figure 7.52 Pressure plot at 25% span - Half_spacing_model F4

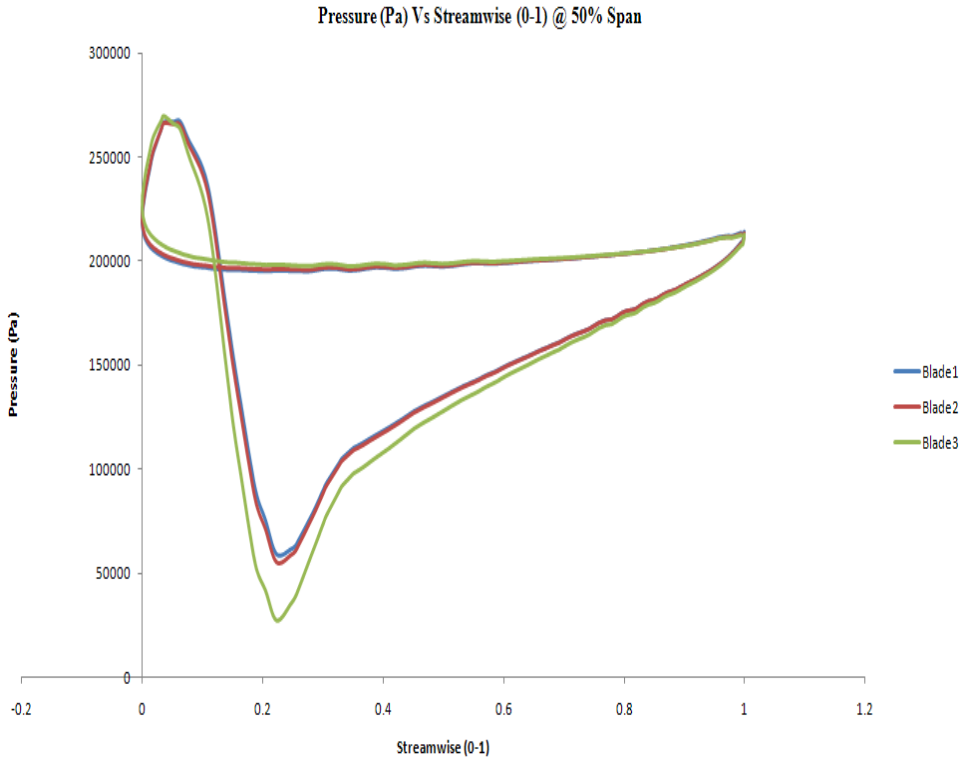

Figure 7.53 Pressure plot at 50% span - Half_spacing_model F4

The layout of the blades are such that the blade three is at the highest point and followed by the blade one and then blade two in clockwise direction. The blade one and blade two are

somewhat in similar vertical position but on either side and hence produces almost similar pressure loading characteristics. The blade three produces the highest force variation as it experiences the largest flow velocities.

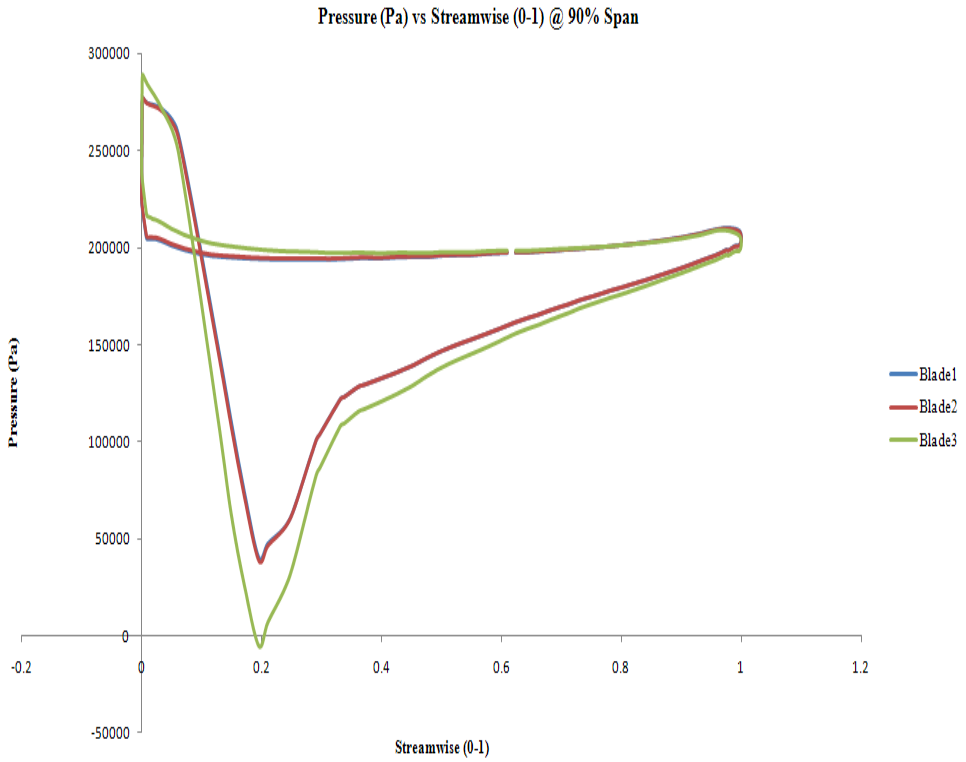

Figure 7.54 Pressure plot at 90% span - Half_spacing_model F4

The Figure 7.55 represents the vorticity plot with blade positioning at 99% span on the rotor plane of rotation. The vorticity plot is colour coded in the same way as the blade loading plots shown above. The blade three denoted with the green plot displays the highest vortices as this blade experiences the highest flow fields. The blade one and blade two denoted with blue and red respectively produce almost similar vortices confirming that they are experiencing identical flow velocities as they are in similar vertical planes. The total vortex generated by all three blades is roughly around $14s^{-1}$.

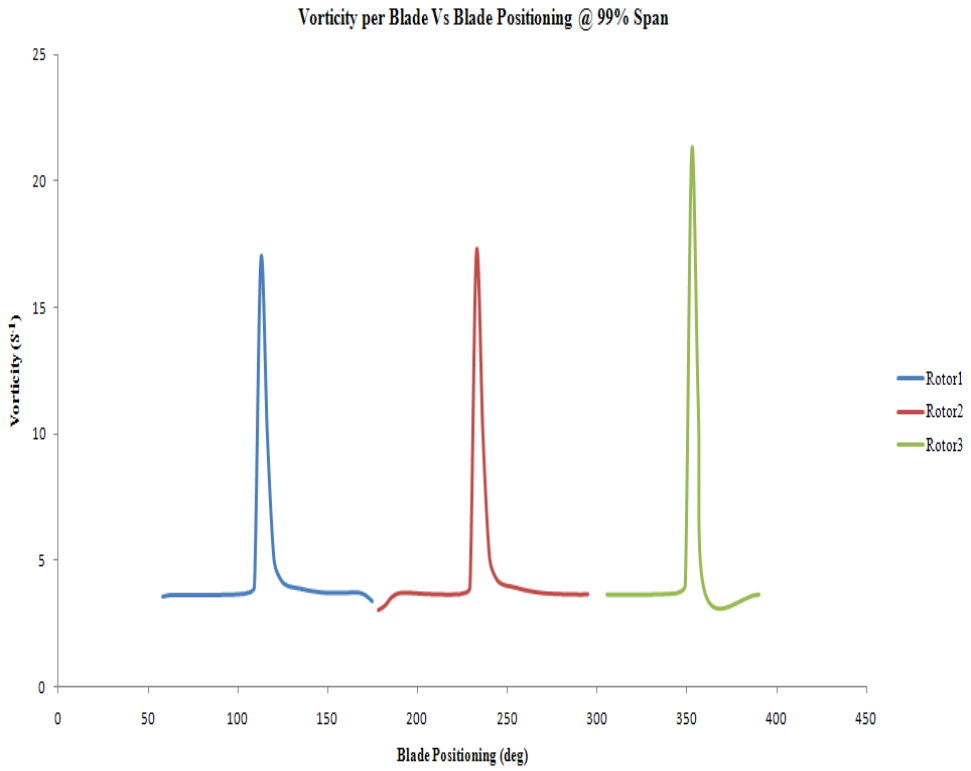

Figure 7.55 Vorticity plot with blade positioning at 99% span - Half_spacing_model F4

The pressure contour plot shown on Figure 7.56 displays the blade-pylon interaction of the Half_spacing_model for the F4 case.

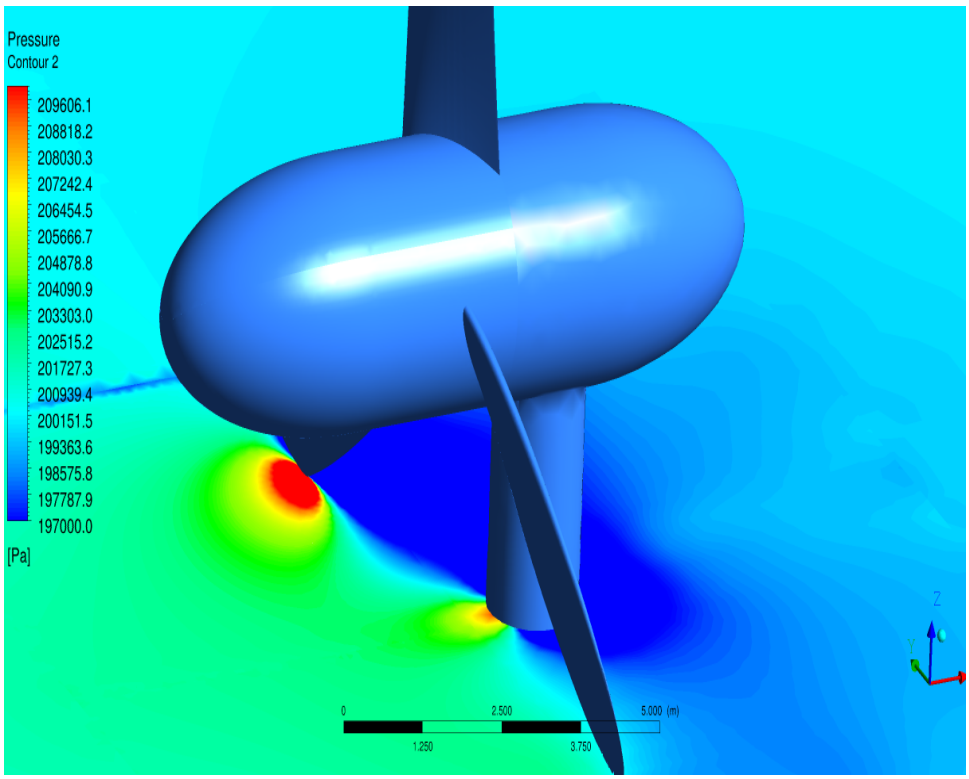

Figure 7.56 Blade-pylon interaction - Half_spacing_model F4

The stagnation points on red, in front of the pylon and on the leading edge of blade 2 is clearly visible. The low pressure area downstream of the rotor is visible as well and the lowest pressure drop is observed to be just behind the pylon and the blades. As seen with the previous plots the pressures involved in Figure 7.56 are higher than that of the corresponding datum model plot, implying that there is a lot more activity around this area for the Half_spacing_model.

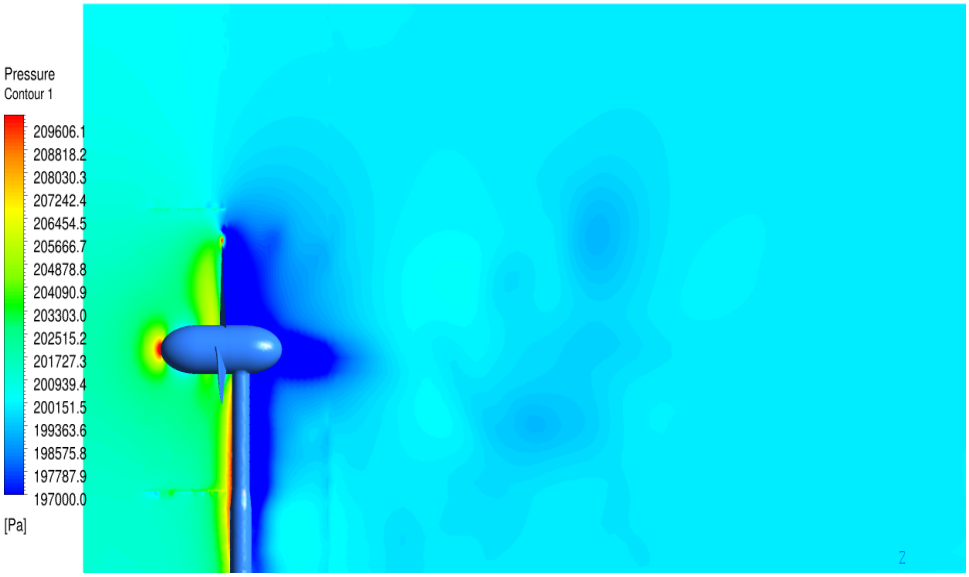

Figure 7.57 Pressure distribution in the meridional plane - Half_spacing_model F4

The Figure 7.57 displays the wake distribution across the model from the inlet through to the outlet. The immediate wake which is between $1 - 2D$ downstream of the rotor is observed to be the most affected area. Further downstream of the rotor between $3 - 4D$ (far wake) the pressure gradually builds up to the free stream pressure values. The pressure range for this plot is the same as above implying that the model has a higher pressure activity when compared to the corresponding datum model plot.

Figures 7.58, 7.59 and 7.60 represent vector plots at a similar location as before for timesteps at 2080, 2090 and 2120. These timesteps correspond to actual simulation times of $8.640s$, $8.728s$ and $8.960s$ respectively.

All these three vector plots suggests that there is a lot more activity and is more disorganised when compared with the vector plots for the F3 Half_spacing_model. This means that the higher flow velocities cause adverse pressure situations in and around the rotor-pylon system.

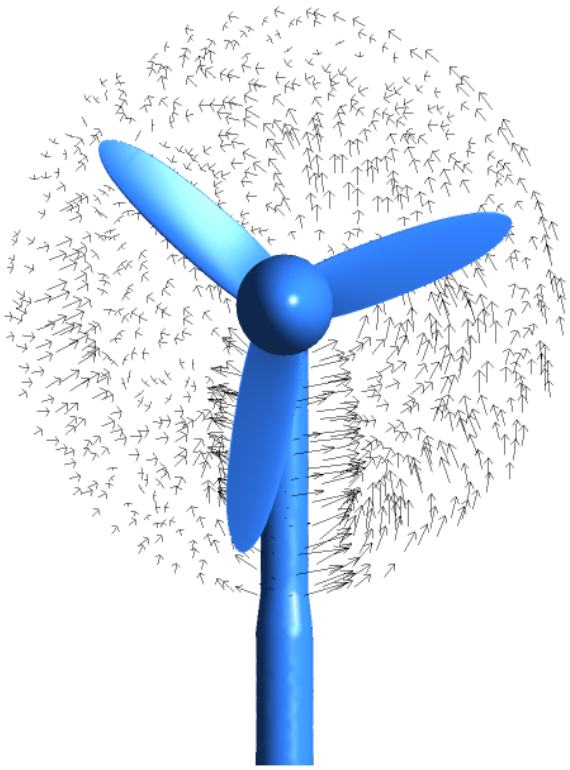

Figure 7.58 Vector plot at 2080 timestep - Half_spacing_model F4

It is evident on all the vector plots that there is a lot of flow recirculation and unsteadiness around because of the higher flow velocities and short hub spacing involved.

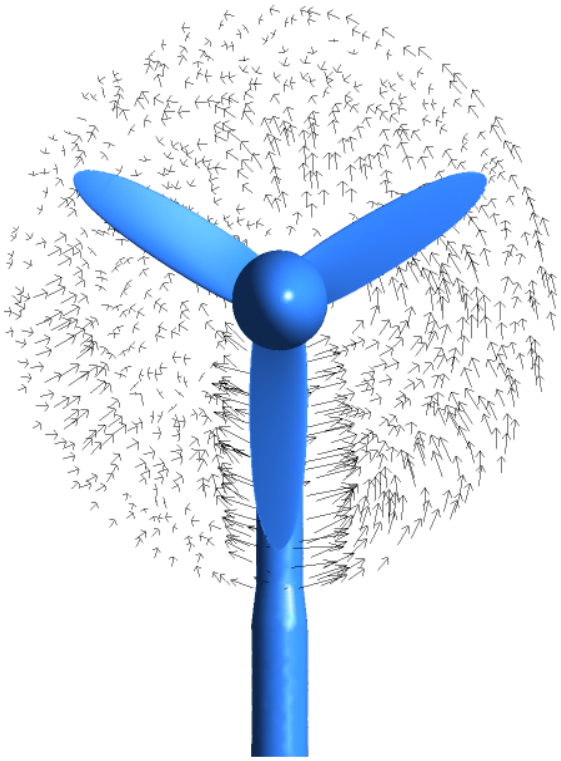

Figure 7.59 Vector plot at 2090 **timestep - Half_spacing_model F4**

The flow field around the blade closest to the pylon is highly charged up which could be interpreted from the size of the vectors.

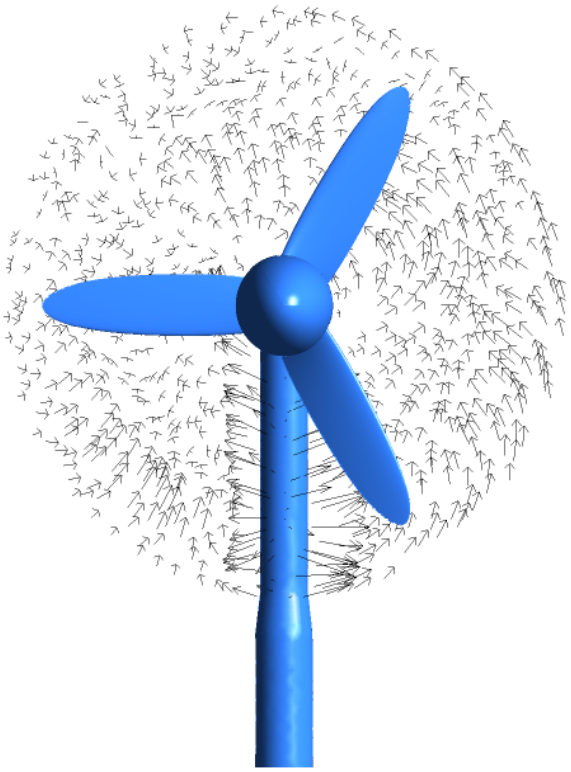

Figure 7.60 Vector plot at 2120 **timestep - Half_spacing_model F4**

The total torque generated by the turbine is approximately calculated to be $423kNm$ and the total thrust produced by the turbine is approximately at $327kN$. The total power generated by the turbine is calculated to be around $930kW$. The Figure 7.61 display the variation of the total axial thrust and torque loads with simulation time for the Half_spacing_model F4 case.

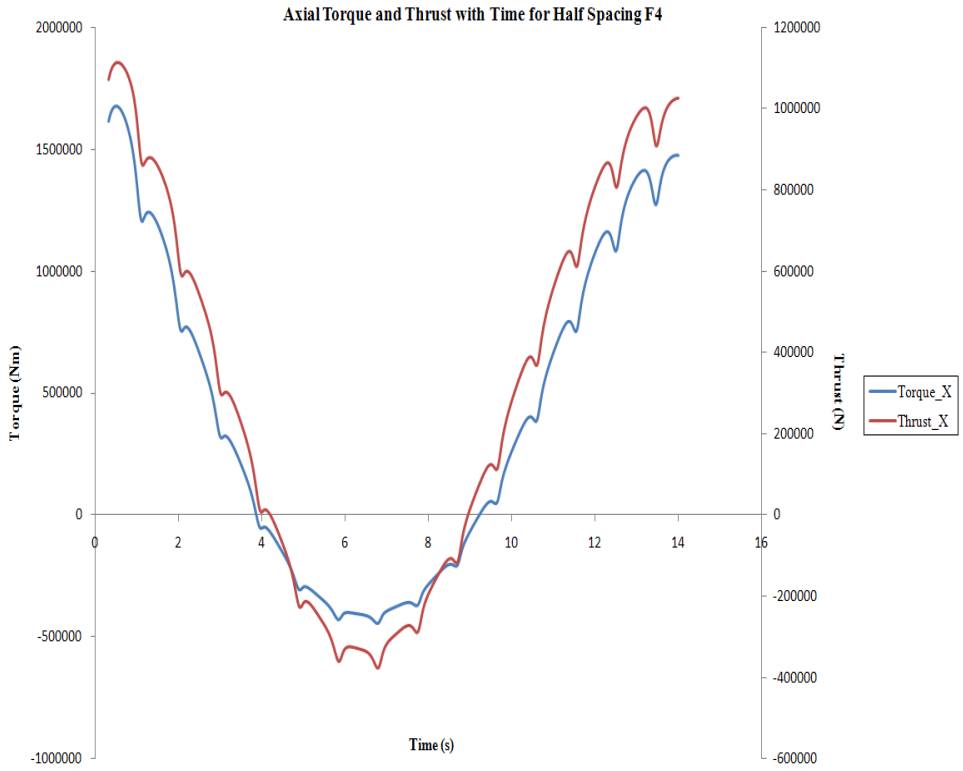

Figure 7.61 Thrust and Torque loads - Half_spacing_model F4

The individual axial thrust and axial torque per blade is presented in Figure 7.62 and Figure 7.63 respectively.

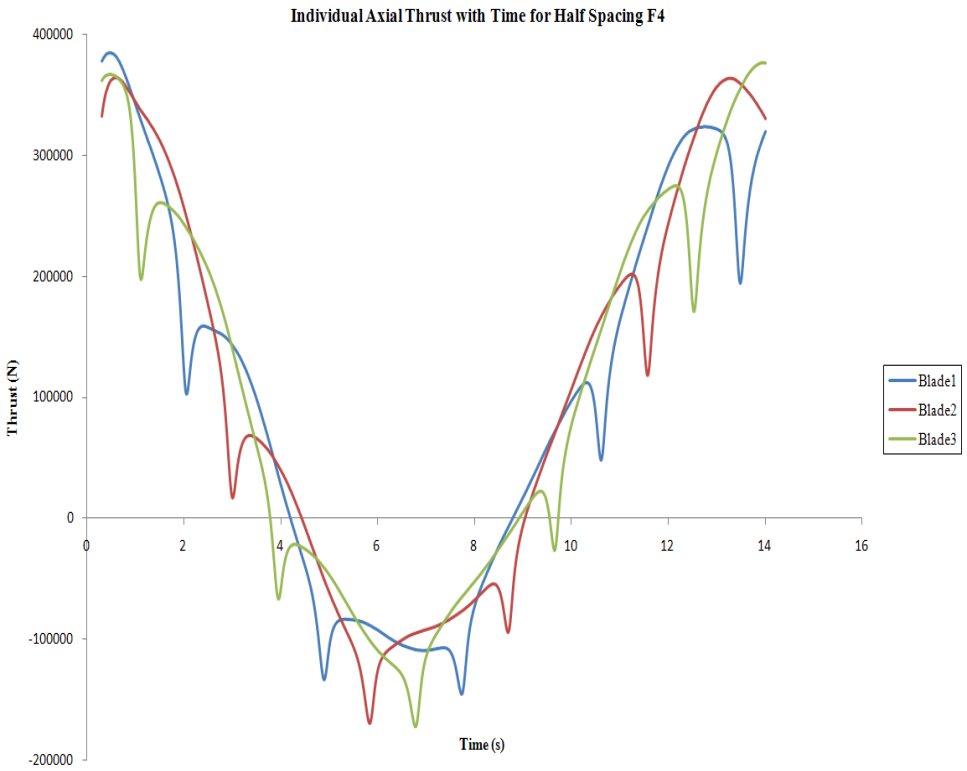

Figure 7.62 Individual Axial Thrust loads - Half_spacing_model F4

The variation of the total loads shown on Figure 7.61 are larger in comparison to the total loads on the F4 datum model. As discussed earlier, this means that the unsteady cyclic loads are much higher for the Half_spacing_model than when compared to the normal_spacing_model on any flow parameter.

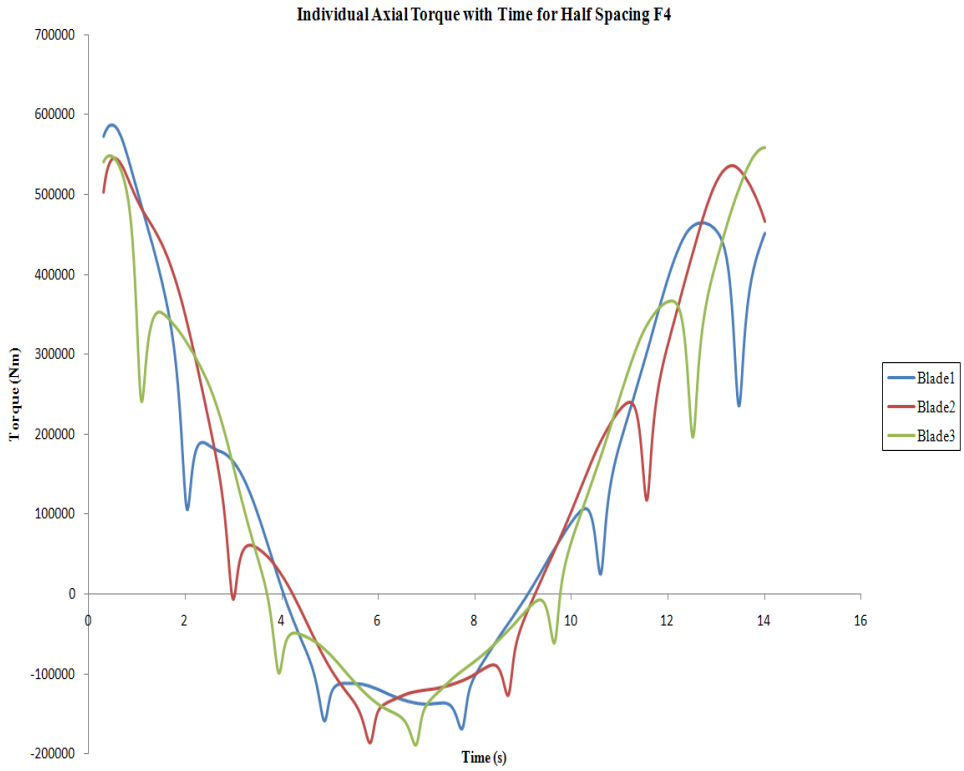

Figure 7.63 Individual Axial Torque loads - Half_spacing_model F4

Individual thrust loads per blade shown on Figure 7.62 also undergoes a large variation when compared to the corresponding plot from the datum model. The variation of the individual torque loads per blade shown on Figure 7.63 are relatively similar, although the torque produced is slightly higher for the datum model.

7.6 Regular Wave for Normal Spacing F3 & F4 Cases

F3 and F4 parameters for the shear profile boundary layer was used in conjunction with the frequent (regular) wave of $1.5m$ in wave height and $10s$ in wave period was analysed for the normal_spacing_model. The pressure loading plots and axial velocity component contour plots are analysed to discuss the wake and blade-pylon characteristics of the models. Analysis of the vortices created by the turbine blades are discussed. Vector plots, circumferential velocity plots are also analysed to help understand the physics. Finally, axial torque and thrust plots are compared and its performance characteristics are compared.

7.6.1 F3 case (maximum torque)

The pressure loading plots displayed on Figure 7.64, Figure 7.65 and Figure 7.66 are for the normal_spacing_model regular waves F3 case. The blade loading plots shown below on Figures 7.64, 7.65 and 7.66 were taken at 25%, 50% and 90% blade span locations

respectively.

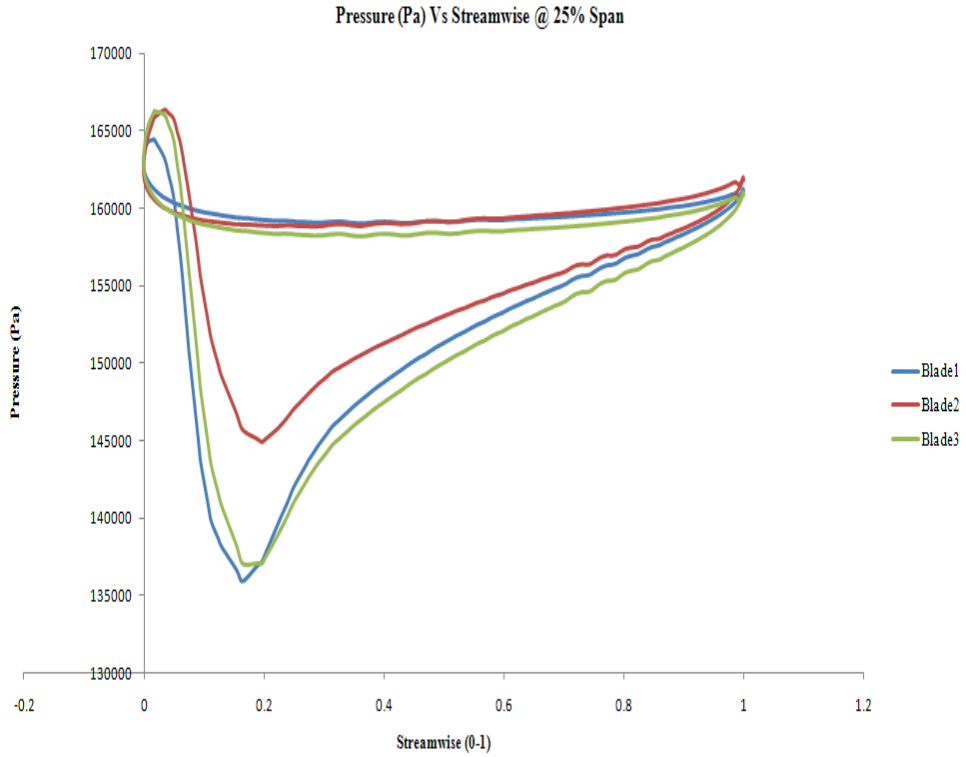

Figure 7.64 Pressure plot at 25% span - normal_spacing_model F3

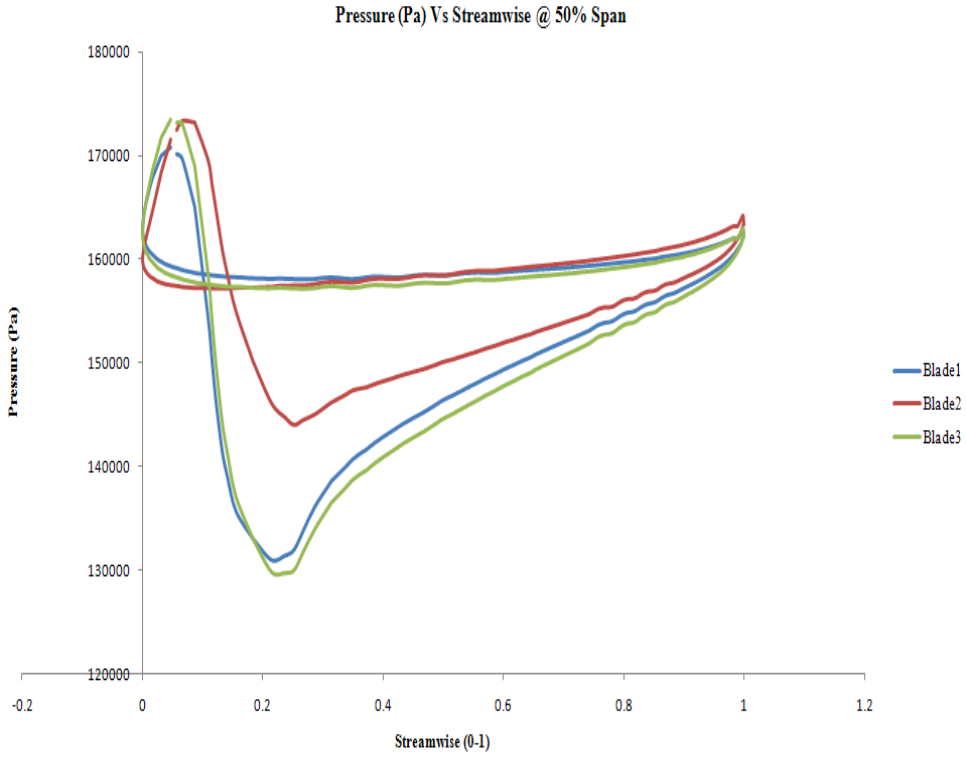

Figure 7.65 Pressure plot at 50% span - normal_spacing_model F3

The blade orientation of the model when the blade loading plots were taken was such that the blade two was almost next to the pylon at the bottom and the blade one and blade three at two o'clock and 11 o'clock positions. As expected the blade two denoted with the red line produces the least pressure distribution. The blade one and blade three colour coded with blue and green lines respectively produce almost similar blade loading distributions as they are in a similar height. The green line produces slightly higher lift characteristics as it is just in a slightly higher plane than the blade one.

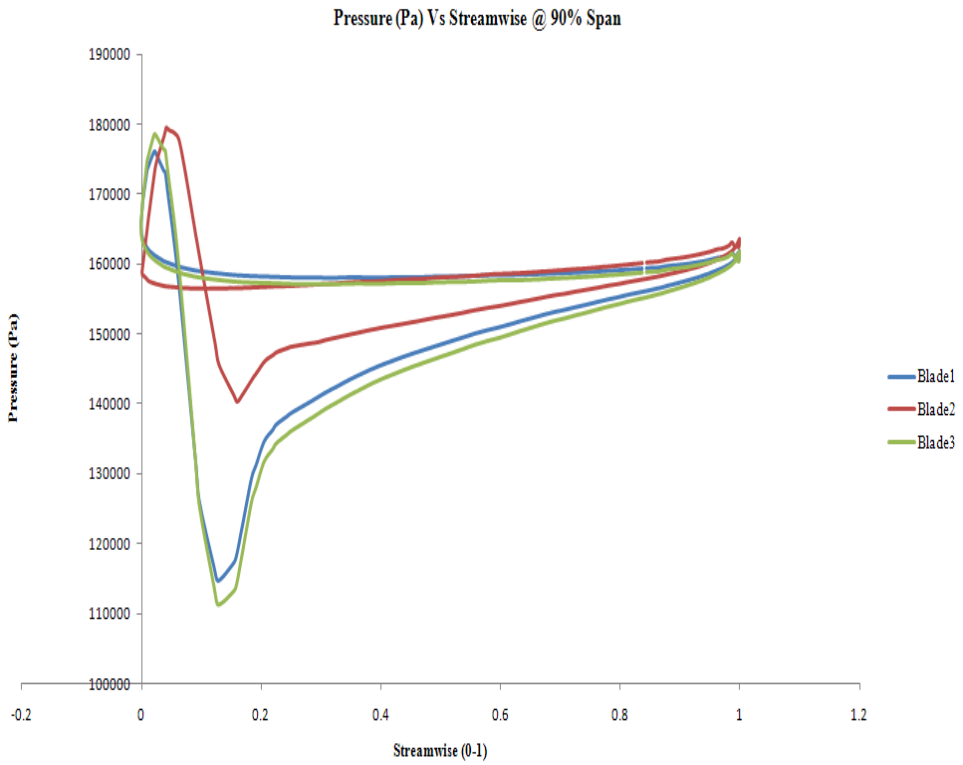

Figure 7.66 Pressure plot at 90% span - normal_spacing_model F3

The Figure 7.67 shows the vorticity plot with blade positioning at 99% span. This plot is colour coded similarly to the blade loading plots shown above. It could be seen from vorticity plot, that the blade two produces the least vortices as compared to the blade one and blade three. The blade three produces the largest vortices and confirms the prediction on the blade loading plots shown above. The total vortices generated from the blade is roughly just over $5.6s^{-1}$.

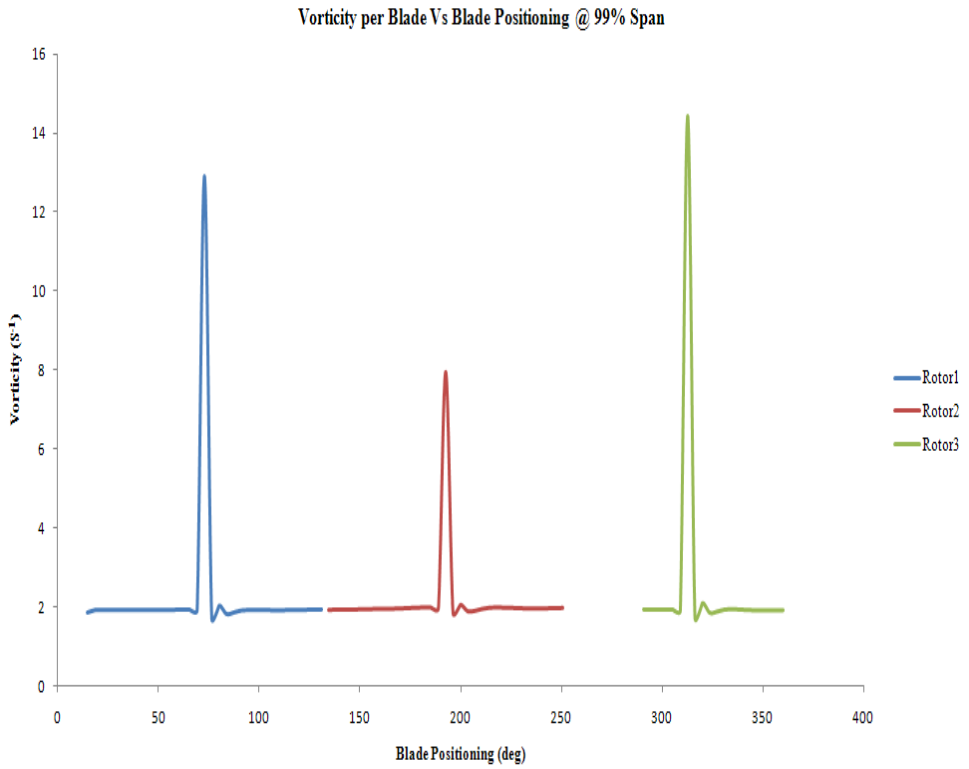

Figure 7.67 Vorticity plot with blade positioning at 99% span - normal_spacing_model F3

The blade-pylon velocity contour plot for the model is shown on Figure 7.68. The axial velocity contour plot is plotted instead of the usual pressure plot because this plot gives a direct information about the actual velocities around the concerned areas, therefore these plots give a different perspective to the simulation results. The stagnant areas in front of the pylon, and just aft of the pylon are shown on dark blue areas of low velocities. Some of these dark blue areas experience flow recirculation as shown on Figure 7.68 by negative velocities. This means that there are turbulent areas just in front and behind the pylon.

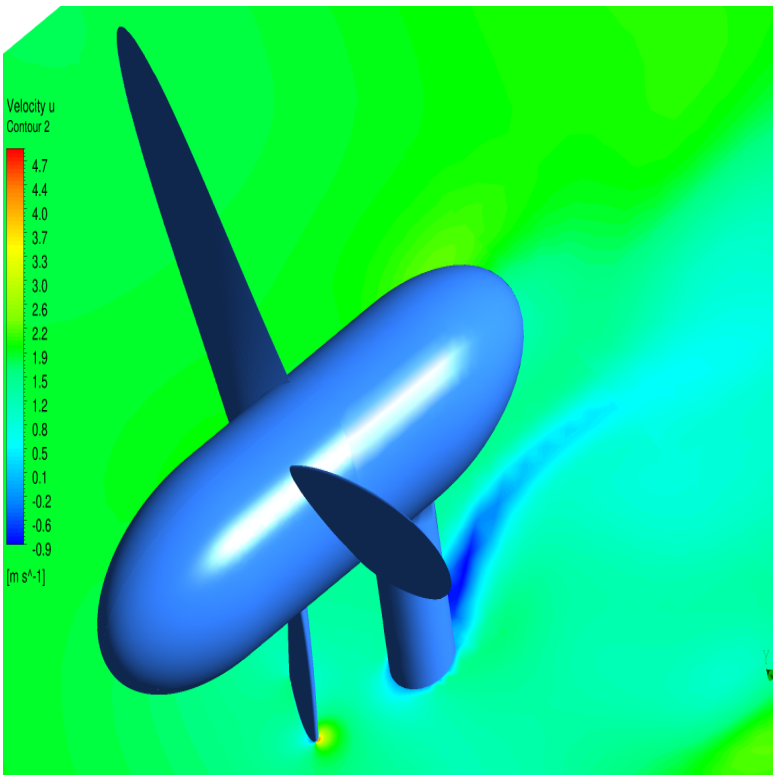

Figure 7.68 Blade-pylon interaction - normal_spacing_model F3

The Figure 7.69 displays the wake distribution plot also using an axial velocity contour plot. The flow recirculation with negative flows is shown clearly in this plot. A strong wake is shown to be extending to at least 3D downstream of the rotor. The wake begins to improve at roughly after 3D downstream of the rotor. Even at the model outlet, which is roughly around 4D downstream of the rotor, the flow has not fully recovered.

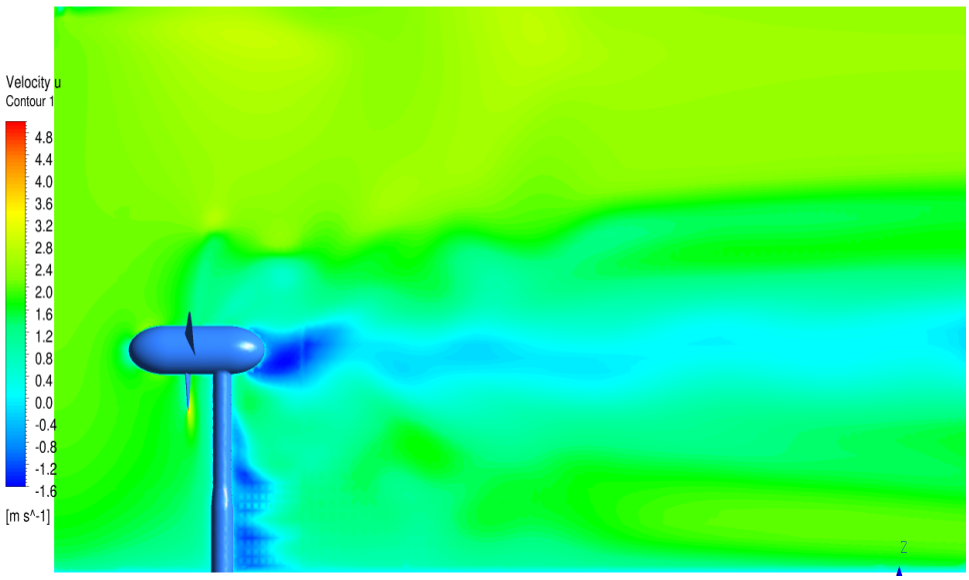

Figure 7.69 Velocity distribution in the meridional plane - normal_spacing_model F3

As with the sub section 7.4.1, three transient results at 4600, 4800 and 5100 corresponding to a simulation time of $6.4801s$, $6.8401s$ and $7.3801s$ were analysed using vector plots, vorticity plots, pressure plots and velocity plots. The plots were taken at exactly the same positions as the previous corresponding plots.

The vector plot on Figure 7.70 displays the flow field a metre or so downstream of the rotor plane of rotation at the timestep corresponding to 4600. This plot is similar to its corresponding plot in sub section 7.4.1 except that this plot is low in intensity. This could be due to the low intensity regular wave as opposed to the extreme wave in the previous sub section.

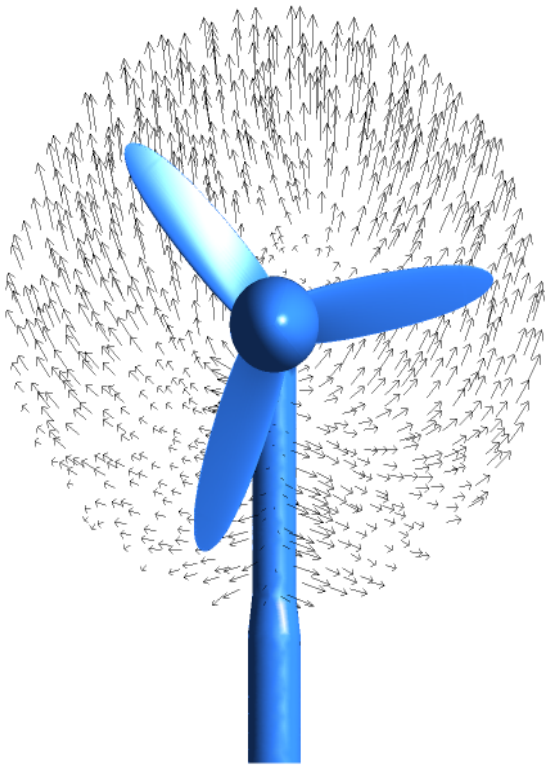

Figure 7.70 Vector plot at 4600 timestep - normal_spacing_model F3

The vorticity plot on Figure 7.71 show the vortices created by the blades for the same location. Again the previous corresponding plot has a slightly higher intensity in the vortices.

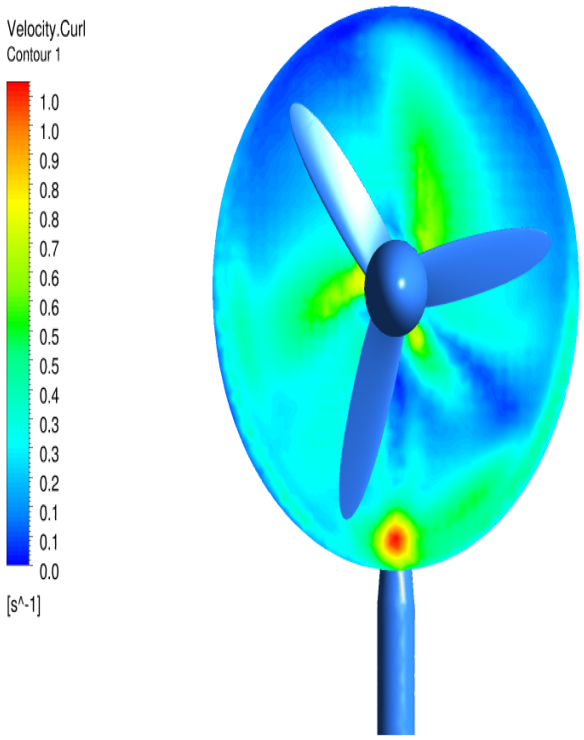

Figure 7.71 Vorticity plot at 4600 **timestep - normal_spacing_model F3**

Figure 7.72 displays a pressure plot at the same location. As seen with the corresponding plot on sub section 7.4.1, the area in front of the pylon experiences a higher pressure.

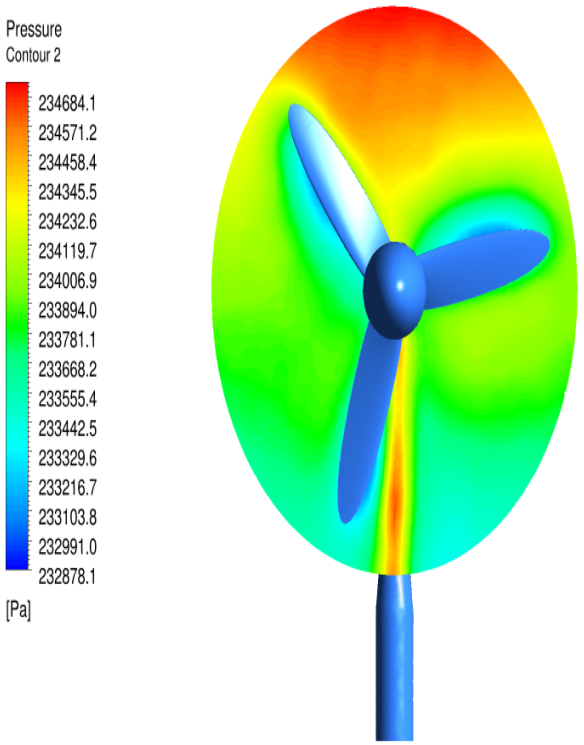

Figure 7.72 Pressure plot at 4600 **timestep - normal_spacing_model F3**

The circumferential velocity is plotted on Figure 7.73. The circumferential velocity plot is also very similar except that the intensity on the plot 7.73 is slightly lower than the corresponding previous plot on sub section 7.4.1.

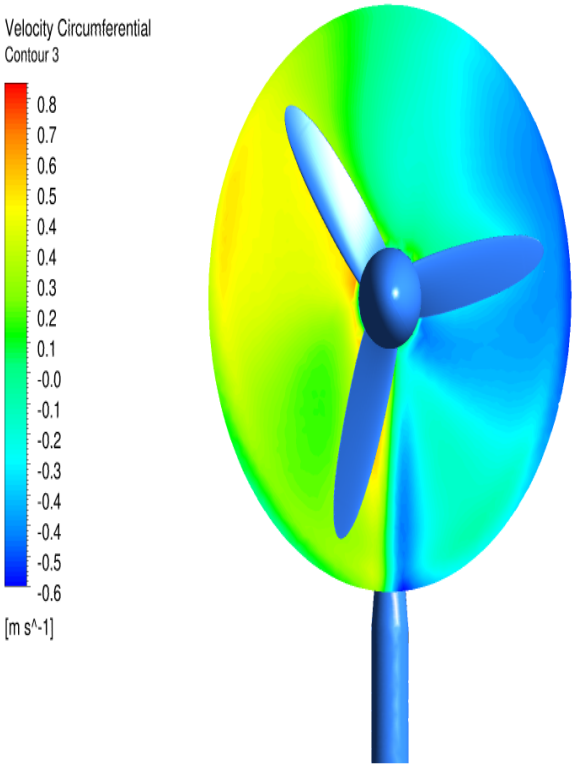

Figure 7.73 Circumferential velocity plot at 4600 **timestep - normal_spacing_model F3**

Axial velocity is plotted on Figure 7.74 at a similar location in the previous corresponding plot. The range displayed in Figure 7.74 is slightly higher than that of the corresponding plot in sub section 7.4.1 suggesting that velocities have slightly recovered than the extreme wave case.

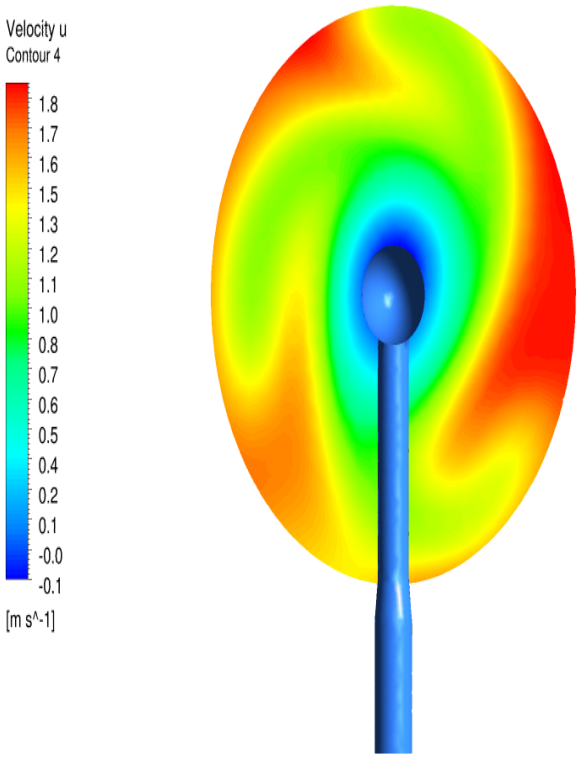

Figure 7.74 Axial velocity plot at 4600 **timestep - normal_spacing_model F3**

The vector plot on Figure 7.75 displays the flow field at exactly the same location as previously although now corresponding to a timestep of 4800. The plot is similar to the previous plot at the timestep corresponding to 4600 but there is a disturbance at the blade 2 (blade in front of the pylon) also the flow intensities are higher around the blade 2.

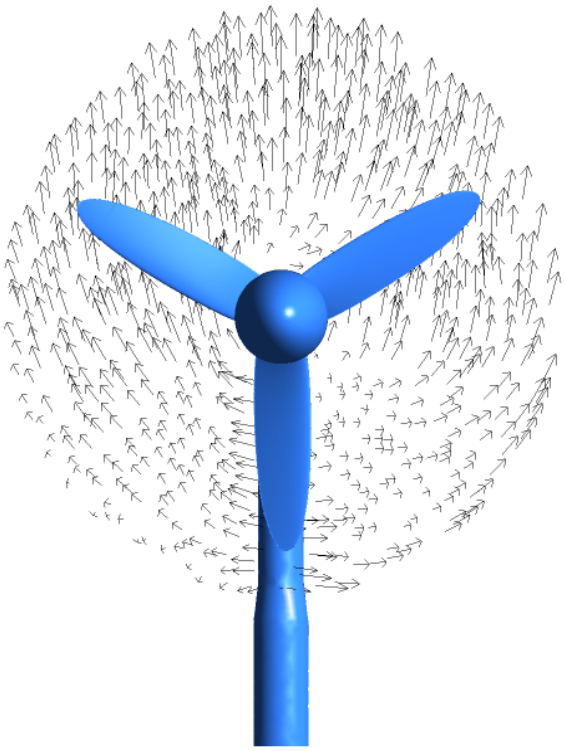

Figure 7.75 Vector plot at 4800 **timestep - normal_spacing_model F3**

The vorticity plot on Figure 7.76 show the vortices created by the blades. The range of the vorticity plot is similar to the previous timestep of 4600. The vortices seem to have developed from the previous plot.

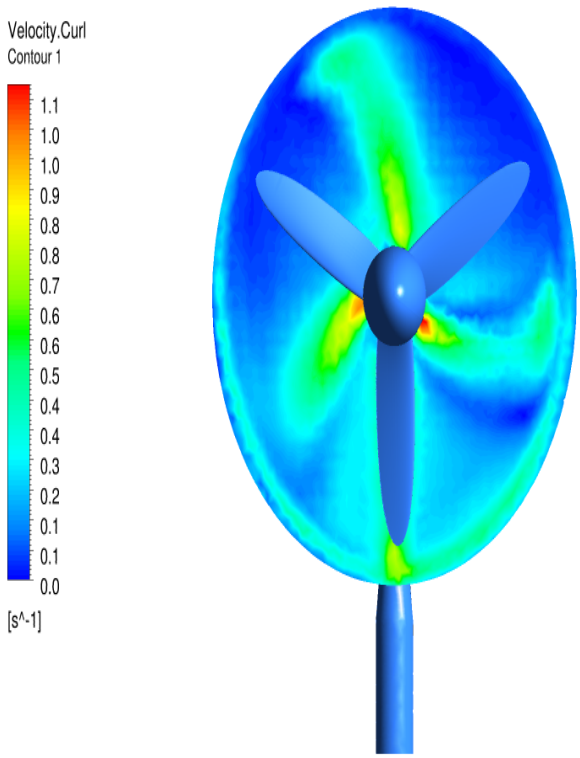

Figure 7.76 Vorticity plot at 4800 **timestep - normal_spacing_model F3**

Figure 7.77 displays a pressure plot. The blade 2 is now in front of the high pressure area in front of the pylon. The intensity seems to have increased from the previous timestep.

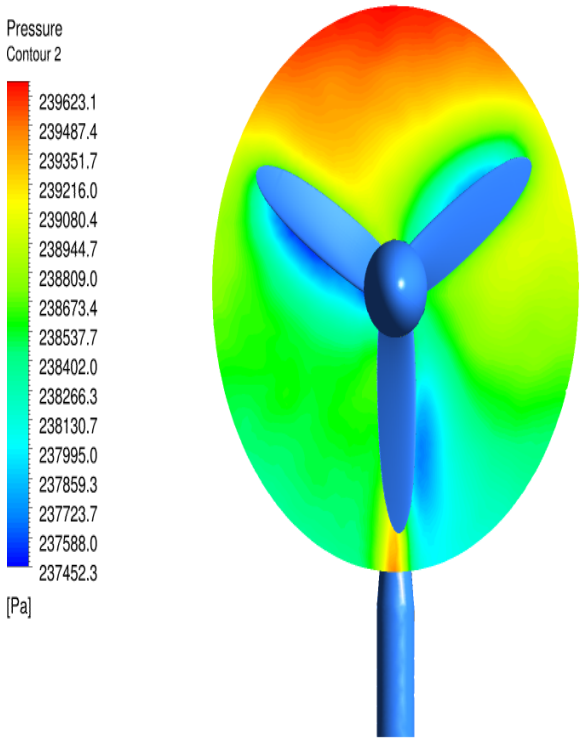

Figure 7.77 Pressure plot at 4800 **timestep - normal_spacing_model F3**

The circumferential velocity is plot on Figure 7.78. Again, the plot is similar to the previous plot at timestep 4600. The range of the circumferential velocity plot seems to have increased slightly.

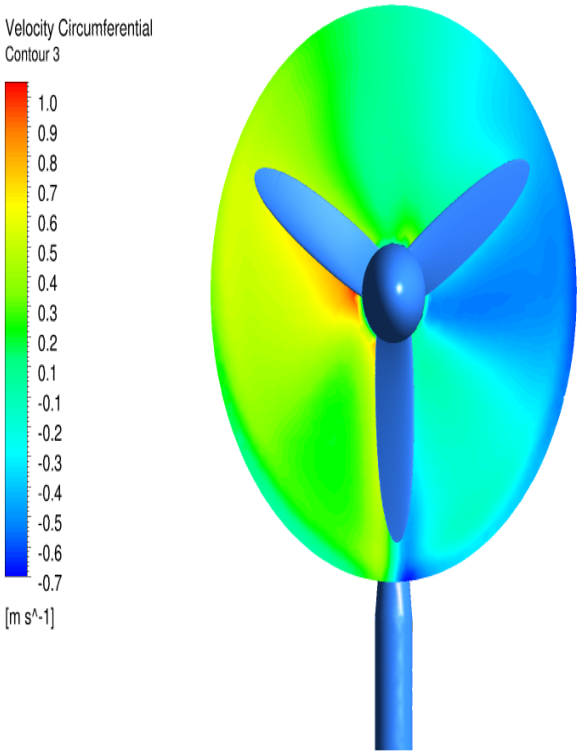

Figure 7.78 Circumferential velocity plot at 4800 timestep - normal_spacing_model F3

Axial velocity is plotted on Figure 7.79. This is also similar to the previous plot at 4600 timestep and the velocities also seem to have recovered slightly.

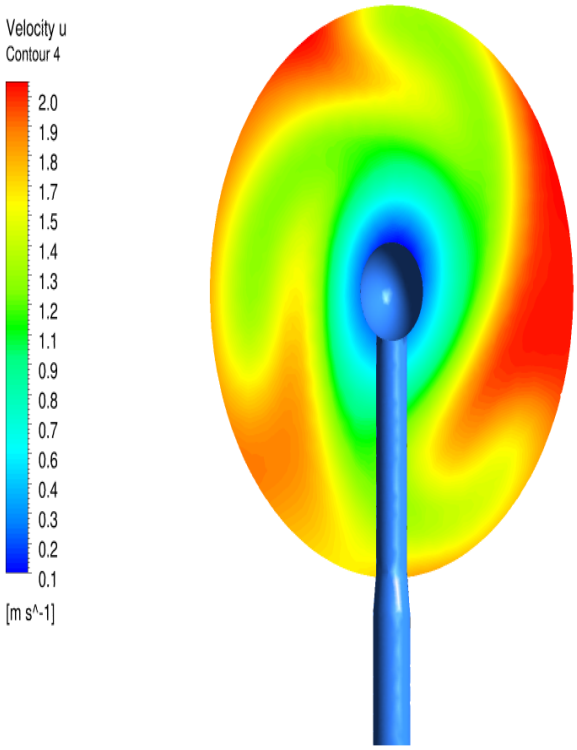

Figure 7.79 Axial velocity plot at 4800 **timestep - normal_spacing_model F3**

The vector plot on Figure 7.80 displays the flow field at the same location as above for the timestep corresponding to 5100. The intensity around the blade 2 is more or less the same but the flow field just before the blade 2 and blade 3 is highly turbulent and has swirling properties.

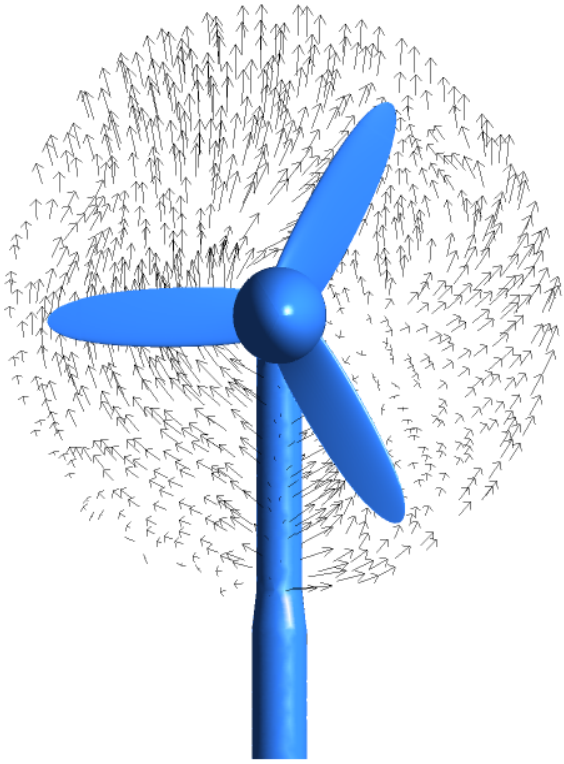

Figure 7.80 Vector plot at 5100 **timestep - normal_spacing_model F3**

The vorticity plot on Figure 7.81 show the vortices created by the blades. The range and the intensity seems to have increased slightly when compared to the corresponding plot for the timestep at 4800. Also, the vortex created by the blade 2 seems to be distorted by the fact that the pylon is present as the other vortices have been illustrated without any issue.

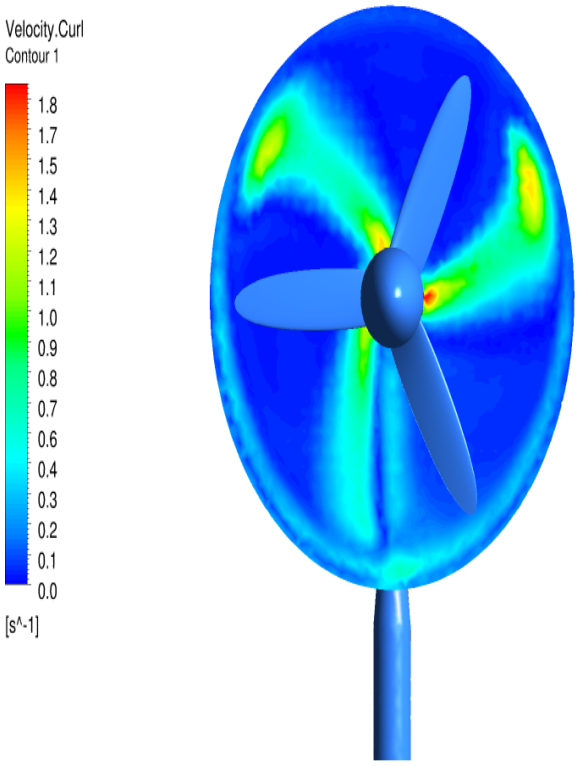

Figure 7.81 Vorticity plot at 5100 **timestep - normal_spacing_model F3**

Figure 7.82 displays a pressure plot, the range in this plot has increased compared to the previous plot.

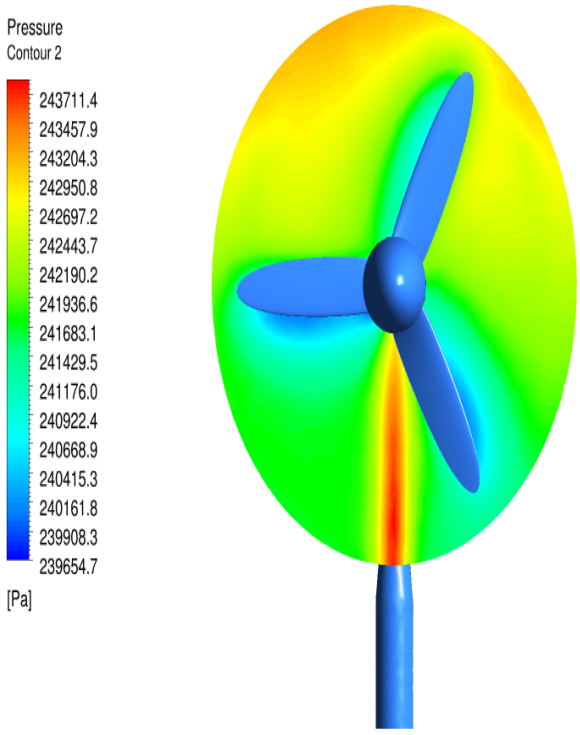

Figure 7.82 Pressure plot at 5100 **timestep - normal_spacing_model F3**

The circumferential velocity is plot on Figure 7.83. The range of the circumferential velocity plot seems to have increased from the previous corresponding plot.

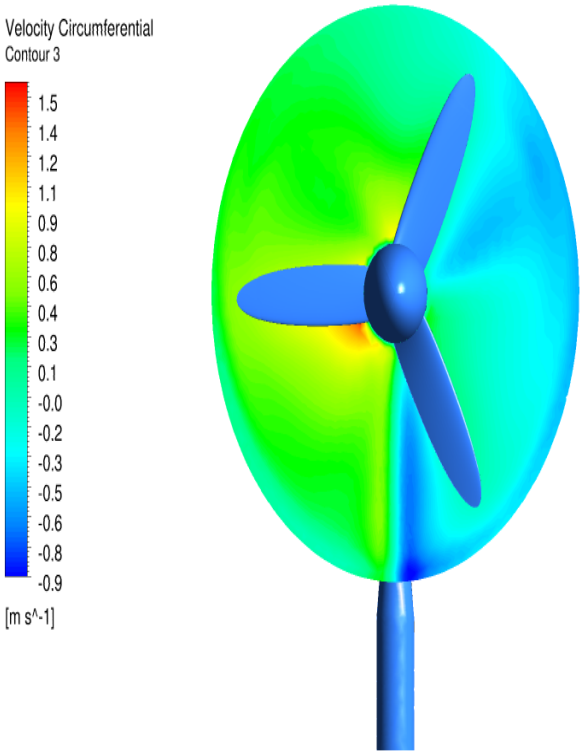

Figure 7.83 Circumferential velocity plot at 5100 **timestep - normal_spacing_model F3**

Axial velocity is plotted on Figure 7.84. The velocity has recovered when compared to the previous corresponding plot.

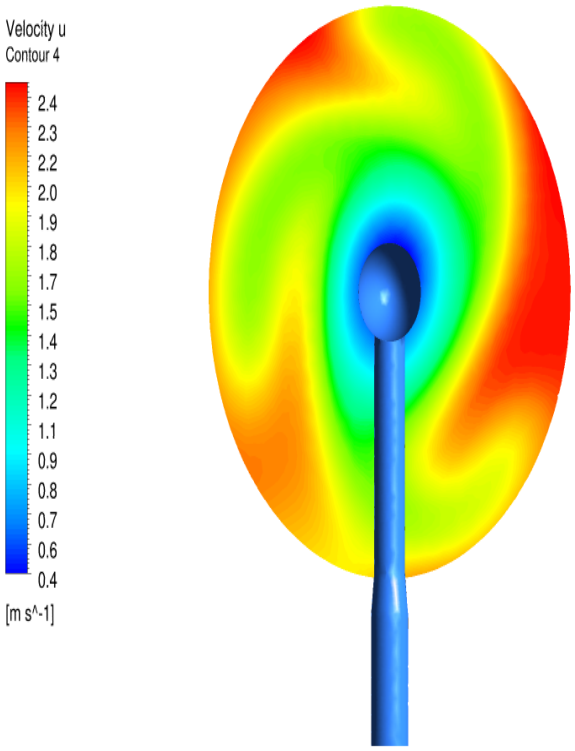

Figure 7.84 Axial velocity plot at 5100 timestep - normal_spacing_model F3

The total torque generated by the turbine is approximately calculated to be $617kNm$ and the total thrust produced by the turbine is approximately at $308kN$. The total power generated by the turbine is calculated to be around $600kW$. The total axial thrust and total axial torque curves are plotted on the Figure 7.85. Again, like the previous corresponding plot on sub section 7.4.1, the negative loads are due to the flow increasing and decreasing between the time spectrum. Only this time the effect is smaller. The lowest point in the plot signifies that it's half the wave time period at $5.0s$.

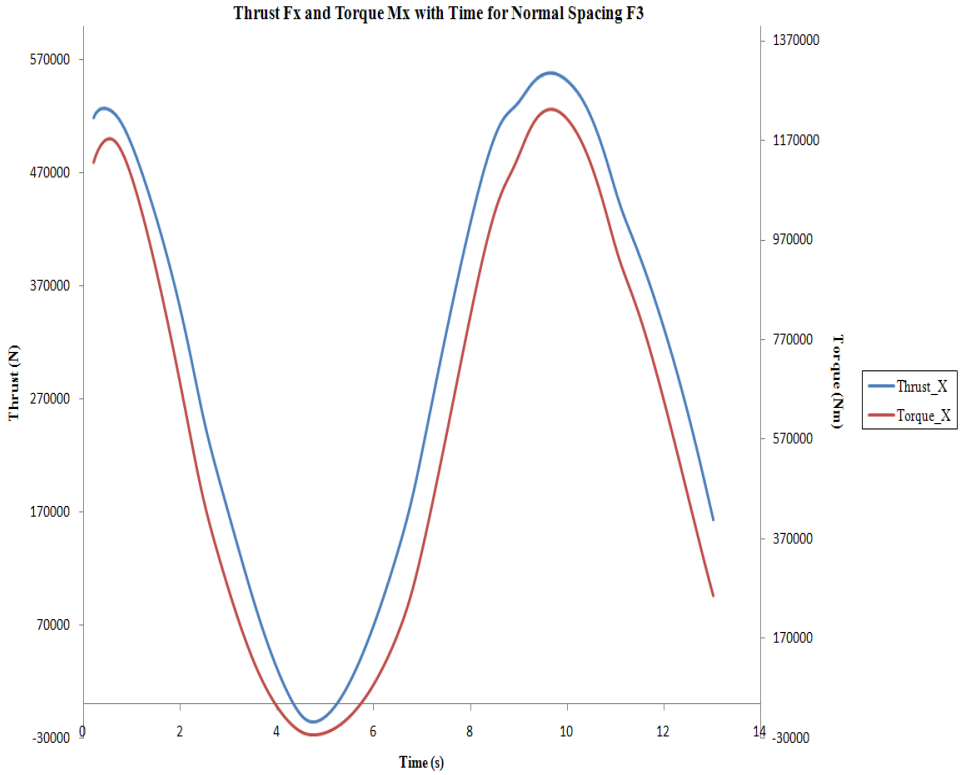

Figure 7.85 Thrust and Torque loads for normal_spacing_model F3

The axial thrust and axial torque variation per blade are shown on Figure 7.86 and Figure 7.87 respectively. Again, the plots behave exactly as the corresponding previous plots. This is because the one full rotation is approximately about $6.5s$ and the half wave period is roughly close to this value at $5.0s$. Therefore, the point at which the lowest loads are generated (half wave period) is superimposed to the one full revolution.

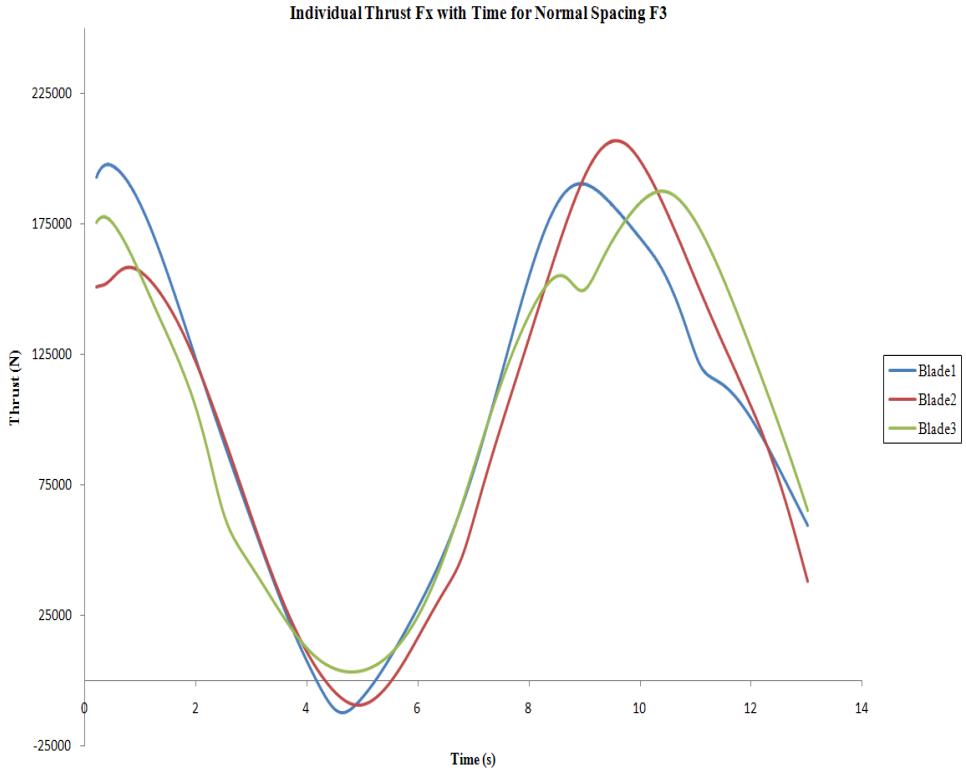

Figure 7.86 Individual Axial Thrust loads for normal_spacing_model F3

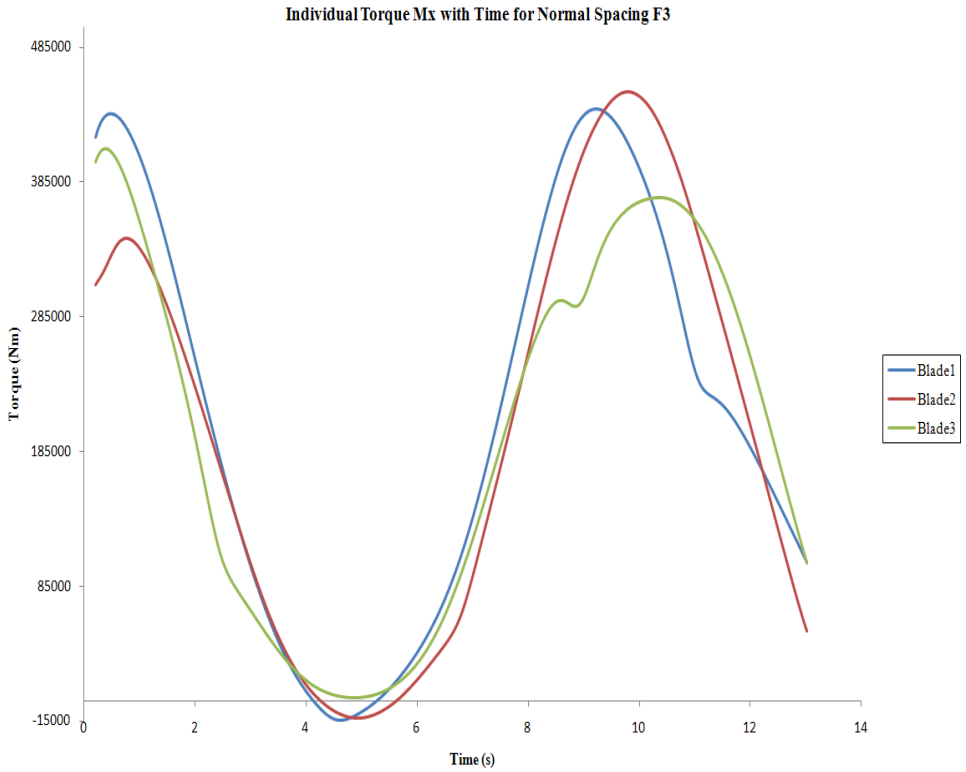

Figure 7.87 Individual Axial Torque loads for normal_spacing_model F3

The severity in terms of the unsteady cyclic loads as seen in the extreme wave normal_spacing_model F3 case is not visible on these three performance plots. Nevertheless,

the cyclic loads presented on the regular are still demanding and needs careful design to address these unsteady loads.

7.6.2 F4 case (maximum thrust)

The Figure 7.88, Figure 7.89 and Figure 7.90 represent the blade loading plots for the regular waves F4 case at 25%, 50% and 90% span locations respectively.

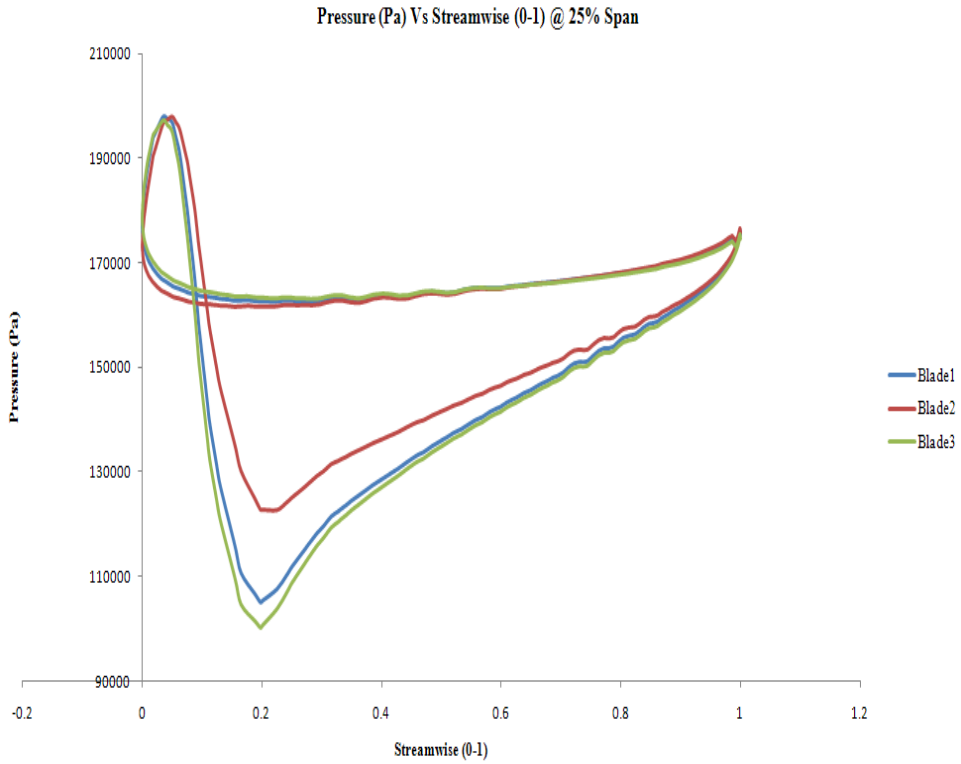

Figure 7.88 Pressure plot at 25% span - normal_spacing_model F4

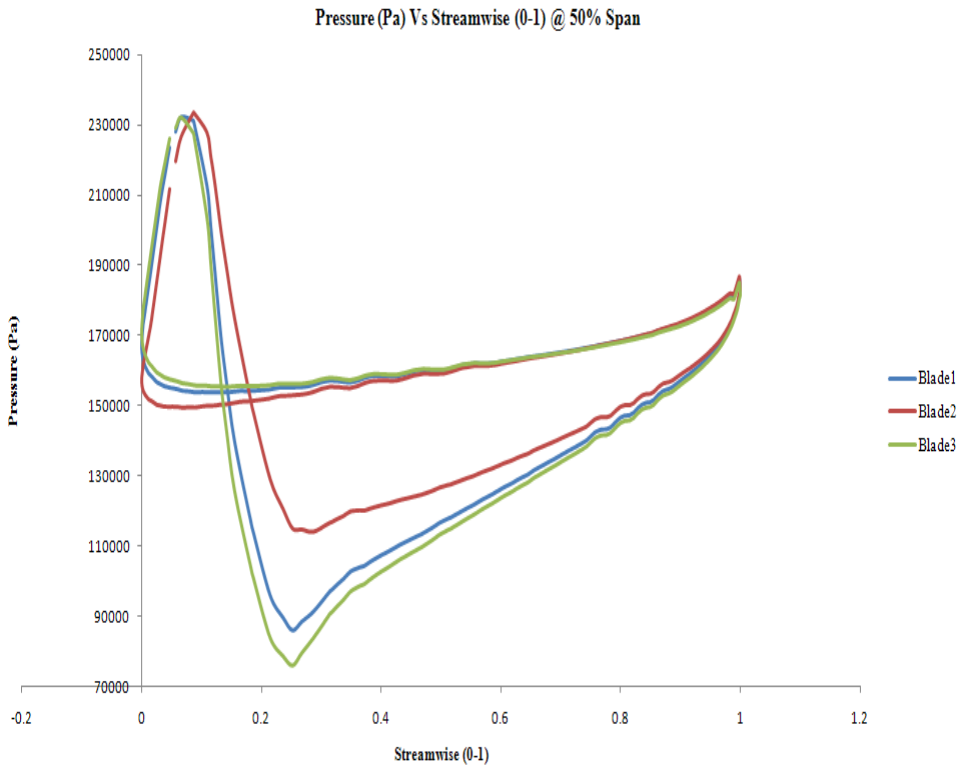

Figure 7.89 Pressure plot at 50% span - normal_spacing_model F4

The layout of the blades on the model when the blade loading plots were taken was in a such a way that the blade two was at the lowest location and blade three at 11 o'clock position and the blade one at about the two o'clock position. From the layout, it is evident that the blade two should produce the least pressure loading plot as is confirmed by these blade loading plots. The highest produced pressure loading plot is denoted in green and is for the blade three. And the blade one follows closely behind denoted on the blue line.

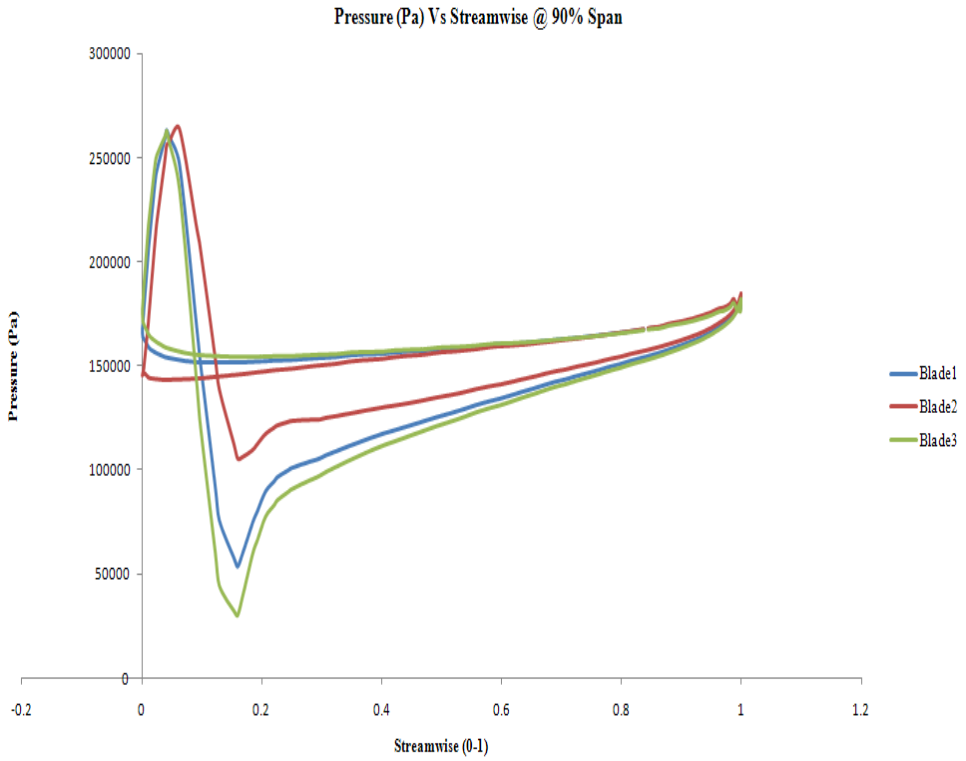

Figure 7.90 Pressure plot at 90% span - normal_spacing_model F4

As expected the F4 case produces the larger blade loading plots compared to the F3 cases for the same wave parameters,

The Figure 7.91 shows the vorticity plot with blade positioning at 99% span. This plot is colour coded in the same manner as the blade loading plots shown above. It could be seen from Figure 7.91, that the blade two produces the least vortices as compared to the blade one and blade three. The blade three produces the largest vortices and confirms the prediction on the blade loading plots shown above. The total average vortices generated from the blade is roughly just over $13s^{-1}$.

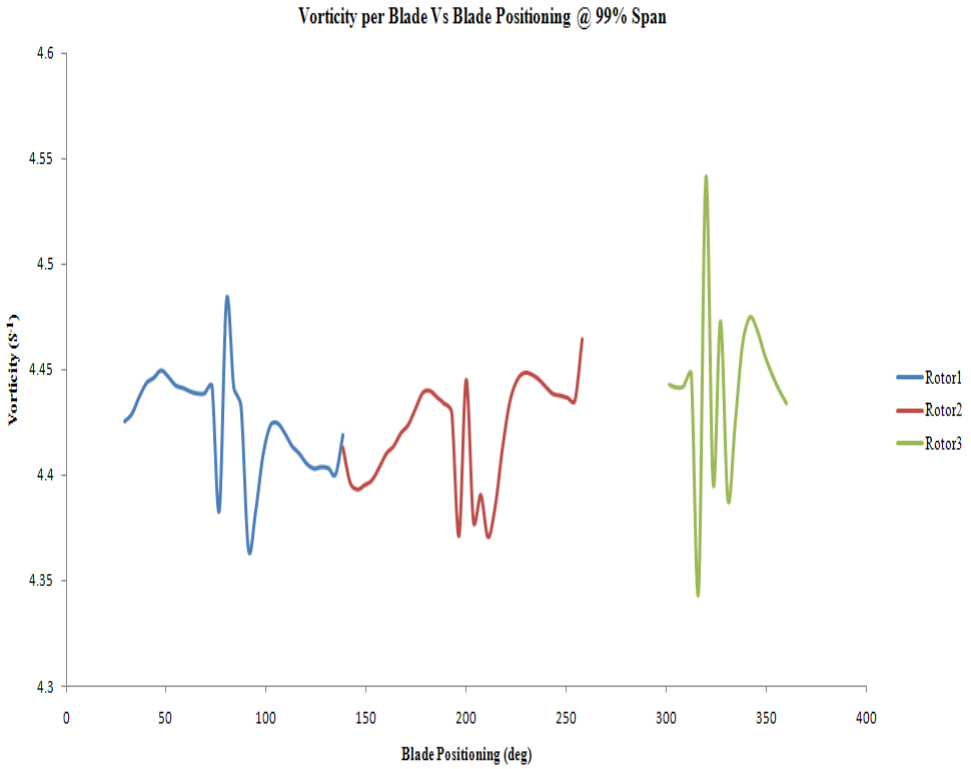

Figure 7.91 Vorticity plot with blade positioning at 99% span - Half_spacing_model F4

The Figure 7.92 displays an axial velocity contour plot for the interaction of the blade-pylon spacing. The low pressure areas aft of the pylon are shown through the blue areas denoting the low velocity areas. The low pressure areas are shown immediately in front and immediately behind the pylon.

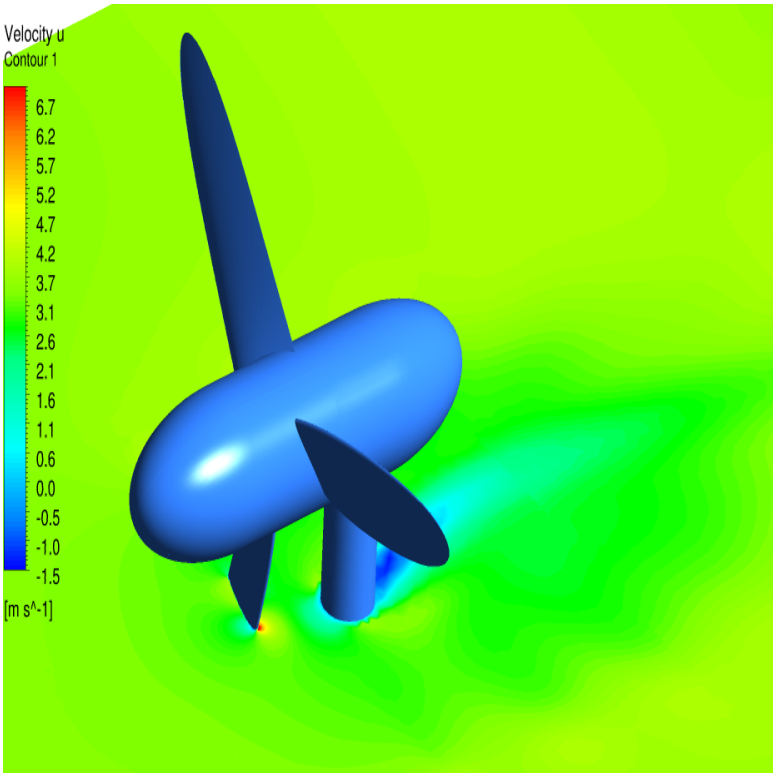

Figure 7.92 Blade-pylon interaction - normal_spacing_model F4

The Figure 7.93 displays an axial velocity contour plot to discuss the features of the wake distribution of the model. The low velocity areas caused by the turbine-pylon wake are clearly visible in the green, light blue and dark blue areas. The area close to the top water surface undergoes the highest velocity because of the combination of the waves and the shear flow being the highest at this level. The F4 cases exhibits this clearly than that of the F3 case. As seen from the previous wake distribution plots the wake is extreme in the so called near wake regions i.e. typically between $1 - 2D$ downstream of the rotor.

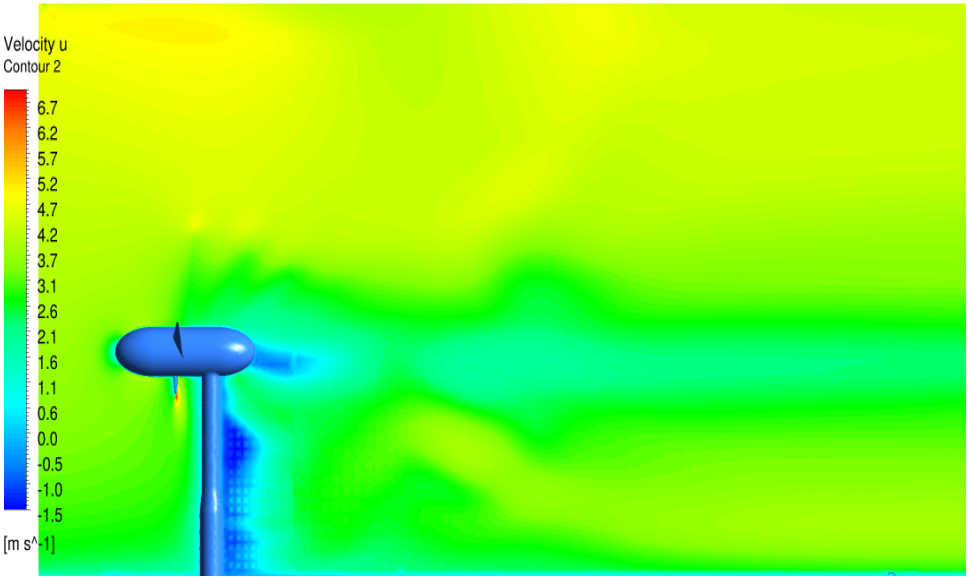

Figure 7.93 Axial velocity distribution in the meridional plane - normal_spacing_model F4

Additional qualitative plots similar to the plots discussed in regular and extreme F3 and F4 normal_spacing_model cases are discussed. Plots when the blade 2 first experiences the presence of the pylon, plots when the blade 2 is in front of the pylon and plots after blade 2 had passed the pylon have been documented. The three transient results at 2080, 2090 and 2120 corresponding to a simulation time of $8.640s$, $8.728s$ and $8.960s$ were loaded on to ANSYS CFX and vector plots, vorticity plots, pressure plots and velocity plots were plotted for these timesteps.

The locations utilised for these plots are similar to the previous plots.

The vector plot on Figure 7.94 displays the flow field approximately a metre or so downstream of the rotor plane of rotation at the timestep corresponding to 2080. The flow field is more energetic and disorganised when compared to the corresponding F3 case plot. The flow around the blade 2 is clearly disturbed and in an excited state.

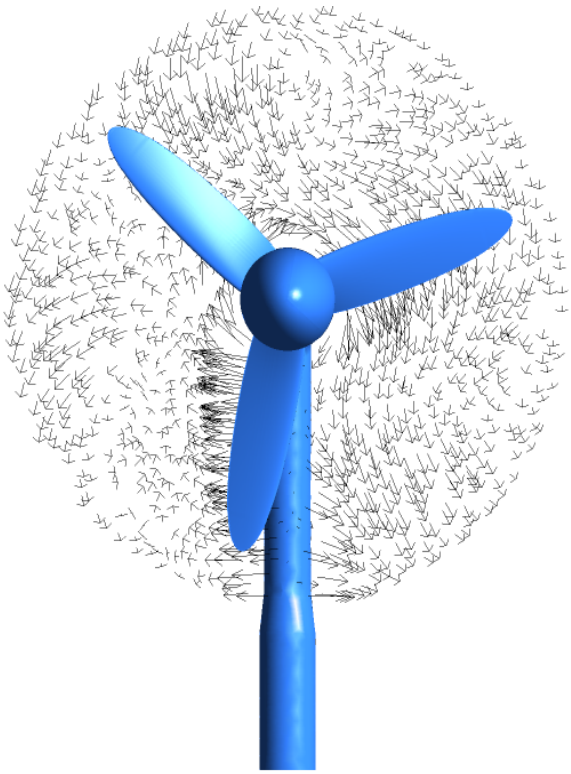

Figure 7.94 Vector plot at 2080 **timestep - normal_spacing_model F4**

The vorticity plot on Figure 7.95 show the vortices created by the blades for the same axial location. Clearly, the vortices are energised by the higher flow field as opposed to the corresponding F3 case.

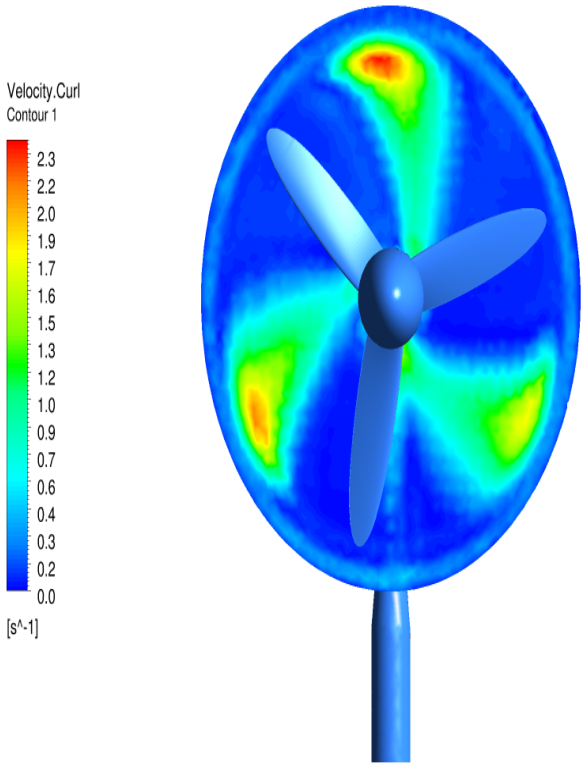

Figure 7.95 Vorticity plot at 2080 **timestep - normal_spacing_model F4**

Figure 7.96 displays a pressure plot at the same location and on this plot it seems very similar, but the pressure range is relatively large when compared to the any similar pressure plot in the F3 cases.

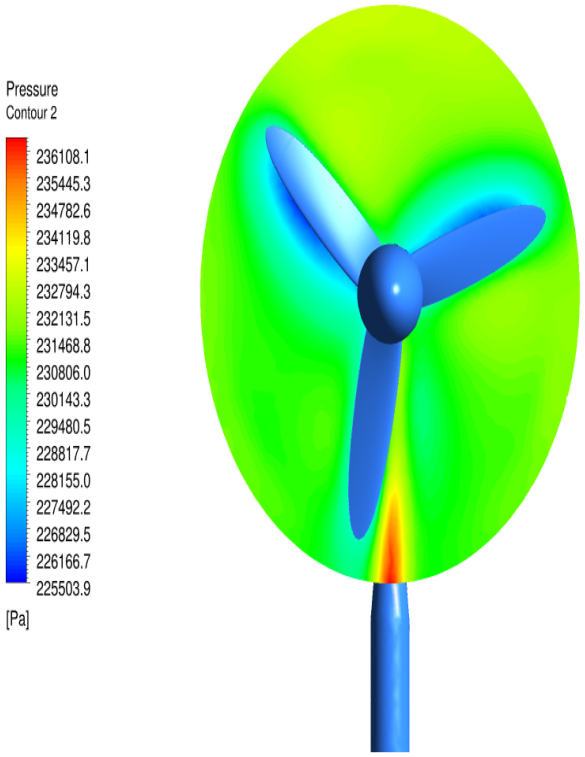

Figure 7.96 Pressure plot at 2080 **timestep - normal_spacing_model F4**

The circumferential velocity is plot on Figure 7.97 at the same location. Again, the range associated in the plot is higher than that of the corresponding F3 plot. This is due to the fact that the flow is energised in the F4 case.

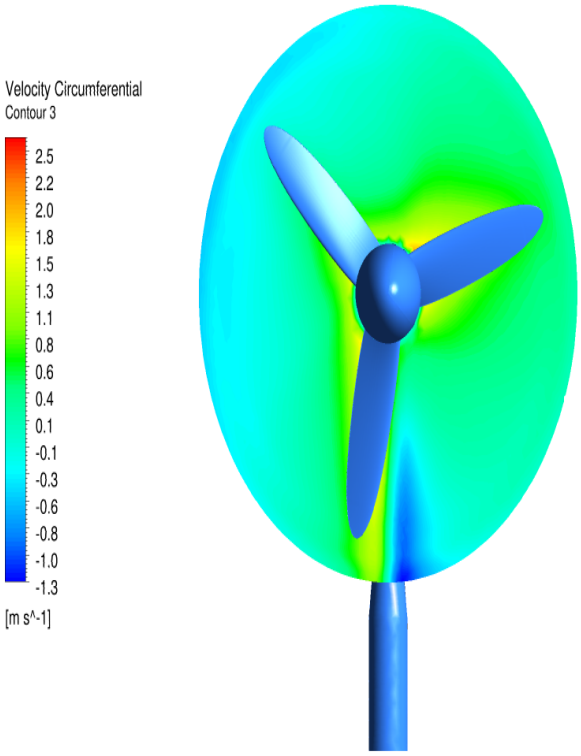

Figure 7.97 Circumferential velocity plot at 2080 **timestep - normal_spacing_model F4**

Axial velocity is plotted on Figure 7.98 at the second surface positioned approximately at $3D$ downstream of the rotor. The flow is without doubt more energised than the flow in the F3 case. It is clearly shown the plot range.

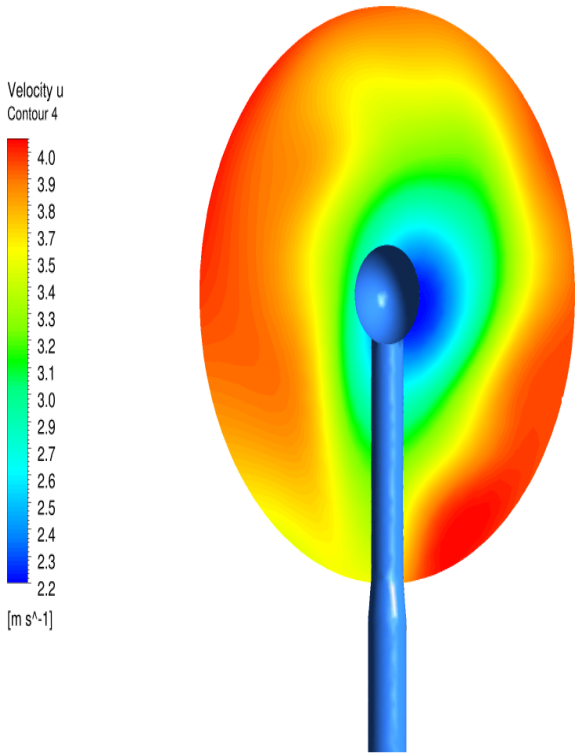

Figure 7.98 Axial velocity plot at 2080 **timestep - normal_spacing_model F4**

The vector plot on Figure 7.99 displays the flow field. This vector plot is for the timestep corresponding to 2090. The flow is relatively similar to the previous corresponding plot at timestep 2080, although the flow around the blade 2 seems to be chaotic and energised by the presence of the pylon.

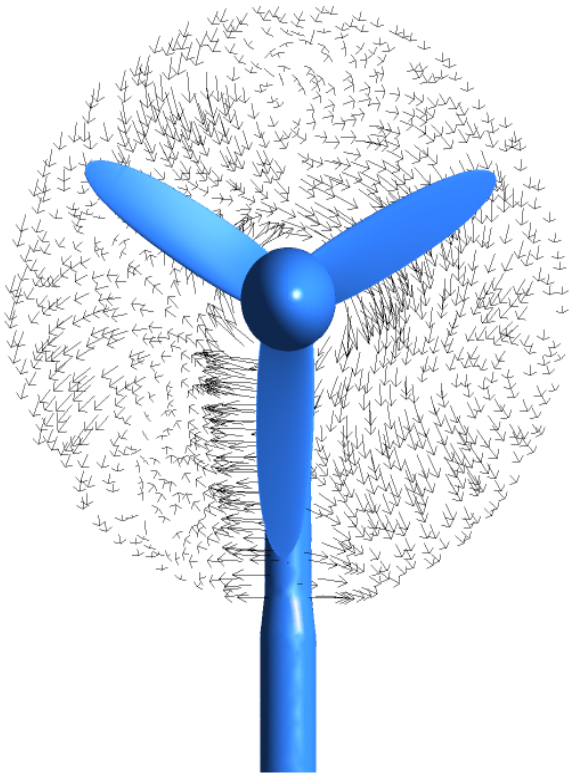

Figure 7.99 Vector plot at 2090 **timestep - normal_spacing_model F4**

The vorticity plot on Figure 7.100 show the vortices created by the blades for the same axial location. Vortices are similar to the previous plot, the intensity has increased only slightly.

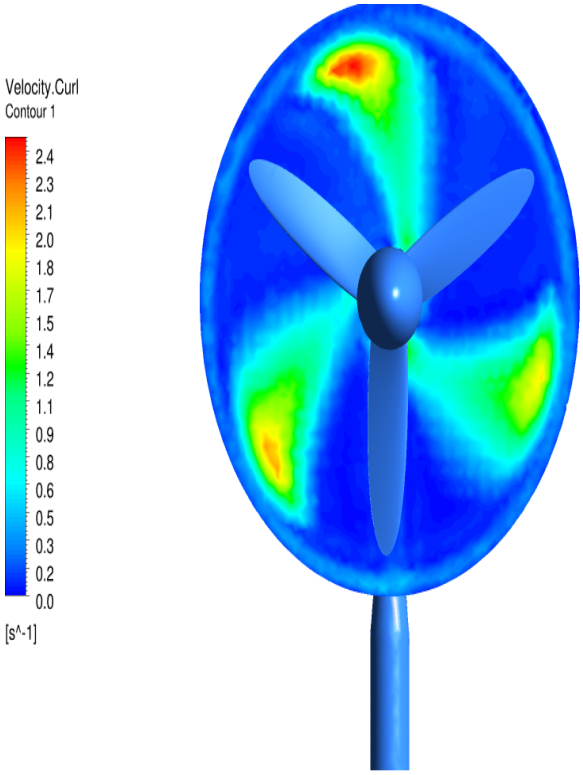

Figure 7.100 Vorticity plot at 2090 **timestep - normal_spacing_model F4**

Figure 7.101 displays a pressure plot at the same location and on this plot it seems very similar, the pressure range is relatively large as in the previous plot.

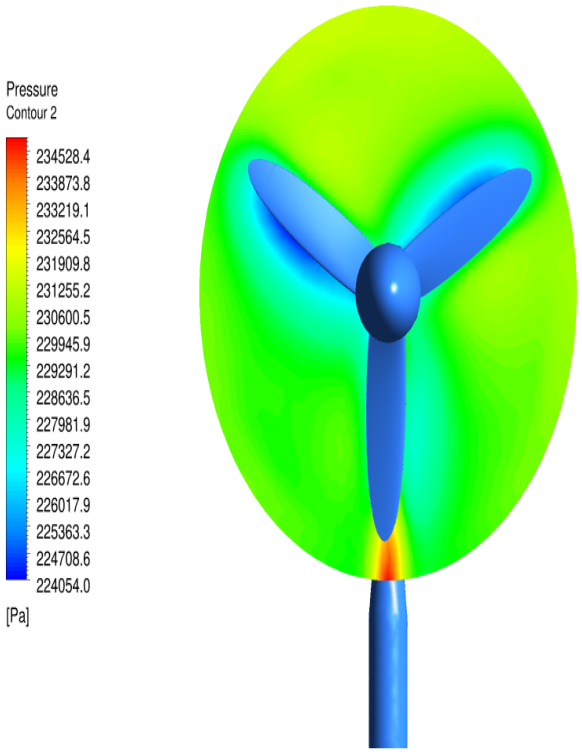

Figure 7.101 Pressure plot at 2090 **timestep - normal_spacing_model F4**

The circumferential velocity is plot on Figure 7.102 at the same location. This plot too has the same features as the previous plot. It is observed that there is a slight increase in the circumferential velocity in this plot.

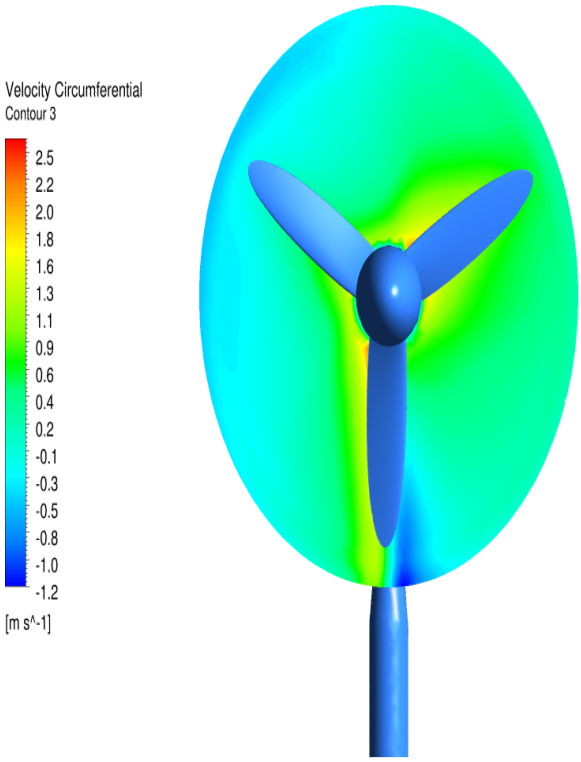

Figure 7.102 Circumferential velocity plot at 2090 **timestep - normal_spacing_model F4**

Axial velocity is plotted on Figure 7.103 at the second surface positioned approximately at $3D$ downstream of the rotor. The plot is very similar to the previous plot.

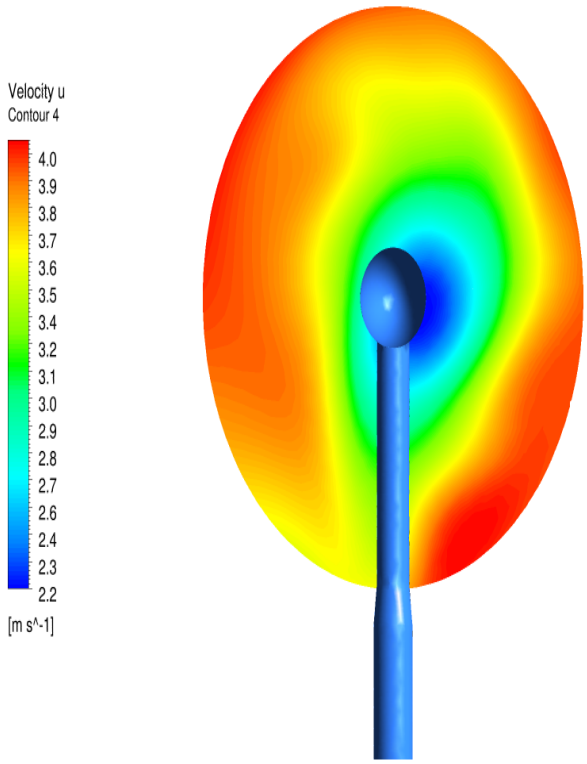

Figure 7.103 Axial velocity plot at 2090 **timestep - normal_spacing_model F4**

The vector plot on Figure 7.104 displays the flow field. This vector plot is for the timestep corresponding to 2120. The flow seems to be chaotic especially around the blade 2 and blade one areas.

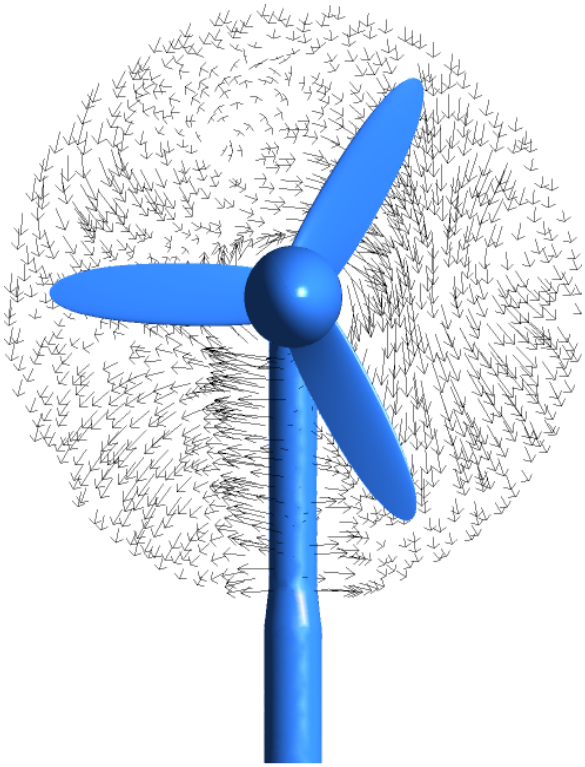

Figure 7.104 Vector plot at 2120 **timestep - normal_spacing_model F4**

The vorticity plot on Figure 7.105 show the vortices created by the blades for the same axial location. The intensity has increased in this plot when compared to the previous plots.

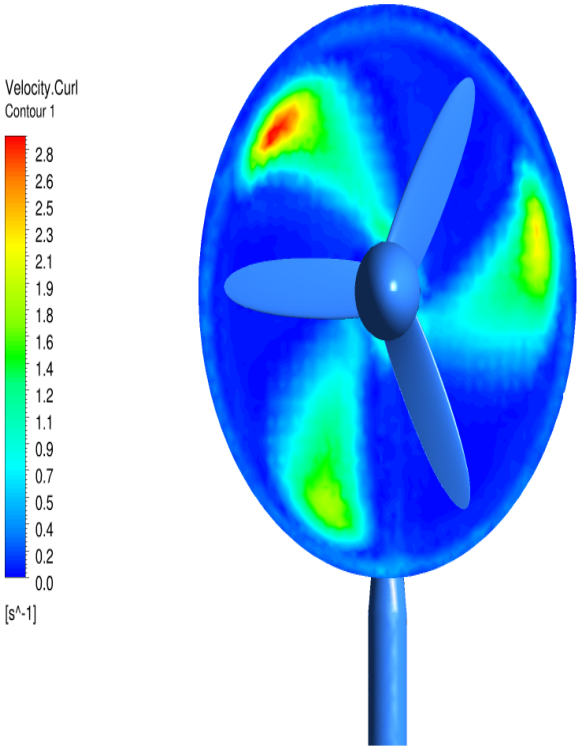

Figure 7.105 Vorticity plot at 2120 **timestep - normal_spacing_model F4**

Figure 7.106 displays a pressure plot at the same location and on this plot it seems very similar, the pressure range seemed to have become larger than the other plots.

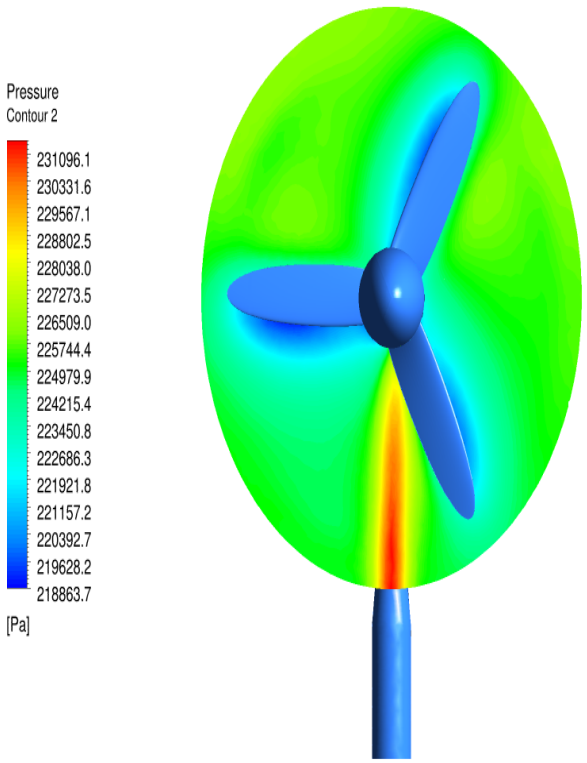

Figure 7.106 Pressure plot at 2120 **timestep - normal_spacing_model F4**

The circumferential velocity is plot on Figure 7.107 at the same location. This plot too has the same features as the previous plot. It is observed that there is a slight increase in the circumferential velocity in this plot.

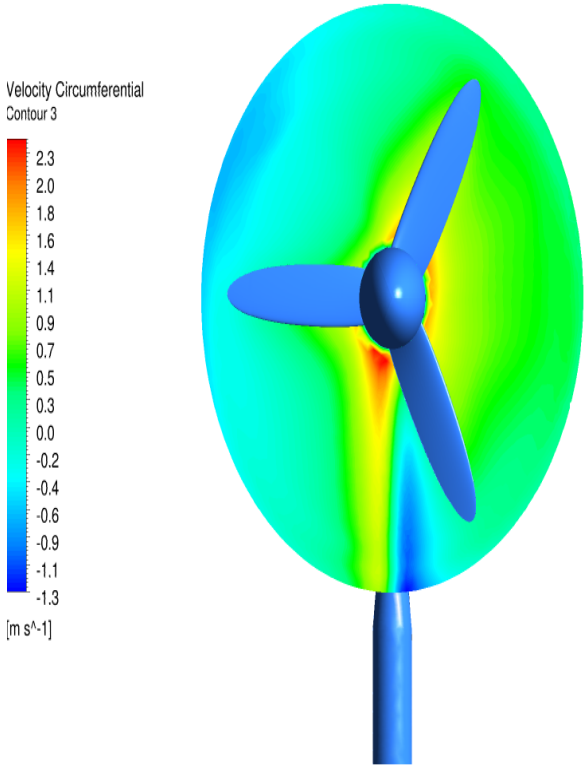

Figure 7.107 Circumferential velocity plot at 2120 **timestep - normal_spacing_model F4**

Axial velocity is plotted on Figure 7.108 at the second surface positioned approximately at $3D$ downstream of the rotor. The plot is very similar to the previous plot.

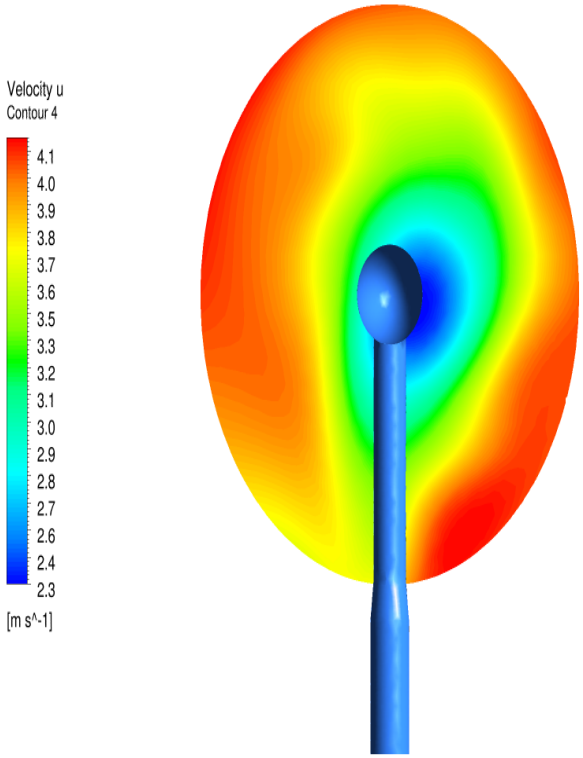

Figure 7.108 Axial velocity plot at 2120 timestep - normal_spacing_model F4

The total torque generated by the turbine is approximately calculated to be $502kNm$ and the total thrust produced by the turbine is approximately at $362kN$. The total power generated by the turbine is calculated to be around $1104kW$. The minimum torque and thrust produced coincides at roughly $5.0s$ of the simulation time. This occurs at the half wave period mark and is clearly shown on Figure 7.109. The maximum torque and thrust occurs at the start of the simulation and at $10.0s$ at the wave period.

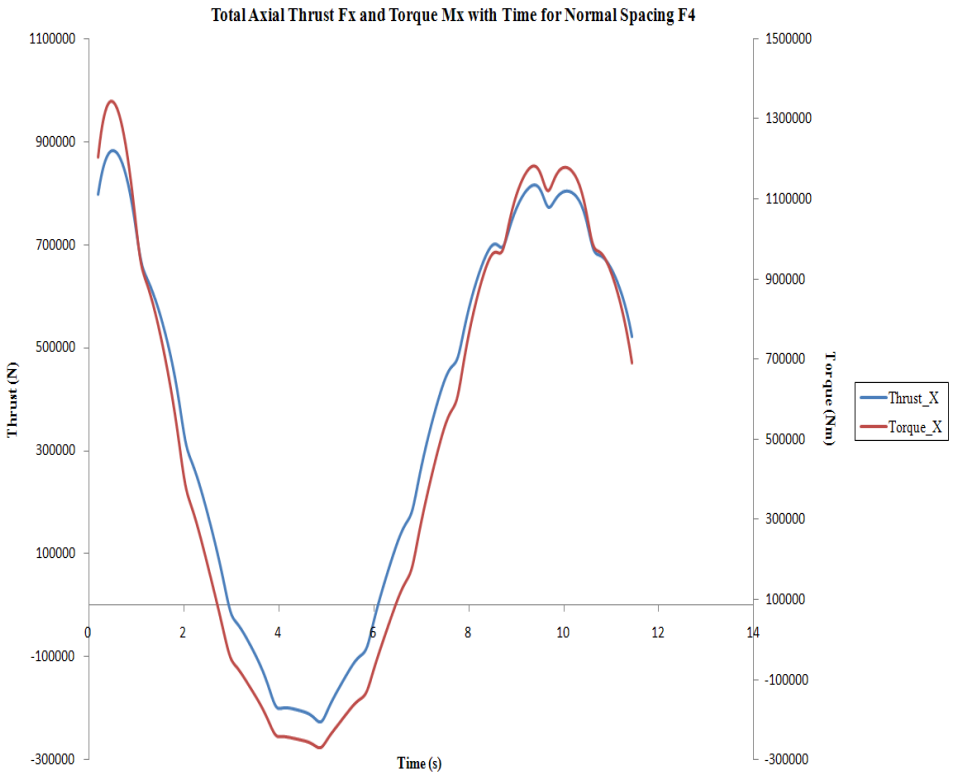

Figure 7.109 Thrust and Torque loads for normal_spacing_model F4

The axial thrust and axial torque variation per blade are shown on Figure 7.110 and Figure 7.111 respectively. On both these plots it is clear that each blade passes the pylon before by one full revolution occurring approximately at $2.8s$. All three blades experience the lowest loads at half the wave period, $5.0s$.

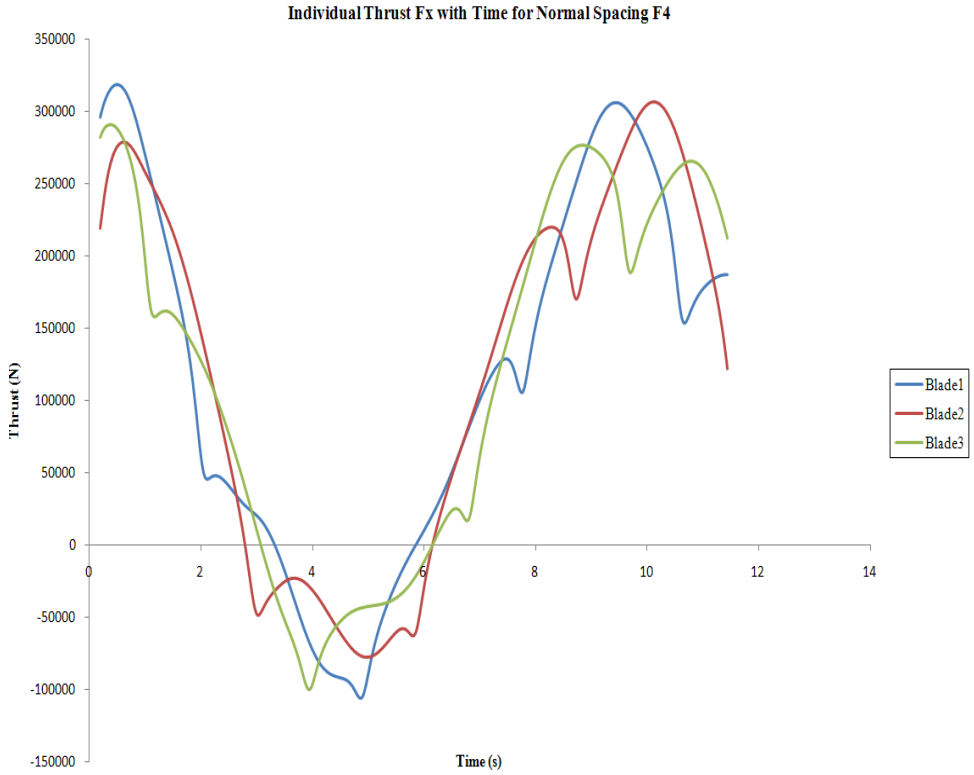

Figure 7.110 Individual Axial Thrust loads for normal_spacing_model F4

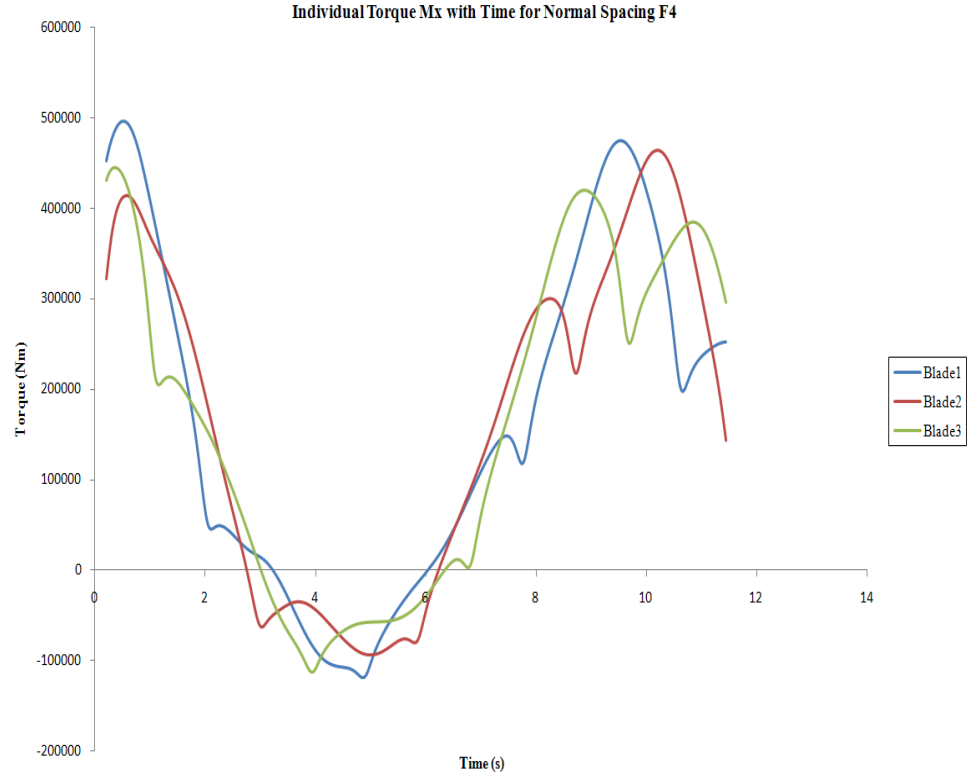

Figure 7.111 Individual Axial Torque loads for normal_spacing_model F4

7.7 Regular Wave for Half Spacing F3 & F4 Cases

F3 and F4 parameters for the shear profile boundary layer was used in conjunction with the frequent (regular) wave of $1.5m$ in wave height and $10.0s$ in wave period was analysed for the Half_spacing_model. The blade loading distribution plots are analysed and as seen from the Chapter 7.6, the axial velocity component contour plots are analysed to discuss the wake and blade-pylon characteristics of the models. Analysis of the vortices created by the turbine blades are discussed by means of plots. Finally, axial torque and thrust plots are compared and its performance characteristics are compared.

7.7.1 F3 case (maximum torque)

The Figure 7.112, Figure 7.113 and Figure 7.114 represent the blade loading plots for the Half_spacing_model F3 case together with the regular wave parameters. The pressure loading plots displayed Figures 7.112 to 7.114 were obtained at 25%, 50% and 90% span.

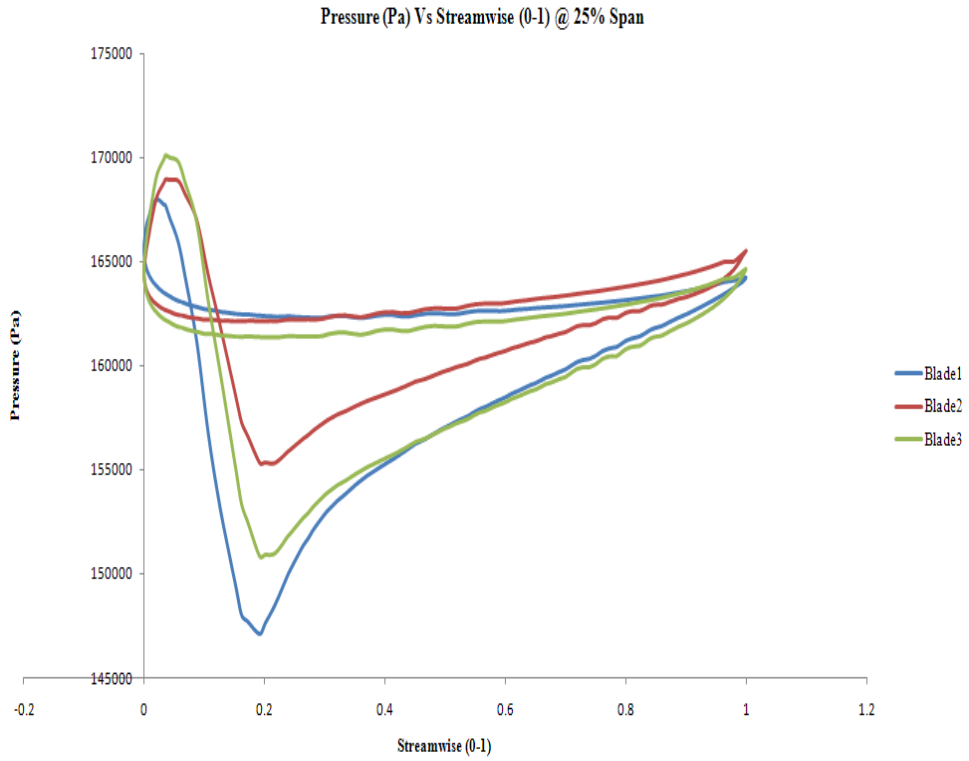

Figure 7.112 Pressure plot at 25% span - Half_spacing_model F3

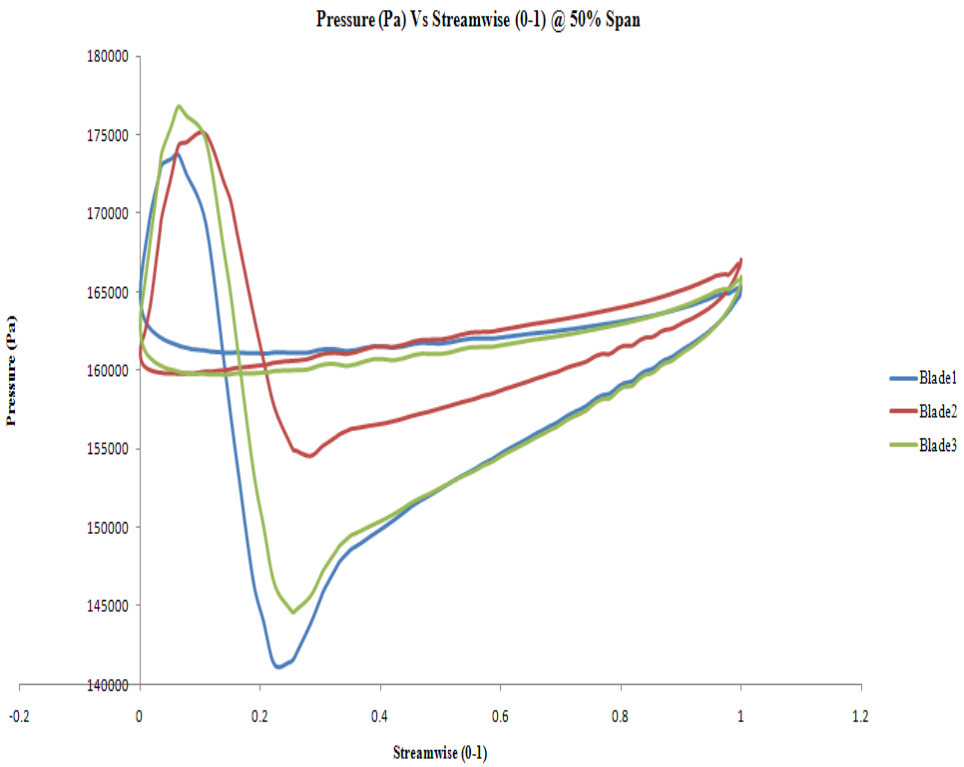

Figure 7.113 Pressure plot at 50% span - Half_spacing_model F3

These pressure plots were taken at the end of the simulation therefore the layout of the blades were such that the blade two was at the lowest point next to the pylon. The blade one was between the 1 o'clock and the 2 o'clock position and the blade three between the 10 o'clock and 11 o'clock position. The blade loading plots describe its blades positioning precisely. The blade two yields the lowest lift characteristics. The blade one is slightly at a higher position than the blade three and hence, produces the highest pressure loading plot.

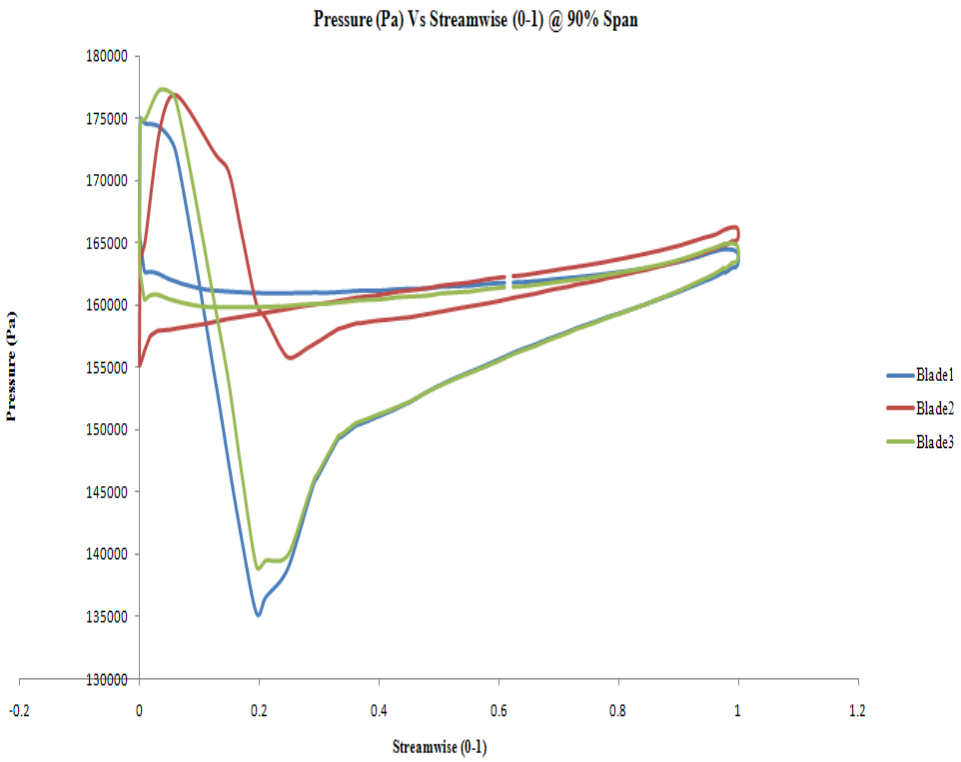

Figure 7.114 Pressure plot at 90% span - Half_spacing_model F3

The Figure 7.115 shows the vorticity plot with blade positioning at 99% span. This plot is colour coded in the same manner as the blade loading plots shown above. It could be seen from plot, that the blade two produces the least vortices when compared to the blade one and blade three. The blade one produces the largest average vortex which also confirms the prediction on the blade loading plots shown above. The total vortices generated from the blade is roughly just over $5.8s^{-1}$.

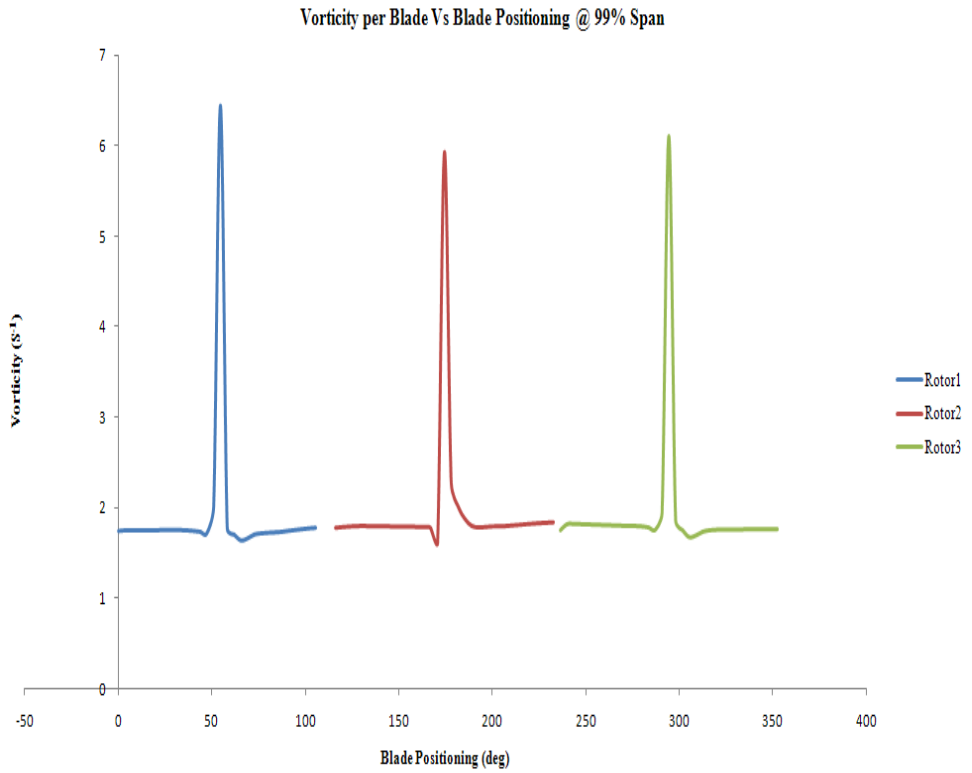

Figure 7.115 Vorticity plot with blade positioning at 99% span - Half_spacing_model F3

Similar to the previous regular wave contour plot, the Figure 7.116 displays an axial velocity contour plot for the interaction of the blade-pylon spacing. The low pressure areas aft of the pylon are shown through the blue areas denoting the low velocity areas. The low pressure areas are shown immediately in front and immediately behind the pylon.

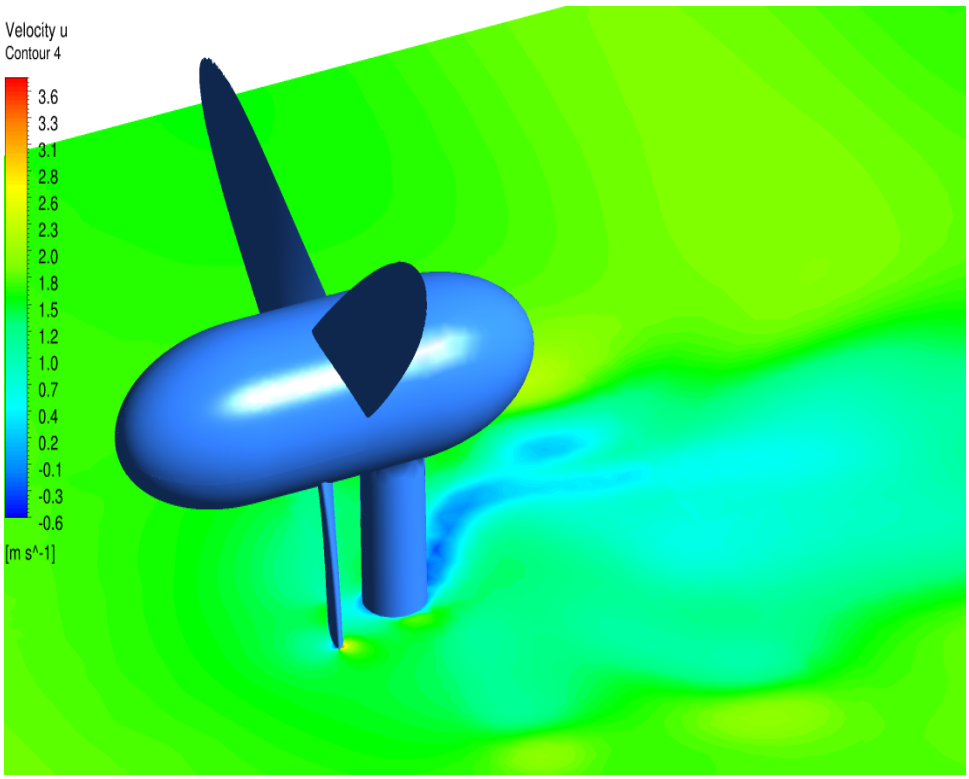

Figure 7.116 Blade-pylon interaction - Half_spacing_model F3

The Figure 7.117 displays an axial velocity contour plot to discuss the features of the wake distribution of the model. The low velocity areas caused by the turbine-pylon wake are clearly visible in the green, light blue and dark blue areas. The area close to the top water surface undergoes the highest velocity because of the combination of the waves and the shear flow being the highest at this level and is shown on red and orange contours. As seen from the previous wake distribution plots the wake is extreme in the so called near wake regions i.e. typically between $1 - 2D$ downstream of the rotor.

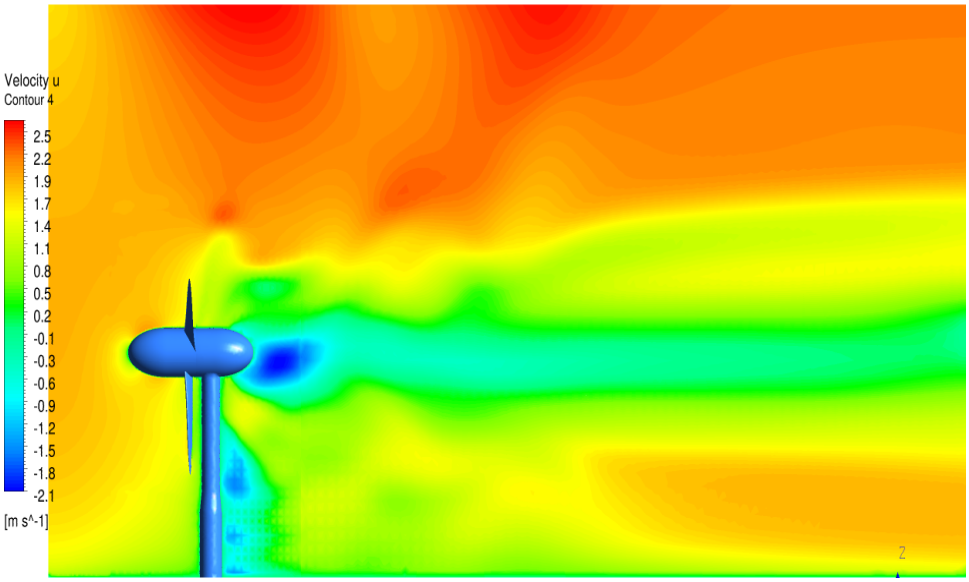

Figure 7.117 Axial Velocity distribution in the meridional plane - Half_spacing_model F3

Figures 7.118, 7.119 and 7.120 represent vector plots at a similar location as before for timesteps at 4600, 4800 and 5100. These timesteps correspond to actual simulation times of $6.4801s$, $6.8401s$ and $7.3801s$ respectively.

All these three vector plots suggests that there is a lot more activity and is more disorganised when compared with the vector plots for the F3 normal_spacing_model. This suggests that the shorter hub spacing causes chaotic and turbulent behaviour around the rotor-pylon system.

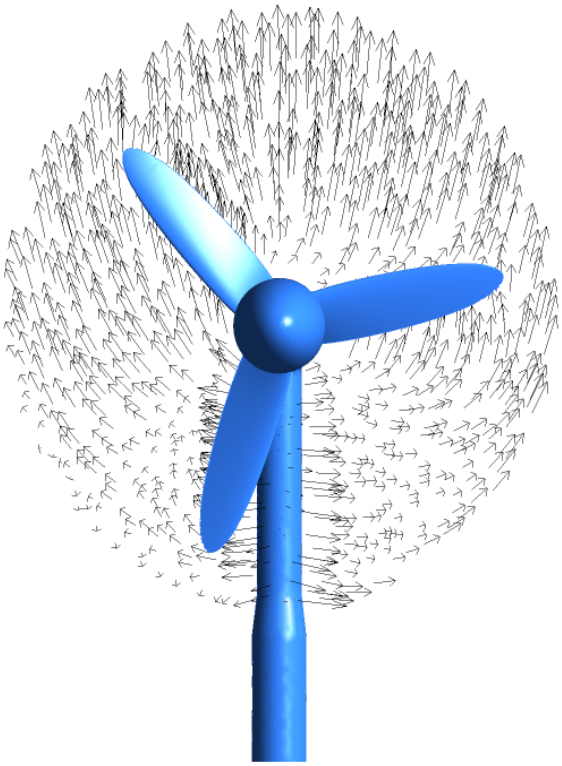

Figure 7.118 Vector plot at 4600 **timestep - Half_spacing_model F3**

It is evident on all the vector plots that there is a lot of flow recirculation and unsteadiness around because short hub spacing involved.

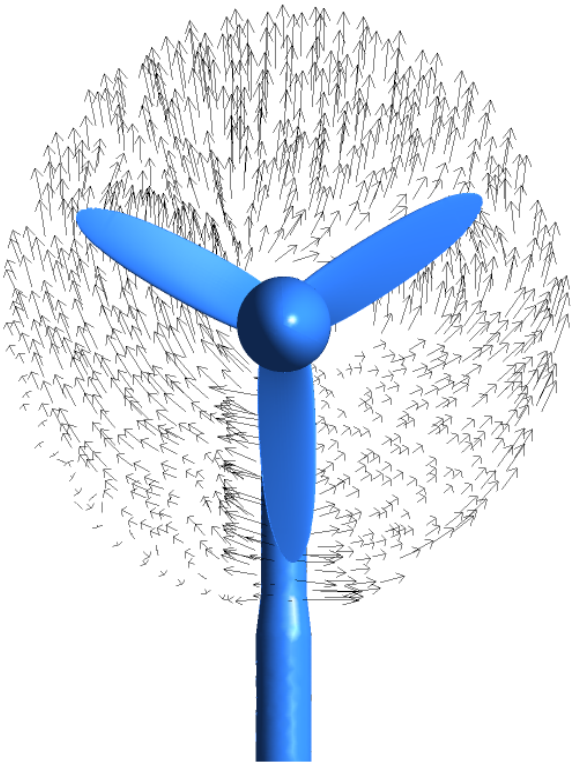

Figure 7.119 Vector plot at 4800 **timestep - Half_spacing_model F3**

The flow field around the blade closest to the pylon is highly chaotic and intense which could be interpreted from the size of the vectors. The flow around the blade 3 and the blade 1 is experiencing highly turbulent flows.

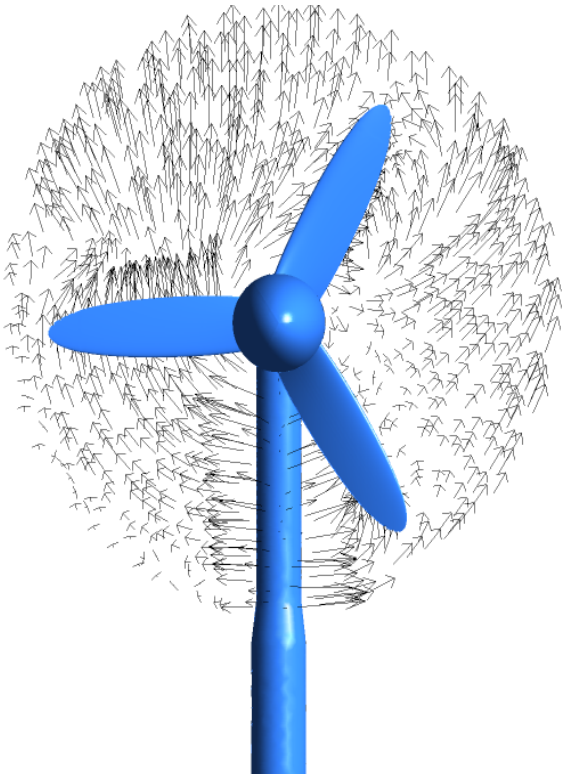

Figure 7.120 Vector plot at 5100 timestep - Half_spacing_model F3

The total torque generated by the turbine is approximately calculated to be $437kNm$ and the total thrust produced by the turbine is approximately at $286kN$. The total average power generated by the turbine is calculated to be around $425kW$. The Figure 7.121 shows the total thrust and torque variation with simulation time. The minimum torque and thrust produced coincides at roughly $5.0s$ of the simulation time. This occurs at the half wave period mark and is clearly shown on Figure 7.121. The maximum total average torque and thrust occurs at the start of the simulation and at $10.0s$ at the wave period.

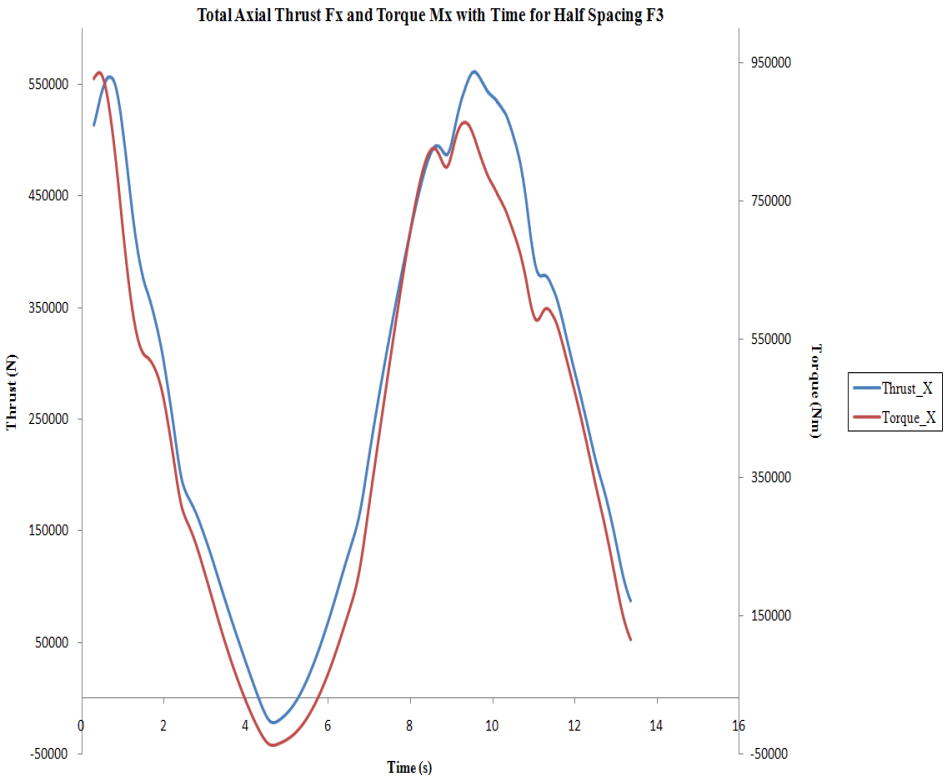

Figure 7.121 Thrust and Torque loads for Half_spacing_model F3

The axial thrust and axial torque variation per blade are shown on Figure 7.122 and Figure 7.123 respectively. The individual thrust variation (not the average thrust) is slightly higher in these plots than when compared to the corresponding F3 normal_spacing_model. The normal_spacing_model produces better torque loads.

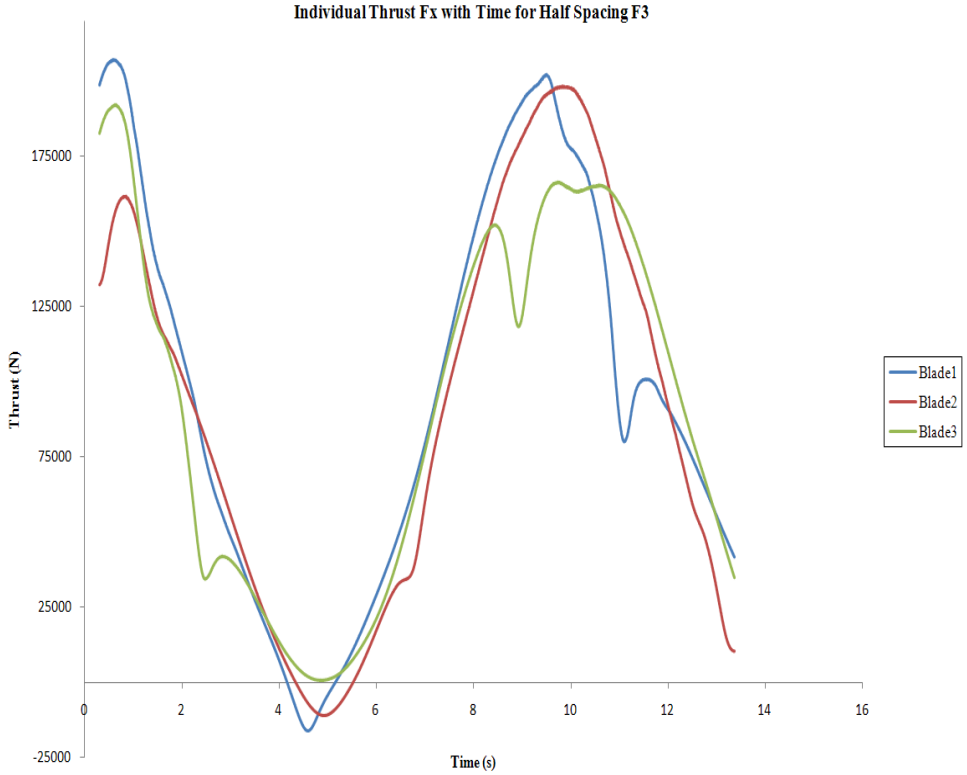

Figure 7.122 Individual Axial Thrust loads for Half_spacing_model F3

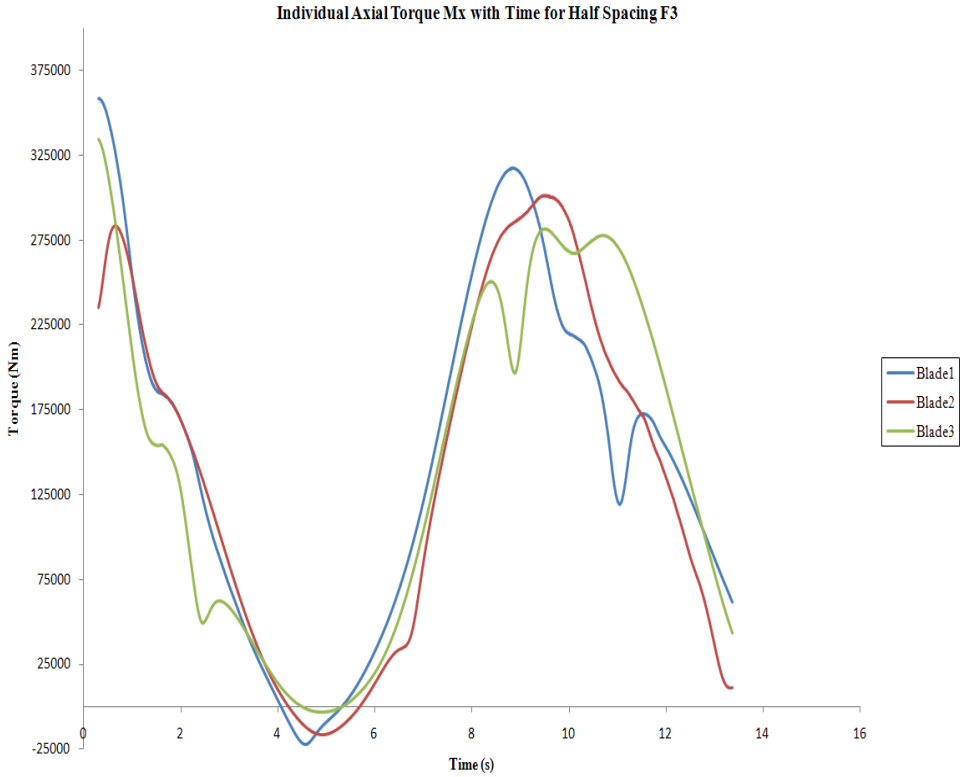

Figure 7.123 Individual Axial Torque loads for Half_spacing_model F3

7.7.2 F4 case (maximum thrust)

The Figures 7.124, 7.125 and 7.126 shown below represents the blade loading plots for the Half_spacing_model F4 case used in conjunction with the regular wave parameters at 25%, 50% and 90% span.

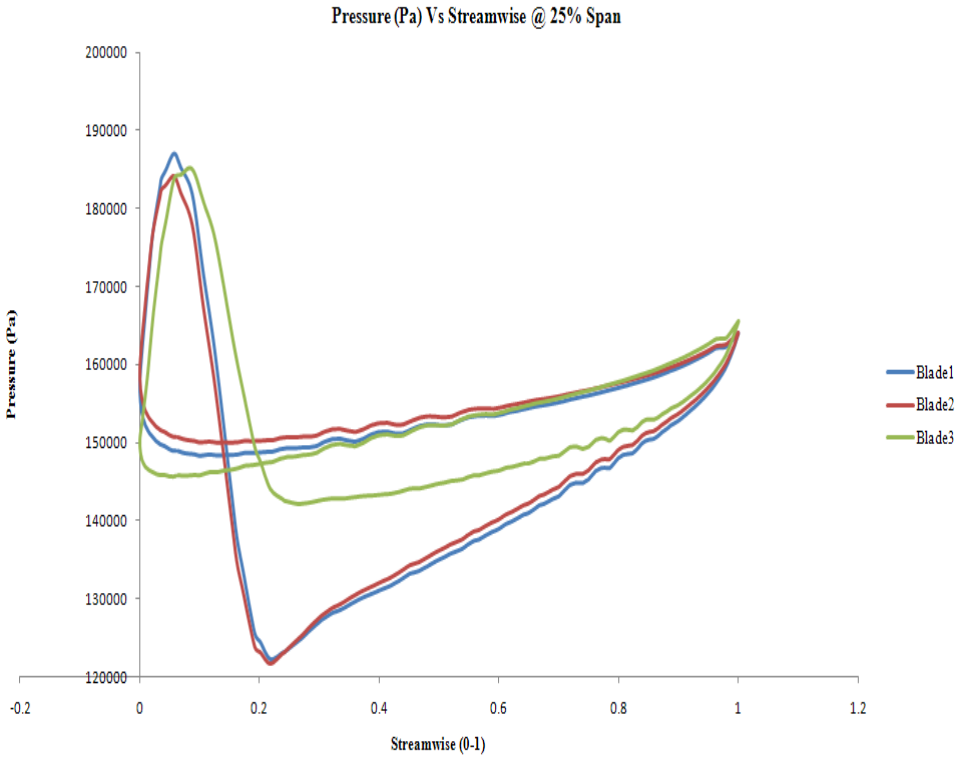

Figure 7.124 Pressure plot at 25% span - Half_spacing_model F4

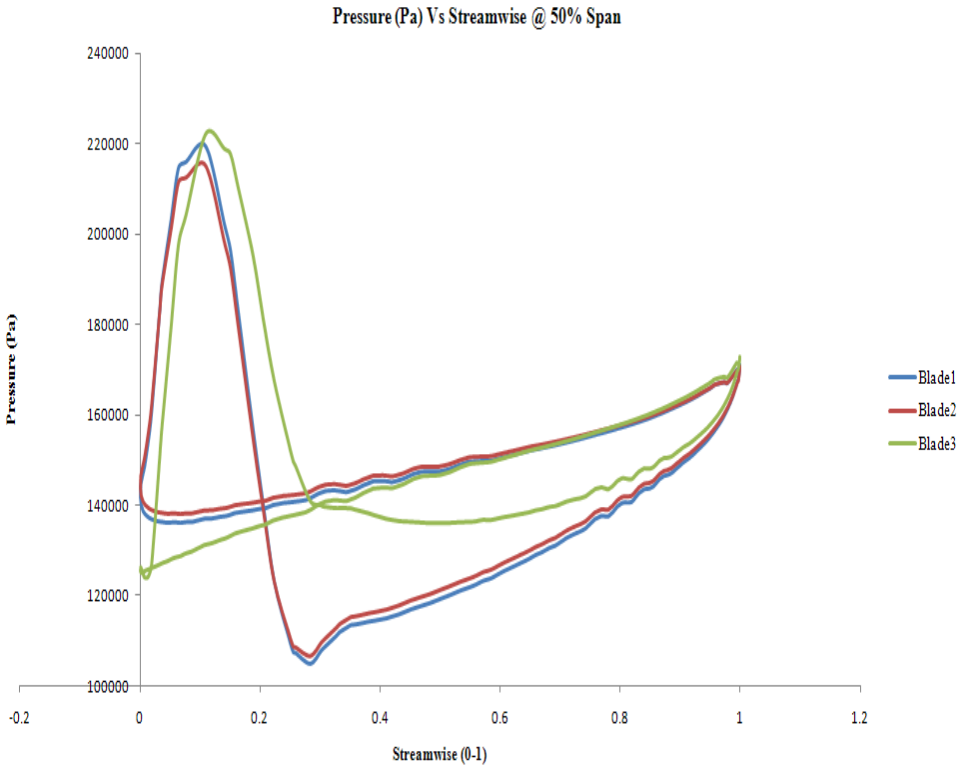

Figure 7.125 Pressure plot at 50% span - Half_spacing_model F4

The blade orientation of the model is such that the blade three is at the bottom most position in front of the pylon. The blade one is at the 11 o'clock position and the blade two is at the 3 o'clock position. From the orientation of the blades, it could be rationalised that the blade three denoted on the green plot produces the least force as opposed to the blade one and blade two. From the blade loading plots it is evident that the blade one produces the highest force and closely followed by the blade two.

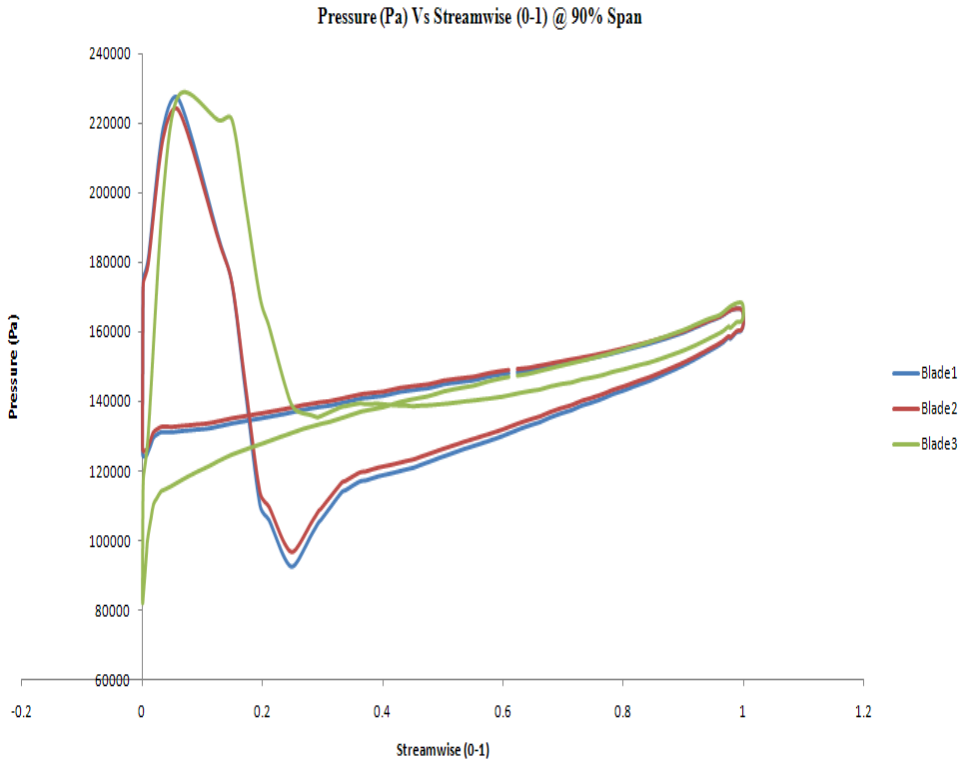

Figure 7.126 Pressure plot at 90% span - Half_spacing_model F4

The Figure 7.127 shows the vorticity plot with blade positioning at 99% span. This plot is colour coded in the same manner as the blade loading plots shown above. It could be seen from the vorticity plot that the blade three produces the least vortices when compared to the blade one and blade two. The blade one produces the largest total vortex which also confirms the prediction on the blade loading plots shown above. The total vortices generated from the blades are roughly just over $9s^{-1}$.

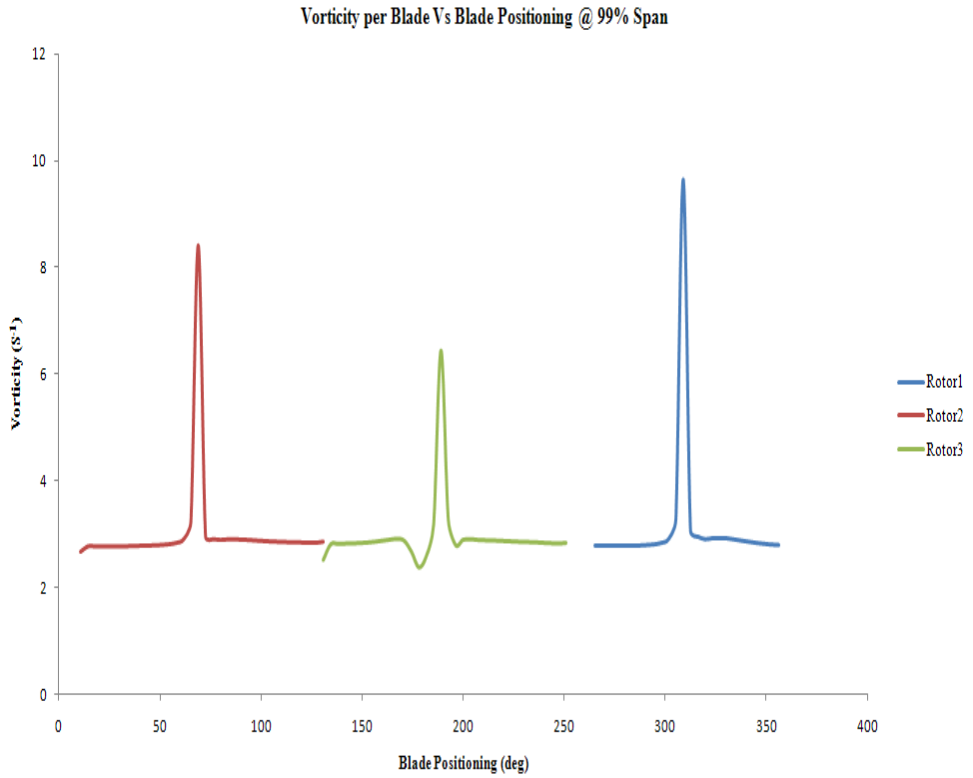

Figure 7.127 Vorticity plot with blade positioning at 99% span - Half_spacing_model F4

As with the other blade-pylon and meridional plane plots for regular waves section the Figure 7.128 displays an axial velocity contour plot for the interaction of the blade-pylon spacing. The low pressure areas aft of the pylon are shown through the light blue/green areas denoting the low velocity areas. The low pressure areas are shown immediately in front and immediately behind the pylon.

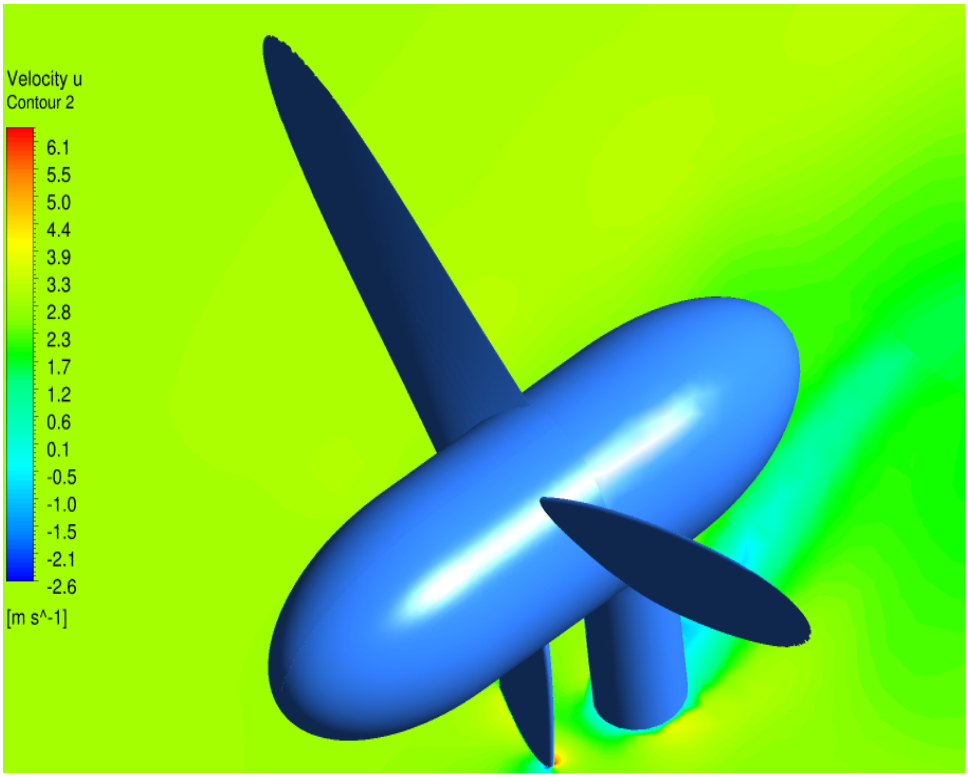

Figure 7.128 Blade-pylon interaction - Half_spacing_model F4

The Figure 7.129 displays an axial velocity contour plot to discuss the features of the wake distribution of the model. The low velocity areas caused by the turbine-pylon wake are clearly visible in the green, light blue and dark blue areas. The area close to the top water surface undergoes the highest velocity because of the combination of the waves and the shear flow being the highest at this level and is shown on yellow and dark yellow contours. As seen from the previous wake distribution plots the wake is extreme in the so called near wake regions i.e. typically between $1-2D$ downstream of the rotor. The far wake improves several diameters downstream of the rotor.

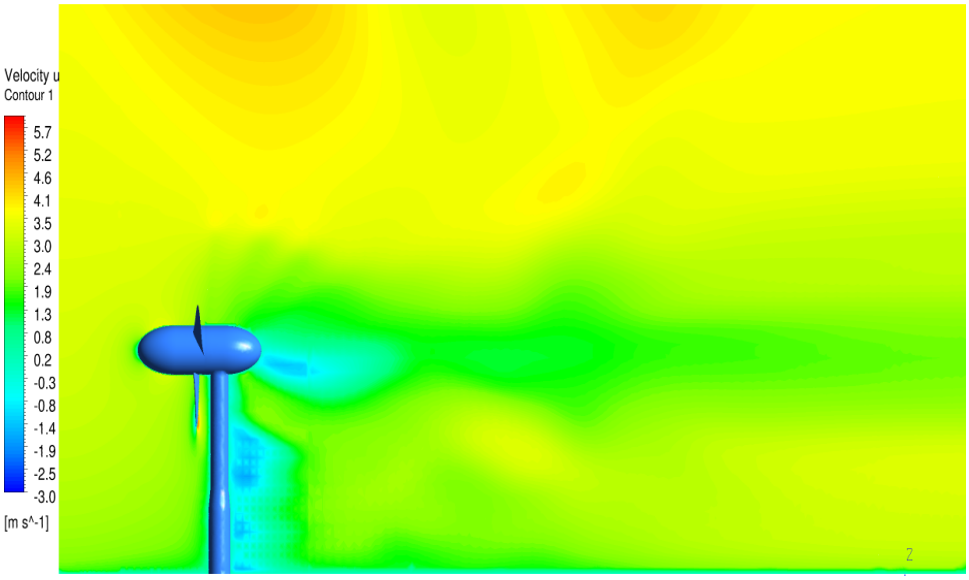

Figure 7.129 Axial Velocity distribution in the meridional plane - Half_spacing_model F4

Figures 7.130, 7.131 and 7.132 represent vector plots at a similar location as before for timesteps at 2080, 2090 and 2120. These timesteps correspond to actual simulation times of $8.640s$, $8.728s$ and $8.960s$ respectively.

These three vector plots suggests that there is a lot more energy in the flow and is even more disorganised when compared with the vector plots for the F3 Half_spacing_model.

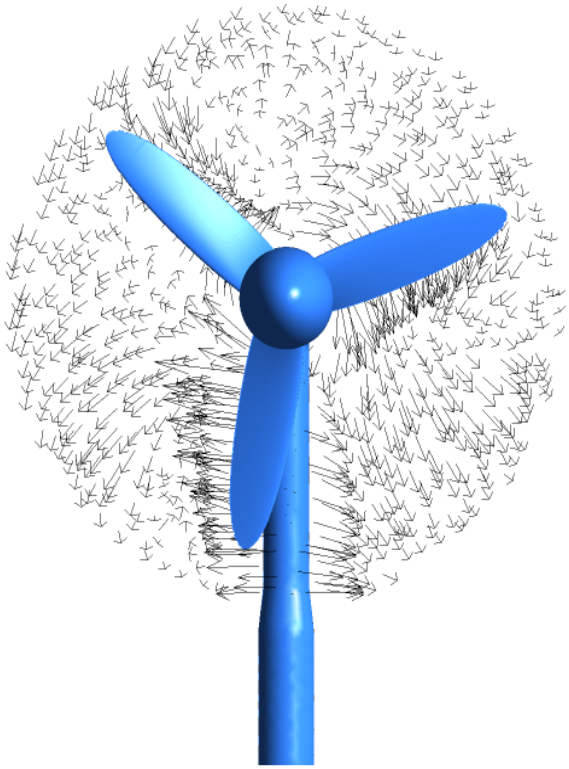

Figure 7.130 Vector plot at 2080 **timestep - Half_spacing_model F4**

All the vector plots exhibit a lot of flow recirculation and unsteadiness around partly because short hub spacing involved and also due to the high flows associated with this simulation.

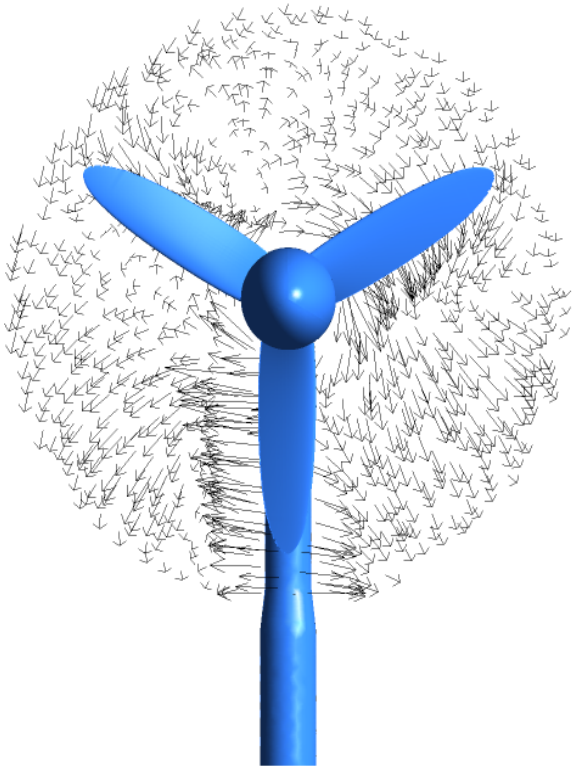

Figure 7.131 Vector plot at 2090 **timestep - Half_spacing_model F4**

In Figure 7.132, the flow field around the blade closest to the pylon is highly chaotic and intense which could be interpreted from the size and orientation of the vectors. The flow around the blade at the 9 o'clock position and in particular the blade at 1 o'clock position are experiencing highly turbulent flows.

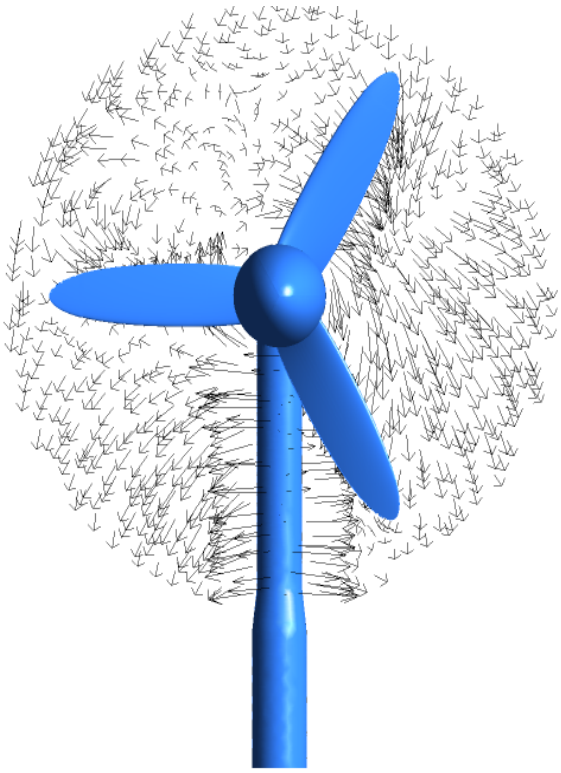

Figure 7.132 Vector plot at 2120 **timestep - Half_spacing_model F4**

The total torque generated by the turbine is approximately calculated to be $431kNm$ and the total thrust produced by the turbine is approximately at $358kN$. The total power generated by the turbine is calculated to be around $948kW$. The minimum torque and thrust produced coincides at roughly $5.0s$ of the simulation time. This occurs at the half wave period mark and is clearly shown on Figure 7.133. The maximum total torque and thrust occurs at the start of the simulation and at $10.0s$ at the wave period due to the cosine effect of the waves.

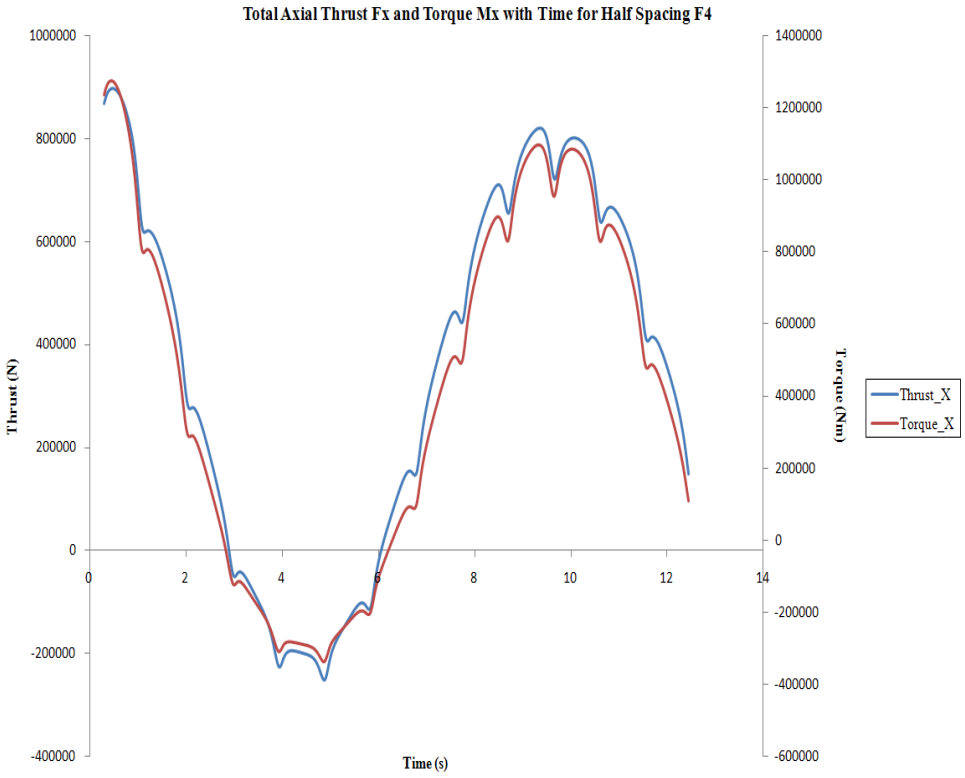

Figure 7.133 Thrust and Torque loads for Half_spacing_model F4

The axial thrust and axial torque variation per blade are shown on Figure 7.134 and Figure 7.135 respectively. The individual thrust and the individual torque variations are significantly higher that of the corresponding F3 Half_spacing_model case. It is clear from the three performance loading plots that the 3 blade pass the pylon at the lowest point in each revolution at every $2.8s$ approximately.

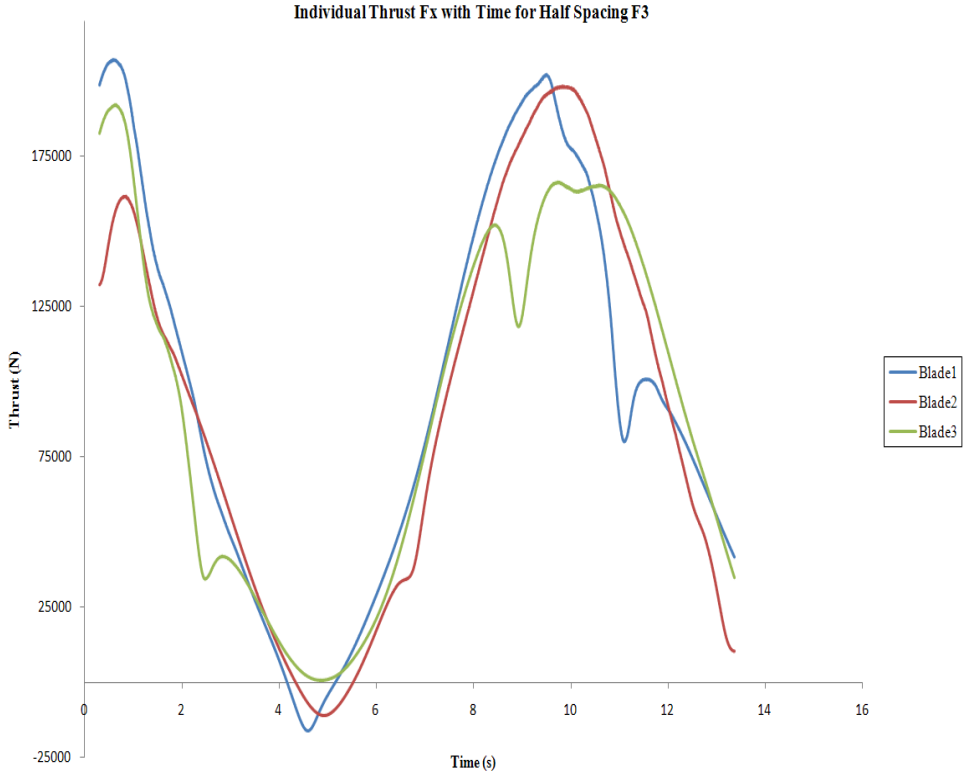

Figure 7.134 Individual Axial Thrust loads for Half_spacing_model F4

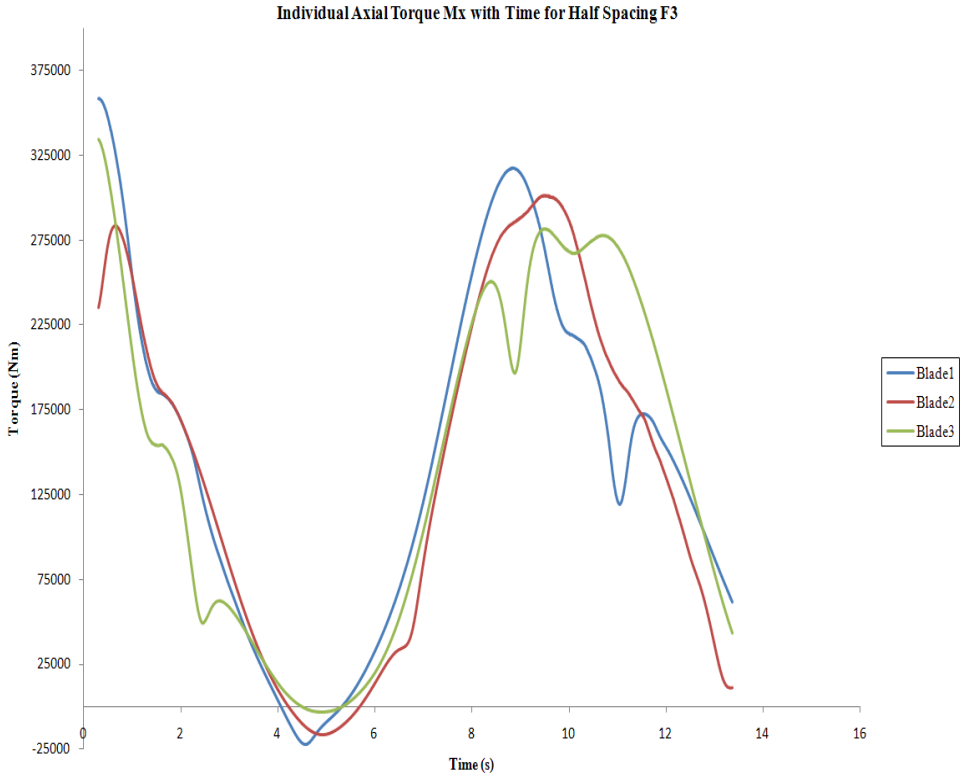

Figure 7.135 Individual Axial Torque loads for Half_spacing_model F4

7.8 Chapter Closure

The progressive small amplitude linear wave theory parameters have been discussed which are in the intermediate water depth range. The model underwent a few changes in terms of its inlet boundary conditions as CEL expressions were introduced and a new local coordinate system was established to introduce these new expressions at the domain inlet. The F3 cases were only run for two revolutions as the model had to be rotated every 0.1 degree rather than the usual 1.0 degree on the F4 cases.

Blade loading plots, vorticity plots, pressure and axial velocity contour plots, vector plots, circumferential velocity plots and performance plots have been analysed extensively for the normal_spacing_model and Half_spacing_model which included the two wave parameters in combination with the F3 and F4 cases. A total of 8 simulations were done for this chapter.

The torque and power generated by the normal_spacing_model F3 cases for the extreme waves and the regular waves were approximately 1.2times the transient no waves F3 case. The thrust produced by these parameters are in the region of approximately 1.0times the transient no waves F3 case. And the torque and power generated by the normal_spacing_model F4 cases for the two wave parameters are roughly around 1.5times the transient no waves F4 case. The thrust variation was roughly around 1.2times the transient no waves F4 case.

The torque and power generated by the Half_spacing_model F3cases for the extreme and regular wave parameters were approximately 1.0times the transient no waves F3 case. The thrust was approximately 1.0times the transient no waves F3 case. The torque and power generated by the Half_spacing_model F4 cases for the two wave parameters were approximately 1.4times the transient no waves F4 case. The thrust produced by the turbine was approximately around 1.2times the transient no waves F4 case.

These increments in the variation of thrust, torque and power could be accounted for by the addition of the waves. This is shown to have increased the unsteady cyclic loads imposed on the turbine and on average are about 1.2times the no waves cases. Therefore, when designing a tidal turbine, a great consideration has to be given to the effect of waves and site specific wave and current combinations, as these will give a sound understanding of what loads the rotor is going to experience on site specific conditions.

Some residual plots of the simulations have been attached in the Appendix D, Figure D.3 displays the convergence residuals for the F4 normal_spacing_model extreme wave case. Figure D.4 represents the residual plot for the F3 Half_spacing_model extreme wave case. The normal_spacing_model F3 regular wave residual plot is attached on Appendix D,

Figure D.5. And finally, Figure D.6 displays the mass and momentum residual convergence plot for Half_spacing_model F4 regular wave case.

The total thrust and torque loads about the Y and Z axis for each of the 8 simulations are plotted in Appendix D, Figures D.7 to D.22 present these plots.

Chapter 8

Conclusions

8.1 General Considerations

The work contained in this thesis reflects the current state of the art in terms of numerical modelling of horizontal axis tidal turbines employing a 3D numerical approach. The study includes steady-state and transient models of the turbine. For the latter case, wave effects were simultaneously accounted for through the prescription of a transient axial velocity variation. After a comprehensive review of the importance of renewable energy, theories relating to tidal turbines, current modelling practices and the available turbulence models, a range of steady state CFD examinations were carried out using the SSG Reynolds Stress Model available in the commercial ANSYS CFX code.

The performance of the models described in the Chapters 5, 6 and 7 were highly dependant upon the skill of the user to input and describe the appropriate boundary conditions which in turn produced a realistic representation of the flow. For these types of application of CFD the inaccuracies inherent in the models themselves can quite easily become secondary to the inaccuracies caused by inappropriate boundary condition formulation.

Whilst a conclusions section was included at the end of each chapter, conclusions for the work in a more overall context are included here. Recommendations for further study on the topic covered in this thesis are also included at the end of this chapter.

8.2 Steady State Simulations

The set of simulations conducted and documented on Chapter 5 were done as part of the initial preparations for the more complex transient analysis that were to follow. The steady state results for normal_spacing_model returned a good degree of agreement with the BEMT approach employed by Freeman (2009a). The turbine design philosophy and its intentions

were discussed in Chapter 5. The initial role of the CFD computations was to offer a substantiation of the behaviour of the turbine according to the design principles laid out in, Freeman (2009c). In addition CFD offers a truly three dimensional representation of the flow surrounding the blades and can expose areas of inefficiency that are not identified in the BEMT approach.

Several models with different blade-pylon spacing were created in order to find the best compromise blade spacing. The results showed that there is a performance penalty in the operation of the turbine in close proximity to the pylon. However the significant effect of that operation is in terms of the structural loadings, and hence given the cyclical nature of the interaction, the fatigue, of the turbine components. However there is also a structural penalty in the extension of the shaft to accommodate a larger spacing.

The investigation of the effects of turbulence was carried out employing two approaches. Results obtained with an inlet profile distribution were compared with equivalent data acquired with an uniform inlet turbulence value. The 5% turbulence intensity formulation of the ANSYS code and the mathematically derived profile representative of the distribution of turbulence in a boundary layer had similar effects on the turbine performance. However a similar exercise carried out with 10% turbulence yielded different results. This confirms that for higher turbulence intensities the use of a turbulence profile is required.

The shear boundary layer velocity was off set to 10deg on the Y-plane to replicate the effect of the flow being yawed for the normal_spacing_model. As expected the 10deg yaw caused the performance of the turbine to drop by an average of 4% for the standard rated power case. Further investigation of the yaw cases revealed that a higher variation of loads were experienced by the blades as opposed to the normal F3 case.

8.3 Transient Simulations - no waves

Although the steady state results offer good agreement with the BEMT code and the experimental testing done in France, the convergence achieved by this solving technique was always problematic. It is extremely difficult to achieve good convergence for a steady state analysis where some of the features of the flow have a tendency to behave in a time-varying way. This is true for the turbine model for the cylindrical pylon and the blade tips to mention just two. The results obtained from the steady state results were used as initial guesses for the transient no-wave models. On average the rated power and overspeed cases for the normal_spacing_model and the Half_spacing_model simulations took approximately 3.5 days to complete the total simulation time on a 16-processor job. It was evident from the initial transient no waves results that the results must be taken between the third and the

fourth revolution as the results were unsteady (in terms of achieving the cyclic behaviour of the model) between the first and the second revolutions. Approximately $400GB$ of disk space was used to store the transient files for these simulations.

On average the normal_spacing_model for the transient no waves models predicts the thrust, torque and power parameters to be 1.2times the steady state values. The steady state results have under predicted the simulation results. However this discrepancy must be examined with caution given the limited convergence obtained for the steady state results. The transient no waves rated power normal_spacing_model over predicts by approximately 10% when compared to the steady state results. The overspeed case over predicts by approximately 18%. The Half_spacing_model for the transient no waves over predicts by approximately 22%. The unsteady data reveals that the drag generated by the model is higher than the steady state predicted values and the power and torque generated by the turbine is also higher.

8.4 Transient Simulations - with waves

After the run of successful sets of transient no-wave simulations, it was decided that waves needed to be modelled to extend the realism of the model. The decision to employ only the horizontal component of the wave velocity particle was taken in the light of the fact that it is this component which essentially contributes to the thrust variations due to the wave effects. The focus on this form of loading arises from the basic concept of the turbine device, its freestanding nature. This is the reason why the axial loadings are above all, the main concern in this study.

The input of the boundary conditions were improved and enhanced by the addition of the CEL codes at the inlet rather than that of the interpolated file previously used in the models. As discussed in Chapter 7, due to the complexity of the simulation, the rated power cases for both the datum model and the shorter hub spacing model were made to rotate every 0.1 degree. The overspeed cases performed well with the 1.0 degree rotation. The storage space for the rated power and the overspeed cases for these cases were extremely large. As mentioned on Chapter 7, these cases were run on 16-processor jobs and yet took a very long to reach the final solution stage.

The torque variation for the rated power case for the normal_spacing_model and Half_spacing_model extreme wave is on average 1.5times and 1.4times the transient no-wave values respectively. The thrust variation for the extreme wave is about same for the transient no waves values for both types of models. The torque for the overspeed case normal_spacing_model and the Half_spacing_model extreme wave is about approximately 1.5 and 1.4 times the transient

no-wave values. The thrust for both models for the extreme wave is approximately 1.2times the no-wave transient values.

8.5 Future Work

The geometry of the blades employed in this study made the generation of the mesh an exceedingly involved affair. In addition the quality of the resultant mesh was lower than what is desirable. It is recommended that an improved mesh be created on a more griding tolerant geometry in a follow up study. In addition a mesh dependency study ought also to be conducted in order to identify the discretisation error in the model.

The inclusion of wave driven transient conditions ought to be extended to polychromatic waves, JONSWAP or Pierson-Moskowitz wave spectra. This could eventually be complemented by non-linear wave representation to characterise large storm conditions.

The effects of turbulence on the loadings of the rotor were mentioned before in an important paper by McCann. The inclusion of actual turbulence contributions, rather than modelled effects as done in this work, would require the employment of an LES model. With the LES method, time dependent equations are solved for the turbulent motion and are filtered in a way to remove very fine time and length scales. These methods require very fine grids and small timesteps and could give the structure of turbulent flows such as pressure fluctuations which cannot be obtained from a RANS formulation. In terms of blade loadings the contribution is due to large scale eddy structures which are described by LES with the turbulent motion at or near Kolmorogov scales being unimportant. To allow for the appropriate use of these models site specific turbulence data along with the site specific details of the BL velocity profiles with wave data must be available.

Lastly the employment of a varying rotational speed, reflecting the inertial behaviour of the machine to incident flow conditions, needs to be modeled. This would support an investigation into the “added mass” issue and is a highly recommended for the future work. When the turbine rotates through the fluid (water), a volume of the surrounding water is shifted, this adds inertia to the rotor system. This force can be significant and is dependent on the fluid density, radius of the rotor and the added mass coefficient. When the turbine accelerates the added mass increases, thereby greatly increasing the difficulty in the turbine system to yaw, if necessary. This will also change the response of the turbine system in dynamic unsteady conditions.

References

Ahlström, A. (2008), *Aeroelastic Simulation of Wind Turbine Dynamics*, PhD, Royal Institute of Technology, Sweden.

Akensivie, F. (2004), *In the Wake of a Marine Current Turbine*. MSc, University of Strathclyde, Glasgow.

Alinot, C. and Masson, C. (2005), "$k-\epsilon$ Model for the Atmospheric Boundary Layer Under Various Thermal Stratifications.", *Journal of Solar Energy Engineering*, vol. 127, no. 4, pp. 438-443.

Alinot, C. and Masson, C. (2002),*Aerodynamic simulations of wind turbines operating in atmospheric boundary layer with various thermal stratifications*, AIAA 2002-0042, American Institute of Aeronautics and Astronautics, Nevada.

Amaral Teixeira, J., (2010), *Discussion on the comparisons of steady state solutions and transient solutions with and without waves*, Cranfield University.

Amaral Teixeira, J., (2008), *Discussion on the aspects of numerically modelling the HATT*, Cranfield University.

ANSYS-CFX (2009), *ANSYS CFX Release 12.1 User Manual*, ANSYS.

ANSYS-CFX (2007), *ANSYS CFX Release 11.0 User Manual*, ANSYS.

ANSYS-CFX (2005), *ANSYS CFX Release 10.0 User Manual*, ANSYS.

Baddour, E. (2004), *Energy from waves and tidal currents towards 20yy*, Institute for Ocean Technology, National Research Council, Canada.

Bahaj, A. S., Batten, W. M. J. and McCann, G. (2007a), "Experimental verifications of numerical predictions for the hydrodynamic performance of horizontal axis marine current turbines", *Journal of Renewable Energy*, vol. 32, no. 15, pp. 2479-2490.

Bahaj, A. S., Molland, A. F., Chaplin, J. R. and Batten, W. M. J. (2007b), "Power and thrust

measurements of marine current turbines under various hydrodynamic flow conditions in a cavitation tunnel and a towing tank", *Renewable Energy*, vol. 32, no. 3, pp. 407-426.

Bahaj, A. S. and Myers, L. (2006), "Wake studies of a 1/30th scale horizontal axis marine current turbine", *Ocean Engineering*, vol. 34, pp. 758-762.

Bahaj, A. S. and Myers, L. E. (2003), "Fundamentals applicable to the utilisation of marine current turbines for energy production", *Renewable Energy*, vol. 28, no. 14, pp. 2205-2211.

Bahaj, A. S., Myers, L. E., Jorge, N. and Thomson, M. D. (2007c), "Characterising the wake of horizontal axis marine current turbines", *Proceedings of the 7th Wave and Tidal Energy Conference*, Porto, Portugal.

Baker, A. C. (1991), *Tidal Power*, 1st Ed, Peter Peregrinus Ltd., London.

Baldock, A. (2005), *Tidal Stream Energy Resource and Technology Summary Report*, 107799/D/2200/04, Carbon Trust, UK.

Balme, R., Le Saux, K., Elghali, B. S. E., Benbouzid, M. E. H., Charpentier, J. F., Hauville, F. and Drouen, L. (2007), "A Simulation Model for the Evaluation of the Electrical Power Potential Harnessed by a Marine Current Turbine in the Raz de Sein", *IEEE Journal of Oceanic Engineering*, vol. 32, no. 4, pp. 786-797.

Barltrop, N., Varyani, K. S., Grant, A., Clelland, D. and Pham, X. (2006), "Wave-current interactions in marine current turbines", *Proceedings of the Institution of Mechanical Engineers, Part M: Journal of Engineering for the Maritime Environment*, vol. 220, no. 4, pp. 195-203.

Batten, W. M. J., Bahaj, A. S., Molland, A. F. and Chaplin, J. R. (2008), "The prediction of hydrodynamic performance of marine current turbines", *Renewable Energy*, vol. 33, no. 5, pp. 1085-1096.

Billingham, J. and King, A. C. (2000), *Wave Motion*, 1st Ed, Cambridge University Press, UK.

Bowditch, N. (1995), *The American Practical Navigator - An Epitome of Navigation*, National Imagery and Mapping Agency, US.

Burchard, H., Craig, P. D., Gemmrich, J. R., Hans van, H., Mathieu, P., Markus Meier, H. E., Nimmo Smith, W. A. M., Prandke, H., Rippeth, T. P., Skyllingstad, E. D., Smyth, W. D., Welsh, D. J. S. and Wijesekera, H. W. (2008), "Observational and numerical modeling methods for quantifying coastal ocean turbulence and mixing", *Progress in Oceanography*,

vol. 76, pp. 399-442.

Butterfield, S. (2008), *Wind Turbine Dynamics: Workshop on Research Needs for Wind Resource Characterisation*, , National Renewable Energy Laboratory, US.

Carbon Trust (2005), *Tidal streams and tidal stream energy device design*, Carbon Trust, UK.

Carpenter, C. (1996), *Flightwise*: Principles of Aircraft Flight, 1st Ed, The Crowood Press Ltd, UK.

Chapman, J., Masters, I. and Orme, J. A. C. (2006), "Rotor Performance Prediction for Tidal Current Turbines", *A Joint Conference of the Association for Computational Mechanics in Engineering (UK) and the Irish Society for Scientific and Engineering Computation*, April 2006, Belfast, N. Ireland, Queen's University, Queen's University, Belfast, pp. 103.

Davidson, P. A. (2004), *Turbulence - An introduction to Scientist and Engineers*, 1st Ed, Oxford University Press, Oxford.

Dean, R. G. and Dalrymple, R. A. (1991), *Advanced Series on Ocean Engineering - Water Wave Mechanics for Engineers and Scientists*, Volume 2, World Scientific Publishing Co. Ltd., Singapore.

Deardorff, J. W. (1970), "A numerical study of three-dimensional turbulent channel flow at large Reynolds numbers", *Journal of Fluid Mechanics*, vol. 41, no. 2, pp. 453-480.

Douglas, J. F., Gasiorek, J. M., Swaffield, J. A. and Jack, L. B. (2005), *Fluid Mechanics*, 5th Ed, Pearson Education Limited, England.

DTI (2007), *Economic Viability of a Simple Tidal Stream Energy Capture Device*, TP/2/ERG/6/1/15527/REP, DTI Technology Programme, UK.

Egarr, D. A., O'Doherty, T., Morris, S. and Ayre, R. G. (2004), "Feasibility study using computational fluid dynamics for the use of a Turbine for extracting energy from the tide", Behnia, M., Lin, W. and McBain, G. D., *Proceedings of the fifteenth Australasian Fluid Mechanics conference*, 13-17 December 2004, Sydney, The University of Sydney, Sydney, Australia.

Fan, R., Chaplin, J. R. and Yang, G. (2010), "CFD Investigation of performance for Marine Current Turbine based on RANS simulations", *Key Engineering Materials*, vol. 419-420, pp. 309-312.

Freeman, C., (2009a), *Discussion on the comparison of the steady state CFD results with the steady state 2D BEMT based results*, Cranfield University.

Freeman, C. and Amaral Teixeira, J., (2009b), *Discussion on the physics of turbulence, boundary layer profiles and waves*, Cranfield University.

Freeman, C., Amaral Teixeira, J. and Day, I. J. (2009c), "Design of a Gravity Stabilised Fixed Pitch Tidal Turbine of $400kW$", *Proceedings of the 8th European Wave and Tidal Energy Conference*, 9 September 2009, Uppsala, Sweden, Uppsala University, Sweden, pp. 376.

Griffiths, R. T. and Woollard, M. G. (1978), "Performance of the Optimal Wind Turbine", *Applied Energy*, vol. 4, no. 4, pp. 261-272.

Groeneweg, J. and Battjes, J. A. (2003), "Three-dimensional wave effects on a steady current.", *Journal of Fluid Mechanics*, vol. 478, pp. 325-343.

Guéna, F., Daviau, J., Majastre, H., Bischoff, V., Ruer, J. and Tartivel, C. (2006), "Design and operational features of a tidal stream turbine", *Offshore Wind and other marine renewable Energies in Mediterrenean and European Seas (OWEMES)*, 20-22 April 2006, Italy, OWEMES, Rome.

Hammons, T. J. (1993), "Tidal Power", *Proceedings of the IEEE*, vol. 81, no. 3, pp. 419-433.

Hau, E. (2003), *Wind Turbines: Fundamentals, Technologies, Application, Economics*, 2nd Ed, Springer-Verlag Berlin Springer, Germany.

Holmes, B. and Brydan, I. (2003), "Tidal Stream Instability", *Proceedings of the 5th European Wave Energy Conference*, 17-20 September, University College Cork, Ireland, Hydraulics & Maritime Research Centre, Cork, Ireland.

Janajreh, I., Talab, I. and Macpherson, J., (2010), *Numerical Simulation of Tower Rotor Interaction for Downwind Wind Turbine*, Article ID 860814, Hindawi Publishing Corporation.

Johnstone, C. M., Nielsen, K., Lewis, T., Sarmento, A. and Lemonis, G. (2006), "EC FPVI co-ordinated action on ocean energy: A European platform for sharing technical information and research outcomes in wave and tidal energy systems.", *Journal of Renewable Energy*, vol. 31, no. 2, pp. 191-196.

Jonsson, I. G. (1990), "Wave-current interactions", in Le Mehauté, B. and Hanes, D. M. (eds.) The Sea - *Ocean Engineering Science*, Volume 9, Wiley, US, pp. 65-120.

Kemp, P. H. and Simons, R. R. (1983), "The interaction between waves and currents. Waves propagating against the current", *Journal of Fluid Mechanics*, vol. 130, pp. 73-89.

Le Gouriérès, D. (2008), *Les éoliennes : Théorie, conception et calcul pratique*, Editions Du Moulin Cadiou, France.

Lilly, D. K. (1967), "The representation of small-scale turbulence in numerical simulation experiments", *In Proceedings of the IBM Scientific Computing Symposium on Environmental Sciences*, Nov 14 - 16, NY, Yorktown Heights, pp. 195.

Marsh, G. (2004), "Tidal turbines harness the power of the sea", *Reinforced Plastics*, vol. 48, no. 6, pp. 44-47.

Masters, I., Orme, J. A. C. and Chapman, J. (2007), "Towards Realistic Marine flow conditions for tidal stream turbines", *Proceedings of the 7th European Wave And Tidal Energy Conference*, Porto, Portugal.

McCann, G. N. (2007), "Tidal current turbine fatigue loading sensitivity to wave and turbulence - a parametric study", *Proceedings of the 7th European Wave And TIdal Energy Conference*, Porto, Portugal.

McNerney, G. M., van Dam, C. P. and Yen-Nakafuji, D. T. (2003), *Blade-wake interaction noise for turbines with downwind rotors*, AIAA 2003-1184, American Institute of Aeronautics and Astronautics.

Murtagh, P. J., Basu, B. and Broderick, B. M. (2005), "Along-wind response of a wind turbine tower with blade coupling subjected to rotationally sampled wind loading", *Engineering Structures*, vol. 27, pp. 1209-1219.

Nezu, I. and Nakagawa, H. (1995), "Turbulence measurements in unsteady free-surface flows." *Flow Measuring Instruments*, vol. 6, no. 1, pp. 49-59.

Nicholls-Lee, R. F. and Turnock, S. R. (2007), *Enhancing Performance of a Horizontal Axis Tidal Turbine Using Adaptive Blades*, Oceans 2007 - Europe, Institute of Electrical and Electronics Engineers, UK.

NOAA Tides and Currents (2010), *Spring and Neap tides*, available at: http://co-ops.nos.noaa.gov/images/restfig3.gif (accessed 05/12).

Open University (2010b), *A typical C_L & C_D variation for an aerofoil*, available at: http://weblab.open.ac.uk/firstflight/graphs (accessed 07/20).

Open University (2010a), *Positive and negative pressure gradients on an aerofoil*, available at: http://weblab.open.ac.uk/firstflight/forces/ (accessed 07/20).

Pelamis Wave Power (2008), *Wave Energy Resource*, available at: http://www.pelamiswave.com/wave-energy/the-resource (accessed 10/27).

Peregrine, D. H. (1976), "Interaction of water waves and currents", *Advances in Applied Mechanics*, vol. 16, no. C, pp. 9-117.

Pesmajoglou, S. D. and Graham, J. M. R. (2000), "Prediction of aerodynamic forces on horizontal axis wind turbines in free yaw and turbulence", *Journal of Wind Engineering and Industrial Aerodynamics*, vol. 86, pp. 1-14.

Pessé, M. (2008), *Review And Assessment of Carbon Dioxide Capture Technologies For Existing Pulverised Coal-Fired Power Plants*, MSc, Cranfield University, Bedfordshire.

Piomelli, U. (1999), "Large eddy simulation:achievements and challenges", *Progress in Aerospace Sciences*, vol. 35, pp. 335-362.

Ranga, D. K. K. J. (2009), *Advanced Turbulence Models: Large Eddy Simulations*, Computational Engineering Techniques for Industrial Processes, Applied Mathematics and Computing Group, Cranfield University, Bedfordshire.

Schumann, U. (1975), "Subgrid Scale Model for Finite Difference Simulations of Turbulent Flows in Plane Channels and Annuli", *Journal of Computational Physics*, vol. 18, pp. 376-404.

Simms, D., Schreck, S., Hand, M. and Fingersh, L. J. (2001), *NREL Unsteady Aerodynamics Experiment in the NASA-Ames Wind Tunnel: A Comparison of Predictions to Measurements*, NREL/TP-500-29494, National Renewable Energy Laboratory, US.

Smagorinsky, J. (1963), "General circulation experiments with the primitive equations, the basic experiment", *Monthly Weather Review*, vol. 91, no. 3, pp. 99-164.

Sustainable Development Commission (2007), *Turning the tide - Tidal Power in the UK*, SDC, UK.

Thai Marine Meteorological Centre (2010), *The types of tides*, available at: http://www.marine.tmd.go.th/marinemet_html/wwr249.gif (accessed 05/10).

Thai Technics (2008), Blade element nomenclature, available at: http://www.thaitechnics.com/propeller/prop_intro.html (accessed 03/10).

The University of Maine (2010), Wave nomenclature, available at: http://misclab.umeoce.maine.edu/boss/classes/SMS_491_2003/waves/wave_a.jpg (accessed 07/06).

Thomas, G. P. (2003), "On the importance of wave-current interactions to tidal stream and marine current generators.", *Proceedings of the Fifth European Wave Energy Conference*, 17-20 September, Cork, Ireland, Hydraulics & Maritime Research Centre, Cork, Ireland, pp. 167.

Thomas, G. P. and Klopman, G. (1997), "Wave-current interactions in the near-shore region", in Hunt, J. N. (ed.) Gravity waves in water of finite depth, *Advances in Fluid Mechanics*, Computational Mechanics Publications, UK, pp. 255-319.

Tucker, M. J. (1991), "Chapter 8", in *Waves in Ocean Engineering, measurement analysis, interpretation*, 4th Ed, Ellis Horwood Limited, New York, pp. 231-266.

Versteeg, H. and Malalasekera, W. (1995), *An introduction to Computational Fluid Dynamics*. 2nd Ed, Pearson Education Limited, England.

Von Karman Institute for Fluid Dynamics (2000b), *Introduction to the modelling of turbulence*. Lecture Series (2000-2004), Von Karman Institute for Fluid Dynamics, Belgium.

Von Karman Institute for Fluid Dynamics (2000a), *Introduction to the modelling of turbulence*. Lecture Series (1997-2003), Von Karman Institute for Fluid Dynamics, Belgium.

Webb, I., Seaman, C. and Jackson, G. (2005), *Marine Energy challenge - "Oscillating Water Column Wave Energy Converter Evaluation Report"*, 115214-00, Carbon Trust, U.K.

www.geographical.co.uk - Royal Geographical Society (with the Institute of British Geographers), (2003),*Setting the agenda for the UK's green-energy future*, Renewable-energy special ed., Circle Publishing Ltd, London.

Zahle, F., Johansen, J. and Sorensen, N. (2009), "Wind turbine rotor-tower interaction using an incompressible overset grid method", *Wind Energy*, vol. 12, no. 6, pp. 594-619.

Bibliography

Anwar, H. O. (1981), "A study of the turbulent structure in a tidal flow." *Estuarine, Coastal and Shelf Science*, vol. 13, no. 4, pp. 373-387.

Anwar, H. O. and Atkins, R. (1980), "Turbulence Measurements in Simulated Tidal Flow." *Journal of the Hydraulics Division*, vol. 106, no. 8, pp. 1273-1289.

Baker, A. C. and Wishart, S. J. (1986), "Tidal power for small estuaries", *Third International Symposium on Wave, Tidal, OTEC and Small Scale Hydro Energy "Water for Energy"*, Brighton, UK, pp. 115.

Bernard, P. S. and Wallace, M. (2002), *Turbulent Flow: Analysis, Measurement and Prediction*, 1st Ed, John Wiley & Sons Ltd., United States.

Biran, A. and Breiner, M. (2002), *MatLab 6 for Engineers*, 3rd Ed, Pearson Education Limited.

Bowden, K. F. (1962), "Measurements of Turbulence near the Sea Bed in a Tidal Current." *Journal of Geophysical Research*, vol. 67, no. 8, pp. 3181-3186.

Boyle, G. (2004), *Renewable Energy*, 2nd Ed, Oxford University Press, Oxford.

Brighenti, A. (2008),*Numerical Investigation of OWC Buoys*, MSc, Cranfield University, Bedfordshire.

Brodeur, P. and Masson, C. (2006), *Numerical simulations of wind distributions over very complex terrain*. AIAA 2006-1362, American Institute of Aeronautics and Astronautics, Nevada.

Burton, T., Sharpe, D., Jenkins, N. and Bossanyi, E. (2001), *Wind Energy Handbook*, 1st Ed, John Wiley & Sons Ltd., UK.

Cohen, H., Rogers, G. F. C., Saravanamuttoo, H. I. H. and Straznicky, P. V. (2008), *Gas Turbine Theory*, 6th Ed, Prentice Hall, UK.

Davies, A. M. (1986), "A Three-Dimensional Model of the Northwest European Continental Shelf, with Application to the M4 Tide", *Journal of Physical Oceanography*, vol. 16, no. 5, pp. 797-813.

Falnes, J. (2002), *Ocean Waves and Oscillating Systems*, 1st Ed, Cambridge University Press, UK.

Fantini, E. (2007), *Free Surface Flow CFD Simulation for Developing the OWC Technology*, MSc, Cranfield University, Bedfordshire.

Gasch, R. and Twele, J. (2002), *Wind Power Plants: Fundamentals, Design, Construction and Operation*, Solarpraxis AG, Germany, Berlin.

Groeneweg, J. (1999), *Wave-current interactions in a generalized Lagrangian mean formulation*, PhD, Delft University of Technology, Netherlands.

Groeneweg, J. and Klopman, G. (1998), "Changes in mean velocity profiles in the combined wave-current motion described in GLM formulation.", *Journal of Fluid Mechanics*, vol. 370, no. 1, pp. 271-296.

Hahn, M. (2008), *Implicit Large-Eddy Simulation of Low-Speed Separated Flows Using High-Resolution Methods*, PhD, Cranfield University, Bedfordshire.

Heathershaw, A. D. (1979), "The turbulent structure of the bottom boundary layer in a tidal current." *Geophysical Journal of the Royal Astronomical Society*, vol. 58, no. 2, pp. 395-430.

Kreyszig, E. (2005), *Advanced Engineering Mathematics*, 9th Ed, John Wiley & Sons, US.

Lamport, L. (2001), *A Document Preparation System LATEX- User's Guide and Reference Manual*, 2nd Ed, Addison-Wesley, US.

Manwell, J. F., McGowan, J. G. and Rogers, A. L. (2002), *Wind Energy Explained - Theory, Design and Application*, John Wiley & Sons Ltd., England.

Nettel, S. (1992), *Wave Physics*, 1st Ed, Springer-Verlag, US.

Patel, M. (1989), *Dynamics of offshore structures*, 1st Ed, Butterworths, London.

Pope, S. (2000), *Turbulent Flows*. 1st Ed, Cambridge University Press, Cambridge.

Sanderse, B. (2009), *Aerodynamics of wind turbine wakes*, ECN-e–09-016, Energy Research Centre of the Netherlands, Netherlands.

Schlichting, H. (1979), *Boundary Layer Theory*, 7th Ed, McGraw Hill, Berlin.

Srensen, B. (2000), *Renewable Energy*, 2nd Ed, Academic Press, UK.

Szasz, R. Z. and Fuchs, L. (2010), *Computations of the Flow around a Wind Turbine: Grid Sensitivity Study and the Influence of Inlet Conditions*, DOI: 10.1007/978-3-642-14139-

3_42, SpringerLink.

The Open University (1984), *Mathematical Methods and Fluid Mechanics - UNIT 13 - The wave equation*, 1st Ed, The Open University Press, UK.

The Open University (1984), *Mathematical Methods and Fluid Mechanics - UNIT 14 - Water waves*, 1st Ed, The Open University Press, UK.

Thorpe, S. A. (2007), *An Introduction to Ocean Turbulence*, 1st Ed, Cambridge University Press, UK.

Tritton, D. J. (2007), *Physical Fluid Dynamics*, 2nd Ed, Oxford University Press, UK.

Williams, J. J., Thorne, P. D. and Heathershaw, A. D. (1989), "Measurements of turbulence in the benthic boundary layer over a gravel bed." *Sedimentology*, vol. 36, no. 6, pp. 959-971.

Appendices

Appendix A

Appendices for Chapter 4

[Data]					
x [m]	y [m]	z [m]	u [m s^-	v [m s^-	w [m s^-1]
-11	-20	-13.75	0	0	0
-11	-20	-13.25	1.4716	0	0
-11	-20	-12.75	1.6247	0	0
-11	-20	-12.25	1.7216	0	0
-11	-20	-11.75	1.7939	0	0
-11	-20	-11.25	1.852	0	0
-11	-20	-10.75	1.9008	0	0
-11	-20	-10.25	1.9432	0	0
-11	-20	-9.75	1.9806	0	0
-11	-20	-9.25	2.0142	0	0
-11	-20	-8.75	2.0447	0	0
-11	-20	-8.25	2.0728	0	0
-11	-20	-7.75	2.0987	0	0
-11	-20	-7.25	2.1228	0	0
-11	-20	-6.75	2.1454	0	0
-11	-20	-6.25	2.1667	0	0
-11	-20	-5.75	2.1867	0	0
-11	-20	-5.25	2.2058	0	0
-11	-20	-4.75	2.2238	0	0
-11	-20	-4.25	2.2411	0	0
-11	-20	-3.75	2.2576	0	0
-11	-20	-3.25	2.2734	0	0
-11	-20	-2.75	2.2885	0	0
-11	-20	-2.25	2.3031	0	0
-11	-20	-1.75	2.3171	0	0
-11	-20	-1.25	2.3307	0	0
-11	-20	-0.75	2.3438	0	0
-11	-20	-0.25	2.3565	0	0
-11	-20	0.25	2.3687	0	0
-11	-20	0.75	2.3806	0	0
-11	-20	1.25	2.3922	0	0
-11	-20	1.75	2.4034	0	0
-11	-20	2.25	2.4143	0	0
-11	-20	2.75	2.425	0	0
-11	-20	3.25	2.4353	0	0
-11	-20	3.75	2.4455	0	0
-11	-20	4.25	2.4553	0	0
-11	-20	4.75	2.4649	0	0
-11	-20	5.25	2.4744	0	0
-11	-20	5.75	2.4836	0	0
-11	-20	6.25	2.4926	0	0
-11	-20	6.75	2.5014	0	0
-11	-20	7.25	2.51	0	0
-11	-20	7.75	2.5184	0	0
-11	-20	8.25	2.5267	0	0
-11	-20	8.75	2.5348	0	0
-11	-20	9.25	2.5428	0	0
-11	-20	9.75	2.5506	0	0
-11	-20	10.25	2.5583	0	0
-11	-20	10.75	2.5659	0	0
-11	-20	11.25	2.5733	0	0
-11	-20	11.75	2.5806	0	0
-11	-20	12.25	2.5877	0	0
-11	-20	12.75	2.5948	0	0
-11	-20	13.25	2.6017	0	0
-11	-20	13.75	2.6086	0	0
-11	-20	14.25	2.6153	0	0

Figure A.1 BL velocity profile

Hub diameter $3.0m$											
Section	1	2	3	4	5	6	7	8	9	10	11
Distance from root (m)	0	0.6	1.2	1.8	2.4	3.0	3.6	4.2	4.8	5.4	6.0
Chord (m)	1.913	1.913	1.931	1.935	1.901	1.837	1.674	1.347	0.748	0.44	0.44
Twist (deg)	26.07	26.07	23.02	20.25	16.16	14.29	12.8	11.8	11.07	10.94	10.94
Thickness $(\%)$	15.65	15.65	15.44	15.22	14.64	14.08	12.85	10.56	5.75	3.38	3.38
Pitch Axis $(\%)$	50	50	50	50	50	50	50	50	50	50	50
Twist Axis $(\%)$	50	50	50	50	50	50	50	50	50	50	50
Pre-Bend (m)	0	0	0	0	0	0	0	0	0	0	0
Cross-sectional area (m^2)	0.394	0.394	0.394	0.389	0.360	0.323	0.245	0.130	0.021	0.004	0.004

Table A.1 NACA0015 Blade Profile

Appendix B

Appendices for Chapter 5

2 m/s profile boundary condition

[Name]
Profile2ms
[Spatial Fields]
x y z
[Data]

x [m]	y [m]	z [m]	u [m s^-1]	v [m s^-1]	w [m s^-1]	ke [m^2 s^-2]	ed [m^2 s^-3]
-11	-20	-13.75	0	0	0	0	0
-11	-20	-13.25	1.471561	0	0	0.440534662	0.0151954
-11	-20	-12.75	1.624735	0	0	0.279911318	0.00769613
-11	-20	-12.25	1.721625	0	0	0.214687354	0.00516954
-11	-20	-11.75	1.793853	0	0	0.177852852	0.00389792
-11	-20	-11.25	1.851958	0	0	0.153692968	0.00313129
-11	-20	-10.75	1.900828	0	0	0.136410198	0.00261826
-11	-20	-10.25	1.943151	0	0	0.123323122	0.00225065
-11	-20	-9.75	1.980575	0	0	0.113005923	0.00197421
-11	-20	-9.25	2.014182	0	0	0.104624367	0.0017587
-11	-20	-8.75	2.044728	0	0	0.097654974	0.00158593
-11	-20	-8.25	2.072759	0	0	0.091751195	0.00144431
-11	-20	-7.75	2.098684	0	0	0.086673675	0.00132609
-11	-20	-7.25	2.12282	0	0	0.082251317	0.0012259
-11	-20	-6.75	2.145413	0	0	0.078358278	0.00113991
-11	-20	-6.25	2.166663	0	0	0.074899751	0.00106528
-11	-20	-5.75	2.186732	0	0	0.071802833	0.0009999
-11	-20	-5.25	2.205752	0	0	0.069010462	0.00094214
-11	-20	-4.75	2.223837	0	0	0.066477276	0.00089074
-11	-20	-4.25	2.24108	0	0	0.064166725	0.00084471
-11	-20	-3.75	2.257562	0	0	0.062048994	0.00080324
-11	-20	-3.25	2.273353	0	0	0.060099504	0.00076568
-11	-20	-2.75	2.288511	0	0	0.058297791	0.00073151
-11	-20	-2.25	2.30309	0	0	0.056626669	0.00070028
-11	-20	-1.75	2.317135	0	0	0.055071586	0.00067164
-11	-20	-1.25	2.330687	0	0	0.053620136	0.00064526
-11	-20	-0.75	2.343783	0	0	0.052261664	0.00062089
-11	-20	-0.25	2.356453	0	0	0.050986972	0.00059832
-11	-20	0.25	2.368728	0	0	0.049788066	0.00057734
-11	-20	0.75	2.380632	0	0	0.048657968	0.00055779
-11	-20	1.25	2.39219	0	0	0.047590553	0.00053954
-11	-20	1.75	2.403422	0	0	0.046580424	0.00052245
-11	-20	2.25	2.414347	0	0	0.045622802	0.00050643
-11	-20	2.75	2.424984	0	0	0.044713442	0.00049136
-11	-20	3.25	2.435348	0	0	0.043848557	0.00047717
-11	-20	3.75	2.445454	0	0	0.043024757	0.00046379
-11	-20	4.25	2.455315	0	0	0.042238996	0.00045114
-11	-20	4.75	2.464945	0	0	0.041488535	0.00043917
-11	-20	5.25	2.474353	0	0	0.040770895	0.00042783
-11	-20	5.75	2.483552	0	0	0.040083833	0.00041706
-11	-20	6.25	2.492551	0	0	0.03942531	0.00040682
-11	-20	6.75	2.501359	0	0	0.038793472	0.00039708
-11	-20	7.25	2.509985	0	0	0.038186624	0.0003878
-11	-20	7.75	2.518436	0	0	0.037603218	0.00037895
-11	-20	8.25	2.526721	0	0	0.037041834	0.00037049
-11	-20	8.75	2.534846	0	0	0.036501167	0.00036241
-11	-20	9.25	2.542817	0	0	0.035980019	0.00035468
-11	-20	9.75	2.550642	0	0	0.035477282	0.00034727
-11	-20	10.25	2.558325	0	0	0.034991935	0.00034017
-11	-20	10.75	2.565872	0	0	0.034523032	0.00033335
-11	-20	11.25	2.573288	0	0	0.034069698	0.00032681

Figure B.1 BL velocity profile with 5% TI profile

# 2 m/s profile boundary condition					
[Name]					
Profile2ms					
[Spatial Fields]					
x	y	z			
[Data]					
x [m]	y [m]	z [m]	u [m s^-	v [m s^-	w [m s^
-11	-20	-13.75	0	0	0
-11	-20	-13.25	1.4492	0.2555	0
-11	-20	-12.75	1.6001	0.2821	0
-11	-20	-12.25	1.6955	0.299	0
-11	-20	-11.75	1.7666	0.3115	0
-11	-20	-11.25	1.8238	0.3216	0
-11	-20	-10.75	1.872	0.3301	0
-11	-20	-10.25	1.9136	0.3374	0
-11	-20	-9.75	1.9505	0.3439	0
-11	-20	-9.25	1.9836	0.3498	0
-11	-20	-8.75	2.0137	0.3551	0
-11	-20	-8.25	2.0413	0.3599	0
-11	-20	-7.75	2.0668	0.3644	0
-11	-20	-7.25	2.0906	0.3686	0
-11	-20	-6.75	2.1128	0.3725	0
-11	-20	-6.25	2.1337	0.3762	0
-11	-20	-5.75	2.1535	0.3797	0
-11	-20	-5.25	2.1722	0.383	0
-11	-20	-4.75	2.1901	0.3862	0
-11	-20	-4.25	2.207	0.3892	0
-11	-20	-3.75	2.2233	0.392	0
-11	-20	-3.25	2.2388	0.3948	0
-11	-20	-2.75	2.2537	0.3974	0
-11	-20	-2.25	2.2681	0.3999	0
-11	-20	-1.75	2.2819	0.4024	0
-11	-20	-1.25	2.2953	0.4047	0
-11	-20	-0.75	2.3082	0.407	0
-11	-20	-0.25	2.3207	0.4092	0
-11	-20	0.25	2.3327	0.4113	0
-11	-20	0.75	2.3445	0.4134	0
-11	-20	1.25	2.3558	0.4154	0
-11	-20	1.75	2.3669	0.4173	0
-11	-20	2.25	2.3777	0.4192	0
-11	-20	2.75	2.3881	0.4211	0
-11	-20	3.25	2.3983	0.4229	0
-11	-20	3.75	2.4083	0.4246	0
-11	-20	4.25	2.418	0.4264	0
-11	-20	4.75	2.4275	0.428	0
-11	-20	5.25	2.4368	0.4297	0
-11	-20	5.75	2.4458	0.4313	0
-11	-20	6.25	2.4547	0.4328	0
-11	-20	6.75	2.4634	0.4344	0
-11	-20	7.25	2.4719	0.4359	0
-11	-20	7.75	2.4802	0.4373	0
-11	-20	8.25	2.4883	0.4388	0
-11	-20	8.75	2.4963	0.4402	0
-11	-20	9.25	2.5042	0.4416	0
-11	-20	9.75	2.5119	0.4429	0
-11	-20	10.25	2.5195	0.4442	0
-11	-20	10.75	2.5269	0.4456	0
-11	-20	11.25	2.5342	0.4468	0
-11	-20	11.75	2.5414	0.4481	0

Figure B.2 BL velocity profile with the 10° yaw

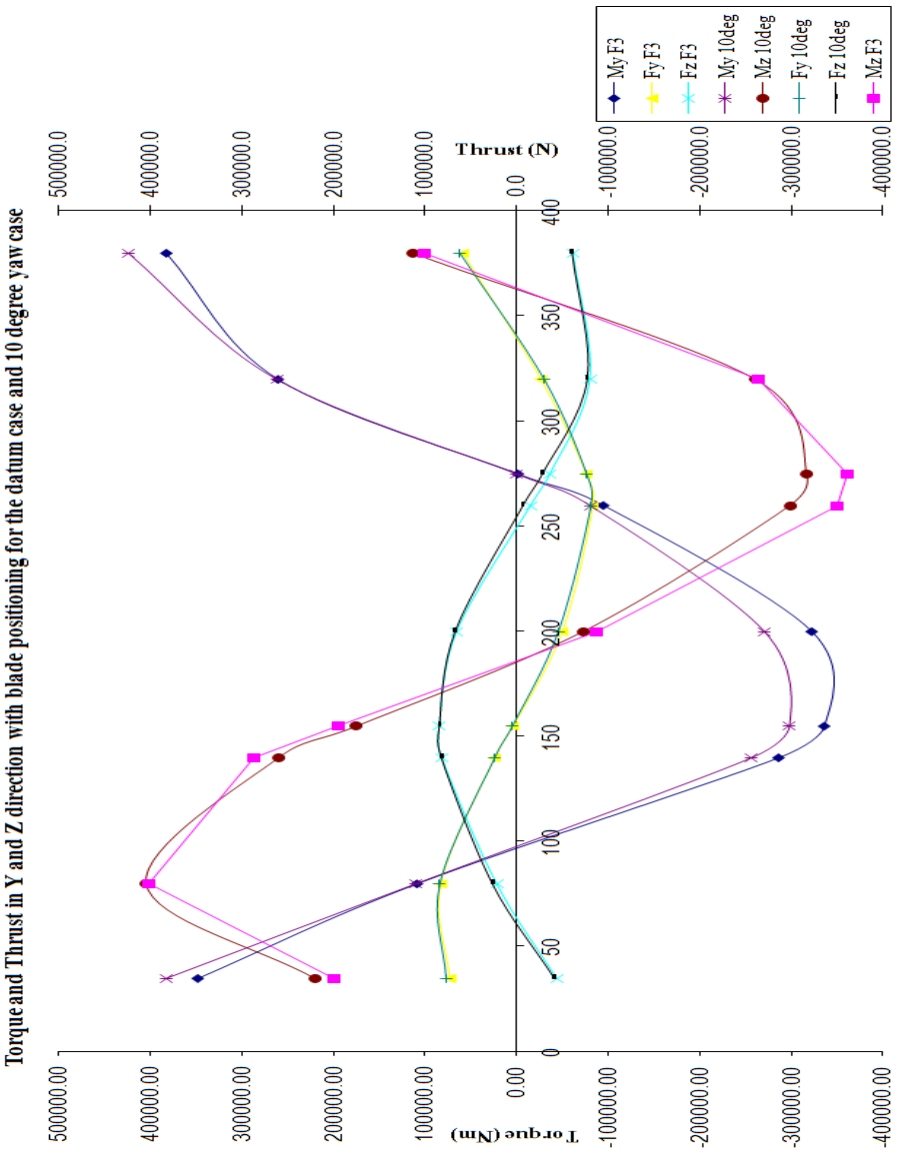

Figure B.3 Comparison of thrust and torque about Y and Z axes for 10° yaw case and standard case

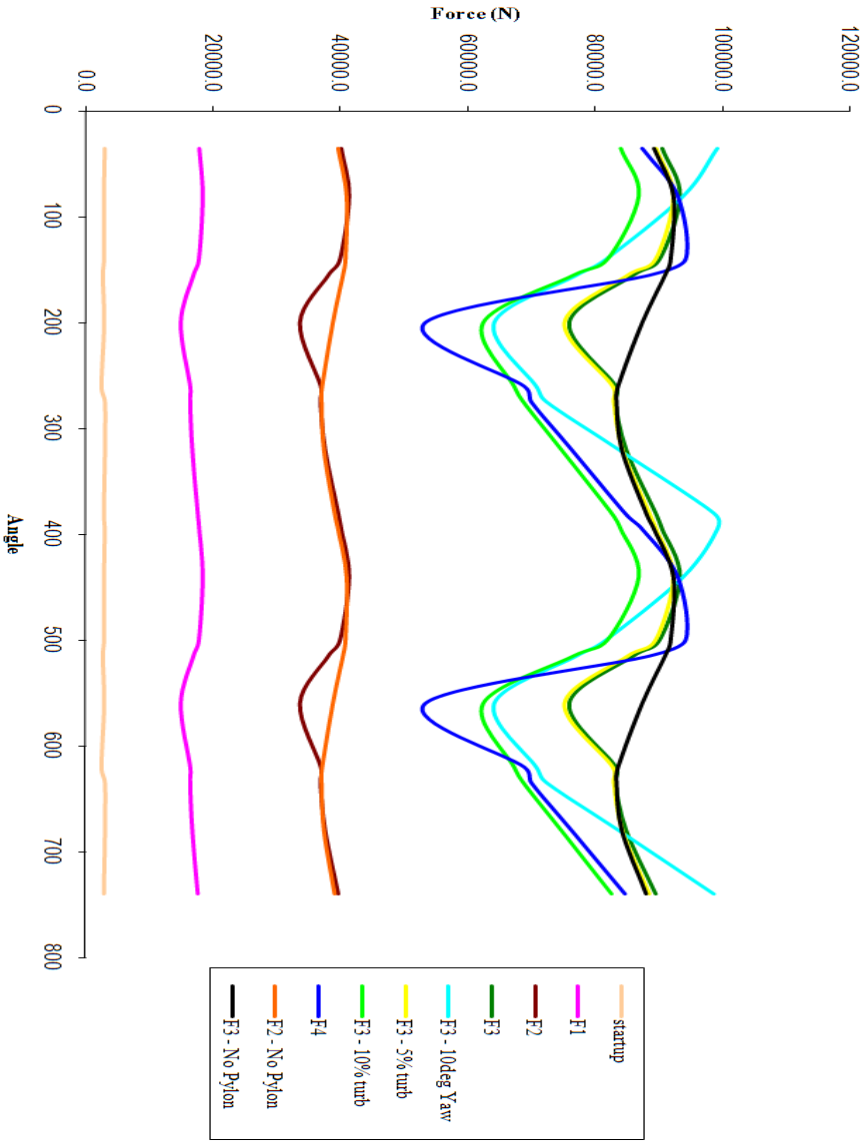

Figure B.4 Comparison of axial thrust for all CFD models

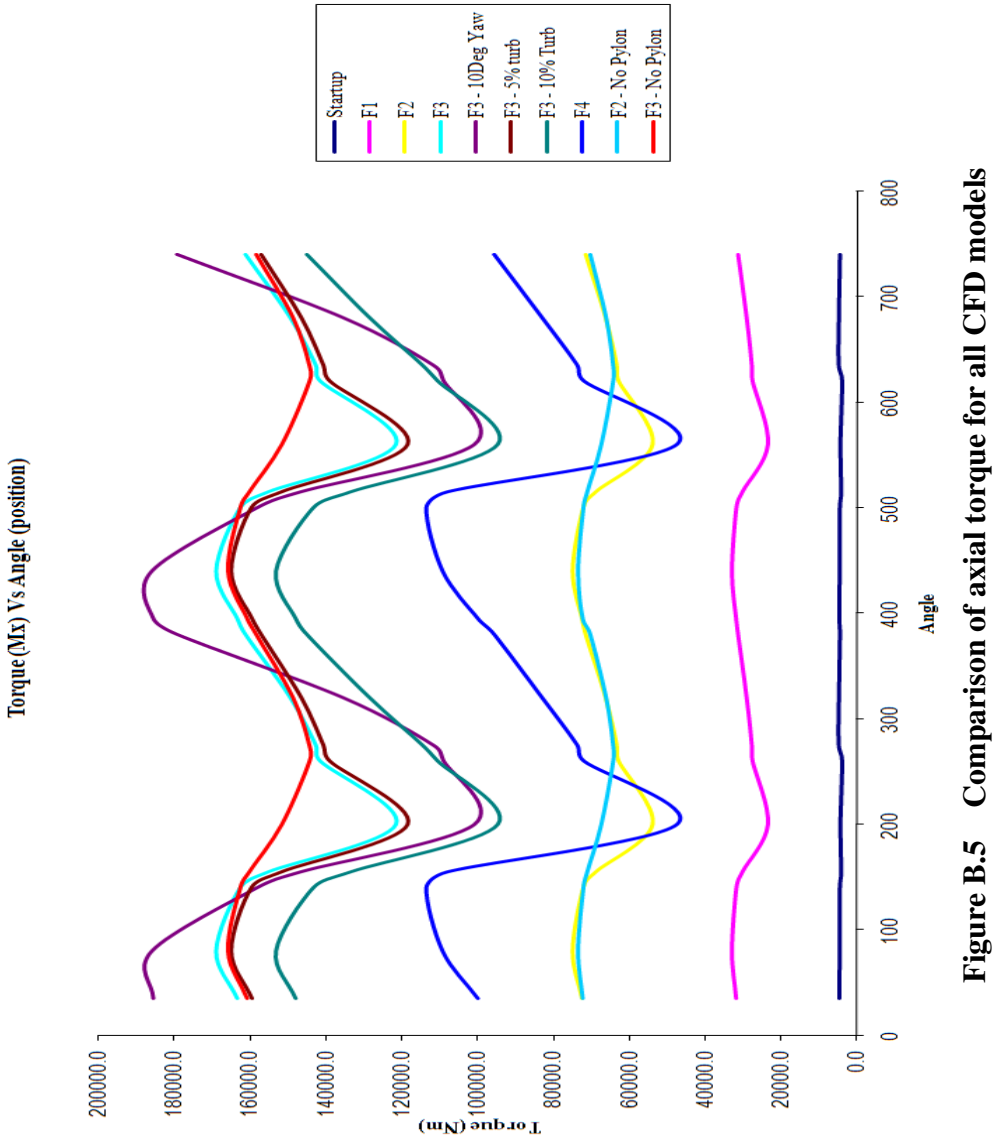

Figure B.5 Comparison of axial torque for all CFD models

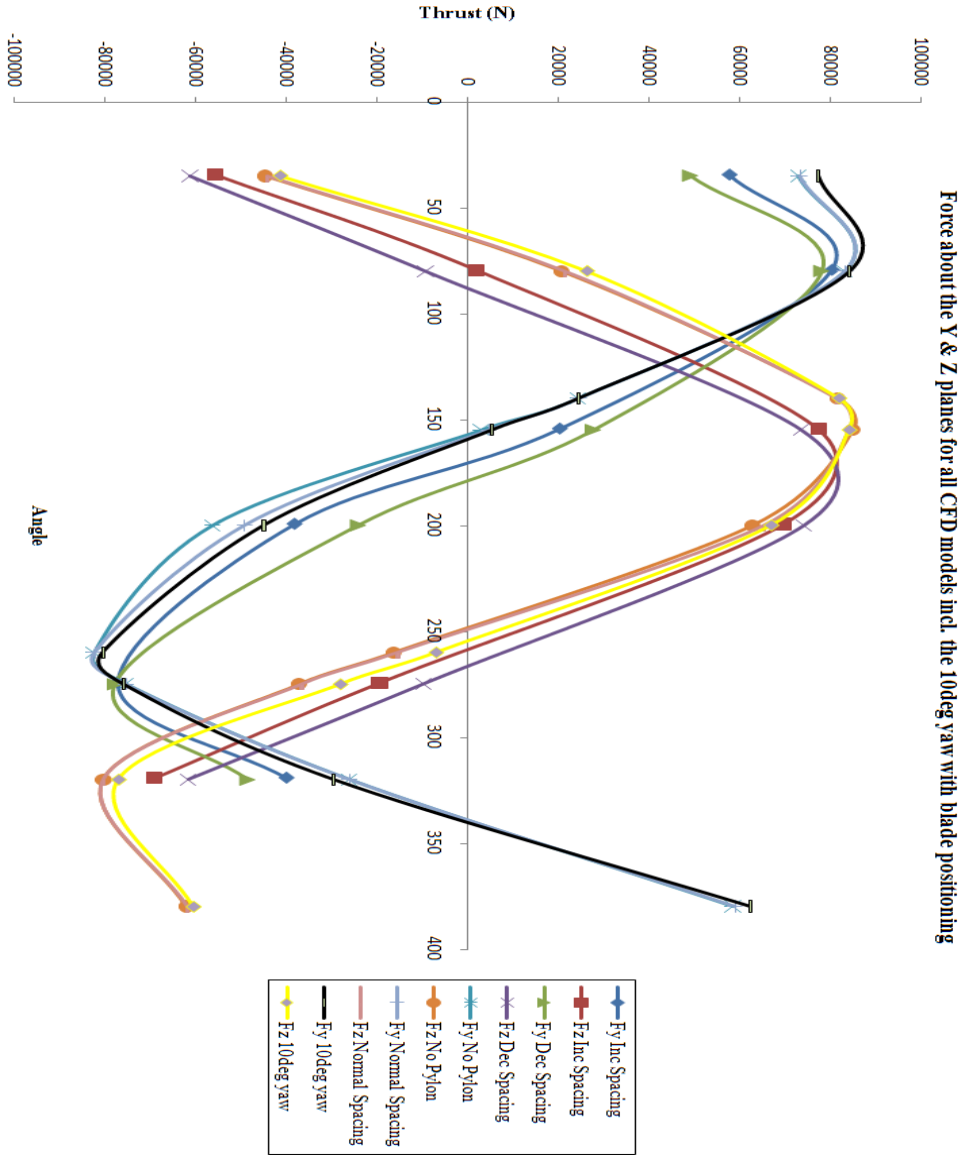

Figure B.6 Comparison of thrust about the Y and Z axes for all CFD models

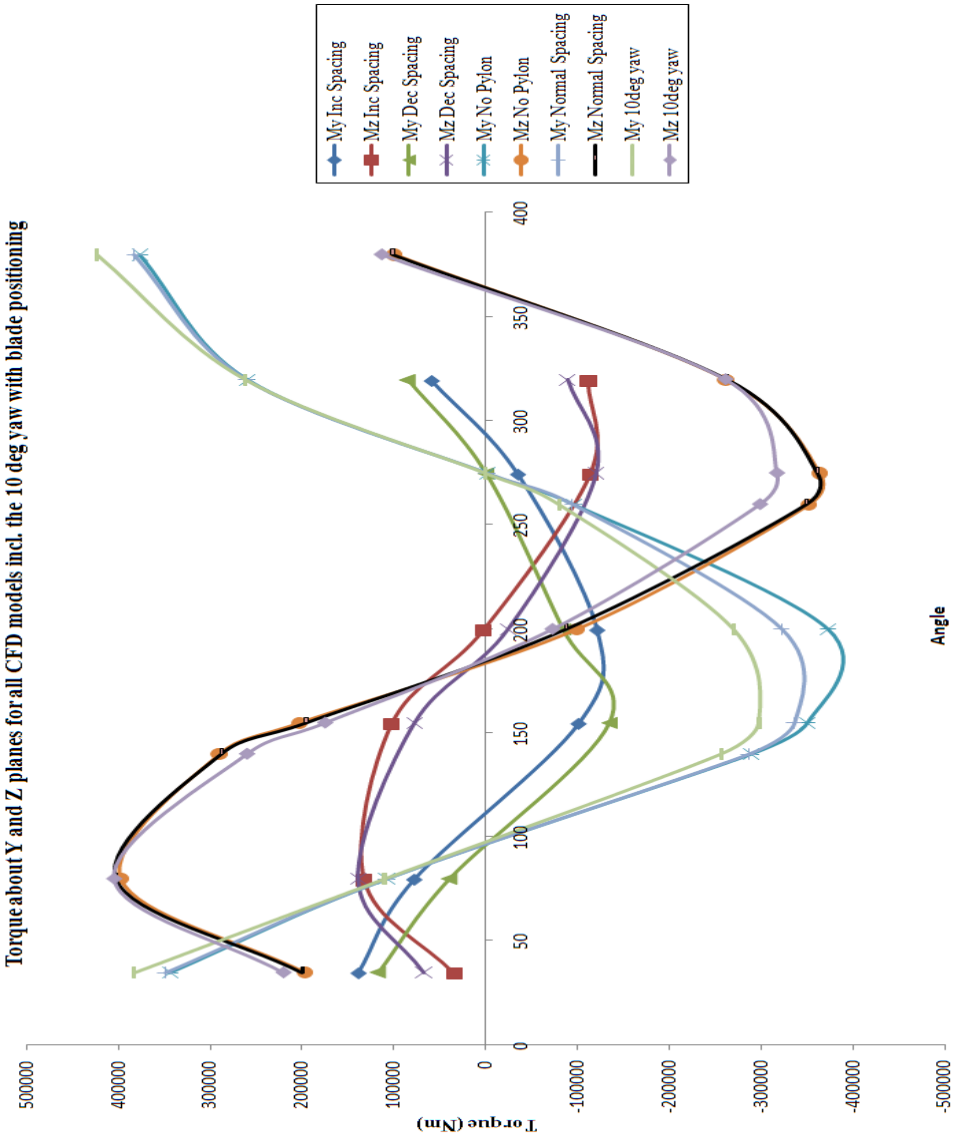

Figure B.7 Comparison of torque about the Y and Z axes for all CFD models

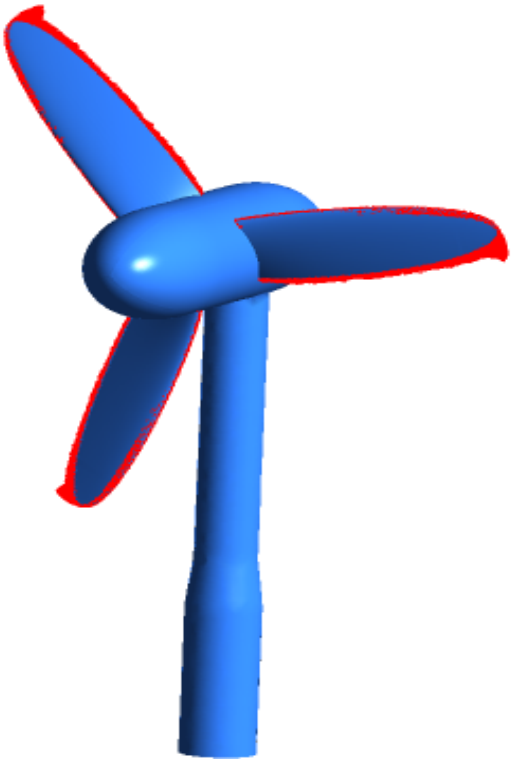

Figure B.8 Vorticity around the blades for the F3 Normal Spacing model

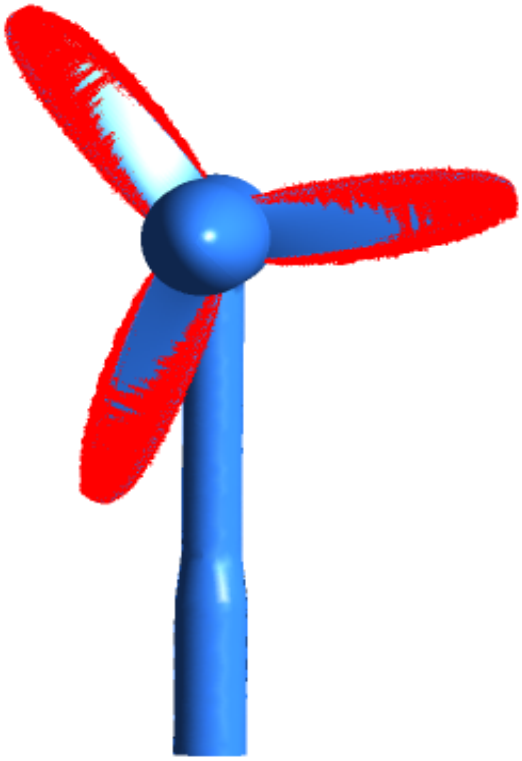

Figure B.9 Vorticity around the blades for the F4 Normal Spacing model

Appendix C

Appendices for Chapter 6

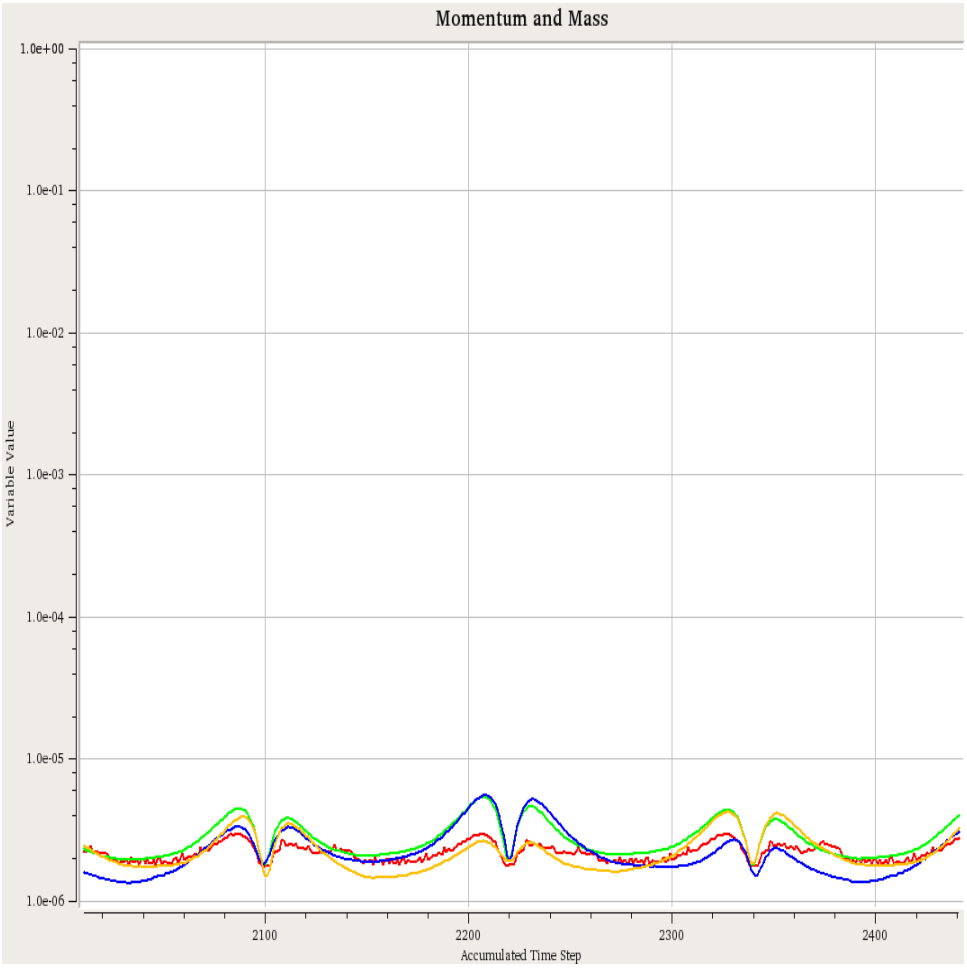

Figure C.1 Transient residual convergence - normal_spacing_model F3

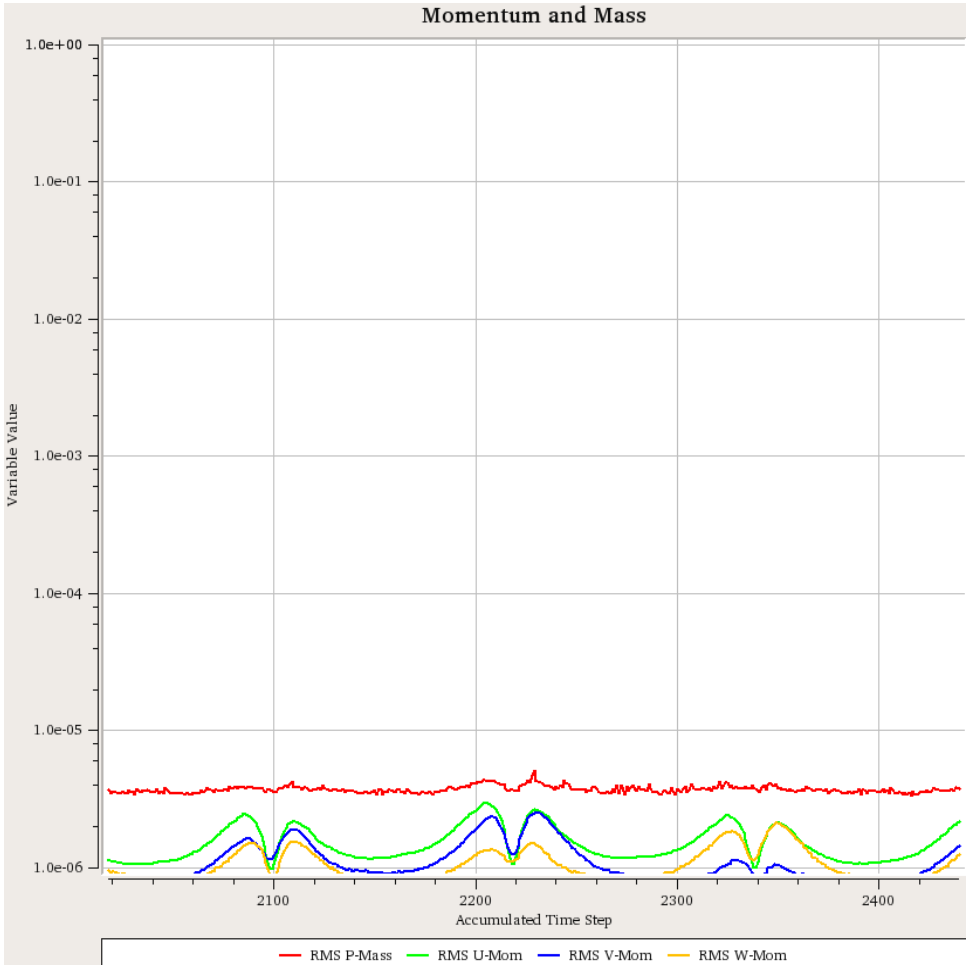

Figure C.2 Transient residual convergence - normal_spacing_model F4

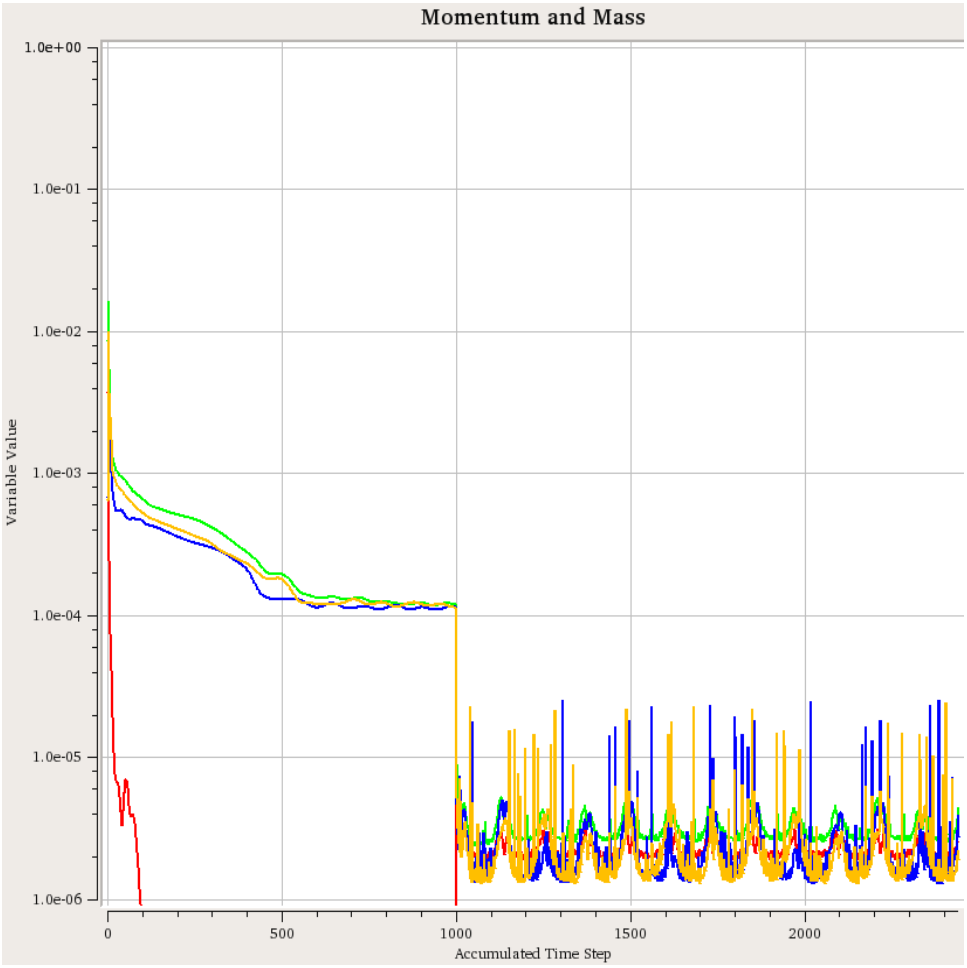

Figure C.3 Transient residual convergence - Half_spacing_model F3

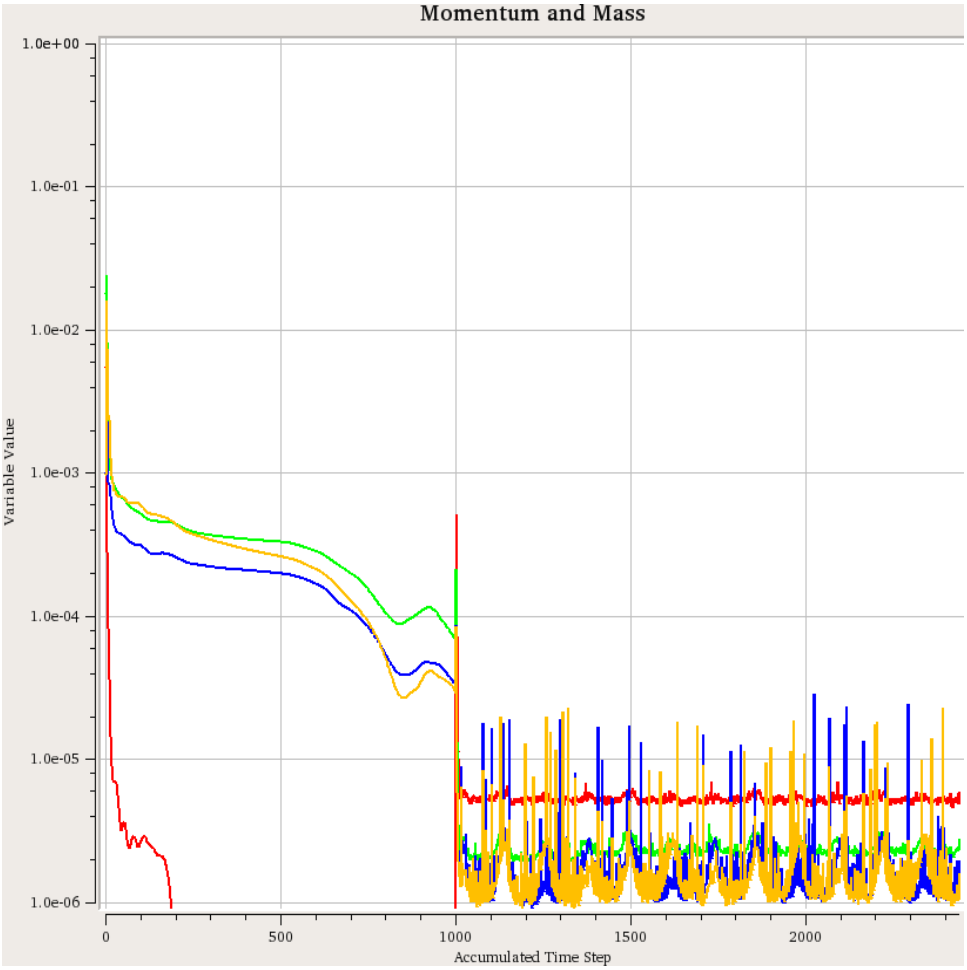

Figure C.4 Transient residual convergence - Half_spacing_model F4

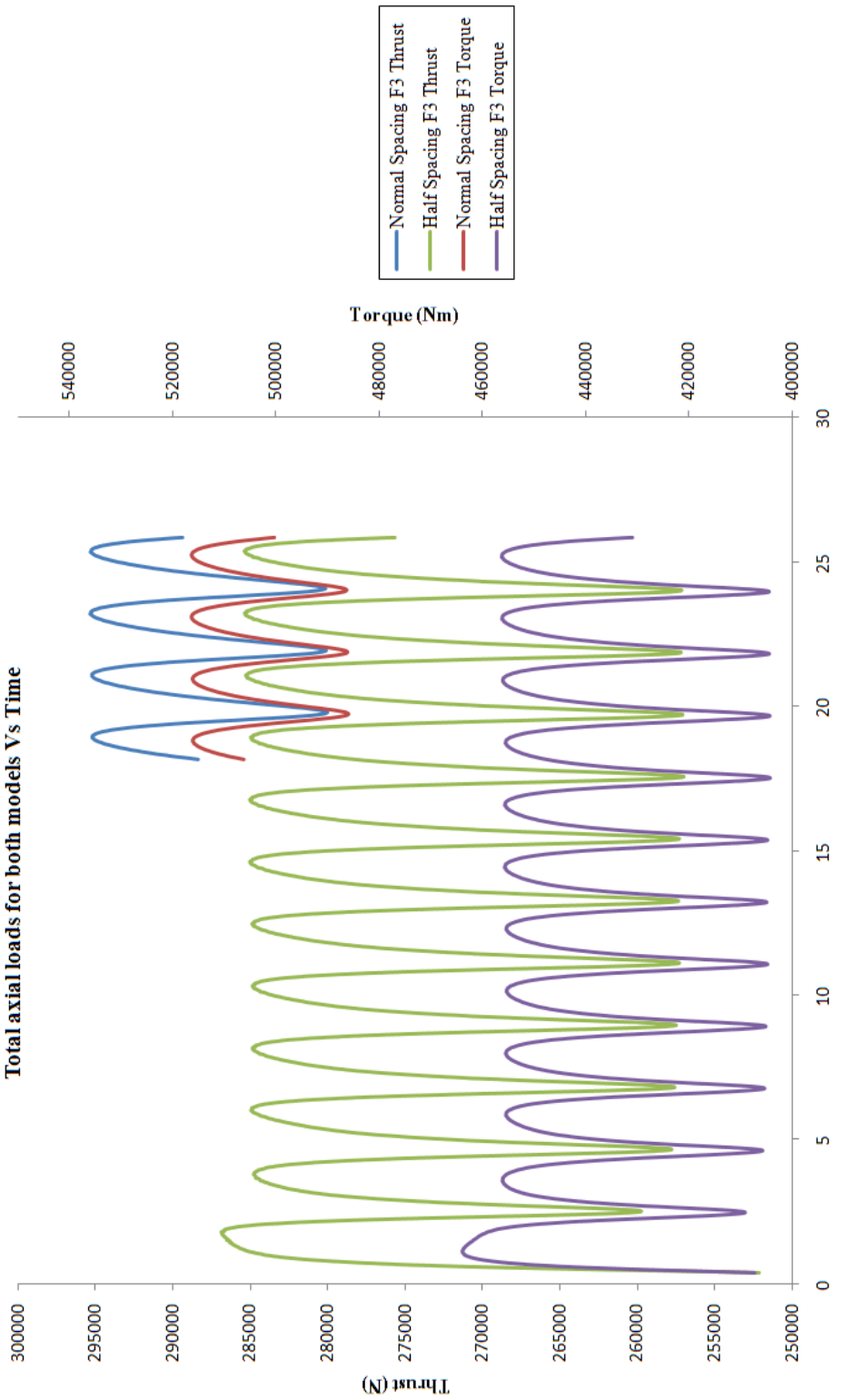

Figure C.5 Comparison of total thrust and torque for both F3 cases

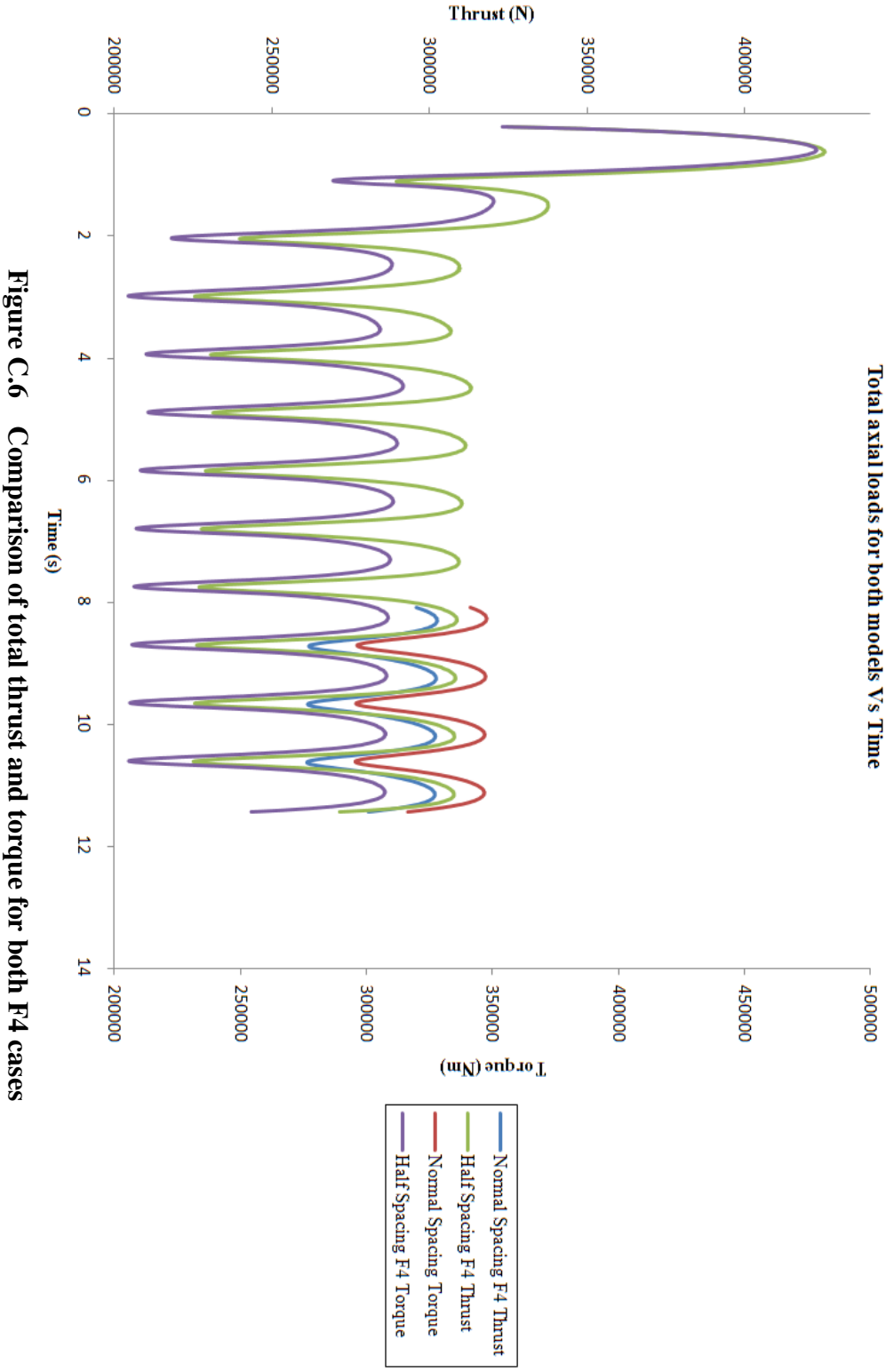

Figure C.6 Comparison of total thrust and torque for both F4 cases

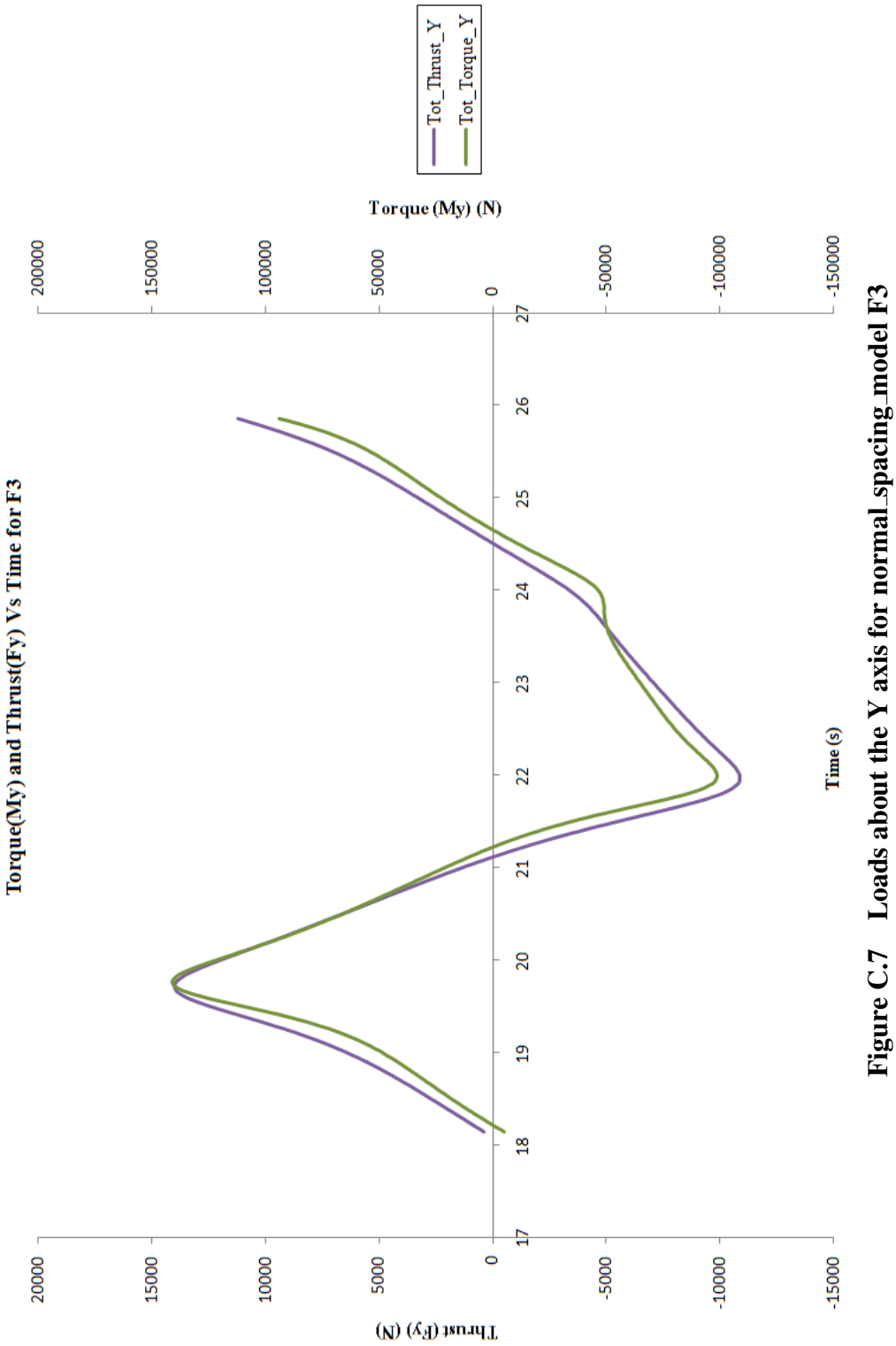

Figure C.7 Loads about the Y axis for normal_spacing_model F3

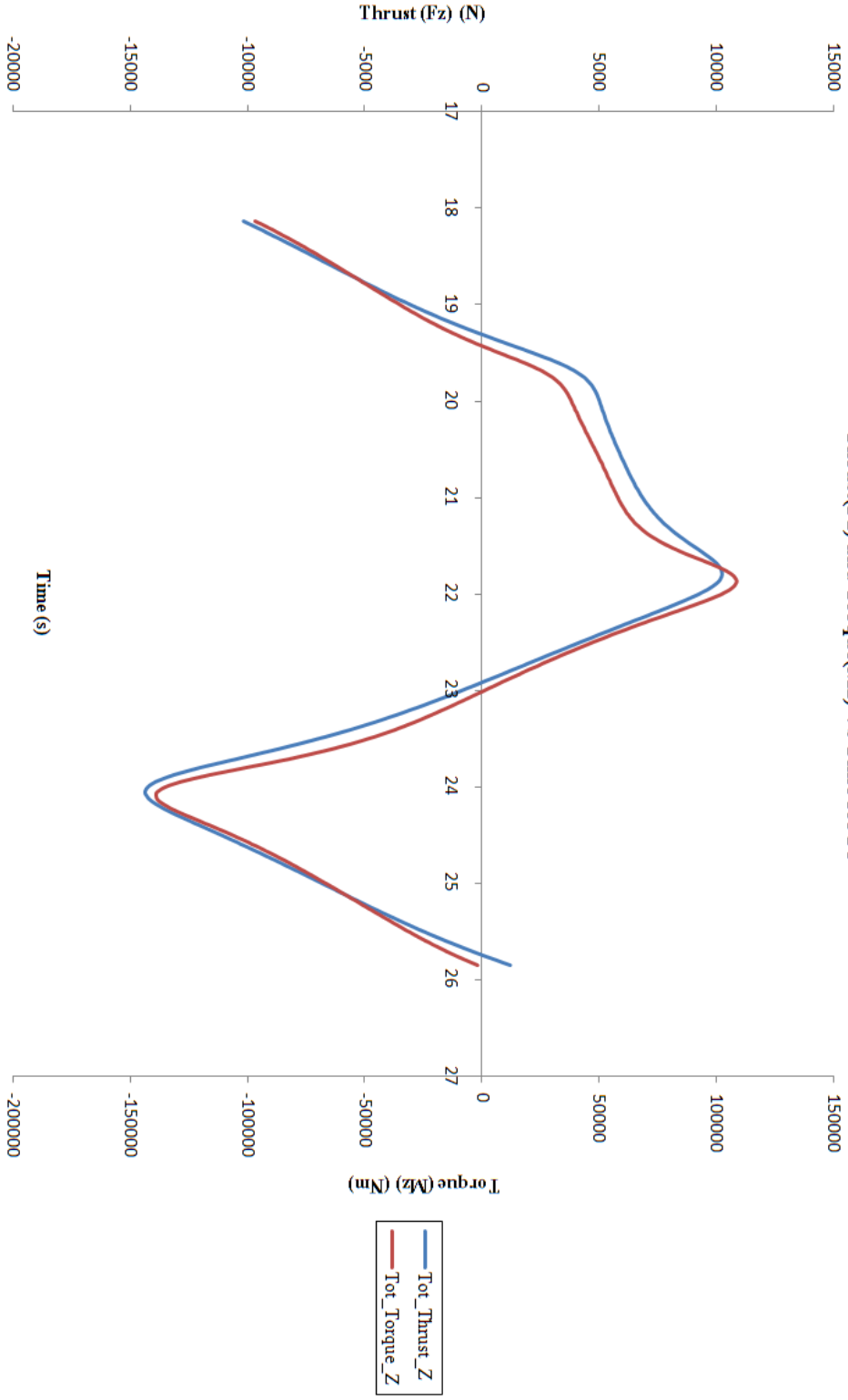

Figure C.8 Loads about the Z axis for normal_spacing_model F3

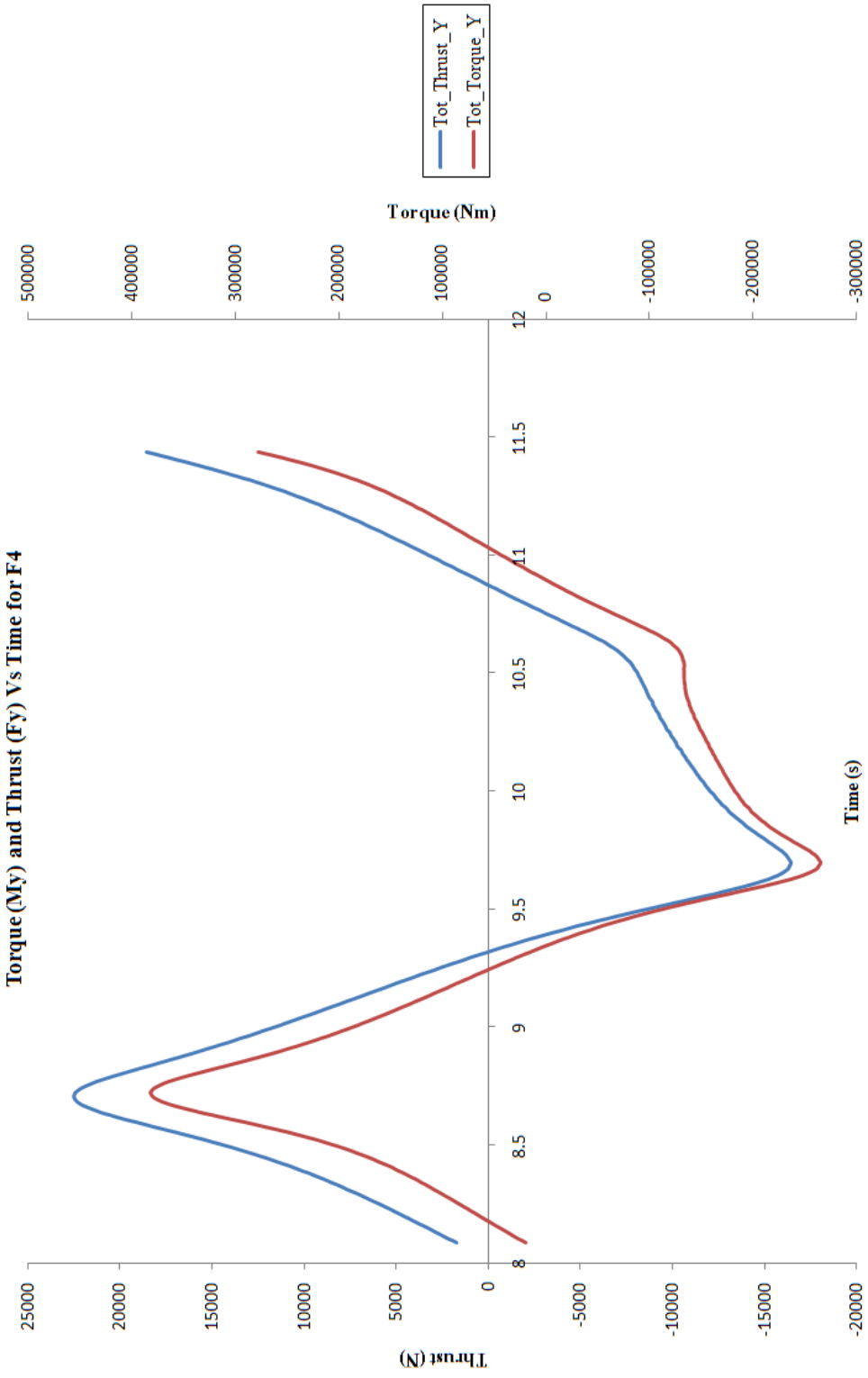

Figure C.9 Loads about the Y axis for normal_spacing_model F4

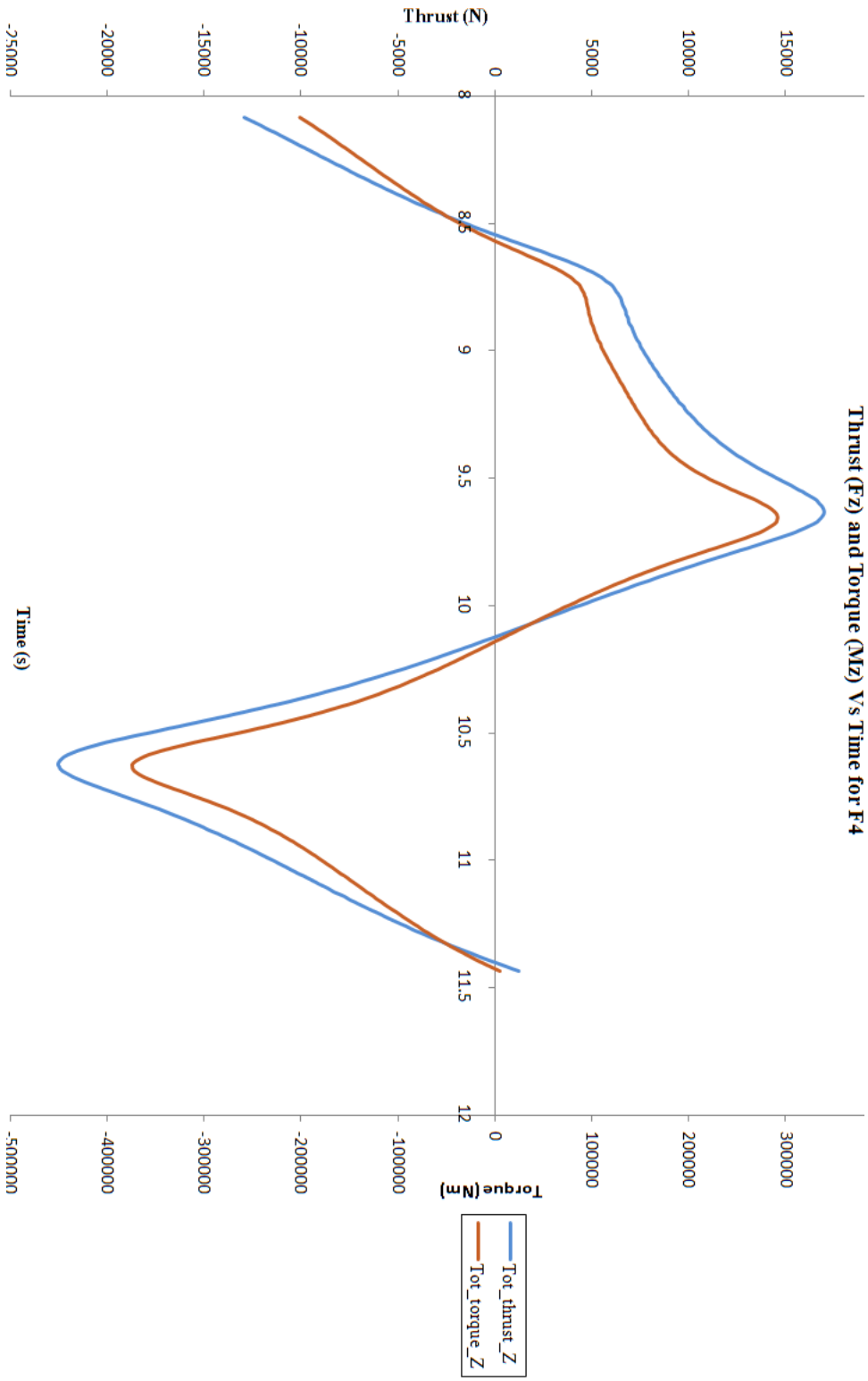

Figure C.10 Loads about the Z axis for normal_spacing_model F4

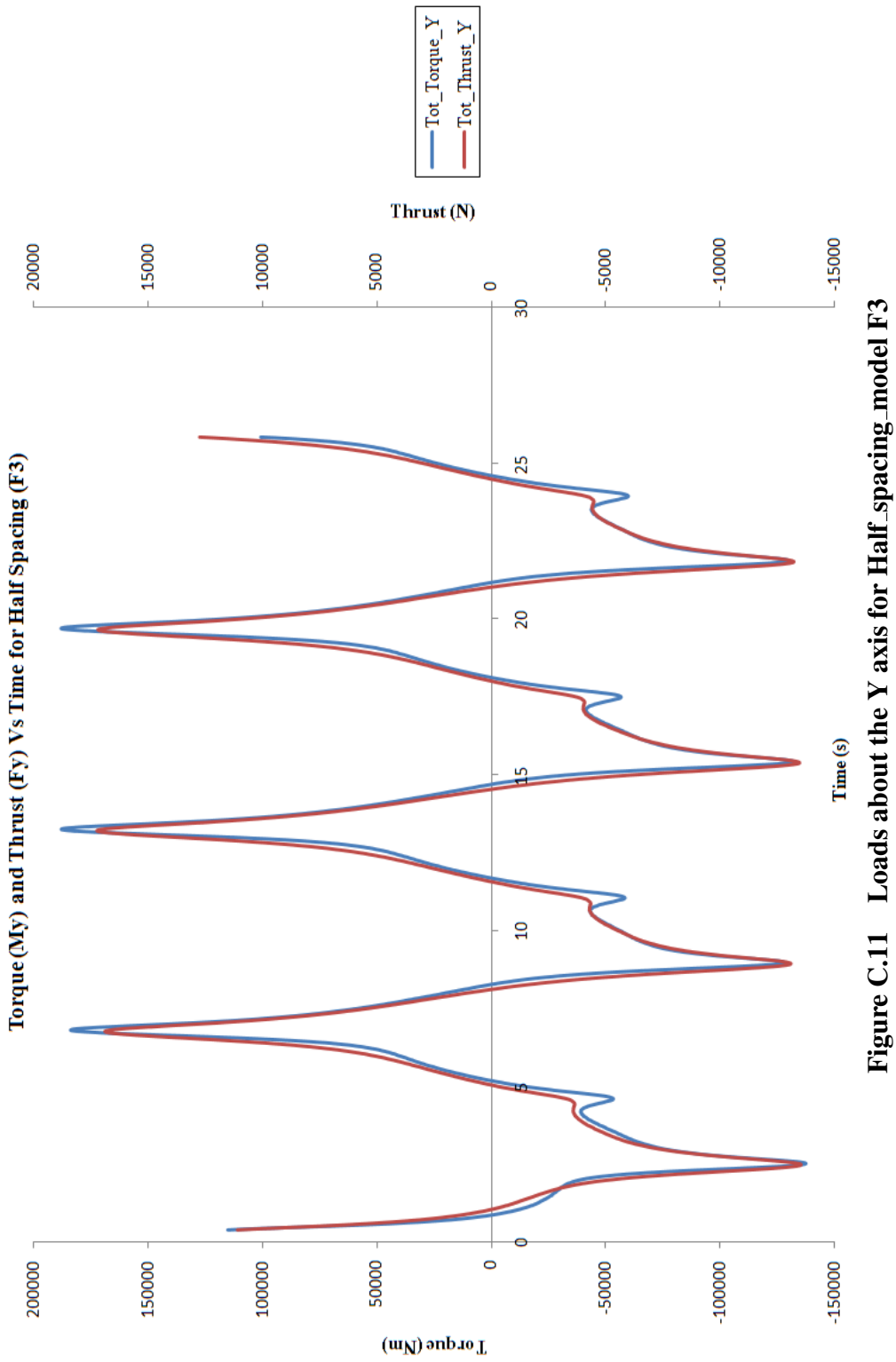

Figure C.11 Loads about the Y axis for Half_spacing_model F3

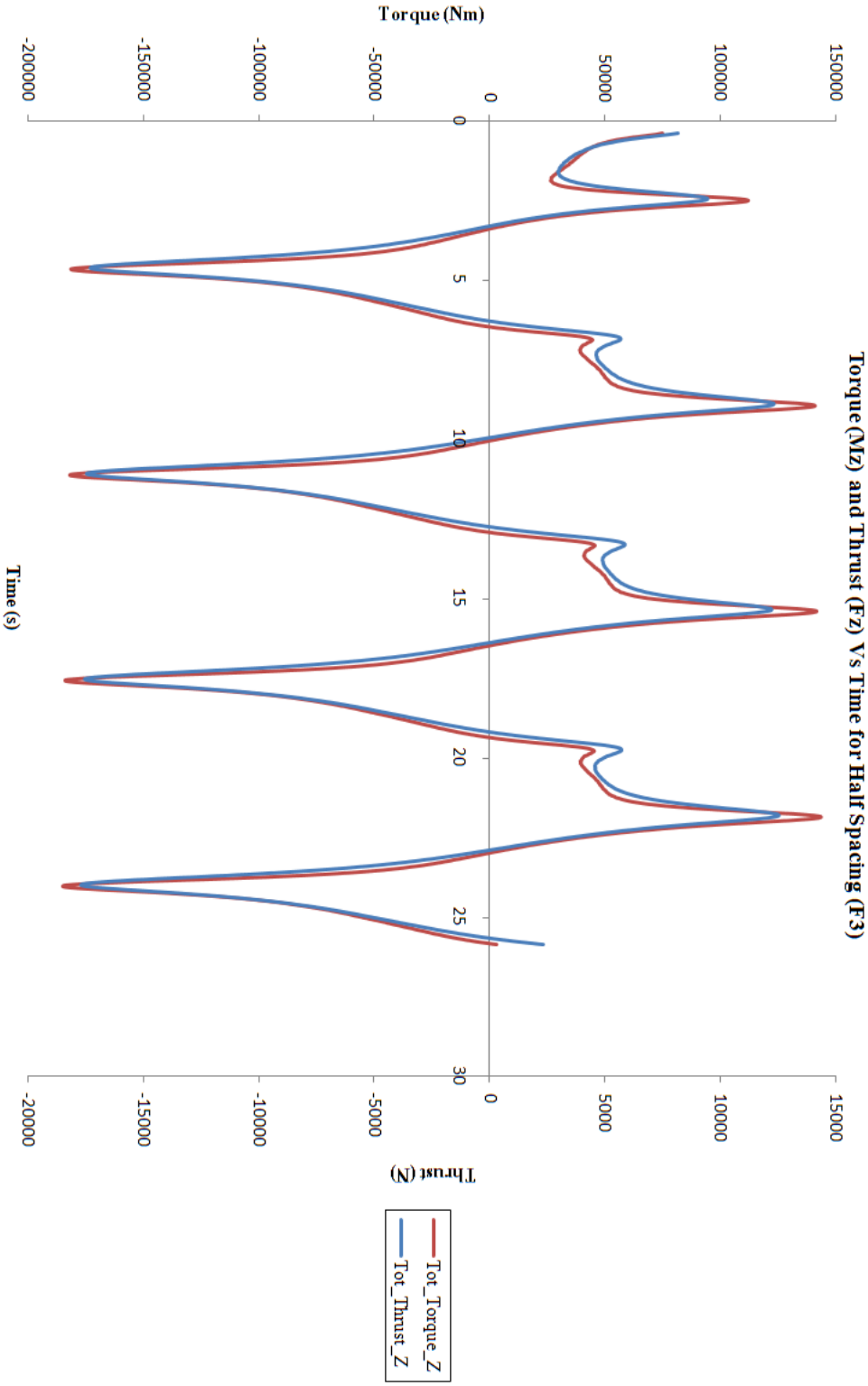

Figure C.12 Loads about the Z axis for Half_spacing_model F3

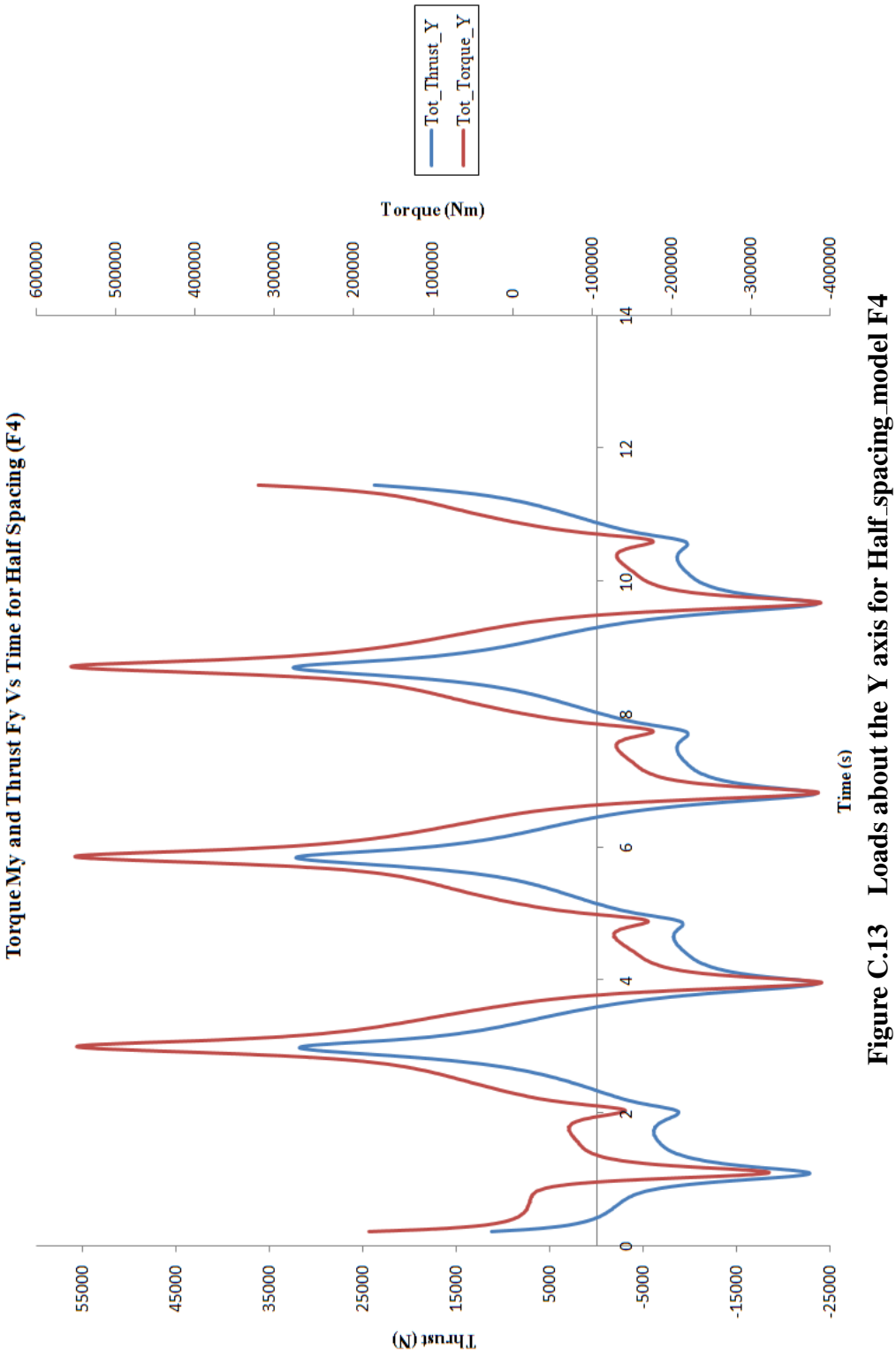

Figure C.13 Loads about the Y axis for Half_spacing_model F4

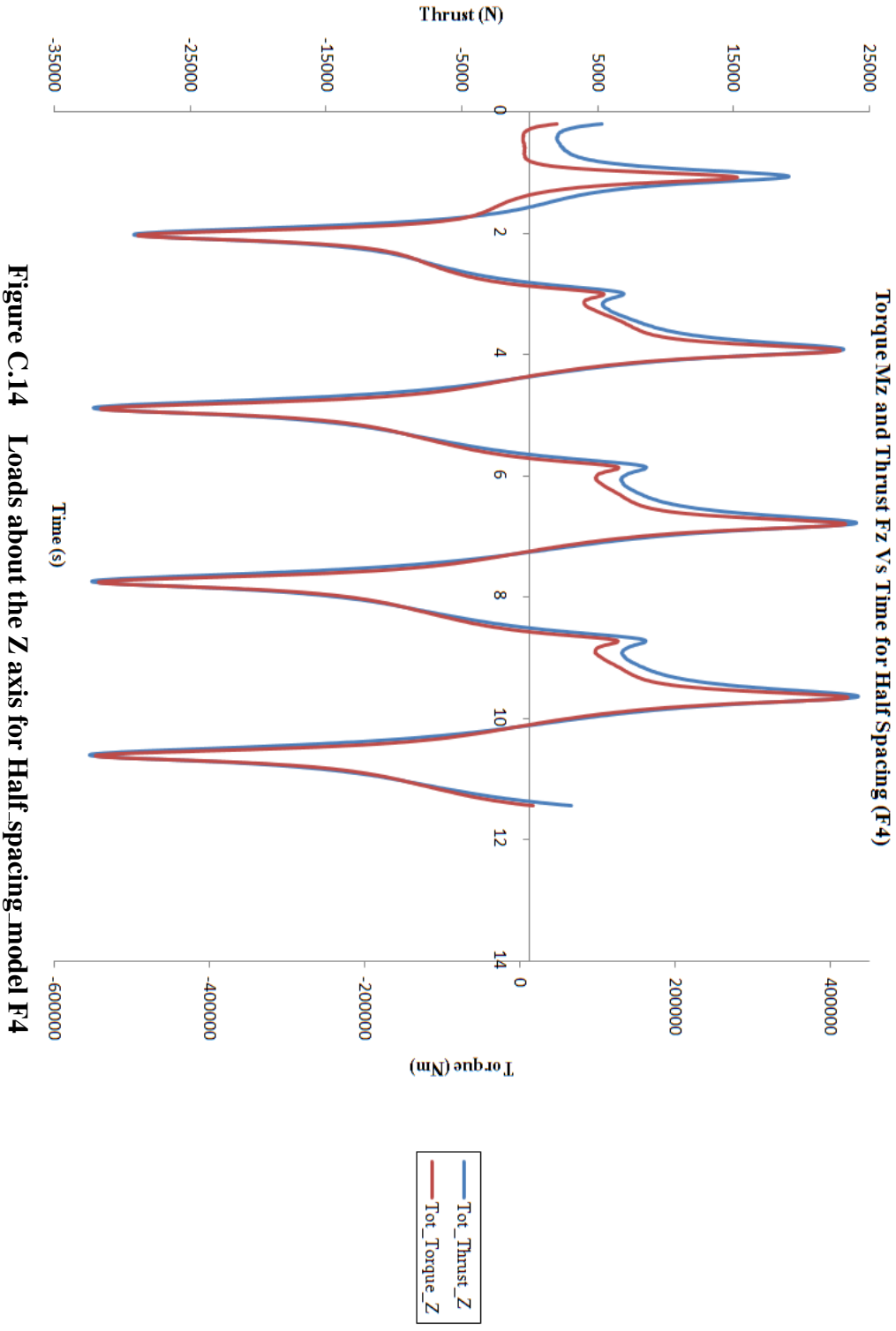

Figure C.14 Loads about the Z axis for Half_spacing_model F4

Appendix D

Appendices for Chapter 7

```
+--------------------------------------------------------------------+
|                                                                    |
|                CFX Command Language for Run                        |
|                                                                    |
+--------------------------------------------------------------------+

LIBRARY:
  CEL:
    EXPRESSIONS:
      H = 3.0 [m]
      P = 14.0 [s]
      Vref = 2.7 [m/s]
      Zref = 35 [m]
      Vcurrent = Vref*(z/Zref)^(1/7)
      a = H/2
      lambda = (g*(P)^(2))/(2*pi)
      k = (2*pi)/(lambda)
      omega = (2*pi)/P
      VwaveH = \
        (a*omega)*((cosh(k*(Zref+z)))/(sinh(k*Zref)))*(cos((k*x)-(omega*t)))
      Vcomb = VwaveH+Vcurrent
    END
```

Figure D.1 CEL user expressions for Extreme wave F3 case

```
COORD FRAME: CEL1cs
  Axis 3 Point = -11 [m], -20 [m], 21.25 [m]
  Coord Frame Type = Cartesian
  Option = Axis Points
  Origin Point = -11 [m], -20 [m], -13.75 [m]
  Plane 13 Point = 10 [m], -20 [m], 5 [m]
  Reference Coord Frame = Coord 0
END
SOLUTION UNITS:
  Angle Units = [rad]
  Length Units = [m]
  Mass Units = [kg]
  Solid Angle Units = [sr]
  Temperature Units = [K]
  Time Units = [s]
END
SIMULATION TYPE:
  Option = Transient
  EXTERNAL SOLVER COUPLING:
    Option = None
  END
  INITIAL TIME:
    Option = Automatic with Value
    Time = 0 [s]
  END
  TIME DURATION:
    Option = Total Time
    Total Time = 28 [s]
  END
  TIME STEPS:
    Option = Timesteps
    Timesteps = 0.0018 [s]
  END
END
DOMAIN: Default Domain
  Coord Frame = Coord 0
  Domain Type = Fluid
  Fluids List = Water
  Location = BODY, BODY 2, CREATED_MATERIAL_45, CREATED_MATERIAL_46
  BOUNDARY: Box Side 1
    Boundary Type = INTERFACE
    Location = OUT 3
    BOUNDARY CONDITIONS:
      MASS AND MOMENTUM:
```

Figure D.2 Local coordinate system in the CCL file

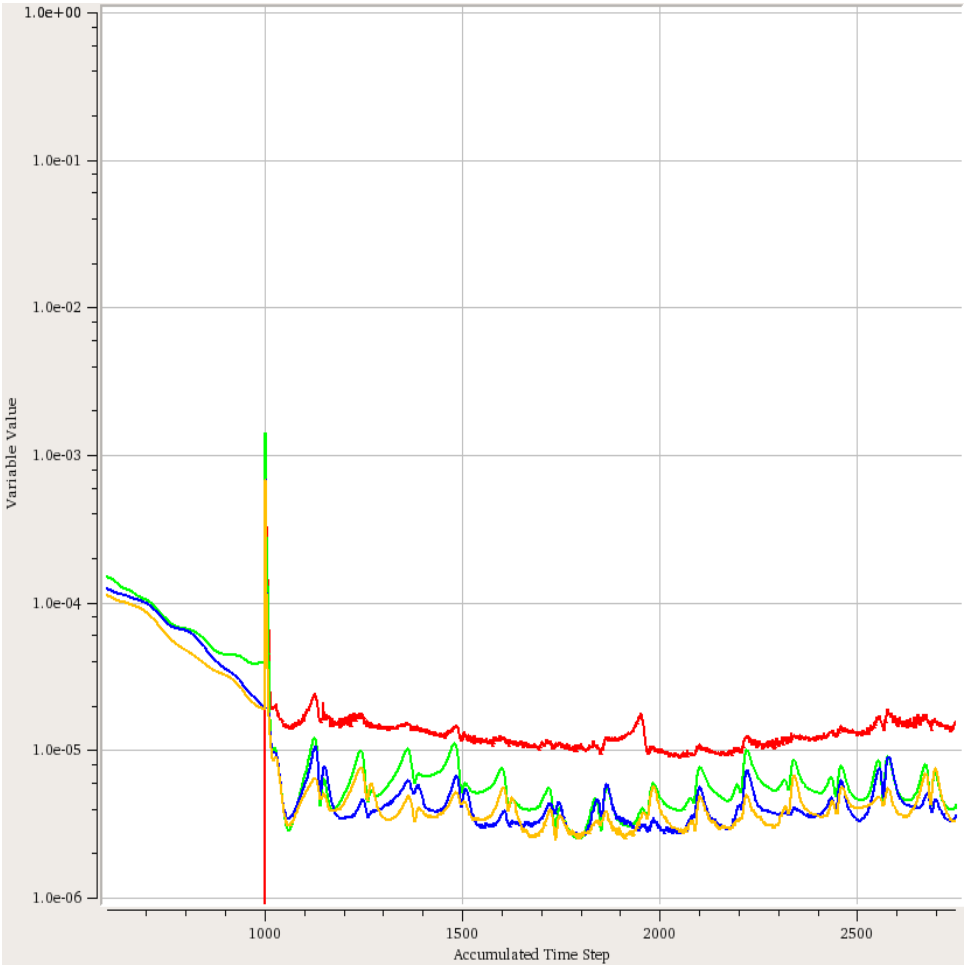

Figure D.3 Residual convergence - Extreme wave normal_spacing_model F4

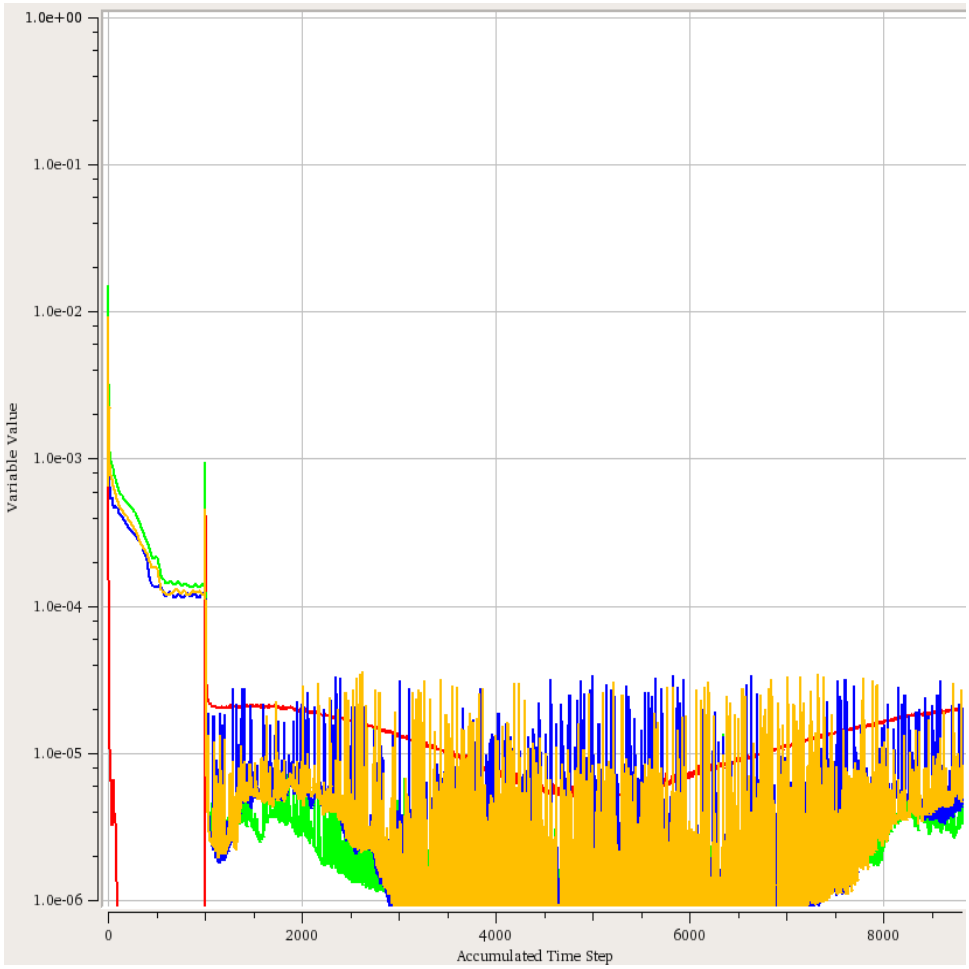

Figure D.4 Residual convergence - Extreme wave Half_spacing_model F3

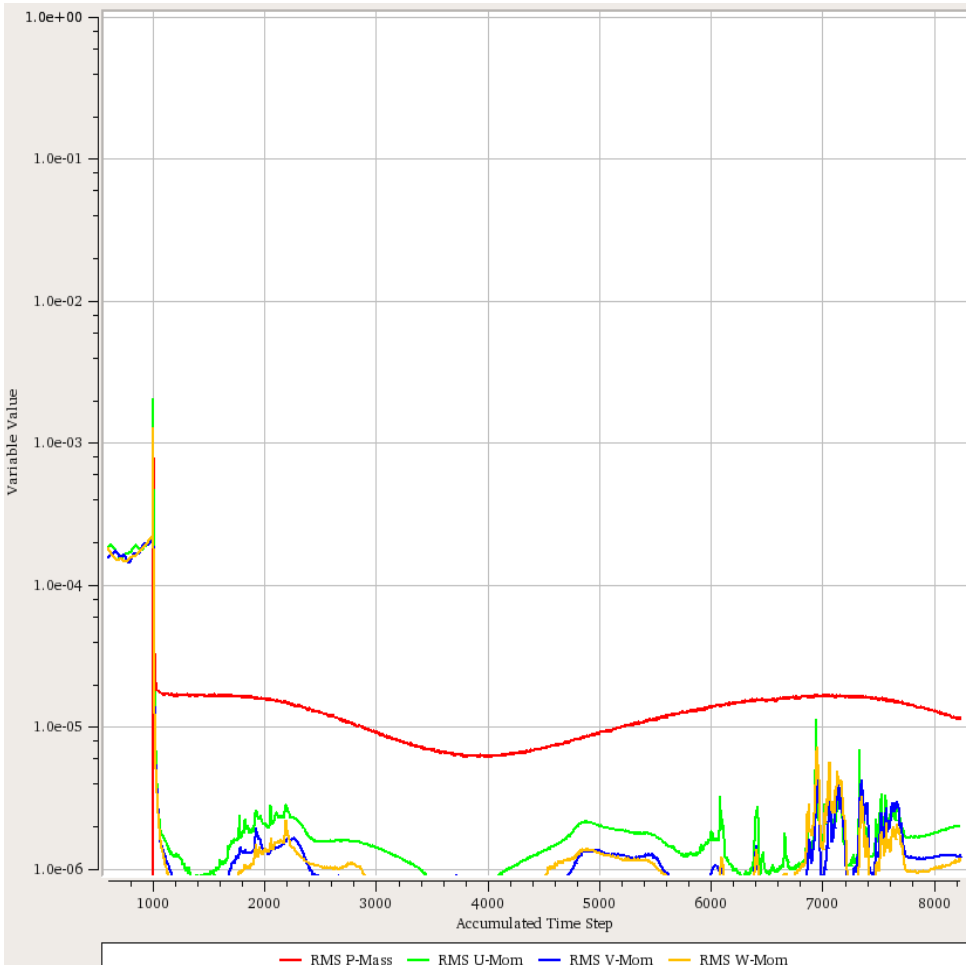

Figure D.5 Residual convergence - Regular wave normal_spacing_model F3

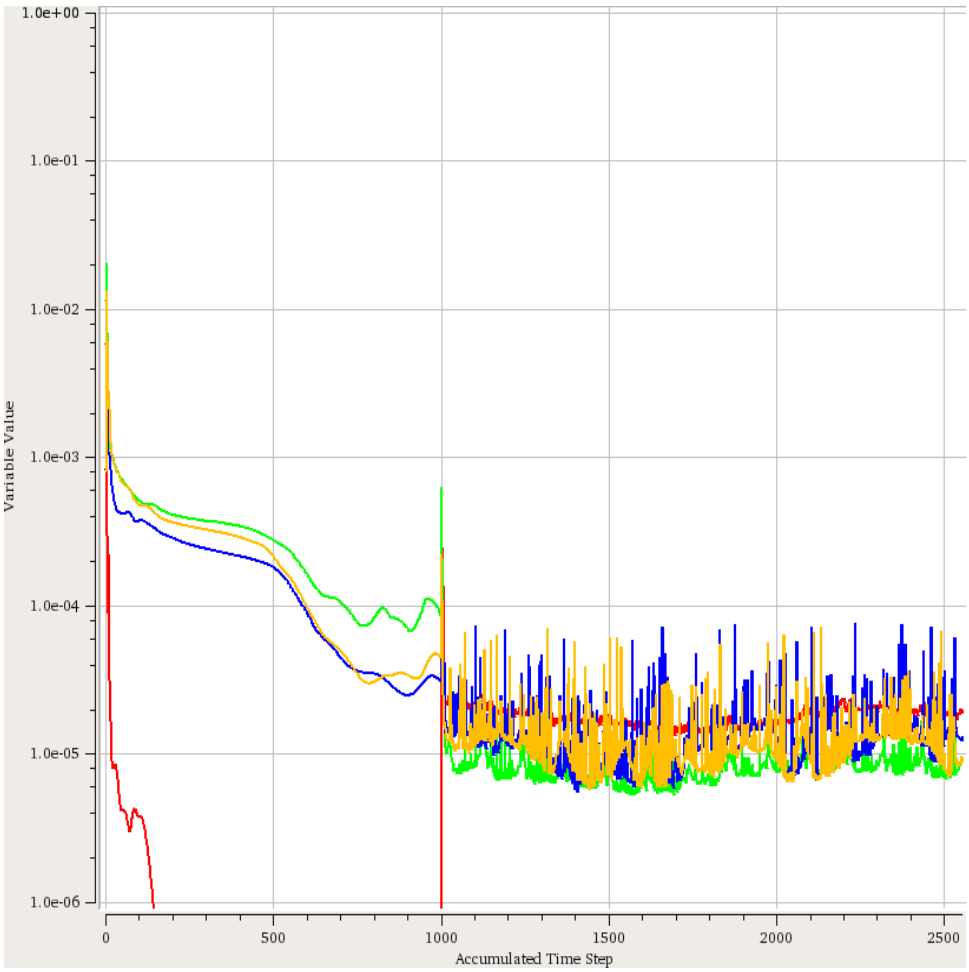

Figure D.6 Residual convergence - Regular wave Half_spacing_model F4

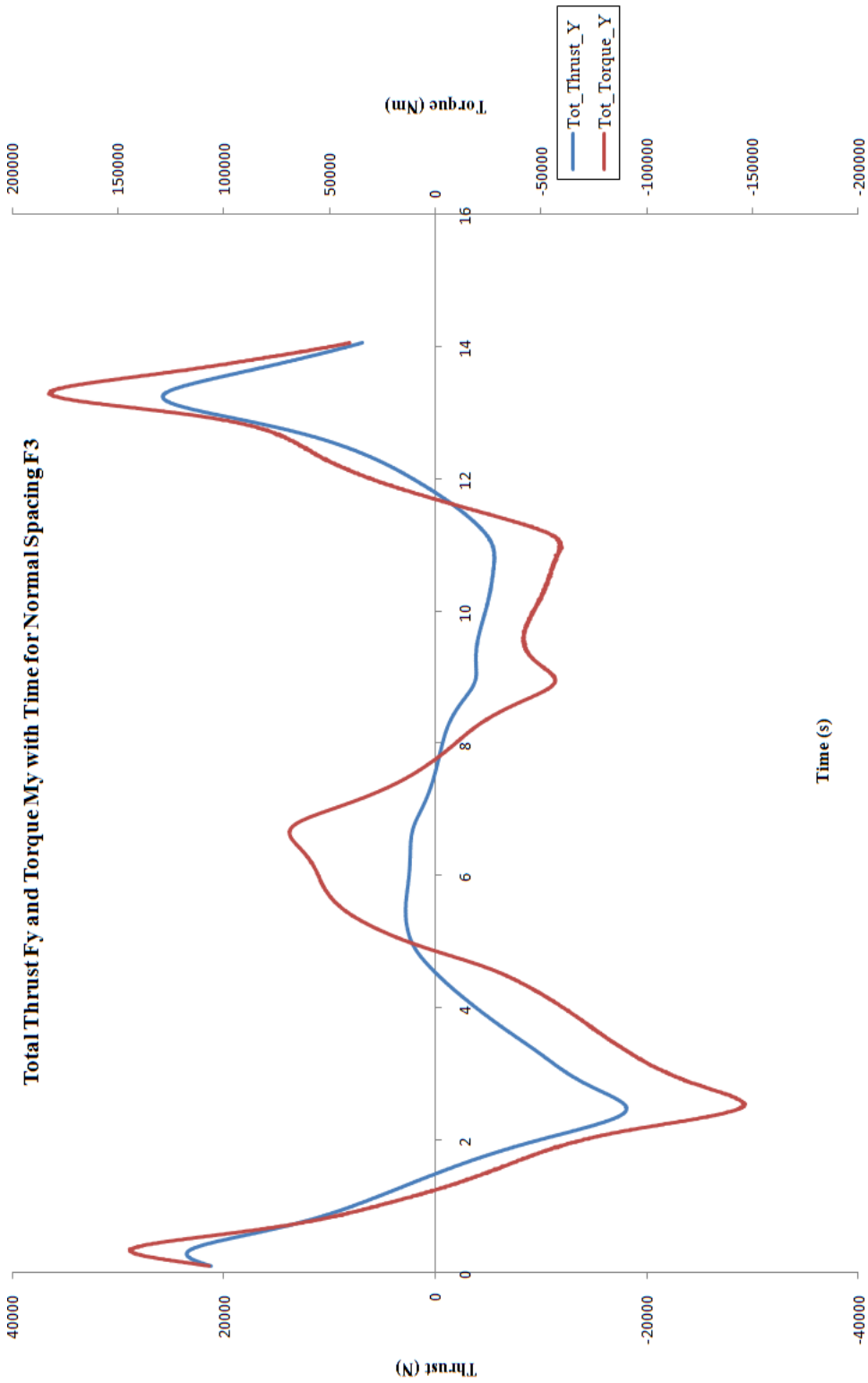

Figure D.7 Loads about the Y axis for Extreme wave normal_spacing_model F3

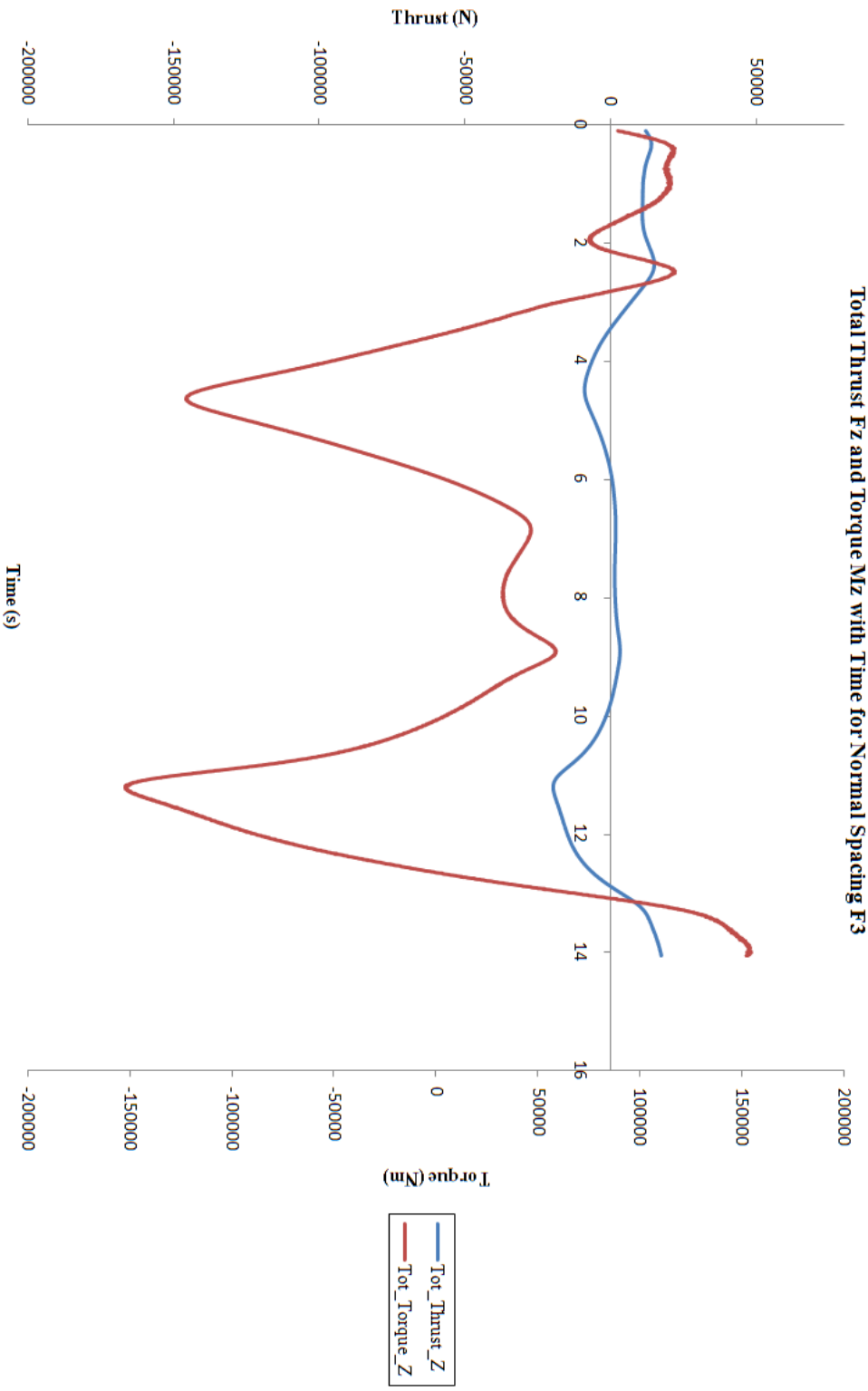

Figure D.8 Loads about the Z axis for Extreme wave normal_spacing_model F3

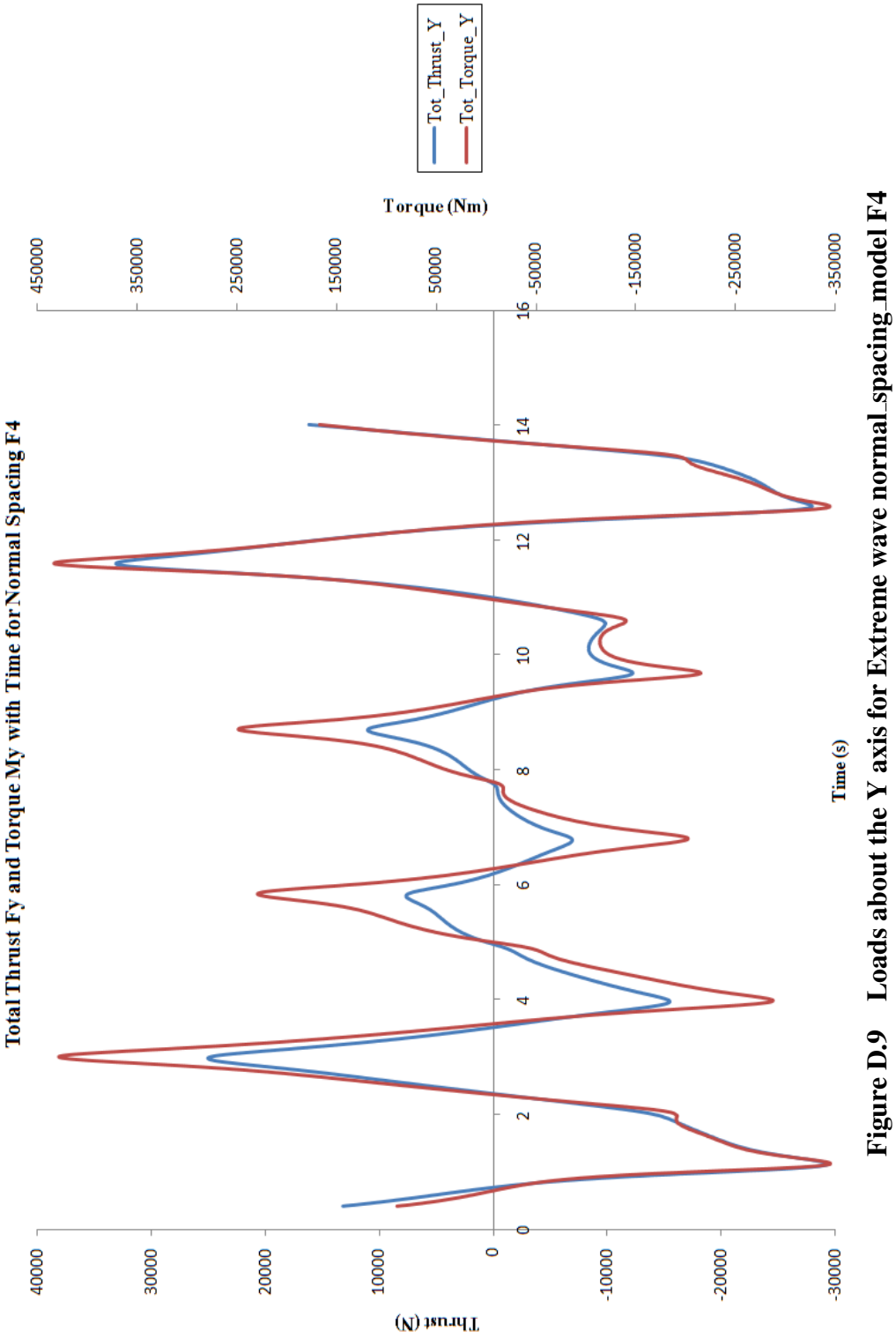

Figure D.9 Loads about the Y axis for Extreme wave normal_spacing_model F4

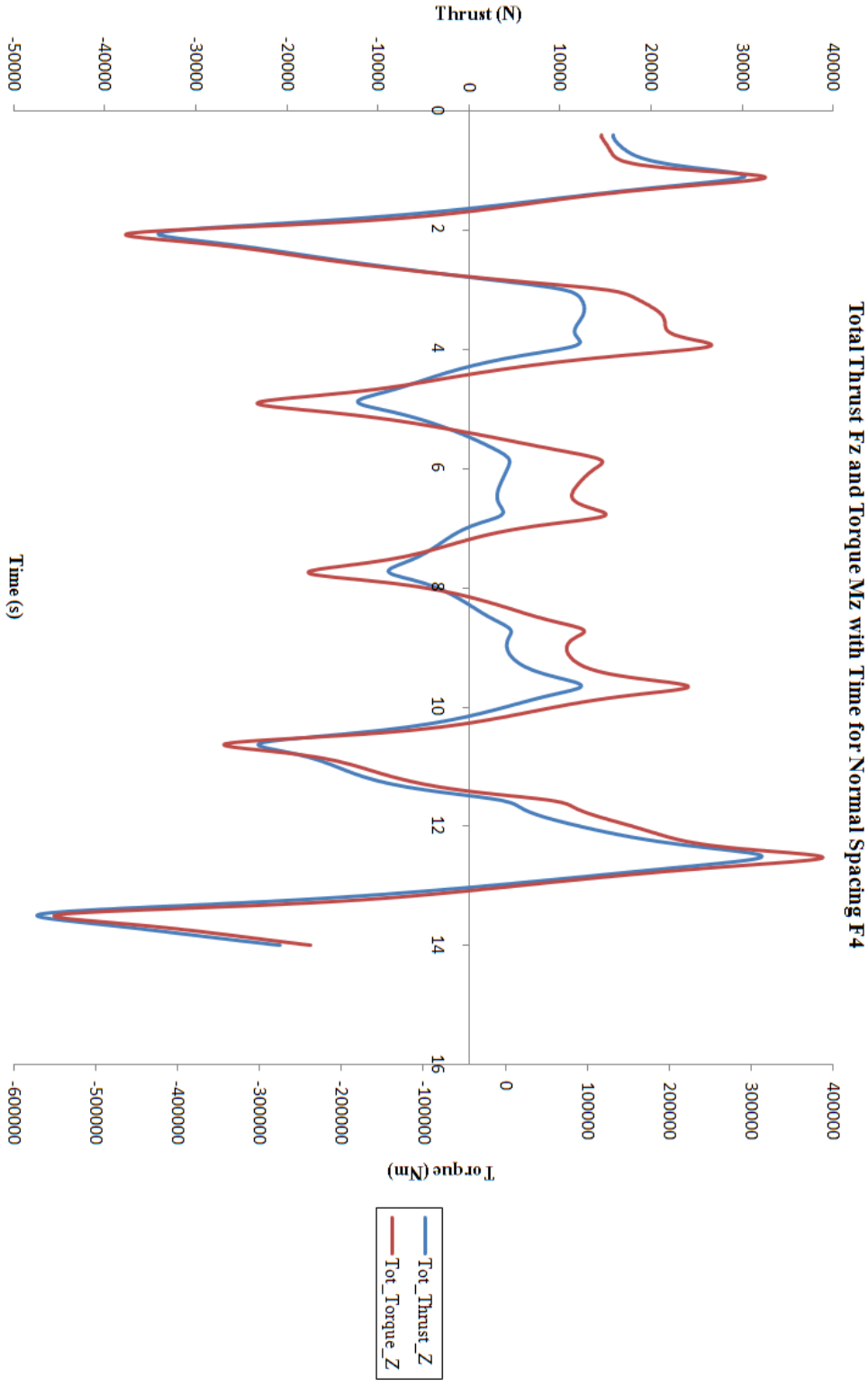

Figure D.10 Loads about the Z axis for Extreme wave normal_spacing_model F4

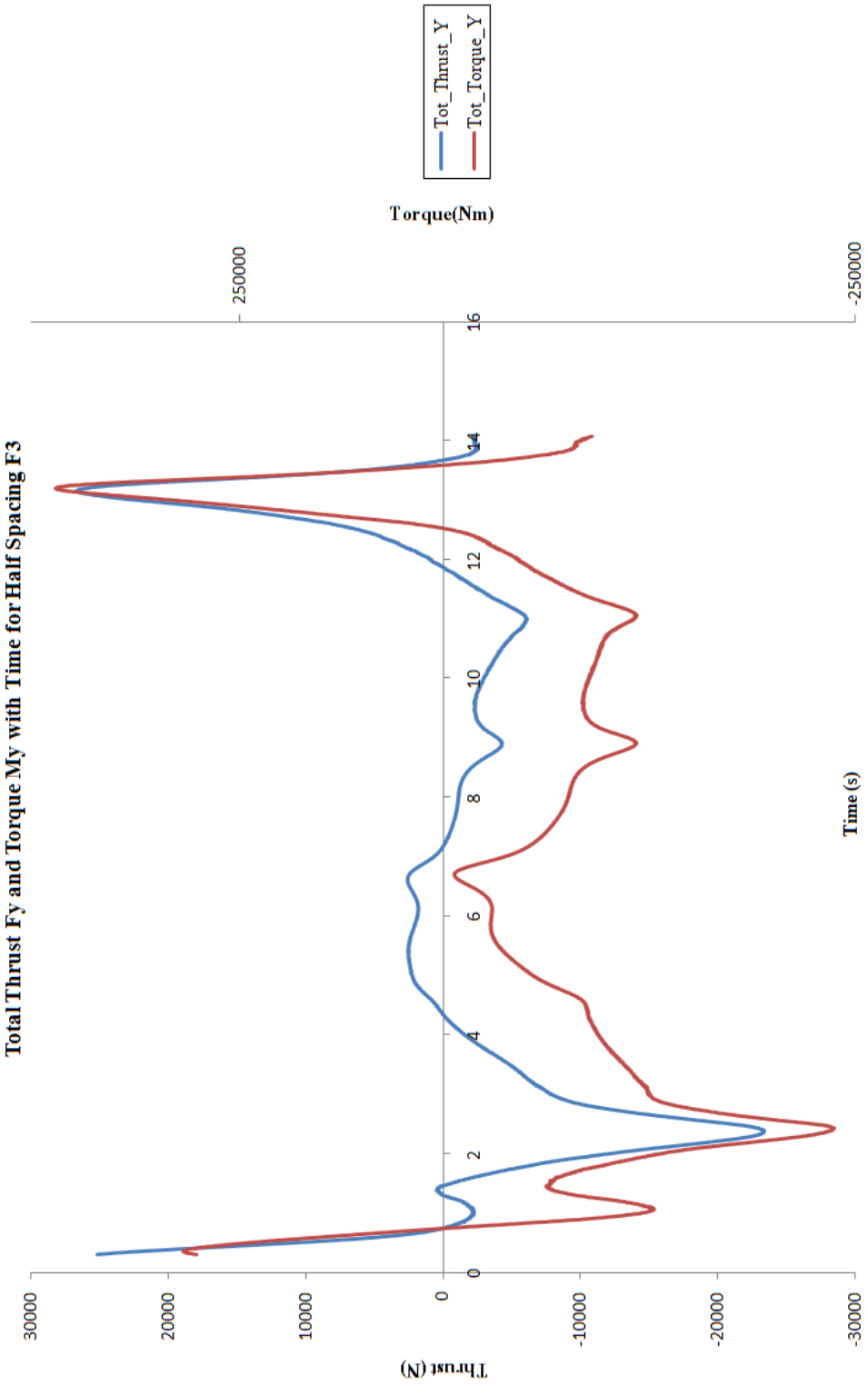

Figure D.11 Loads about the Y axis for Extreme wave Half_spacing_model F3

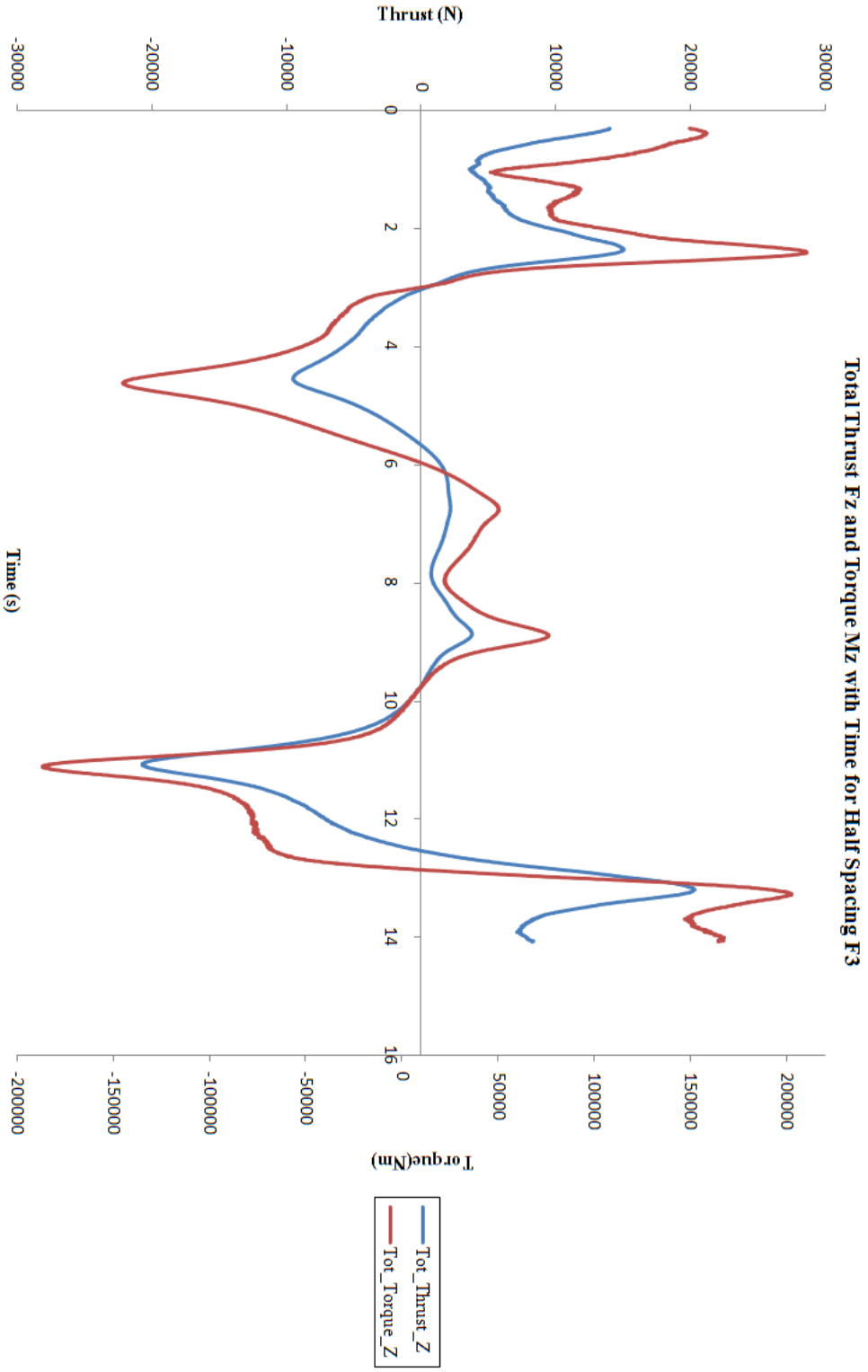

Figure D.12 Loads about the Z axis for Extreme wave Half_spacing_model F3

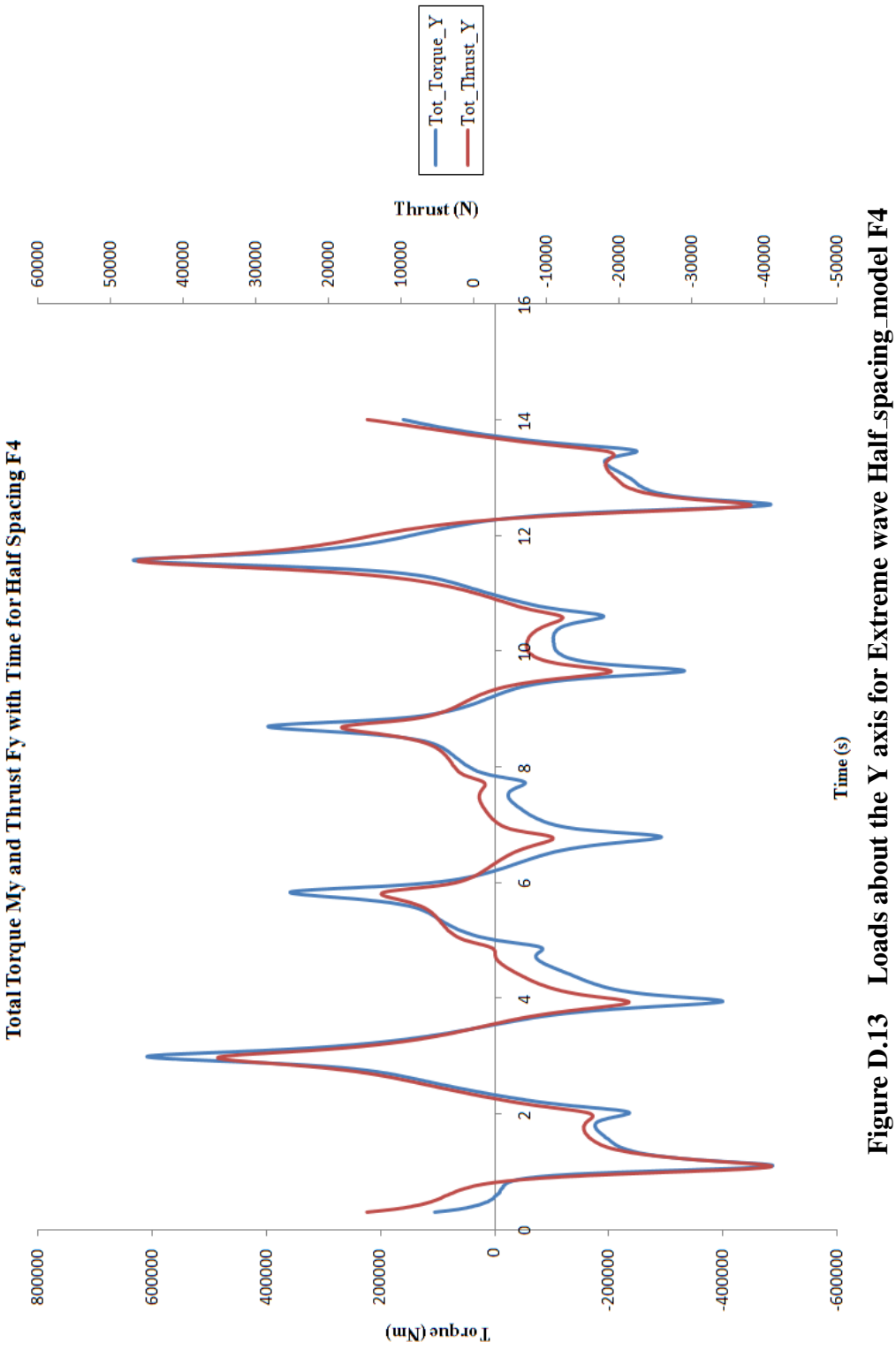

Figure D.13 Loads about the Y axis for Extreme wave Half_spacing_model F4

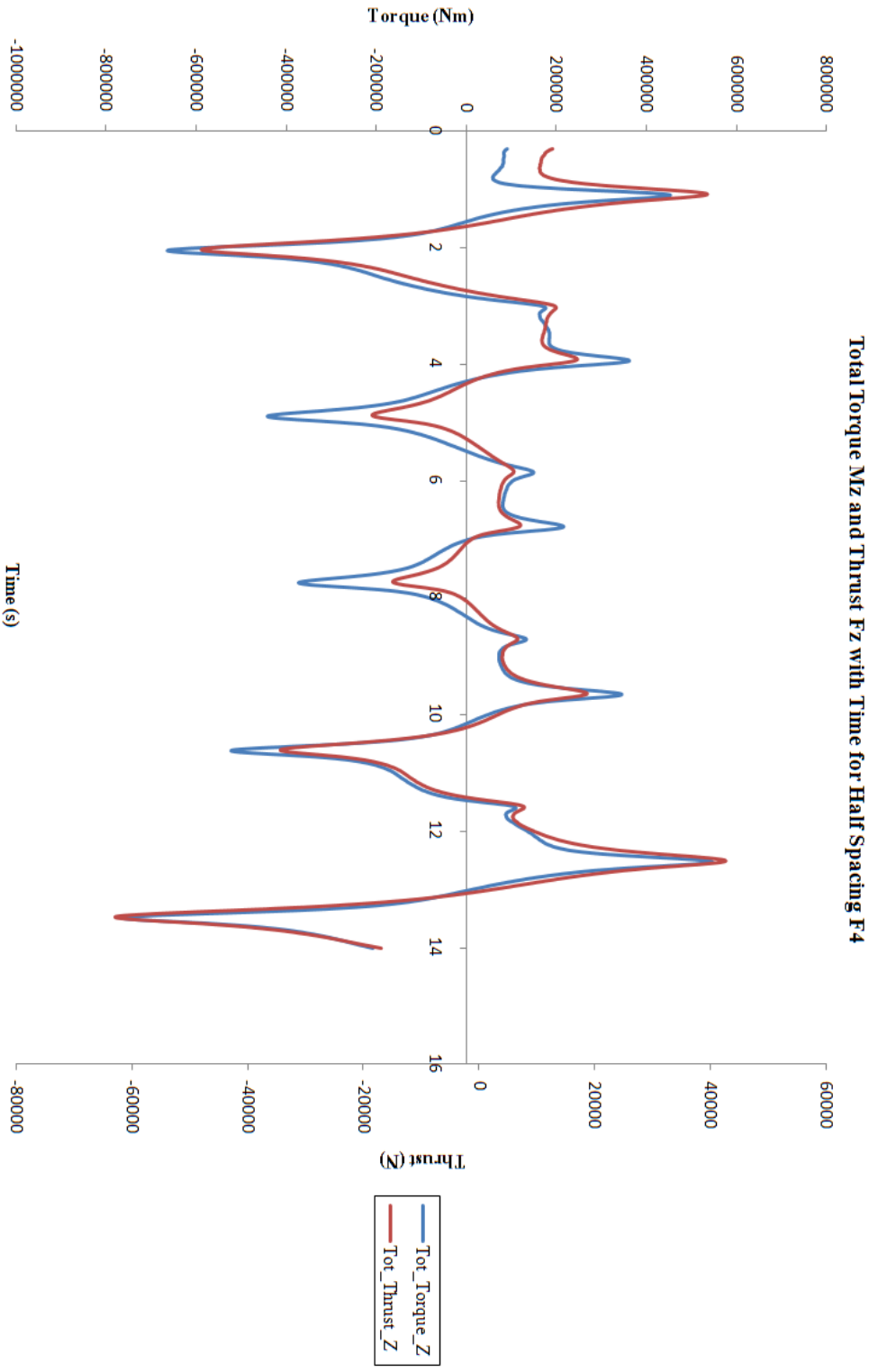

Figure D.14 Loads about the Z axis for Extreme wave Half_spacing_model F4

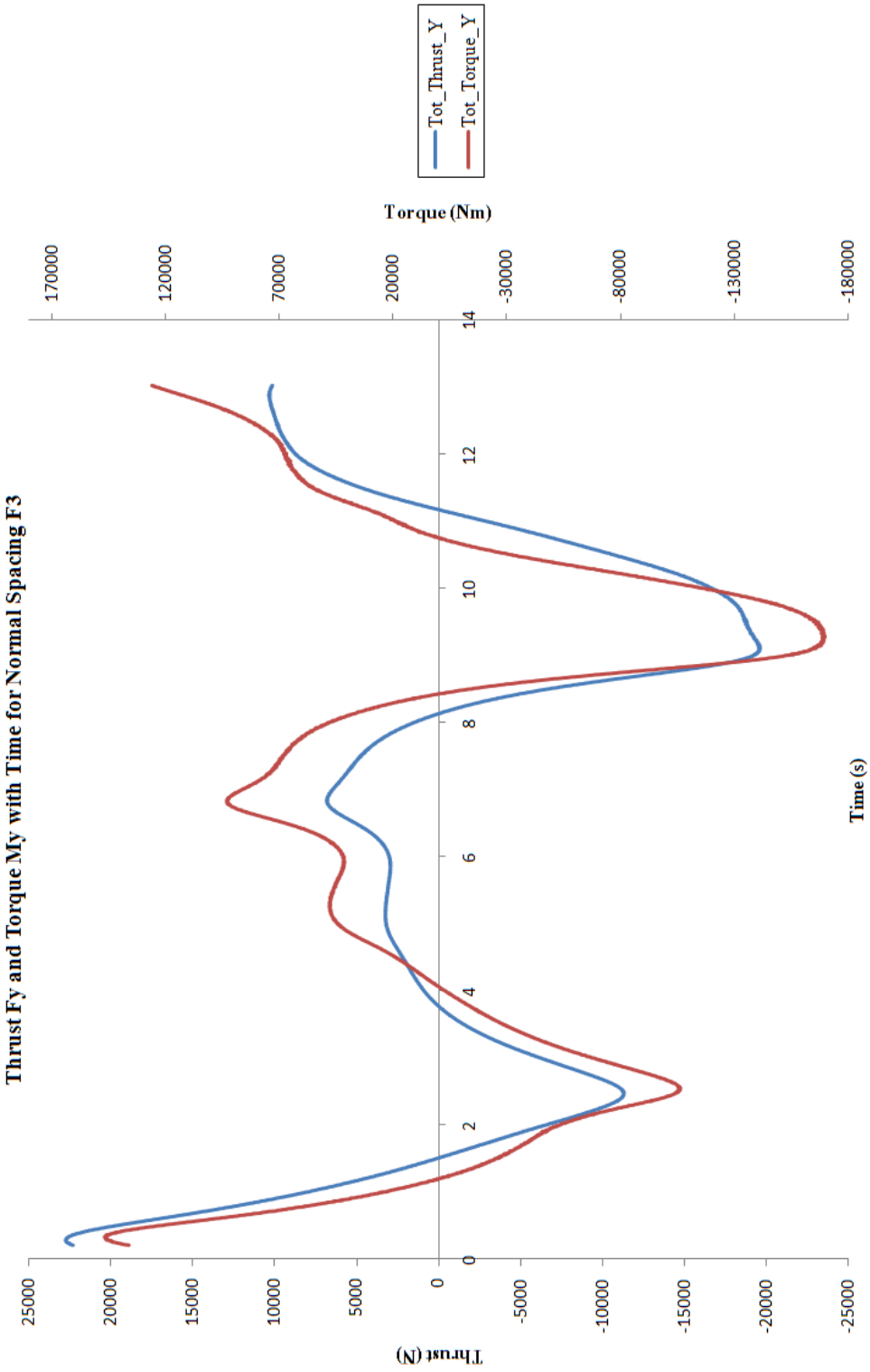

Figure D.15 Loads about the Y axis for Regular wave normal_spacing_model F3

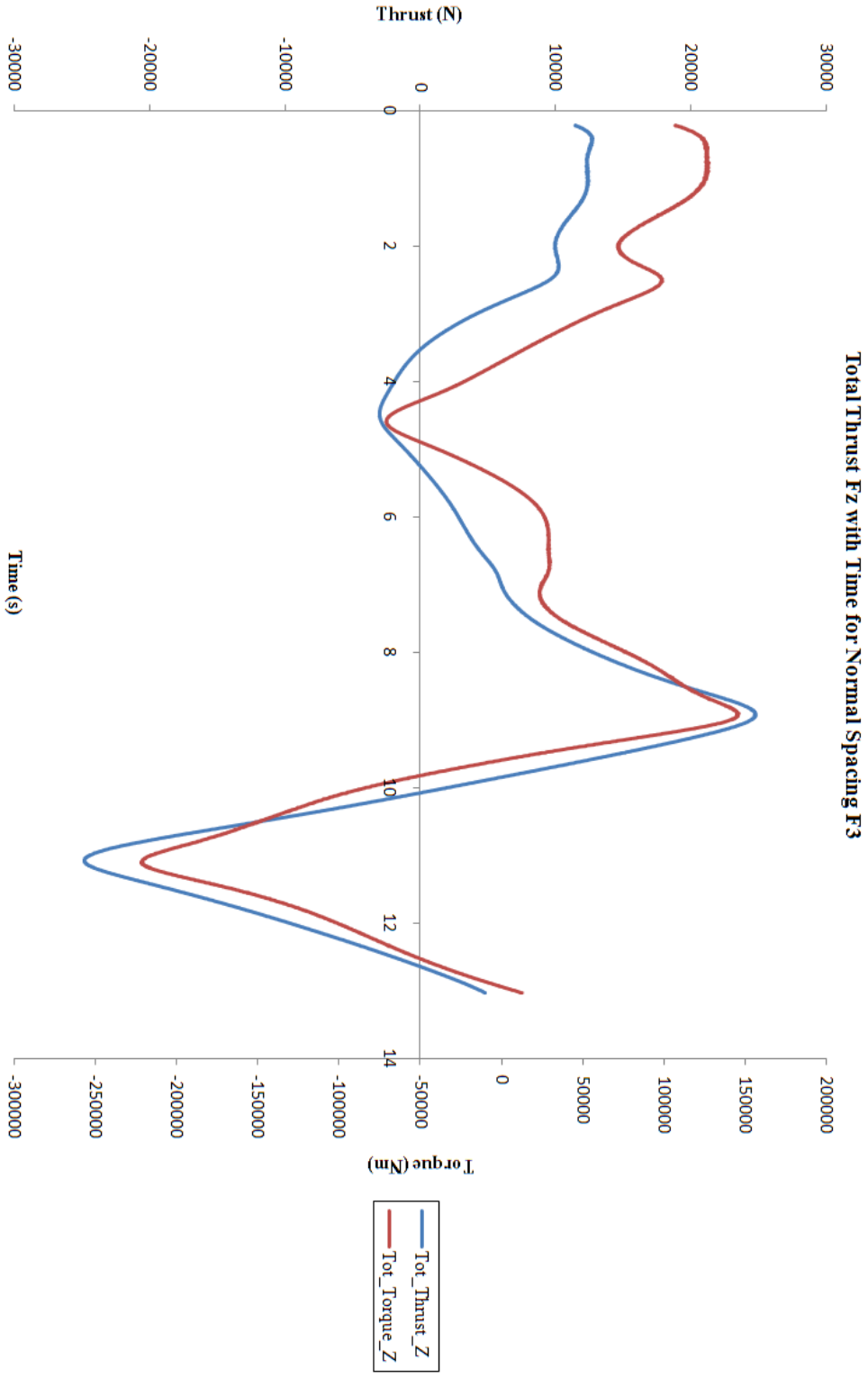

Figure D.16 Loads about the Z axis for Regular wave normal_spacing_model F3

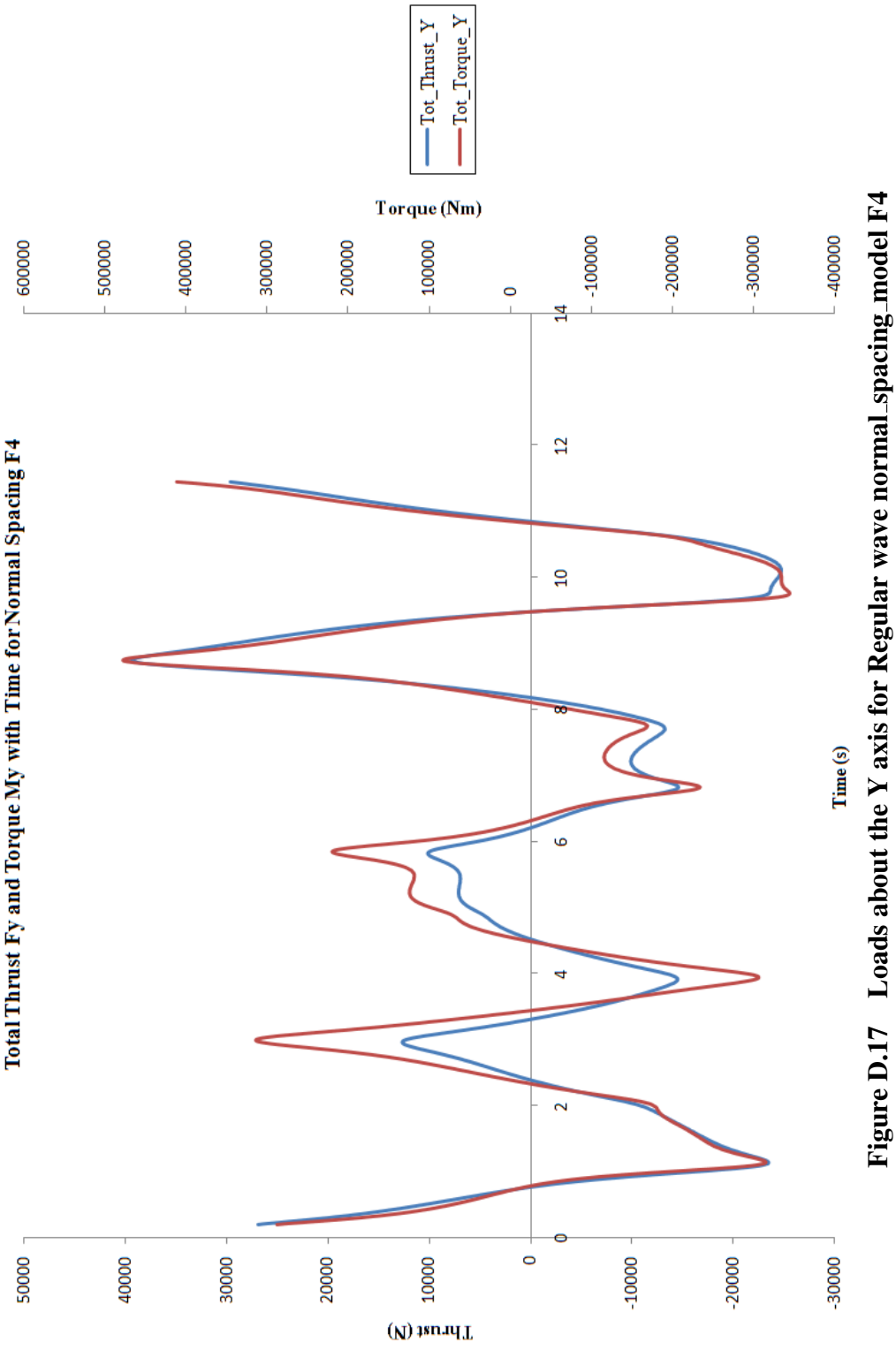

Figure D.17 Loads about the Y axis for Regular wave normal_spacing_model F4

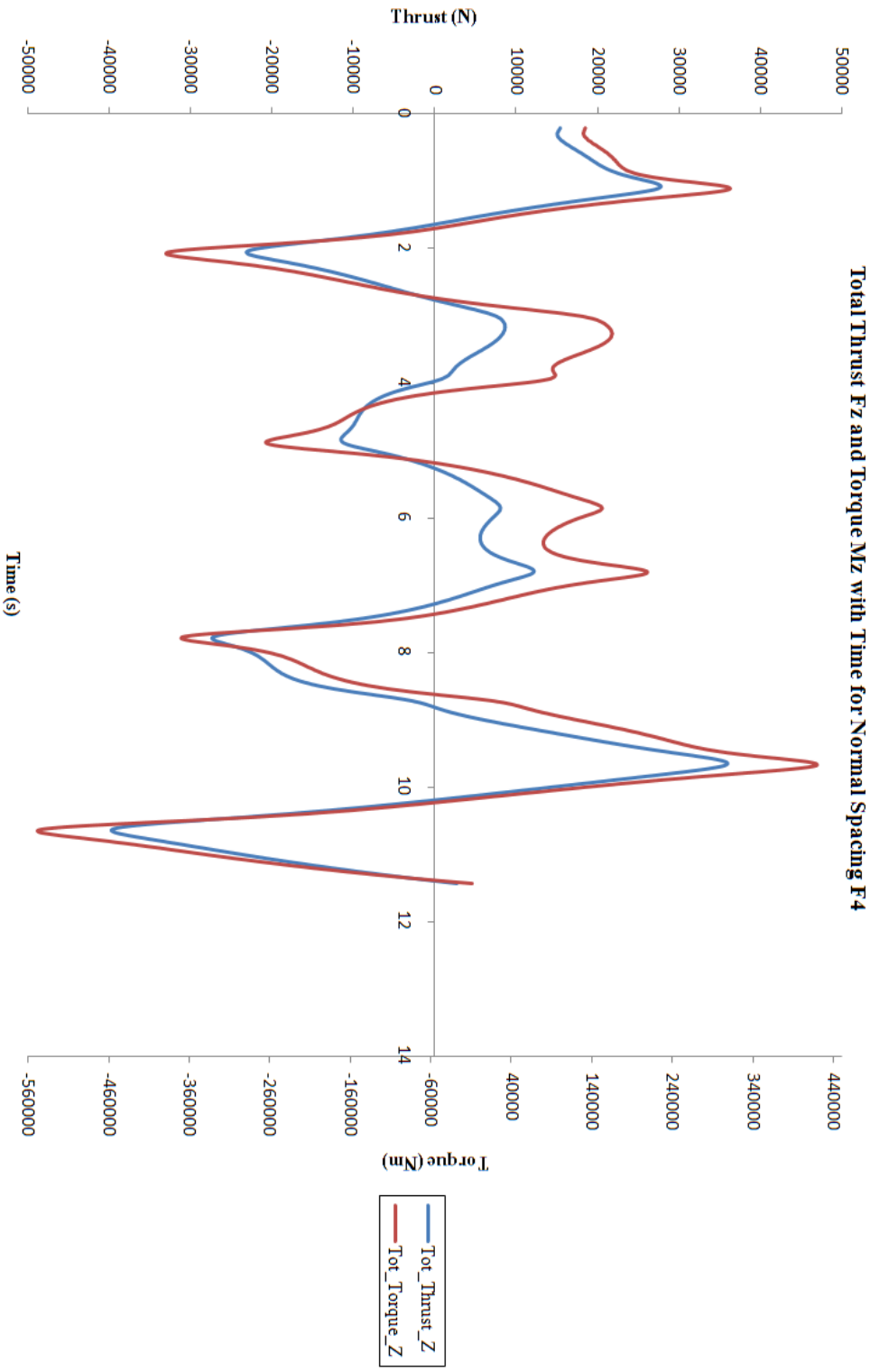

Figure D.18 Loads about the Z axis for Regular wave normal_spacing_model F4

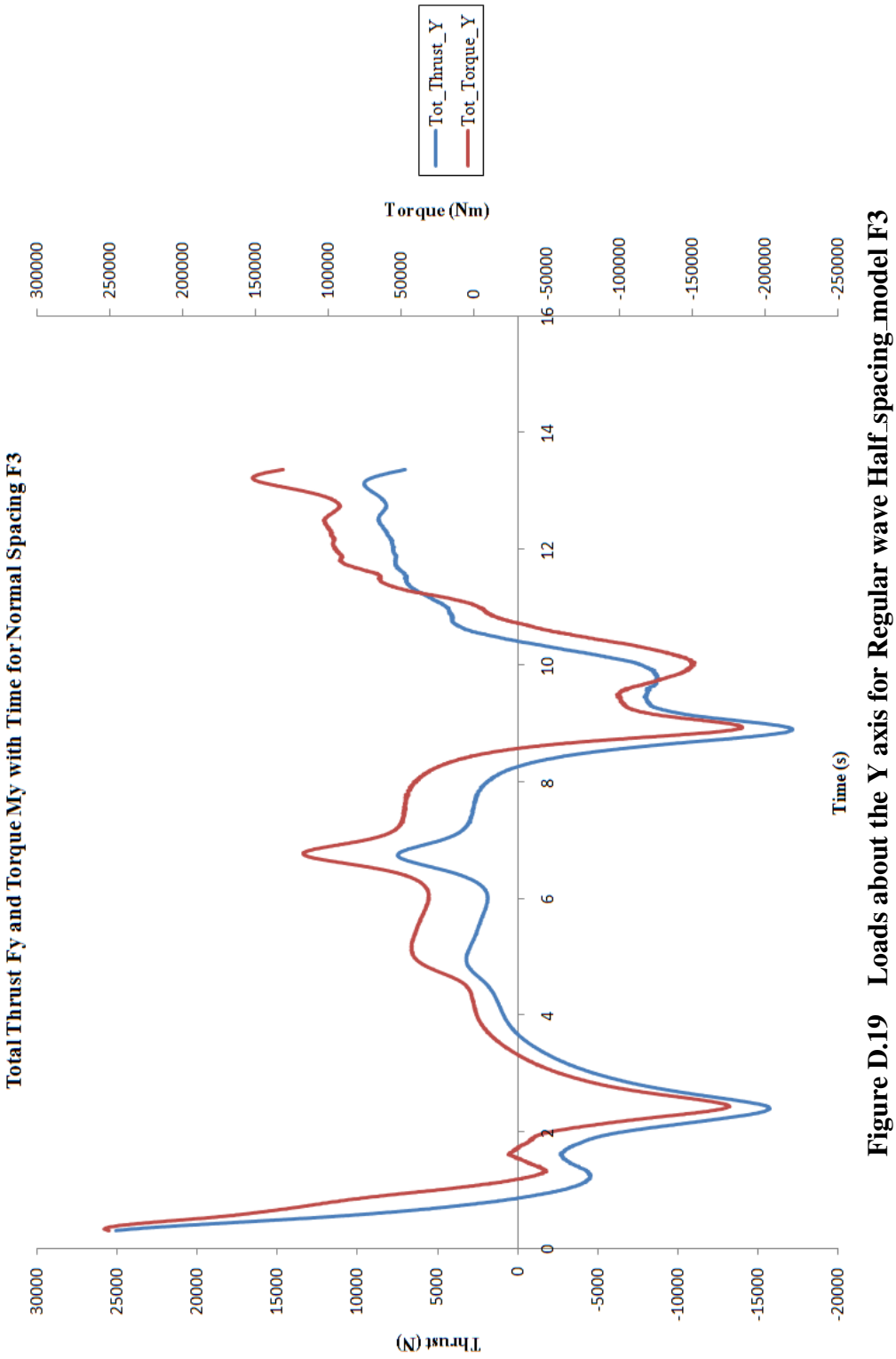

Figure D.19 Loads about the Y axis for Regular wave Half_spacing_model F3

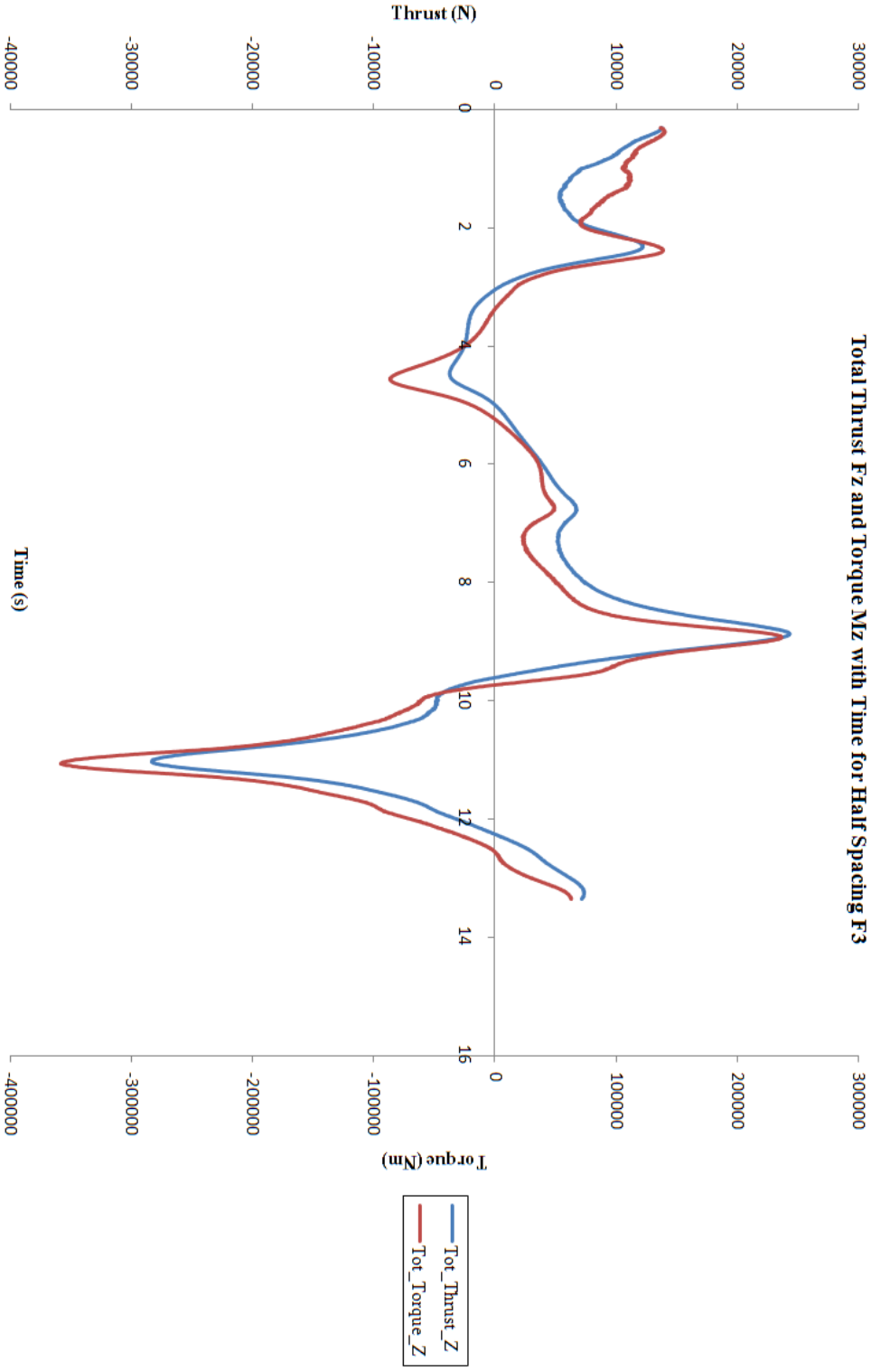

Figure D.20 Loads about the Z axis for Regular wave Half_spacing_model F3

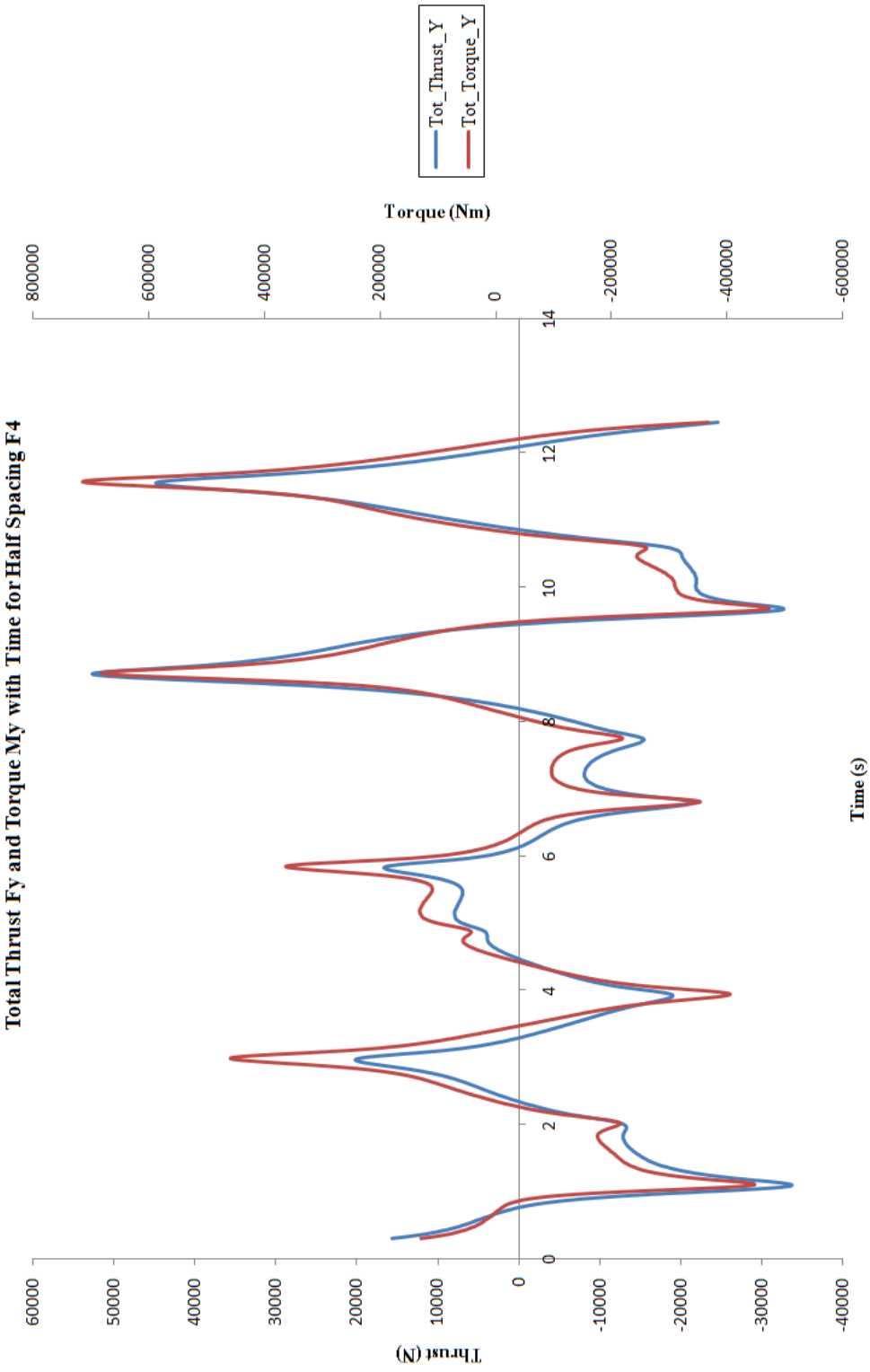

Figure D.21 Loads about the Y axis for Regular wave Half_spacing_model F4

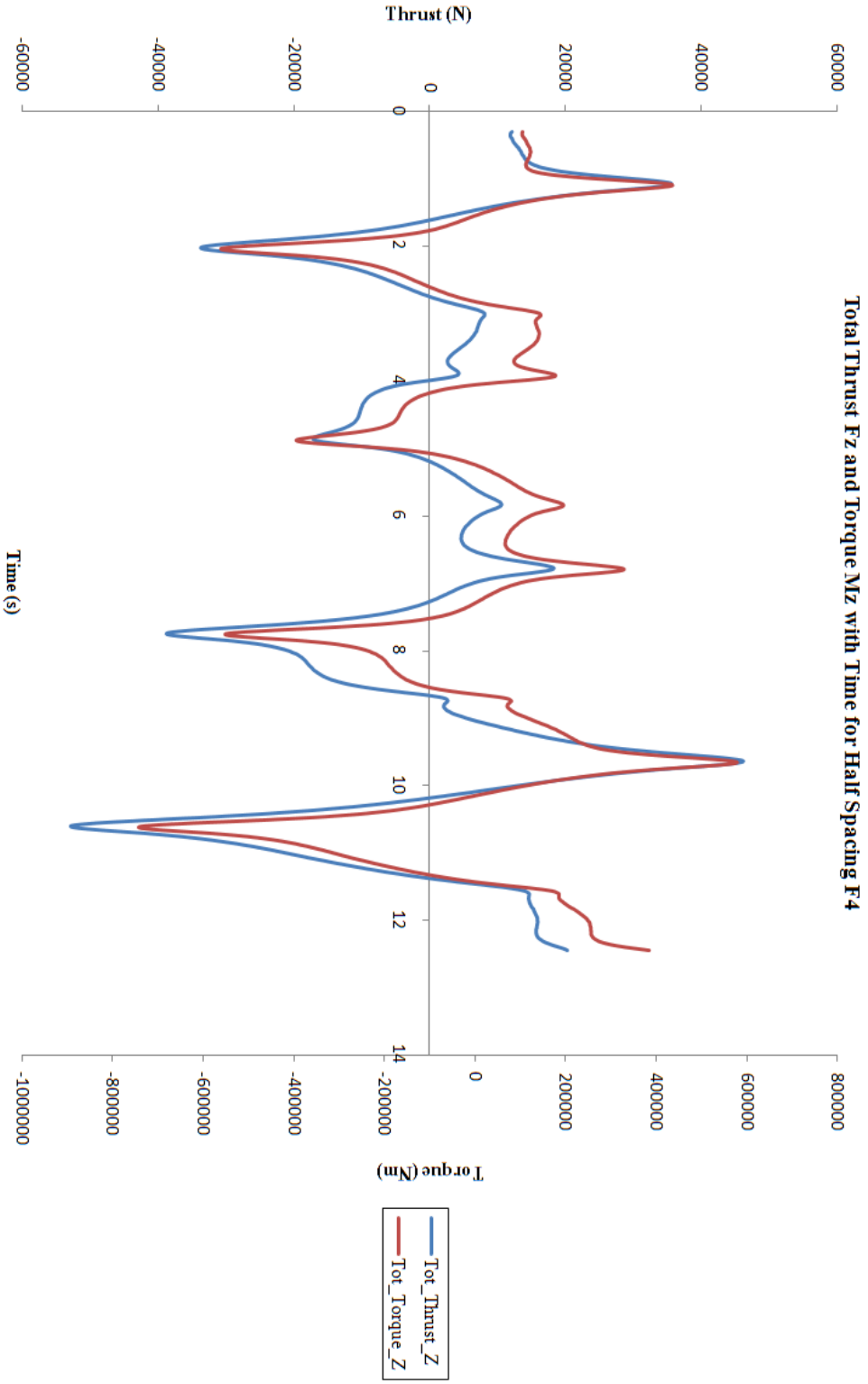

Figure D.22 Loads about the Z axis for Regular wave Half_spacing_model F4